ISSN 1520-295X

Seismic Response of Low Aspect Ratio Reinforced Concrete Walls

by

Bismarck N. Luna, Jonathan P. Rivera, Siamak Epackachi and Andrew S. Whittaker

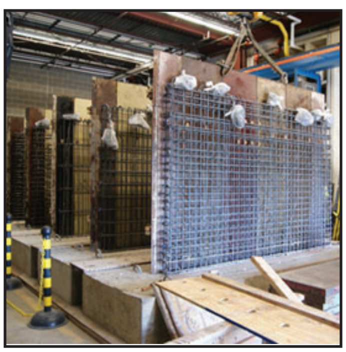
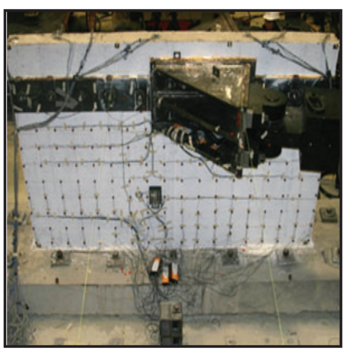

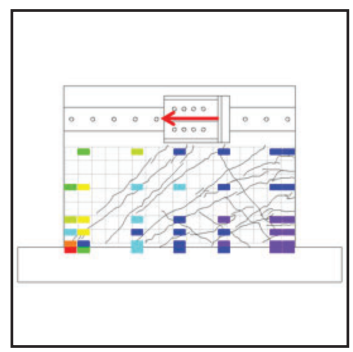

Technical Report MCEER-18-0002

Revision 01, September 10, 2019; originally published April 21, 2018

This research was conducted at the University at Buffalo, State University of New York, and was supported primarily by the National Science Foundation under Grant Number CMMI-0829978.

Seismic Response of Low Aspect Ratio Reinforced Concrete Walls
Revision 01

by

Bismarck N. Luna,[1] Jonathan Rivera,[2] Siamak Epackachi[3] and Andrew S. Whittaker[4]

Revision 01 Publication Date: September 10, 2019
Publication Date: April 21, 2018
Submittal Date: July 19, 2016

Technical Report MCEER-18-0002

National Science Foundation Grant Number CMMI-0829978

1 Development Specialist, Praxair; former Graduate Student, Department of Civil, Structural and Environmental Engineering, University at Buffalo, State University of New York
2 Senior Engineer, Thornton Tomasetti; former Graduate Student, Department of Civil, Structural and Environmental Engineering, University at Buffalo, State University of New York
3 Assistant Professor, Department of Civil Engineering, Amirkabir University of Technology; former Graduate Student, Department of Civil, Structural and Environmental Engineering, University at Buffalo, State University of New York
4 SUNY Distinguished Professor and MCEER Director, Department of Civil, Structural and Environmental Engineering, University at Buffalo, State University of New York

MCEER
University at Buffalo, State University of New York
212 Ketter Hall, Buffalo, NY 14260

Preface

MCEER is a national center of excellence dedicated to the discovery and development of new knowledge, tools and technologies that equip communities to become more disaster resilient in the face of earthquakes and other extreme events. MCEER accomplishes this through a system of multidisciplinary, multi-hazard research, in tandem with complimentary education and outreach initiatives.

Headquartered at the University at Buffalo, The State University of New York, MCEER was originally established by the National Science Foundation in 1986, as the first National Center for Earthquake Engineering Research (NCEER). In 1998, it became known as the Multidisciplinary Center for Earthquake Engineering Research (MCEER), from which the current name, MCEER, evolved.

Comprising a consortium of researchers and industry partners from numerous disciplines and institutions throughout the United States, MCEER's mission has expanded from its original focus on earthquake engineering to one which addresses the technical and socio-economic impacts of a variety of hazards, both natural and man-made, on critical infrastructure, facilities, and society.

The Center derives support from several Federal agencies, including the National Science Foundation, Federal Highway Administration, Department of Energy, Nuclear Regulatory Commission, and the State of New York, foreign governments and private industry.

The main objective of this report is to improve the profession's understanding of the seismic behavior of low aspect ratio reinforced concrete shear walls by analyzing data from tests of 12 large scale wall specimens at the Structural Engineering and Earthquake Simulation Laboratory at the University at Buffalo. This report 1) documents the design, construction, test setup, instrumentation and testing of the 12 reinforced concrete shear wall specimens, 2) presents information from the 12 tests, including global force-displacement relationships, drifts and forces at the initiation of cracking of concrete and yielding of reinforcement, patterns of concrete cracking, modes of failure, strain distributions at peak strength, and contributions to total lateral drift and out-of-plane displacements, and 3) provides a technical basis for the effective elastic stiffness of reinforced concrete shear walls for use in design practice, and equations for peak shear strength of low aspect ratio walls suitable for inclusion in standards such as ACI 318, ACI 349 and ASCE 43.

Erratum: Some of the entries in columns 4 and 5 of Table 6.8 have been revised.

ABSTRACT

Low aspect ratio reinforced concrete (RC) walls are widely used for low- and medium-rise buildings and safety-related nuclear structures. Studies have demonstrated that the seismic performance of conventional low aspect ratio walls cannot be estimated accurately using existing predictive equations or hysteretic models. To improve the profession's understanding of the cyclic response of low aspect ratio walls, the US National Science Foundation funded a Network for Earthquake Engineering Simulation (NEES) research project on shear walls of conventional and composite construction.

Twelve large-size, low aspect ratio, rectangular, RC shear wall specimens were designed, constructed and tested at the NEES facility at the University at Buffalo. The primary objective was to gather and analyze data to better characterize the performance of low aspect ratio RC walls during earthquake shaking. The global force-displacement relationships are analyzed and discussed. Deformation of the reinforced concrete panels was computed from a dense array of 3D non-contact transducers, and used to estimate a) contributions to total displacement of flexure, shear and sliding, and b) principal compressive and tensile strains, and shear strains, as a function of total displacement.

The initial stiffness of the test specimens was substantially smaller than values calculated using equations in design standards and revisions are recommended. Restrained shrinkage at the foundation-wall junction is identified as the primary cause for the differences in stiffness.

The concrete cracking patterns and rebar and concrete strain distributions are presented and used to identify how forces flow from the centerline of loading to the foundation. The traditionally assumed failure modes of diagonal tension (rebar yielding) and diagonal compression (concrete crushing) are coupled. New equations for the peak shear strength of low aspect ratio walls with and without boundary elements (contained within the web of the wall) are proposed for possible inclusion in codes and standards of practice.

ACKNOWLEDGEMENTS

Funding for this project was provided in part by the National Science Foundation (NSF), through the Network for Earthquake Engineering Simulation Research Program, Grant CMMI-0829978. The financial support from NSF is greatly acknowledged.

All of the experiments described in this report were conducted in the Structural Engineering and Earthquake Simulation Laboratory at the University at Buffalo, with technical support of the laboratory staff, including Messrs. Christopher Budden, Jeffrey Cizdziel, Goran Josipovic, the late Duane Kozlowski, Louis Moretta, Mark Pitman, Robert Staniszewski, Scot Weinreber and Christopher Zwierlein. LPCiminelli, Inc. is acknowledged for their assistance in the construction of the Phase II wall specimens. Mr. Joshua Rocks, Ms. Emma Lejeune, Dr. Caglar Goksu, Dr. Joshua Pugh, Dr. Catherine Whyte, Professor Bozidar Stojadinovic and Professor Laura Lowes were involved in different aspects of the NSF project. The authors thank each of these individuals for their contributions to the project.

TABLE OF CONTENTS

TABLE OF CONTENTS (CONT'D)

TABLE OF CONTENTS (CONT'D)

Page

TABLE OF CONTENTS (CONT'D)

Page

TABLE OF CONTENTS (CONT'D)

Page

LIST OF FIGURES

LIST OF FIGURES (CONT'D)

Figure Page

LIST OF FIGURES (CONT'D)

LIST OF FIGURES (CONT'D)

LIST OF FIGURES (CONT'D)

LIST OF FIGURES (CONT'D)

LIST OF FIGURES (CONT'D)

Figure Page

LIST OF FIGURES (CONT'D)

Figure Page

LIST OF FIGURES (CONT'D)

Figure Page

LIST OF FIGURES (CONT'D)

Figure Page

LIST OF FIGURES (CONT'D)

LIST OF FIGURES (CONT'D)

LIST OF FIGURES (CONT'D)

Figure Page

LIST OF FIGURES (CONT'D)

Figure Page

LIST OF TABLES

LIST OF TABLES (CONT'D)

Table Page

LIST OF SYMBOLS

A_{cv}	=	Effective wall area equal to the product of wall length and web thickness
A_{eff}	=	Effective wall area, equal to $A_w/1.2$ for walls with rectangular cross section and $A_w/1.1$ for walls with flanges, per Sozen and Moehle (1993)
A_g	=	Gross cross sectional area of the wall
A_{sy}	=	Area of vertical reinforcement per Moehle (2015)
$A_{s,be}$	=	Total area of vertical reinforcement in one boundary element
A_v	=	Area of horizontal reinforcement within distance *s* per ACI 318-11
	=	Total area of the vertical reinforcement per Wood (1990) equation
A_w	=	Area of the web cross section
b_f	=	Width of flange
b_w	=	Thickness of the compression strut per Moehle (2015)
c	=	Distance from the toe of the wall in compression to the bottom of the nearest diagonal crack
D	=	Undeformed length of diagonal of the quadrilateral panel opposite α_{io}
d	=	Distance of the extreme compression fiber to the centroid of the tensile reinforcement
E_c	=	Modulus of elasticity of concrete
$E_c I_g$	=	Flexural rigidity of the wall section
F_c	=	Compressive force at the bottom of struts in section B of the wall
F_{cx}	=	Shear force acting at the bottom of segment A
F_{cy}	=	Vertical component of the force in the concrete in compression per (6-2)
	=	Normal force acting at the bottom of segment A

f_c = Axial stress in the concrete at the bottom of segment A

$f_c^{'}$ = Compressive strength of concrete

F_h = Force carried by the horizontal reinforcement along a crack

F_{hw} = Force carried by the horizontal reinforcement on the web

F_s = Force associated with aggregate interlock

f_u = Ultimate stress of reinforcement

F_{cy} = Vertical component of the force in the concrete in compression per (6.4)

F_v = Force carried by the vertical reinforcement along a crack

F_{vbe} = Force carried by the vertical reinforcement on the boundary elements per Gulec and Whittaker (2011)

F_{vw} = Force carried by the vertical reinforcement on the web per Gulec and Whittaker (2011)

F_{vwc} = Force carried by the vertical reinforcement in compression

F_{vwt} = Force carried by the vertical reinforcement in tension

f_y = Yield stress of reinforcement

F_y = Force in the vertical reinforcement over the width of a strut

$f_{\bar{y}}$ = Stress in vertical reinforcement
= Average of yield and ultimate stress of reinforcement (for SW2 through SW7)
= f_y (for SW8, SW9 and SW10)
= 1.25 f_y per (6.34) and (6.42)

G_c = Shear modulus of concrete

G_cA_g = Shear rigidity of the wall section

h = Wall thickness per ACI 318-11

H	=	Undeformed length of horizontal side of the quadrilateral panel adjacent to α_{io}
h_w	=	Height of the wall, taken as the distance from the top of the foundation to the centerline of loading
h_s	=	Total height of the rectangular grid of the wall
I_{eff}	=	Effective moment of inertia
I_g	=	Gross moment of inertia of the wall section (reinforcement ignored)
K_{abq}	=	Initial stiffness calculated from ABAQUS models
K_{eff}	=	Initial stiffness of the wall calculated using I_{eff} and A_{eff}
K_f	=	Stiffness of the flexural spring
K_i	=	Measured initial stiffness of the wall
K_m	=	Measured initial stiffness of the wall per Sozen and Moehle (1993)
K_s	=	Stiffness of the shear spring
K_T	=	Theoretical initial stiffness
K_{41-13}	=	*Cracked* stiffness of wall specimen per ASCE 41-13 (ASCE, 2013)
K_{43-05c}	=	*Cracked* stiffness of wall specimen per ASCE 43-05 (ASCE, 2005)
$K_{43-05uc}$	=	*Uncracked* stiffness of wall specimen per ASCE 43-05 (ASCE, 2005)
l_{be}	=	Length of each boundary element
l_w	=	Length of the wall
l_{web}	=	Length of the web of the wall
M_{cr}	=	Cracking moment of the wall determined by cross section analysis
M_{OOP}	=	Out-of-plane moment at the base of the wall

M_u	=	Factored moment per ACI 318-14
n_u	=	Axial load on the wall per unit length per Moehle (2015)
N_u	=	Factored axial compressive force per ACI 318-11
	=	Axial load on the wall
p	=	Axial load per unit length at the centerline of loading
P	=	Axial load on the wall per Gulec and Whittaker (2011)
s	=	Center-to-center spacing of horizontal reinforcement per ACI 318-11
s_x	=	Spacing of the vertical reinforcement per Moehle (2015)
t_f	=	Thickness of flange
t_w	=	Thickness of the wall
V_B	=	Undeformed length of the bottom side of the quadrilateral panel
V	=	Undeformed length of vertical side of the quadrilateral panel adjacent to α_{io}
V_c	=	Nominal shear force carried by concrete
V_L	=	Undeformed length of the left side of the quadrilateral panel
v	=	Shear force per unit length at the centerline of loading
v_n	=	Uniform shear stress acting at the top and bottom of the strut per Moehle (2015)
V_n	=	Nominal shear strength of a wall
$V_{n,be}$	=	Peak shear strength of a wall with boundary elements
V_{na}	=	Contribution of segment A to the shear resistance of the wall without boundary elements
$V_{na,be}$	=	Contribution of segment A to the shear resistance of the wall with boundary elements

V_{nb} = Contribution of segment B to the shear resistance of the wall without boundary elements

$V_{nb,be}$ = Contribution of segment B to the shear resistance of the wall with boundary elements

V_{nc} = Contribution of the horizontal reinforcement to the shear resistance of the wall without boundary elements

$V_{nc,be}$ = Contribution of the horizontal reinforcement to the shear resistance of the wall with boundary elements

V_R = Undeformed length of the right side of the quadrilateral panel

V_s = Nominal shear strength provided by shear reinforcement

V_n = Peak shear strength of the wall

V_T = Undeformed length of the top side of the quadrilateral panel

V_u = Factored shear force per ACI 318-11

x = Width of a concrete compression strut in section B of the wall

α = Angle of crack with respect to the horizontal per Gulec and Whittaker (2011)

α_c = Coefficient defining the relative contribution of concrete strength to nominal wall shear strength

α_{io} = Undeformed angle of the ith corner of the quadrilateral

β_{1-7} = Coefficients of the terms of the equation for peak strength per Gulec and Whittaker (2011)

γ_{xy} = Mean shear strain of the quadrilateral element equal to the average of the change in angle of the four corners

ΔD = Change in length of the diagonal of the quadrilateral panel

ΔH = Change in length of the horizontal side of the quadrilateral panel

Δ_r = Reference displacement or displacement related to yield

ΔV = Change in length of the vertical side of the quadrilateral panel

ε_x	=	Horizontal strain (concrete panels)
ε_y	=	Vertical strain (concrete panels)
	=	Yield strain of reinforcement
ε_1	=	First principal strain (concrete panels)
ε_2	=	Second principal strain (concrete panels)
θ	=	Crack angle with respect to the horizontal
θ_p	=	Orientation of the principal strains
μ	=	Coefficient of friction
λ	=	Modification factor per ACI 318-11 reflecting the reduced mechanical properties of lightweight concrete relative to normal weight concrete of the same compressive strength
υ	=	Poisson's ratio of concrete
ρ_{be}	=	Boundary element vertical reinforcement ratio
ρ_l	=	Vertical reinforcement ratio on the web
ρ_t	=	Horizontal reinforcement ratio on the web

CHAPTER 1
INTRODUCTION

1.1 General

Low aspect ratio reinforced concrete (RC) shear walls (height-to-length ratio of two and less) are widely used in low- and medium-rise buildings and safety-related nuclear structures for resistance to lateral wind and seismic loadings. For this reason, it is important that the cyclic hysteretic (inelastic) response of these walls be understood well to enable code-based design and seismic performance (risk) assessment.

Recent studies by Gulec et al. (2008), Gulec and Whittaker (2009), Gulec et al. (2010), and Gulec and Whittaker (2011) demonstrated that the seismic response of conventional low aspect ratio walls cannot be accurately estimated using existing predictive equations or hysteretic models. Standards of practice in the United States and abroad provide equations to estimate the maximum shear strength of a RC shear wall but these are inaccurate and insufficiently parameterized (e.g., Gulec et al., 2008; Del Carpio et al., 2012). Equations for *uncracked* and *cracked* stiffness are available for design but have not been validated by large-scale testing.

To improve the profession's understanding of the cyclic response of low aspect ratio walls, the US National Science Foundation (NSF) funded a Network for Earthquake Engineering Simulation (NEES) research project on shear walls of conventional and composite construction. Sixteen rectangular, low aspect ratio concrete shear walls were built and tested at the NEES facility at the University at Buffalo (UB): 12 conventionally reinforced concrete walls and four steel-plate concrete composite walls. Two additional RC shear walls were built and tested using hybrid simulation at the University of California, Berkeley.

This report addresses the response of the 12 RC shear walls tested at UB. Data presented in this report provides valuable information to enable the characterization of the hysteretic response of low aspect ratio RC shear walls.

1.2 Research objectives

The main objective of this research is to improve the profession's understanding of the seismic behavior of low aspect ratio RC shear walls by analyzing data from tests of large-scale shear walls. Specifically, this research:

1. Documents the design, construction, test setup, instrumentation and testing of 12 RC large-scale shear walls.
2. Curates and archives data from the reversed cyclic tests of 12 RC shear walls.
3. Presents information from the 12 tests, including global force-displacement relationships, drifts and forces at the initiation of cracking of concrete and yielding of reinforcement, patterns of concrete cracking, modes of failure, strain distributions at peak strength, and contributions to total lateral drift and out-of-plane displacements.
4. Develops a technical basis for the effective elastic stiffness of RC shear walls for use in design practice.
5. Develops equations for peak shear strength of low aspect ratio walls suitable for inclusion in standards such as ACI 318, ACI 349 and ASCE 43.

1.3 Report organization

This report has seven chapters, a list of references, and five appendices. Chapter 2 presents a literature review of topics related to experimental and analytical studies of low aspect ratio RC shear walls. Chapter 3 discusses the experimental testing of the 12 RC shear walls at UB. Descriptions of the 1) test specimens, 2) pre-test numerical analysis, 3) specimen construction, 4) loading apparatus, 5) material properties, 6) test setup, 7) instrumentation, 8) loading protocol, and 9) test procedures are provided. The results of analysis of data from testing of the 12 RC shear walls specimens are presented in Chapter 4, including 1) global force-displacement relationships, 2) drifts and shearing forces at initiation of cracking of concrete and yielding of reinforcement, 3) cracking patterns and modes of failure, 4) vertical, horizontal, shear and principal strain distributions, 5) contributions of flexure, shear and sliding to the total lateral drift, 6) out-of-plane displacements, and 7) strength and stiffness degradation. Chapter 5 provides a technical basis for the effective elastic lateral stiffness of RC shear walls suitable for use in design practice. New equations for peak shear strength of rectangular low aspect ratio RC shear walls with and without boundary elements are presented in Chapter 6. Summary, conclusions and recommendations are presented in Chapter 7. Chapter 8 is a list of references used in this research. Appendix A provides CAD drawings of the 12 RC wall specimens and loading apparatus used for testing. Appendix B presents the strut-and-tie modeling of the foundation of SW8. Instrumentation of each wall specimen is presented in Appendix C. Drawings that identify the locations of 1) Krypton LED sensors, 2) strain gages on vertical and horizontal reinforcement, 3) string potentiometers and Temposonics, and 4) linear potentiometers are provided. Appendix C also provides pertinent information on the laboratory equipment used during testing. Appendix D shows the reference displacements and loading protocols for testing the walls. Photographs of the specimens at different stages of the tests are presented in Appendix E.

CHAPTER 2
LITERATURE REVIEW

2.1 Introduction

A literature review of the topics related to the experimental and analytical studies of low aspect ratio reinforced concrete (RC) shear walls is presented in this chapter. Experimental research programs on low aspect ratio RC walls conducted by other researchers are presented in Section 2.2. The different failure modes of low aspect ratio walls are discussed in Section 2.3. Section 2.4 presents equations in the literature and building codes and standards that are used to predict the nominal peak shear strength of low aspect ratio walls. The recently published equation of Moehle (2015) is included for completeness. Section 2.5 describes prior work on the effective stiffness of low aspect ratio walls.

2.2 Experimental research on the behavior of low aspect ratio reinforced concrete shear walls

A significant number of researchers have studied and reported the response of low aspect ratio RC shear walls. Using these data, Gulec and Whittaker (2009) compiled a comprehensive database that reported information on tests of 434 low aspect ratio walls. Key information from these experimental programs is provided in the literature review of Gulec and Whittaker and is not repeated here. Table 2.1 summarizes information from experimental programs on low aspect ratio RC shear walls conducted from 2008 up until the time of this writing: augmenting information in the Gulec and Whittaker database.

2.3 Failure modes of low aspect ratio RC walls

According to Paulay and Priestley (1992), the modes of failure of low aspect ratio RC walls under lateral loading are 1) diagonal tension, 2) diagonal compression, and 3) sliding shear, where failure is defined as decrease in resistance with an increase in displacement.

Lateral loading on RC shear wall specimen results in the formation of diagonal cracks in the web of the wall. Reversed cyclic loading on a wall specimen results in the formation of two sets of diagonal cracks that are approximately orthogonal. Figure 2.1 shows a typical cracking pattern of a low aspect ratio RC wall specimen subjected to reversed cyclic loading.

Table 2.1. Review of experimental programs on low aspect ratio reinforced concrete walls

Reference	Information
Athanasopoulou (2010)	Nine large-scale low aspect ratio rectangular shear wall specimens were tested under reversed cyclic loading. Four walls were constructed using regular concrete and five walls were constructed using high-performance fiber reinforced concrete material (HPFRC). The height-to-length ratios were 1.0 and 1.3. Axial loads were not applied to the specimens.
El-Sokkary and Galal (2013)	Three rectangular shear wall specimens with length, height and width of 1200 *mm*, 1045 *mm* and 80 *mm*, respectively, were tested under reversed cyclic loading. A constant axial stress of 0.7 MPa was applied to the specimens during testing. Two of the three specimens were retrofitted with Fiber-Reinforced Polymer (FRP).
Farvashany et al. (2008)	Seven large-scale high-strength concrete (HSC) shear wall specimens were loaded monotonically to failure. The height-to-length ratio of the walls was 1.25. The compressive strength of concrete varied from 11.6 ksi to 14.5 ksi. Axial stress considered were 0 ksi, 0.6 ksi, 1.2 ksi and 2.9 ksi. Horizontal reinforcement ratios of 0.47% and 0.75% and vertical reinforcement ratios of 0.75% and 1.26% were used.
Kuang and Ho (2008)	Eight large-scale, non-seismically detailed, rectangular RC walls with aspect ratios of 1.0 and 1.5, were tested under reversed cyclic loading. The length and thickness of the walls were 1200 *mm* and 100 *mm*, respectively. Axial loads were not applied to the specimens.

Table 2.1. Review of experimental programs on low aspect ratio reinforced concrete walls (continued)

Reference	Information
Orakcal et al. (2009)	Six wall piers and eight wall spandrel ($3/4$-scale) were tested under reversed cyclic loading. The wall piers and wall spandrels had an aspect ratio of 0.9 and 1.0, respectively. Two wall piers were tested with an axial load of $0.05 f_c^{'} A_g$ and another two with an axial load of $0.1 f_c^{'} A_g$.
Park et al. (2014)	Eight shear wall specimens with height to width ratio of 1.0 were tested under reversed cyclic loading. Seven specimens have rectangular sections with boundary elements. One specimen have a barbell shape cross section.
Parulekar et al. (2014)	A rectangular RC wall with length, width and thickness of 3 *m*, 1.2 *m* and 0.4 *m*, respectively, was tested under reversed cyclic loading. An axial of 60 tons was applied to the specimen.
Thomson et al. (2009)	Three shear wall specimens were tested under reversed cyclic loading to validate a proposed simplified model for simulating damage to low aspect ratio shear walls. Two specimens had a height-to-width ratio of 1.25 and the third had a height-to-width ratio of 1.5.
Whyte and Stojadinovic (2013)	Two rectangular low aspect ratio RC wall specimens, 8” thick and 10’ long, with height-to-length ratio of 0.54 were tested using hybrid simulation techniques. No axial load was imposed on the specimens.

2.3.1 Diagonal tension

A diagonal tension failure is characterized by wide diagonal cracks and yielding of horizontal and vertical reinforcement. Walls with low horizontal and/or vertical web reinforcement ratios are vulnerable to this type of failure. Figure 2.2 is a photograph of a wall that has failed in diagonal tension.

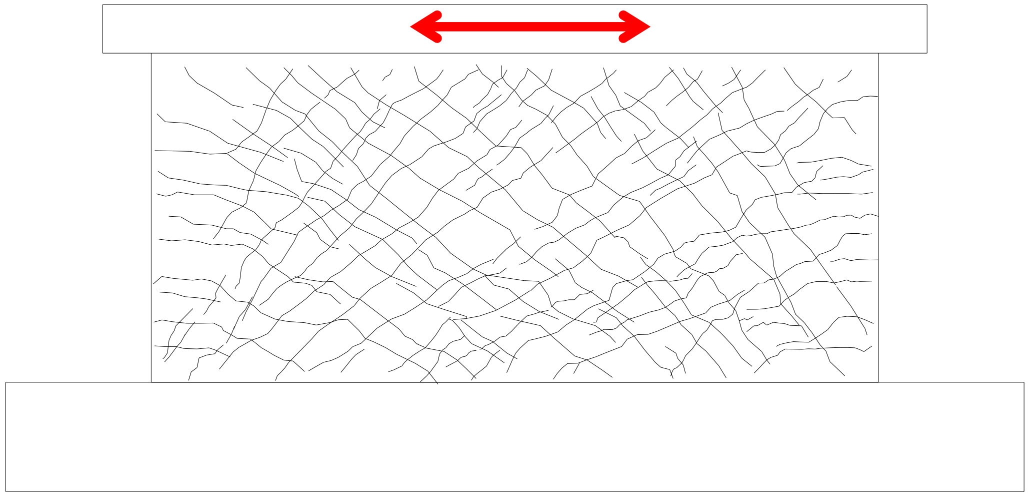

Figure 2.1. Typical cracking pattern for a low aspect ratio shear wall subjected to reversed cyclic lateral loading

Figure 2.2. Diagonal tension failure

2.3.2 Diagonal compression

If sufficient horizontal and vertical reinforcement is provided in the web of a wall to prevent diagonal tension failure, the concrete compression struts that serve to transfer lateral loads to a foundation may crush, resulting in a diagonal compression failure. Figure 2.3 shows a diagonal compression failure.

The formation of two sets of diagonal shear cracks from reversed cyclic loading can substantially decrease the integrity of concrete compression struts. According to Paulay and Priestley (1992), diagonal compression failure results in a drastic loss of strength and should be avoided if the goal is to achieve ductile response. ACI 318-14 (ACI, 2014) imposes an upper limit of $10\sqrt{f_c^{'}}$ on the average horizontal shear stress to avoid diagonal compression failure.

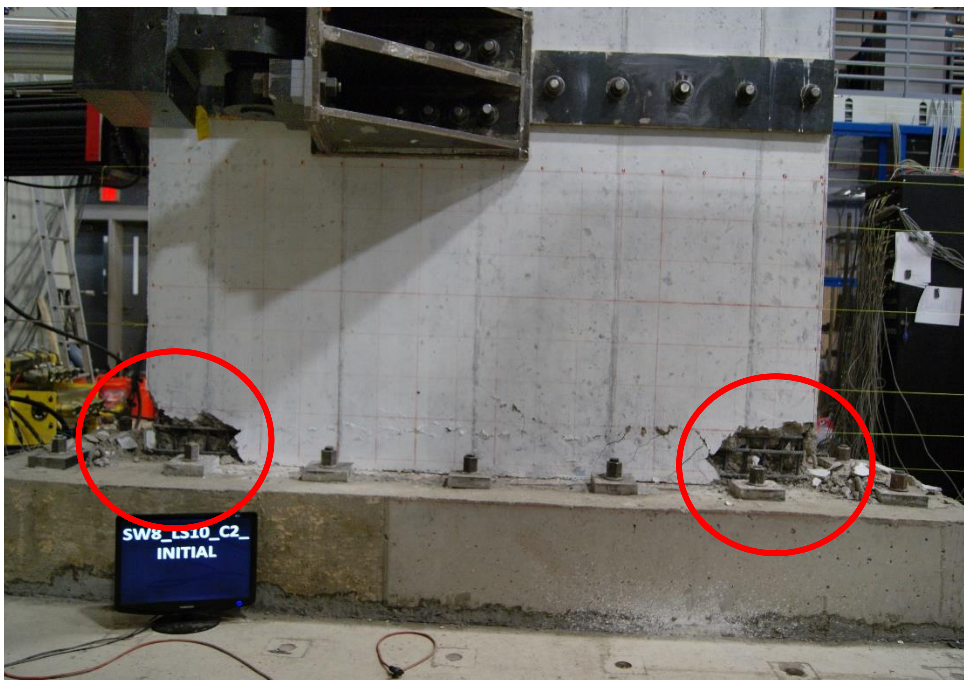

Figure 2.3. Diagonal compression failure

2.3.3 Sliding shear

Reversed cyclic loading can result in yielding in both tension and compression of vertical reinforcement at the base of a wall. The cyclic yielding of this reinforcement may result in a horizontal crack at the base of the wall and subsequent sliding of the wall on its foundation at small levels of lateral load. The wall will slide until it rotates sufficiently for its compression toe to bear directly on the foundation below. Figure 2.4 is a photograph of a damaged wall after sliding.

Figure 2.4. Sliding shear failure

2.4 Estimation of peak shear strength

Equations are available in the literature and in codes and standards of practice to predict the nominal shear strength of RC walls. Each equation uses design variables such as compressive strength of concrete, yield strength of reinforcement, reinforcement ratio and aspect ratio. This section presents five equations used to calculate the nominal shear strength of RC shear walls, together with the recently published equation of Moehle (2015).

2.4.1 Chapter 11 of ACI 318-14

Section 11.5 of ACI 318-14 (ACI, 2014) provides equations for the peak shear strength of low aspect ratio shear walls. The nominal shear strength is given by

$$V_n = V_c + V_s \leq 10\sqrt{f_c^{'}}dt_w \tag{2.1}$$

where V_c (lb) is the nominal shear force carried by concrete, V_s (lb) is the nominal shear strength provided by shear reinforcement, $f_c^{'}$ (psi) is the compressive strength of concrete, d (in) is the distance of the extreme compression fiber to the centroid of the tensile reinforcement (taken as $0.8l_w$, where l_w is the length of the wall), and t_w (in) is the thickness of the wall. The concrete contribution, V_c, is the smaller of:

$$V_c = 3.3\lambda\sqrt{f_c^{'}}dt_w + \frac{N_u d}{4l_w} \tag{2.2}$$

$$V_c = \left[0.6\lambda\sqrt{f_c^{'}} + \frac{l_w\left(1.25\lambda\sqrt{f_c^{'}} + \frac{0.2N_u}{l_w t_w}\right)}{\frac{M_u}{V_u} - \frac{l_w}{2}}\right]dt_w \tag{2.3}$$

where N_u (lb) is the factored axial compressive force, M_u (lb-in) is the factored moment, V_u is the factored shear force and $\lambda = 1.0$ for normal weight concrete. If $\left(M_u/V_u - l_w/2\right)$ is negative, (2.3) is not applicable. The rebar contribution, V_s, is given by

$$V_s = \frac{A_v f_y d}{s} \tag{2.4}$$

where s (in) is the spacing of horizontal reinforcement and A_v (in^2) is the area of horizontal reinforcement within distance s. The minimum horizontal reinforcement ratio, ρ_t, shall not be less than 0.0025. The spacing s must not exceed the smallest of $l_w/5$, $3h$ and 18 inches. The minimum vertical reinforcement ratio, ρ_l, must not be less than the greater of 0.0025 and that given by (2.5):

$$\rho_l = 0.0025 + 0.5\left(2.5 - \frac{h_w}{l_w}\right)\left(\rho_t - 0.0025\right) \tag{2.5}$$

The spacing of the vertical reinforcement should not exceed the smallest of $l_w/3$, $3h$ and 18 inches.

2.4.2 Chapter 18 of ACI 318-14

The nominal peak shear strength in section 18.10 of ACI 318-14 (ACI, 2014) is given by

$$V_n = \left(\alpha_c\lambda\sqrt{f_c^{'}} + \rho_t f_{yh}\right)A_w \le 10\sqrt{f_c^{'}}A_w \tag{2.6}$$

where α_c is the coefficient defining the relative contribution of concrete strength and is equal to 3.0 for $h_w/l_w \leq 1.5$, 2.0 for $h_w/l_w \geq 2.0$ and varies linearly between 3.0 and 2.0 for h_w/l_w between 1.5 and 2.0; $\lambda = 1.0$ for normal weight concrete; $f_c^{'}$ (psi) is the compressive strength of concrete; ρ_t is the horizontal reinforcement ratio; f_{yh} (psi) is the yield stress of the horizontal web reinforcement; and A_w (in^2) is the area of the wall.

2.4.3 Barda et al. (1977)

The equation of Barda et al. (1977) to predict the peak shear strength was derived based on tests of eight low aspect ratio walls with heavily reinforced flanges. The equation is applicable for rectangular walls and for walls with boundary elements. The nominal peak strength, V_n, is given by

$$V_n = \left(8\sqrt{f_c^{'}} - 2.5\sqrt{f_c^{'}}\frac{h_w}{l_w} + \frac{N_u}{4l_w t_w} + \rho_l f_{yv}\right) d t_w \qquad (2.7)$$

where $f_c^{'}$ (psi) is the compressive strength of concrete, h_w (in) is the height of the wall, l_w (in) is the length of the wall, N_u (lb) is the factored axial compressive force, t_w (in) is the thickness of the web, ρ_l is the vertical web reinforcement ratio, f_{yv} (psi) is the yield stress of vertical web reinforcement, and d (in) is the distance of the extreme compression fiber to the centroid of the tensile reinforcement.

2.4.4 Wood (1990)

Experimental data from the tests of 143 low aspect ratio walls were used to derive the Wood (1990) equation for peak shear strength, which is based on shear friction.. Wood’s equation for peak average shear stress is:

$$6\sqrt{f_c^{'}} \leq \frac{A_v f_{yv}}{4A_{cv}} \leq 10\sqrt{f_c^{'}} \qquad (2.8)$$

where $f_c^{'}$ (psi) is the compressive strength of concrete, A_{cv} (in^2) is the effective wall area equal to the product of wall length and web thickness, A_v (in^2) is the total area of vertical reinforcement in the wall, and f_{yv} (psi) is the yield stress of the vertical reinforcement.

2.4.5 Gulec and Whittaker (2011)

Gulec and Whittaker (2011) developed an empirical equation for peak shear strength of low aspect ratio rectangular walls using data from 74 rectangular walls tested by others. The peak shear strength, V_n, is given by:

$$V_n = \frac{1.5\sqrt{f_c'}A_w + 0.25F_{vw} + 0.20F_{vbe} + 0.40P}{\sqrt{h_w/l_w}} \le 10\sqrt{f_c'}A_w \tag{2.9}$$

where f_c' (psi) is the compressive strength of concrete, A_w (in^2) is the area of the wall, F_{vw} (lb) is the force attributed to the vertical web reinforcement (equal to the product of the total area of the vertical reinforcement and reinforcement yield stress), F_{vbe} (lb) is the force attributed to the boundary reinforcement (equal to the product of the total area of vertical boundary element reinforcement and the reinforcement yield stress), P (lb) is the axial compressive force, h_w (in) is the height of the wall, and l_w (in) is the length of the wall.

2.4.6 Moehle (2015)

Moehle (2015) presents an equation for nominal shear strength of low aspect ratio RC walls, which assumes: 1) normal and shear stresses along a diagonal crack are resisted only by reinforcement, that is, the effect of aggregate interlock is not included, 2) all vertical reinforcement yield in tension, and 3) diagonal cracks form at a constant angle to the horizontal. The nominal shear strength, V_n, is given by:

$$V_n = \left(N_u + \rho_l f_y A_{cv}\right)\frac{1}{\tan\theta} \tag{2.10}$$

where N_u is the total axial load, ρ_l is the vertical reinforcement ratio, A_{cv} is the gross-cross sectional area of the wall, and θ is the orientation of the cracks with respect to the horizontal.

2.5 Effective lateral stiffness

In 1980, the United Stated Nuclear Regulatory Commission (NRC) funded the Seismic Category I Structures Program to investigate the seismic response of low-rise RC shear walls. RC shear walls were identified as the most important, yet least understood, seismic resisting components in safety-related nuclear structures. Initial stiffness was a subject of study. The initial phase of the program involved tests of small-scale isolated shear walls (1/30 scale, 1-inch thick) and 3-dimensional box-like micro-concrete structures. Tests results indicated that the resonant frequency of the specimens was lower than the theoretical value by a factor of 2 or more, suggesting that lateral stiffness was smaller than the theoretical *uncracked* stiffness by a factor of 4 or more (Farrar et al., 1990). Subsequent tests of 10 scaled box-type RC structures (seven specimens made with $3/8$-inch aggregate concrete and three specimens made with micro-concrete), subjected to static and dynamic tests, showed no appreciable difference between measured and theoretical *uncracked* stiffness (Farrar et al., 1991; Farrar and Baker, 1993). They noted that the best correlation between the theoretical and measured stiffness occured when the flanges were assumed to be fully effective in resisting bending and they included the flanges in the calculation of the theoretical flexural stiffness of the 10 box-type RC structures.

Sozen and Moehle (1993) compiled and examined the lateral stiffness of 41 RC wall specimens tested by Maier and Thürlimann (1985), Inada (1986) and Rothe (1992). Sozen and Moehle compared the measured stiffness with the theoretical *uncracked* stiffness calculated using the strength-of-materials approach. In calculating the shear component of the theoretical *uncracked* stiffness, the total cross-sectional area of the wall, A_g, was replaced by an effective wall area, A_{eff}, equal to $A_w/1.2$ for walls with rectangular sections and $A_w/1.1$ for walls with flanges, where A_w is the area of the web: total depth multiplied by web thickness. For the 41 test specimens considered, the ratio of the measured to theoretical *uncracked* stiffness ranged between 0.33 and 1.2 with mean and median values of 0.73 and 0.7, respectively. They attributed the increased flexibility of the test specimens to 1) cracks invisible to the eye present before the test, and 2) deformability of the base girder and noted that the data provided no clear relationship between imposed axial stress and measured initial stiffness.

The Working Group on the Stiffness of Concrete Shear Wall Structures of the ASCE Dynamic Analysis Committee (Murray et al., 1994) prepared a report to address the differences between measured and calculated initial stiffness of low rise RC shear walls, as observed in experimental data available in literature, particularly those reported in the initial tests of the Seismic Category I Structures Program. To address variations in stiffness, the Working Group suggested upper and lower bound values on the elastic and shear moduli of *uncracked* concrete to be used modeling the stiffness of RC walls: E_c and G_c were increased by 25% to calculate upper bound values and reduced by 25% to calculate lower bound values. The upper bound value accounted for $f_c^{'}$ greater than the minimum specified 28-day concrete compressive strength. The lower bound value was based on experimental data and was assumed to account for the uncertainty of concrete quality in the field.

Building codes and standards of practice provide recommendations for the effective stiffness of low aspect ratio RC shear walls by specifying reductions in the flexural and shear rigidities. Different reductions in the flexural and shear rigidities are used to estimate effective stiffness of *uncracked* and *cracked* walls. For *uncracked* walls, ASCE 43-05 (ASCE, 2005) recommends no reduction in flexural and shear rigidities. For *cracked* walls, ASCE 43-05 recommends a 50% reduction in both flexural and shear rigidities, and ASCE 41-13 (ASCE, 2013) recommends a reduction of 50% in flexural rigidity and no reduction in shear rigidity.

CHAPTER 3
EXPERIMENTAL PROGRAM

3.1 Introduction

This section discusses the program for the testing of 12 shear walls at the Network for Earthquake Engineering Simulation (NEES) facility at the University at Buffalo (UB). Section 3.2 presents the test specimens. Section 3.3 discusses the pre-test numerical analysis. The construction of the test specimens and details on the loading apparatus are presented in Sections 3.4 and 3.5, respectively. Material properties are identified in Section 3.6. The test setup, instrumentation and loading protocol are discussed in Sections 3.7, 3.8 and 3.9, respectively. The test procedures are described in Section 3.10.

3.2 Specimen details

Twelve large-size, low aspect ratio, rectangular, reinforced concrete (RC) shear wall specimens were built and tested at the NEES facility at UB. The walls were named SW1 to SW12. The design variables considered in developing the portfolio of test specimens included: 1) wall aspect ratio, h_w/l_w where h_w is the distance from the top of the foundation to the centerline of loading and l_w is the length of the wall; 2) day-of-test concrete compressive strength, $f_c^{'}$; 3) vertical and horizontal reinforcement ratios: ρ_l, ρ_t; 4) yield and ultimate strengths of the reinforcement: f_y, f_u; 5) splices in vertical reinforcement and; 6) boundary elements.

The length and thickness of the test specimens were limited by the capacity of the NEES actuators at UB to 120 inches and 8 inches, respectively. Three aspect ratios were considered; 0.33, 0.54 and 0.94. The horizontal and vertical reinforcement ratios in each of SW1 through SW8 were identical. The vertical reinforcement in specimens SW2 and SW3 were coupled mechanically using ZAP Screwlok model 4ZB (http://www.barsplice.com/) Type-2 mechanical couplers at approximately 14 inches above the top of the foundation; all other specimens were constructed with continuous vertical reinforcement. Specimens SW8, SW9 and SW10 had the same vertical reinforcement ratio but different horizontal reinforcement ratios. SW11 and SW12 had boundary elements. There were lap splices on some of the vertical reinforcements of SW8 through SW12 to avoid thru-holes in the wall. The construction and testing of the 12 specimens was executed in two phases: Phase I (SW1-SW7) and Phase II (SW8-SW12). The Phase I walls were constructed and tested first. The Phase II walls were designed after preliminary analysis of data from the testing of the Phase I walls.

The longitudinal bars of the foundation block of Phase I specimens consisted of ten #8 bars, five each on top and bottom. The transverse reinforcement consisted of #5 four-leg ties with 135-degree hooks spaced at three inches on center. Similarly, the longitudinal bars of the foundation block of Phase II specimens consisted of ten #8 bars, five each on top and bottom. The transverse reinforcement consisted of #4 four-leg ties with 135-degree hooks. The ties were spaced at four inches on center for four feet lengths from each end and eight inches on center in the remainder.

All vertical and horizontal reinforcement in the webs of SW1 and SW4 through SW12 were #4 Grade 60 ASTM A615 (ASTM, 2014a). The vertical and horizontal reinforcement in the webs of SW2 and SW3 were #4 Grade 60 ASTM A706 (ASTM, 2014b). The vertical bars on the boundary elements of SW11 and SW12 where #5 Grade 60 ASTM A615. Regular, normal weight concrete was used for all of the foundations and the Phase I walls. Self-consolidating concrete was used for Phase II walls. The properties of the walls are summarized in Table 3.1. The construction plans and details for all 12 walls are presented in Appendix A.

Table 3.1. Properties of the wall specimens

Wall	h_w/l_w [1]	Web		Boundary element		f_c' (ksi)	f_y (ksi)	f_u (ksi)
		ρ_l (%)	ρ_t (%)	ρ_l (%)	ρ_t (%)			
SW1	0.94	0.67	0.67	-	-	3.6	67	102
SW2	0.54	1.0	1.0	-	-	7.0	63	87
SW3		0.67	0.67	-	-	7.8	63	87
SW4		0.33	0.33	-	-	4.2	67	102
SW5	0.33	1.0	1.0	-	-	4.3	67	102
SW6		0.67	0.67	-	-	3.8	67	102
SW7		0.33	0.33	-	-	3.8	67	102
SW8	0.54	1.5	1.5	-	-	3.5	67	102
SW9		1.5	0.67	-	-	4.3	67	102
SW10		1.5	0.33	-	-	4.6	67	102
SW11		0.67	0.67	1.5	1.5	5.0	67	102
SW12		0.33	0.33	2.0	2.0	5.0	67	102

1. Wall length of 10 feet for all specimens.

Axial loads were not applied to the specimens because 1) axial stresses in low aspect ratio walls are typically small as measured by a fraction of the product of their cross sectional area and the concrete compressive strength, and 2) applying and maintaining even low axial loads on a wall with an area of approximately 1,000 square inches at the relatively large lateral displacements expected in the experiments would have been extremely difficult.

3.3 Pre-test numerical analysis

Numerical simulations of the cyclic response of the wall specimens were performed to help design and detail the test specimens and the test fixture. Upper bound estimates of material strength were used to establish the maximum size of the test specimens, which was dictated by 1) the capacity of the NEES actuators, and 2) the need to construct walls of different aspect ratios with identical plan dimensions. VecTor2 ver. 2.8 (Vecchio and Wong, 2002), a nonlinear finite element program for the analysis of RC structures, was used to simulate the response of each test specimen to monotonic and reversed cyclic loading using the Modified Compression Field Theory (Vecchio and Collins, 1986) and Popovics (1973) model to represent the pre- and post-peak response of concrete in compression. An average mesh size of 15 $\times$ 1.4 inches for walls with an aspect ratio of 0.33; 2.5 $\times$ 2.7 inches for walls with an aspect ratio of 0.54; and 5.7 $\times$ 4.9 inches for SW1 were used for the models. Figure 3.1 shows the predicted monotonic and cyclic base shear versus story drift relationships for all the specimens for 1) a concrete compressive strength of 6 ksi, 50% greater than the target of 4 ksi; and 2) rebar yield strength of 75 ksi, 25% greater than the proposed minimum specified value of 60 ksi. The predicted peak shear strength for SW5 was 732 kips: the greatest for the Phase I walls, and this resistance, with a margin, was used to design the test fixture. The predicted peak shear force for SW8 was 821 kips: the greatest for the Phase II walls but still within the capacity of the actuators and the designed text fixture.

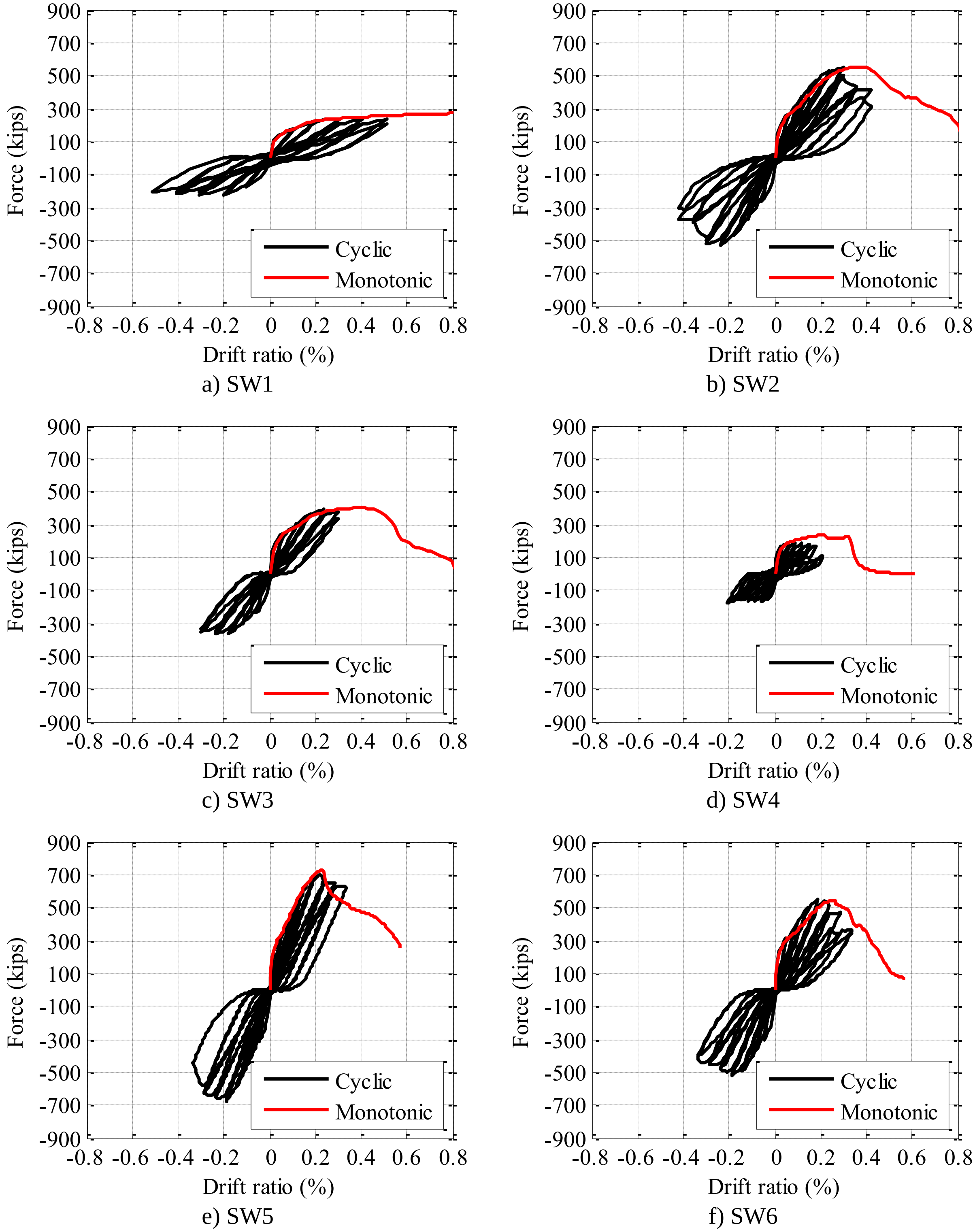

Figure 3.1. VecTor2 predicted force-displacement relationships

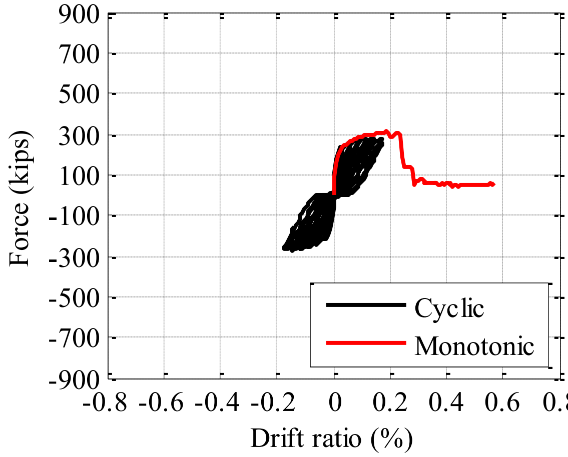

g) SW7

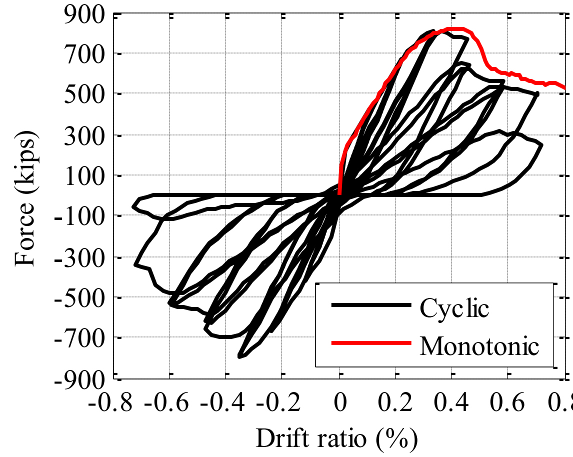

h) SW8

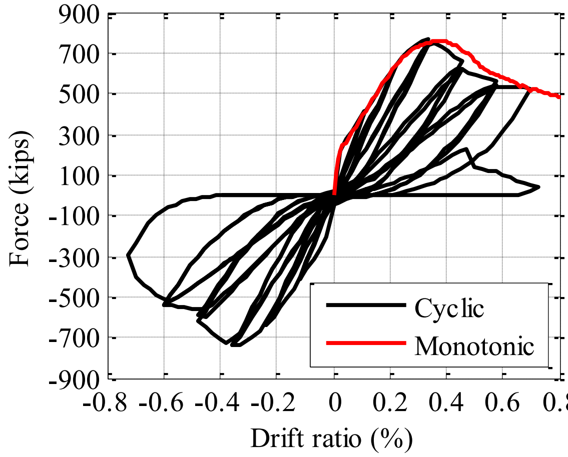

i) SW9

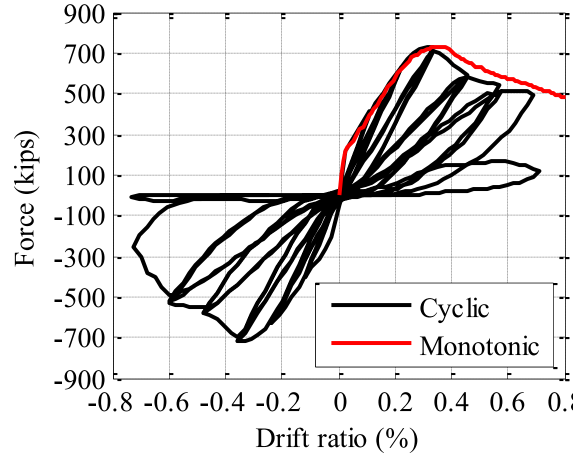

j) SW10

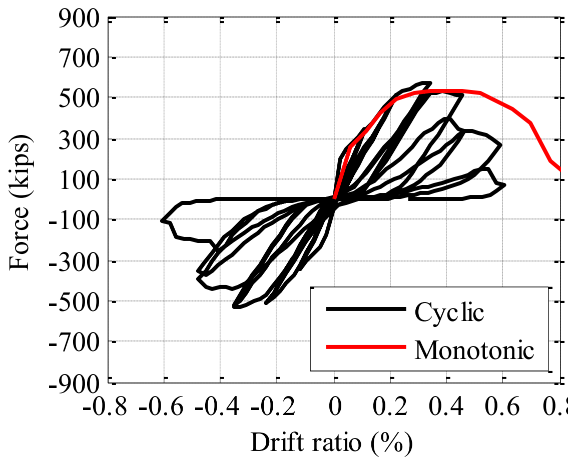

k) SW11

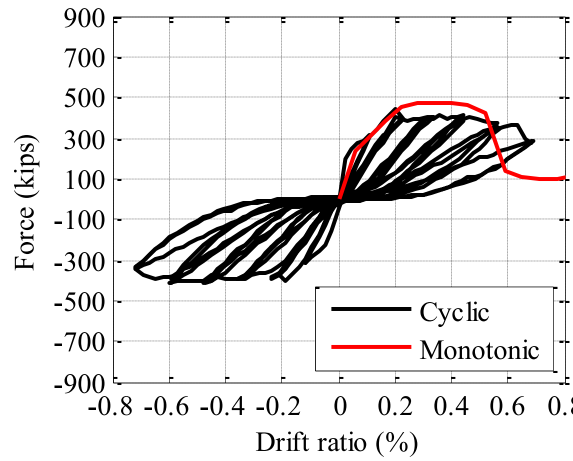

l) SW12

Figure 3.1. VecTor2 predicted force-displacement relationships (continued)

3.4 Construction of walls

3.4.1 Phase I specimens

Phase I specimens (SW1-SW7) were constructed in two stages: the foundations preceded the wall sections. The foundations of the seven specimens were cast on July 2, 2009. The walls of SW1, SW4, SW5, SW6 and SW7 were cast on August 24, 2009; the walls of SW2 and SW3 were cast on December 23, 2009.

The foundations of Phase I specimens had plan dimensions of 14 × 3 inches and a height of 18.5 inches. The formwork for the foundations of the seven walls was fabricated in the Structural Engineering and Earthquake Simulation Laboratory (SEESL). The rebar cages were fabricated off-site. Figure 3.2 is a photograph of some of the Phase I pre-fabricated rebar cages. Fourteen 2-inch diameter steel pipes were used to form thru-holes in the foundation blocks. These holes were used to pass Dywidag Threadbar anchors (Dywidag) to post tension the foundation block to the strong floor. Before the rebar cages were placed inside the foundation formwork, 2-inch diameter wooden plugs, arranged in a grid to align with the positions of the 2-inch diameter steel pipes, were nailed to the soffit of the formwork. These wooden plugs were used as installation guides for the steel pipes. Rebar chairs were placed on the formwork to obtain the desired concrete cover. Figure 3.3 shows some of the Phase I rebar cages before they were lowered into the foundation formwork. The vertical reinforcement in the wall was tied to the foundation reinforcement before casting the foundation concrete. The bottom of the vertical reinforcement had 90º hooks and sat on top of the bottom longitudinal bars in the foundation. Four #5 bar lifting lugs were installed in the reinforcement cage to facilitate later movement of the specimen. Figure 3.4 shows a rebar cage positioned inside the formwork with the 2-inch diameter pipes, the vertical reinforcement of the wall, and the lifting lugs.

A boom concrete pump was used to transport concrete to the foundation formwork. Vibrators were used to consolidate the concrete. Concrete samples were obtained and placed in standard 6-inch diameter by 12-inch tall cylinders for later concrete compressive strength testing; per ASTM C31/31M-08 (ASTM, 2008) and ASTM C39/39M-05 (ASTM, 2005). Figure 3.5 and Figure 3.6 are photographs taken during the casting of the foundations.

Figure 3.2. Pre-fabricated reinforcement cages for the Phase I foundations

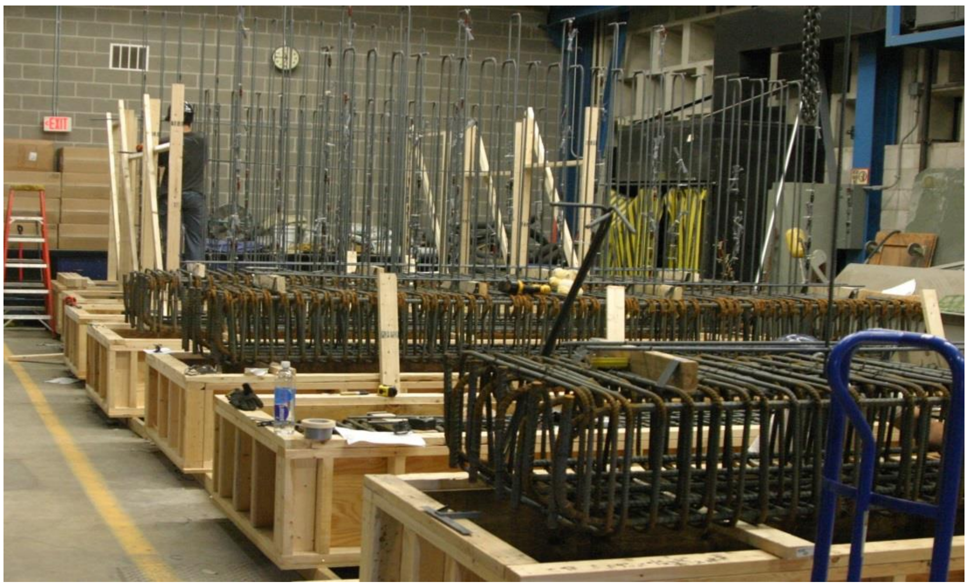

Figure 3.3. Phase I rebar cages prior to placement in formwork

Figure 3.4. Rebar cage positioned inside formwork, Phase I foundation

Figure 3.5. Pumping of concrete for Phase I foundations


Figure 3.6. Pouring of Phase I foundation concrete

The construction joints between the foundation blocks and the to-be-constructed walls above were chipped to expose aggregate. The horizontal reinforcement was then tied to the vertical reinforcement. The horizontal bars had 90º hooks at their ends. Rebar chairs were tied onto the horizontal reinforcement before the formwork for the walls were installed. Two-inch diameter PVC pipes were inserted through the wall formwork to create thru-holes for later installation of the loading apparatus.

Strain gages on the horizontal and vertical reinforcements of the walls were installed before concrete was poured. Strain gages YFLA-5-5L, made by Tokyo Sokki Kenkyujo Co., Ltd. (http://www.tml.jp/e/) were used. Specifications for the YFLA-5-5L strain gages are provided in Appendix C. The manufacturer's installation recommendations were followed. The surface of the reinforcement where the gages were attached was prepared by grinding using a #36 grit disc, mechanical sanding using a #120 sandpaper, and finished using #220 sandpaper. The surfaces were cleaned by M-Prep Conditioner A and M-Prep Neutralizer 5A before the gages were installed. High strength CN adhesive was used to attach the gages to the reinforcement. Tokyo Sokki Kenkyujo Co., Ltd. coating materials were used for waterproofing the bonded gages. The coating materials include W-1 microcrystalline wax, butyl rubber SB and VM tapes, and two-component (AW106 resin and HV953U hardener) epoxy. The gages were wrapped with electrical tape after the application of the waterproofing materials. The gages and the reinforcing bars were carefully and redundantly labeled using blue tape and a marker before they were brought into the construction area.

Figure 3.7 is a photograph of SW5 prior to finishing the wall formwork. Wires for the strain gages were bundled and were let out on one face of the wall. A boom concrete pump was used to pour concrete in the walls. Internal and external vibrators were used to consolidate the concrete. Concrete samples were obtained per ASTM C31/31M-08 and ASTM C39/39M-05. The walls were wrapped with plastic to facilitate hydration during curing and sprayed twice daily for seven days. The small holes and imperfections on the surface of the concrete walls were roughened, cleaned and patched with SikaTop 123 Plus (http://usa.sika.com/).

Figure 3.7. SW5 prior to finishing of wall formwork

3.4.2 Phase II specimens

The Phase II walls (SW8-SW12) were built at SEESL by LPCiminelli Inc., a construction company in Buffalo, NY. Similar to the Phase I walls, the specimens were constructed in two stages: foundations then walls. The foundations were cast on March 20, 2012; the walls were cast on March 27, 2012.

The foundations of Phase II specimens had plan dimensions of 14 feet by 4 feet; their height was 18 inches. The rebar cages for the foundations were assembled on-site. Fourteen 2-inch diameter PVC pipes formed thru-holes in the foundation block for later installation of Dywidag bars. Before the rebar cages were placed into the formwork, 2-inch diameter wooden plugs were attached to the soffit of the formwork to guide the installation of PVC pipes. Rebar chairs were placed on the formwork to obtain the required concrete cover. Figure 3.8 is a photograph of the rebar cage and foundation formwork for SW10.

Figure 3.8 Foundation formwork and rebar cage for a Phase II wall

The heights of the stirrups for the foundations of the Phase II walls were fabricated 2 inches shorter than specified. The effect of the reduced height of the rebar cage was investigated using strut-and-tie models. Additional longitudinal and transverse reinforcement were needed to accommodate the reduction in height and maintain the capacity of the foundation. Appendix B presents the strut-and-tie model of the foundation of SW8. The details of the supplemental reinforcement are also given in Appendix B. Figure 3.9 shows the foundation of SW8 prior to the installation of the supplemental reinforcement. Figure 3.10 and Figure 3.11 show the locations of the supplemental reinforcement on the foundation of SW8 and SW12, respectively.

Figure 3.9. SW8 foundation details

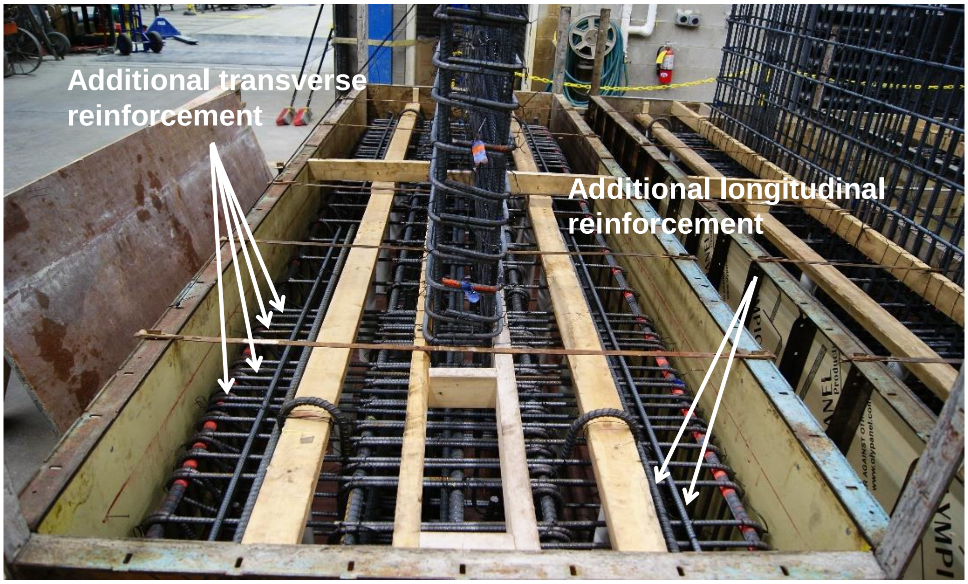

Figure 3.10. Supplemental reinforcement in the foundation of SW8

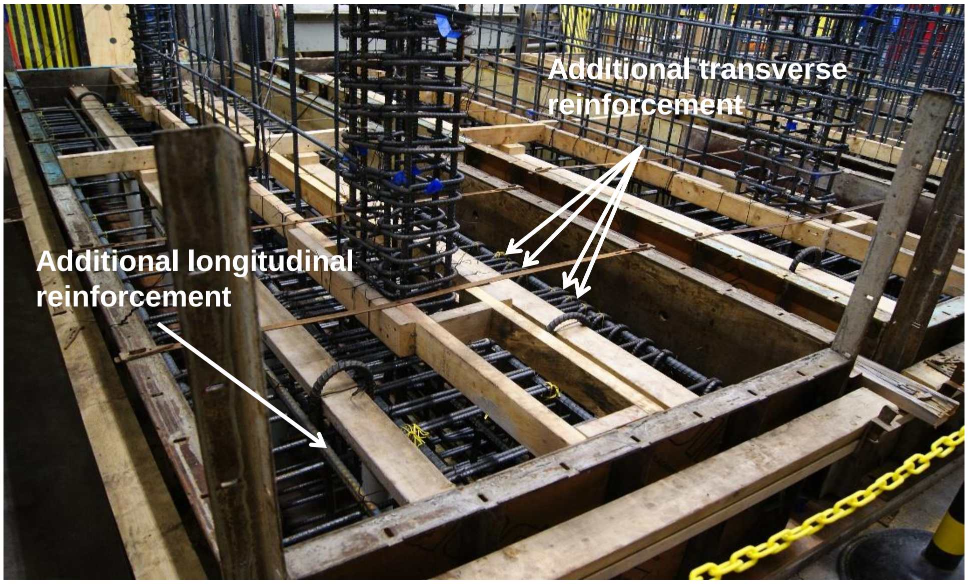

Figure 3.11. Supplemental reinforcement in the foundation of SW12

Strain gages (YFLA-5-5L) were installed on the horizontal and vertical reinforcement of the walls, as described previously. The horizontal and vertical rebars (with the strain gages attached) were installed after the rebar cages were positioned in the foundation formwork. The 90º hooks at the bottom of the vertical reinforcement, originally detailed to sit on top of the bottom longitudinal bars of the foundation, were placed beneath the longitudinal reinforcement to account for the reduced depth of the rebar cage. Strain gage wires were bundled and were let of the top of the wall. Four #6 bars lifting lugs were installed on the reinforcement cage to facilitate later movement of the specimen. Figure 3.12 shows the Phase II walls prior to casting concrete.

A conveyor belt was used to pour the foundation concrete. Vibrators were used to consolidate the concrete. Concrete samples were obtained and placed in standard cylinders, per ASTM C31/31M-08 and ASTM C39/39M-05.

The construction joints between the foundation blocks and the to-be-constructed walls above were chipped to expose the aggregate. Rebar chairs were tied onto the horizontal reinforcements before the formwork for the walls was installed. Two-inch diameter PVC pipes were inserted through the wall formwork to create thru-holes for later installation of the loading apparatus. Figure 3.13 shows wall formwork, Figure 3.14 is a photograph of the completed formwork setup prior to the pouring of concrete in the walls. Self-consolidating concrete was used for the walls. Concrete samples were obtained and placed in standard cylinders per ASTM C31/31M-08 and ASTM C39/39M-05. The small holes and imperfections on surface of the concrete walls were roughened, cleaned and patched with SikaTop 123 Plus. The walls were wrapped with plastic to facilitate hydration during curing and sprayed twice daily for seven days. Figure 3.15 is a photograph of the Phase II walls during curing.

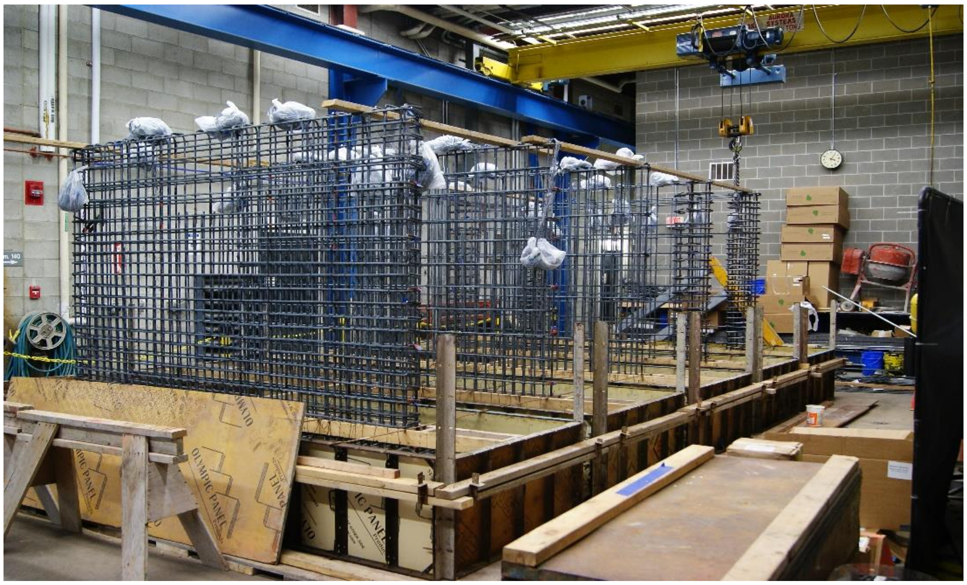

Figure 3.12. Phase II walls prior to foundation concrete casting

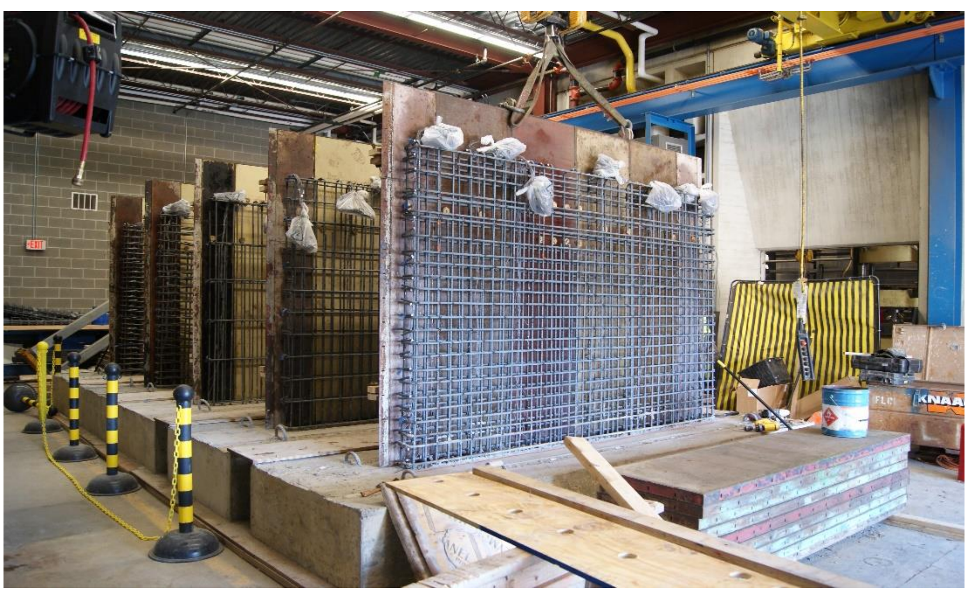

Figure 3.13. Installation of Phase II wall formwork


Figure 3.14. Phase II specimens prior to pouring of concrete on the walls


Figure 3.15. Curing of Phase II wall specimens

3.5 Loading apparatus

The loading apparatus consisted of two sets of custom-made steel plates and brackets, one set for each face of the wall. Drawings of the loading plates and brackets are presented in Appendix A. The plates and brackets were analyzed using ABAQUS version 6.5.1 (Dassault Systemes Simulia Corp., 2014) and designed such that at maximum load on the actuators, the elastic deformations were minimal and the stresses were well below yield. The geometry of the brackets was dictated by the geometry of the strong wall and strong floor and the desire to have the centerline of the actuators intersect beyond the end of the specimen. Having the intersection of the centerline of the actuators (instant center) beyond the end of the specimen permits better control of the lateral displacement of the centerline of loading of the wall. ASTM A572 (ASTM, 2013) Grade 50 steel plate was used for the steel plate. The mechanical properties of ASTM A572 steel plate are summarized in Table 3.2. The plates and brackets were post tensioned to either side of the specimens using 1.5-inch diameter B-7 threaded rods. Eight rods were used to clamp the brackets and plates to the specimens and another eight rods were used to clamp the remainder of the plate to the specimen. The target load in each rod was 82 kips. Additional shear blocks were welded to the loading plate after testing the first three specimens to provide an additional margin against slipping. The drawings of the additional shear blocks are presented in Appendix A.

Table 3.2. Summary of the mechanical properties of steel plate and reinforcing bars (from ASTM A572, ASTM A615 and ASTM A706)

	Steel plate	Reinforcing bars	
	A572	A615	A706
Grade	50	60	60
Minimum tensile strength (ksi)	65	90	80[1]
Minimum yield strength (ksi)	50	60	60
Maximum yield strength (ksi)	-	-	78
1. Not more than 1.25 times the actual yield strength			

3.6 Material properties

3.6.1 Concrete

Concrete samples for all batches of concrete were obtained, placed in standard 6-inch diameter by 12-inch tall cylinders, and tested in accordance with ASTM C31/31M-08 and ASTM C39/39M-05. The cylinders were tested for uniaxial compressive strength. The target 28 day compressive strengths of the concrete in the walls and in the foundations were 4 ksi and 5 ksi, respectively. The cylinders of wall concrete were tested 7, 14, 28 and 56 days after casting and on the days of testing of the corresponding specimens. The cylinders from the foundations of the Phase I specimens were tested 7, 14, 28 and 42 days after casting; the cylinders from the Phase II foundations were tested 7, 14, 28 and 56 days after casting.

After testing each Phase I specimen, core samples were taken and tested for uniaxial compressive strength per ASTM C42/C42M (ASTM, 2010). A 4-inch diameter core bit was used to cut core samples around the loading area (assumed undamaged) of SW1, SW2, SW3, SW4, SW6 and SW7. Reinforcement was avoided. The 4-inch diameter core bit produced 3.5-inch diameter cores. The heights of the cores (equal to the 8-inch thickness of the specimens) were trimmed to 7 inches to maintain an aspect ratio of two. A 3-inch diameter core bit was used for SW5 to produce 2.5-inch diameter cores. The heights of the 2.5-inch diameter cores were reduced to 5 inches, also to achieve an aspect ratio of 2. Four core samples were taken from each of the Phase I specimens and tested in compression. No cores were taken from the Phase II specimens. The small spacing of the vertical reinforcement in SW8, SW9 and SW10 made it nigh-on impossible to cut core samples without cutting reinforcement.

The compressive strengths of the concrete in the walls are summarized in Table 3.3. Results are presented in Figure 3.16. The compressive strength of the foundation concrete is summarized in Table 3.4 and results are plotted in Figure 3.17. The values reported are the average values obtained from testing two cylinders for the Phase I specimens and three cylinders for Phase II specimens and are rounded to the nearest tenth of a ksi. The average 28-day wall cylinder strength of all specimens, except SW2 and SW3, varied between 3.0 ksi and 3.6 ksi (10% to 25% less than the target 28-day strength of 4 ksi); the average 28-day wall concrete cylinder strengths of SW2 and SW3 were 5.1 ksi and 6.2 ksi, respectively. The average 28-day foundation concrete cylinder strengths varied between 4.5 ksi and 5.4 ksi. The average value of the compressive strengths from the cores extracted from specimens SW2, SW3, SW4 and SW6 were within 10% of the average cylinder strength on the day of testing. The average core strength from specimen SW1 and SW7 were 22% and 21% less than the average cylinder strength. Micro cracks in the cores, not visible to the eye, are a possible cause of this difference.

Table 3.3. Uniaxial compressive strength of concrete in the walls (ksi)

Wall	Cylinders					Core	Core / Day of test
	Days after casting				Day of test		
	7	14	28	56			
SW1	2.1	2.7	3.1	3.6	3.6	2.8	0.78
SW2	3.9	4.2	5.1	6.0	7.0	6.3	0.90
SW3	4.7	5.7	6.2	7.4	7.8	7.4	0.95
SW4	2.3	2.9	3.3	3.8	4.2	4.5	1.07
SW5	2.0	2.8	3.0	3.3	4.3	3.0	0.70
SW6	2.0	2.8	3.0	3.3	3.8	4.1	1.08
SW7	2.0	2.8	3.0	3.3	3.8	3.0	0.79
SW8	2.1	2.9	3.5	-	3.5	-	-
SW9	2.1	2.9	3.5	-	4.3	-	-
SW10	2.1	2.8	3.6	4.2	4.6	-	-
SW11	2.1	2.8	3.6	4.2	5.0	-	-
SW12	2.1	2.8	3.6	4.2	5.0	-	-

Table 3.4. Uniaxial compressive strength of concrete in the foundations (ksi)

Wall	Days after casting				
	7	14	28	42	56
SW1	3.0	3.6	4.5	4.9	-
SW2	3.0	3.6	4.5	4.9	-
SW3	3.1	3.9	5.0	5.5	-
SW4	3.1	3.9	5.0	5.5	-
SW5	3.0	3.9	4.8	5.0	-
SW6	3.0	3.9	4.8	5.0	-
SW7	3.0	3.9	4.8	5.0	-
SW8	4.1	4.6	5.3	-	5.8
SW9	4.1	4.6	5.3	-	5.8
SW10	3.9	4.7	5.4	-	5.8
SW11	3.7	4.8	5.4	-	5.7
SW12	3.7	4.8	5.4	-	5.7

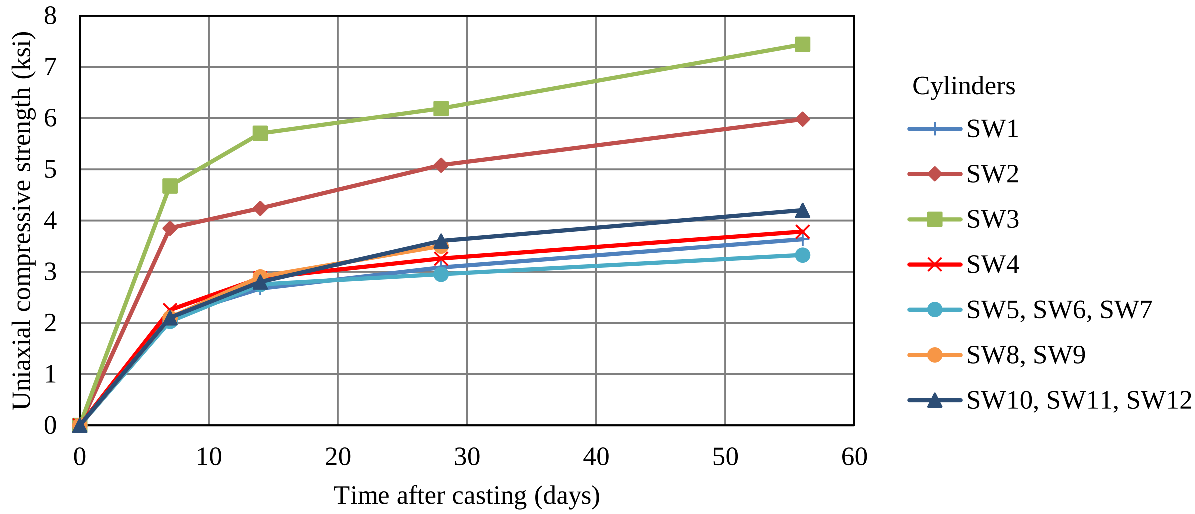

Figure 3.16. Concrete compressive strength from cylinder tests: walls

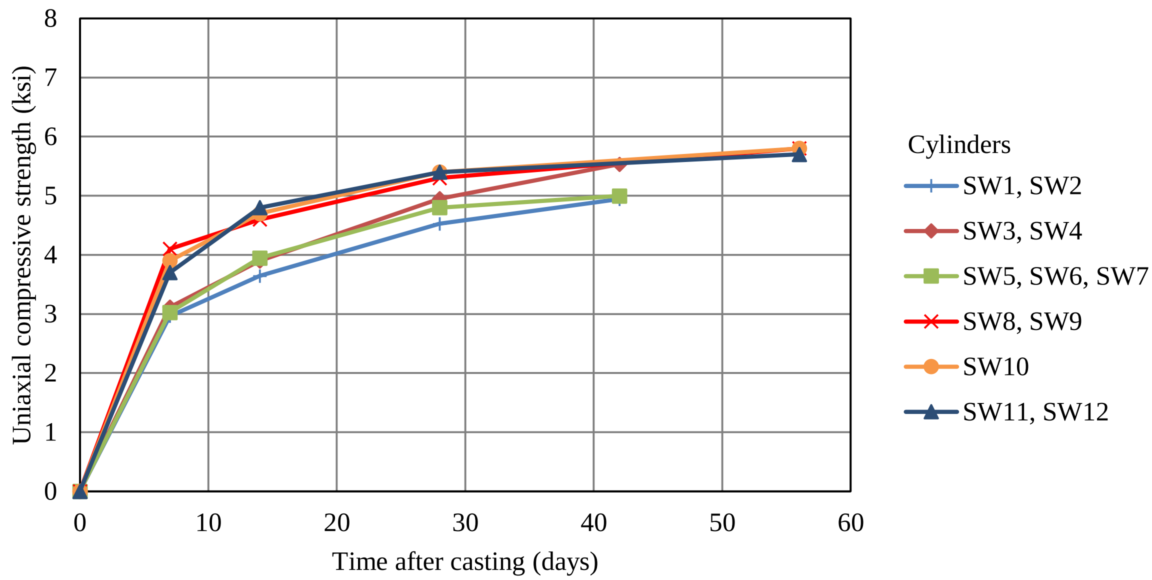

Figure 3.17. Concrete compressive strength from cylinder tests: foundations

3.6.2 Reinforcement

The Phase I specimens were constructed using two different batches of Grade 60 reinforcement. Grade 60 ASTM A615 reinforcement was used for SW1, SW4, SW5, SW6 and SW7 and Grade 60 ASTM A706 reinforcement was used for SW2 and SW3. The mechanical properties of the A615 and A706 reinforcement are presented in Table 3.2. Randomly selected pieces of reinforcement, eight from the A615 stock and five from the A706 stock, were tested. ASTM A615 Grade 60 reinforcement was used for the Phase II specimens. Five randomly selected (three #4 bars and two #5 bars) pieces were tested. All of the tested steel specimens were 16 inches long: 4 inches at each end of each specimen were used to grip the specimen in the testing machine. A 2-inch extensometer was used to measure the strain on the test specimens.

Type-2 mechanical splices were installed on the vertical reinforcement in SW2 and SW3. Two steel coupons with the mechanical splice at their middle were tested. The total length of these test specimens was 23 inches: 4 inches at each end were used to hold the specimen in the testing machine, 4 inches on each side of the mechanical coupler, and a coupler length of 7 inches. The rupture zones in the two test specimens were outside the limits of the couplers (see Figure 3.18).

Figure 3.18. Rupture zone in the Type-2 mechanical coupler tensile test

Sample stress-strain relationships for the reinforcement used are presented in Figure 3.19. Stress was calculated as the ratio of the measured force to the cross sectional area of the reinforcement. Strain was calculated by dividing the measured elongation (by the extensometer) by the gage length of 2 inches. The stress-strain relationships for the mechanically coupled A706 rebar had no well-defined yield plateau. The two steel coupons of mechanically coupled A706 rebar achieved the tensile strengths of the rebar.

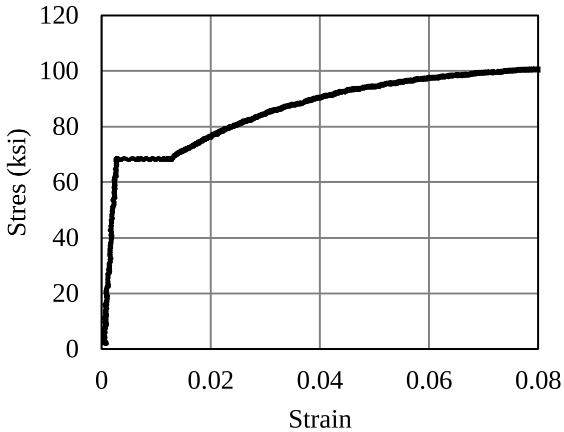

a) ASTM A615 rebar

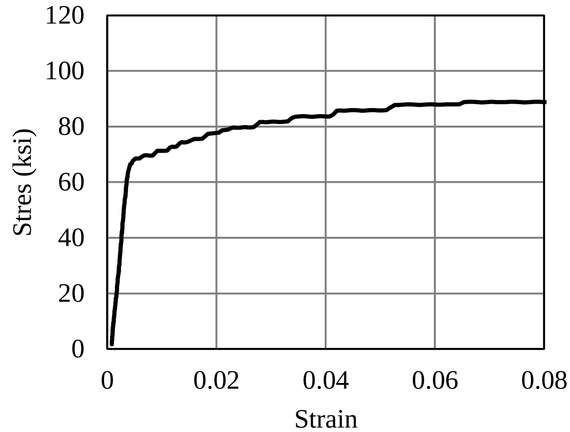

b) ASTM A706 rebar

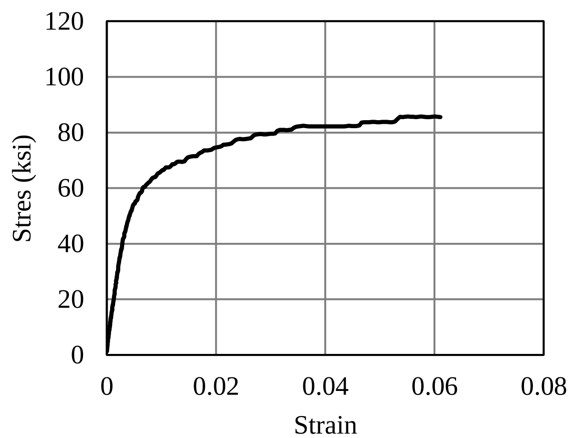

c) ASTM A706 rebar with Type-2 mechanical coupler

Figure 3.19. Stress-strain relationships for reinforcement

Table 3.5 summarizes the yield and tensile stresses of the reinforcement used for the Phase I and Phase II specimens. The average yield and ultimate strengths of the A615 reinforcement used for Phase I specimens were 67.3 ksi and 102.7 ksi, respectively. The average yield and ultimate strengths of the A615 rebars used for Phase II specimens were 67.3 ksi and 102.4 ksi, respectively. The reinforcement used for all the specimens met the requirements of Section 20.2.2.5 of ACI 318-14 (ACI, 2014). None of the tested A615 reinforcement had a yield strength greater than 78 ksi and the ratio of the tensile strength-to-yield strength of the tested A615 reinforcement was greater than 1.25.

Table 3.5. Reinforcement material properties

Reinforcement (specimen)	Sample	f_y (ksi)	f_u (ksi)	$\frac{f_u}{f_y}$	Ave. f_y (ksi)	Ave. f_u (ksi)	Ave. $\frac{f_u}{f_y}$
A615 (SW1, SW4, SW6, SW6, SW7)	1	67.8	104.2	1.54	67.3	102.7	1.53
	2	65.8	99.9	1.52			
	3	65.4	100.2	1.53			
	4	67.9	102.6	1.51			
	5	69.1	105.1	1.52			
	6	69.4	105	1.51			
	7	69.8	105	1.50			
	8	63.4	99.4	1.57			
A706 (SW2, SW3)	1	61	82.9	1.36	63.0	87.7	1.39
	2	65.5	85.8	1.31			
	3	59.6	85.7	1.44			
	4	67.4	91.9	1.36			
	5	61.5	92.1	1.50			
A706 w/ coupler (SW2, SW3)	1	61.8	88.5	1.43	62.3	87.9	1.41
	2	62.7	87.3	1.39			
A615 #4 (SW8 through SW12)	1	65.8	98.5	1.50	67.3	102.4	1.52
	2	68.4	102.9	1.50			
	3	69	103.7	1.50			
A615 #5 (SW11, SW12)	1	67.1	101.1	1.51			
	2	66.1	105.7	1.60			

3.7 Test setup

The typical test setup involved the following main steps: 1) positioning the wall specimen, 2) wall surface preparation, 3) installation of the loading apparatus, and 4) instrumentation. These steps are described as follows.

The specimen was lifted into the testing area using the four lifting lugs. The footprint of the foundation was marked on the strong floor using duct tape. Before the specimen was lowered to the floor, the Dywidag bars at the four corners of the foundations were installed to facilitate alignment of the specimen. The initial task was to ensure that the specimen was level and that the centerline of loading was horizontal, noting that the strong floor and the bottom of the foundation of the specimen were not perfectly flat. This task was achieved by placing steel shims and cement grout between the foundation and strong floor. Steel shims were placed at the four corners of the foundation. The height of the shim at each corner was adjusted to provide at least ¼ inches of clearance between the underside of the foundation and the top of the strong floor, while simultaneously keeping the centerline of loading horizontal. After these objectives were achieved, the specimen was temporarily removed from its location. The shims were secured to the strong floor using duct tape. The thru-holes on the strong floor were covered with duct tape and rubber foam (weather_strip) tape was installed on its perimeter to prevent the cement grout from covering the thru-holes and/or flowing into the laboratory sub-basement. The cement grout was then poured under a gravity head into the cavity between the foundation and strong floor. After repositioning the specimen, the alignment of the centerline of loading was rechecked before the Dywidag bars were placed. The grout was allowed to cure for at least three days before the Dywidag bars were post-tensioned to the strong floor. The Dywidag bars were post-tensioned from below the strong floor to minimize the bar extension above the top of the foundation. The Dywidag bars were post-tensioned to about 50% of yield (95 kips) for the first six wall specimens tested and to around 80% of yield (152 kips) for the remaining six specimens.

The wall preparation consisted of painting the surface with a mixture of white latex paint and water using a volumetric ratio of 1:1. This was intended to make cracks easier to locate and to make the chalk line grids on the two faces of the wall more visible. For the Phase I walls, two thin coats of the paint mixture were applied after the specimens had been placed for testing. For the Phase II specimens, the first coat was applied after the construction of the walls and the second coat was applied after the walls had been placed for testing.

The next step in the setup was to install the loading plates and brackets on the two sides of the wall. The gap between the loading plate and wall surface, created by the 0.25-inch thick shims on the four corners of the plate, was filled with Hydro-Stone gypsum cement (http://www.usg.com). Rubber foam tape was attached on the inside perimeter of the loading plate (except on the top portion to facilitate pouring of the Hydro-Stone) and on the perimeter of the thru-holes. The plates were lifted and temporarily secured by putting the B-7 rods, nuts and washers on the thru-holes at the two ends of the plates/wall. The nuts were loosely tightened to enable the leveling of the loading plate. The centerlines of the loading plates and wall were aligned. Post jacks placed at each bottom end of the plates were used to adjust the height of the plates and facilitate alignment. Once the plates and wall were aligned and leveled, the remaining B-7 rods were attached and their nuts were slightly tightened, enough to hold the plates in place. The perimeter of the loading plates with rubber foam tape attached were caulked with silicone rubber sealant. Hydro-Stone was poured from the top of the plates and was allowed to cure for at least one day before the loading brackets were attached. The B-7 rods were installed and tensioned to approximately 80% of yield (82 kips). Figure 3.20 and Figure 3.21 are photographs of the installations of the loading plates and brackets. The actuators were then carefully attached to the bracket and the mounting block on the strong wall using four B-7 rods on each end of the actuators. Each actuator was leveled horizontally before the nuts of the B-7 rods were tightened.

Two grids of chalk lines were marked on each face of the wall to enable accurate placement of instruments. Figure 3.22 is a photograph of SW2 after setup and before testing. Figure 3.23 is a CAD plan view of the setup.

Figure 3.20. Loading plate installation

3.8 Instrumentation

The instrumentation plan for each wall is presented in Appendix C. Four drawings are presented for each wall to show the locations of 1) Krypton LED sensors, 2) strain gages on vertical reinforcement, 3) strain gages on the horizontal reinforcement, and 4) string potentiometers and Temposonics. Specimen SW4 has a supplementary drawing showing the locations of linear potentiometers. The following are abbreviations used in the drawings: SP – string potentiometer, TP – Temposonic, LP – linear potentiometer, and S – strain gage.

Figure 3.21. Loading bracket installation

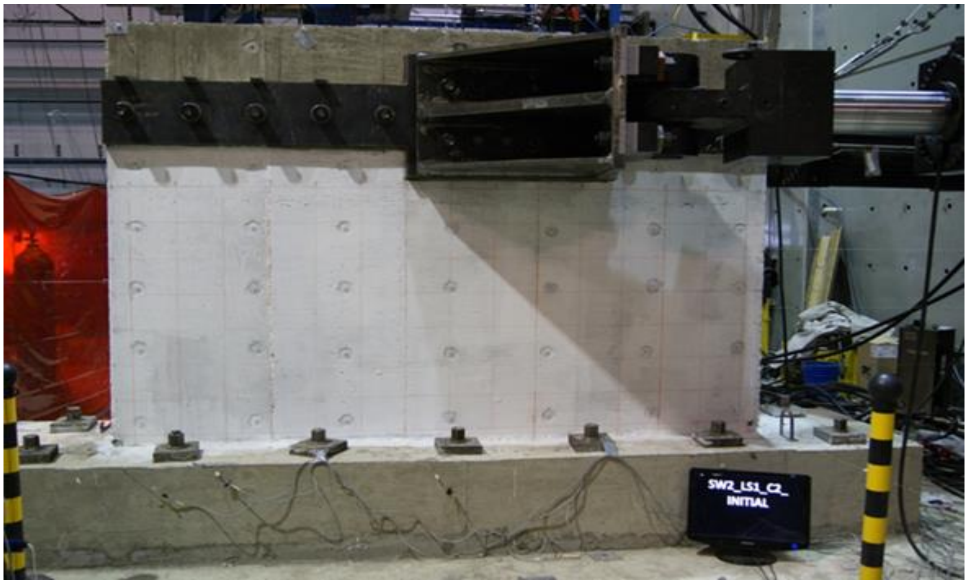

Figure 3.22. Photograph of SW2 after setup

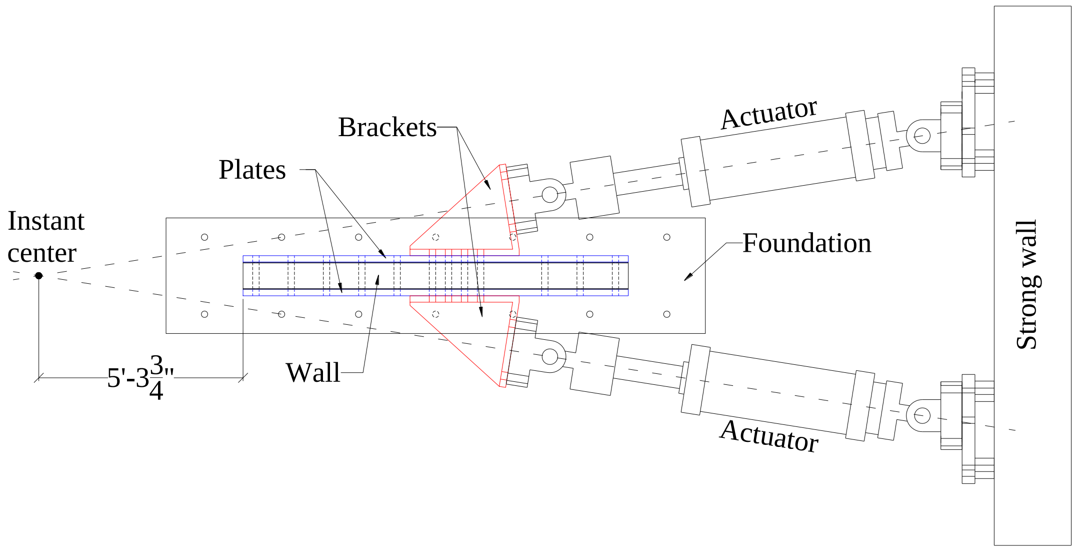

Figure 3.23. Plan view of typical specimen setup

String potentiometers, linear potentiometers and Temposonics were used to measure the in-plane and out-of-plane displacements of each wall. The Krypton K600 Optical Measurement System (Nikon Metrology, 2013) was used to monitor displacements across one face of each wall, using LED sensors installed on a rectangular grid. Data from this dense grid of sensors enabled calculation of the contributions of flexure, shear and base slip to the total lateral displacement. String potentiometers and LED sensors were installed to monitor lateral displacement and rotation of the foundation. A rectangular grid was marked on the opposite face of the wall to the LED sensors to monitor cracks and to facilitate interpretation of GigaPan (GigaPan Systems, 2013) images of the *cracked* wall. Strain gages capable of measuring 15% strain were installed on the horizontal and vertical reinforcements in each wall as described previously. An average of 52 and 84 strain gages were installed on Phase I and Phase II walls, respectively. The detailed specifications of each instrument are provided in Section C.2 of Appendix C. Figure 3.24 is a photograph of some instrumentation installed on SW8.

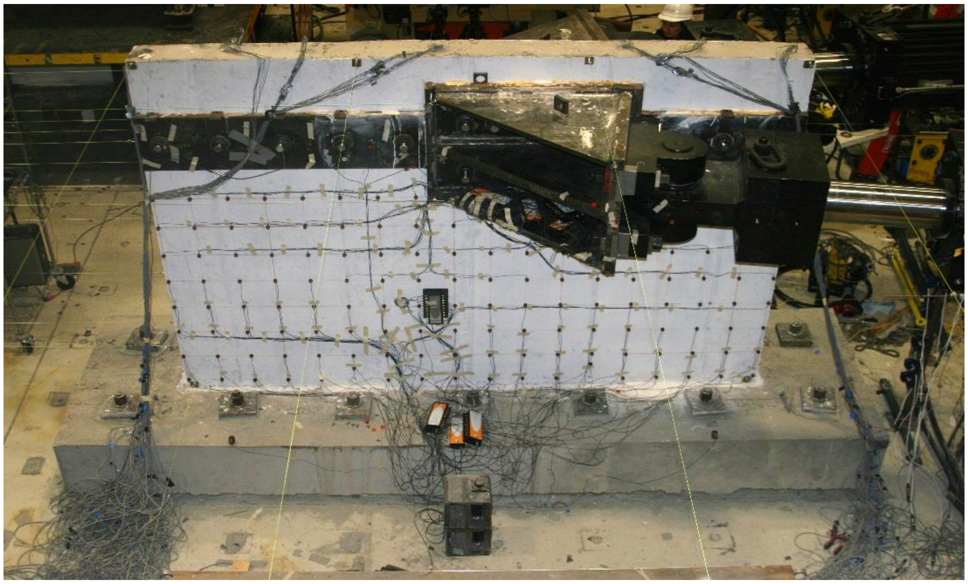

Figure 3.24. SW8 instrumentation

Lateral loads were applied to the walls using two high force-capacity actuators that were horizontally inclined by nine degrees with respect to the longitudinal axis of the walls (see Figure 3.23). The actuators have a load capacity of 440 kips and 600 kips in tension and compression, respectively. The specifications for the actuators are presented in Section C.2 of Appendix C. Displacement transducers in the actuators were used to control the lateral displacement of the walls. (Discrepancies between the input and actual displacements were inevitable with this control strategy at very small values of displacement because of nonlinear slip and movement within each actuator clevis.) Load cells in the actuators were used to measure the applied load.

Two data acquisition systems (DAQ) were used to collect and process data from the instrumentation. Pacific Instruments Model 6000 DAQ (http://www.pacificinstruments.com/) collected data from the string potentiometers, linear potentiometers, Temposonics and load cells and displacement transducers within the actuators. The specifications for the Model 6000 DAQ are provided in Section C.2 of Appendix C. The Krypton system DAQ collected data from the Krypton camera and LED sensors. To enable data synchronization, a single controller was used to simultaneously trigger the two DAQs to start collecting data.

3.9 Loading protocol

The test specimens were subjected to reversed cyclic, displacement controlled loadings to indirectly simulate the effect of earthquake shaking. The guidelines provided by ATC-24 (ATC, 1992), ACI 374.1-05 (ACI, 2005) and a 2009 working draft of ACI 374.2R-13 (ACI, 2013) were considered in the development of the loading protocol.

The first step in developing the loading protocol for a given wall was to simulate its load-displacement relationship (monotonic loading) using the finite element software VecTor2 ver. 2.8. The material models and average mesh size used in modeling each wall specimen were similar to those used in the pre-test modeling (Section 3.2). A uniaxial concrete compressive strength of 4 ksi and a reinforcement yield strength of 60 ksi were used. A reference displacement (a displacement related to yield), Δ_r , was determined for each wall using the predicted load-displacement relationship and an equal energy assumption. Figure 3.25 shows the derived reference displacement for SW5. The derivation of the reference displacement for each wall is presented in Appendix D.

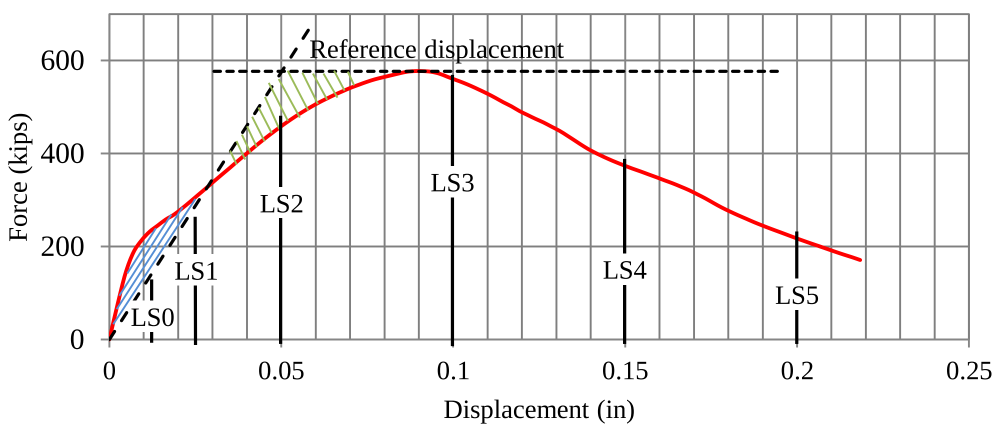

Figure 3.25. Reference displacement for SW5

The different displacement increments of the loading protocol, referred to as load steps (LS), were anchored to fractions/multiples of Δ_r . Load step LS0 was the first load step for SW1 and SW5 through SW12; LS1 was the first load step for SW2, SW3 and SW4. Load step LS0 was to $0.25\Delta_r$ and was used for the calculation of initial stiffness. Load step LS1 was to $0.5\Delta_r$.

Succeeding load steps were displacement increments of either $0.5\Delta_r$ or Δ_r. The first load step for each wall comprised three displacement cycles and subsequent load steps comprised two displacement cycles. The loading protocol for SW5 is shown in Figure 3.26. The loading protocols for all the walls are presented in Appendix D. The displacement loading rate for all the specimens ranged from approximately 0.005 in/sec to 0.01 in/sec.

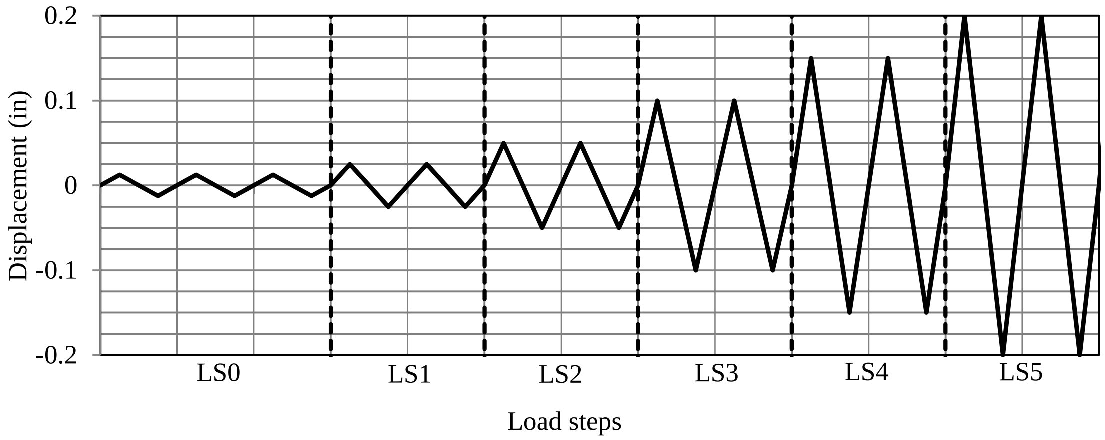

Figure 3.26. Loading protocol for SW5

3.10 Test procedures

The 12 wall specimens were tested in Testing Area 2 of the Structural Engineering and Earthquake Simulation Laboratory (SEESL). The sequence and dates of testing of the 12 walls are presented in Table 3.6. The first specimen (SW4) was tested on February 28, 2011 and the last specimen (SW12) was tested on August 22, 2012. The testing schedule was dictated by the availability of laboratory equipment for setting up the specimen and the instrumentation for testing. There were other concurrent projects at the laboratory during the duration of the setup and testing of the 12 walls.

A four-field alpha-numeric string, separated by underscores, was used to organize the data collected from the testing of each wall specimen. The following is a sample of the string.

SW1_LS1_C1_Initial

SW1_LS1_C1_Peak1

SW1_LS1_C1_Mid

SW1_LS1_C1_Peak2

SW1_LS1_C2_Initial

The first field is the name of the specimen being tested; the second field is the load step (defined by the loading protocol); the third field is the cycle of loading (three cycles for the first load step and two cycles for all subsequent load steps); and the fourth field refers to the point of the cycle where data is currently being collected. In the fourth field of the string, *Initial* refers to the initial zero displacement for a given cycle; *Peak1* refers to the positive direction of loading to the target displacement of the current load step (pushing the specimen); *Mid* refers to the unloading to zero displacement from *Peak1*; and *Peak2* refers to the negative direction of loading to the target displacement of the current load step (pulling the specimen).

Table 3.6. Testing sequence and dates of the 12 wall specimens

Test No.	Phase	Specimen	Testing start date	Testing end date
1	Phase I	SW4	February 28, 2011	March 10, 2011
2		SW3	May 3, 2011	May 11, 2011
3		SW2	May 25, 2011	June 1, 2011
4		SW1	July 12, 2011	July 19, 2011
5		SW7	September 30, 2011	October 6, 2011
6		SW6	November 22, 2011	December 1, 2011
7		SW5	January 31, 2012	February 13, 2012
8	Phase II	SW8	April 23, 2012	April 27, 2012
9		SW9	May 17, 2012	May 21, 2012
10		SW10	June 7, 2012	June 18, 2012
11		SW11	July 30, 2012	August 1, 2012
12		SW12	August 22, 2012	August 27, 2012

The data manually collected at the different points of every cycle (*Initial*, *Peak1*, *Mid* and *Peak2*) include 1) crack propagation, 2) crack width measurements, and 3) photograph of the whole wall. Incremental photographs of the different sections of wall were taken using GigaPan System (which were later stitched together to come up with a very high resolution photograph of the wall) during *Peak1* and *Peak2*. Digital photographs of the significant damages to the walls were taken and logged.

CHAPTER 4

SPECIMEN PERFORMANCE

4.1 Introduction

This chapter presents results of the analysis of data from the reversed cyclic testing of the 12 shear wall specimens introduced in Chapter 3. Section 4.2 presents the measured global force-displacement relationships. Section 4.3 summarizes the initiation of cracking of concrete and yielding of reinforcement. The cracking patterns and modes of failure of the specimens are described in Section 4.4. Crack angles are discussed in Section 4.5. Vertical, horizontal, shear and principal strain distributions are presented in Section 4.6. Contributions of flexure, shear and sliding to the total lateral drift, and out-of-plane displacements, are discussed in Sections 4.7 and 4.8, respectively. Loss of stiffness and peak strength with repeated cycling is described in Section 4.9. Additional analysis of data from the reversed cyclic testing of the 12 shear wall specimens can be found in Rivera (2018) and Rivera et. al. (2018). Data from the tests have been curated and archived at NEES Project Warehouse (Luna et al., 2013a and 2013b).

4.2 Global force-displacement relationships

Figure 4.1 presents the measured force-drift relationships and the cyclic backbone curves (solid red piecewise linear lines) for the 12 walls. The peak points of the first cycle at each displacement increment were connected to form the backbone curves. The two blue dashed lines in each panel identify the peak shear strength in the first and third quadrants of loading. The values inside the parentheses in the subtitles of Figure 4.1 (and succeeding figures, unless otherwise specified) correspond to 1) aspect ratio, 2) horizontal reinforcement ratio, 3) vertical reinforcement ratio, 4) concrete compressive strength and 5) boundary elements reinforcement ratio (for SW11 and SW12). The in-plane forces were calculated using load cells in the actuators. The lateral displacements were calculated from: in-plane string potentiometers (SP7) for walls SW2, SW3 and SW4; and in-plane Temposonics (TP7) for walls SW1 and SW5 thru SW12. SP7 and TP7 were attached at the centerline of loading at the east end of the wall specimens. The resolution of the string potentiometers and Temposonics used in the tests were 0.0025 and 0.00025 inch, respectively. Significant noise is present in the collected data from the string potentiometers at small drifts (see Figure 4.2). The drift ratio for each wall was calculated by dividing the lateral displacement at the centerline of loading by the distance between the centerline of loading and the top of the foundation.

Walls SW8, SW9 and SW10 have an aspect ratio of 0.54 and a vertical reinforcement ratio of 1.5%. The horizontal reinforcement ratios of the three walls vary from 0.33% to 1.5%. Their cyclic backbone curves are plotted in Figure 4.3a. Some of the key observations from the response of these walls are: 1) the hysteretic responses of SW8 and SW9 are quantitatively similar, measured here in terms of peak strength and loss of stiffness and strength with repeated cycling beyond the displacement corresponding to peak strength, 2) the *pinching* of the hysteresis loops is due to sliding at the base, which occurs after the peak strength is attained, 3) the peak shear strengths of SW8 and SW9 are similar in quadrant 1, although SW9 has much less horizontal reinforcement, which suggests that above a threshold value, the effect of the horizontal reinforcement ratio on peak strength is small, and 4) the ability of the wall to sustain significant lateral load at displacements greater than that at peak strength is affected by the horizontal reinforcement ratio.

Walls SW11 and SW12 are the two walls with boundary elements. Their backbone curves are plotted in Figure 4.3b. A plateau can be observed in the hysteretic response of the two walls, which suggests that boundary elements help maintain peak shear strength for cycles at displacements beyond peak strength. The two walls have about the same average vertical reinforcement ratio (0.84% for SW11 and 0.77% for SW12), same day-of-test concrete compressive strength and comparable peak shear strengths (slightly higher for SW11 on the first quadrant of loading). These results suggest that the distribution of the total vertical reinforcement along the length of the wall does not appear to have a significant effect on peak shear strength, noting that the amount and distribution of horizontal reinforcement is expected to have little influence on the shear strength of low aspect ratio walls (Barda et al., 1977; Gulec and Whittaker, 2011).

Walls SW5, SW6 and SW7 have an aspect ratio of 0.33 and reinforcement ratios of 1.0%, 0.67% and 0.33%, respectively. Their backbone curves are plotted in Figure 4.3c. The concrete compressive strength of SW6 and SW7 are identical but the peak shear strength of SW6 is significantly greater than SW7 which suggests that the vertical reinforcement ratio has significant effect on peak shear strength (the effect of horizontal reinforcement on peak strength is small per observation from SW8, SW9 and SW10). Although the concrete compressive strength of SW5 is only marginally greater than SW6, the peak shear strength of SW5 is approximately 150 kips (667 kN) greater than SW6. These observations confirm the expected behavior of RC walls that the peak shear strength is greater for walls with higher reinforcement ratio.

Walls SW2, SW3 and SW4 have an aspect ratio of 0.54 and reinforcement ratios of 1.0%, 0.67% and 0.33%, respectively. Their backbone curves are plotted in Figure 4.3d. The peak shear strength of SW2 is greater than SW3 although its concrete compressive strength is smaller. The peak shear strength of SW4 is much less than SW3, which was expected because the concrete strength and reinforcement ratios are substantially smaller in SW4. Similar to prior observations (on SW5, SW6 and SW7), peak shear strength is greater for walls with greater reinforcement ratio.

Specimens SW1, SW3 and SW6 have the same horizontal and vertical reinforcement ratios and aspect ratios of 0.94, 0.54 and 0.33, respectively. Their backbone curves are plotted in Figure 4.3e. The measured peak strength in the first quadrant of loading is greater for SW6 than SW3, even though SW6 has a significantly lower concrete compressive strength than SW3 which suggests that aspect ratio has significant effect on peak shear strength. SW6 and SW1 have a similar concrete compressive strength but the measured peak shear strength is greater for SW6 than SW1. These results support past observations that peak shear strength is greater for walls with lower aspect ratios, all other parameters being equal.

4.3 Initiation of cracking of concrete and yielding of reinforcement

Table 4.1 summarizes the values of the lateral forces and drift ratios corresponding to the onset of 1) visible diagonal (shear) cracking in concrete, 2) visible horizontal cracking in concrete near the base of the wall, and 3) tensile yielding of the boundary vertical reinforcing bars. Diagonal cracking in the webs of the walls was first observed at lateral forces between 57 kips (SW1) and 221 kips (SW9), average shear stresses between $1.0\sqrt{f_c^{'}}$ (SW1) and $3.8\sqrt{f_c^{'}}$ (SW8), and drift ratios between 0.02% (SW5) and 0.12% (SW11). For walls with an aspect ratio of 0.54 and equal horizontal and vertical reinforcement ratio (SW2, SW3, SW4 and SW8), the force and drift ratio corresponding to the initiation of diagonal cracking increase with the increase in reinforcement ratio. Horizontal cracks formed near the base of the wall at lateral forces between 57 kips (SW1) and 623 kips (SW8), average shear stresses between $1.0\sqrt{f_c^{'}}$ (SW1) and $11.0\sqrt{f_c^{'}}$ (SW8), and drift ratios between 0.055% (SW1) and 0.94% (SW11). The force and drift ratio at the onset of horizontal cracking near the base of the wall were significantly smaller for SW1 than the other walls. Wall SW1 has an aspect ratio of 0.94 and was the tallest of the walls tested. There were no visible horizontal cracks near the base of walls SW10 and SW12. (SW10 and SW12 both failed in diagonal tension.) Tensile yielding of vertical reinforcement at the boundaries of the walls initiated at lateral forces between 87 kips (SW1) and 448 kips (SW9), average shear stresses between $1.5\sqrt{f_c'}$ (SW1) and $7.3\sqrt{f_c'}$ (SW8), and drift ratios between 0.10% (SW7) and 0.40% (SW10). Tensile yielding of the vertical reinforcement at the boundaries of SW1 occurred at a significantly smaller lateral force than in the other specimens, which is expected due to its higher aspect ratio.

4.4 Cracking and modes of failure

Diagonal cracks were observed on the webs of the shear-critical walls SW2 through SW12. A greater number of diagonal cracks were observed in the walls with higher horizontal and vertical reinforcement ratios. Fewer but wider cracks were observed in walls with lower horizontal and vertical reinforcement ratios. In SW11 and SW12, the walls with boundary elements, the orientation of the diagonal cracks on the web transitioned to horizontal at the web-boundary element junctions. (Moehle (2015) presents similar horizontal cracking patterns in the boundary flanges of slender structural walls.) Wall SW1, the wall with an aspect ratio of 0.94, had diagonal cracks at its mid-section and flexural cracks near its ends. Figure 4.4 shows the cracking patterns on one face of the 12 walls after two cycles of loading at displacement corresponding to peak strength. Shaded segments in Figure 4.4 identify spalled concrete.

In general, the lateral displacement at the centerline of loading at load steps prior and corresponding to peak shear strength was mainly due to the opening of the diagonal shear cracks throughout the web of the wall specimens (discussed in Section 4.6.2.2). The contributions of flexural cracks and sliding at the base of the wall were insignificant during load steps prior and corresponding to peak shear strength.

The shear-critical walls SW2 through SW12 failed either by diagonal tension or diagonal compression. Diagonal tension was chosen to describe a failure associated with wide cracks and measured horizontal rebar strains substantially greater than yield; diagonal compression was assumed otherwise. (Diagonal compression was related to the crushing of concrete near the toes of the walls.) Wall SW1 failed in a combination of flexure and shear. Figure 4.5 presents photographs of the damage to all the wall specimens at the end of testing. Additional photographs of damage to the specimens are provided in Appendix E.

Significant sliding at the base of the walls was observed in all the specimens except SW4 at load steps following the one corresponding to peak strength. Spalling of concrete along the base and at the toes of the wall was also observed. The vertical reinforcement near the base and near the toes of all walls, except SW2, SW5 and SW10, buckled and resulted into more spalling of concrete.

Spalling and crushing of concrete at the boundaries of all walls, except SW2, SW5 and SW10, made it possible to verify the condition of the 90º hooks to the horizontal reinforcement. None of the 90º hooks on the horizontal reinforcement at the boundaries of these low aspect ratio walls opened or disengaged during the testing. Yielding of horizontal reinforcement was observed from the strain gage data. These observations suggest that the 90º hooks are sufficient in the boundaries of low aspect ratio walls and that 135º hooks are unnecessary.

Specimens SW8 and SW10 have the same vertical reinforcement ratio (1.5%) and horizontal reinforcement ratios of 1.5% and 0.33%, respectively. The concrete compressive strength of SW10 is about 1.1 ksi greater than in SW8. Photographs of the damage to walls SW8 and SW10 are presented in Figure 4.6 at drift ratios of 1.3% (SW8) and 1.4% (SW10). The red arrows identify the direction of loading at the instant the photograph was taken. Although the drift ratios are similar, the damage to the two walls is very different: SW10 failed in diagonal tension whereas SW8 failed in diagonal compression. Wall SW10 had fewer but wider diagonal cracks than SW8. The amount and distribution of horizontal reinforcement affects the distribution and size of cracks in low aspect ratio RC shear walls.

4.5 Crack angles

Figure 4.4 presents patterns of concrete cracking for all the walls after two cycles of loading at displacement corresponding to peak strength. The rectangular grid of each wall are also shown. The vertical and horizontal lines (of the rectangular grid) were marked with letters and numbers, respectively, to facilitate the identification of cracks. The distances between the gridlines for each wall specimen are provided in Section C.2. A crack angle, θ, for each wall is determined by averaging the angles that the major cracks make with respect to the horizontal. Cracks that propagated diagonally over more than half the height of the wall were considered major. Table 4.2

identifies the major cracks for each wall and their angle with respect to the horizontal. The cracks were named with a combination of letters and numbers (e.g., A1-D5). The first combination of letter and number (A1) identifies where the crack originates, that is, at the intersection of vertical line A and horizontal line 1. The second combination of letter and number (D5) identifies where the crack ends. If the beginning (or ending) of a crack falls in between vertical or horizontal lines, the crack name will contain two letters and/or two numbers (e.g., AB1-D45). The angle of each crack is determined using the known distances between gridlines. The crack angle for each wall and the average crack angle for walls with the same aspect ratio are summarized in Table 4.3. The average crack angle for walls with aspect ratios of 0.94, 0.54 and 0.33 are 46°, 41° and 42°, respectively. (The angle of a crack with respect to the horizontal is typically assumed to be 45°.) The average crack angles are useful when analyzing the forces acting on the concrete compression struts and evaluating the equilibrium of different sections of the wall, both of which are needed to estimate the peak shear strength of low aspect ratio walls. The crack angles presented in this section are used in Chapter 6 to formulate equations for the peak shear strength of low aspect ratio RC walls with and without boundary elements.

4.6 Strain fields

Strain fields together with cracking patterns can help identify how forces flow through shears walls, in this case from the centerline of loading to the foundation. Data gathered from the strain gages attached to the horizontal and vertical reinforcement of the walls are presented to show the general distribution (in-plane) of strain. Data from the Krypton LED sensors attached on the face of the walls were processed and used to calculate the in-plane strain fields. The strain data obtained from strain gages should be similar/comparable to the strain measured from the Krypton LED sensors if there is a good bond between concrete and reinforcement in the walls. Comparisons of the strain data obtained from the strain gages and Krypton LED sensors are presented in Section 4.6.2.1.

4.6.1 Strain gage data

Strain gages were attached to the horizontal and vertical reinforcement of each wall. The Phase I and Phase II walls had an average of 52 and 84 strain gages, respectively. The installation of the strain gages are described in Section 3.4 and the locations are provided in Section C.2. Each wall had two curtains of reinforcement and the strain gages in each wall were all installed on just one curtain. A few strain gages in each wall did not function properly prior to testing, likely due to damage to the gages and/or their connecting wires sustained during the casting of concrete. Figure 4.7 shows the strains on the vertical reinforcement (measured from strain gages S8, S11 and S14) versus displacement at the centerline of loading of SW9. Strain gages S8 and S14 are located at the ends of the wall while strain gage S11 is located near the middle of the wall (see Figure C.21). Yielding of the reinforcement, as can be seen in panels A and B of Figure 4.7, started at around 2000 microstrains which was typically observed from all the strain gages of all the walls.

Figure 4.8 presents strains on the vertical reinforcement of each wall at peak lateral strength. The red arrow identifies the direction of loading. Positive strain corresponds to tension and negative strain corresponds to compression. The cracking patterns and the rectangular grid are also shown.

Several strain gages failed on SW1, particularly those near the bottom and at the ends of the wall. Almost all the vertical reinforcement with attached strain gages yielded in tension for walls SW2, SW3 and SW4 (aspect ratio of 0.54 and vertical reinforcement ratio of 1%, 0.67% and 0.33%, respectively). (The yielding was throughout the height of the wall for SW2 and SW3.) Similarly, all vertical reinforcement with attached strain gages yielded in tension over the height of the walls SW5, SW6 and SW7 (aspect ratio of 0.33 and vertical reinforcement ratio of 1%, 0.67% and 0.33%, respectively). For SW8, a wall with an aspect ratio of 0.54 and vertical reinforcement ratio of 1.5%, only about one-half of the vertical reinforcement yielded in tension. It appears that above a certain vertical reinforcement ratio threshold, between 1% and 1.5%, peak strength is achieved without all the vertical reinforcement yielding in tension. (Some equations for peak strength available in literature (e.g., Wood, 1990; Moehle, 2015) assume that all vertical reinforcement yields in tension.) Wall SW10 had a vertical and horizontal reinforcement ratio of 1.5% and 0.33%, respectively, and it failed in diagonal tension. The vertical reinforcement in SW10 did not yield, except that at the boundaries of the wall.

Figure 4.9 presents strains in the horizontal reinforcement of each wall at peak lateral strength. The strains in all the horizontal reinforcement of all the walls were tensile (positive). Yielding was measured mostly at the mid-depth of the wall. The strains in the horizontal reinforcement were small at the ends of the wall. In general, the magnitude of the strains measured on the horizontal reinforcement were significantly smaller than the strains measured on the vertical reinforcement, which suggests the contribution of the horizontal reinforcement to the total resisting force of a low aspect ratio wall is significantly smaller than the contribution of the vertical reinforcement.

The distributions of strain in the vertical and horizontal reinforcement for walls SW8, SW2 and SW3 were compared at 0.7% drift ratio. Walls SW8, SW2 and SW3 had an aspect ratio of 0.54 and reinforcement ratios (vertical and horizontal) of 1.5%, 1% and 0.67%, respectively. The lateral forces measured at the centerline of loading corresponding to 0.7% drift were 623 kips, 530 kips and 402 kips for walls SW8, SW2 and SW3, respectively. Figure 4.10 and Figure 4.11 show the distributions of strains on the vertical and horizontal reinforcement, respectively, of SW2 and SW3 at 0.7% drift ratio. For SW2 and SW3, the strains were measured during the load step that corresponds to the first excursion to 0.7% drift ratio. A drift ratio of 0.7% corresponds to the peak strength of SW8 and the distribution of strains on the vertical and horizontal reinforcement of SW8 at 0.7% drift ratio are presented in Figure 4.8h and Figure 4.9h, respectively. Tensile yielding of the vertical reinforcement of SW8 occurred only near the end of the wall in tension. Most of the vertical reinforcement of SW2 yielded in tension. All vertical reinforcement of SW3 yielded in tension. Tensile strains in the vertical reinforcement of the three walls were greatest in SW3 and smallest in SW8, confirming that the greater the vertical reinforcement ratio, the smaller the strain (and stress) at peak strength. All measured strains on the horizontal reinforcement of walls SW8, SW2 and SW3 were tensile, with maximum strains measured at the mid-length of the walls. The horizontal reinforcement yielded at the mid-length of walls SW2 and SW3 whereas none of the horizontal reinforcement in SW8 yielded.

4.6.2 Krypton LED data

Data gathered from the Krypton LED sensors were principally used to estimate the in-plane strain fields in the wall specimens at displacements, equal to or less than those at peak lateral strength. Four strains were calculated: 1) vertical strain, 2) horizontal strain, 3) shear strain, and 4) principal strain. The grid of Krypton LED sensors generated quadrilateral panels on the surface of the wall specimen. (The grid of Krypton LED sensors for each wall are presented in Section C.2.) The strains were calculated for each panel using the displacements measured by Krypton LED on each corner/node, which requires two assumptions, namely, 1) the response is linearly elastic, and 2) deformations are small. The first assumption is poor but necessary because the locations of cracks were not known prior to the installation of the LEDs. (Strains in a given panel are considered average values. For panels of LEDs that include cracks, average tensile strains will overestimate concrete tensile strain.)

A quadrilateral panel and the notations used to calculate the strains are presented in Figure 4.12. The vertical strains, ε_y, at the left and right of the panel were calculated by dividing the change in length of the side, ΔV, by the original length of the side (V_L or V_R). The horizontal strains, ε_x, at the top and bottom of the panel were calculated by dividing the change in length of the side, ΔH, by the original length of the side (V_T or V_B). To determine the average shear strain for the panel, the change in angle at each of the four corners were determined. The initial angle of each corner, α_{io}, was calculated using the law of cosines and is given by:

$$\alpha_{io} = \cos^{-1} \frac{H^2 + V^2 - D^2}{2HV} \qquad (i = 1, 2, 3, 4) \tag{4.1}$$

where *H* and *V* are the original lengths of the two sides of the panel adjacent to α_{io}, and *D* is the original length of the diagonal opposite to α_{io}. The final angle of each corner, α_i, was calculated by:

$$\alpha_i = \cos^{-1} \frac{(H + \Delta H)^2 + (V + \Delta V)^2 - (D + \Delta D)^2}{2(H + \Delta H)(V + \Delta V)} \qquad (i = 1, 2, 3, 4) \tag{4.2}$$

where ΔD is the change in length of the diagonal and all other variables are previously defined above. The change in angle for each corner was calculated by subtracting the initial angle from the final angle. The average shear strain, γ_{xy}, in each quadrilateral element was calculated as the average of the change in angle of the four corners. Average shear strains were used to calculate the shear deformations of the walls. The principal strains in each panel were estimated by:

$$\varepsilon_{1,2} = \frac{\varepsilon_x + \varepsilon_y}{2} \pm \sqrt{\left(\frac{\varepsilon_x - \varepsilon_y}{2}\right)^2 + \left(\frac{\gamma_{xy}}{2}\right)^2} \tag{4.3}$$

where the subscripts 1 and 2 correspond to the first (maximum) and second (minimum) principal strains, respectively. Generally, for the 12 walls tested here, the first principal strain is tensile and the second is compressive. The orientation of the principal strains (along which the principal strains act) for each panel, θ_p, was calculated by:

$$\tan 2\theta_p = \frac{\gamma_{xy}}{\varepsilon_x - \varepsilon_y} \tag{4.4}$$

Birely (2012) analyzed Krypton LED data from tests of four slender RC walls to determine in-plane strain fields. The LED sensors on the slender RC walls were arranged in a rectangular grid. She calculated axial and shear strains from LED displacements by geometry (method presented above) and a finite element formulation. Birely improved the usability of the strain information by averaging values of the strain quantity from the surrounding panels. A similar method was used here to calculate the strain fields.

The accuracy of the geometry-based method for predicting strains was evaluated using a finite element formulation described in Epackachi (2014). Strain fields in SW8 were established using both methods, using the finite element formulation as a benchmark. Strains were calculated at peak strength using a square panel of 16 LEDs. The axial and shear strains calculated using the geometry-based method described above were within 5% and 3%, respectively, of those calculated using the finite element formulation, providing confidence in the axial and shear strain data presented below.

The dimensions of the rectangular grid used for the Krypton LEDs for each wall specimen are provided in Section C.2. Walls SW2, SW3 and SW4, the first three specimens tested, had fewer LED sensors near the top of the grid due to unavailability of LED sensors at the time of testing. The upper part of wall SW1 (tallest of the walls tested, with an aspect ratio of 0.94) did not have LEDs near the top of the wall due to a limitation on the field of view of the Krypton camera.

4.6.2.1 Horizontal and vertical strain fields

The vertical and horizontal strain distributions calculated from the Krypton LED data of each wall at peak strength are presented in Figure 4.13 and Figure 4.14, respectively. The red arrow identifies the direction of loading. Positive strain is tensile. The cracking patterns and the rectangular grids with strain data are also shown. The color map is comparable to the color legend used for the strain gage data presented in the previous section.

The distributions of vertical strains at peak strength along the height and length of the 12 walls are qualitatively similar, defining three segments in each wall: information used in Chapter 6 to develop an equation for peak shear strength. The tensile and compressive vertical strains are greatest at the toes of the walls, and the former are greater than the latter. Much of the cross sections of the walls are subjected to positive (tensile) vertical strains.

The horizontal strains at peak strength in the 12 walls are positive (tensile). The horizontal strains are greatest at mid-length of the walls, where the widest cracks were observed. Greater average horizontal strains were calculated in the vicinity of diagonal cracks (e.g., see panels d and g of Figure 4.14) for the reason given previously. Figure 4.5j is a photograph of SW10 after testing. Concrete spalled from the edges of the concrete compression strut that formed between two wide diagonal cracks. The (blue) band of high average horizontal strain (Figure 4.14j) identifies the compression strut, noting that the calculated average strains overestimate those in the concrete alone because the calculation cannot accommodate the presence of discrete cracks.

Figure 4.15 presents ranges of strain on vertical reinforcement in SW8 at drift ratios less than that at associated with peak strength: 0.35% and 0.5%. Figure 4.16 presents vertical strains calculated from the Krypton LED sensors at 0.35% and 0.5% drift ratios. In general, the gage- and LED-calculated strains are in good agreement.

4.6.2.2 Shear and principal strain fields

The shear strain fields calculated using the LED data are presented in Figure 4.17. The distributions of the principal strains, ε_1 and ε_2, are shown in Figure 4.18 and Figure 4.19, respectively, where ε_1 corresponds to the first (maximum) principal strain and ε_2 corresponds to the second (minimum) principal strain. The observed pattern of cracking and the associated rectangular grid are also shown in the figures. Two color legends were used for the shear and ε_1

strain distributions: one for SW1 through SW7 and another for SW8 through SW12. The calculated shear and ε_1 strains in SW8 through SW12 were generally smaller than SW1 through SW7 and the use of different legends improves the presentation of the strain fields in the walls. Two color legends were used for ε_2: one for SW1 through SW5 and SW12, and another for SW6 through SW11.

There are three segments in each wall that are characterized by substantially different amplitudes of shear strain. Figure 4.20 identifies the three segments on the web of a wall, with and without boundary elements. The orientations of the boundaries between segments A and B, and segments B and C, is the same as that of the diagonal cracks. The shear strains are small in segments A and great in segments B. There are no-to-few cracks in segment A but a large number of cracks in segment B. The high local displacements caused by the cracks produce high average shear strains in segment B. The lateral displacement at the centerline of loading is due primarily to the opening of diagonal cracks, since sliding at the base of the wall is minimal at displacement corresponding to peak strength. The magnitude of the shear strains in segment C lies between those in segments A and B.

The distributions of principal strain ε_1 in the 12 walls are presented in Figure 4.18. The key observations from Figure 4.18 are: 1) the magnitude of ε_1 in segment B in all the walls is relatively high, which corresponds to the greater number and width of cracks in that region, and 2) the magnitude of ε_1 in segment A in all the walls is relatively small because there are few-to- no cracks and any crack was narrow. The distributions of principal strain ε_2 in the 12 walls are presented in Figure 4.19. For all the walls, the magnitude of ε_2 is significantly greater in segment B than in segments A and C. The magnitude of ε_2 is small and moderate in segments A and C, respectively. The orientations of the principal strains, θ_p , of each of the walls are shown in Figure 4.21. There is a very good agreement between the orientations of the principal strains and the patterns of cracking in all the 12 walls, which provides significant confidence in the strain calculations presented in this section.

4.7 Displacement components

Data collected from the Krypton LED sensors were used to calculate the components of total displacement at the centerline of loading of the walls. The components of the total displacement are 1) shear deformation, 2) flexural deformation, and 3) sliding at the base of the wall.

Figure 4.22 shows a typical grid of the Krypton LED sensors. The distances between the gridlines for each wall specimen are provided in Section C.2. (Note that SW1, SW2, SW3 and SW4 had fewer LED sensors near the top of the grid than the other walls.) To facilitate the calculation of the contribution of each component to the total deformation, the Krypton LED grid was divided into horizontal strips, as shown in Figure 4.22. The height of the strips were identical in each wall.

Birely (2012) explored different methods of determining the shear deformation in a RC wall specimen using data from a rectangular grid of Krypton LED sensors. The most appropriate method involves 1) calculating the average shear strain of all the panels in a strip, 2) determining the shear deformation of each strip by multiplying the average shear strain in each strip by the height of the strip, and 3) adding the shear deformations in each strip. This procedure was utilized here to determine the shear component of the total deformation of the walls. The sum of the shear displacements of all the strips were multiplied by the ratio of h_w/h_s (h_w is the distance from the foundation to the centerline of loading of the wall and h_s is the total height of the grid as shown in Figure 4.22 to determine the total shear component of the displacement at the centerline of loading.

The Krypton LEDs at the bottom of the grid of all the walls were located 2 inches above the foundation. The component of the total displacement that corresponds to the sliding at the base of the wall was calculated as the average horizontal displacement of all the LED sensors located at the bottom of the grid, noting that there was no movement (sliding) of the foundation. The flexural component of the total lateral displacement at the centerline of loading was calculated as the difference between the total lateral displacement and the sum of shear and base sliding displacements.

Figure 4.23 presents the shear, flexure and base sliding components of the total lateral displacement at the centerline of loading as a function of drift ratio. From this figure, it can be observed that

1) The contribution of base sliding prior to achieving peak shear strength is relatively small for all of the walls bar SW4. This indicates that equations for peak shear strength of low aspect ratio RC walls that are based on sliding (shear friction) at the base of the wall is not appropriate.
2) Significant sliding at the base of the walls is observed after achieving peak shear strength.
3) The shear component of the total displacement of walls SW5, SW6 and SW7 (aspect ratio of 0.33) is significantly greater than those due to flexure and base sliding at displacements less than or equal to those associated with peak shear strength.
4) The contribution of flexure to the total lateral displacement is significantly greater in SW1 (aspect ratio of 0.94) than in the remaining walls.

There is no post-peak strength LED data for some of the walls. Many LEDs at the bottom of the grid had to be removed from some of the walls during post-peak strength displacement increments to prevent their damage due to crushing of concrete. It was difficult or impossible to evaluate shear strain and base sliding at the bottom panel of the rectangular grid with many missing LEDs.

4.8 Out-of-plane displacement

Out-of-plane (OOP) displacement and twisting of RC shear walls can occur in the field during earthquake shaking. Building framing system can translate and rotate in plan (twist) during an earthquake due to 1) irregular framing, 2) accidental torsion, 3) non-uniform yielding of member in the lateral-force-resisting system, and 4) torsional ground motions. The loading apparatus used during the tests of the 12 specimens did not prevent the walls from moving OOP. String potentiometers, attached on the top of the wall approximately 16 inches above the centerline of loading, were used to monitor OOP displacements. The OOP displacement and twisting of the walls, normalized by their height, in the first and third quadrants of loading to peak strength are presented in Table 4.4. The effects of OOP displacement on initial stiffness and peak shear strength are discussed in Chapter 5 and Chapter 6, respectively.

4.9 Strength and stiffness degradation

Walls in buildings and safety related nuclear structures are expected to maintain their strength for multiple cycles of loading at and beyond the displacement corresponding to peak shear strength.

Figure 4.24 shows the loss of stiffness in SW1 with repeated cycling to the displacement corresponding to peak strength. To quantify the loss of stiffness in the 12 walls, shear strengths V_1, V_2 and V_3 (marked with open red circles in Figure 4.24) were extracted from the first quadrant hysteresis loops of each specimen. Force V_1 corresponds to the peak shear strength at a displacement *D*; forces V_2 and V_3 correspond to the shear strength at the second and third excursions to the displacement *D*. Table 4.5 presents the ratios V_2/V_1 and V_3/V_1, which is related to the loss of stiffness of the wall with repeated cycling to displacements corresponding to peak strength. On the second (third) excursion to *D*, the secant stiffness to shear strength is as low as 60% (40%) of the secant stiffness to peak shear strength. Walls SW9 and SW10 (vertical reinforcement ratio of 1.5% and horizontal reinforcement ratio of 0.67% and 0.33%, respectively) had the smallest loss of stiffness after two excursions to D. The 12 walls show a rapid loss of maximum resistance after achieving peak shear strength, at either the same lateral displacement (in a subsequent cycle) or a greater displacement. It is evident from the ratios presented in Table 4.5 that these 12 walls show a rapid loss of stiffness after achieving peak shear strength.

The force-displacement relationships of the walls without boundary elements (see panels a to j of Figure 4.1) show a rapid loss of maximum resistance at cycles of displacement beyond that associated with peak shear strength. Walls SW11 and SW12, the two walls with boundary elements, maintained their resistance for multiple cycles of loading at displacements greater than that associated with peak strength (see panels k and l of Figure 4.1).

Table 4.1. Summary of forces and drift ratios at the initiation of cracking in concrete and yielding of reinforcement

Wall	Diagonal cracking			Horizontal cracking near the base of the wall			Tensile yielding of boundary vertical reinforcement		
	Force (kips)	Avg. shear stress $\left(\times\sqrt{f_c'}\right)$	Drift ratio (%)	Force (kips)	Avg. shear stress $\left(\times\sqrt{f_c'}\right)$	Drift ratio (%)	Force (kips)	Avg. shear stress $\left(\times\sqrt{f_c'}\right)$	Drift ratio (%)
SW1	57	1.0	0.055	57	1.0	0.055	87	1.5	0.12
SW2	153	1.9	0.079	341	4.2	0.31	371	4.6	0.35
SW3	132	1.6	0.060	132	1.6	0.060	134	1.6	0.12
SW4	84	1.4	0.044	160	2.6	0.14	141	2.3	0.11
SW5	68	1.1	0.020	551	8.8	0.47	310	4.9	0.23
SW6	124	2.1	0.060	280	4.7	0.23	245	4.1	0.20
SW7	139	2.3	0.060	273	4.6	0.41	149	2.5	0.10
SW8	215	3.8	0.10	623	11.0	0.70	413	7.3	0.29
SW9	221	3.5	0.10	485	7.7	0.31	448	7.1	0.27
SW10	127	2.0	0.021	-	-	-	416	6.4	0.40
SW11	201	3.0	0.12	381	5.6	0.39	296	4.4	0.26
SW12	94	1.4	0.057	-	-	-	314	4.6	0.32

Table 4.2. Crack angles at load step corresponding to peak strength

Wall	Crack ID	No. of grids (horizontal)	Run (in)	No. of grids (vertical)	Rise (in)	Angle (º)	Ave. Angle (º)
SW1	B5-EF10	4.5	47.25	5	52.5	48.0	45.8
	AB2-HI10	6.5	68.25	8	84	50.9	
	FG78-J10	3.5	36.75	2.5	26.25	35.5	
	BC23-F67	3.5	36.75	4	42	48.8	
SW2	A1-G8	6	48	7	49	45.6	39.2
	D4-H8	4	32	4	28	41.2	
	BC2-H78	5.5	44	5.5	38.5	41.2	
	DE3-IJ8	5	40	5	35	41.2	
	BC1-J78	7.5	60	6.5	45.5	37.2	
	D1-L8	8	64	7	49	37.4	
	J45-M7	3	24	2.25	15.75	33.3	
	GH1-K4	3.5	28	3	21	36.9	
SW3	BC3-G8	4.5	36	5	35	44.2	38.7
	B1-H8	6	48	7	49	45.6	
	CD12-J8	6.5	52	6	42	38.9	
	CD1-K8	7.5	60	7	49	39.2	
	H4-M8	5	40	4	28	35.0	
	G23-NO8	7.5	60	5.5	38.5	32.7	
	H2-M6	5	40	4	28	35.0	
SW4	A12-F8	5	46.6	6	48	45.9	43.3
	F1-L8	6	55.9	6	48	40.7	
SW5	A1-DE5	3.5	22.75	4	29	51.9	42.7
	B1-F5	4	26	4	29	48.1	
	CD1-GH5	4	26	4	29	48.1	
	EF2-J5	4.5	29.25	3	21.75	36.6	
	F1-I34	3	19.5	2.5	18.125	42.9	
	H2-L5	4	26	3	21.75	39.9	
	IJ2-MN5	4	26	3	21.75	39.9	
	IJ1-N5	4.5	29.25	4	29	44.8	
	L23-PQ5	4.5	29.25	2.5	18.125	31.8	
SW6	B1-FG5	4.5	29.25	4	29	44.8	42.4
	C1-H5	5	32.5	4	29	41.7	
	D1-I5	5	32.5	4	29	41.7	
	F1-J4	4	26	3	21.75	39.9	
	HI1-M5	4.5	29.25	4	29	44.8	
	J1-O5	5	32.5	4	29	41.7	

Table 4.2. Crack angles at load step corresponding to peak strength (continued)

Wall	Crack ID	No. of grids (horizontal)	Run (in)	No. of grids (vertical)	Rise (in)	Angle (º)	Ave. Angle (º)
SW7	C1-H5	5	32.5	4	29	41.7	41.2
	GH1-L5	4.5	29.25	4	29	44.8	
	KL3-N5	2.5	16.25	2	14.5	41.7	
	J1-M3	3	19.5	2	14.5	36.6	
SW8	CD2-F56	3	21	3.5	24.5	49.4	41.7
	C1-I67	6	42	6.5	45.5	47.3	
	FG5-J8	3.5	24.5	3	21	40.6	
	E2-L8	7	49	6	42	40.6	
	FG2-M8	6.5	45.5	6	42	42.7	
	G2-NO8	7.5	52.5	6	42	38.7	
	H2-NO7	6.5	45.5	5	35	37.6	
	H1-P7	8	56	6	42	36.9	
SW9	Q3-M8	4	28	5	35	51.3	42.8
	Q1-KL8	6.5	45.5	7	49	47.1	
	OP1-I8	6.5	45.5	7	49	47.1	
	O1-H8	8	56	7	49	41.2	
	NO1-F8	8.5	59.5	7	49	39.5	
	M1-D8	9	63	7	49	37.9	
	J23-C8	7	49	6.5	45.5	42.9	
	KL1-C7	8.5	59.5	6	42	35.2	
SW10	R1-LM8	5.5	38.5	7	49	51.8	41.3
	PQ1-JK8	6	42	7	49	49.4	
	P1-H8	8	56	7	49	41.2	
	N2-F8	8	56	6	42	36.9	
	N1-D8	10	70	7	49	35.0	
	LM1-DE6	7.5	52.5	5	35	33.7	
SW11	CD3-HI8	5	35	5	35	45.0	40.1
	B1-J8	8	56	7	49	41.2	
	D1-JK8	6.5	45.5	7	49	47.1	
	F3-LM8	6.5	45.5	5	35	37.6	
	F1-OP8	9.5	66.5	8	56	40.1	
	G1-N5	7	49	4	28	29.7	
SW12	P45-LM8	3.5	24.5	3.5	24.5	45.0	40.1
	Q1-JK8	6.5	45.5	7	49	47.1	
	L4-H8	4	28	4	28	45.0	
	O1-F8	9	63	7	49	37.9	
	NO1-KL3	3	21	2	14	33.7	
	IJ3-CD8	6	42	5	35	39.8	
	HI3-C67	5.5	38.5	3.5	24.5	32.5	

Table 4.3. Summary of the crack angles at peak strength

Aspect ratio	Wall	Crack angle	Avg. crack angle
0.94	SW1	45.8	45.8
0.54	SW2	39.2	40.9
	SW3	38.7	
	SW4	43.3	
	SW8	41.7	
	SW9	42.8	
	SW10	41.3	
	SW11	40.1	
	SW12	40.1	
0.33	SW5	42.7	42.1
	SW6	42.4	
	SW7	41.2	

Table 4.4. Out-of-plane displacement and twisting (normalized by the height of the wall)

Wall	Measured drift ($\times 10^{-3}$)		Measured twist (rad/in $\times 10^{-6}$)	
	First quadrant (2)	Third quadrant (3)	First quadrant (4)	Third quadrant (5)
SW1	7.5	-1.9	53.1	-5.3
SW2	-21.5	-2.9	-133.8	43.1
SW3	-7.1	-1.1	-43.1	15.4
SW4	-10.3	-1.1	-69.2	-1.5
SW5	-10.5	-0.2	-48.8	22.0
SW6	-5.1	0.5	-34.1	4.9
SW7	-4.4	-1.7	-4.9	17.1
SW8	-0.3	-0.5	3.1	18.5
SW9	1.8	0.6	23.1	-0.3
SW10	0.2	2.6	-4.6	24.6
SW11	0.9	0.6	-6.2	10.8
SW12	-1.5	0.9	-6.2	16.9

Table 4.5. Reduction in peak strength with repeated cycling

Wall	$\frac{V_2}{V_1}$	$\frac{V_3}{V_1}$
SW1	0.84	0.79
SW2	0.79	0.70
SW3	0.60	0.42
SW4	0.72	0.67
SW5	0.92	0.40
SW6	0.86	0.79
SW7	0.84	0.75
SW8	0.80	0.68
SW9	0.86	0.80
SW10	0.92	0.90
SW11	0.82	0.75
SW12	0.77	0.73

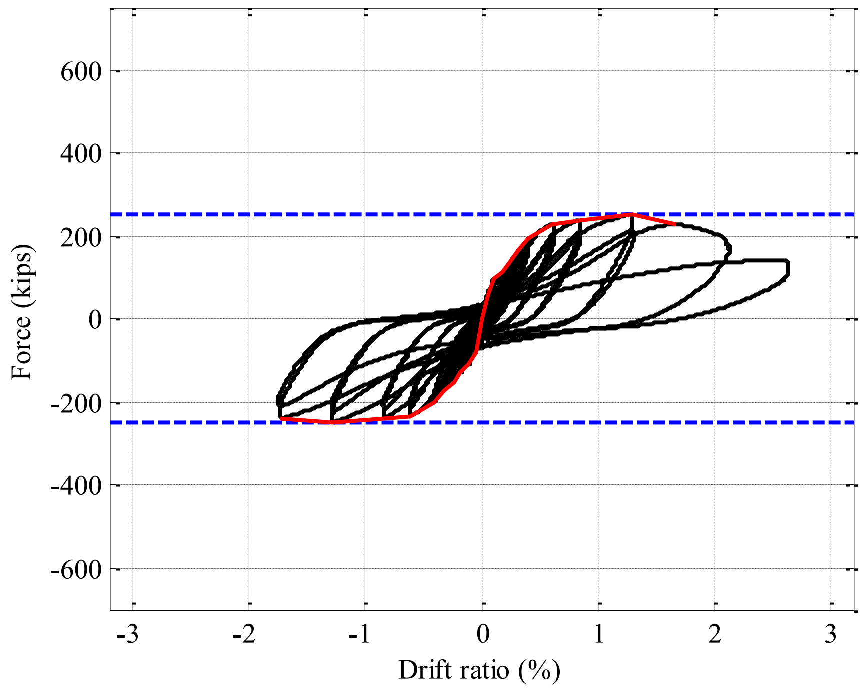

a) SW1 (0.94, 0.67%, 0.67%, 3600 psi)

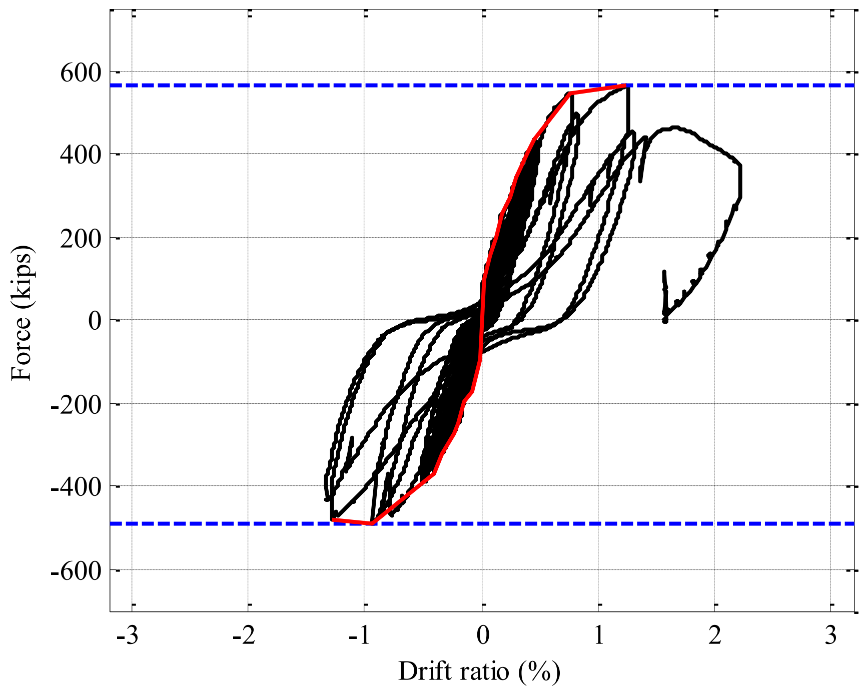

b) SW2 (0.54, 1.0%, 1.0%, 7000 psi)

Figure 4.1. Global force-displacement relationships of the wall specimens

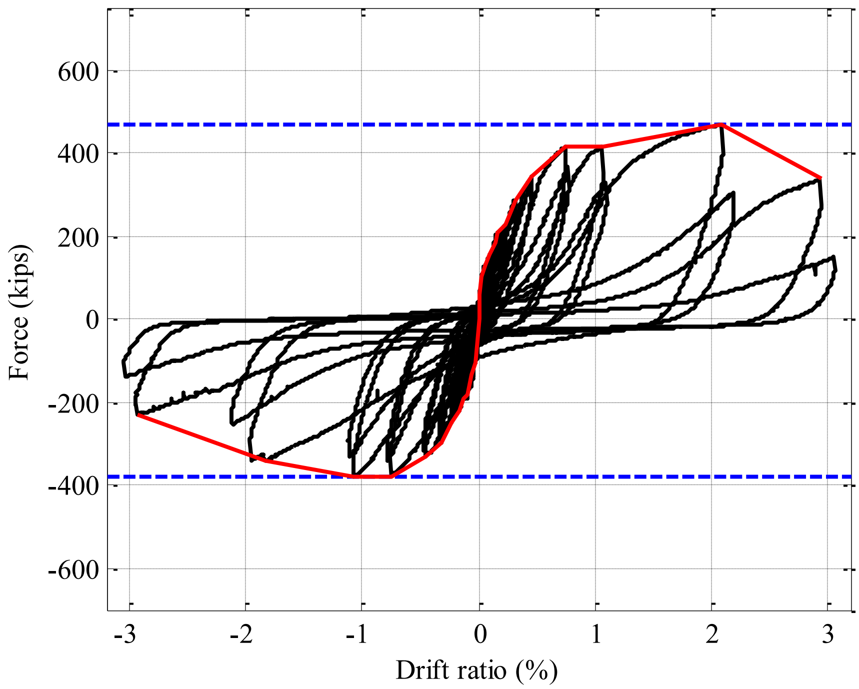

c) SW3 (0.54, 0.67%, 0.67%, 7800 psi)

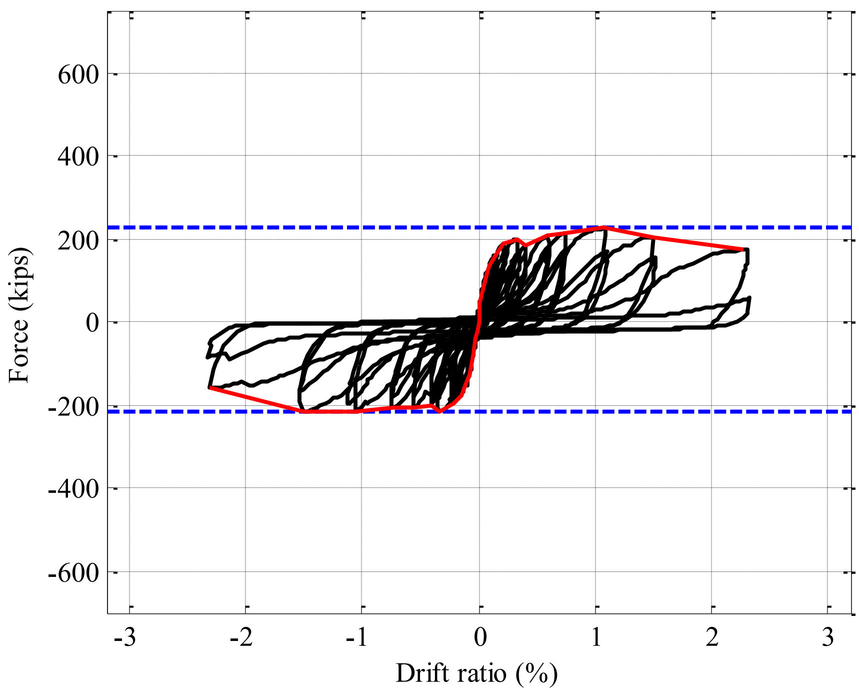

d) SW4 (0.54, 0.33%, 0.33%, 4200 psi)

Figure 4.1. Global force-displacement relationships of the wall specimens (continued)

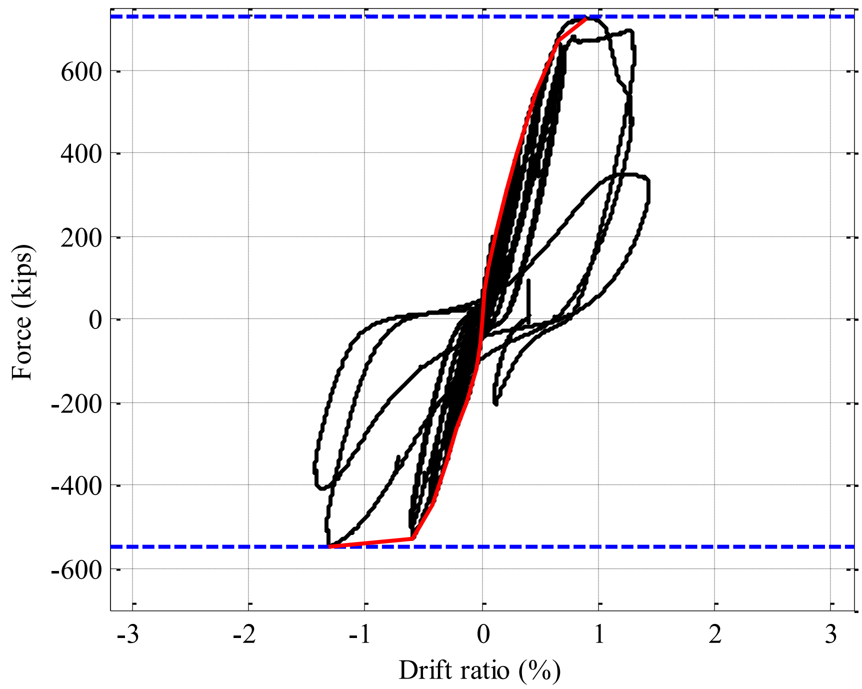

e) SW5 (0.33, 1.0%, 1.0%, 4300 psi)

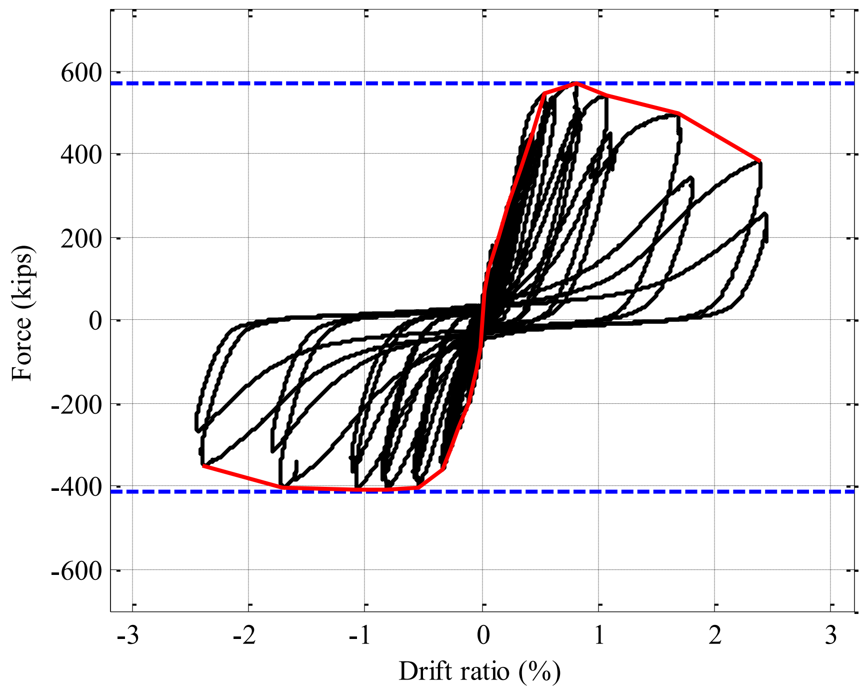

f) SW6 (0.33, 0.67%, 0.67%, 3800 psi)

Figure 4.1. Global force-displacement relationships of the wall specimens (continued)

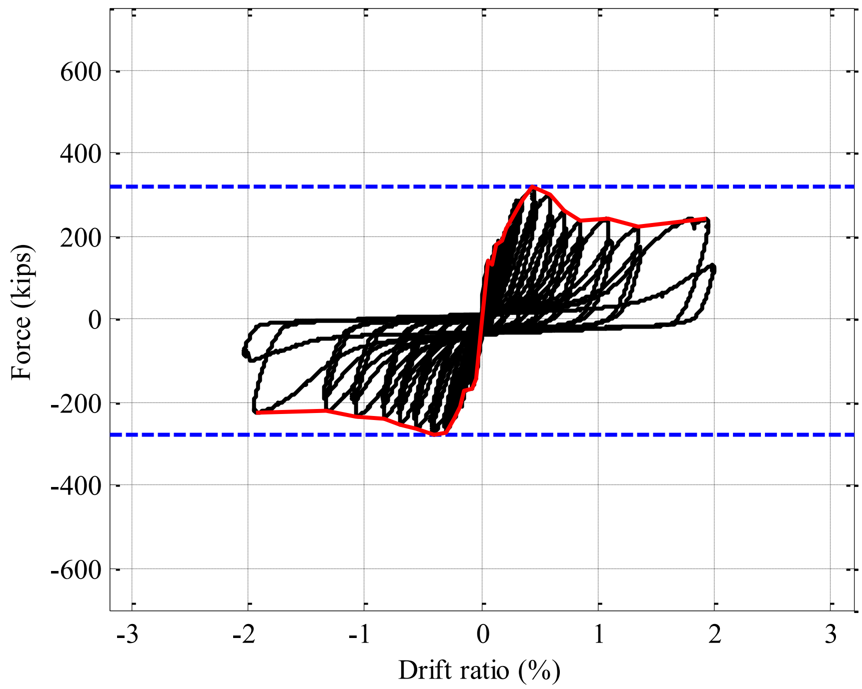

g) SW7 (0.33, 0.33%, 0.33%, 3800 psi)

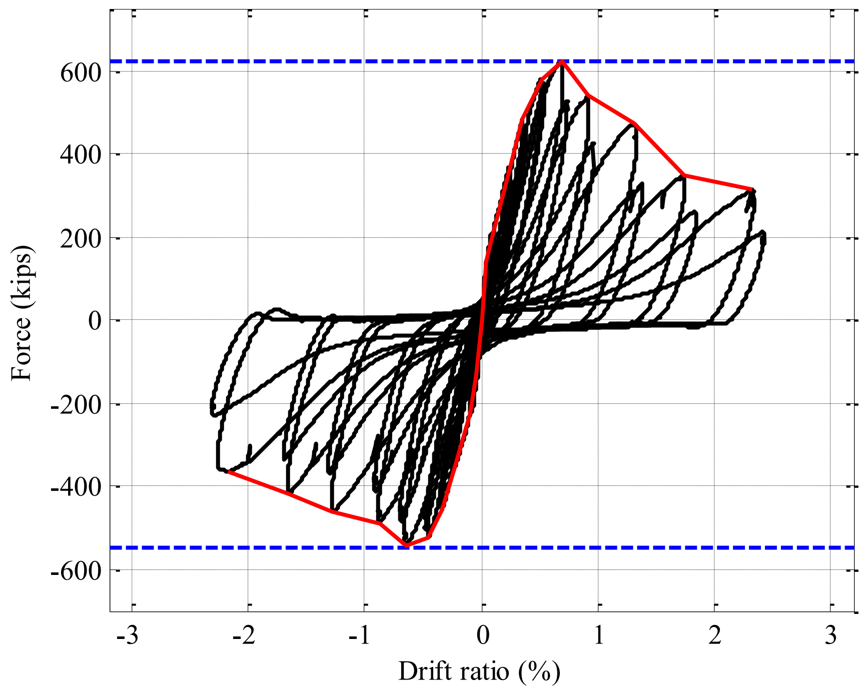

h) SW8 (0.54, 1.5%, 1.5%, 3500 psi)

Figure 4.1. Global force-displacement relationships of the wall specimens (continued)

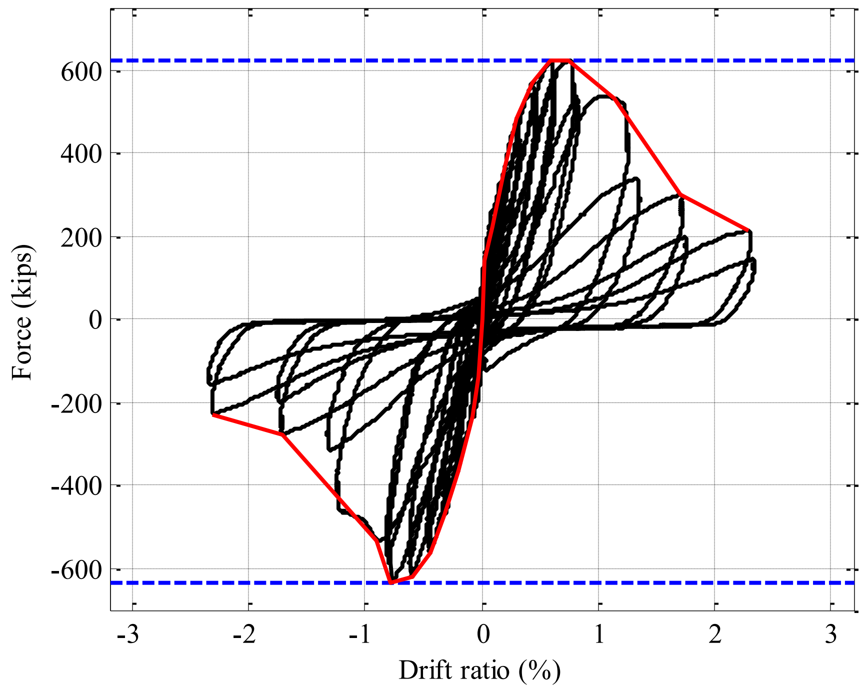

i) SW9 (0.54, 0.67%, 1.5%, 4300 psi)

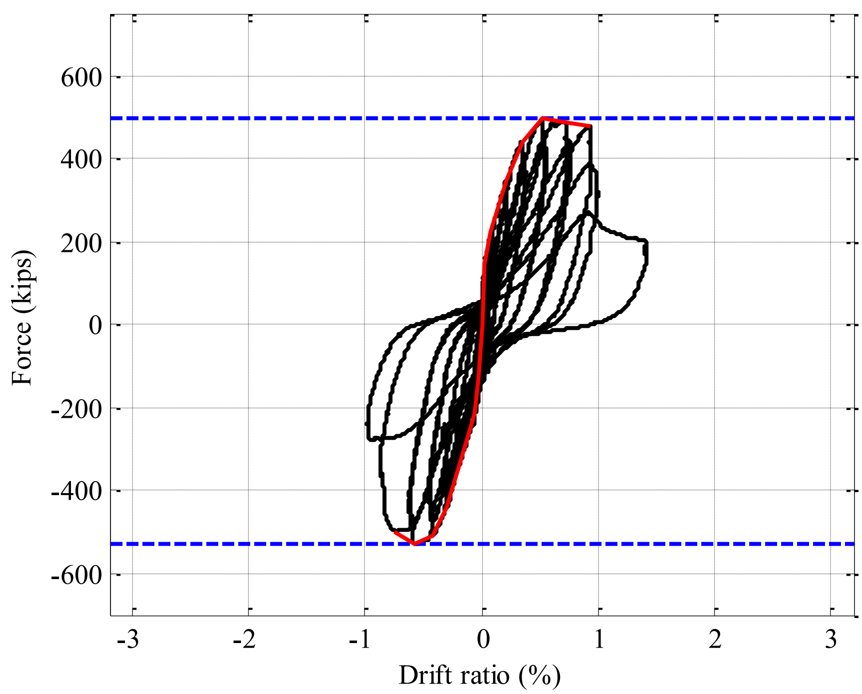

j) SW10 (0.54, 0.33%, 1.5%, 4600 psi)

Figure 4.1. Global force-displacement relationships of the wall specimens (continued)

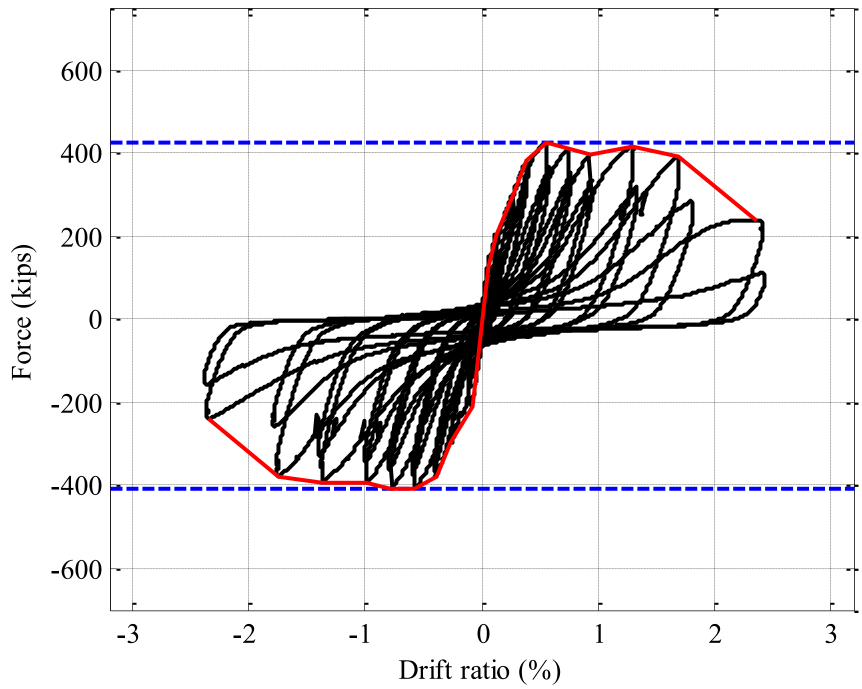

k) SW11 (0.54, 0.67%, 0.67%, 1.5% be, 5000 psi)

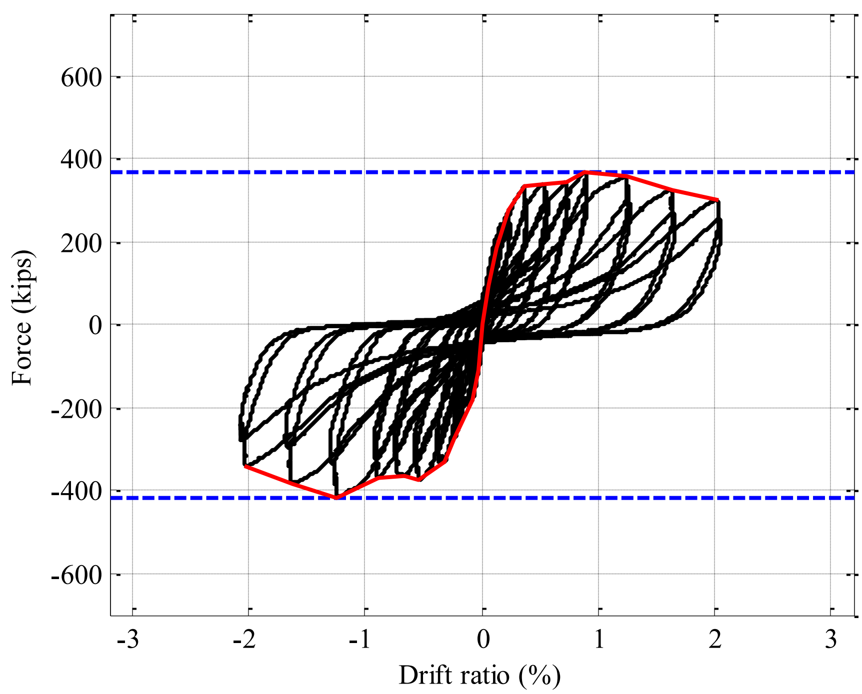

l) SW12 (0.54, 0.33%, 0.33%, 2.0% be, 5000 psi)

Figure 4.1. Global force-displacement relationships of the wall specimens (continued)

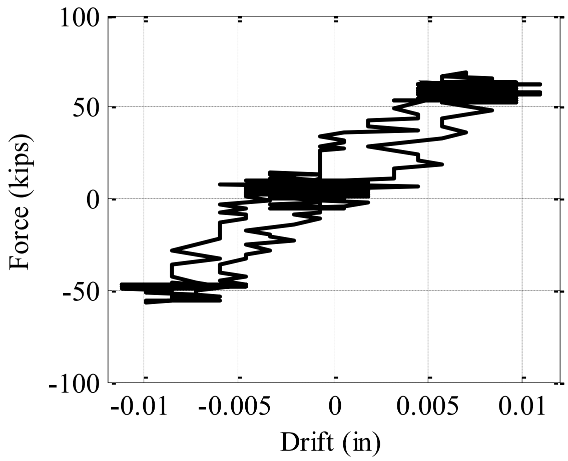

a) String potentiometers

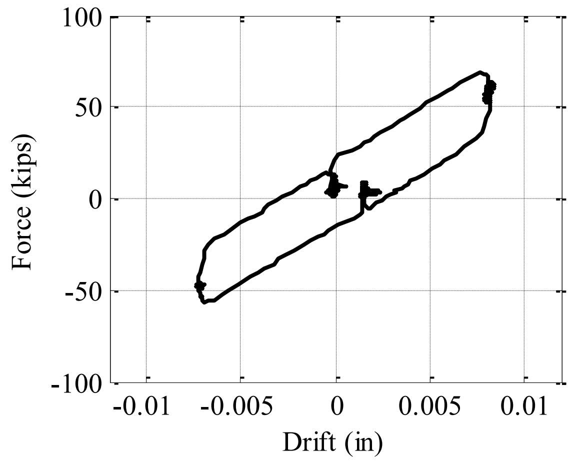

b) Temposonics

Figure 4.2. Comparison of data collected from string potentiometers and Temposonics at small drifts

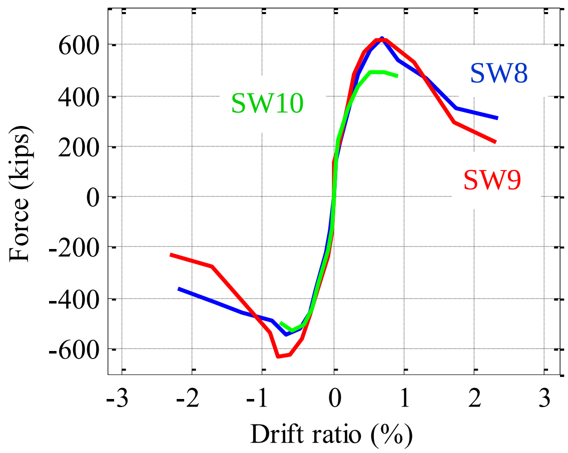

a) SW8, SW9 and SW10

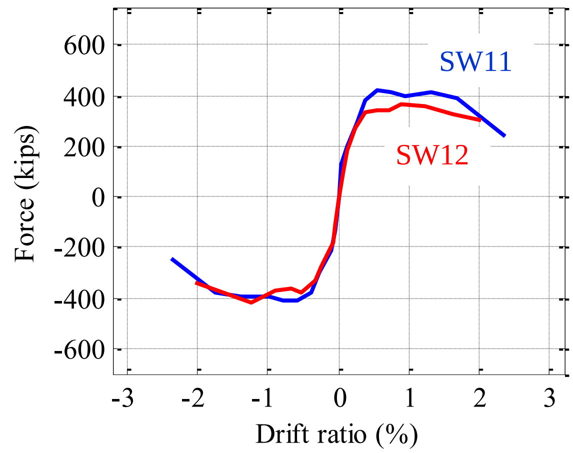

b) SW11 and SW12

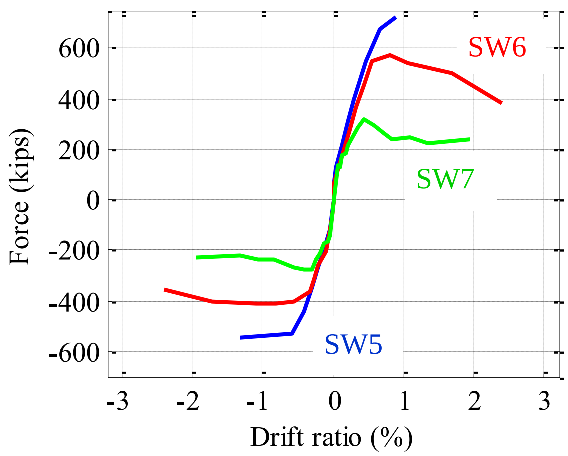

c) SW5, SW6 and SW7

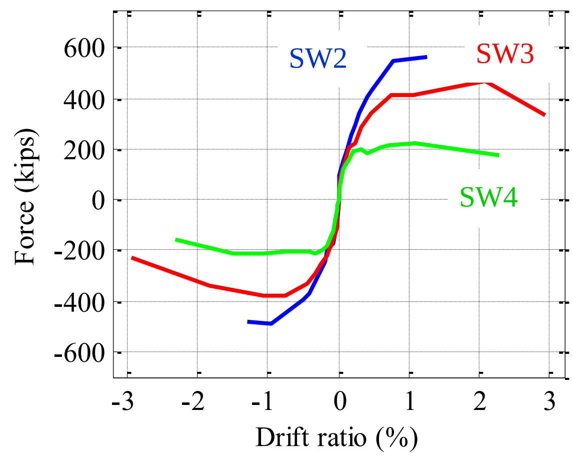

d) SW2, SW3 and SW4

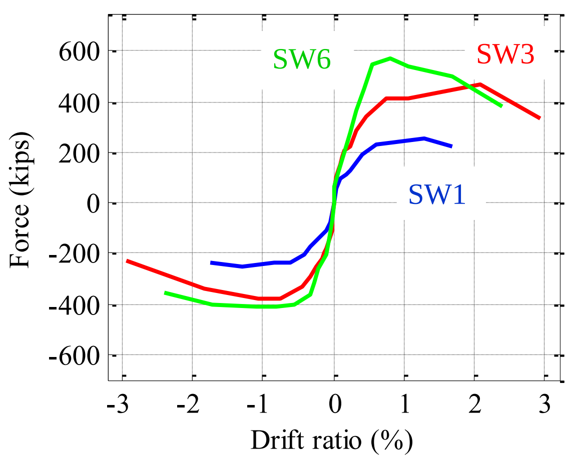

e) SW1, SW3 and SW6

Figure 4.3. Cyclic backbone curves

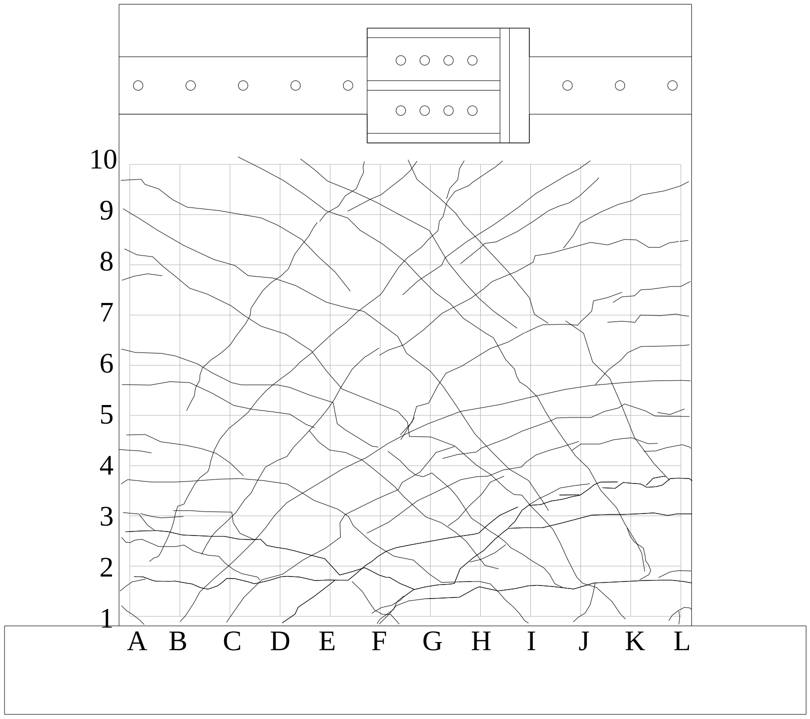

a) SW1 (0.94, 0.67%, 0.67%, 3600 psi)

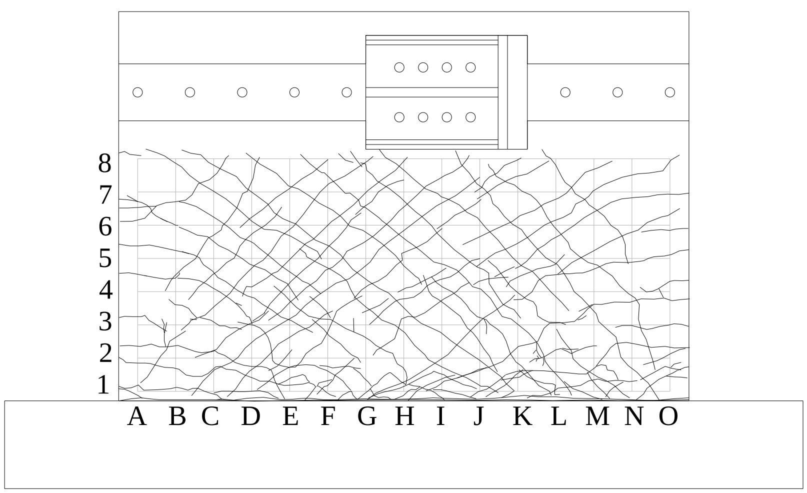

b) SW2 (0.54, 1.0%, 1.0%, 7000 psi)

Figure 4.4. Cracking patterns after two cycles of loading at displacement corresponding to pea k strength

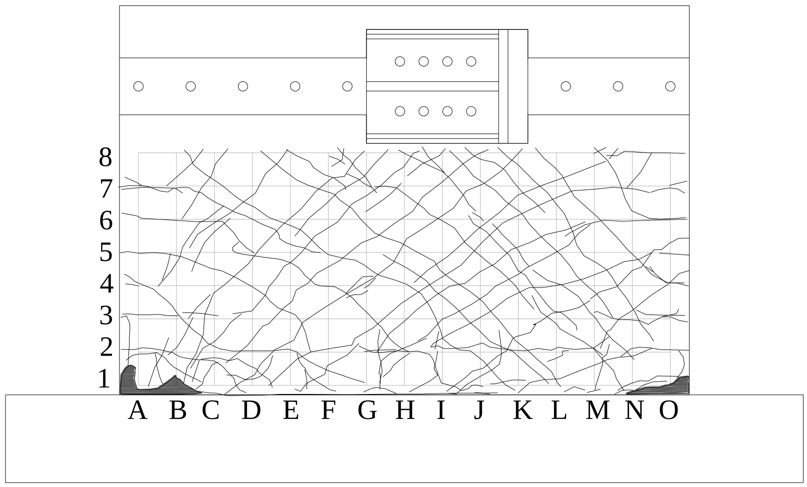

c) SW3 (0.54, 0.67%, 0.67%, 7800 psi)

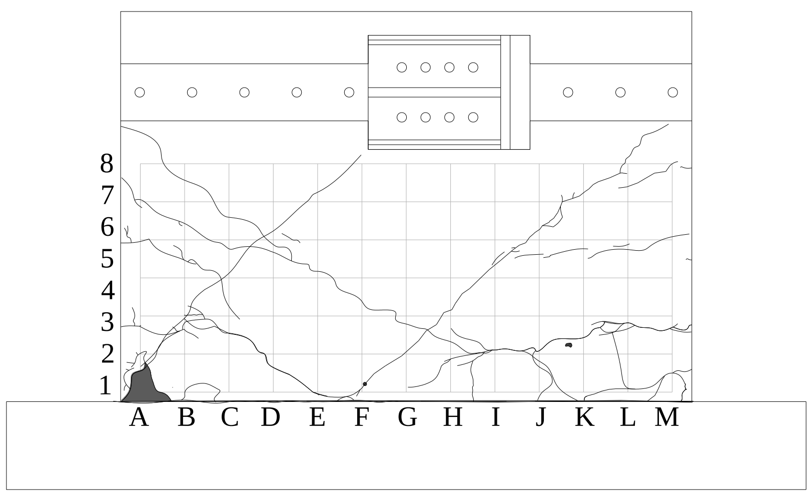

d) SW4 (0.54, 0.33%, 0.33%, 4200 psi)

Figure 4.4. Cracking patterns after two cycles of loading at displacement corresponding to pea k strength (continued)

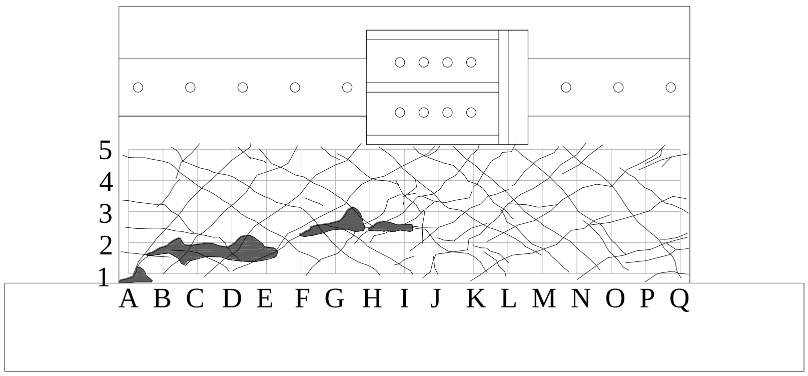

e) SW5 (0.33, 1.0%, 1.0%, 4300 psi)

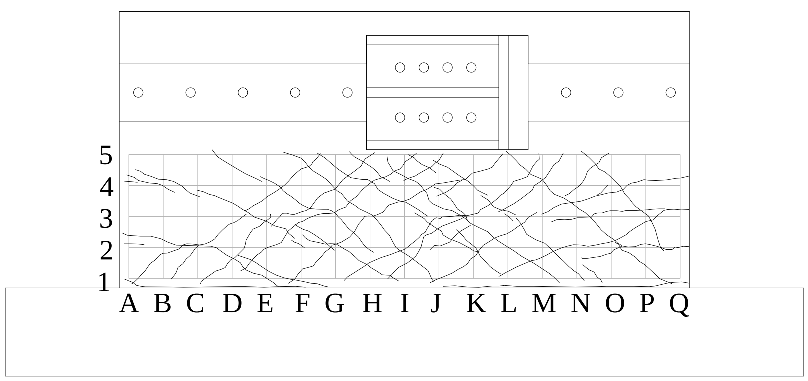

f) SW6 (0.33, 0.67%, 0.67%, 3800 psi)

Figure 4.4. Cracking patterns after two cycles of loading at displacement corresponding to pea k strength (continued)

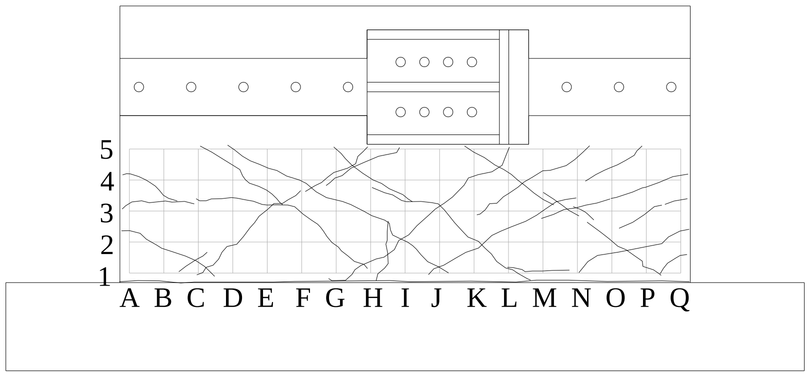

g) SW7 (0.33, 0.33%, 0.33%, 3800 psi)

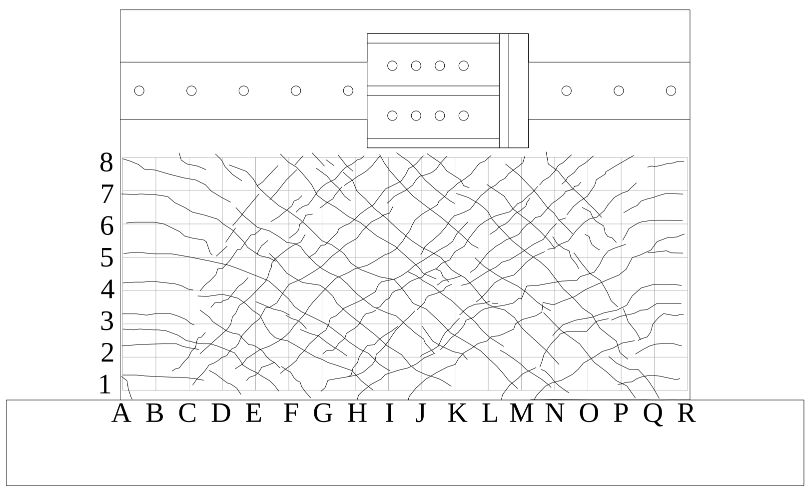

h) SW8 (0.54, 1.5%, 1.5%, 3500 psi)

Figure 4.4. Cracking patterns after two cycles of loading at displacement corresponding to pea
k strength (continued)

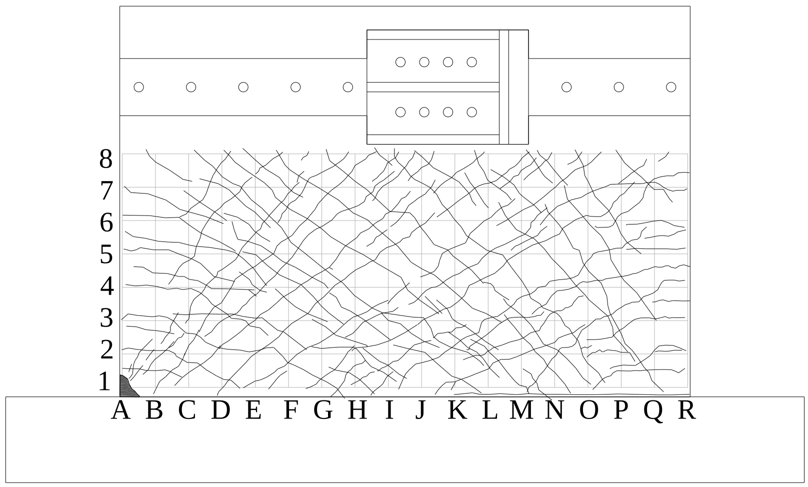

i) SW9 (0.54, 0.67%, 1.5%, 4300 psi)

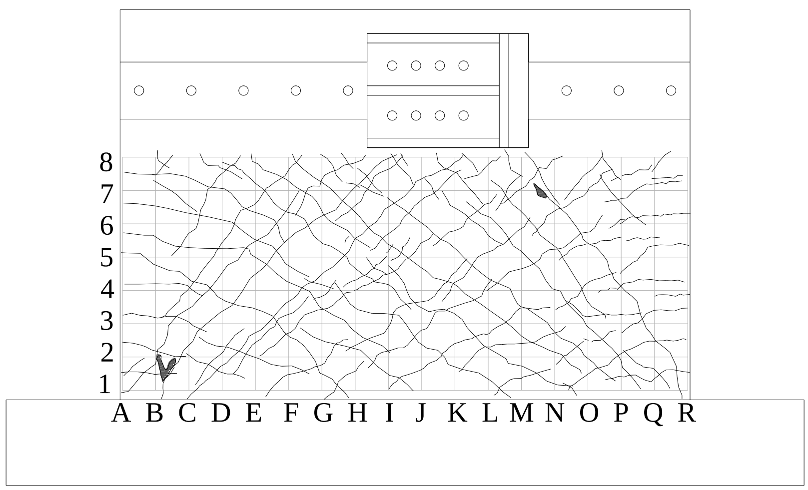

j) SW10 (0.54, 0.33%, 1.5%, 4600 psi)

Figure 4.4. Cracking patterns after two cycles of loading at displacement corresponding to pea k strength (continued)

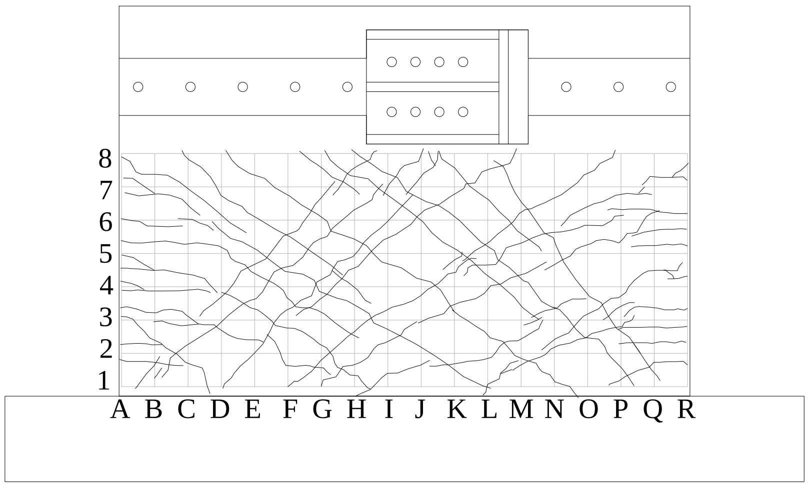

k) SW11 (0.54, 0.67%, 0.67%, 1.5% be, 5000 psi)

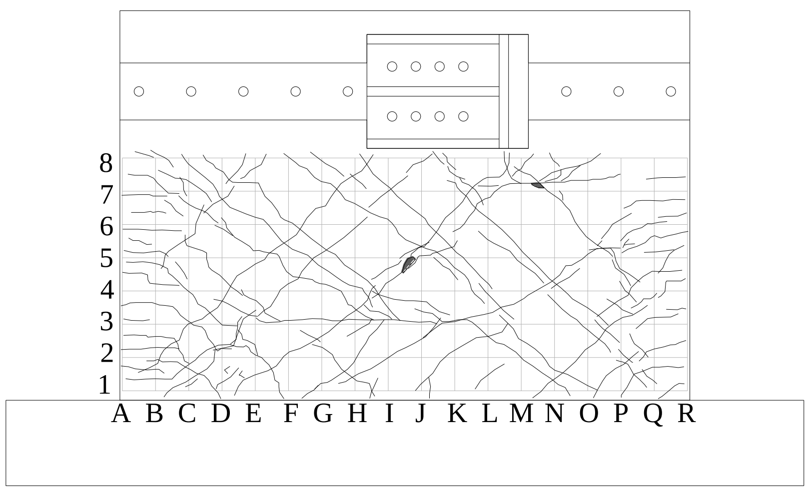

l) SW12 (0.54, 0.33%, 0.33%, 2.0% be, 5000 psi)

Figure 4.4. Cracking patterns after two cycles of loading at displacement corresponding to pea k strength (continued)

a) SW1 (0.94, 0.67%, 0.67%, 3600 psi)

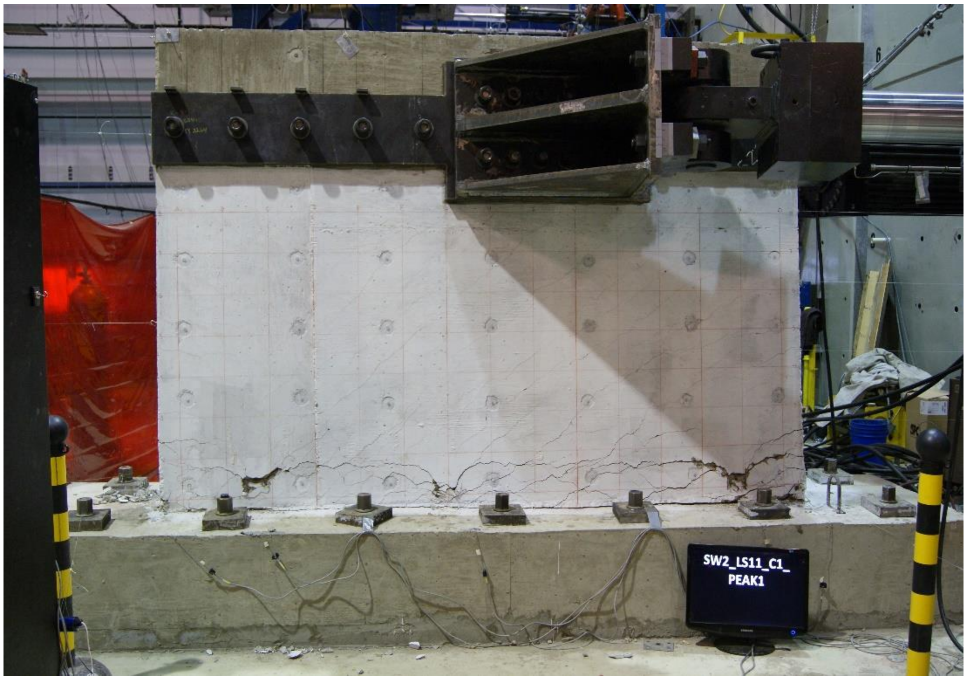

b) SW2 (0.54, 1.0%, 1.0%, 7000 psi)

Figure 4.5. Damage state of the walls at the end of testing

c) SW3 (0.54, 0.67%, 0.67%, 7800 psi)

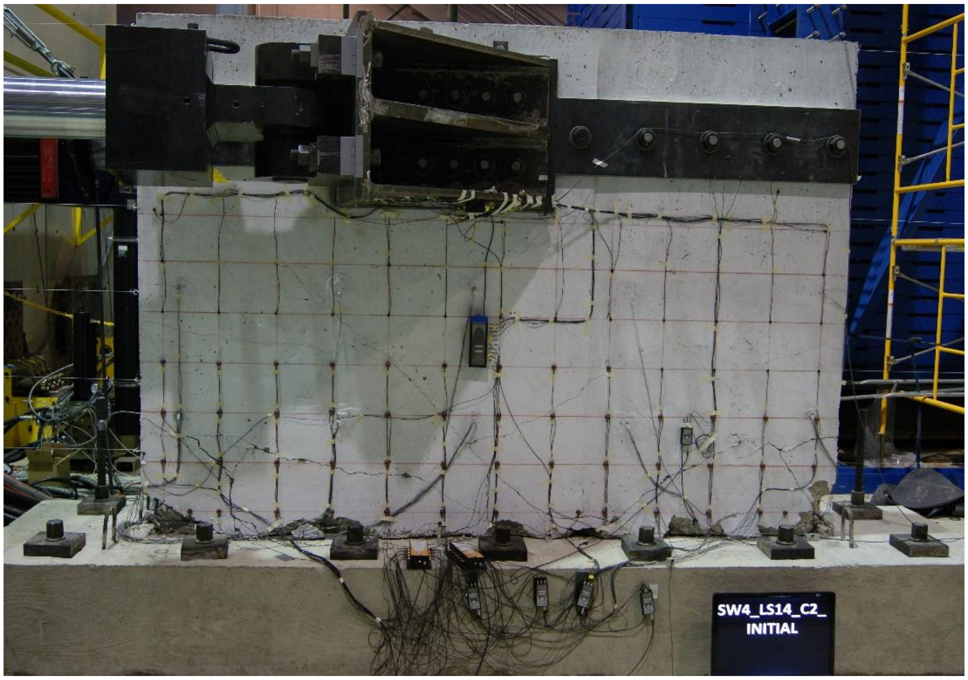

d) SW4 (0.54, 0.33%, 0.33%, 4200 psi)

Figure 4.5. Damage state of the walls at the end of testing (continued)

e) SW5 (0.33, 1.0%, 1.0%, 4300 psi)

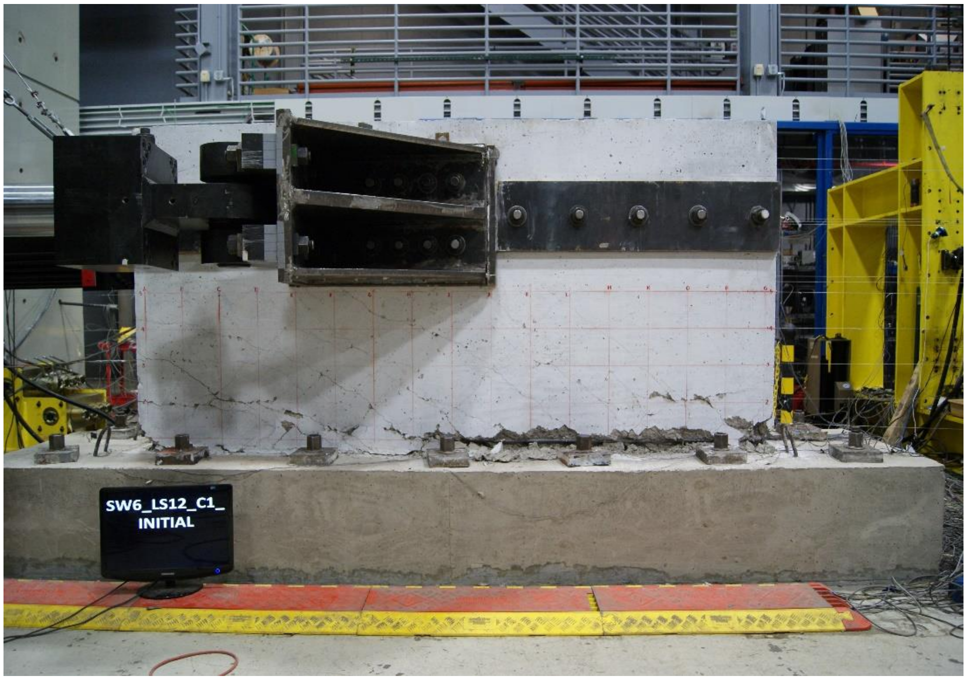

f) SW6 (0.33, 0.67%, 0.67%, 3800 psi)

Figure 4.5. Damage state of the walls at the end of testing (continued)

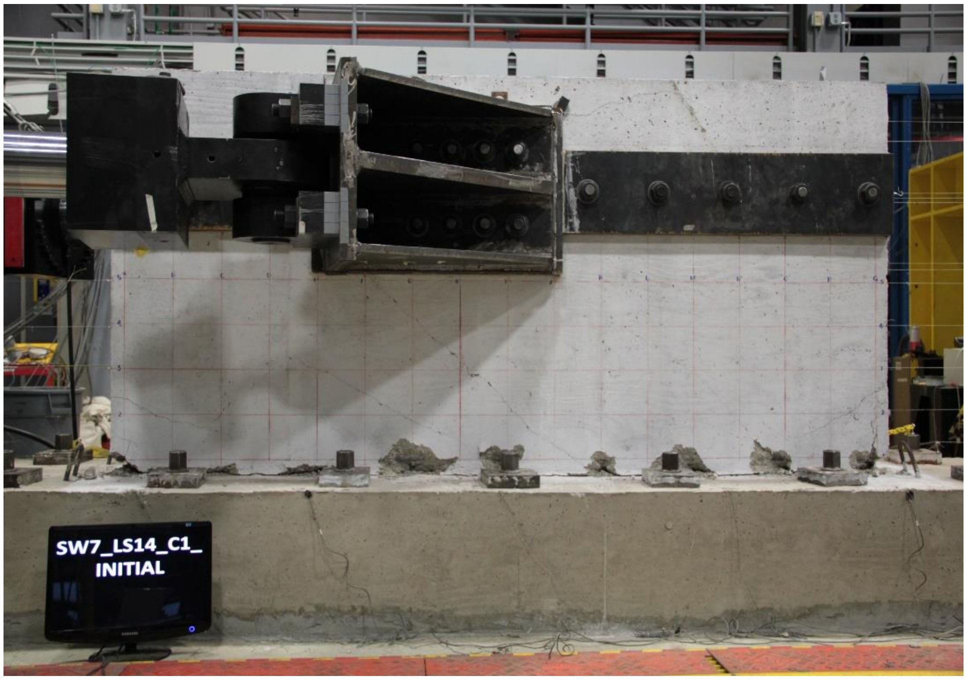

g) SW7 (0.33, 0.33%, 0.33%, 3800 psi)

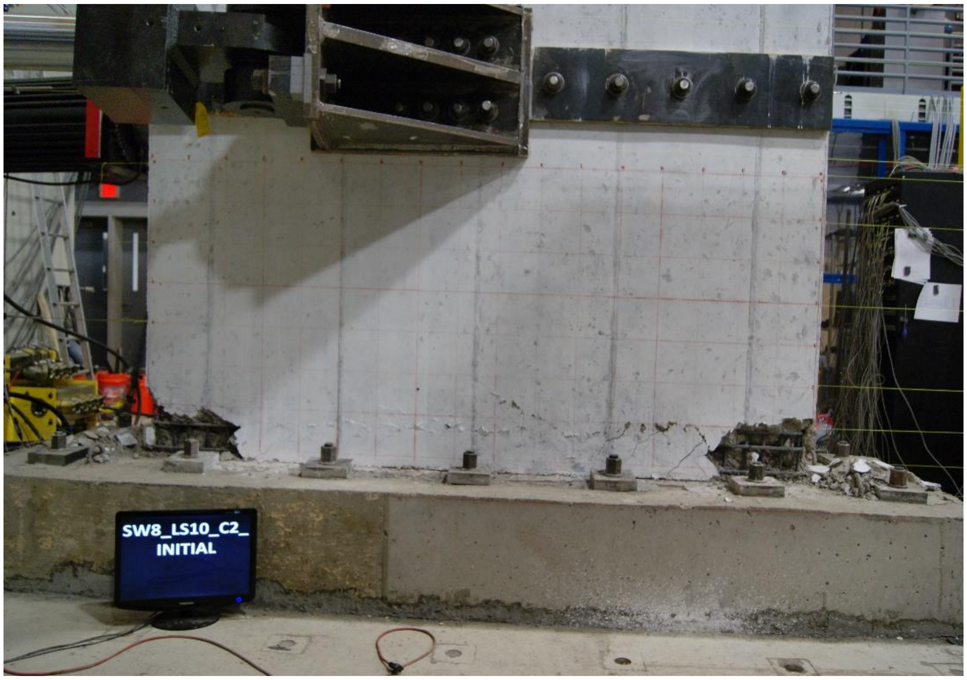

h) SW8 (0.54, 1.5%, 1.5%, 3500 psi)

Figure 4.5. Damage state of the walls at the end of testing (continued)

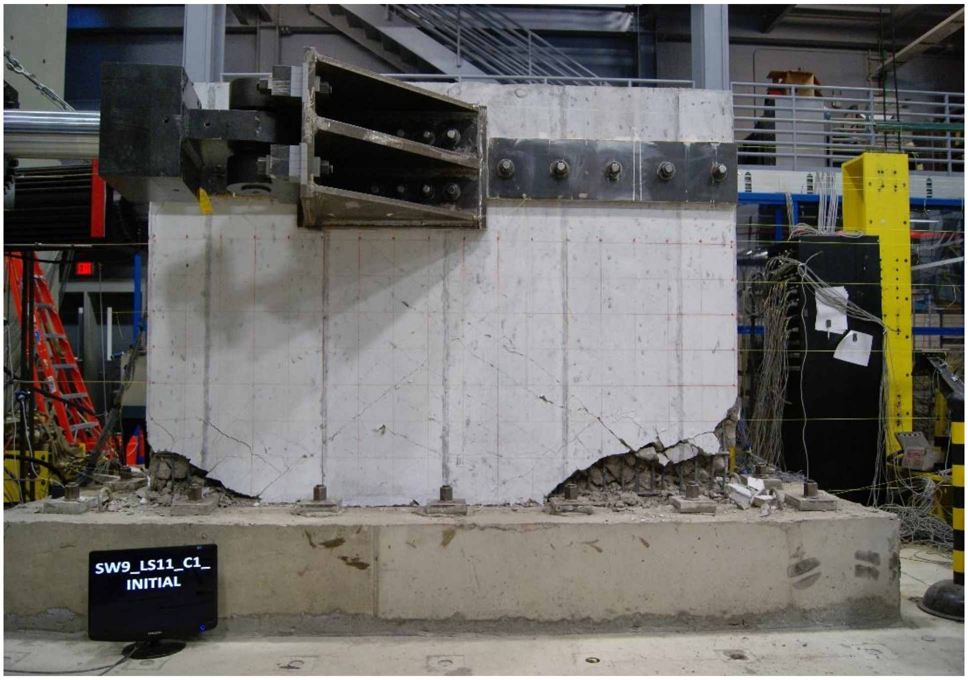

i) SW9 (0.54, 0.67%, 1.5%, 4300 psi)

j) SW10 (0.54, 0.33%, 1.5%, 4600 psi)

Figure 4.5. Damage state of the walls at the end of testing (continued)

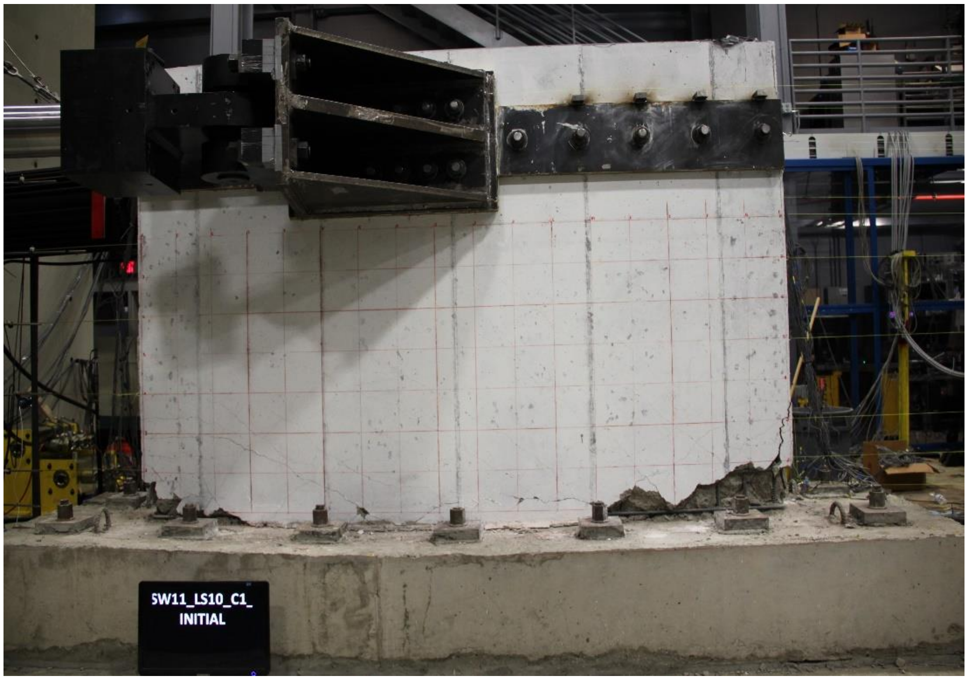

k) SW11 (0.54, 0.67%, 0.67%, 1.5% be, 5000 psi)

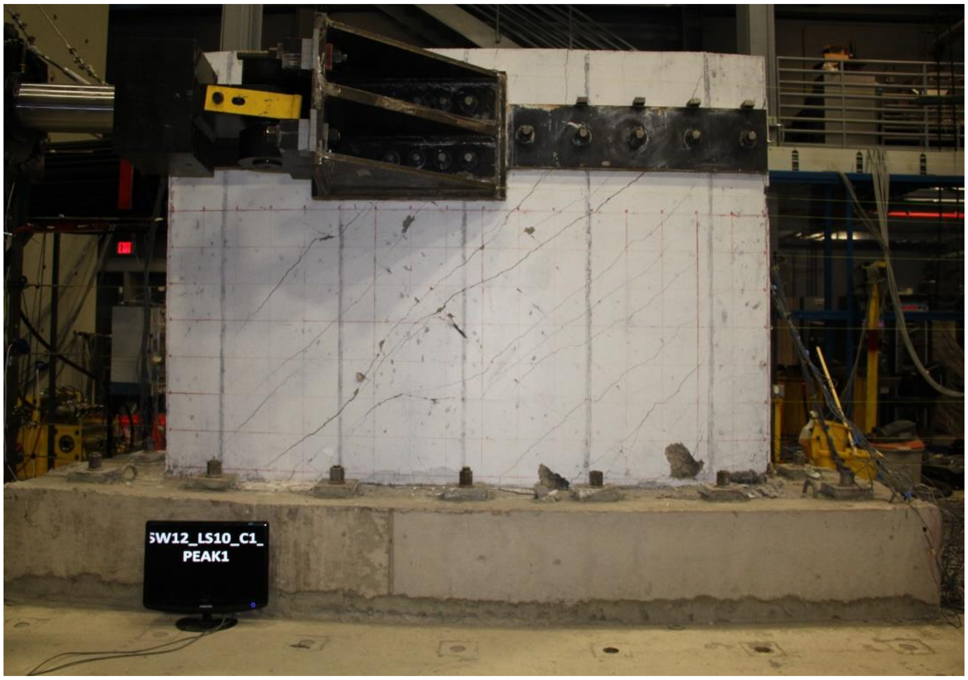

l) SW12 (0.54, 0.33%, 0.33%, 2.0% be, 5000 psi)

Figure 4.5. Damage state of the walls at the end of testing (continued)

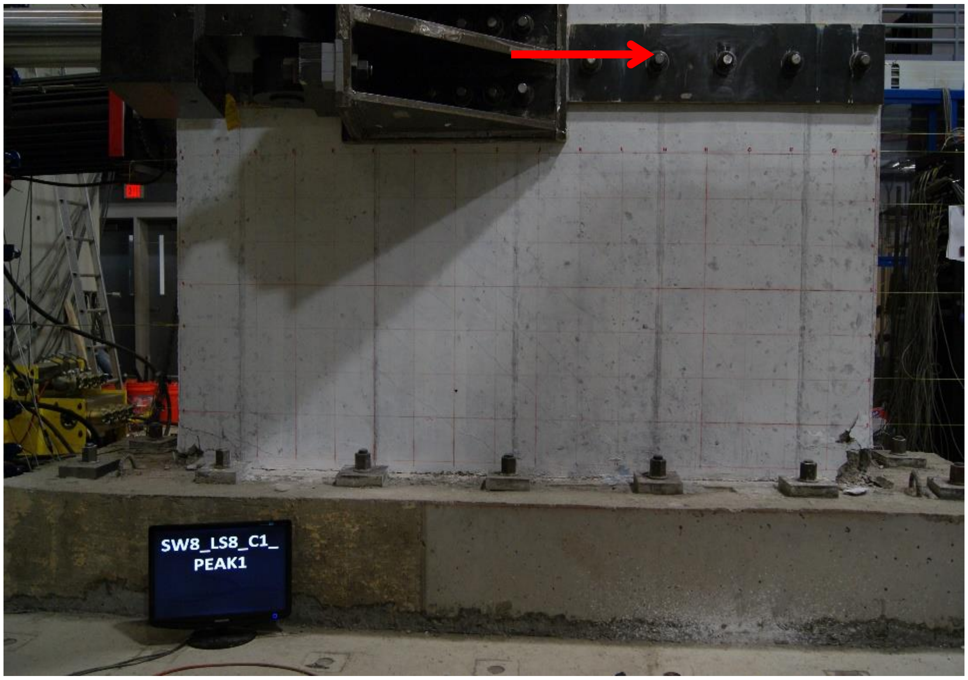

a) SW8 (drift ratio = 1.3%)

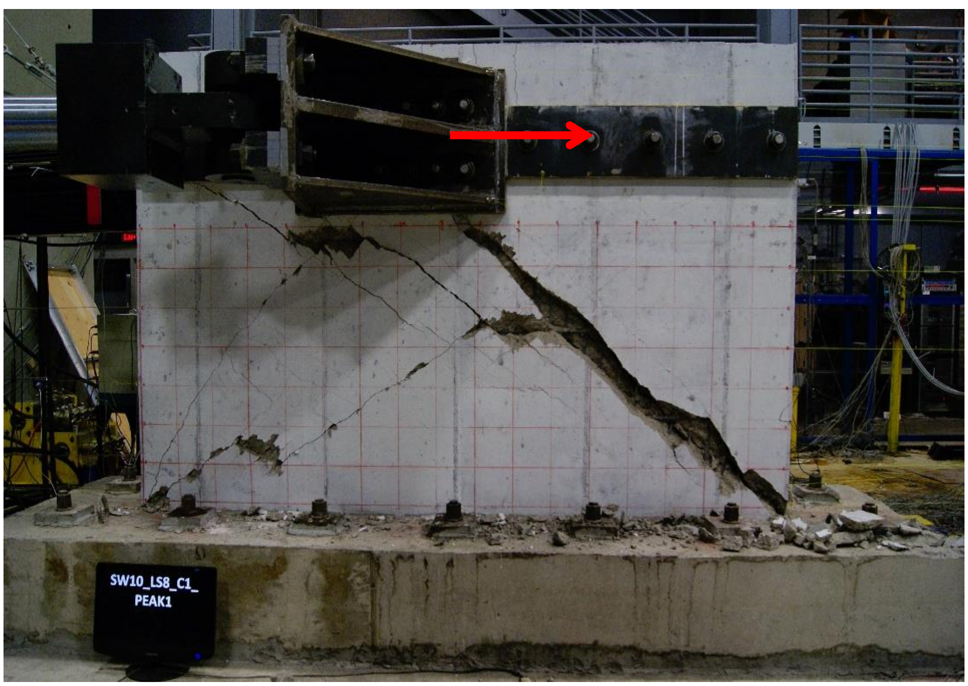

b) SW10 (drift ratio = 1.4%)

Figure 4.6. Photographs of damage to SW8 and SW10

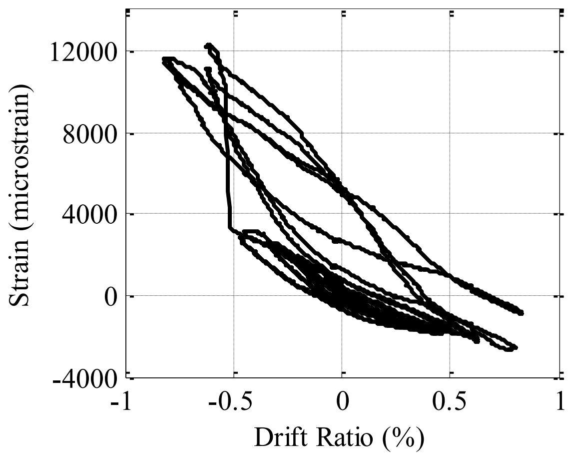

a) Strain gage S14

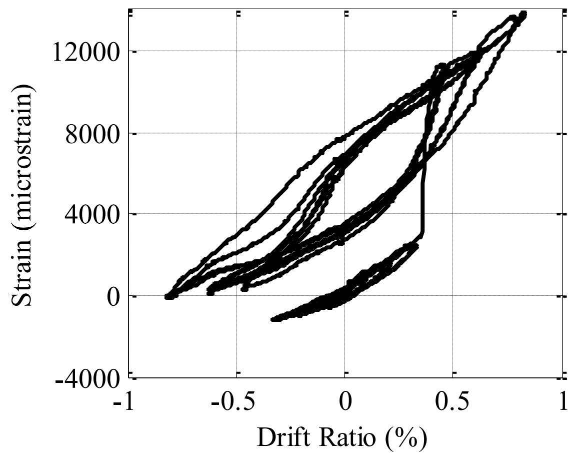

b) Strain gage S8

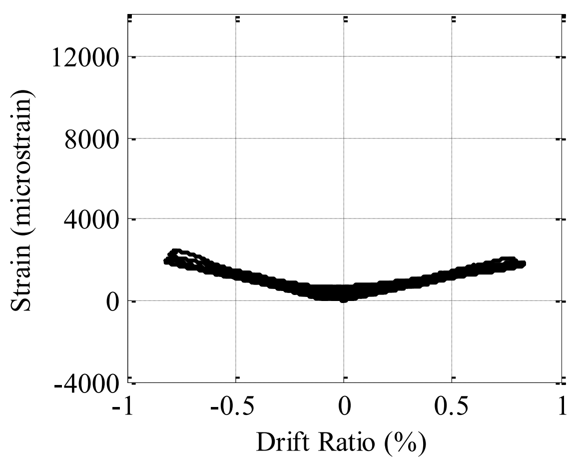

c) Strain gage S8

Figure 4.7. Strains on the vertical reinforcement versus displacement at the centerline of loadin g of SW9

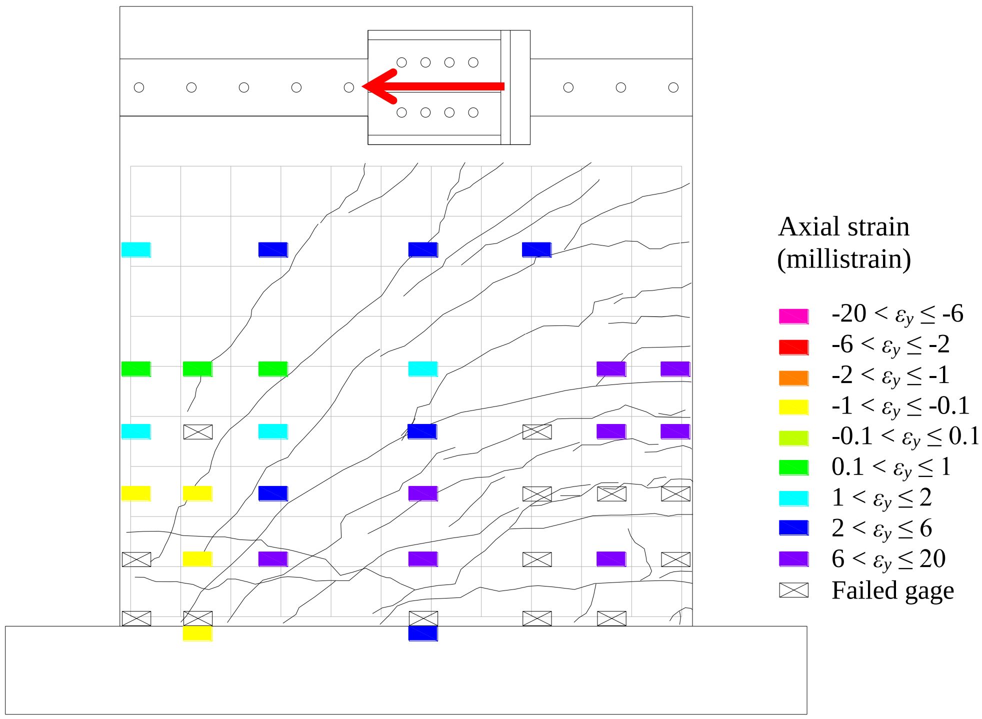

a) SW1 (0.94, 0.67%, 0.67%, 3600 psi)

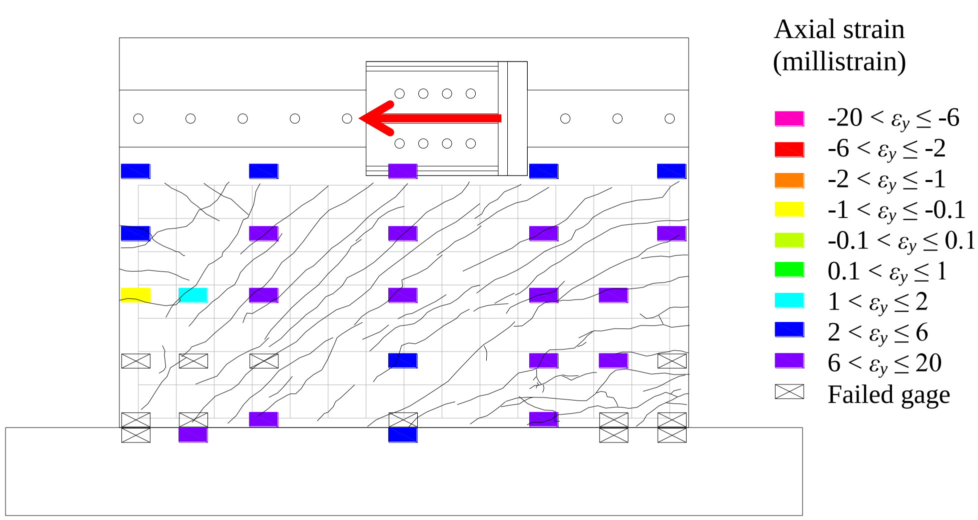

b) SW2 (0.54, 1.0%, 1.0%, 7000 psi)

Figure 4.8. Strains on vertical reinforcement at peak strength

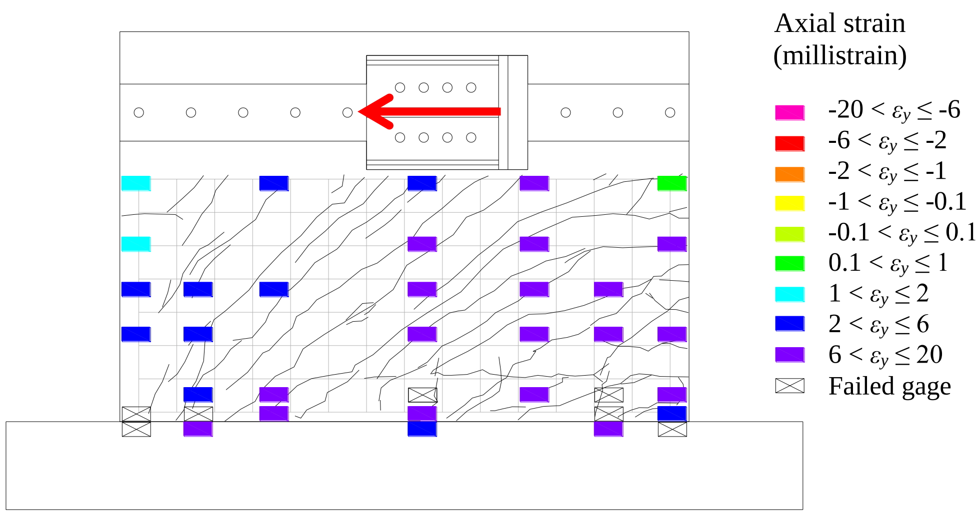

c) SW3 (0.54, 0.67%, 0.67%, 7800 psi)

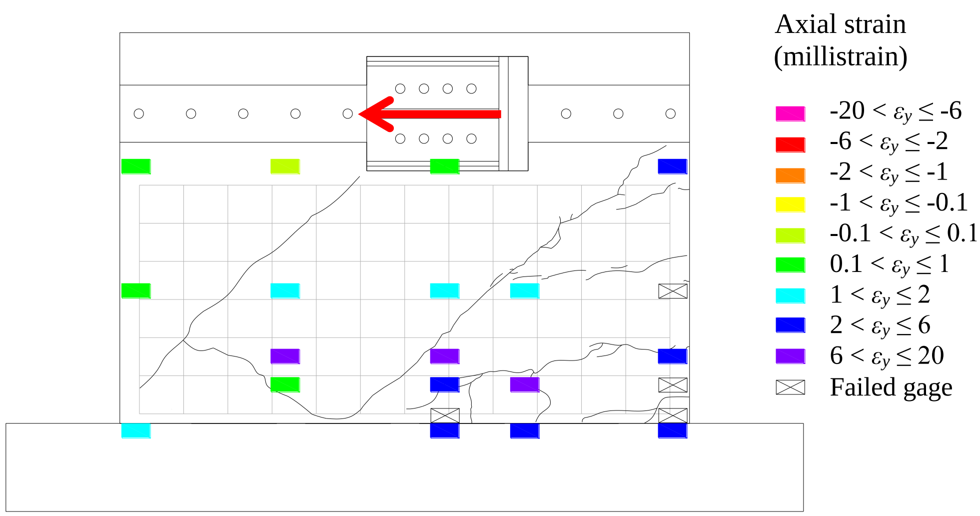

d) SW4 (0.54, 0.33%, 0.33%, 4200 psi)

Figure 4.8. Strains on vertical reinforcement at peak strength (continued)

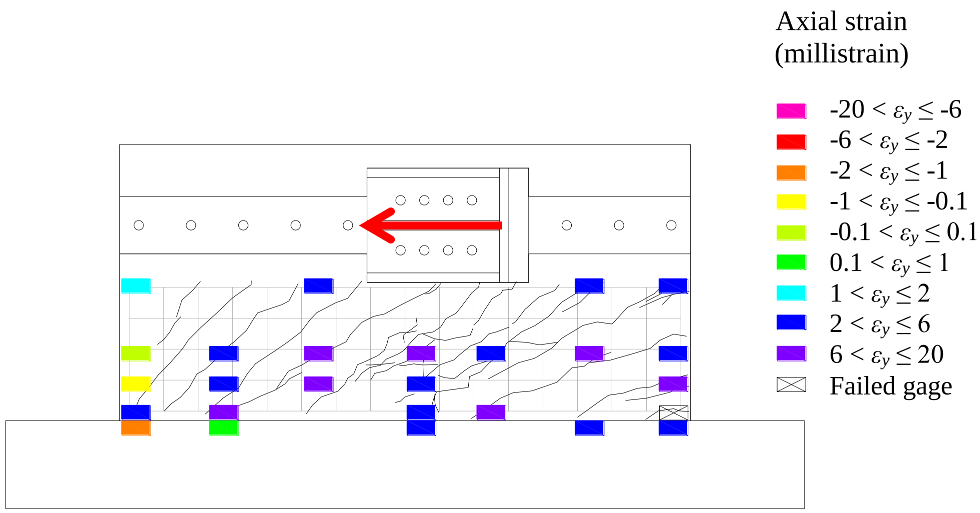

e) SW5 (0.33, 1.0%, 1.0%, 4300 psi)

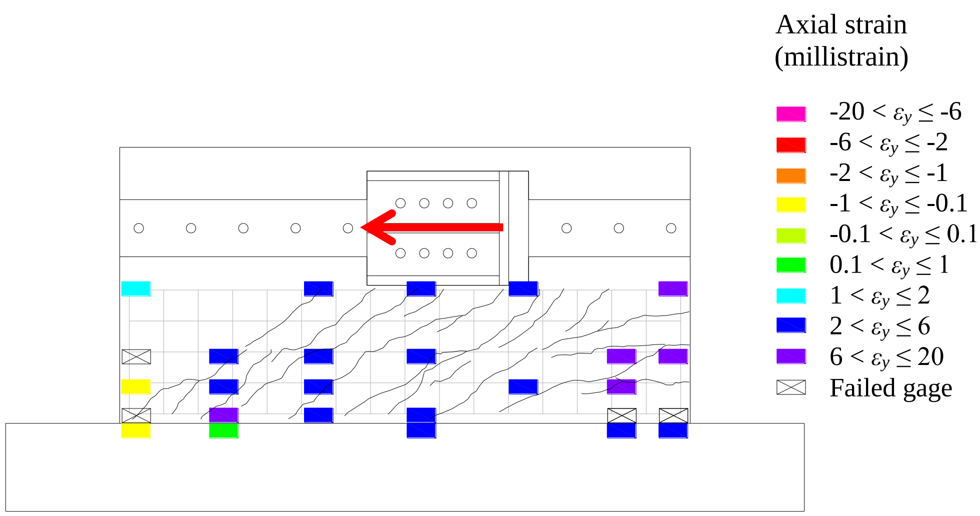

f) SW6 (0.33, 0.67%, 0.67%, 3800 psi)

Figure 4.8. Strains on vertical reinforcement at peak strength (continued)

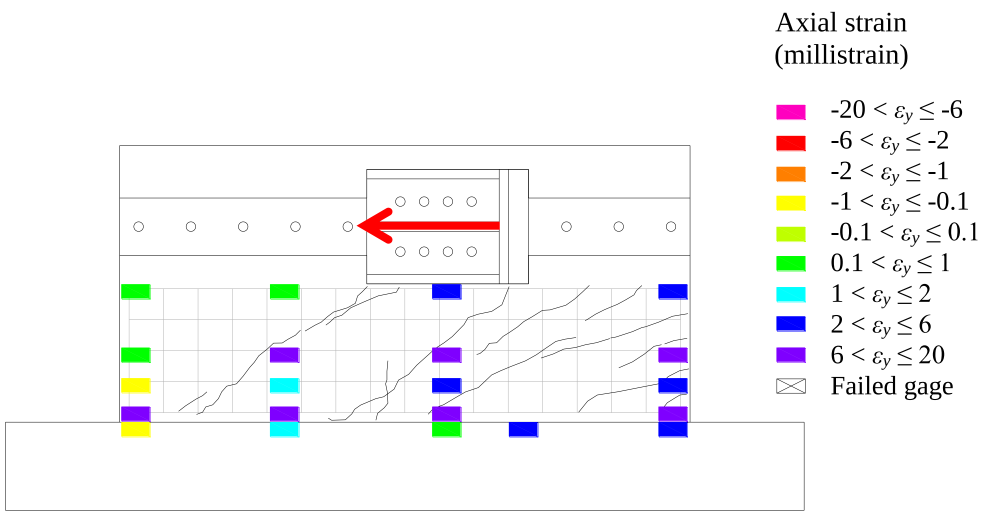

g) SW7 (0.33, 0.33%, 0.33%, 3800 psi)

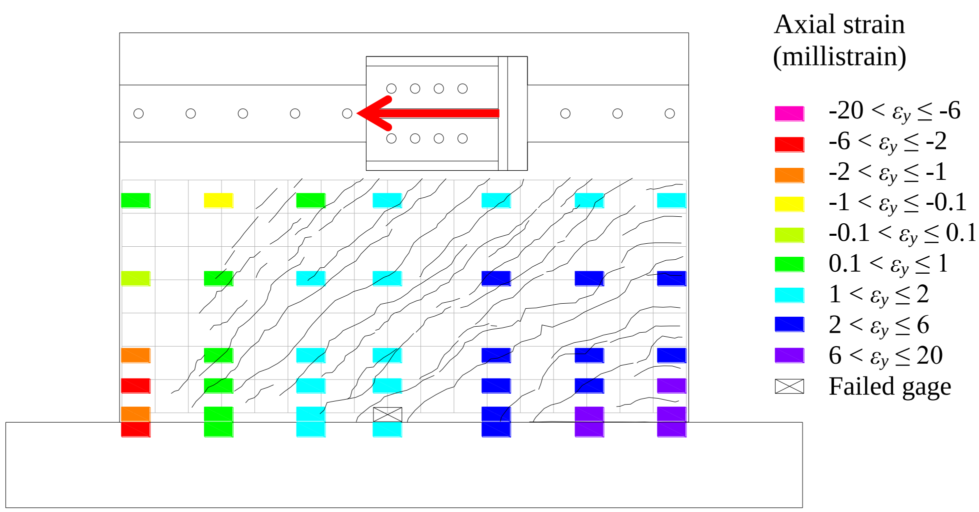

h) SW8 (0.54, 1.5%, 1.5%, 3500 psi)

Figure 4.8. Strains on vertical reinforcement at peak strength (continued)

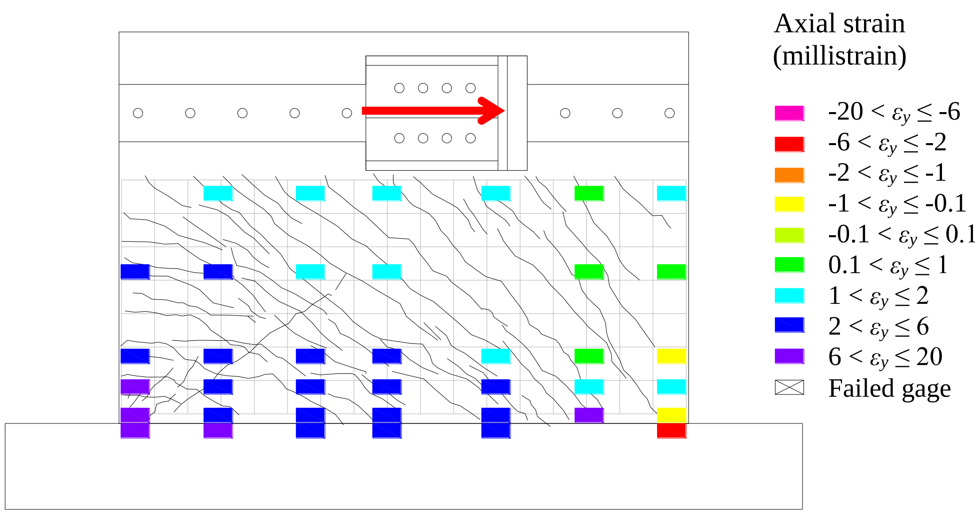

i) SW9 (0.54, 0.67%, 1.5%, 4300 psi)

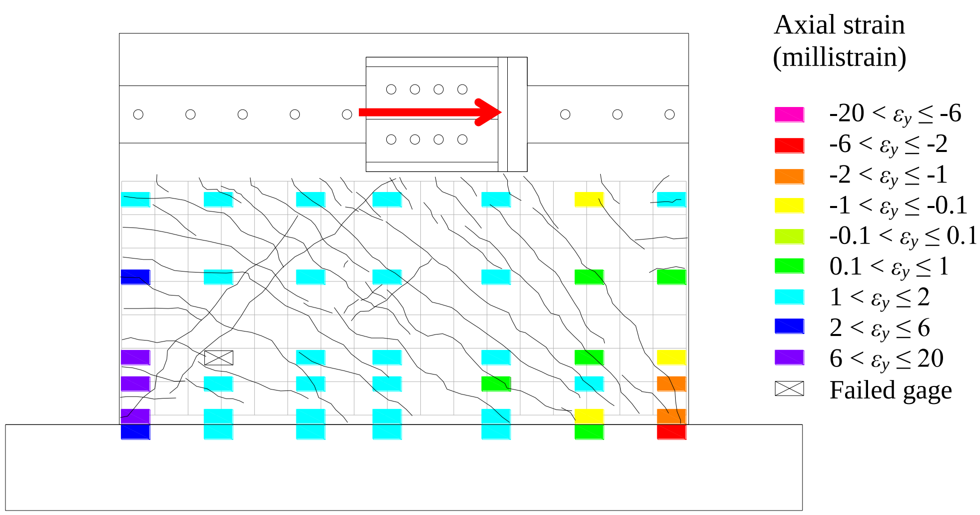

j) SW10 (0.54, 0.33%, 1.5%, 4600 psi)

Figure 4.8. Strains on vertical reinforcement at peak strength (continued)

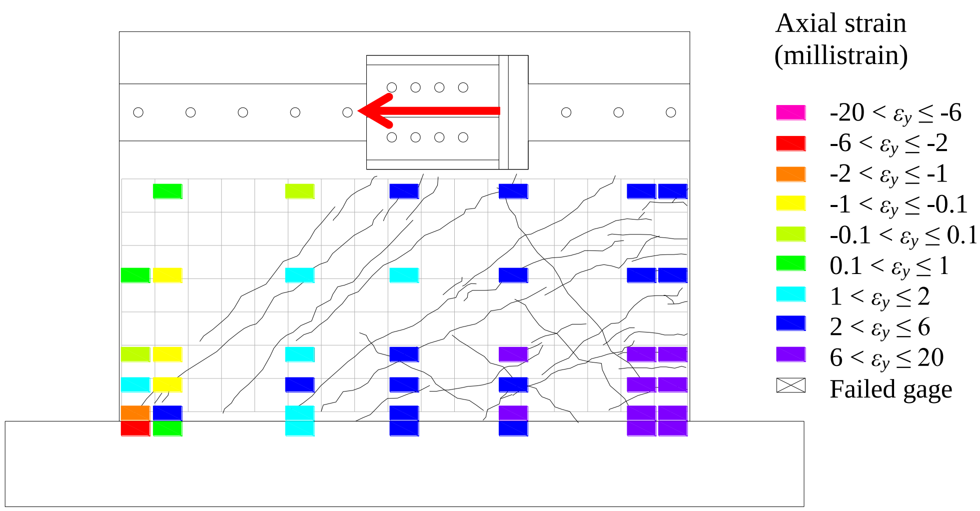

k) SW11 (0.54, 0.67%, 0.67%, 1.5% be, 5000 psi)

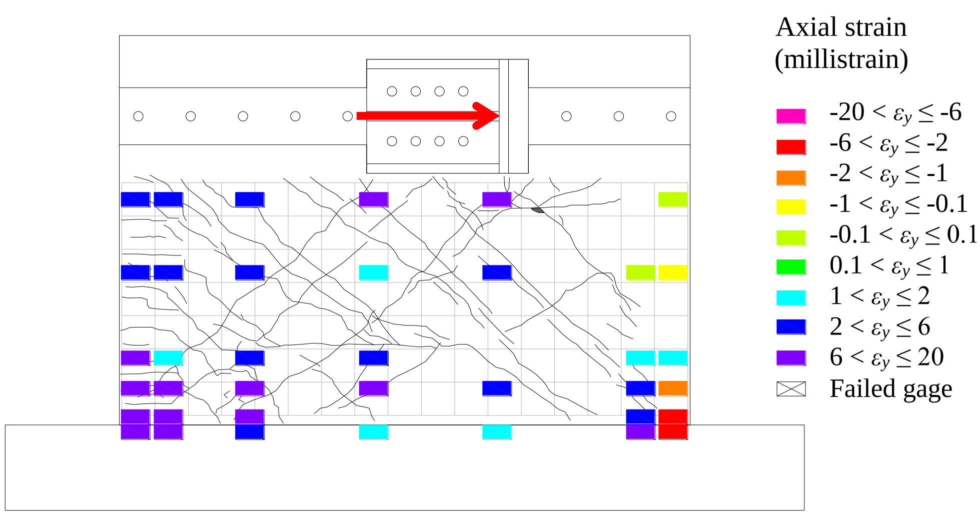

l) SW12 (0.54, 0.33%, 0.33%, 2.0% be, 5000 psi)

Figure 4.8. Strains on vertical reinforcement at peak strength (continued)

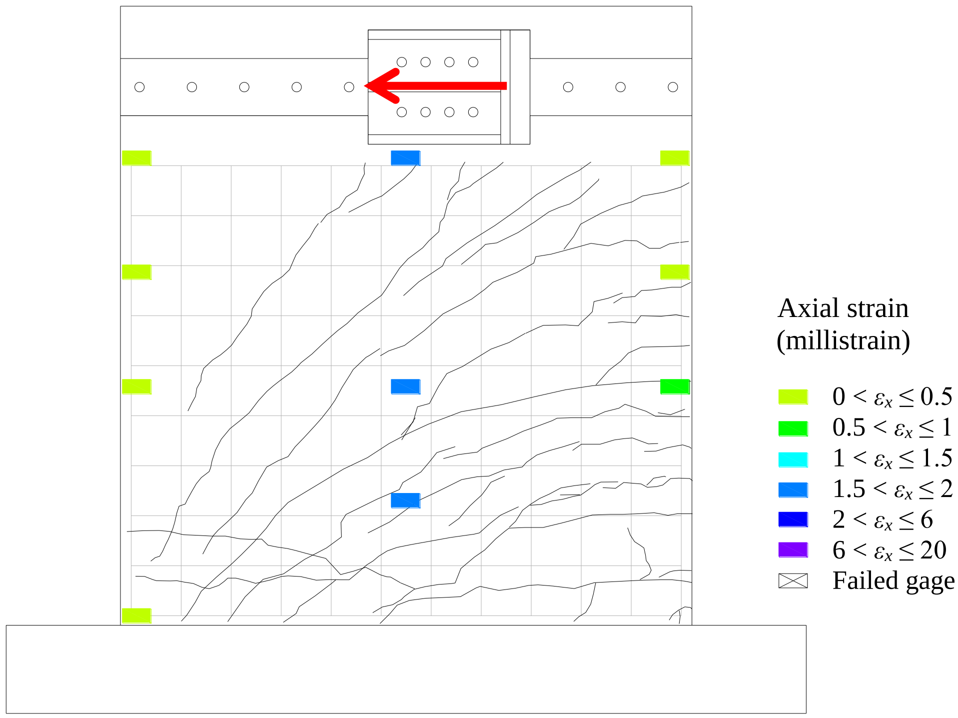

a) SW1 (0.94, 0.67%, 0.67%, 3600 psi)

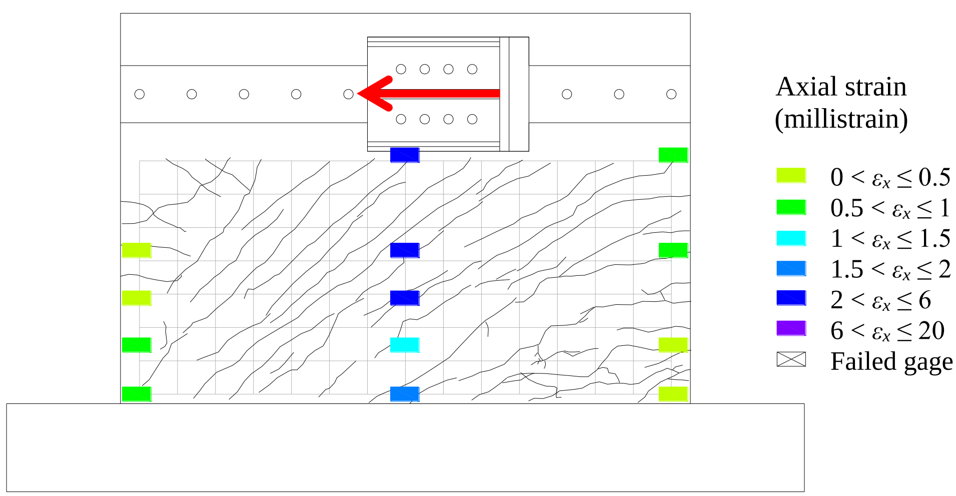

b) SW2 (0.54, 1.0%, 1.0%, 7000 psi)

Figure 4.9. Strains on horizontal reinforcement at peak strength

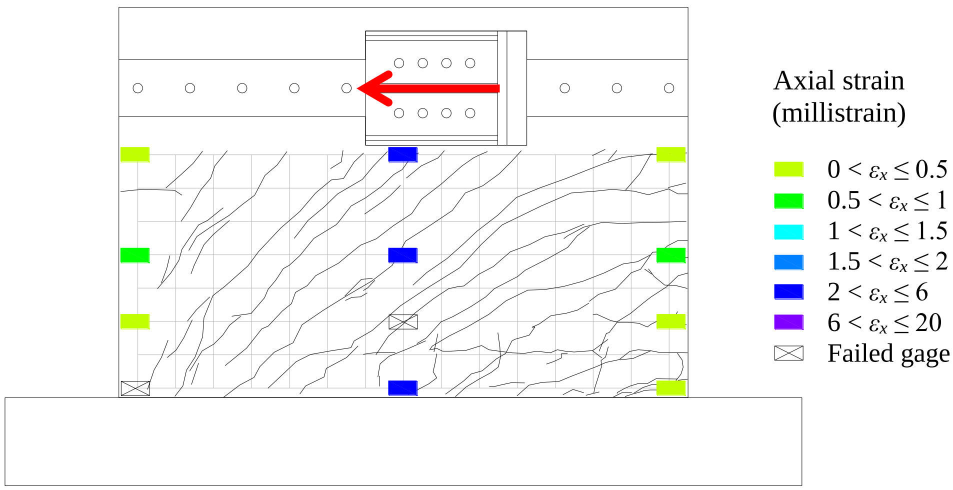

c) SW3 (0.54, 0.67%, 0.67%, 7800 psi)

d) SW4 (0.54, 0.33%, 0.33%, 4200 psi)

Figure 4.9. Strains on horizontal reinforcement at peak strength (continued)

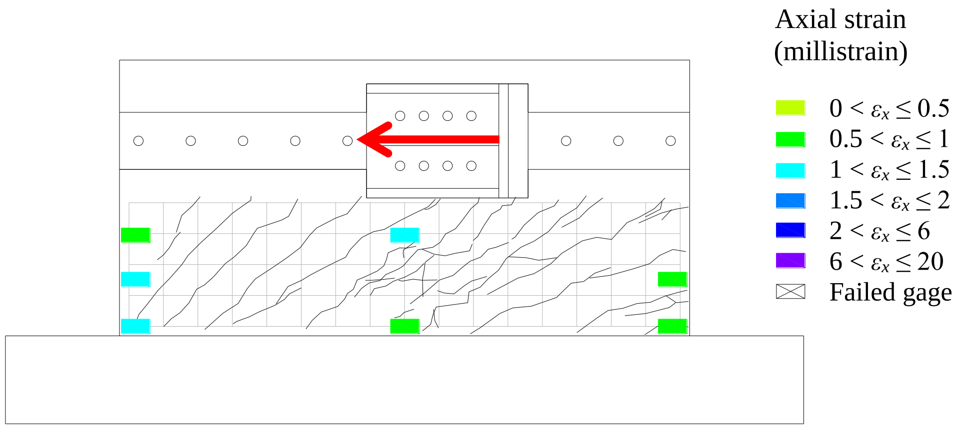

e) SW5 (0.33, 1.0%, 1.0%, 4300 psi)

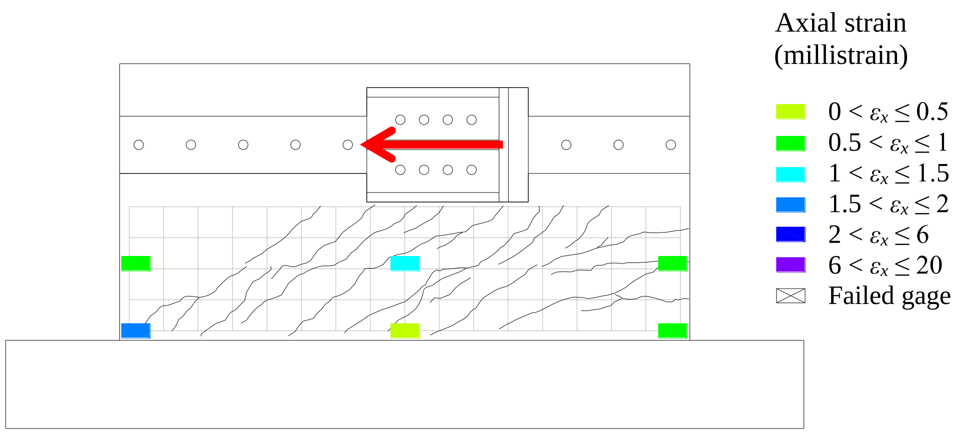

f) SW6 (0.33, 0.67%, 0.67%, 3800 psi)

Figure 4.9. Strains on horizontal reinforcement at peak strength (continued)

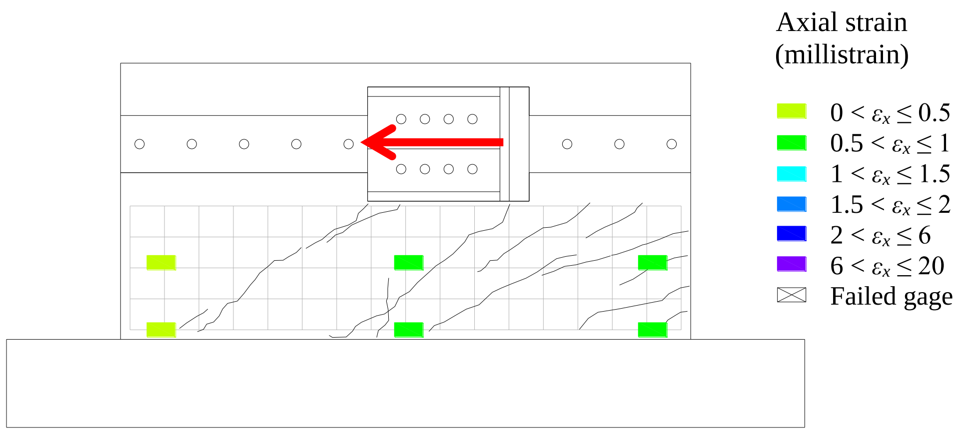

g) SW7 (0.33, 0.33%, 0.33%, 3800 psi)

h) SW8 (0.54, 1.5%, 1.5%, 3500 psi)

Figure 4.9. Strains on horizontal reinforcement at peak strength (continued)

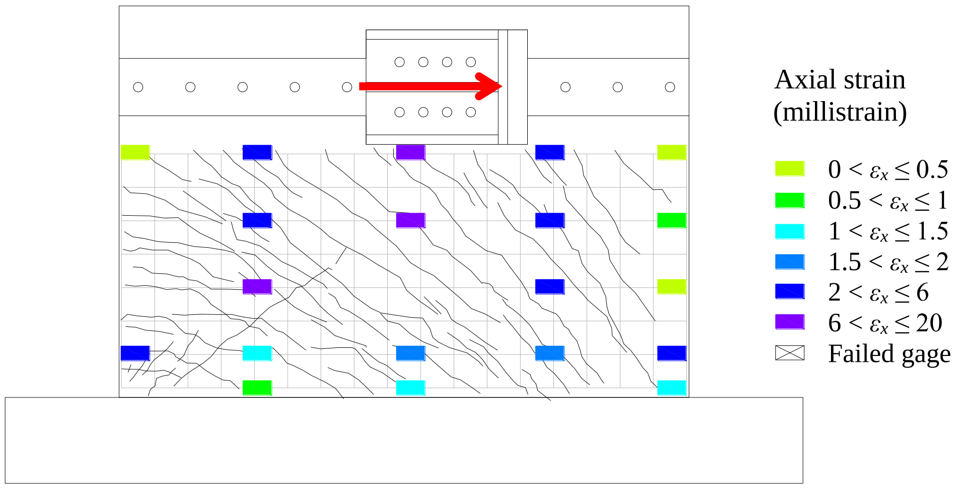

i) SW9 (0.54, 0.67%, 1.5%, 4300 psi)

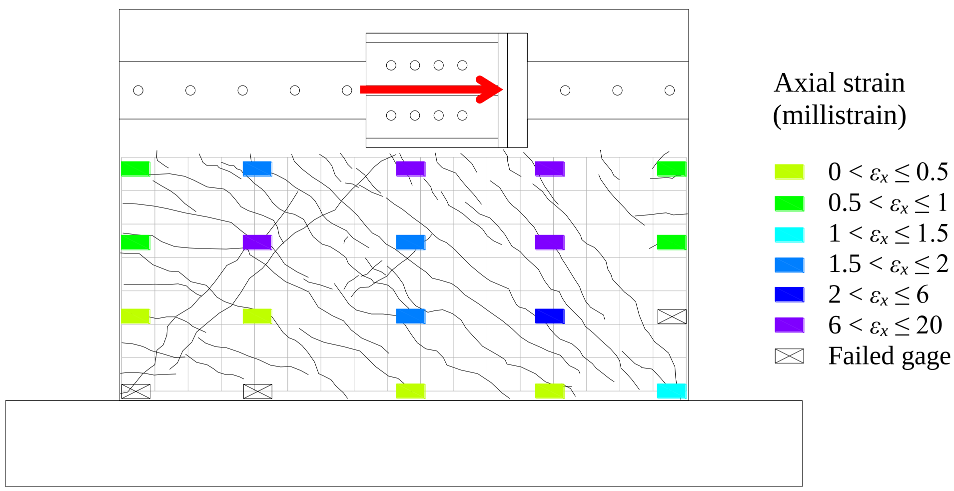

j) SW10 (0.54, 0.33%, 1.5%, 4600 psi)

Figure 4.9. Strains on horizontal reinforcement at peak strength (continued)

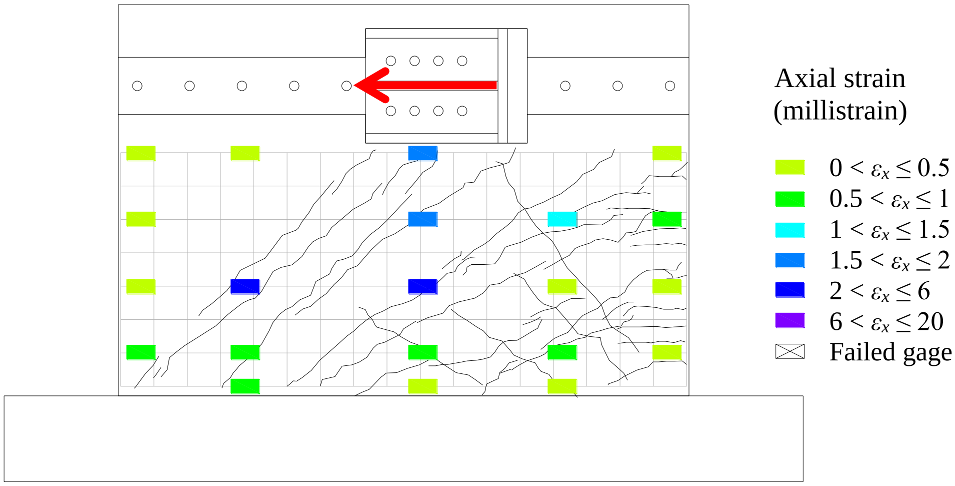

k) SW11 (0.54, 0.67%, 0.67%, 1.5% be, 5000 psi)

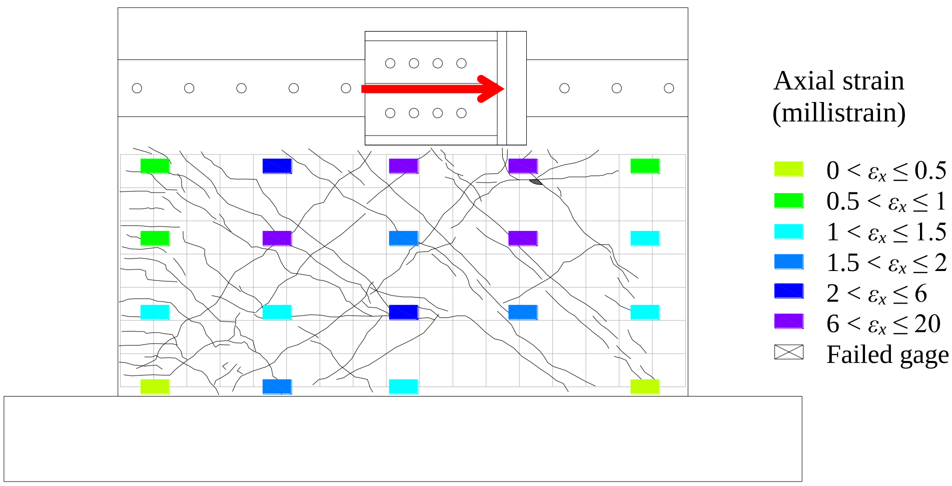

l) SW12 (0.54, 0.33%, 0.33%, 2.0% be, 5000 psi)

Figure 4.9. Strains on horizontal reinforcement at peak strength (continued)

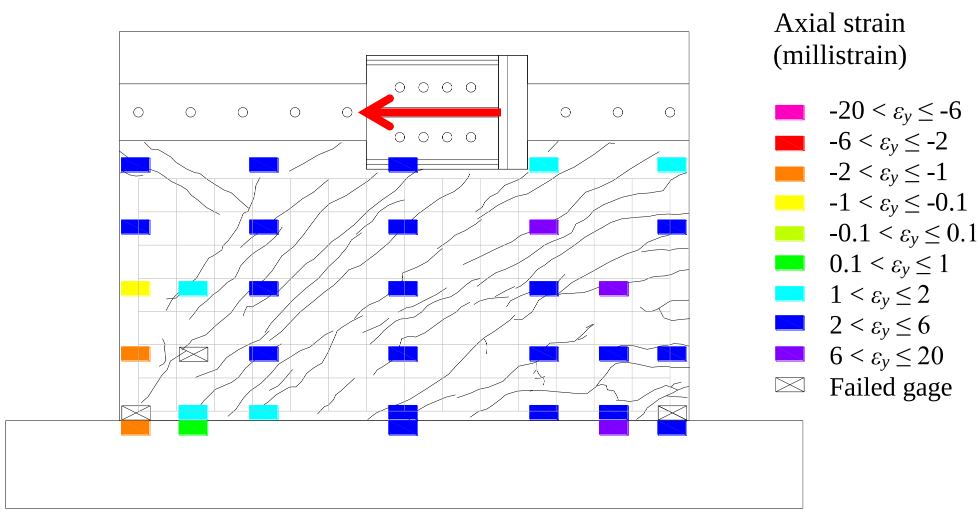

a) SW2 (0.54, 1.0%, 1.0%, 7000 psi)

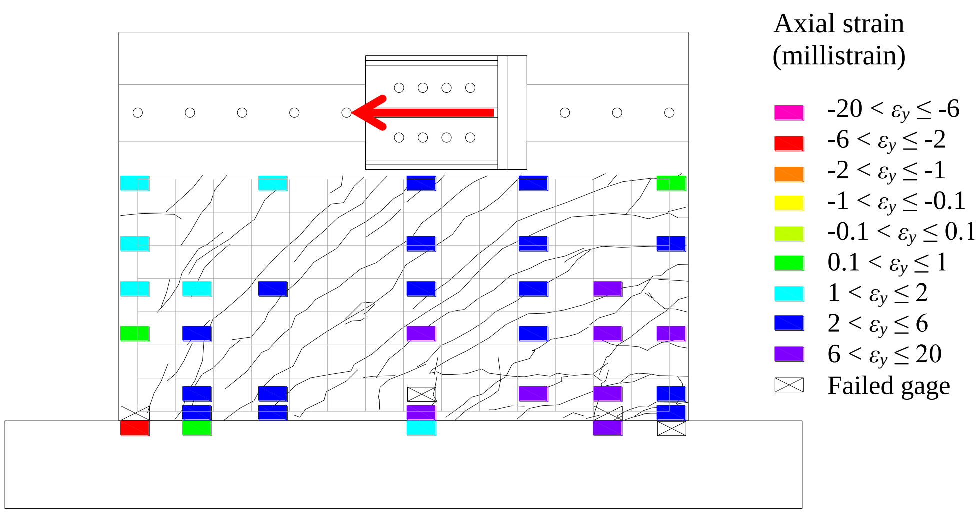

b) SW3 (0.54, 0.67%, 0.67%, 7800 psi)

Figure 4.10. Strains on vertical reinforcement of SW2 and SW3 at 0.7% drift ratio

a) SW2 (0.54, 1.0%, 1.0%, 7000 psi)

b) SW3 (0.54, 0.67%, 0.67%, 7800 psi)

Figure 4.11. Strains on horizontal reinforcement of SW2 and SW3 at 0.7% drift ratio

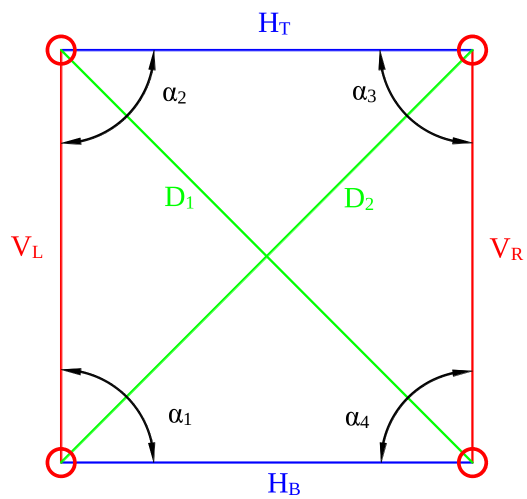

Figure 4.12. Notation for the quadrilateral panel used to calculate strain fields

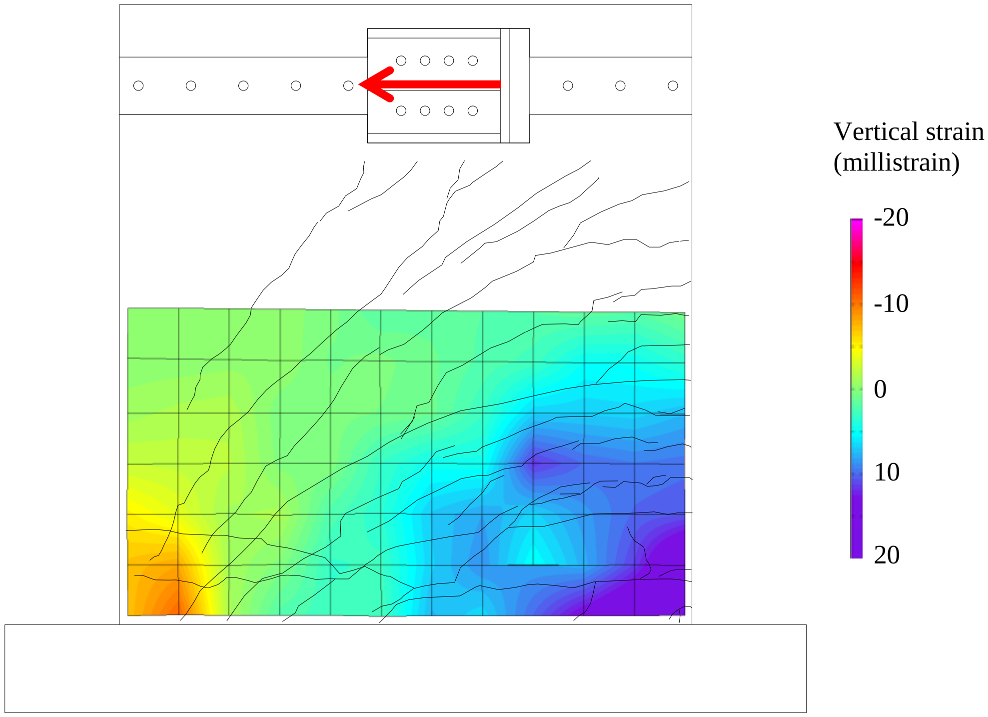

a) SW1 (0.94, 0.67%, 0.67%, 3600 psi)

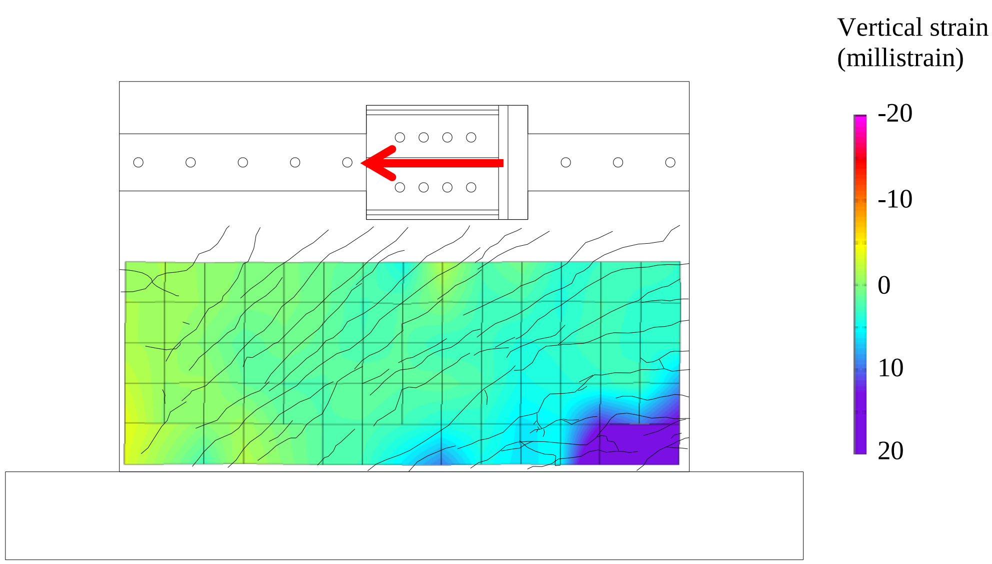

b) SW2 (0.54, 1.0%, 1.0%, 7000 psi)

Figure 4.13. Vertical strain fields at peak strength

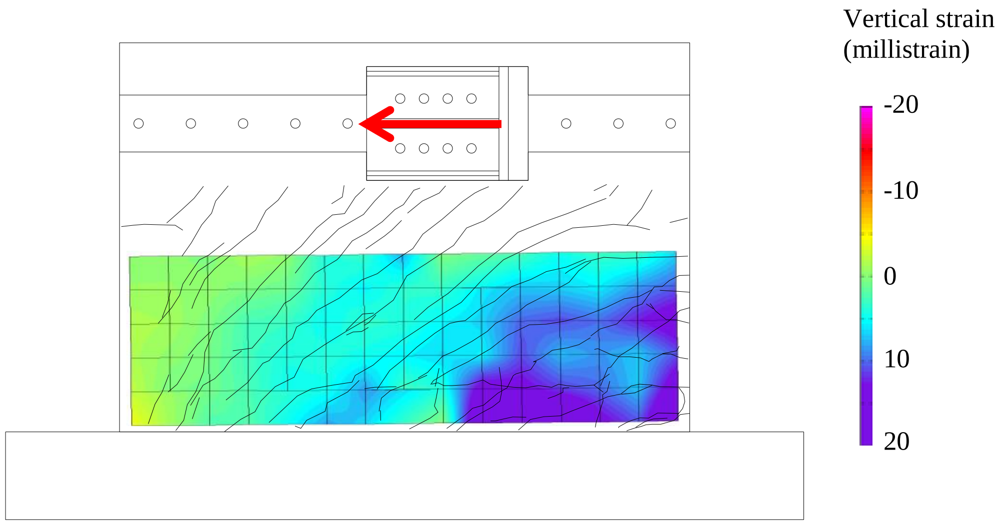

c) SW3 (0.54, 0.67%, 0.67%, 7800 psi)

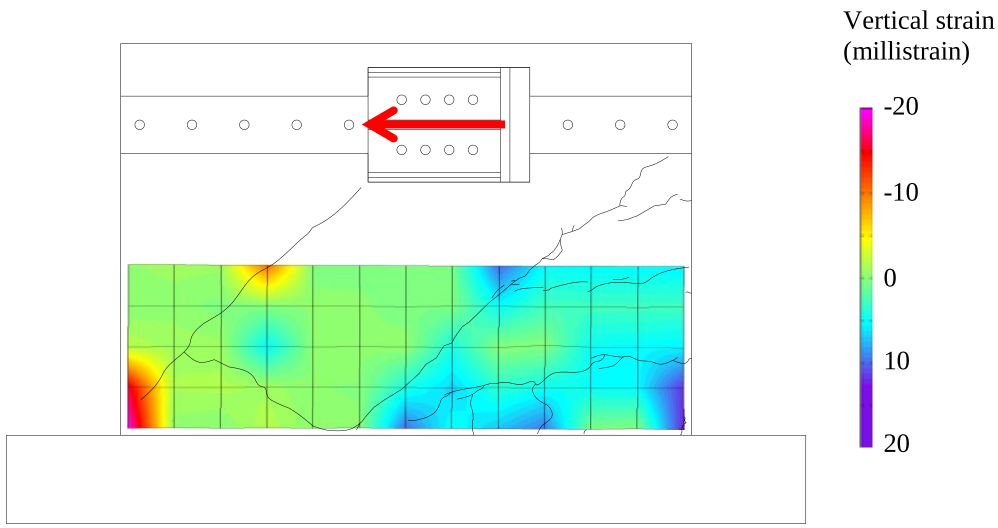

d) SW4 (0.54, 0.33%, 0.33%, 4200 psi)

Figure 4.13. Vertical strain fields at peak strength (continued)

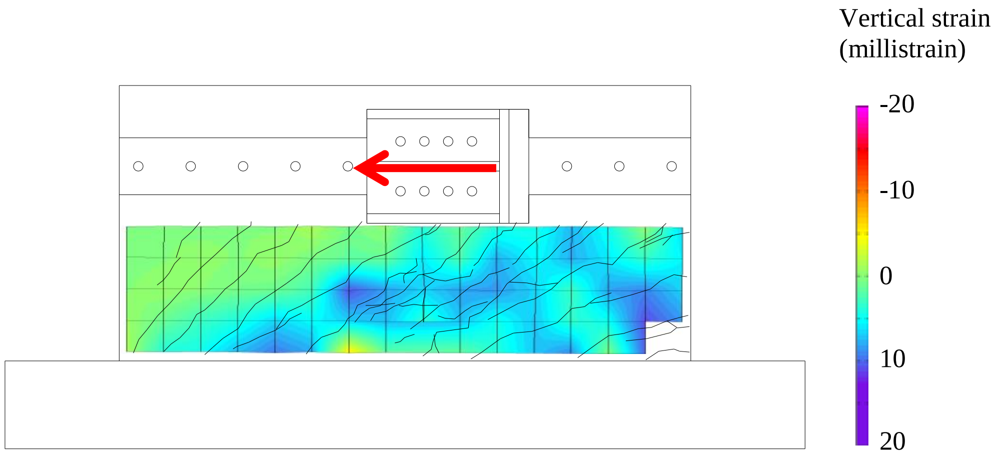

e) SW5 (0.33, 1.0%, 1.0%, 4300 psi)

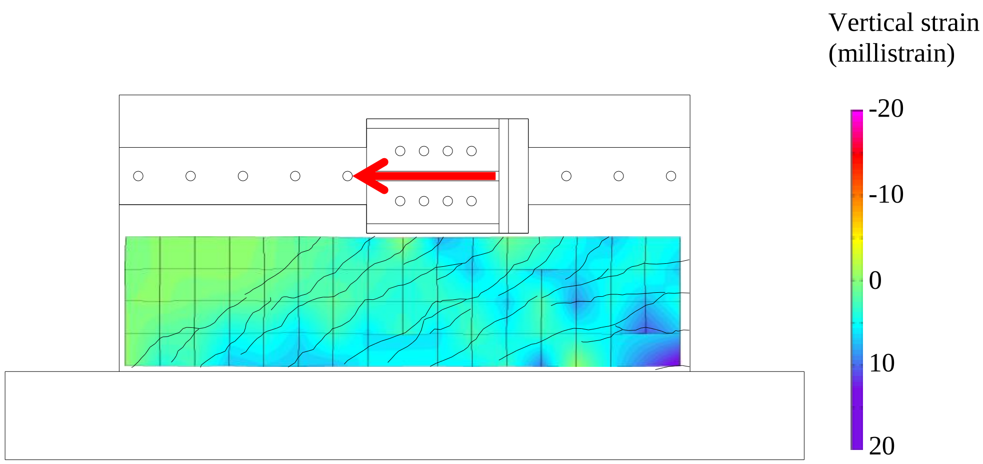

f) SW6 (0.33, 0.67%, 0.67%, 3800 psi)

Figure 4.13. Vertical strain fields at peak strength (continued)

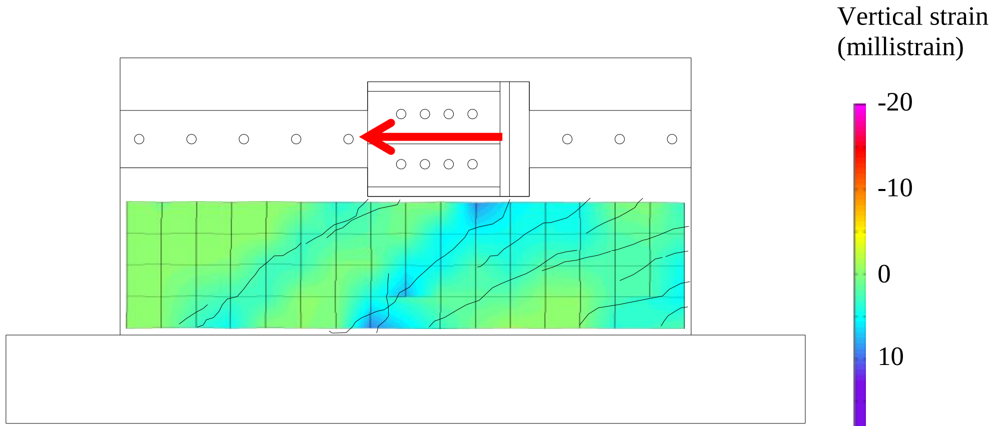

g) SW7 (0.33, 0.33%, 0.33%, 3800 psi)

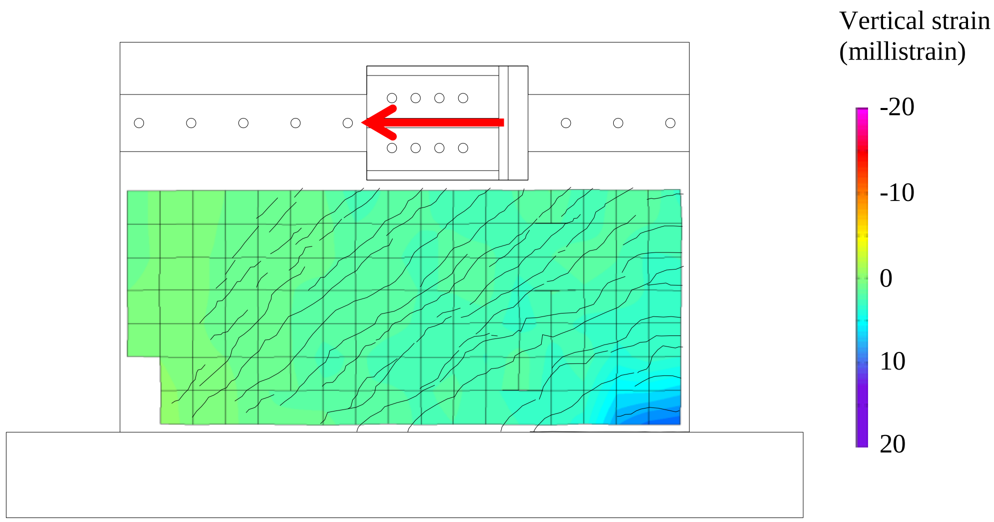

h) SW8 (0.54, 1.5%, 1.5%, 3500 psi)

Figure 4.13. Vertical strain fields at peak strength (continued)

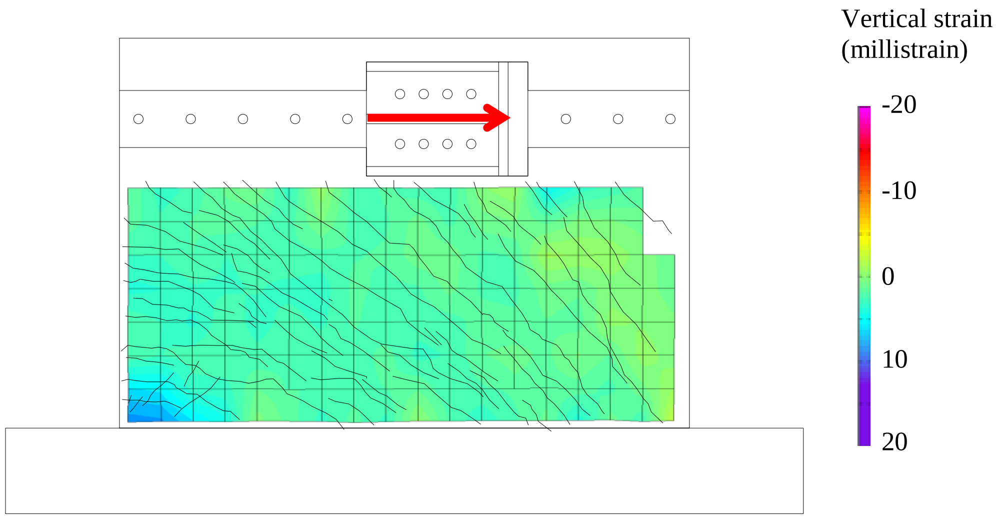

i) SW9 (0.54, 0.67%, 1.5%, 4300 psi)

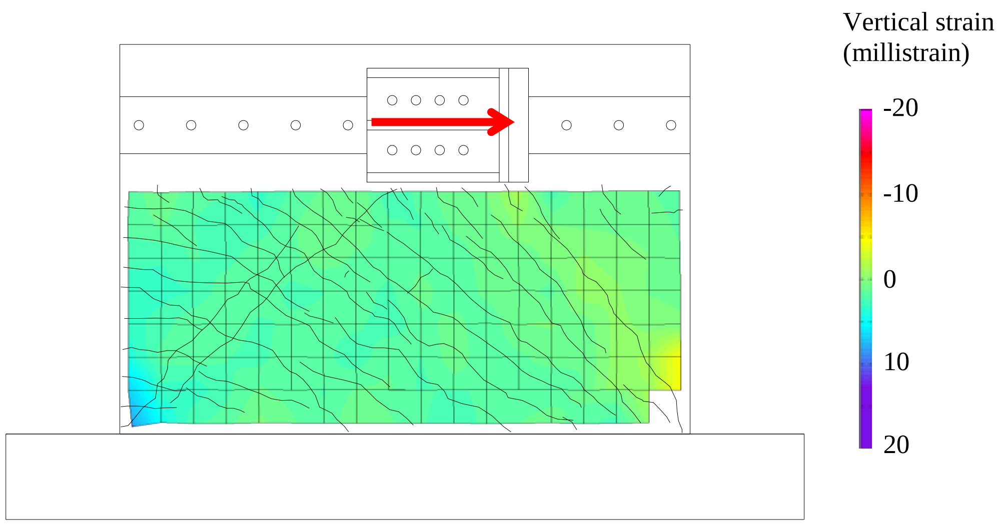

j) SW10 (0.54, 0.33%, 1.5%, 4600 psi)

Figure 4.13. Vertical strain fields at peak strength (continued)

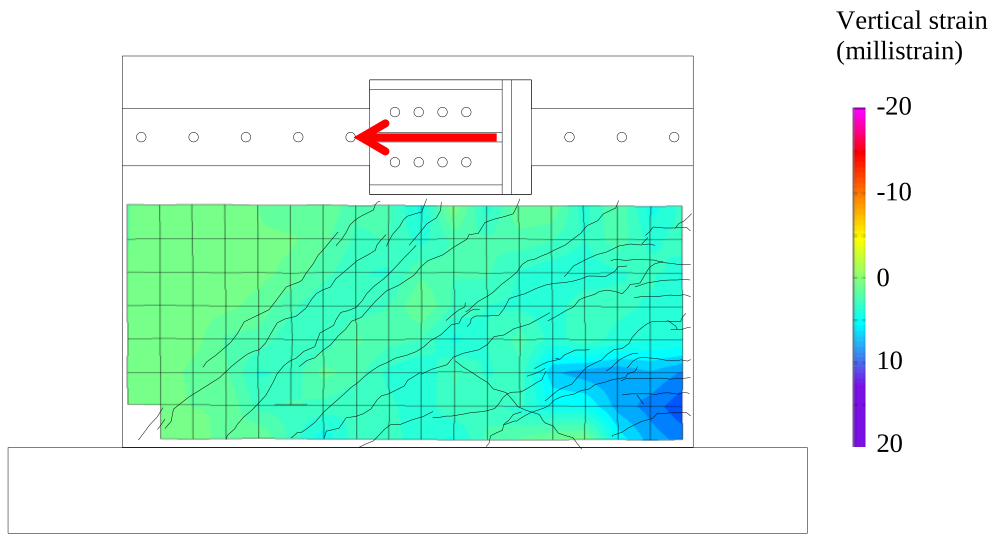

k) SW11 (0.54, 0.67%, 0.67%, 1.5% be, 5000 psi)

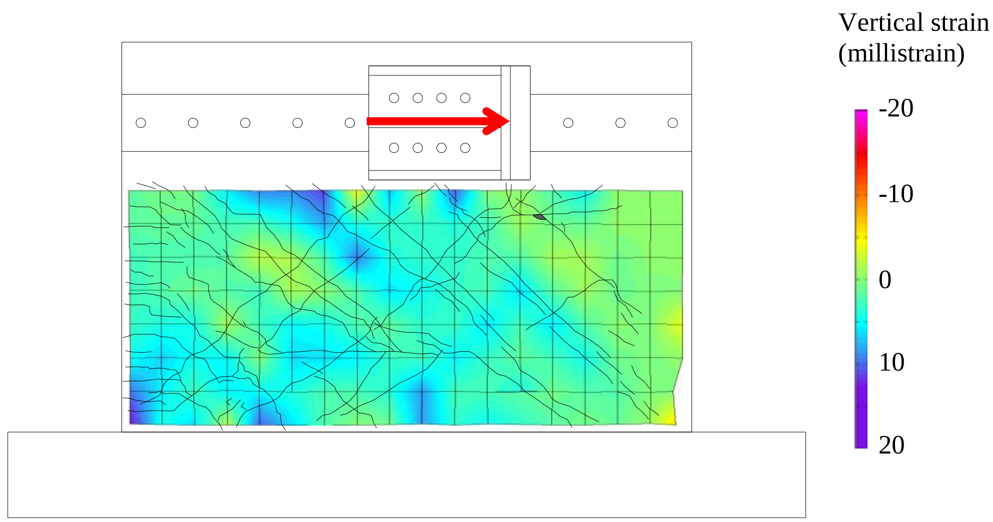

l) SW12 (0.54, 0.33%, 0.33%, 2.0% be, 5000 psi)

Figure 4.13. Vertical strain fields at peak strength (continued)

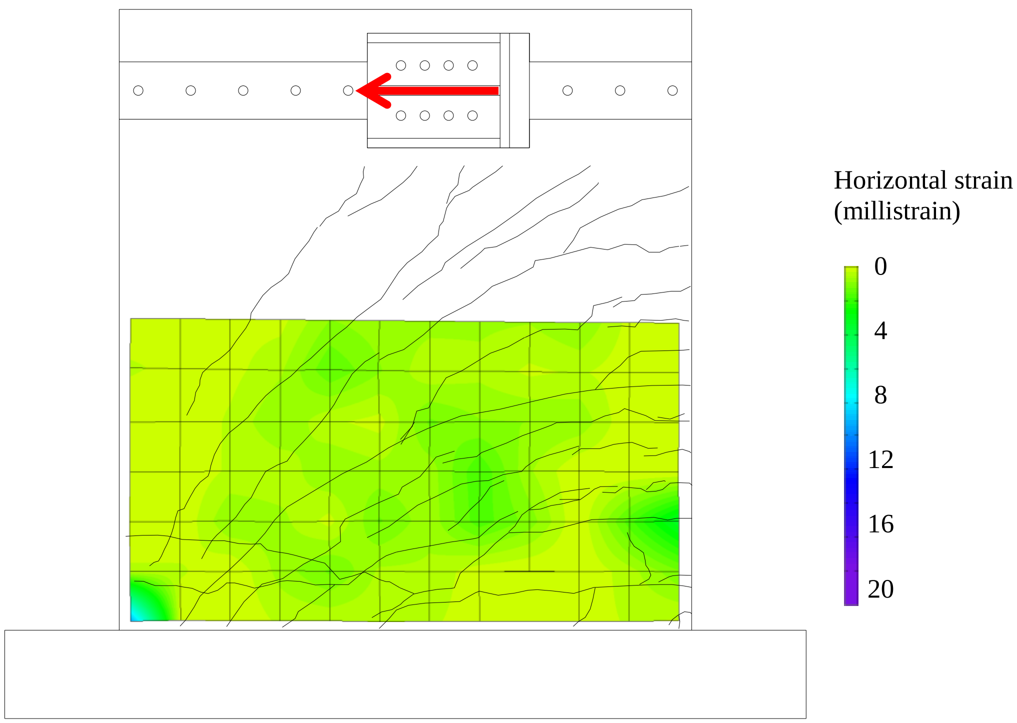

a) SW1 (0.94, 0.67%, 0.67%, 3600 psi)

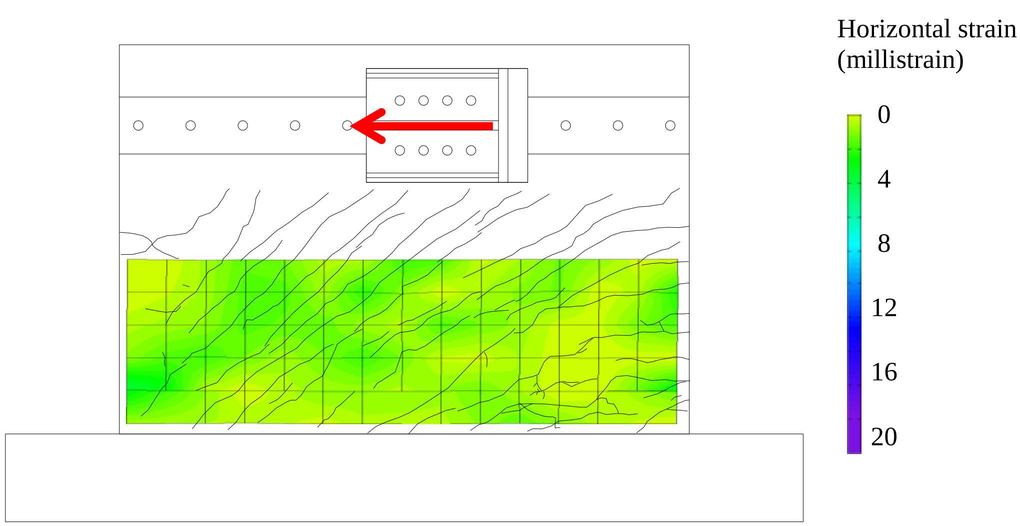

b) SW2 (0.54, 1.0%, 1.0%, 7000 psi)

Figure 4.14. Horizontal strain fields at peak strength

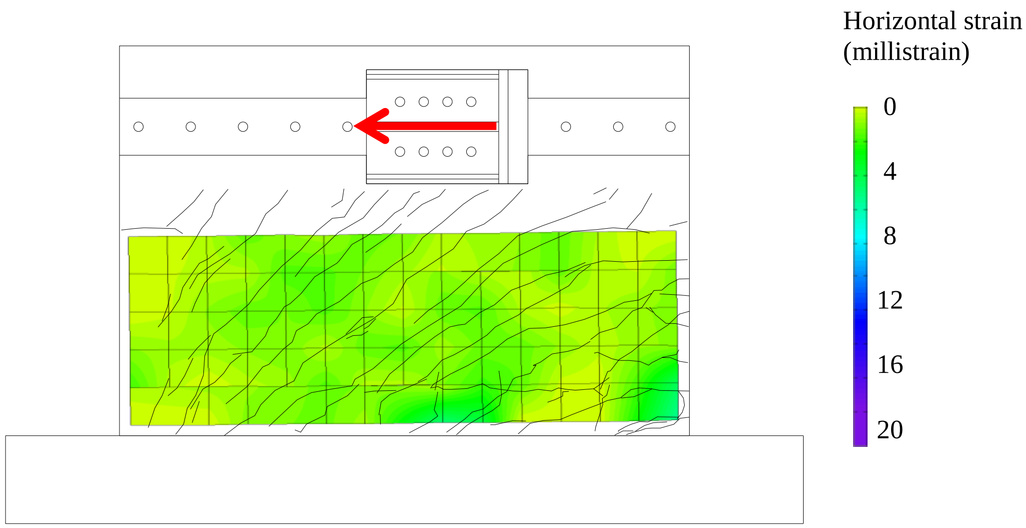

c) SW3 (0.54, 0.67%, 0.67%, 7800 psi)

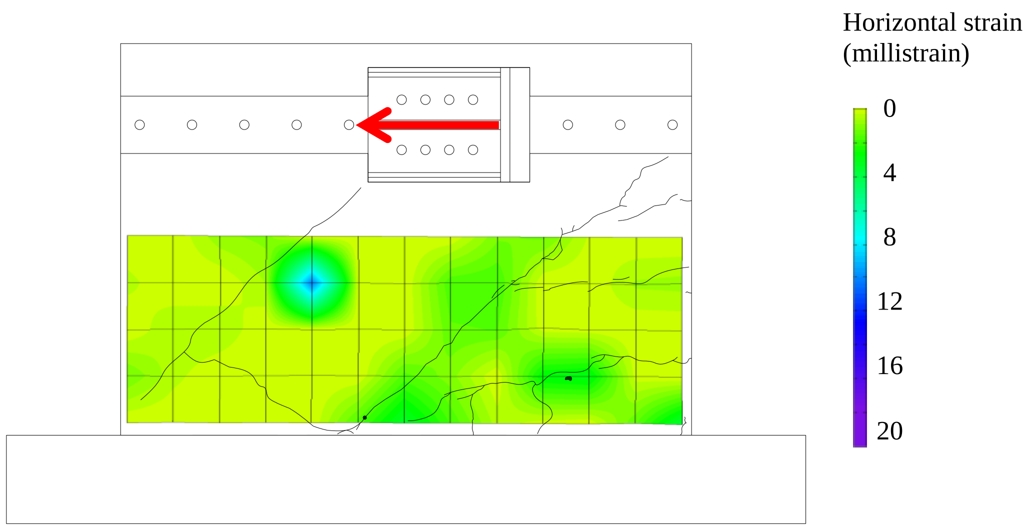

d) SW4 (0.54, 0.33%, 0.33%, 4200 psi)

Figure 4.14. Horizontal strain fields at peak strength (continued)

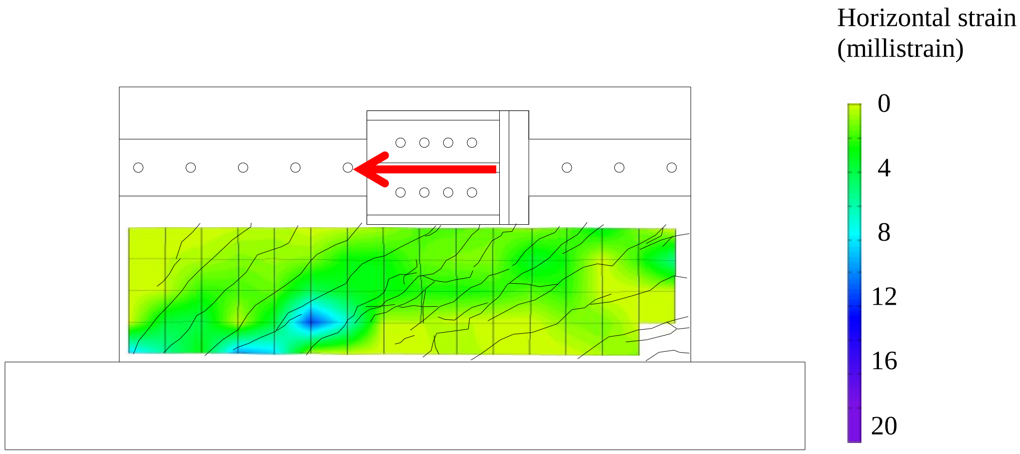

e) SW5 (0.33, 1.0%, 1.0%, 4300 psi)

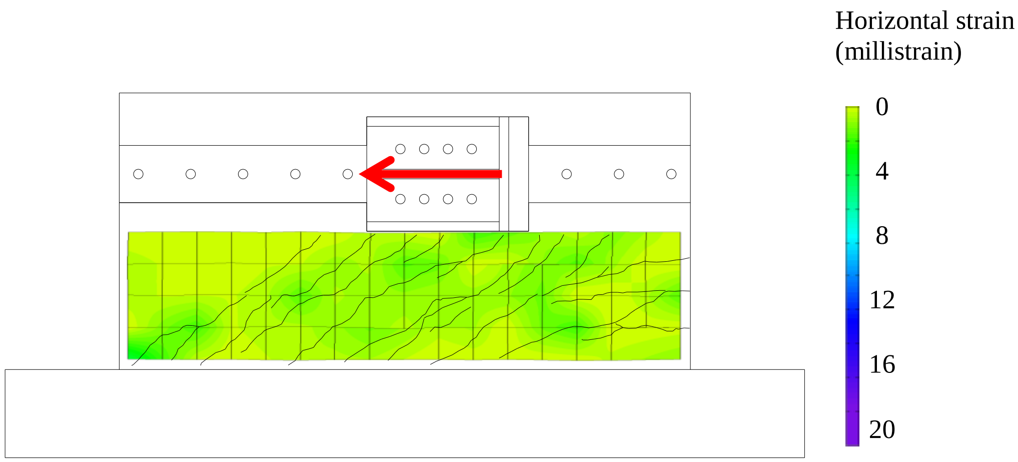

f) SW6 (0.33, 0.67%, 0.67%, 3800 psi)

Figure 4.14. Horizontal strain fields at peak strength (continued)

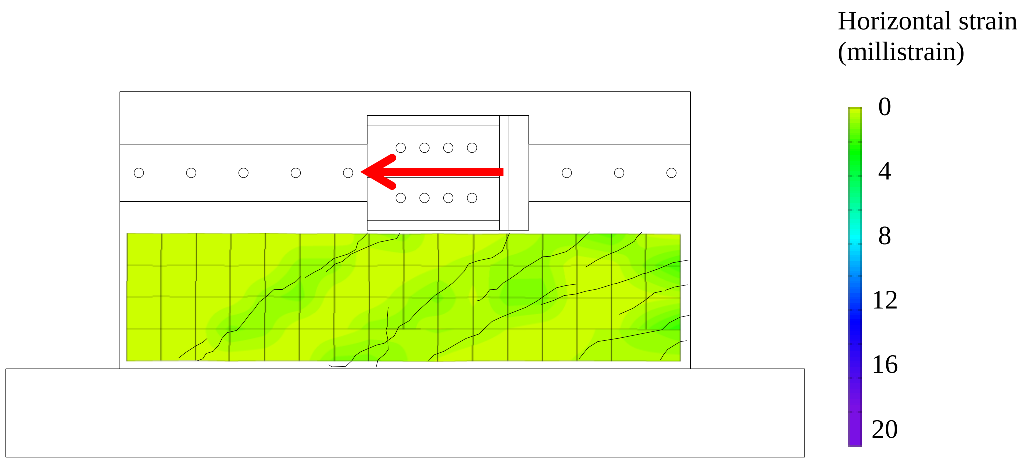

g) SW7 (0.33, 0.33%, 0.33%, 3800 psi)

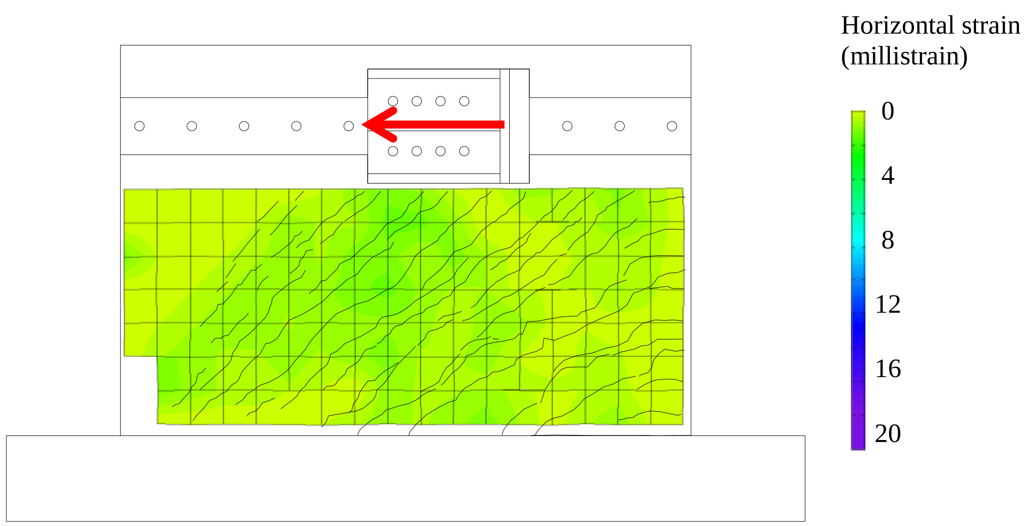

h) SW8 (0.54, 1.5%, 1.5%, 3500 psi)

Figure 4.14. Horizontal strain fields at peak strength (continued)

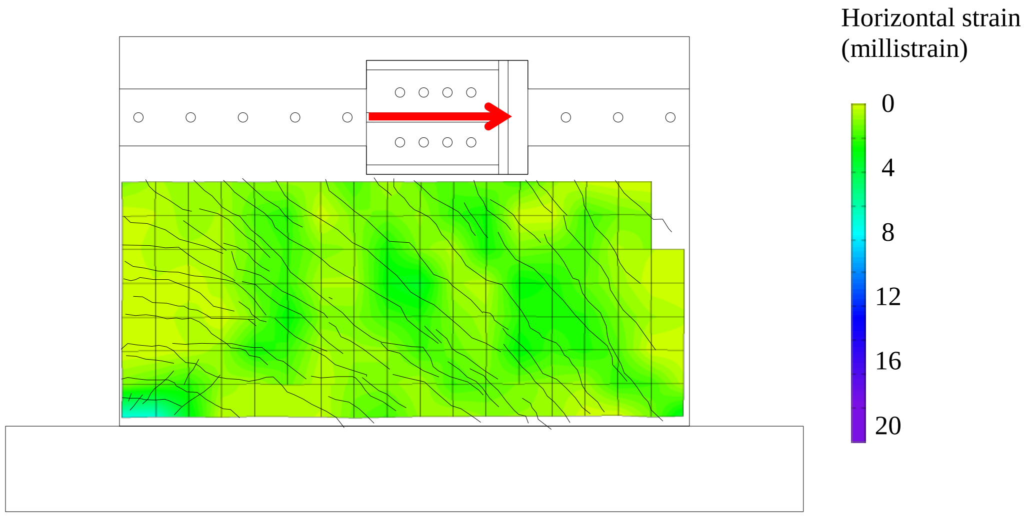

i) SW9 (0.54, 0.67%, 1.5%, 4300 psi)

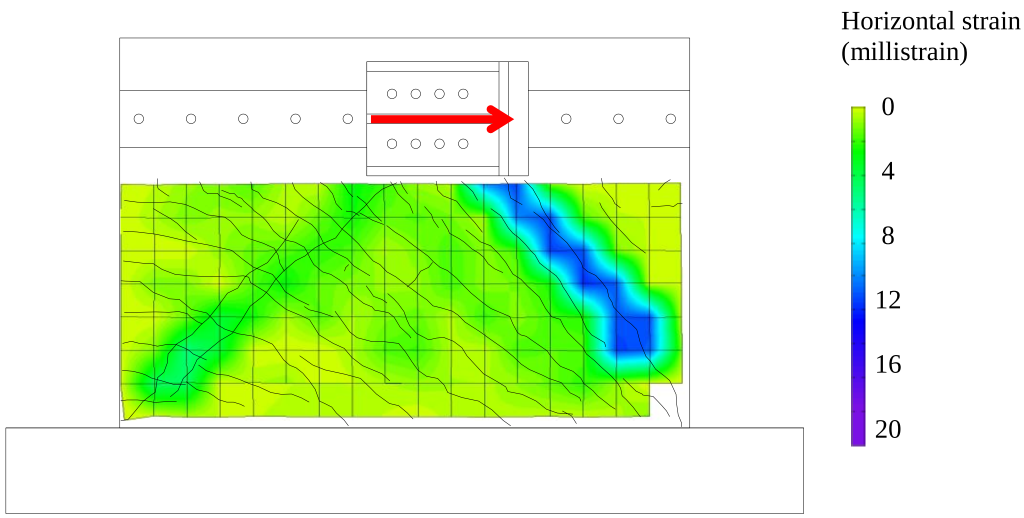

j) SW10 (0.54, 0.33%, 1.5%, 4600 psi)

Figure 4.14. Horizontal strain fields at peak strength (continued)

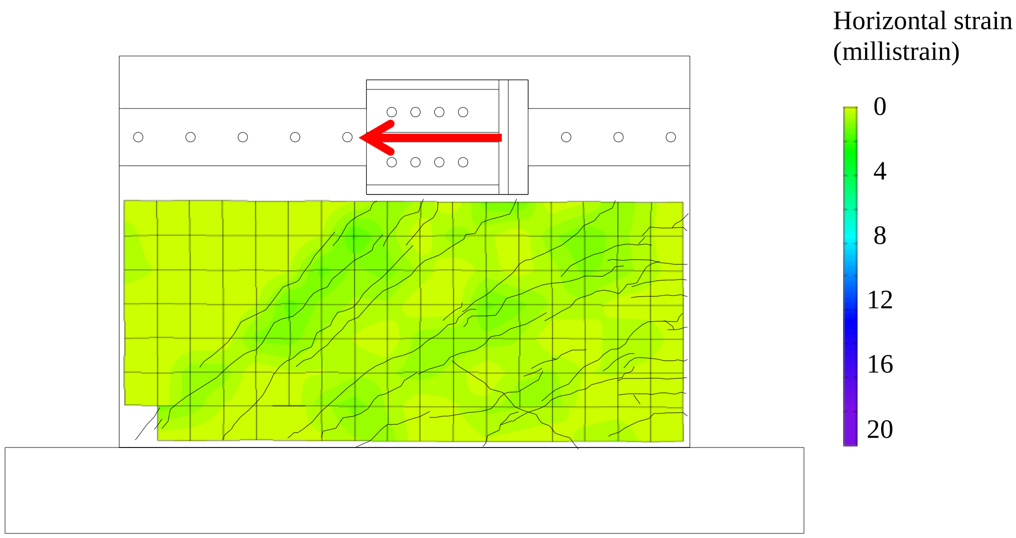

k) SW11 (0.54, 0.67%, 0.67%, 1.5% be, 5000 psi)

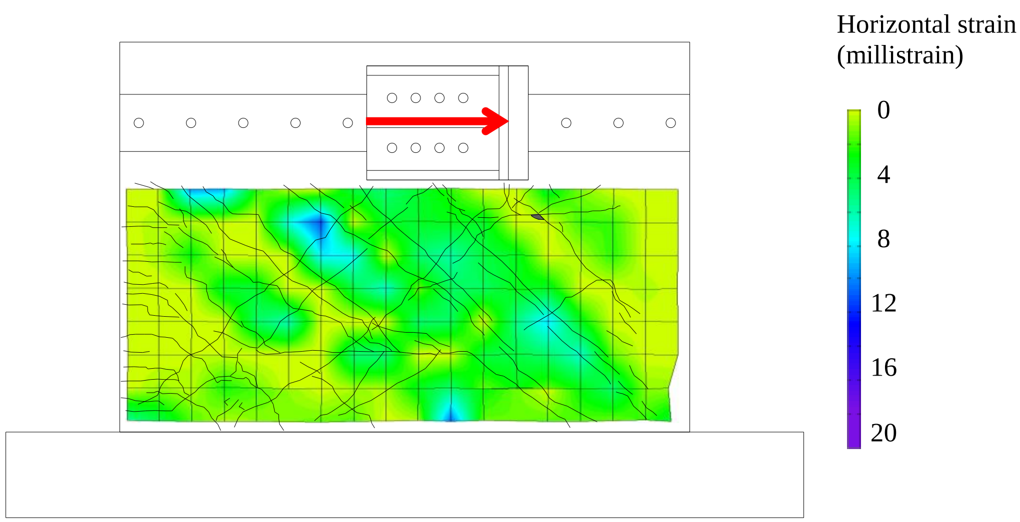

l) SW12 (0.54, 0.33%, 0.33%, 2.0% be, 5000 psi)

Figure 4.14. Horizontal strain fields at peak strength (continued)

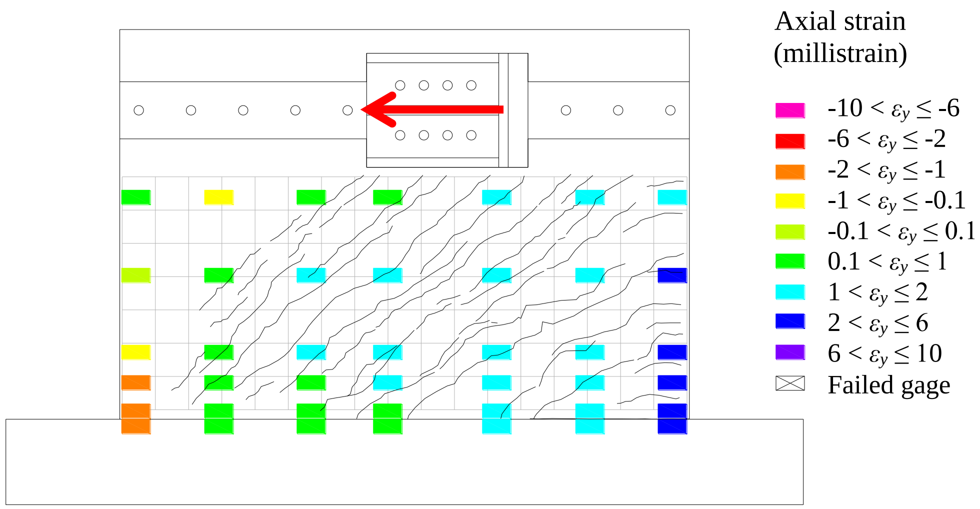

a) 0.35% drift ratio

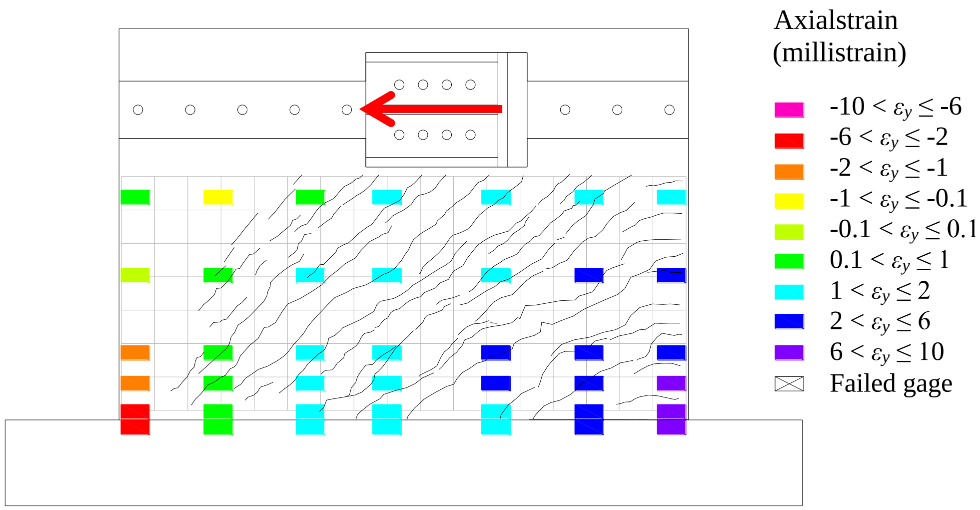

b) 0.5% drift ratio

Figure 4.15. Strains on vertical reinforcement of SW8 (0.54, 1.5%, 1.5%, 3500 psi)

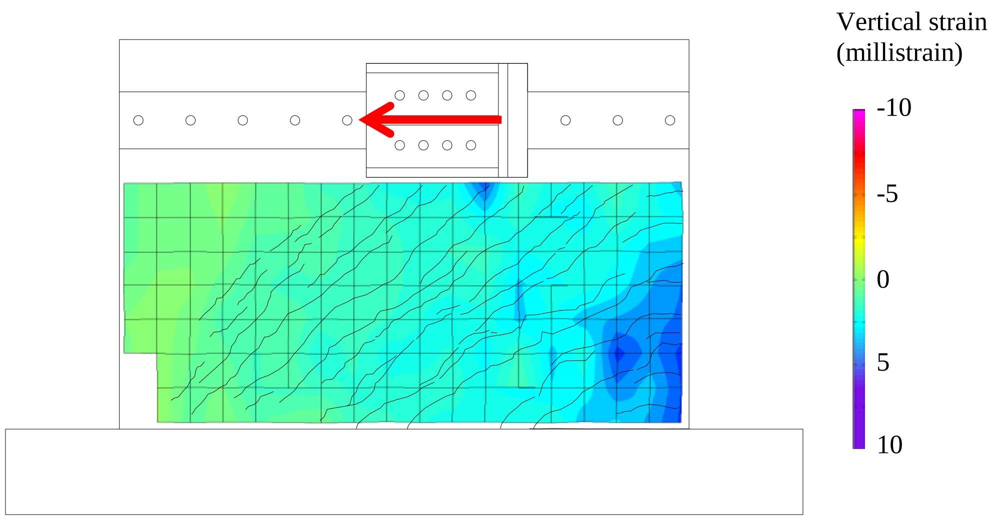

a) 0.35% drift ratio

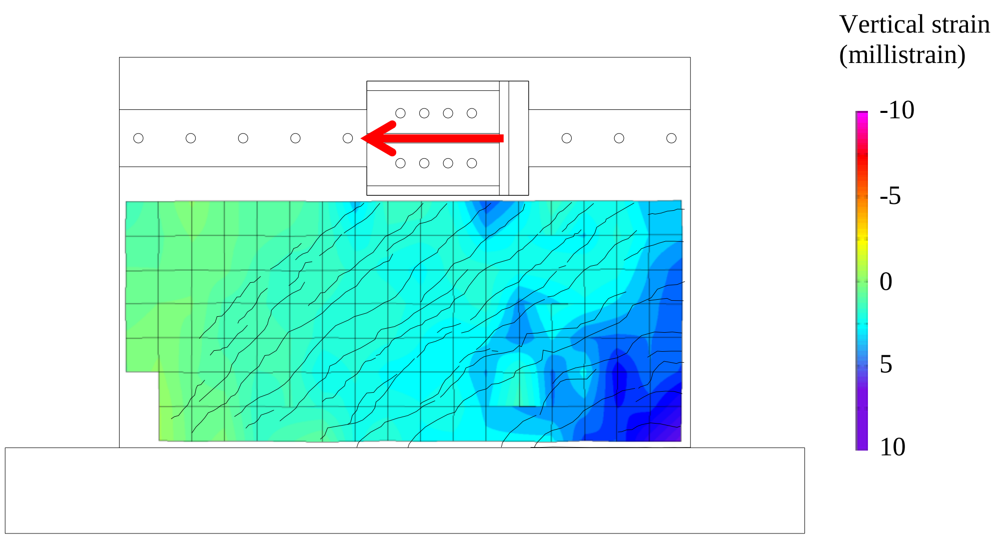

b) 0.5% drift ratio

Figure 4.16. Vertical strain fields on SW8 calculated from Krypton LED sensors

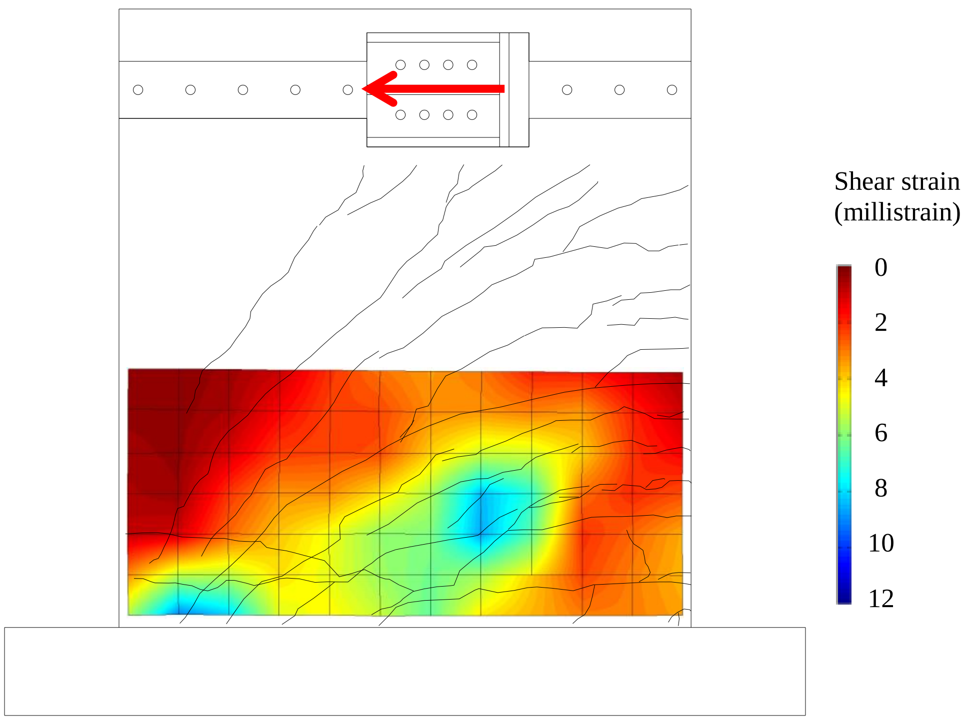

a) SW1 (0.94, 0.67%, 0.67%, 3600 psi)

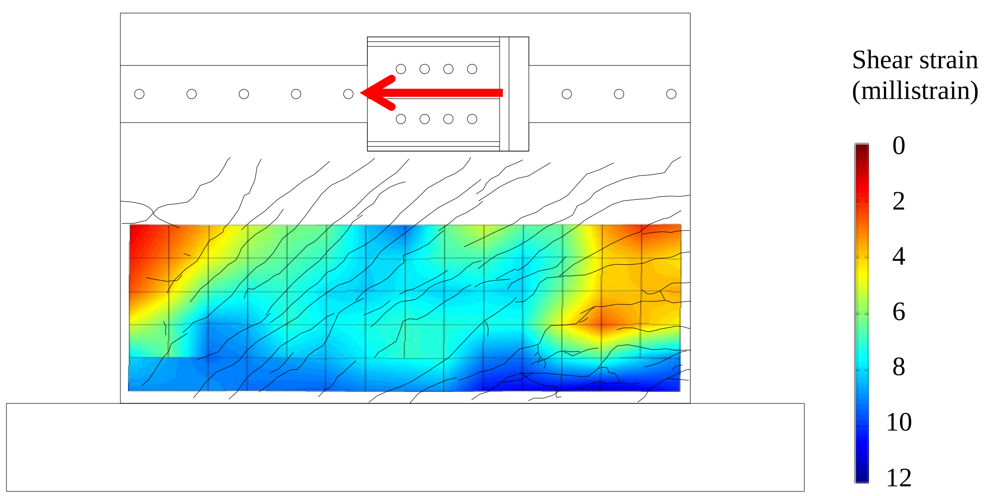

b) SW2 (0.54, 1.0%, 1.0%, 7000 psi)

Figure 4.17. Shear strain fields at peak strength

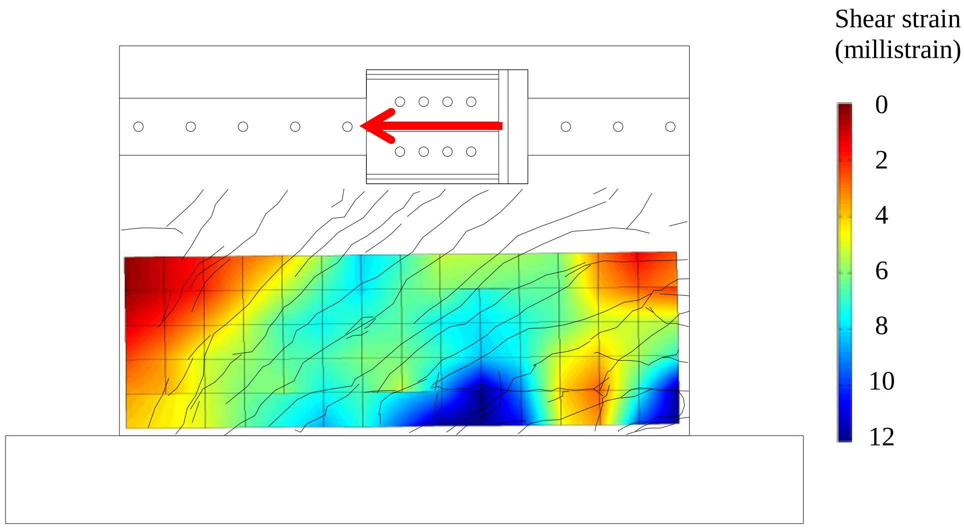

c) SW3 (0.54, 0.67%, 0.67%, 7800 psi)

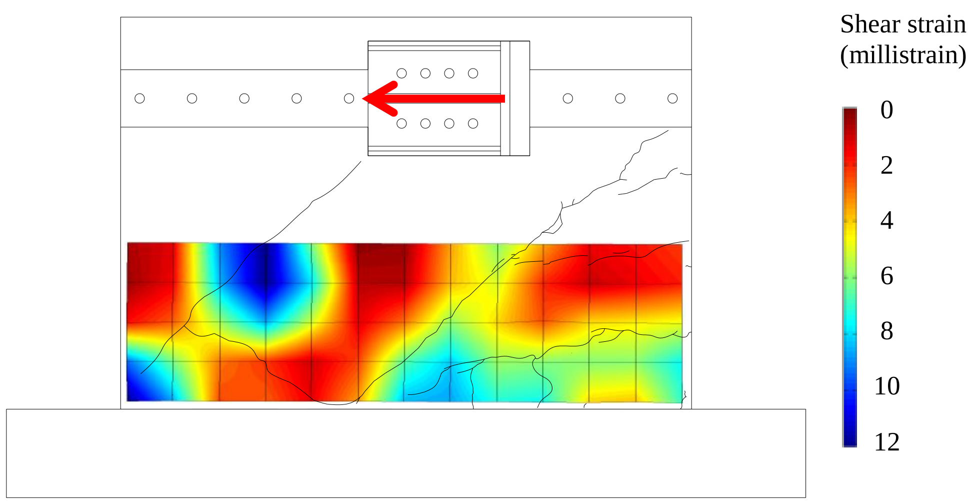

d) SW4 (0.54, 0.33%, 0.33%, 4200 psi)

Figure 4.17. Shear strain fields at peak strength (continued)

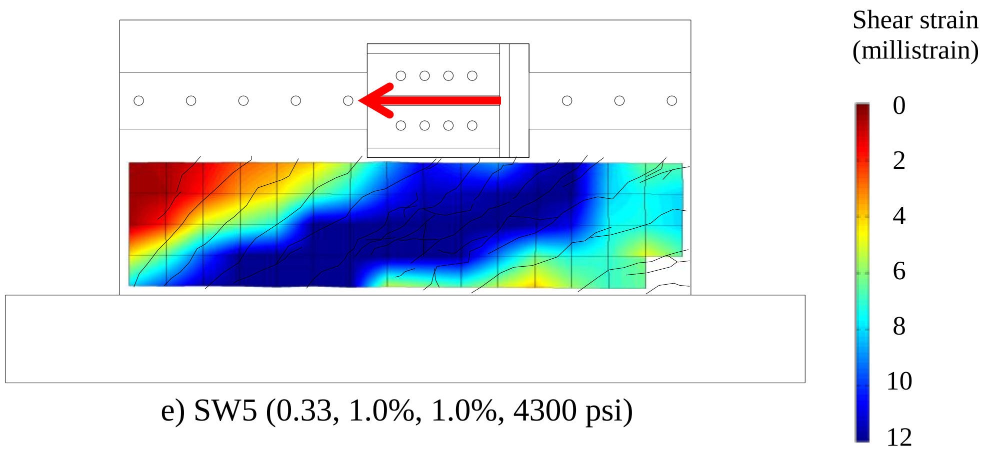

e) SW5 (0.33, 1.0%, 1.0%, 4300 psi)

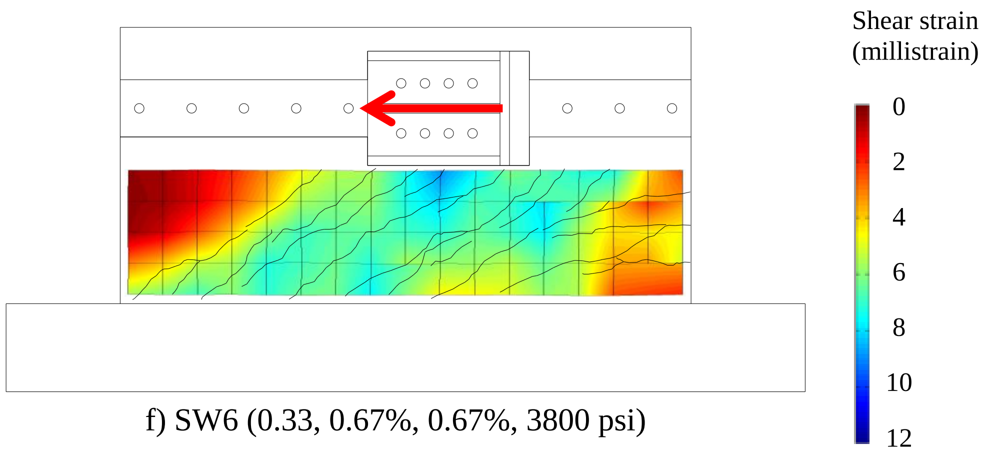

f) SW6 (0.33, 0.67%, 0.67%, 3800 psi)

Figure 4.17. Shear strain fields at peak strength (continued)

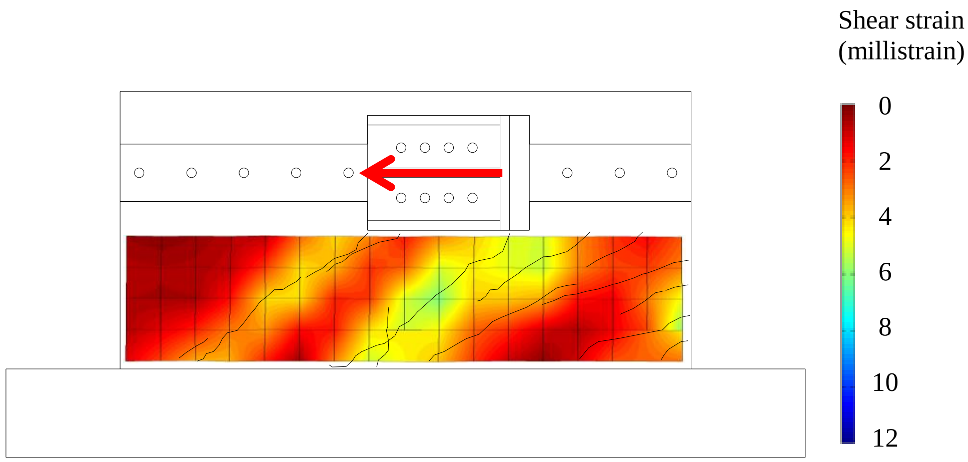

g) SW7 (0.33, 0.33%, 0.33%, 3800 psi)

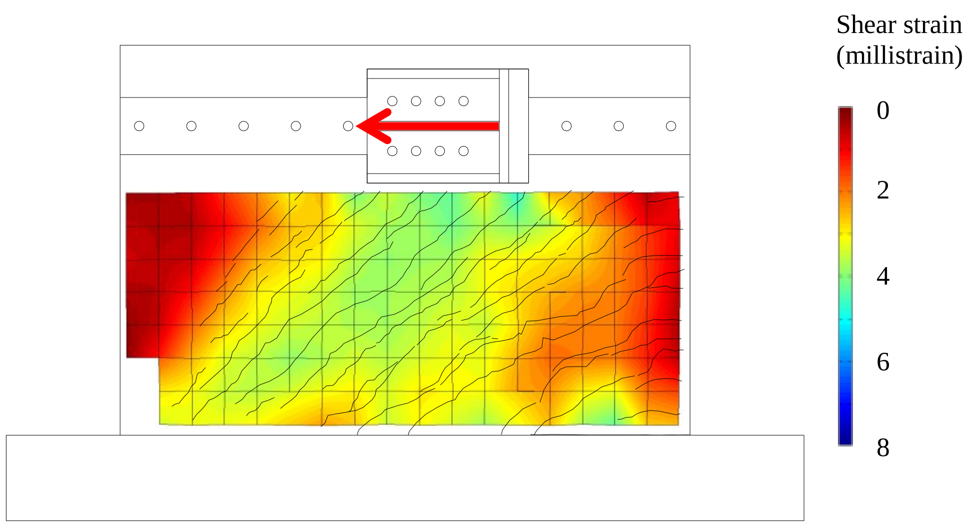

h) SW8 (0.54, 1.5%, 1.5%, 3500 psi)

Figure 4.17. Shear strain fields at peak strength (continued)

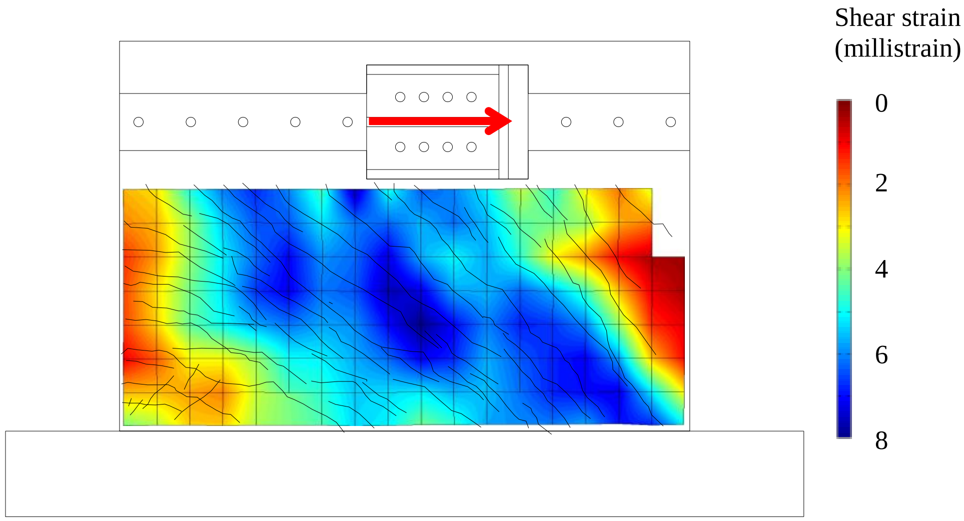

i) SW9 (0.54, 0.67%, 1.5%, 4300 psi)

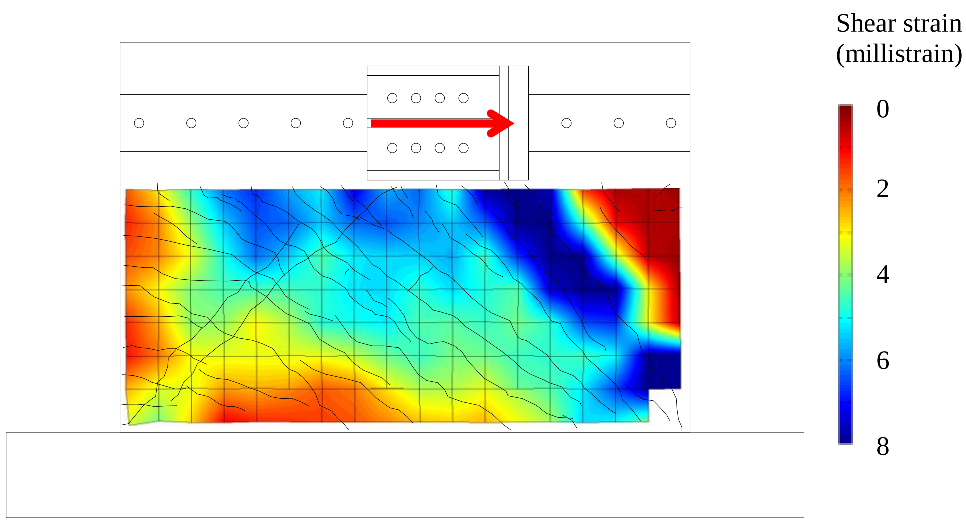

j) SW10 (0.54, 0.33%, 1.5%, 4600 psi)

Figure 4.17. Shear strain fields at peak strength (continued)

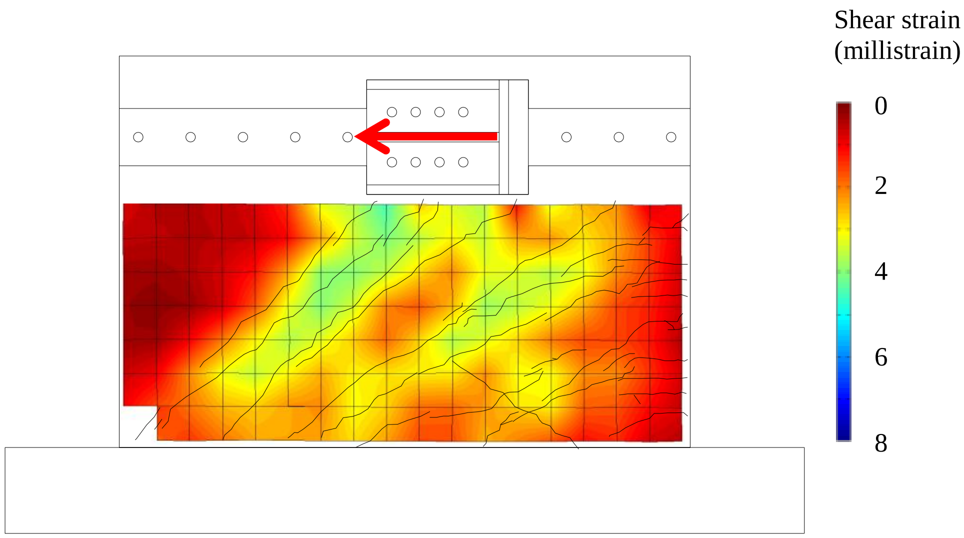

k) SW11 (0.54, 0.67%, 0.67%, 1.5% be, 5000 psi)

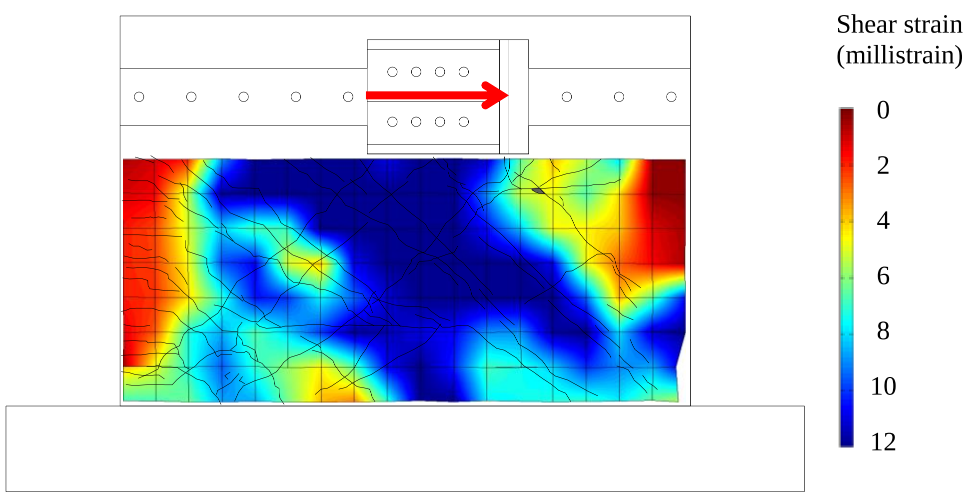

l) SW12 (0.54, 0.33%, 0.33%, 2.0% be, 5000 psi)

Figure 4.17. Shear strain fields at peak strength (continued)

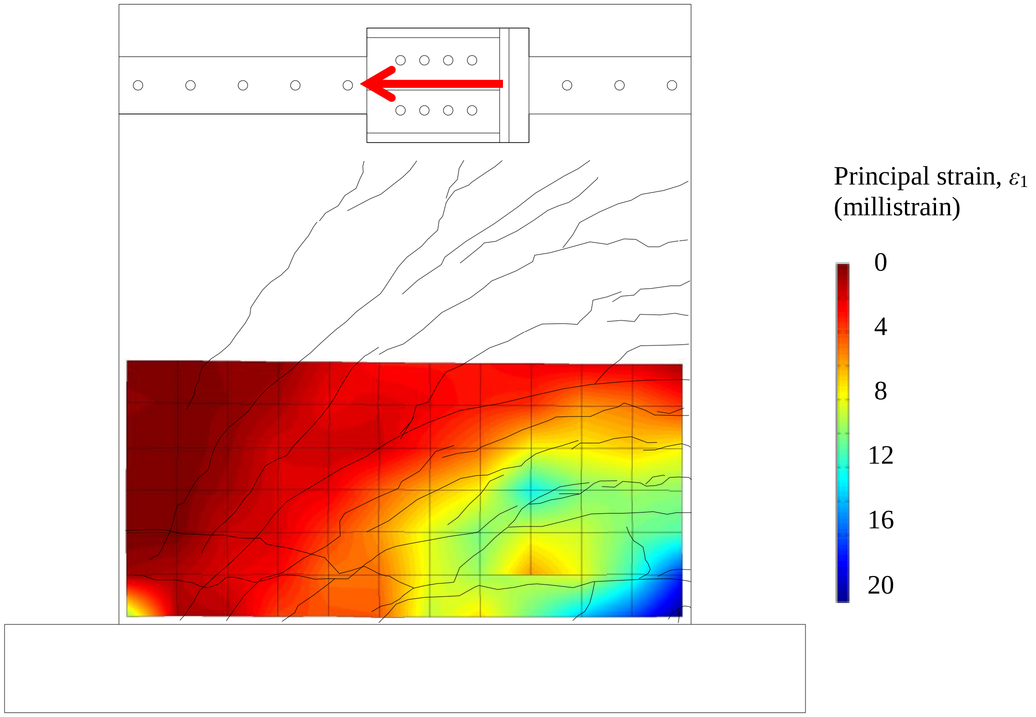

a) SW1 (0.94, 0.67%, 0.67%, 3600 psi)

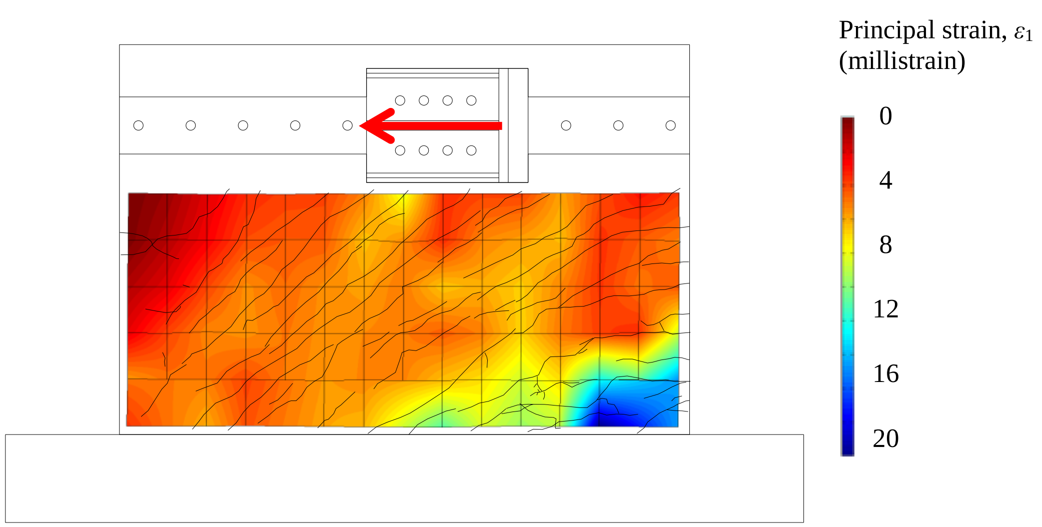

b) SW2 (0.54, 1.0%, 1.0%, 7000 psi)

Figure 4.18. Principal strain, ε_1, fields at peak strength

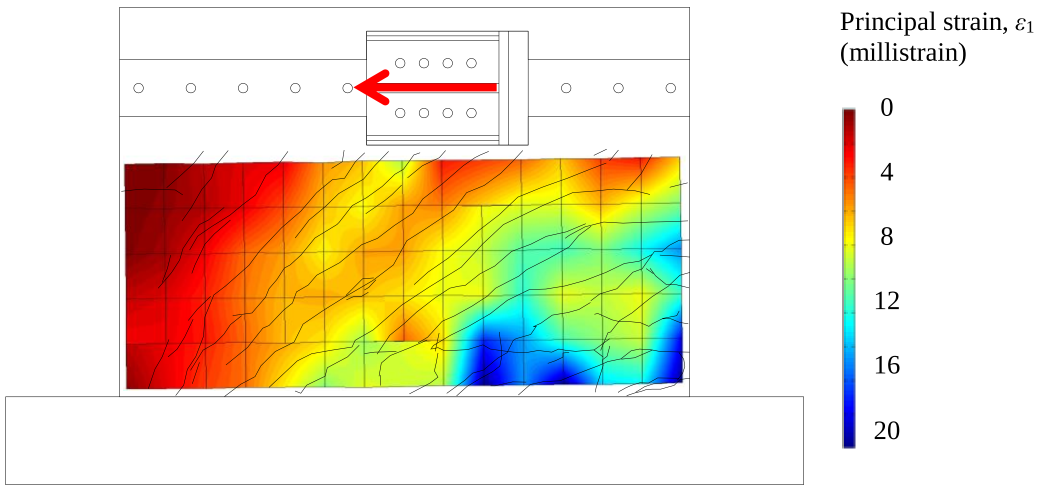

c) SW3 (0.54, 0.67%, 0.67%, 7800 psi)

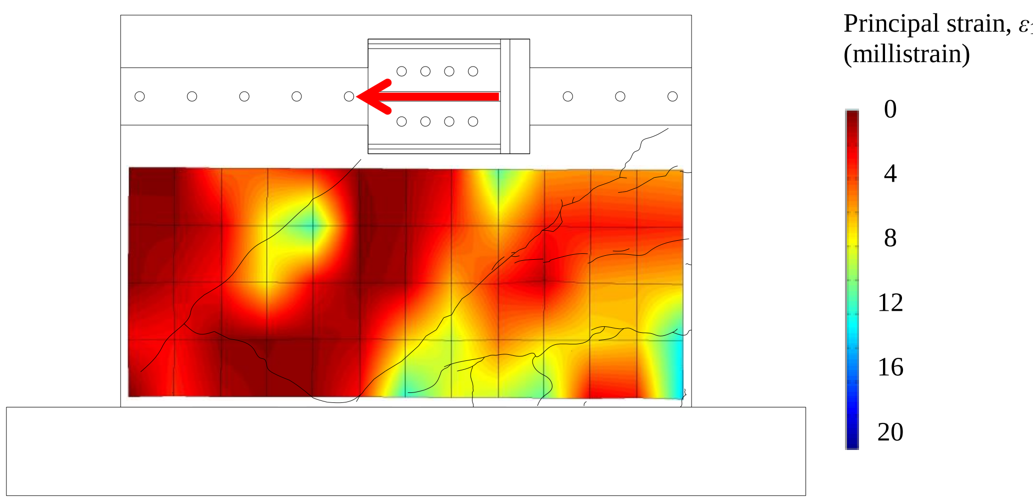

d) SW4 (0.54, 0.33%, 0.33%, 4200 psi)

Figure 4.18. Principal strain, ε_1, fields at peak strength (continued)

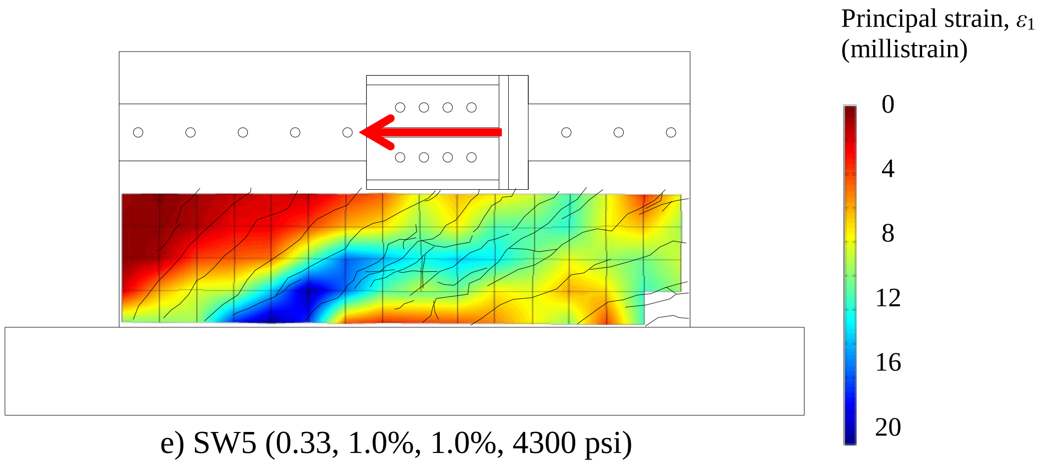

e) SW5 (0.33, 1.0%, 1.0%, 4300 psi)

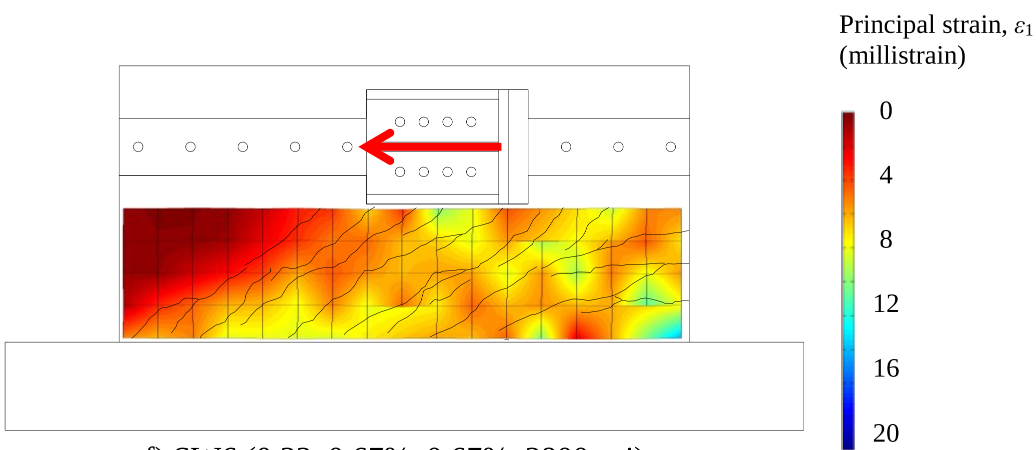

f) SW6 (0.33, 0.67%, 0.67%, 3800 psi)

Figure 4.18. Principal strain, ε_1, fields at peak strength (continued)

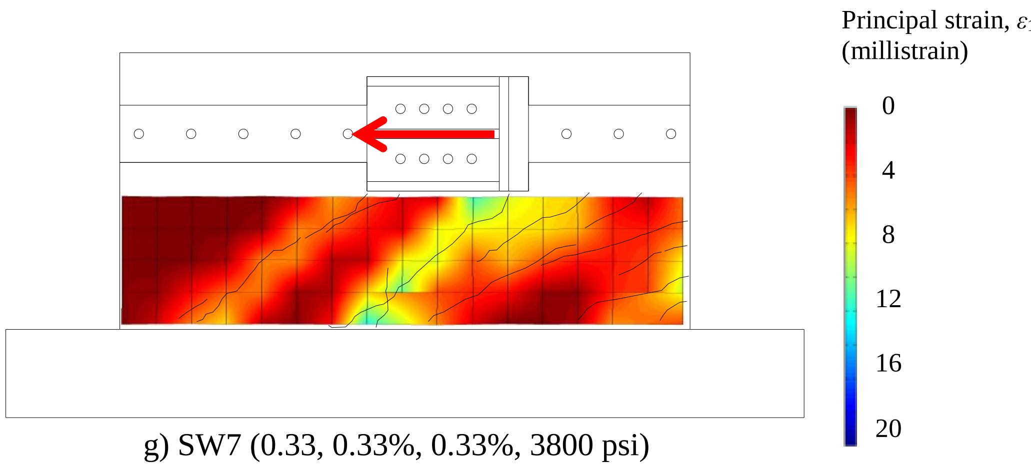

g) SW7 (0.33, 0.33%, 0.33%, 3800 psi)

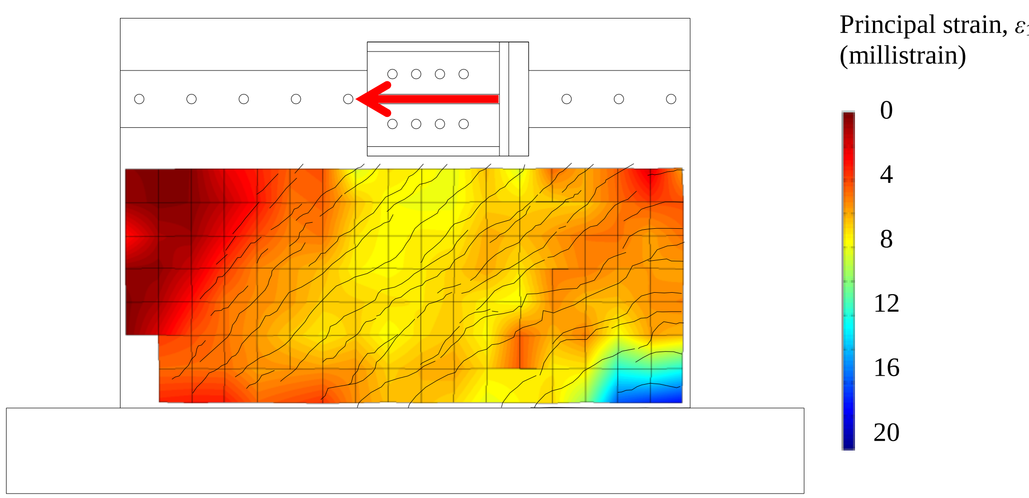

h) SW8 (0.54, 1.5%, 1.5%, 3500 psi)

Figure 4.18. Principal strain, ε_1, fields at peak strength (continued)

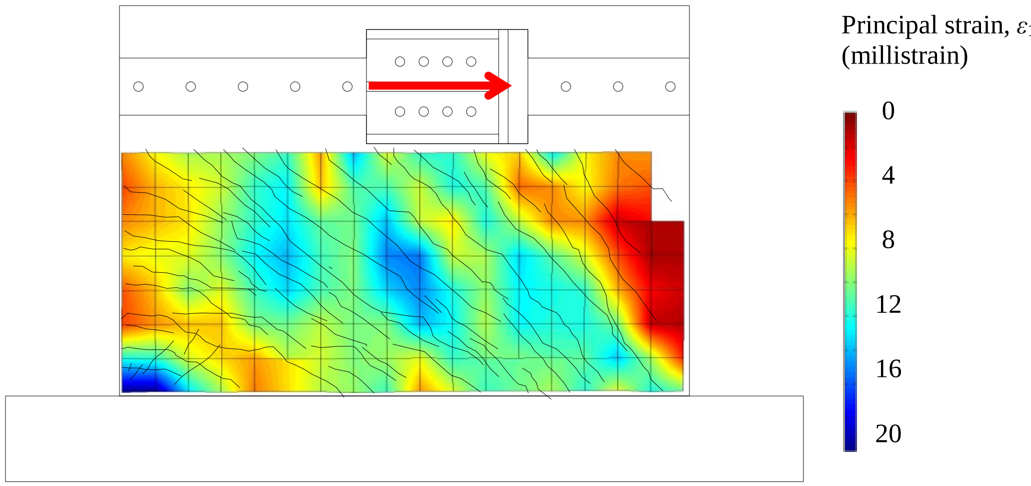

i) SW9 (0.54, 0.67%, 1.5%, 4300 psi)

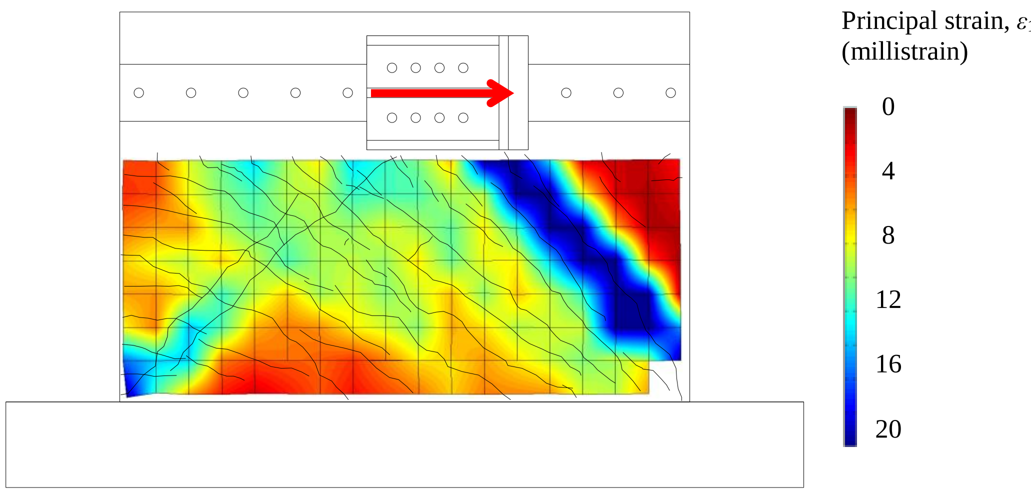

j) SW10 (0.54, 0.33%, 1.5%, 4600 psi)

Figure 4.18. Principal strain, ε_1, fields at peak strength (continued)

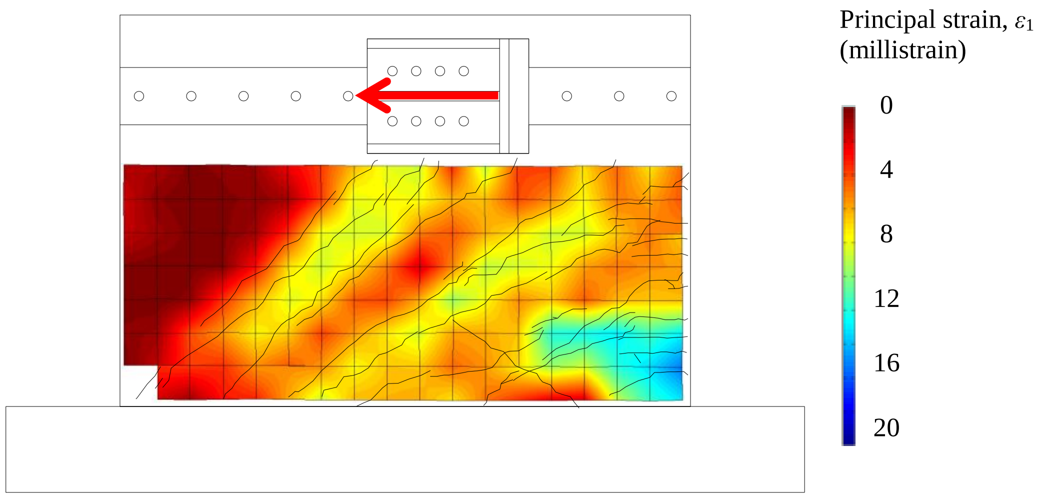

k) SW11 (0.54, 0.67%, 0.67%, 1.5% be, 5000 psi)

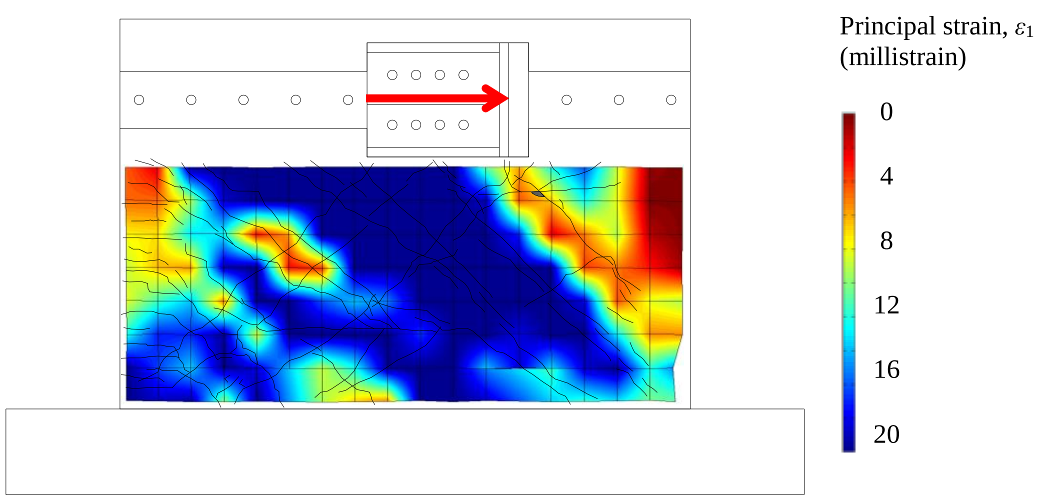

l) SW12 (0.54, 0.33%, 0.33%, 2.0% be, 5000 psi)

Figure 4.18. Principal strain, ε_1, fields at peak strength (continued)

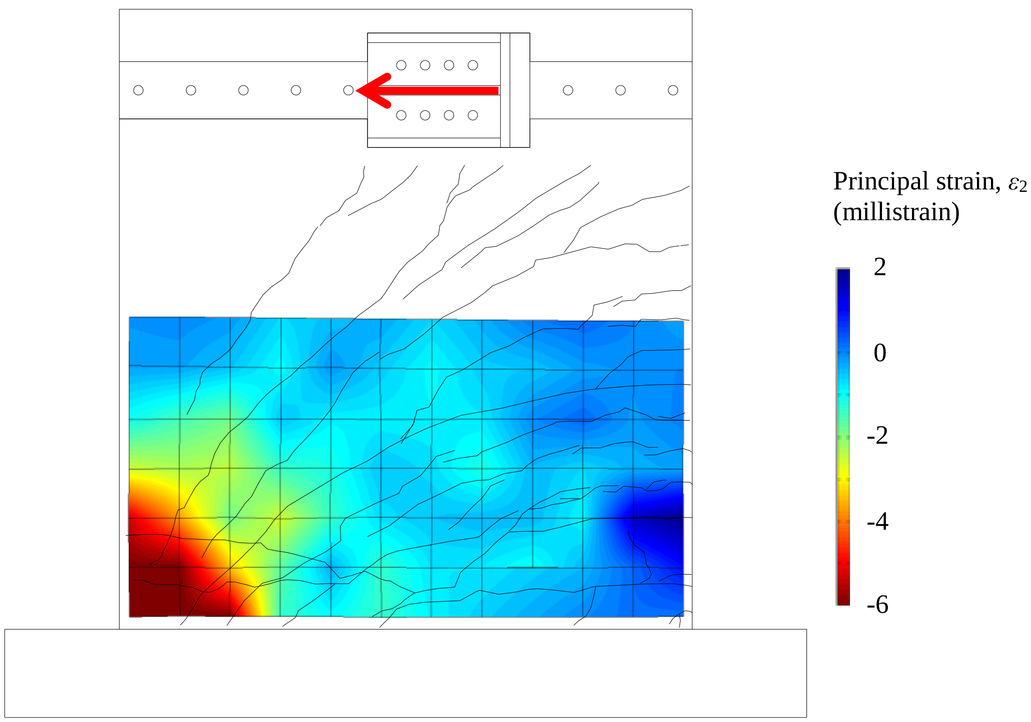

a) SW1 (0.94, 0.67%, 0.67%, 3600 psi)

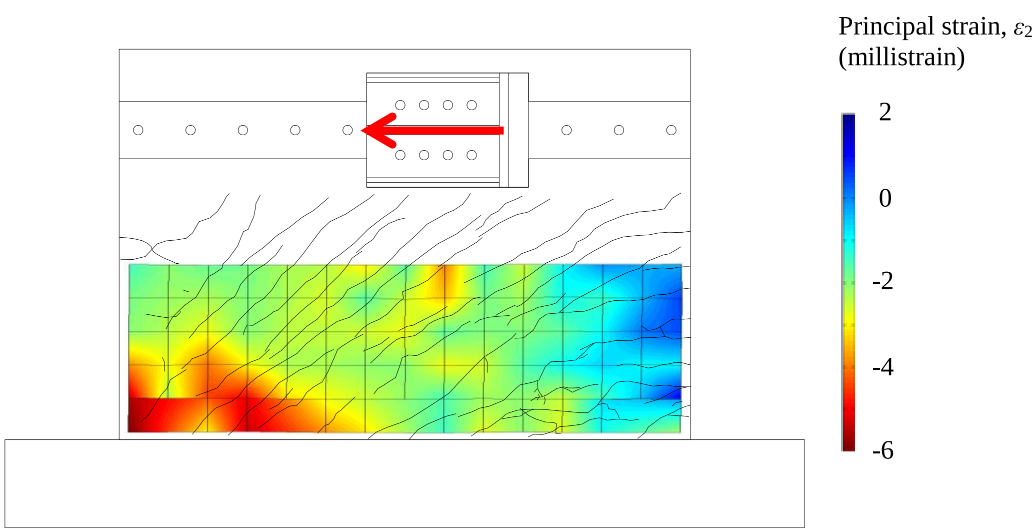

b) SW2 (0.54, 1.0%, 1.0%, 7000 psi)

Figure 4.19. Principal strain, ε_2, fields at peak strength

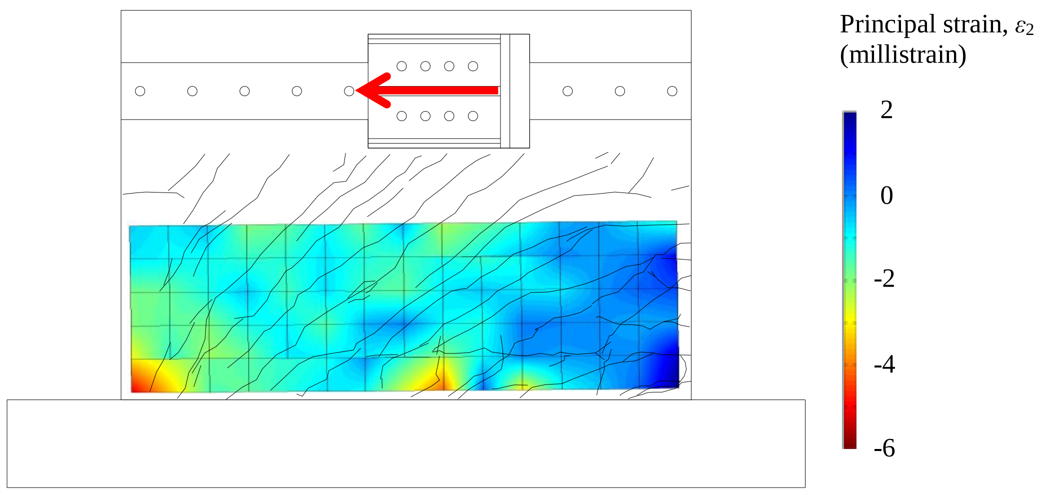

c) SW3 (0.54, 0.67%, 0.67%, 7800 psi)

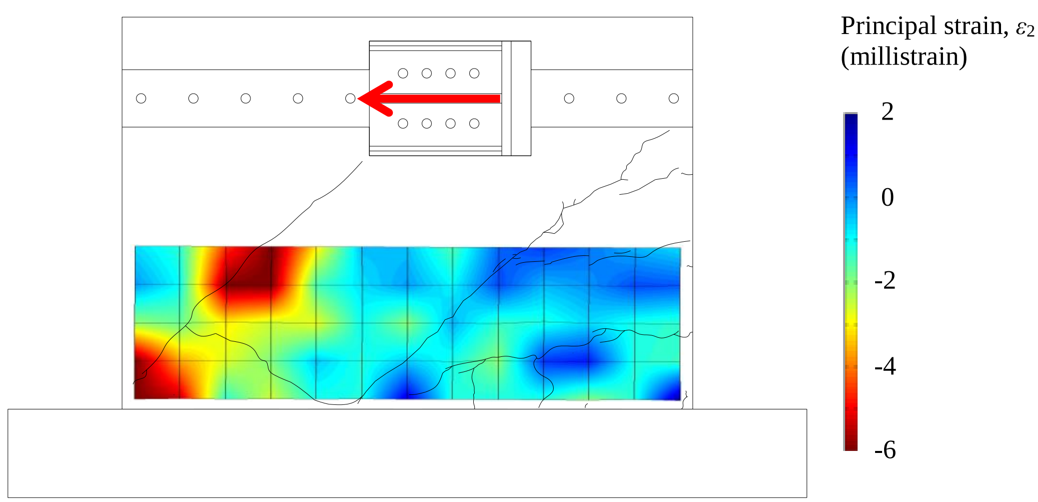

d) SW4 (0.54, 0.33%, 0.33%, 4200 psi)

Figure 4.19 Principal strain, ε_2, fields at peak strength (continued)

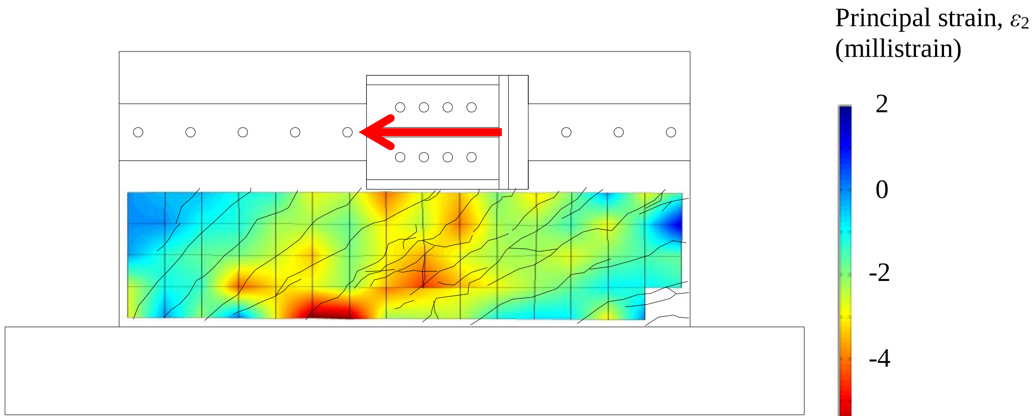

e) SW5 (0.33, 1.0%, 1.0%, 4300 psi)

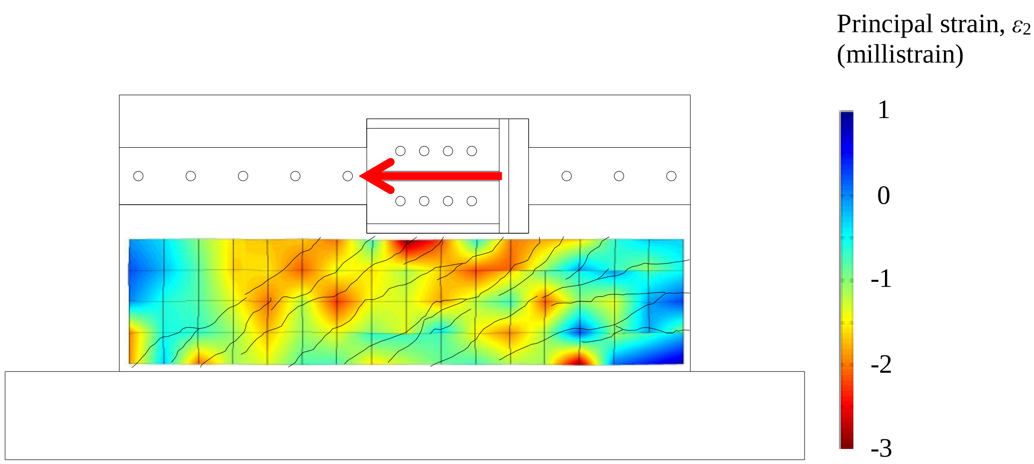

f) SW6 (0.33, 0.67%, 0.67%, 3800 psi)

Figure 4.19. Principal strain, ε_2, fields at peak strength (continued)

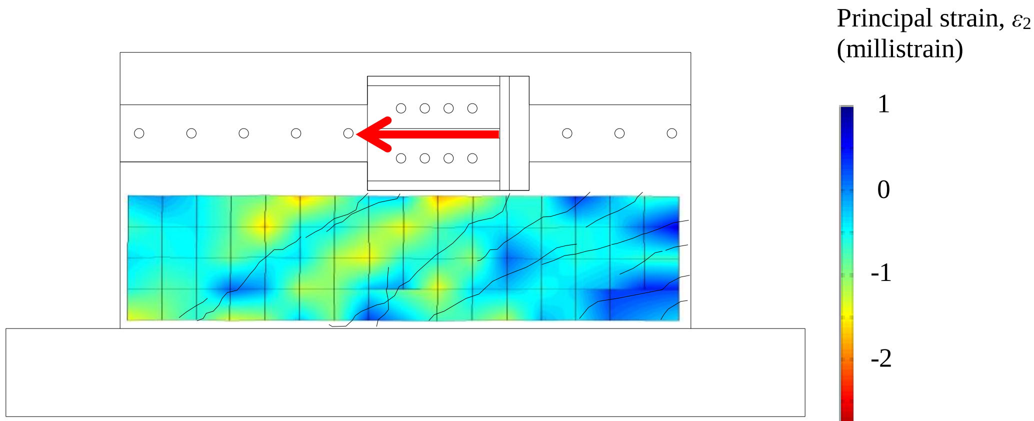

g) SW7 (0.33, 0.33%, 0.33%, 3800 psi)

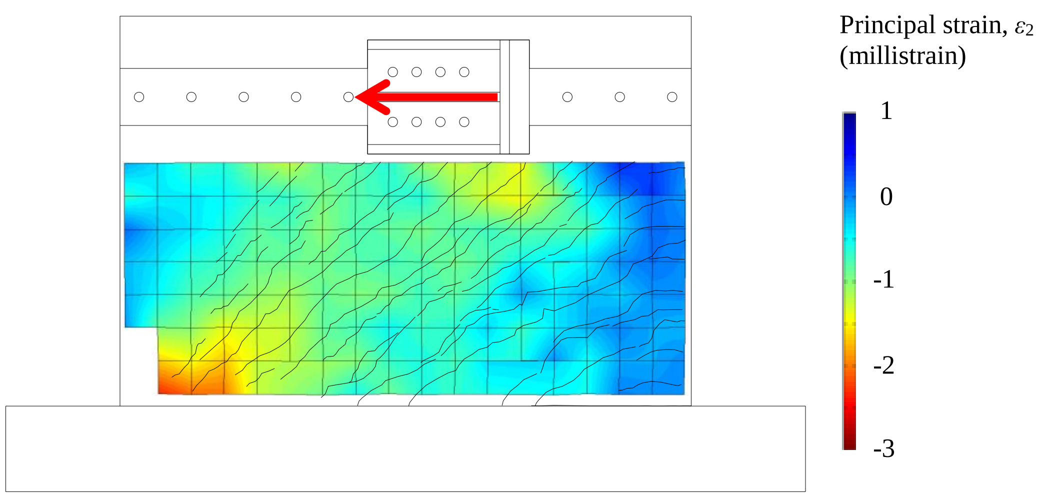

h) SW8 (0.54, 1.5%, 1.5%, 3500 psi)

Figure 4.19. Principal strain, ε_2, fields at peak strength (continued)

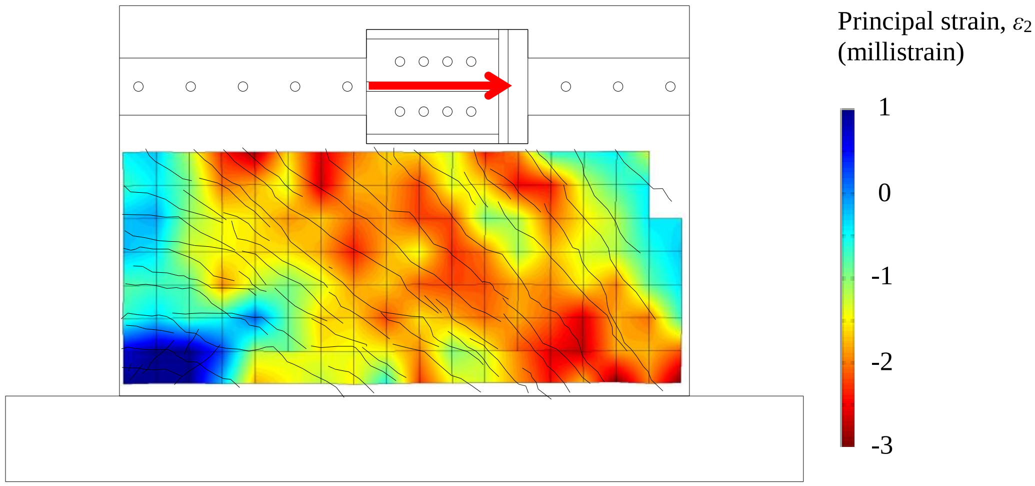

i) SW9 (0.54, 0.67%, 1.5%, 4300 psi)

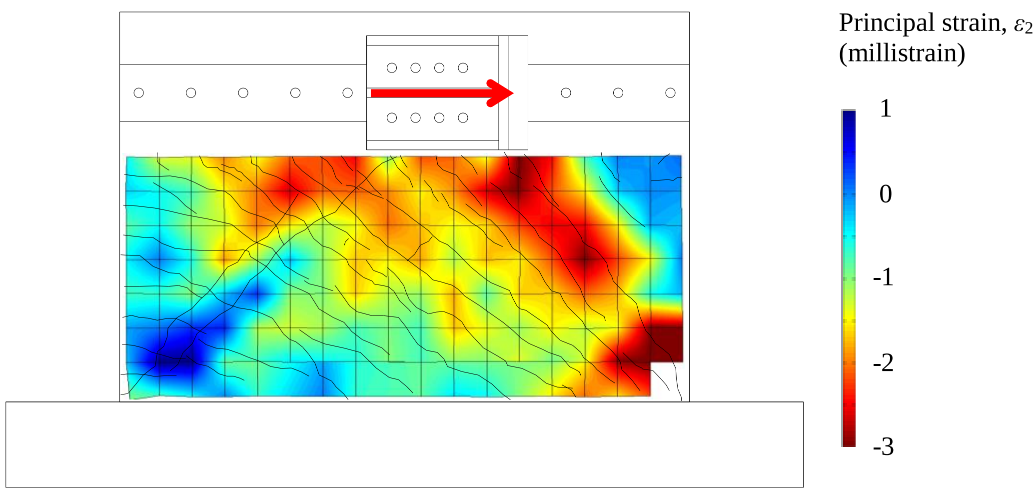

j) SW10 (0.54, 0.33%, 1.5%, 4600 psi)

Figure 4.19. Principal strain, ε_2, fields at peak strength (continued)

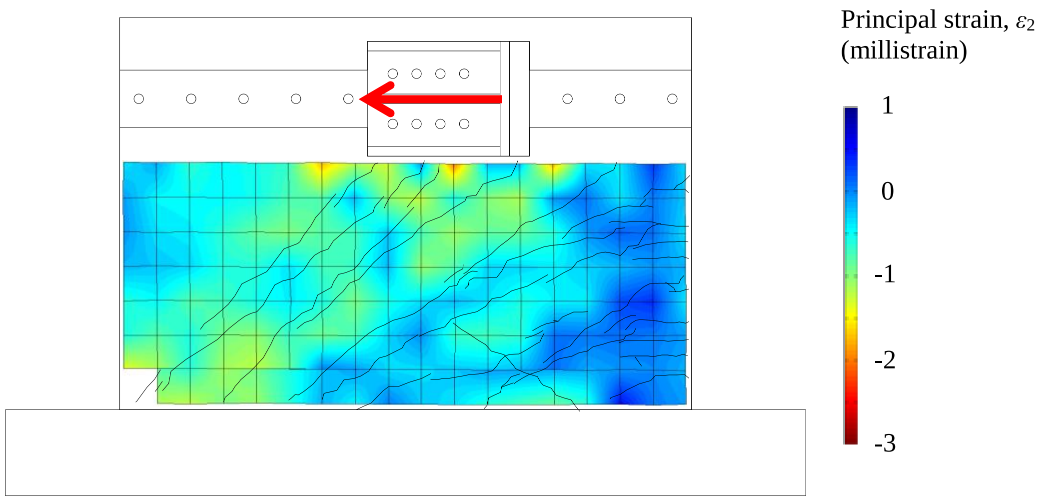

k) SW11 (0.54, 0.67%, 0.67%, 1.5% be, 5000 psi)

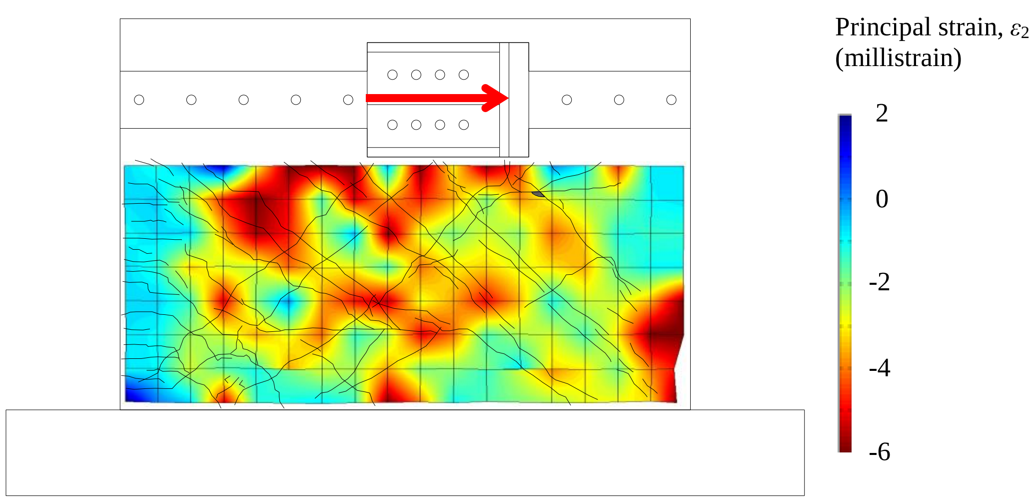

l) SW12 (0.54, 0.33%, 0.33%, 2.0% be, 5000 psi)

Figure 4.19. Principal strain, ε_2, fields at peak strength (continued)

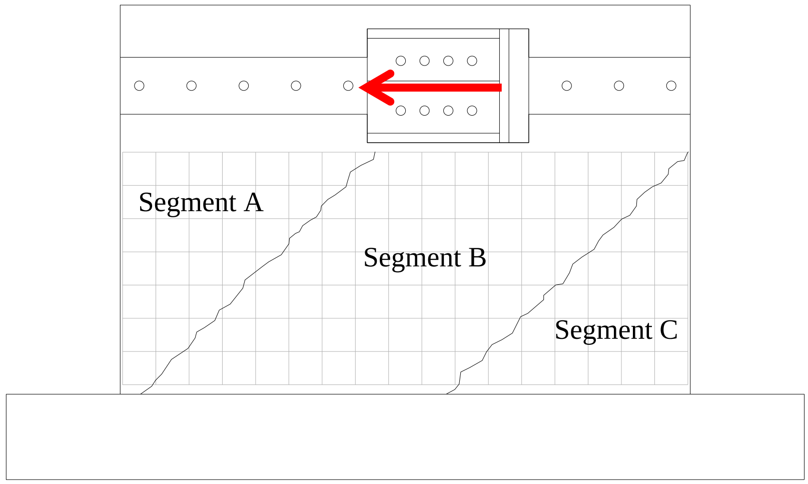

a) Walls without boundary elements

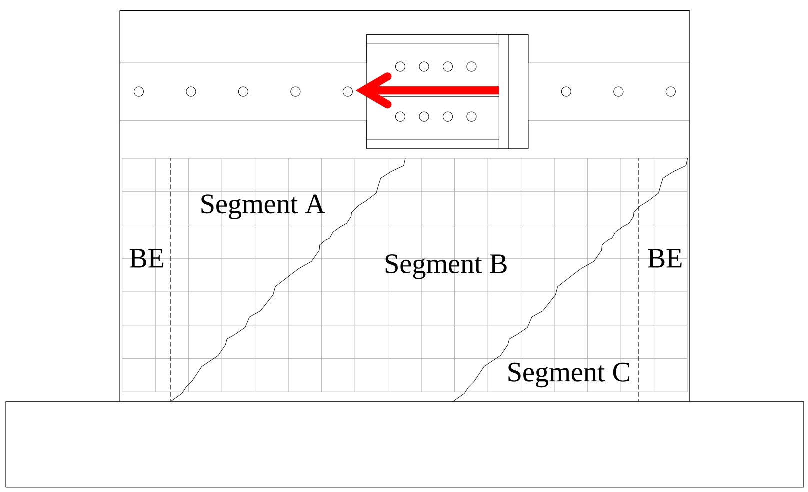

b) Walls with boundary elements

Figure 4.20. Three distinct segments of the walls with different strain distributions

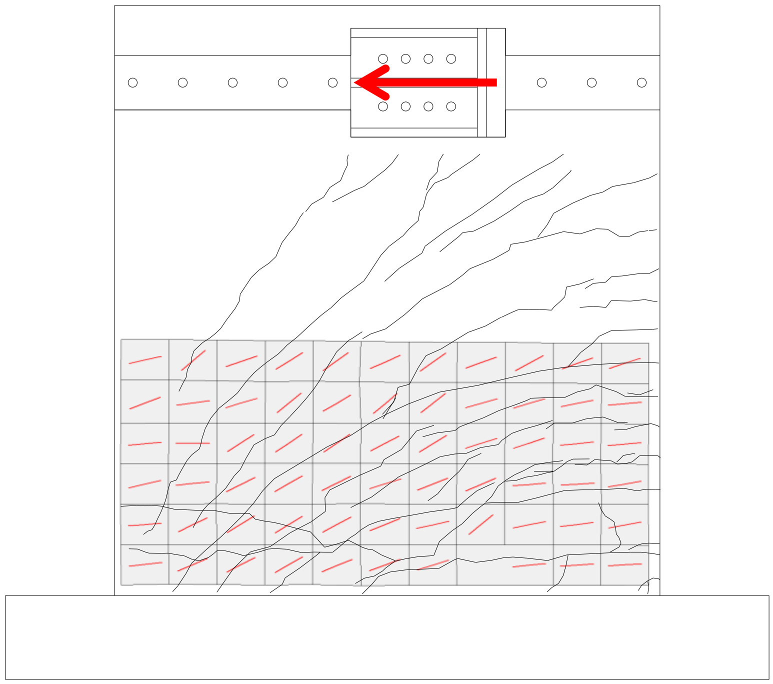

a) SW1 (0.94, 0.67%, 0.67%, 3600 psi)

b) SW2 (0.54, 1.0%, 1.0%, 7000 psi)

Figure 4.21. Orientation of principal strains at peak strength

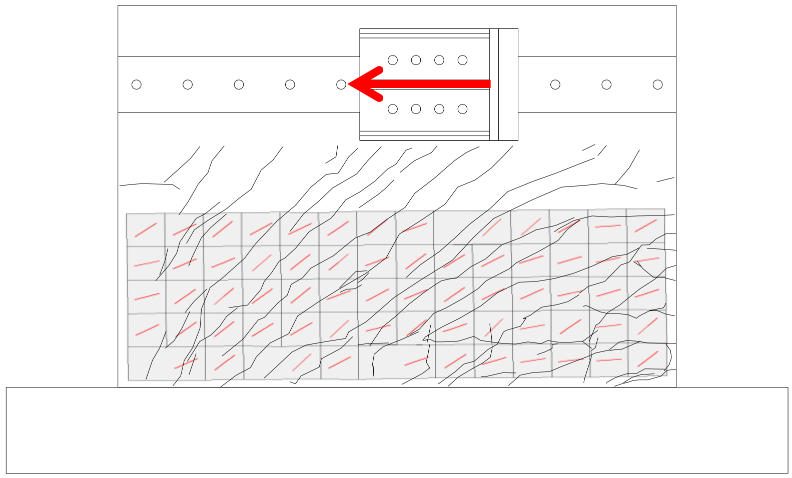

c) SW3 (0.54, 0.67%, 0.67%, 7800 psi)

d) SW4 (0.54, 0.33%, 0.33%, 4200 psi)

Figure 4.21 Orientation of principal strains at peak strength (continued)

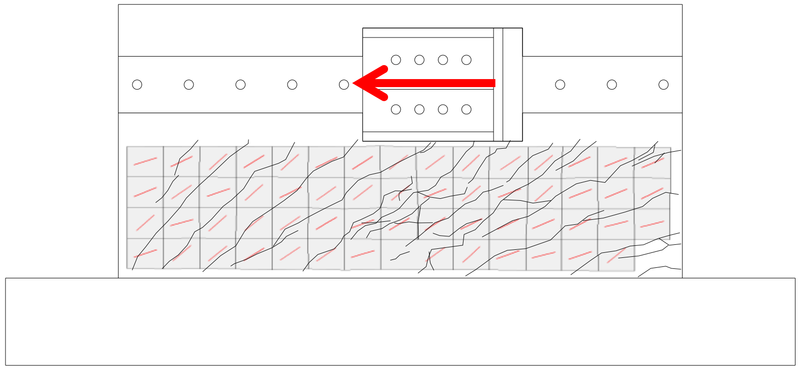

e) SW5 (0.33, 1.0%, 1.0%, 4300 psi)

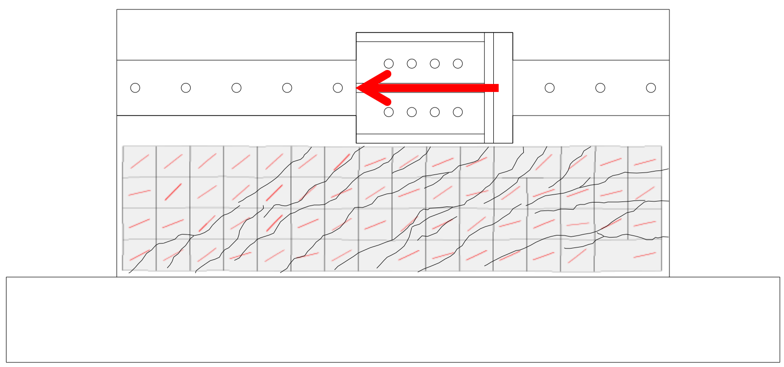

f) SW6 (0.33, 0.67%, 0.67%, 3800 psi)

Figure 4.21 Orientation of principal strains at peak strength (continued)

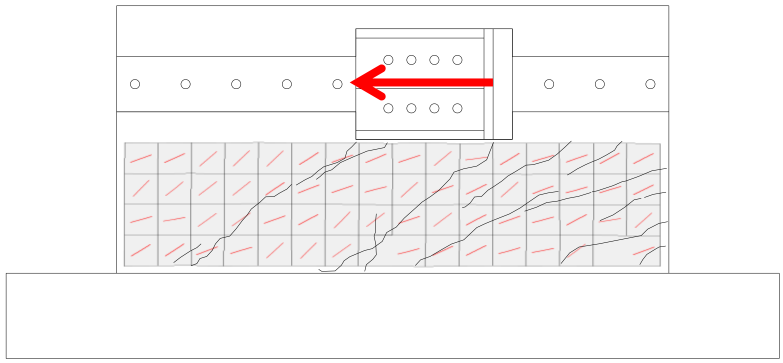

g) SW7 (0.33, 0.33%, 0.33%, 3800 psi)

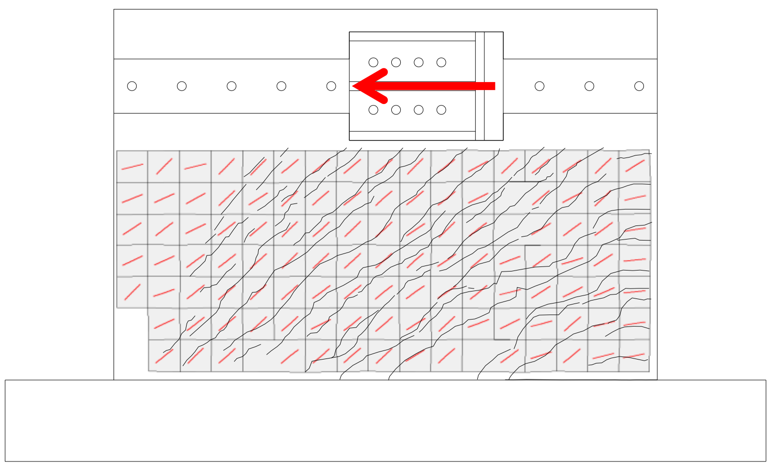

h) SW8 (0.54, 1.5%, 1.5%, 3500 psi)

Figure 4.21 Orientation of principal strains at peak strength (continued)

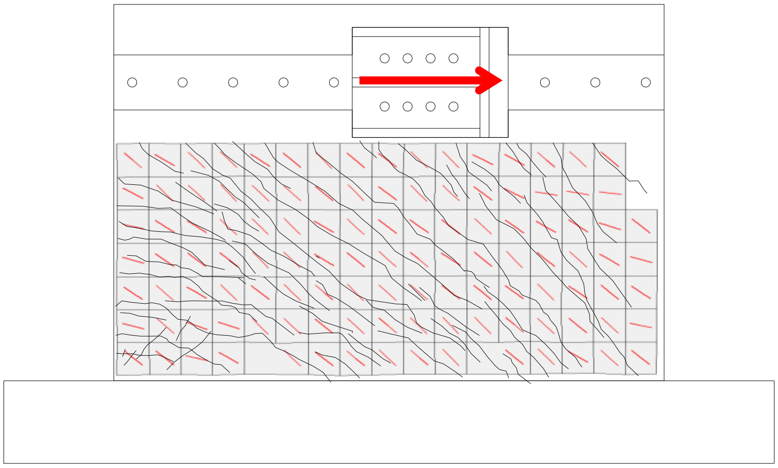

i) SW9 (0.54, 0.67%, 1.5%, 4300 psi)

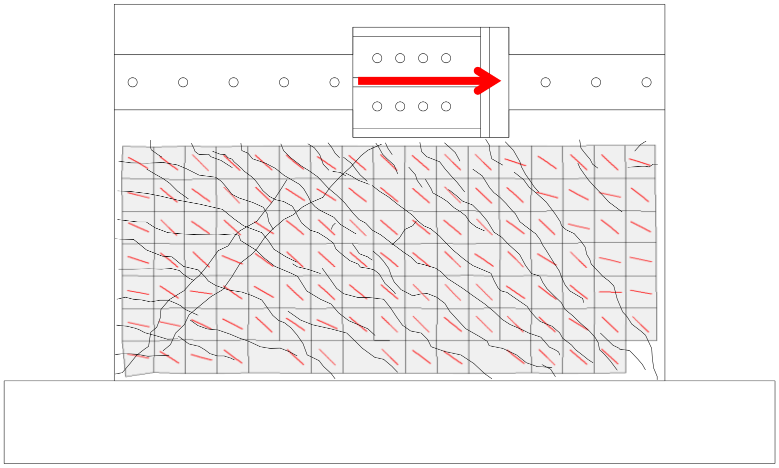

j) SW10 (0.54, 0.33%, 1.5%, 4600 psi)

Figure 4.21 Orientation of principal strains at peak strength (continued)

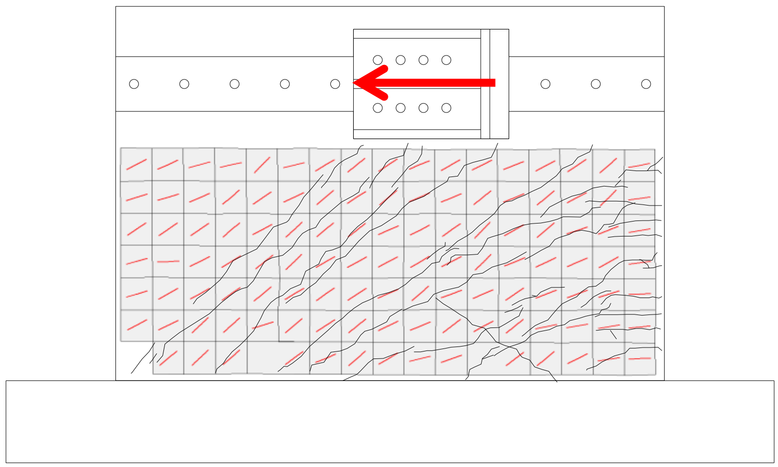

k) SW11 (0.54, 0.67%, 0.67%, 1.5% be, 5000 psi)

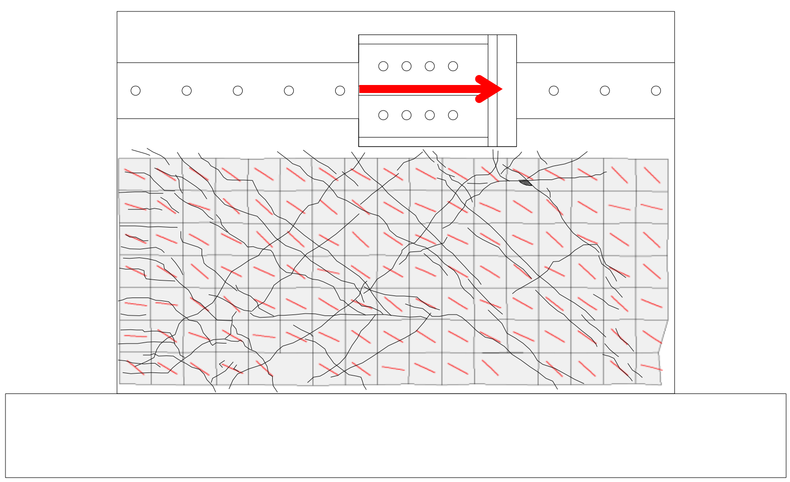

l) SW12 (0.54, 0.33%, 0.33%, 2.0% be, 5000 psi)

Figure 4.21 Orientation of principal strains at peak strength (continued)

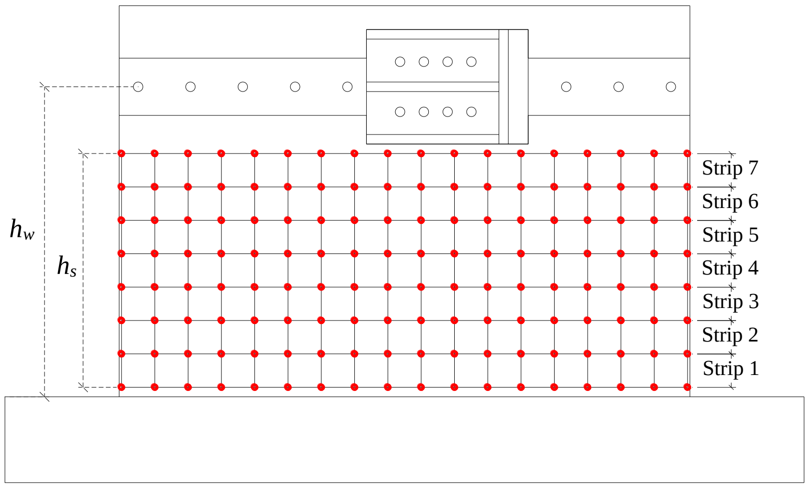

Figure 4.22. Typical grid of Krypton LED sensors

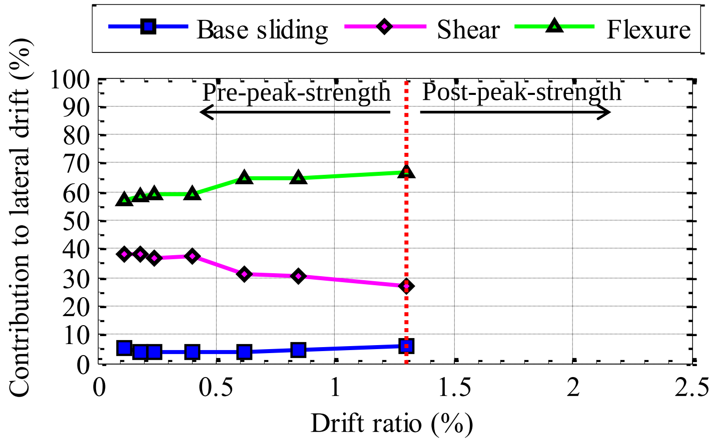

a) SW1 (0.94, 0.67%, 0.67%, 3600 psi)

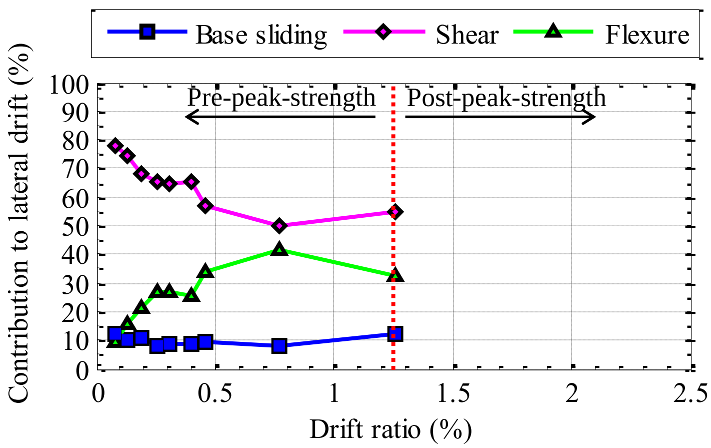

b) SW2 (0.54, 1.0%, 1.0%, 7000 psi)

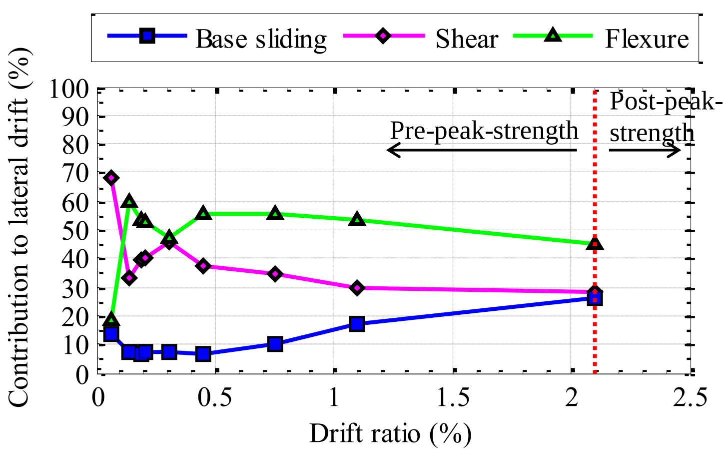

c) SW3 (0.54, 0.67%, 0.67%, 7800 psi)

Figure 4.23. Components of the total lateral displacement

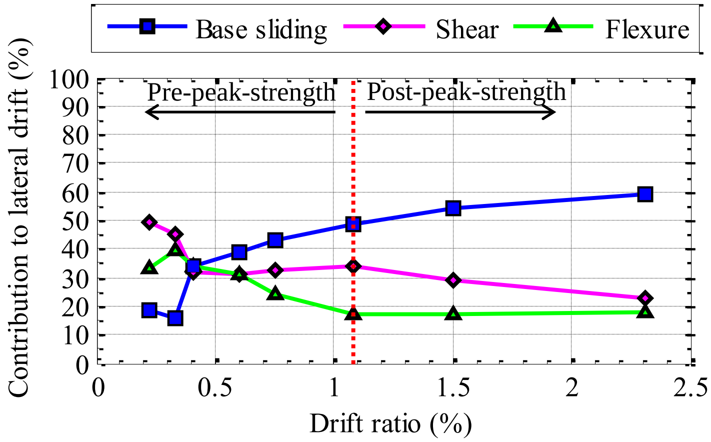

d) SW4 (0.54, 0.33%, 0.33%, 4200 psi)

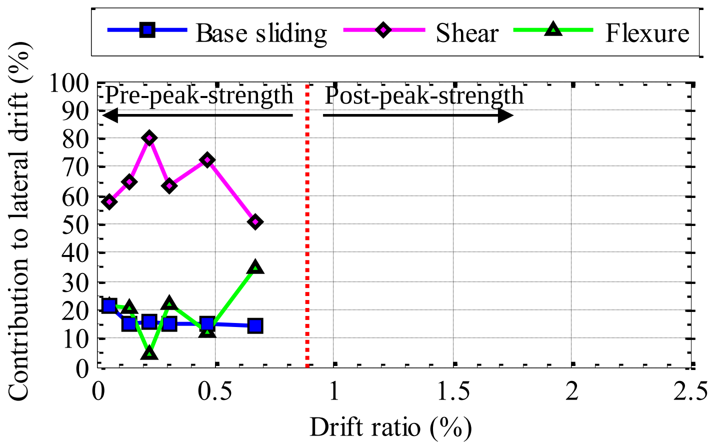

e) SW5 (0.33, 1.0%, 1.0%, 4300 psi)

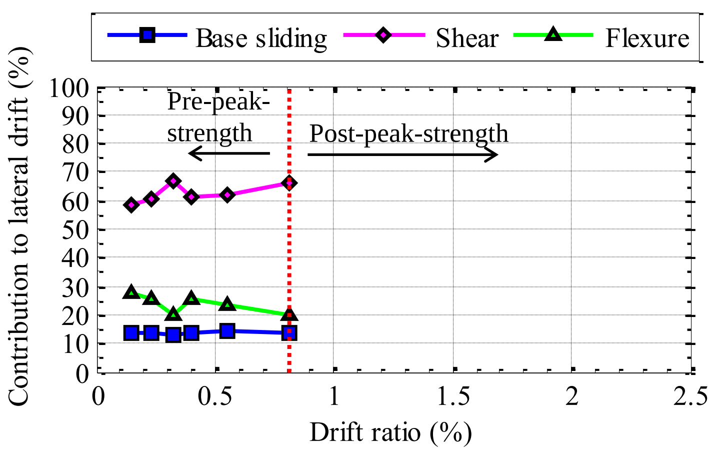

f) SW6 (0.33, 0.67%, 0.67%, 3800 psi)

Figure 4.23. Components of the total lateral displacement (continued)

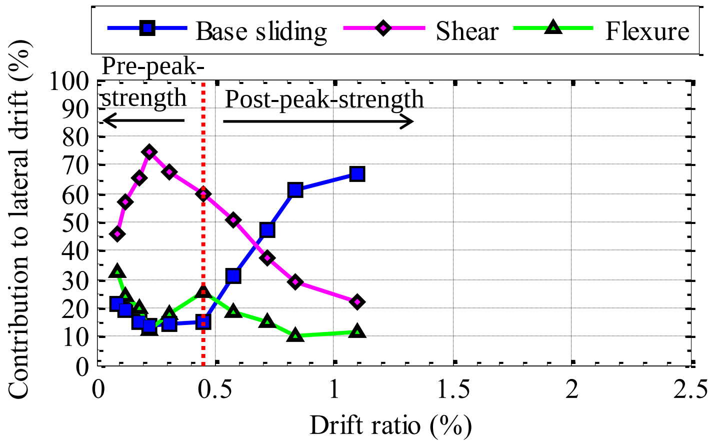

g) SW7 (0.33, 0.33%, 0.33%, 3800 psi)

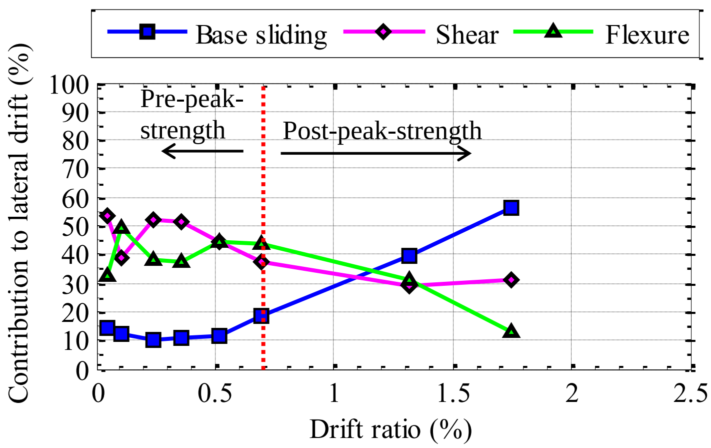

h) SW8 (0.54, 1.5%, 1.5%, 3500 psi)

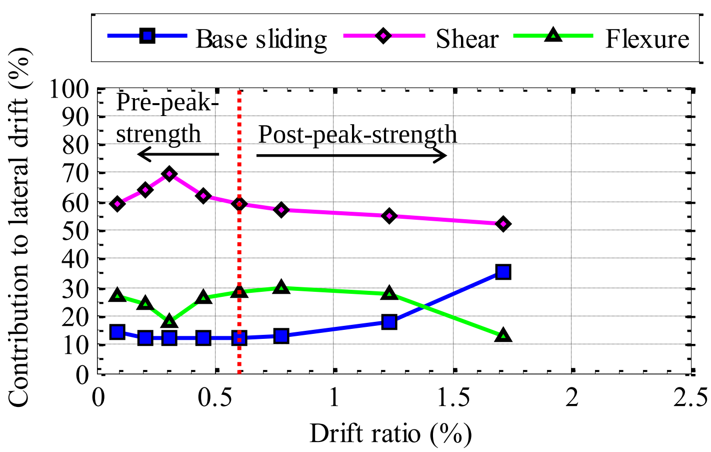

i) SW9 (0.54, 0.67%, 1.5%, 4300 psi)

Figure 4.23. Components of the total lateral displacement (continued)

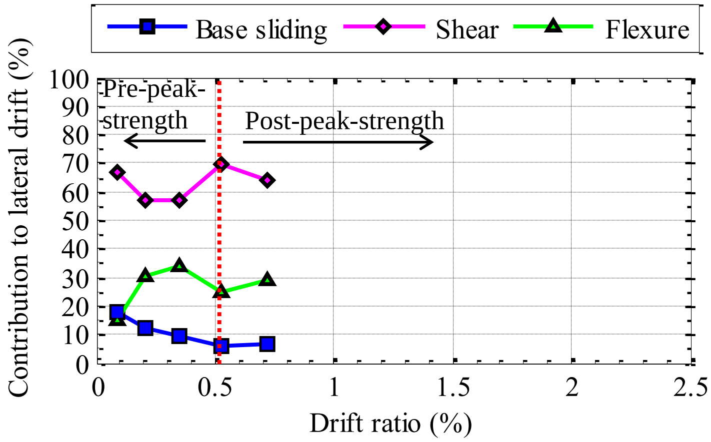

j) SW10 (0.54, 0.33%, 1.5%, 4600 psi)

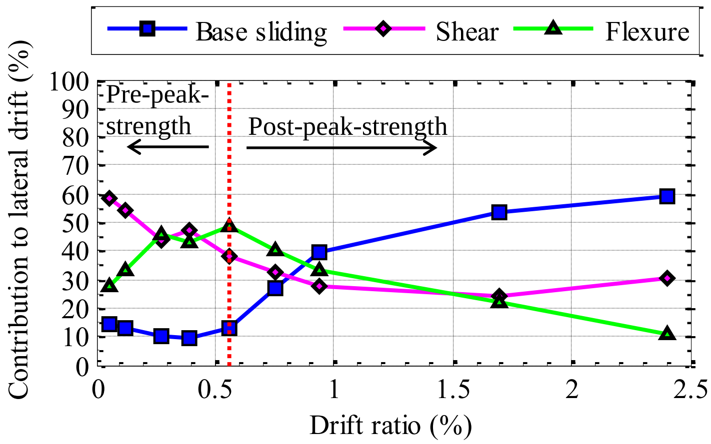

k) SW11 (0.54, 0.67%, 0.67%, 1.5% be, 5000 psi)

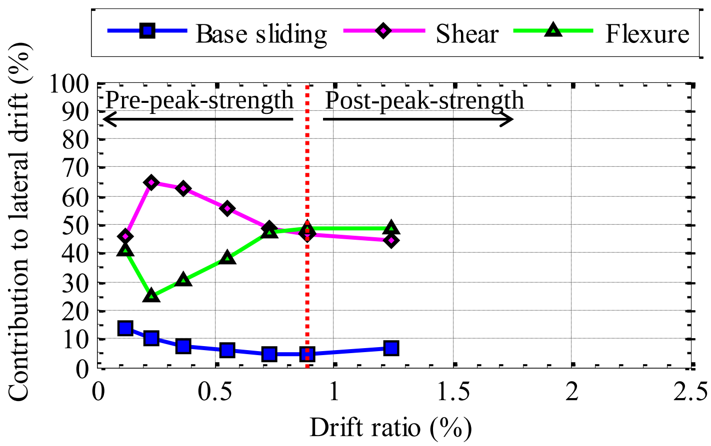

l) SW12 (0.54, 0.33%, 0.33%, 2.0% be, 5000 psi)

Figure 4.23. Components of the total lateral displacement (continued)

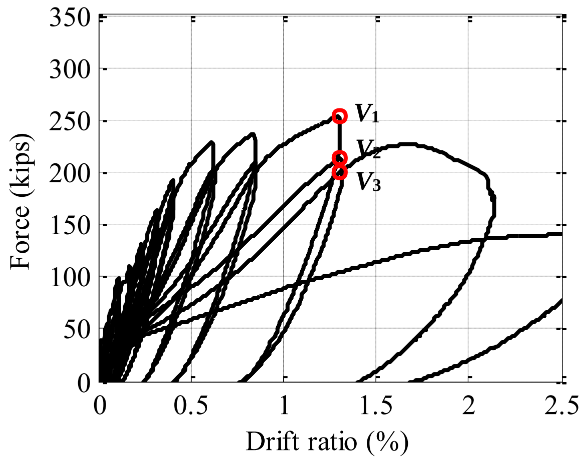

Figure 4.24. First quadrant hysteresis loops, SW1

CHAPTER 5

INITIAL IN-PLANE STIFFNESS OF SHEAR WALLS

5.1 Introduction

A reliable estimate of the in-plane lateral stiffness of reinforced concrete (RC) shear walls is important for the analysis and design of buildings and safety related nuclear structures that implement RC shear walls as the primary components to resist lateral earthquake forces. A theoretical strength-of-materials formulation is routinely used to estimate the lateral stiffness of RC shear walls. In this formulation, the model is fixed against rotation and translation at its base, and flexure and shear springs are arranged in series. The theoretical initial in-plane stiffness, K_t, is given by

$$K_t = \frac{1}{\frac{1}{K_f} + \frac{1}{K_s}}; \qquad K_s = \frac{G_c A_g}{h_w}; \qquad K_f = \frac{3E_c I_g}{h_w^3}; \qquad G_c = \frac{E_c}{2(1+\upsilon)} \tag{5.1}$$

where K_s is the stiffness of the shear spring; K_f is the stiffness of the flexure spring; G_c is the shear modulus of concrete; E_c is the modulus of elasticity of concrete; I_g is the gross moment of inertia of the wall; A_g is the total cross-sectional area of the wall; h_w is the height of the wall measured from the top of the foundation to the centerline of loading; and υ is the Poisson's ratio. ($E_c I_g$ and $G_c A_g$ are commonly referred to as the flexural and shear rigidities, respectively.) In the calculation of the theoretical stiffness of RC walls, I_g and A_g are approximated by the gross concrete section and the reinforcement is ignored. The elastic modulus E_c is estimated using the empirical expression provided in section 19.2.2 of ACI 318-14 (ACI, 2014).

The concrete section is assumed *uncracked* and unreinforced for the calculation of theoretical stiffness. The presence of horizontal construction joints is ignored. Cracking reduces stiffness. Reductions in the flexural and shear rigidities are usually employed to derive a value of *cracked* stiffness from *uncracked* stiffness.

This chapter presents and discusses the initial in-plane lateral stiffness of shear walls, as described in Chapters 3 and 4. The initial stiffness of walls determined from testing are compared and contrasted with those determined from a strength-of-materials formulation and from those based on recommendations in standards for practice. Recommendations for fractions of $E_c I_g$ and $G_c A_g$ for use in practice are provided at the end of the chapter.

5.2 Background information on initial stiffness of RC walls

Important studies on the lateral stiffness of RC shear walls are reviewed in Section 2.5. The profession is well aware the initial stiffness of a RC shear wall is less than that calculated by strength-of-materials formulation, and codes of practice and standards prescribe reductions in the parameters used to calculate initial stiffness to estimate effective lateral stiffness of RC shear walls.

Studies by the United Stated Nuclear Regulatory Commission (NRC) (Farrar et al., 1990; Farrar et al., 1991; Farrar and Baker, 1993) and The Working Group on the Stiffness of Concrete Shear Wall Structures of the ASCE Dynamic Analysis Committee (Murray et al., 1994), as described in Section 2.5, note there are differences between the strength-of-materials-based calculations of initial stiffness and those calculated using test data. The Sozen and Moehle (1993) report on the initial stiffness of RC shear walls is the most comprehensive study to date on the subject. They compiled and examined the lateral stiffness of 41 RC wall specimens tested by Maier and Thürlimann (1985), Inada (1986) and Rothe (1992). The properties of the 41 wall specimens are provided in Table 5.1 and the values of the theoretical *uncracked* and measured stiffness are reproduced in Table 5.2. The axial load on the specimens and the relevant parameters used in the calculations of theoretical *uncracked* stiffness are provided in Table 5.1 and Table 5.2 (the parameters b_f is width of the flange, t_f is the thickness of the flange, and P is the axial load; other parameters used were previously defined in this chapter and in Chapter 3). Sozen and Moehle compared the measured stiffness with the theoretical *uncracked* stiffness calculated using a strength-of-materials formulation. In calculating the shear component of the theoretical *uncracked* stiffness, the total cross-sectional area of the wall, A_g, was replaced by an effective wall area, A_{eff}, equal to $A_w/1.2$ for walls with rectangular sections and $A_w/1.1$ for walls with flanges, where A_w is the area of the web: total depth multiplied by web thickness. (Discussions on shear stiffness with relation to effective shear area can be found in Timoshenko (1940), Cowper (1966), and Renton (1991)) For the 41 test specimens considered, the ratio of measured initial stiffness to theoretical *uncracked* stiffness ranged between 0.33 and 1.2 with median and mean and median values of 0.70 and 0.73, respectively. The ratio was greater than 1.0 in only 4 specimens and each of these specimens was constructed with flanges and the theoretical calculations assumed a rectangular (web) cross section. Sozen and Moehle attributed the increased flexibility of the test specimens to 1) cracks invisible to the eye present before the test, and 2) deformability of the base girder.

Although the profession is aware that the initial stiffness of a RC shear walls is less than the *uncracked* stiffness, there is still no mechanics-based presentation to explain why. The remainder of this chapter provides an explanation and a technical basis for estimating the initial stiffness of RC shear walls for seismic analysis.

Table 5.1. Properties of the wall specimens tested by Maier and Thürlimann, Inada and Rothe (from: Sozen and Moehle (1993))

Ref.[1]	Specimen	Section Type	$f_c^{'}$ (psi)	E_c ($\times 10^6$ psi)	h_w (in)	l_w (in)	t_w (in)	b_f (in)	t_f (in)	$\frac{P}{A_g f_c^{'}}$ (%)
1	S1	Flanged	5350	4.95	52	46.5	3.9	15.7	3.9	6.6
1	S2	Flanged	5350	4.95	52	46.5	3.9	15.7	3.9	25.2
1	S3	Flanged	5320	4.92	52	46.5	3.9	15.7	3.9	6.5
1	S4	Rect.	4770	4.58	52	46.5	3.9	3.9	3.9	6.8
1	S5	Flanged	5410	4.71	52	46.5	3.9	15.7	3.9	6.3
1	S6	Flanged	5160	4.37	52	46.5	3.9	15.7	3.9	6.6
1	S7	Flanged	4950	4.55	52	46.5	3.9	15.7	3.9	27.3
1	S8	Flanged	4660	4.48	52	46.5	3.9	15.7	3.9	7.3
1	S9	Rect.	4230	4.18	52	46.5	3.9	3.9	3.9	7.6
1	S10	Rect.	4500	4.02	52	46.5	3.9	3.9	3.9	7.2
2	O-W	Box	3950	2.86	23.6	32.7	3.1	-	-	2.8
2	B-6	Box	3640	3.24	31.5	32.7	3.1	-	-	0.0
2	B-10	Box	3670	3.36	31.5	32.7	3.1	-	-	0.0
2	B-16	Box	2700	3.63	31.5	32.7	3.1	-	-	0.0
2	B1-1	Box	3940	3.46	23.6	62.2	3.1	-	-	7.2
2	B1-2	Box	3510	3.20	23.6	62.2	3.1	-	-	0.0
2	B1-3	Box	3530	3.13	47.2	62.2	3.1	-	-	8.0

[1] Reference 1 – Maier and Thürlimann (1985), 2 – Inada (1986), 3 – Rothe (1992)

Table 5.1. Properties of the wall specimens tested by Maier and Thürlimann, Inada and Rothe (from: Sozen and Moehle (1993)) (continued)

Ref.[1]	Specimen	Section Type	$f_c^{'}$ (psi)	E_c ($\times 10^6$ psi)	h_w (in)	l_w (in)	t_w (in)	b_f (in)	t_f (in)	$\frac{P}{A_g f_c^{'}}$ (%)
2	B1-4	Box	4340	3.26	47.2	62.2	3.1	-	-	0.0
2	B1-5	Box	4220	3.81	47.2	62.2	3.1	-	-	6.7
2	B1-6	Box	3910	3.10	47.2	62.2	6.3	-	-	0.0
2	B1-7	Box	3510	3.06	47.2	62.2	3.1	-	-	0.0
2	B25A1-12	Box	3830	3.81	47.2	70.9	1.6	-	-	0.0
2	B25A2-18	Box	3670	3.06	47.2	70.9	1.6	-	-	0.0
2	B25A1-24	Box	3490	3.06	47.2	70.9	1.6	-	-	0.0
2	B25A1-18	Box	3610	2.56	47.2	70.9	1.6	-	-	0.0
2	S-1	Flanged	4320	3.64	47.2	62.2	3.1	32.7	3.1	0.0
2	S-2	Flanged	3330	2.96	141.7	186.6	9.4	98.0	9.4	0.0
2	S-3	Flanged	3740	3.23	141.7	186.6	9.4	98.0	9.4	0.0
2	S-4	Flanged	3290	3.21	141.7	186.6	9.4	98.0	9.4	0.0
2	S-5	Flanged	3600	2.99	141.7	186.6	9.4	98.0	9.4	0.0
3	T01	Rect.	3530	2.65	47.2	31.5	3.1	-	-	0
3	T02	Flanged	4500	2.45	47.2	31.5	2.0	3.9	5.9	0
3	T03	Flanged	4310	2.71	47.2	31.5	2.0	3.9	5.9	0
3	T04	Rect.	4180	2.72	47.2	31.5	3.1	-	-	0
3	T05	Rect.	3510	2.86	47.2	31.5	3.1	-	-	0
3	T06	Flanged	4880	2.61	47.2	31.5	2.0	3.9	5.9	0
3	T07	Flanged	4480	2.74	47.2	31.5	2.0	3.9	5.9	8.0
3	T08	Flanged	4440	2.68	47.2	31.5	2.0	3.9	5.9	6.3
3	T09	Flanged	3860	2.44	47.2	31.5	2.0	3.9	5.9	0.0
3	T10	Rect.	4870	2.83	47.2	31.5	3.1	-	-	0.0
3	T11	Rect.	3900	2.74	47.2	31.5	3.1	-	-	5.6

[1] Reference 1 – Maier and Thürlimann (1985), 2 – Inada (1986), 3 – Rothe (1992)

Table 5.2. Stiffness data of the wall specimens tested by Maier and Thürlimann, Inada and Rothe (from: Sozen and Moehle (1993))

Ref.[1]	Specimen	I_g (2) (in^4)	A_{eff} (3) (in^2)	K_s (4) (kips/in)	K_f (5) (kips/in)	K_t (6) (kips/in)	K_m (7) (kips/in)	$\frac{K_m}{K_t}$
1	S1	75000	166	7100	7900	3740	2660	0.69
1	S2	75000	166	7000	7900	3710	2870	0.75
1	S3	75000	166	7000	7900	3710	2040	0.53
1	S4	32900	152	6000	3200	2090	1370	0.65
1	S5	75000	166	6700	7600	3560	1700	0.46
1	S6	75000	166	6200	7000	3290	1280	0.38
1	S7	75000	166	6500	7300	3440	2650	0.75
1	S8	75000	166	6400	7200	3390	1430	0.41
1	S9	32900	152	5500	2900	1900	971	0.50
1	S10	32900	152	5300	2800	1830	894	0.48
2	O-W	1939900	575.6	35870	1260000	34900	22700	0.65
2	B-6	54700	187.1	8820	17000	5800	4080	0.70
2	B-10	54700	187.1	9130	17600	6000	4030	0.67
2	B-16	54700	187.1	9860	19100	6500	2830	0.44
2	B1-1	434000	356.2	29800	342000	27400	24400	0.89
2	B1-2	434000	356.2	27600	316000	25400	17900	0.70
2	B1-3	434000	356.2	11600	38700	8900	6350	0.71
2	B1-4	434000	356.2	12000	40200	9300	9040	0.97
2	B1-5	434000	356.2	14100	47100	10800	7210	0.67
2	B1-6	875000	748.5	24100	77300	18400	12400	0.67
2	B1-7	434000	356.2	11300	37800	8700	7990	0.92
2	B25A1-12	349000	202.9	7330	37900	6100	4050	0.66
2	B25A2-18	349000	202.9	5880	30400	4900	5790	1.18
2	B25A1-24	349000	202.9	5880	30400	4900	5320	1.09
2	B25A1-18	349000	202.9	4920	25500	4100	4460	1.09
2	S-1	225500	178.1	6430	23400	5000	5280	1.06
2	S-2	18270000	1603.0	15700	57000	12300	10700	0.87
2	S-3	18270000	1603.0	17100	62200	13400	10700	0.80
2	S-4	18270000	1603.0	17000	61900	13400	11600	0.87
2	S-5	18270000	1603.0	15800	57600	12400	10300	0.83
3	T01	8200	82.7	2170	619	482	440	0.91
3	T02	9000	56.4	1370	629	431	430	1.00
3	T03	9000	56.4	1510	694	476	300	0.63
3	T04	8200	82.7	2220	634	493	280	0.57

[1] Reference 1 – Maier and Thürlimann (1985), 2 – Inada (1986), 3 – Rothe (1992)

Table 5.2. Stiffness data of the wall specimens tested by Maier and Thürlimann, Inada and Rothe (from: Sozen and Moehle (1993)) (continued)

Ref.[1]	Specimen	I_g (2) (in^4)	A_{eff} (3) (in^2)	K_s (4) (kips/in)	K_f (5) (kips/in)	K_t (6) (kips/in)	K_m (7) (kips/in)	$\frac{K_m}{K_t}$
3	T05	8200	82.7	2340	667	519	400	0.77
3	T06	9000	56.4	1460	669	459	380	0.83
3	T07	9000	82.7	2250	703	535	360	0.67
3	T08	9000	82.7	2200	688	524	360	0.69
3	T09	9000	56.4	1360	325	428	140	0.33
3	T10	8200	82.7	2320	661	514	310	0.60
3	T11	8200	82.7	2250	640	498	300	0.60

[1] Reference 1 – Maier and Thürlimann (1985), 2 – Inada (1986), 3 – Rothe (1992)

5.3 Restrained shrinkage cracking

ACI Standard 209R-92 (ACI, 1992) identifies factors that affect drying shrinkage of concrete. Such shrinkage develops tensile stresses that can lead to cracking (e.g., Gilbert, 1992). Carino and Clifton (1995) estimated unrestrained drying shrinkage strains in concrete of between 400 and 1100 microstrains for standard conditions of seven days of curing, a volume-to-surface ratio of 38 mm, and ambient relative humidity of 40%. Numerical modeling by Palermo and Vecchio (2002) showed that imposing a shrinkage-induced pre-strain of 400 microstrain enabled the accurate simulation of initial stiffness of two large-scale flanged RC walls, physically tested under cyclic displacements.

Schilitter et. al. (2010) (also reported in Raoufi, 2011) investigated the effects of restrained shrinkage cracking in concrete slabs. Finite element models of concrete slabs on top of large concrete foundations were prepared. The influence of foundation thickness on cracking of concrete slab was investigated. The foundation considered in the study had plan dimension of 15.1 × 2.6 feet and its thicknesses ranged between 6 and 18 inches. Results showed that for foundation thicknesses ranging from 10 to 18 inches, the average tensile stress in the slabs exceeded 0.44 ksi after about 64 hours of curing. For concrete with compressive strength of 4 ksi, an average tensile stress of 0.44 ksi may be sufficient to cause cracking.

The wall specimens at UB had foundation footprints of 14 × 3 feet (Phase I specimens) and 14 × 4 feet (Phase II specimens). The thicknesses of the foundations were 18.5 and 18 inches for the Phase I and Phase II specimens, respectively. The foundations of all 12 walls were cast before the corresponding wall sections and the compressive strengths of the concrete in the foundations were greater than those in the walls. Each wall has a construction joint at its base connection to the foundation. Wall web reinforcement ratios ranged between 0.33% and 1.5%. Given the restraint to the base of the wall provided by the already-cast foundation and the steel reinforcement in the wall, cracking of the concrete near the base of each wall was highly likely.

5.4 Effective lateral stiffness of RC shear walls

The generalized load-deformation relationship in ASCE 41-13 (ASCE, 2013) for RC walls is shown in Figure 5.1. Points A, B, C and D represent the state of the unloaded component, effective yield point, nominal strength and loss of significant strength to a residual value, respectively. For walls with response dominated by shear, the strengths associated with points B and C are taken to be the same. The effective lateral stiffness of an RC wall is the slope of line AB, that is, the secant value to the yield point.

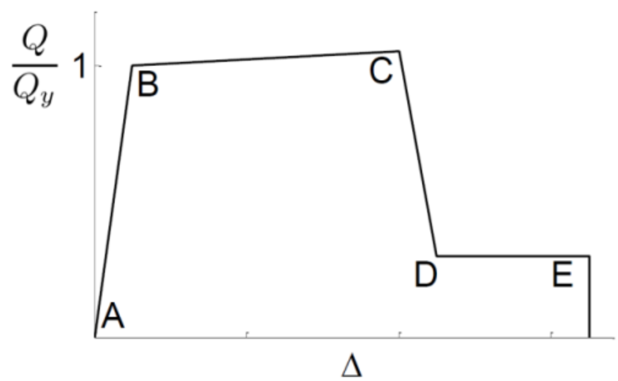

Figure 5.1. ASCE 41-13 force-deformation relationship (ASCE, 2013)

Building codes and standards of practice provide recommendations to estimate the initial stiffness of RC shear walls. Reductions in the flexural and shear rigidities are used to estimate the effective initial stiffness of *uncracked* and *cracked* walls. ASCE 43-05 (ASCE, 2005) recommends no reduction in the flexural and shear rigidities for *uncracked* walls and a 50% reduction in both the flexural and shear rigidities for *cracked* walls. ASCE 41-13 recommends a reduction of 50% in the flexural rigidity but no reduction in the shear rigidity for *cracked* walls.

Table 5.3 presents data on the lateral stiffness obtained from the tests of the 12 specimens. The initial stiffness was calculated from the first cycle of the first load step in each test, which involved force less than 15% of peak strength and a drift ratio of less than 0.025%. No additional axial load was applied to the specimens.

Table5.3. Data for the calculation of initial stiffness, K_i

Wall	Force (kip)	Disp. (in)	Drift Ratio (%)
SW1	15.8	0.0086	0.0076
SW2	-	-	-
SW3	-	-	-
SW4	-	-	-
SW5	68.5	0.0077	0.019
SW6	65.9	0.0087	0.021
SW7	33.1	0.0027	0.0066
SW8	69.8	0.013	0.020
SW9	64.7	0.013	0.020
SW10	68.3	0.013	0.020
SW11	61.4	0.015	0.023
SW12	57.8	0.015	0.023

Data for the initial stiffness of walls SW2, SW3 and SW4 are not presented due to noise in the data collected on the initial loading of the specimens. String potentiometers were used to collect data on the first load step for these three walls whereas data for initial stiffness for the other nine walls were obtained from Temposonics. The precision of the string potentiometers and Temposonics used in the tests were 0.0025 and 0.00025 inch, respectively.

Table 5.4 presents the calculated theoretical *uncracked* stiffness of the 12 walls together with the predicted *uncracked* and *cracked* stiffness using recommendations from ASCE 41-13 and ASCE 43-05. Day-of-test concrete compressive strength, equation 19.2.2.1.b of ACI 318-14 for Young's modulus and Poisson's ratio equal to 0.2 were used in the calculations. The reinforcement was ignored in the stiffness calculations. The measured initial stiffness and secant stiffness at peak strength are also presented in Table 5.4.

Table 5.4. Initial stiffness of the wall specimens (kips/inch)

Wall	Theoretical *uncracked* K_t	ASCE 41-13	ASCE 43-05		Measured	
		cracked K_{41-13}	*uncracked* $K_{43-05uc}$	*cracked* K_{43-05c}	Initial K_i	Secant at peak strength K_s
SW1	4890	3060	4890	2445	1840	170
SW2	19710	14835	19710	9855	-	690
SW3	20810	15660	20810	10405	-	340
SW4	15270	11495	15270	7635	-	320
SW5	30530	26250	30530	15265	8900	1990
SW6	28700	24680	28700	14350	7570	1720
SW7	28700	24680	28700	14350	12260	1730
SW8	13940	10490	13940	6970	5370	1380
SW9	15450	11630	15450	7725	4980	1250
SW10	15980	12025	15980	7990	5250	1400
SW11	16660	12540	16660	8330	4090	1170
SW12	16660	12540	16660	8330	3850	520

Ratios of measured stiffness to predicted stiffness are given in Table 5.5. The ratio of the measured initial stiffness to the theoretical *uncracked* stiffness ranged from 0.23 to 0.43 with a mean of 0.32. The average ratios of the calculated initial stiffness to the effective stiffness recommended by ASCE 41-13 and ASCE 43-05 for *cracked* wall sections are 0.42 and 0.64, respectively. The secant stiffness was calculated at the point of peak shear strength. The secant stiffness at peak resistance is as low as 3% (2%) of the effective stiffness recommended by ASCE 43-05 (ASCE 41-13) for *cracked* wall sections.

The values of initial stiffness of the 12 tested walls are significantly less than those estimated using standards of practice. Since the tests were conducted using large-scale specimens (8 inch thick, 3/4 inch aggregate concrete and two curtains of #4 web reinforcement), possible concerns regarding scaling effects are not relevant.

Table 5.5. Initial stiffness ratios

Wall	$\frac{K_i}{K_t}$	$\frac{K_i}{K_{41-13}}$	$\frac{K_i}{K_{43-05c}}$	$\frac{K_s}{K_{41-13}}$	$\frac{K_s}{K_{43-05c}}$
SW1	0.38	0.60	0.75	0.06	0.07
SW2	-	-	-	0.05	0.07
SW3	-	-	-	0.02	0.03
SW4	-	-	-	0.03	0.04
SW5	0.29	0.34	0.58	0.08	0.13
SW6	0.26	0.31	0.53	0.07	0.12
SW7	0.43	0.50	0.85	0.07	0.12
SW8	0.39	0.51	0.77	0.13	0.20
SW9	0.32	0.43	0.64	0.11	0.16
SW10	0.33	0.44	0.66	0.12	0.18
SW11	0.25	0.33	0.49	0.09	0.14
SW12	0.23	0.31	0.46	0.04	0.06
Average	0.32	0.42	0.64	0.07	0.11

5.5 Effects of cracking on initial stiffness

The initial stiffness of the walls was calculated at drift levels of less than 0.025%. The measured tensile strains in the vertical reinforcement, 2 inches above the foundation, near the tension end of the wall ranged from 150 to 430 microstrain at drift levels of 0.025% and less: sufficient strain to crack the adjacent concrete. The locations of the strain gages on the vertical reinforcement are shown in the Appendix C.

To estimate the effect of cracking at the base of the wall on initial stiffness, an effective moment of inertia and effective wall area were calculated for each wall. The concrete at the base of the wall was assumed to have *cracked* prior to testing due to restrained shrinkage. The location of the neutral axis (NA) was determined for each wall on the basis of strains, compressive or tensile, in the vertical reinforcement. The effective moment of inertia, I_{eff}, was calculated using a *cracked* transformed section (with the crack extending from the tension face to the NA). The *uncracked* length of the wall (compression face to the NA) was used to estimate effective shear area, A_{eff}. The initial stiffness, K_{eff}, of the 12 walls were calculated using the effective moment of inertia and the effective shear area. The values used in the calculation of K_{eff} are presented in Table 5.6. The average of the ratio of K_i to K_{eff} for all the walls, except SW2, SW3 and SW4, is 0.91; the coefficient of variation is 0.11, noting that the number of data points (9) is too small to form a robust estimate of the standard deviation.

Table 5.6. Effective stiffness

Wall	N.A. location, from tension face (in)	I_{eff} (in^4)	$\frac{I_{eff}}{I_g}$	A_{eff} (in^2)	$\frac{A_{eff}}{A_g}$	K_{eff} (kips/in)	$\frac{K_i}{K_{eff}}$
SW1	72	605428	0.52	384	0.40	2078	0.88
SW2	66	607830	0.53	449	0.45	8126	-
SW3	83	564585	0.49	296	0.31	6333	-
SW4	50	595818	0.52	560	0.58	7566	-
SW5	72	612635	0.53	384	0.40	11289	0.79
SW6	83	576598	0.50	296	0.31	8251	0.92
SW7	60	595818	0.52	480	0.50	12762	0.96
SW8	72	639062	0.56	384	0.40	5322	1.01
SW9	77	622245	0.54	344	0.36	5425	0.92
SW10	83	600623	0.52	296	0.31	4939	1.06
SW11	78	588610	0.51	336	0.35	5602	0.73
SW12	90	518938	0.45	240	0.25	4174	0.92
Average			0.51		0.38		0.91

5.6 Effects of out-of-plane displacement

The out-of-plane (OOP) displacement of the 12 RC walls was monitored during testing using two string potentiometers attached at the top corners of the wall, approximately 16″ above the centerline of loading. The OOP displacements of the walls SW1 and SW5 through SW12 were between 0 ± 0.0025 inch: for the in-plane displacements used to estimate initial lateral stiffness: the precision of the string potentiometers.

The OOP moments (M_{OOP}) at the base of the walls due to a 0.005-inch OOP displacement at the centerline of loading of the wall were calculated assuming a modulus of rupture of concrete of $7.5\sqrt{f_c^{'}}$. The values of M_{OOP} and M_{cr} are presented in Table 5.7. The ratio of the OOP moment to the cracking moment ranged between 0.03 (SW1) and 0.26 (SW5, SW6 and SW7). Out-of-plane displacements of the magnitude reported above are highly unlikely to affect initial in-plane lateral stiffness.

Table 5.7. Out-of-plane bending moments

Wall	M_{OOP} (kip-in)	M_{cr} (kip-in)	$\frac{M_{OOP}}{M_{cr}}$
SW1	4443	129600	0.03
SW2	18725	180719	0.10
SW3	19766	190766	0.10
SW4	14504	139984	0.10
SW5	36886	141641	0.26
SW6	34675	133151	0.26
SW7	34675	133151	0.26
SW8	13240	127787	0.10
SW9	14676	141641	0.10
SW10	15179	146498	0.10
SW11	15825	152735	0.10
SW12	15825	152735	0.10

5.7 Numerical modeling of restrained shrinkage

To investigate the effect of restrained shrinkage on the initial stiffness of RC walls, a numerical study was conducted using general purpose finite element code LS-DYNA (LS-DYNA, 2012a, 2012b). The baseline model was validated using test data from Phase I specimens, SW1 through SW7 (Epackachi et al., 2015). The validated model was used to investigate the impact of shrinkage on the in-plane response of planar RC walls. The analysis assumptions and key analysis results are described in the following sub-sections.

5.7.1 Properties of the LS-DYNA model

The concrete wall was modeled using the smeared crack Winfrith model (MAT085) in LS-DYNA (LS-DYNA, 2012b). The Winfrith model was originally developed by Broadhouse (1986) to simulate the local and global responses of reinforced concrete structures subjected to accidental impact loadings (Broadhouse, 1995). The yield surface of the Winfrith model is based on the plastic surface proposed by Ottosen (1977). Up to three orthogonal cracks can be generated in each concrete element. After cracking, tensile strength decays as a linear function of crack width. The shear stress transfer across the crack surface due to the aggregate interlock is estimated as the product of the crack-parallel shear stress and a shear stress factor that is a convex parabolic function of aggregate size and crack width, and varies between 1 and 0 corresponding to a crack width equal to 0 and aggregate size, respectively. The reinforcement was modeled using Mat-

Plastic-Kinematic (MAT003), with isotropic, kinematic, and combined kinematic-isotropic hardening. The hardening can be specified by varying a parameter, β, between 0 and 1: 0 for kinematic, 1 for isotropic, and a value between 0 and 1 for combined kinematic-isotropic hardening.

Beam elements and 1.0 × 1.0 × 1.0 inch solid elements were used to model the reinforcement and the concrete wall, respectively. The beam (reinforcement) elements were tied to the solid (concrete) elements and slip was ignored. Horizontal displacements were applied to the nodes of the concrete and reinforcement elements at a level of the centerline of the loading to simulate the reversed cyclic loading.

Day-of-test concrete compressive strength, calculated fracture energy (G_f, the energy required to propagate a tensile crack of unit area) using Equation 2.1-7 of the CEB-FIP Model Code (1993), a maximum crack width equal to $2G_f / f_t$ where f_t is the concrete tensile strength, and the measured stress-strain relationships derived from the tensile tests of reinforcement were used as input to the LS-DYNA model. For the cyclic analysis of the RC walls, kinematic hardening was considered for the reinforcement by setting the input parameter β to 0 in MAT003.

The LS-DYNA model of SW2 is presented in Figure 5.2. The cyclic loading protocol presented in Section 3.9 was used for the numerical analysis of the RC walls.

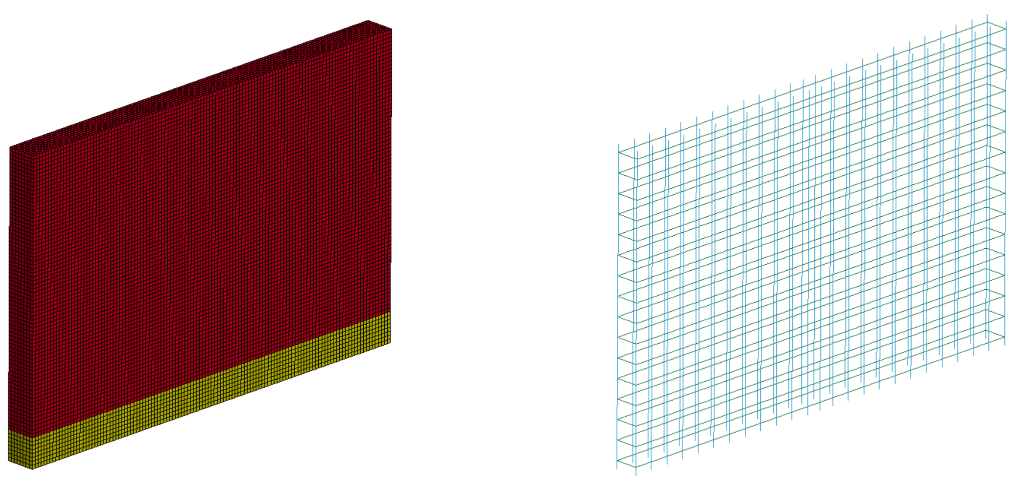

(a) Concrete wall (b) Horizontal and vertical reinforcement

Figure 5.2. LS-DYNA model of SW2

5.7.2 Modeling restrained shrinkage

Shrinkage cannot be directly modeled in LS-DYNA and so was modeled indirectly by applying a thermal load to a zone of concrete elements near the base of the wall. The value of the temperature increment, ΔT, was calculated as

$$\Delta T = \frac{\varepsilon_{sh}}{\alpha_c} \tag{5.2}$$

where ε_{sh} is the shrinkage strain and α_c is the coefficient of thermal expansion of concrete $(= 14.5 \times 10^{-6}\ in/(in\ K))$.

To investigate the impact of shrinkage on the initial stiffness of RC walls, the LS-DYNA model of SW2 was analyzed for three shrinkage strains within the range identified by Carina and Clifton (1995), 400 and 800 microstrain, and 1600 microstrain. The region colored yellow in Figure 5.2 identifies the zone subjected to thermal loading. Two heights above the base, H_T, were considered for thermal loading: 8 inch (wall thickness) and 16 inch (twice the wall thickness). Table 5.8 lists the values of $\mathrm{D}T$ and H_T considered for the analysis. The LS-DYNA models with different values of $\mathrm{D}T$ and H_T were denoted SW2-1 through SW2-5.

Table 5.8. Thermal loading properties

Model	ΔT (K)	H_T (in)	Equivalent shrinkage strain, ε_{sh} (microstrain)
SW2-1	-27	8	400
SW2-2	-54	8	800
SW2-3	-54	16	800
SW2-4	-108	8	1600
SW2-5	-108	16	1600

5.7.3 Analysis results

The measured and predicted cyclic backbone curves and cyclic response of SW2 are presented in Figure 5.3. Figure 5.3b through 5.2f present measured (SW2) and predicted responses (SW2-1 to SW2-5). Restrained shrinkage at the base of the wall has no effect on the peak and post-peak strength of SW2 (see Figure 5.3a) but significantly affects the initial stiffness: as the shrinkage strain or the height of the shrinkage zone is increased, the initial stiffness decreases.

Figure 5.3f shows that the LS-DYNA model with a 1600 microstrain applied over a height of twice the wall thickness at the base of the wall recovers the measured initial stiffness of SW2. However, this calibrated choice of ΔT and H_T cannot be broadly applied to other walls.

5.7.4 Effects of axial load on initial stiffness

Axial loads were not imposed on the 12 walls tested at the University at Buffalo. The effect of axial load on initial stiffness was investigated numerically by using the LS-DYNA models of SW2-2 and SW2-4, listed in Table 5.8, and two axial loads: $0.05A_g f_c'$ and $0.1A_g f_c'$. Each analysis was performed in three sequential stages: 1) thermal loading, 2) axial loading, and 3) cyclic loading. The material models, elements, and boundary conditions introduced previously for the shrinkage analysis were used for the axial-load analysis.

Figure 5.4 presents the cyclic-force displacement relationships of the LS-DYNA model of SW2, with and without shrinkage and axial load. The values of the axial load ratio (i.e., the applied axial compressive force divided by the product of the concrete compressive strength and wall area) and shrinkage strain for the LS-DYNA models are listed in Table 5.9. Figure 5.10 indicates that the axial load has a significant effect on strength and stiffness: as the axial load increases, the peak strength at a given drift increases and the hysteresis loops are less pinched. This is an expected result because more cracks are closed as axial load increases.

Table 5.9. Thermal loading and axial load properties

Model	$P / A_g f_c'$ (%)	Shrinkage strain, ε_{sh} (microstrain)
SW2	0	0
SW2-2	0	800
SW2-4	0	1600
SW2-2-5	5	800
SW2-2-10	10	800
SW2-4-5	5	1600
SW2-4-10	10	1600

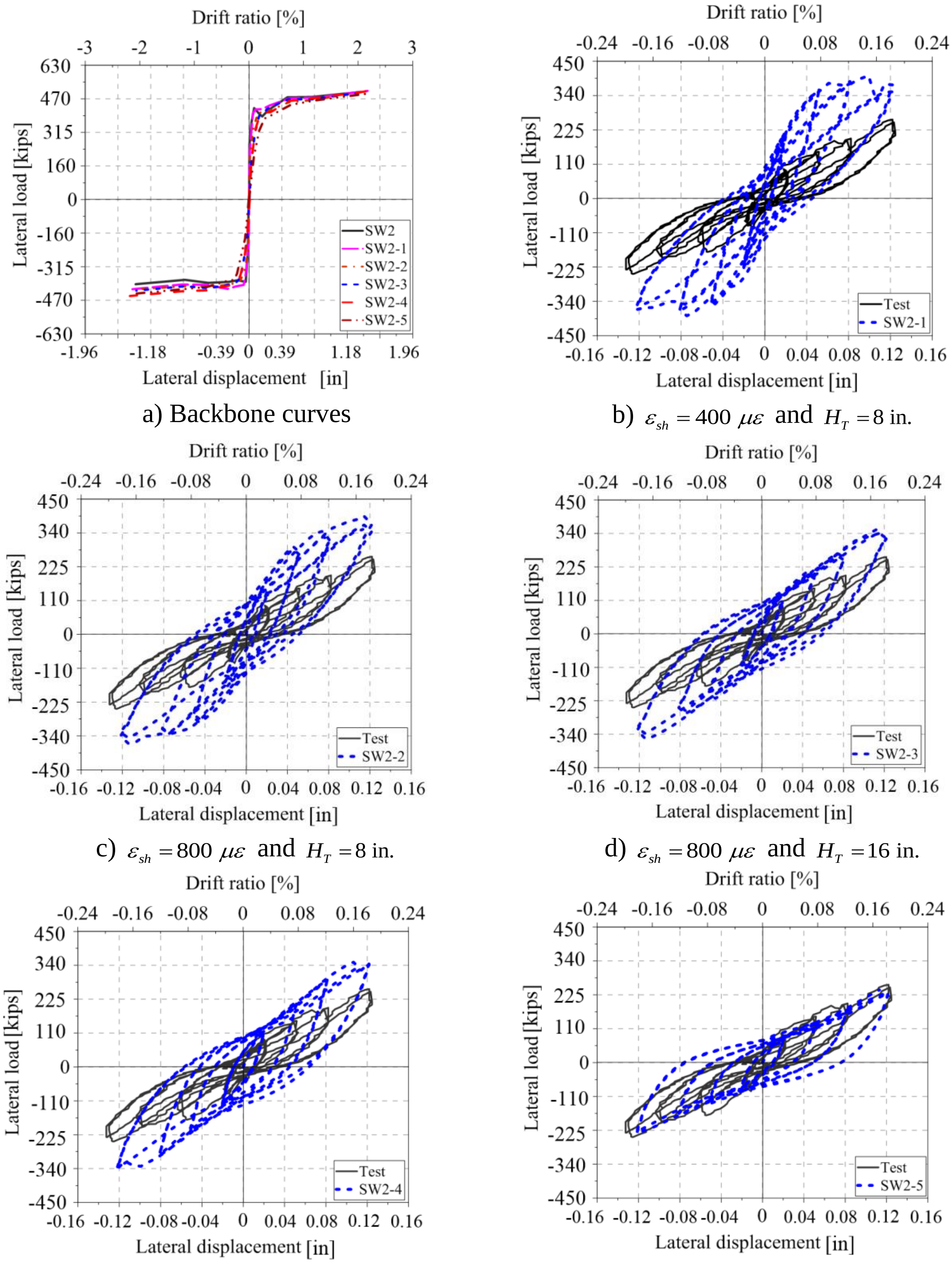

a) Backbone curves

b) $\varepsilon_{sh} = 400\ \mu\varepsilon$ and $H_T = 8$ in.

c) $\varepsilon_{sh} = 800\ \mu\varepsilon$ and $H_T = 8$ in.

d) $\varepsilon_{sh} = 800\ \mu\varepsilon$ and $H_T = 16$ in.

e) $\varepsilon_{sh} = 1600\ \mu\varepsilon$ and $H_T = 8$ in.

f) $\varepsilon_{sh} = 1600\ \mu\varepsilon$ and $H_T = 16$ in.

Figure 5.3. Predicted and measured lateral load - displacement relationships of RC walls

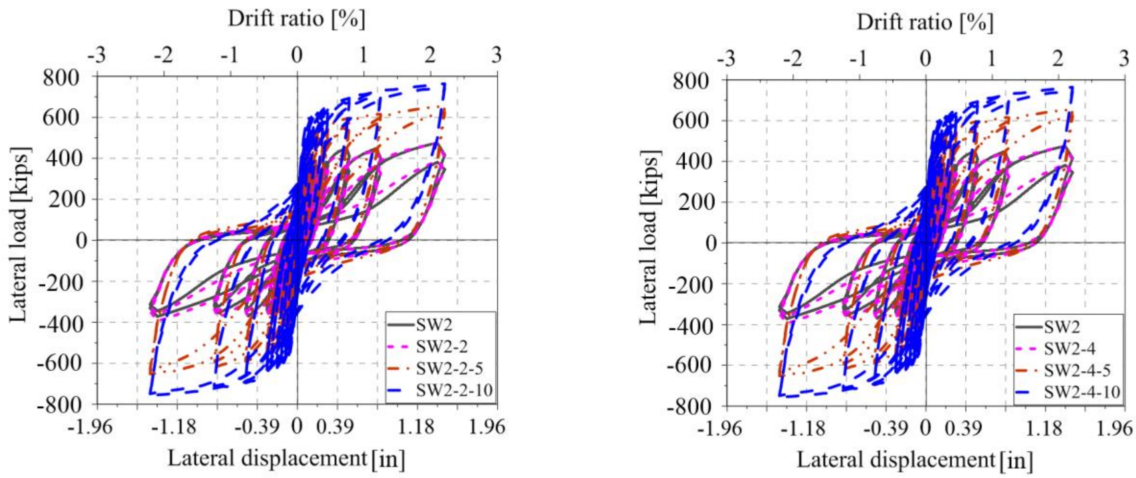

a) $\varepsilon_{sh} = 800\ \mu\varepsilon$ b) $\varepsilon_{sh} = 1600\ \mu\varepsilon$

Figure 5.4. Cyclic force-displacement relationships of RC walls

Figure 5.5 presents cyclic backbone curves for drift ratios up to 0.15%. The axial load has a significant effect on initial stiffness. The initial stiffness of SW2 with no imposed shrinkage and no axial load (SW2 in the legend) was recovered with 800 microstrain of imposed shrinkage and an axial load of $0.05A_g f_c'$ (SW2-2-5 in the legend). However, the initial stiffness of SW2 with no imposed shrinkage and no axial load (SW2) was not recovered for 1600 microstrain of imposed shrinkage and an axial load of $0.1A_g f_c'$ (SW2-4-10 in the legend). Figure 5.5 also shows that an increase in the axial load from $0.05A_g f_c'$ to $0.1A_g f_c'$ has only a small effect on the initial stiffness of the wall with 800 microstrain of imposed shrinkage but significantly increased the initial stiffness of the wall with 1600 microstrain of imposed shrinkage.

In the presence of axial compressive load, fine cracks caused by restrained shrinkage are closed leading to partial to full recovery of *uncracked* initial stiffness. As the shrinkage strains increases, larger axial loads are required to close the shrinkage cracks and recover the *uncracked* initial stiffness.

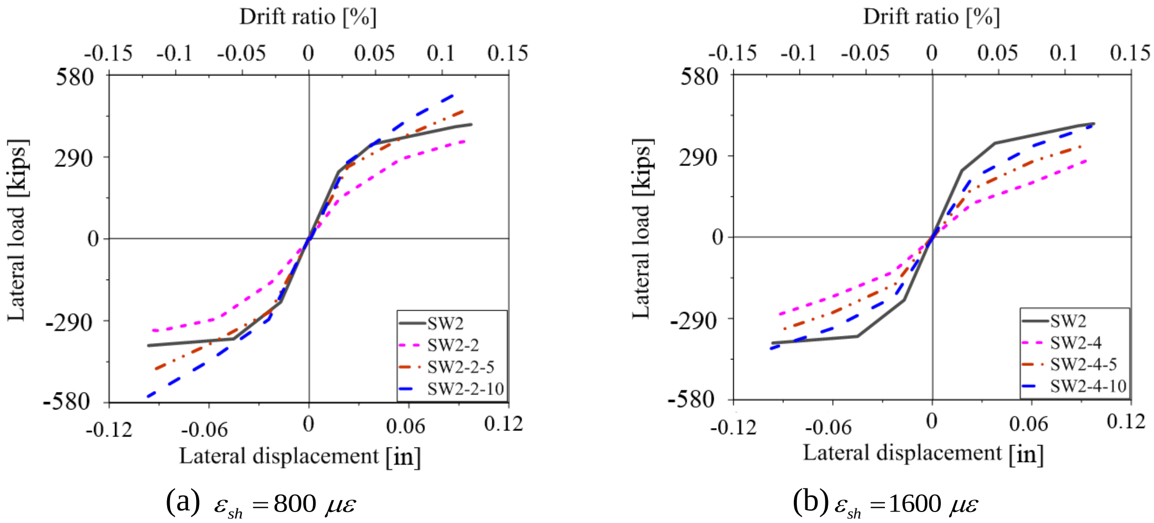

Figure 5.5. Cyclic backbone curves for RC walls

5.8 Recommendations for use in practice

As reported in Table 5.6, the average ratio of the effective moment of inertia to the total (gross) moment of inertia is 0.51 and the average ratio of the effective shear area to the total shear area is 0.38. The effective flexural rigidity of $0.5E_cI_g$ proposed by ASCE 43-05 and ASCE 41-13 can be used for the calculation of initial stiffness of *cracked* walls. However, the shear rigidity proposed by ASCE 43-05 and ASCE 41-13 appears to substantially overestimate the shear stiffness of *cracked* RC walls. Based on the test results of Chapter 4, the flexural and shear rigidity of low aspect ratio RC walls can be taken as $0.5E_cI_g$ and $0.35G_cA_g$, respectively, for the calculation of initial in-plane stiffness if the imposed axial compressive stress is small.

Data from the second load step were analyzed to determine a reasonable range of force (average shear stress) and drifts for which $0.5E_cI_g$ and $0.35G_cA_g$ would provide a reasonable estimate of lateral stiffness. The stiffness measured in the second load step were about one half of the initial stiffness from the first load step for forces ranging between 22% and 52% of peak force and drift ratios ranging from 0.05% to 0.2%. The forces and drift ratios (measured in the second load step) of the walls for which the initial stiffness was reduced to about half had an average of 39% of peak strength and 0.11%, respectively. From these observations it can be generalized that the $0.5E_cI_g$ and $0.35G_cA_g$ for use in effective initial stiffness calculations, are reasonable for forces up to 40% of peak strength and drift ratios of up to 0.1%.

The presence of significant axial compression, sufficient to overcome the effects of restrained shrinkage, will increase the initial stiffness of low aspect ratio walls, but recommendations cannot be made based on the tests described in Chapter 4.

CHAPTER 6

PEAK SHEAR STRENGTH OF SHEAR WALLS

6.1 Introduction

Equations are available in the literature and standards of practice to predict the nominal shear strength of low aspect ratio reinforced concrete (RC) walls but these equations are inaccurate and insufficiently parameterized (e.g., Gulec et al, 2008; Del Carpio et al, 2012). Accurate prediction of the shear strength is important for both code-based design and seismic performance assessment (Gulec et al, 2008). A review of equations that are used to predict the peak shear strength of RC shear walls was presented in Section 2.4.

Section 6.2 presents the shear strength of the 12 walls tested at the University at Buffalo (UB) calculated using equations from chapters 11 and 18 of ACI 318-14 (ACI, 2014), Barda et al. (1977), Wood (1990), Gulec and Whittaker (2011), and Moehle (2015). Each equation uses design variables such as compressive strength of concrete, yield strength of reinforcement, reinforcement ratio and aspect ratio. The resistance calculated using these equations are compared and contrasted with the measured peak shear strength of the 12 walls.

Section 6.3 discusses the effects of the out-of-plane displacement and twisting on peak shear strength of the walls in the first and third quadrant of loading. Section 6.4 reviews the equation for peak strength by Gulec and Whittaker (2011) and provides an alternative equation based on regression analysis using additional data provided by the tests of 12 walls described in Chapter 3. Section 6.5 evaluates the equation proposed by Moehle (2015). Alternate equations for the peak shear strength of rectangular walls without (with) boundary elements are presented in Section 6.6 (6.7) based on load paths identified from analysis of strain, displacement and crack data mined from the tests of the 12 walls. Observations regarding the loss of stiffness and strength at displacements greater than that at peak strength are provided in Section 6.8. Section 6.9 provides closing thoughts on the subject of peak shear strength.

6.2 Peak shear strength of the 12 UB walls

The peak shear strength, corresponding average shear stress and drift ratios in the first and third quadrants of loading of the 12 UB walls are reported in Table 6.1. The nominal shear strength of the 12 walls calculated using equations from chapters 11 and 18 of ACI 318-14 (ACI, 2014), Barda et al. (1977), Wood (1990), Gulec and Whittaker (2011), and Moehle (2015) are presented in Table 6.2. The measured peak shear strength and the nominal shear strength predicted by the six equations are plotted in Figure 6.1. (The measured peak strength reported in Figure 6.1 is the greater of the peak strengths in the first and third quadrants.) It is evident from the figure that 1) there is a significant scatter in the predictions of peak shear strength, and 2) none of the equations are particularly suitable for either design or performance assessment in their current form.

Table 6.1. Peak shear strength and corresponding drift ratio

Wall	First quadrant			Third quadrant			Average
	Peak force (kips)	Avg. shear stress ($\times\sqrt{f_c'}$)	Drift ratio (%)	Peak force (kips)	Avg. shear stress ($\times\sqrt{f_c'}$)	Drift ratio (%)	Peak force (kips)
SW1	253	4.4	1.30	249	4.3	1.28	251
SW2	563	7.0	1.25	490	6.1	0.94	526
SW3	468	5.5	2.09	381	4.5	0.76	423
SW4	226	3.6	1.08	216	3.5	0.33	221
SW5	726	11.5	0.89	547	8.7	1.31	633
SW6	571	9.6	0.81	411	6.9	0.81	491
SW7	318	5.4	0.45	277	4.7	0.41	297
SW8	623	11.0	0.70	546	9.6	0.65	584
SW9	622	9.9	0.60	633	10.1	0.78	627
SW10	495	7.6	0.52	528	8.1	0.58	512
SW11	424	6.2	0.56	408	6.0	0.78	416
SW12	365	5.4	0.89	416	6.1	1.24	391

Table 6.2. Predicted peak shear strength (in kips)

Wall	ACI 318-14 §11.5	ACI 318-14 §18.10	Barda et al. (1977)	Wood (1990)	Gulec and Whittaker (2011)	Moehle (2015)
SW1	461	576	605	346	200	-
SW2	643	803	911	482	369	605
SW3	548	660	775	509	310	405
SW4	334	399	501	373	199	212
SW5	504	630	874	378	437	643
SW6	473	592	683	355	336	431
SW7	326	390	508	355	243	212
SW8	454	568	1074	341	443	965
SW9	504	620	1107	378	456	965
SW10	342	408	1118	391	460	965
SW11	524	635	706	407	280	-
SW12	349	416	531	407	236	-

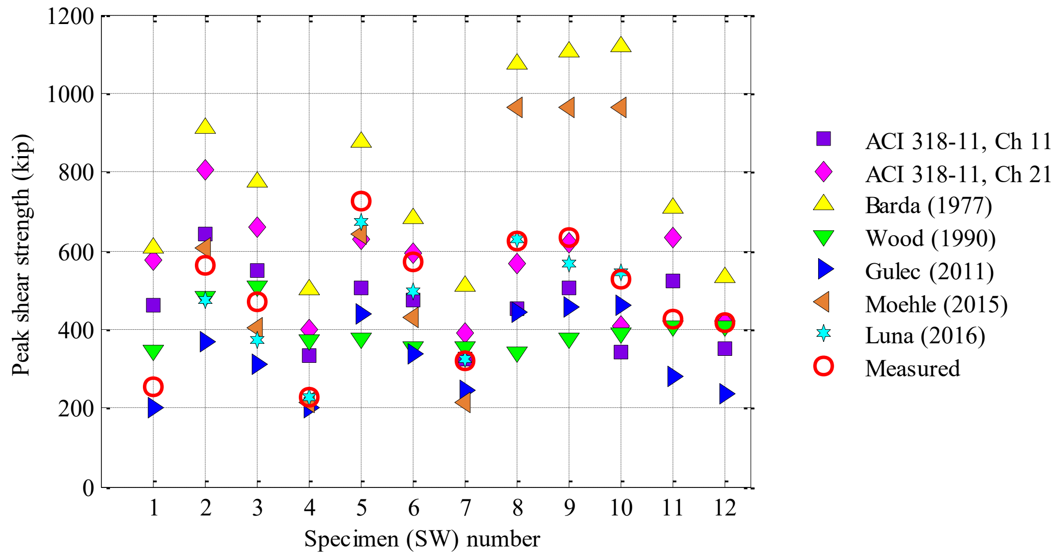

Figure 6.1. Measured and predicted peak shear strength

Table 6.3 shows the ratios of the predicted to measured peak shear strength (greater of peak strengths in the first and third quadrants) of the 12 UB walls. A ratio greater than 1.0 is an over prediction of strength: unconservative for design. The Barda equation produced unconservative predictions for the rectangular walls, with over-predictions by more than a factor of 2 for three of the walls. Of the two ACI-318 equations, the chapter 11 equation provided a mean value of the ratio of predicted to measured strength closer to 1.0 than the chapter 18 equation. The empirical equation derived by Gulec and Whittaker provides conservatively biased estimates of peak shear strength.

The Moehle equation was not used to predict peak strength of SW1, SW11 and SW12 because the crack pattern assumed to derive the equation was not appropriate for these three walls. The cracks on SW1 were a combination of shear and flexural cracks (Figure 4.4a), and the orientation of the cracks on the boundary elements of walls SW11 and SW12 were horizontal (panels k and l of Figure 4.4). The Moehle equation predicted the shear strength of walls SW2 through SW7 reasonably well but significantly over predicted the strength of SW8, SW9 and SW10. Walls SW8, SW9 and SW10 had a vertical reinforcement ratio of 1.5% and different horizontal reinforcement ratios. Moehle's equation is discussed further in Section 6.5.

Table 6.3. Ratio of predicted to measured peak shear strength

Wall	ACI 318-14 §11.5	ACI 318-14 §18.10	Barda et al. (1977)	Wood (1990)	Gulec and Whittaker (2011)	Moehle (2015)
SW1	1.82	2.28	2.39	1.37	0.79	-
SW2	1.14	1.43	1.62	0.86	0.66	1.07
SW3	1.17	1.41	1.66	1.09	0.66	0.87
SW4	1.48	1.77	2.21	1.65	0.88	0.94
SW5	0.69	0.87	1.20	0.52	0.60	0.89
SW6	0.83	1.04	1.20	0.62	0.59	0.75
SW7	1.03	1.23	1.60	1.12	0.76	0.67
SW8	0.73	0.91	1.72	0.55	0.71	1.55
SW9	0.80	0.98	1.75	0.60	0.72	1.52
SW10	0.65	0.77	2.12	0.74	0.87	1.83
SW11	1.24	1.50	1.66	0.96	0.66	-
SW12	0.84	1.00	1.28	0.98	0.57	-
Mean	1.03	1.26	1.70	0.92	0.71	1.12
SD*	0.34	0.42	0.37	0.33	0.10	0.39
COV**	0.33	0.33	0.22	0.36	0.14	0.34

* Standard deviation
** Coefficient of variation

6.3 Peak shear strength in the first and third quadrant of loadings

Significant differences in the measured first and third quadrant peak shear strength were observed in walls SW2, SW3, SW5, SW6, SW7 and SW8. The loading apparatus did not prevent the walls from moving out-of-plane (OOP), and OOP displacement and twisting, which should be anticipated in the field during earthquake shaking, was observed. The OOP displacement and twisting of the walls, normalized by their height, in the first and third quadrants of loading to peak strength are presented in Table 6.4. Data from the OOP string potentiometers attached at the two corners on the top of the wall, approximately 16 inches above the centerline of loading, were used for these calculations. The "measured drift" in Table 6.4 is the average of the OOP displacements measured by the string potentiometers at the two top corners of the walls.

A maximum value of OOP displacement due to OOP loading (at the centerline of the actuators) was estimated for each wall using the cross-section analysis code XTRACT version 3.0.8 (TRC Companies, Inc., 2010). The yield and ultimate moments, and the corresponding curvatures, were calculated using day-of-test concrete compressive strength and a measured rebar stress-strain relationship. The yield and ultimate moments of the 12 walls are summarized in Table 6.5. (The properties of the test specimens, including day-of-test concrete compressive strength and rebar yield and tensile strengths, are presented in Table 3.1.) The maximum OOP displacements were estimated by integrating the moment-curvature relationship over the height of the wall. Interaction with in-plane moments and shears was ignored in the calculation. The calculated maximum OOP displacement was normalized by the height of the wall and reported as drift in the second-to-last column of Table 6.4.

Table 6.4. Out-of-plane displacement and twisting (normalized by the height of the wall)

Wall	Measured drifts ($\times 10^{-3}$)		Measured twist (rad/in $\times 10^{-6}$)		Maximum drift ($\times 10^{-3}$)	$\left\lvert \frac{(2)}{(6)} \right\rvert$
	First quadrant (2)	Third quadrant (3)	First quadrant (4)	Third quadrant (5)	(6)	
SW1	7.5	-1.9	53.1	-5.3	161.9	0.05
SW2	-21.5	-2.9	-133.8	43.1	100.0	0.22
SW3	-7.1	-1.1	-43.1	15.4	80.0	0.09
SW4	-10.3	-1.1	-69.2	-1.5	24.6	0.42
SW5	-10.5	-0.2	-48.8	22.0	70.7	0.15
SW6	-5.1	0.5	-34.1	4.9	58.5	0.09
SW7	-4.4	-1.7	-4.9	17.1	17.1	0.26
SW8	-0.3	-0.5	3.1	18.5	126.2	0.00
SW9	1.8	0.6	23.1	-0.3	126.2	0.01
SW10	0.2	2.6	-4.6	24.6	120.0	0.00
SW11	0.9	0.6	-6.2	10.8	92.3	0.01
SW12	-1.5	0.9	-6.2	16.9	81.5	0.02

The ratios of the first quadrant OOP drift (calculated using the average of the OOP displacements at the ends of the wall) to the calculated maximum OOP drift are presented in the last column of Table 6.4. Five of the six walls (SW2, SW3, SW5, SW6 and SW7) with significant differences in first and third quadrant peak strengths had the greatest ratios of the first quadrant OOP drift to the calculated maximum OOP drift, indicating that OOP drift may have a significant influence on peak in-plane shear strength.

Table 6.5. Cross-section analysis using XTRACT version 3.0.8

Wall	Yield moment (kip-in)	Yield curvature (1/in $\times 10^{-3}$)	Ultimate moment (kip-in)	Ultimate curvature (1/in $\times 10^{-3}$)
SW1	1274	0.45	1497	18.34
SW2	1875	0.44	2238	18.34
SW3	1305	0.42	1493	18.33
SW4	730	0.47	749	18.32
SW5	1837	0.46	2242	18.35
SW6	1278	0.45	1495	18.34
SW7	730	0.45	750	18.32
SW8	2733	0.5	3451	18.39
SW9	2733	0.5	3451	18.39
SW10	2765	0.48	3452	18.37
SW11	1740	0.44	2061	17.45
SW12	1624	0.45	1872	17.45

Figure 6.2 shows the typical OOP displacement and twisting of walls SW2, SW3, SW5, SW6 and SW7 during the first and third quadrants of loading to peak in-plane strength. The red arrow shows the direction of loading and the open red rectangle indicates the final position of the top of the wall at peak strength. Tensile yielding of the vertical reinforcement in these walls was measured at the ends of the walls in the load steps corresponding to peak in-plane strength. The OOP stiffness at peak in-plane shear strength will vary considerably along the length of a wall at peak strength, from a small value at the end in tension under in-plane loading to a relatively large value at the end in compression: the OOP displacements of the top of the walls were larger at the end of the wall in tension than at the end of the wall in compression, as indicated in Figure 6.2. The variation in OOP stiffness along the length of the walls led to twisting of the walls. In the absence of OOP displacement and twisting, the peak shear strength in the first and third quadrants of loading were expected to be similar. Large OOP displacements and twisting resulted in significant differences in peak strength in the first and third quadrants of loading.

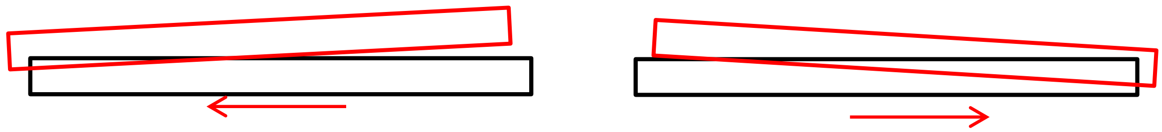

a. First quadrant loading b. Third quadrant loading

Figure 6.2. Typical out-of-plane displacement and twisting of the walls at peak strength

6.4 Gulec and Whittaker (2011) equation for peak shear strength

The functional form of the equation for peak shear strength by Gulec and Whittaker (2011) for rectangular low aspect ratio RC walls was identified using the free-body diagram shown in Figure 6.3. The cut on the wall was made at a typical diagonal crack (observations based on published data of past experiments) that forms as a result of lateral loading on top of a low aspect ratio RC wall. The crack is assumed to be at an angle α with respect to the horizontal. The forces on the free-body diagram include the 1) lateral force at the top of the wall, 2) axial load on the wall, 3) force carried by the vertical boundary element reinforcement, 4) total force carried by the vertical web reinforcement, 5) total force carried by the horizontal web reinforcement, and 6) frictional force associated with aggregate interlock between two cracks. The functional form is:

$$V_n = \frac{\beta_1 \left(f_c^{'} \right)^{\beta_2} A_{eff} + \beta_3 F_{vw} + \beta_4 F_{hw} + \beta_5 F_{vbe} + \beta_6 P}{\left(h_w / l_w \right)^{\beta_7}} \tag{6.1}$$

where β_1 through β_7 are unknown coefficients; $f_c^{'}$ (psi) is the compressive strength of concrete; A_{eff} (in^2) is the area of the wall; F_{vw}, F_{hw}, F_{vbe} (lb) are the vertical and horizontal forces developed in the web, and the vertical force in a vertical boundary element, respectively; P (lb) is the axial compressive force; h_w (in) is the height of the wall; and l_w (in) is the length of the wall.

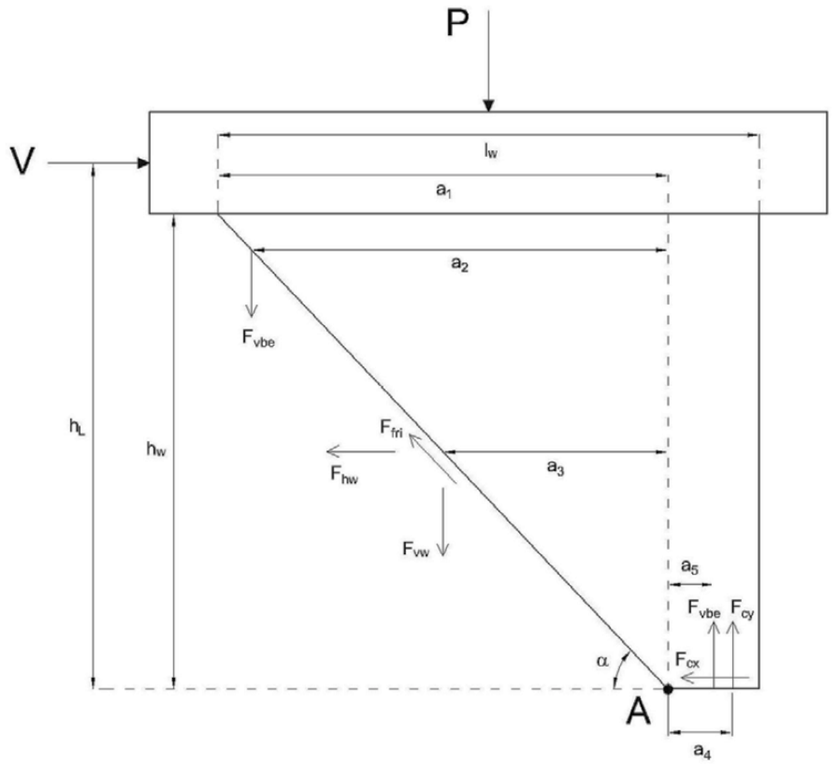

Figure 6.3. Free body diagram used to identify the functional form of Gulec and Whittaker equation for peak strength (reproduced from Gulec and Whittaker, 2009)

The coefficients were determined using nonlinear regression analysis of data from tests of 74 rectangular shear-critical walls conducted by other researchers. The properties of the 74 rectangular walls are summarized in Table 6.6 and Table 6.7. The walls considered in the analysis were tested using a cantilever test fixture and loaded at low rates of strain. For the cyclically loaded specimens, the peak shear strength is taken as the average of the peak shear strengths in the first and third quadrants of loading. The nonlinear solver *fmincon* in MATLAB R2006b (2006), a function that uses Sequential Quadratic Programming to find the minimum of a constrained nonlinear function with multiple variables, was used to determine the coefficients. The coefficient β_2 was set to 0.5 since the concrete contribution to shear strength is traditionally expressed as a function of $\sqrt{f_c'}$. Values of β_1, β_3, β_4, β_5, β_6 and β_7 were determined to be 1.29, 0.26, 0.04, 0.20, 0.39 and 0.58, respectively. The value of β_4, the multiplier for the forces developed in the horizontal reinforcement, indicates that the contribution of the horizontal reinforcement to the peak strength of a low aspect ratio wall was small. The small value of β_6, (=0.39), which premultiplies

P, is attributed to the lack of tests in the dataset performed with relatively large values of applied axial compression. The ratio of the predicted peak strength of the 74 walls using (6.1) (with the coefficients determined from the regression analysis) to the experimentally measured peak shear strength had a median value of 0.99. (The mean value of the ratio was 1.0 since this was the input constraint and the coefficient of variation was 0.135.) The author recreated the code for the regression analysis in MATLAB R2012b (MathWorks, Inc., 2012), and similar results were obtained.

From the cracking pattern observed from the tests of the 12 RC shear walls at UB (10 walls without boundary elements and two walls with boundary elements), it is evident that the free-body diagram assumed by Gulec best applies to walls without boundary elements. The idealized cracking pattern of a wall without boundary elements (based on the observed cracking patterns of SW2 through SW10) is shown in Figure 6.4. For the walls with boundary elements, the orientation of the shear cracks on the webs of the walls changed from diagonal to horizontal at the junction of web-boundary elements, making the assumed free-body diagram for the equation of Gulec inappropriate.

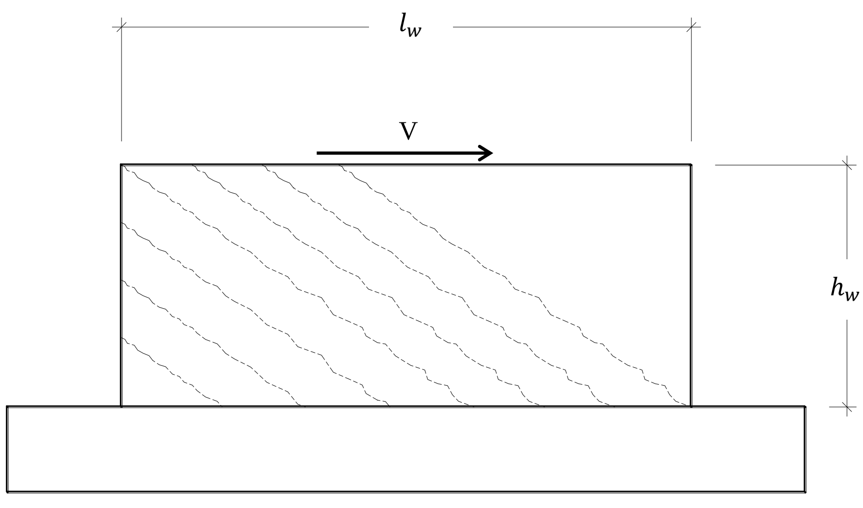

Figure 6.4. Observed cracking pattern (idealized) of a rectangular low aspect ratio RC wall wit hout boundary elements

Table 6.6. Properties of the 74 rectangular walls assembled by Gulec and Whittaker (2011)

Researcher	Wall	t_w (in)	h_w (in)	l_w (in)	h_{be} (in)	ρ_{be} (%)	ρ_l (%)	ρ_t (%)
Cardenas	SW-7	3.00	75.00	75.00	7.50	8.19	0.85	0.27
	SW-8	3.00	75.00	75.00	0.00	0.00	2.87	0.27
	SW-10	3.00	75.00	75.00	7.50	8.19	0.00	0.00
	SW-13	3.00	75.00	75.00	0.00	0.00	2.87	0.93
Pilakoutas	SW4	2.36	47.24	23.62	4.33	6.86	0.50	0.39
	SW5	2.36	47.24	23.62	2.36	12.75	0.59	0.31
	SW7	2.36	47.24	23.62	2.36	12.75	0.59	0.39
	SW8	2.36	47.24	23.62	4.33	7.14	0.50	0.28
	SW9	2.36	47.24	23.62	4.33	7.14	0.50	0.56
Greifenhagen	M1	3.94	24.02	39.37	0.00	0.00	0.34	0.37
	M2	3.94	24.02	39.37	0.00	0.00	0.34	0.00
Hidalgo	1	4.72	78.74	39.37	3.94	8.50	0.25	0.13
	2	4.72	78.74	39.37	3.94	8.50	0.25	0.25
	4	4.72	78.74	39.37	3.94	10.58	0.25	0.38
	6	4.72	70.87	51.18	5.12	6.54	0.26	0.13
	7	4.72	70.87	51.18	5.12	6.54	0.13	0.25
	8	4.72	70.87	51.18	5.12	6.54	0.26	0.25
	9	3.94	70.87	51.18	5.12	7.00	0.26	0.26
	10	3.15	70.87	51.18	5.12	7.31	0.25	0.25
	11	3.94	55.12	55.12	5.51	5.71	0.26	0.13
	12	3.94	55.12	55.12	5.51	5.71	0.13	0.26
	13	3.94	55.12	55.12	5.51	5.71	0.26	0.26
	14	3.15	47.24	66.93	6.69	4.41	0.25	0.13
	15	3.15	47.24	66.93	6.69	4.41	0.13	0.26
	16	3.15	47.24	66.93	6.69	4.41	0.25	0.25
	21	3.94	70.87	51.18	5.12	4.62	0.00	0.00
	22	3.94	70.87	51.18	5.12	4.62	0.00	0.00
	23	3.94	70.87	51.18	5.12	8.54	0.00	0.25
	24	3.94	70.87	51.18	5.12	4.62	0.25	0.00
	25	3.94	55.12	55.12	5.51	4.29	0.00	0.00
	26	3.94	55.12	55.12	5.51	4.29	0.00	0.00
	27	3.94	55.12	55.12	5.51	6.50	0.00	0.25
	28	3.94	55.12	55.12	5.51	4.29	0.25	0.00
	29	3.15	41.34	59.06	5.91	5.00	0.00	0.00
	30	3.15	41.34	59.06	5.91	5.00	0.00	0.00
	31	3.15	41.34	59.06	5.91	6.67	0.00	0.25
	32	3.15	41.34	59.06	5.91	5.00	0.25	0.00

Table 6.6. Properties of the 74 rectangular walls assembled by Gulec and Whittaker (2011) (continued)

Researcher	Wall	t_w (in)	h_w (in)	l_w (in)	h_{be} (in)	ρ_{be} (%)	ρ_l (%)	ρ_t (%)
Hirosawa	72	6.30	62.99	66.93	6.69	5.68	0.51	0.26
	73	6.30	62.99	66.93	6.69	5.68	0.51	0.26
	74	6.30	62.99	66.93	6.69	5.68	0.51	0.57
	75	6.30	62.99	66.93	6.69	5.68	0.51	0.57
	76	6.30	62.99	66.93	6.69	5.68	0.51	1.08
	77	6.30	62.99	66.93	6.69	5.68	0.51	1.08
	79	6.30	62.99	66.93	6.69	2.51	0.51	0.61
	82	6.30	62.99	33.46	3.35	9.91	0.40	0.57
	83	6.30	62.99	33.46	3.35	9.91	0.40	0.57
Rothe	T10	3.15	43.31	31.50	5.91	1.41	0.71	0.51
Wiradinata	Wall-1	3.94	39.37	78.74	12.60	1.25	0.59	0.26
	Wall-2	3.94	19.69	78.74	12.60	1.25	0.59	0.26
Pilette	Wall-4	3.94	39.37	78.74	12.60	1.25	0.59	0.80
	Wall-5	3.94	39.37	78.74	9.84	1.60	1.07	1.20
Doostdar	Wall-7	3.94	59.06	78.74	12.60	1.25	0.59	0.80
	Wall-8	3.94	59.06	59.06	14.17	1.11	0.51	0.80
Salonikios	MSW3	3.94	70.87	47.24	9.45	1.30	0.28	0.28
	MSW6	3.94	70.87	47.24	9.45	1.70	0.57	0.57
	LSW1	3.94	47.24	47.24	9.45	1.70	0.57	0.57
	LSW2	3.94	47.24	47.24	9.45	1.30	0.28	0.28
	LSW3	3.94	47.24	47.24	9.45	1.30	0.28	0.28
Sheu	SWN-1D	3.94	19.69	39.37	0.00	0.00	0.43	0.57
	SWN-5D	3.94	29.53	39.37	0.00	0.00	0.43	0.57
	SW-5	3.94	19.69	39.37	0.00	0.00	0.77	1.03
	SW9	3.94	19.69	39.37	0.00	0.00	0.79	0.57
	SW11	3.94	19.69	39.37	0.00	0.00	0.79	0.57
	SW12	3.94	19.69	39.37	0.00	0.00	0.78	0.57
	SW13	3.94	19.69	39.37	0.00	0.00	0.76	0.00
	SW17	3.94	29.53	39.37	0.00	0.00	0.79	0.57
	SW19	3.94	29.53	39.37	0.00	0.00	0.76	0.00
Synge	Wall-1	3.94	59.06	118.11	9.45	1.89	0.81	1.61
Wallace	wp111-9	6.00	48.00	54.00	7.50	0.87	0.25	0.27
	wp111-10	6.00	48.00	54.00	7.50	0.87	0.25	0.27
	wp1105-8	6.00	48.00	54.00	7.50	0.87	0.25	0.27
	wp1105-7	6.00	48.00	54.00	7.50	0.87	0.25	0.27
	wp110-5	6.00	48.00	54.00	7.50	0.87	0.25	0.27
	wp110-6	6.00	48.00	54.00	7.50	0.87	0.25	0.27

Table 6.7. Additional properties of the 74 rectangular walls assembled by Gulec and Whittaker (2011)

Researcher	Wall	f_c' (psi)	f_{ybe} (ksi)	f_{yl} (ksi)	f_{yt} (ksi)	$\frac{M}{Vl_w}$	$\frac{P}{A_{cv} f_c'}$ (%)	V_{peak} (kips)
Cardenas	SW-7	6240	65	65	60	1.00	0.00	116.70
	SW-8	6160	0	65	68	1.00	0.00	128.10
	SW-10	5850	65	0	0	1.00	0.00	68.70
	SW-13	6300	0	65	66	1.00	0.00	142.10
Pilakoutas	SW4	5352	73	80	80	2.00	0.00	23.54
	SW5	4612	78	80	58	2.00	0.00	25.15
	SW7	4641	78	80	80	2.00	0.00	29.07
	SW8	6643	78	80	58	2.00	0.00	21.29
	SW9	5642	78	80	58	2.00	0.00	22.08
Greifenhagen	M1	7352	0	73	73	0.61	2.20	45.47
	M2	7395	0	73	0	0.61	2.20	45.74
Hidalgo	1	2914	59	59	59	1.00	0.00	44.51
	2	2959	61	61	61	1.00	0.00	60.70
	4	2944	61	61	61	1.00	0.00	72.84
	6	2654	47	47	47	0.69	0.00	69.47
	7	2741	71	71	71	0.69	0.00	81.83
	8	2364	71	71	71	0.69	0.00	84.08
	9	2654	55	55	55	0.69	0.00	58.00
	10	2466	55	55	55	0.69	0.00	42.04
	11	2451	55	55	55	0.50	0.00	52.83
	12	2567	55	55	55	0.50	0.00	68.34
	13	2741	56	56	56	0.50	0.00	64.97
	14	2582	55	55	55	0.35	0.00	57.33
	15	2872	55	55	55	0.35	0.00	82.73
	16	2843	55	55	55	0.35	0.00	81.38
	21	3655	65	0	0	0.69	0.00	58.00
	22	2596	65	0	0	0.69	0.00	49.91
	23	3655	65	0	65	0.69	0.00	74.86
	24	3612	65	65	0	0.69	0.00	52.16
	25	3612	65	0	0	0.50	0.00	79.13
	26	2669	65	0	0	0.50	0.00	58.90
	27	3597	65	0	65	0.50	0.00	110.38
	28	3510	65	65	0	0.50	0.00	58.00
	29	3495	65	0	0	0.35	0.00	90.04
	30	2698	65	0	0	0.35	0.00	80.03
	31	3495	65	0	65	0.35	0.00	87.90

Table 6.7. Additional properties of the 74 rectangular walls assembled by Gulec and Whittaker (2011) (continued)

Researcher	Wall	$f_c^{'}$ (psi)	f_{ybe} (ksi)	f_{yl} (ksi)	f_{yt} (ksi)	$\frac{M}{Vl_w}$	$\frac{P}{A_{cv} f_c^{'}}$ (%)	V_{peak} (kips)
Hidalgo	32	3510	65	65	0	0.35	0.00	77.33
Hirosawa	72	2503	55	59	61	0.94	11.37	173.64
	73	3015	55	59	61	0.94	9.44	174.20
	74	3015	55	59	61	0.94	9.44	177.50
	75	1991	55	59	61	0.94	14.29	182.46
	76	2133	55	59	60	0.94	13.34	178.61
	77	2660	55	59	60	0.94	10.70	196.80
	79	1991	55	59	61	0.94	14.29	132.85
	82	3015	55	59	61	1.88	9.44	71.39
	83	2589	55	59	61	1.88	10.99	68.36
Rothe	T10	4869	73	73	73	1.37	0.00	20.12
Wiradinata	Wall-1	3626	63	63	62	0.50	0.00	119.71
	Wall-2	3191	63	63	62	0.25	0.00	153.99
Pilette	Wall-4	4786	70	70	70	0.50	0.00	90.15
	Wall-5	3916	70	70	70	0.50	0.00	122.41
Doostdar	Wall-7	6527	65	65	65	0.75	0.00	84.30
	Wall-8	6527	65	65	65	1.00	0.00	50.47
Salonikios	MSW3	3494	85	88	88	1.50	7.00	38.97
	MSW6	3988	85	87	87	1.50	0.00	42.13
	LSW1	3219	85	87	87	1.00	0.00	58.47
	LSW2	3132	85	88	88	1.00	0.00	41.61
	LSW3	3466	85	88	88	1.00	7.00	56.53
Sheu	SWN-1D	3869	0	68	68	0.50	12.00	67.24
	SWN-5D	4068	0	68	68	0.75	12.00	55.12
	SW-5	3954	0	70	70	0.50	0.00	54.42
	SW9	3776	0	62	68	0.50	0.00	55.78
	SW11	3776	0	62	68	0.50	0.00	49.85
	SW12	3840	0	65	68	0.50	0.00	55.78
	SW13	4694	0	66	0	0.50	0.00	54.72
	SW17	3769	0	63	68	0.75	0.00	40.52
	SW19	3556	0	66	0	0.75	0.00	35.23
Synge	Wall-1	3945	44	44	55	0.50	0.00	173.84

Table 6.7. Additional properties of the 74 rectangular walls assembled by Gulec and Whittaker (2011) (continued)

Researcher	Wall	f_c' (psi)	f_{ybe} (ksi)	f_{yl} (ksi)	f_{yt} (ksi)	$\frac{M}{Vl_w}$	$\frac{P}{A_{cv} f_c'}$ (%)	V_{peak} (kips)
Wallace	wp111-9	4100	62	62	62	0.44	10.00	169.50
	wp111-10	4550	62	62	62	0.44	10.00	184.50
	wp1105-8	4630	62	62	62	0.44	5.00	146.00
	wp1105-7	4640	62	62	62	0.44	5.00	153.50
	wp110-5	4340	62	62	62	0.44	0.00	91.00
	wp110-6	4500	62	62	62	0.44	0.00	73.00

Figure 6.5a shows a modified version of the free-body diagram used by Gulec that is based on a typical cracking pattern for a wall without boundary elements. Summing moments at point A:

$$V = \frac{P\left(a_1 - \frac{l_w}{2}\right) + F_{vwt}\left(a_2\right) + F_{vwc}\left(a_3\right) + F_{hw}\left(\frac{h_w}{2}\right) + F_{cy}\left(a_4\right)}{h_w} \tag{6.2}$$

where F_{vwt} and F_{vwc} are the forces in the vertical reinforcement in tension and compression, respectively; and F_{cy} is the vertical component of the force in the concrete in compression. Walls SW2 through SW10 had little vertical reinforcement in compression at the instance of peak shear strength, typically only those nearest the end of the wall in compression, and the magnitude of strain in these vertical reinforcement in compression was small. Herein, it is assumed that the total force on the few vertical reinforcement in compression is insignificant. The forces F_{vwt} and F_{vwc} can be approximated by a single term F_{vw} that acts at a distance a_5 from point A (see Figure 6.5b). Considering strain hardening in some of the vertical reinforcement in tension, the force F_{vw} can be approximated using total vertical reinforcement area and yield stress of the vertical reinforcement. Force F_{hw} can also be approximated using the total horizontal reinforcement area and yield stress of the horizontal reinforcement. Equation (6.2) can be written as:

$$V = \frac{P\left(a_1 - \frac{l_w}{2}\right) + F_{vw}\left(a_5\right) + F_{hw}\left(\frac{h_w}{2}\right) + F_{cy}\left(a_3\right)}{h_w} \tag{6.3}$$

The functional form of a modified equation for a rectangular wall without boundary elements, based on the equilibrium expression in (6.3), can be expressed as:

$$V_n = \frac{\beta_1\sqrt{f_c'}A_{eff} + \beta_2 F_{vw} + \beta_3 F_{hw} + \beta_4 P}{\left(h_w/l_w\right)^{\beta_5}} \tag{6.4}$$

where the concrete contribution term is expressed in terms of $\sqrt{f_c'}$.

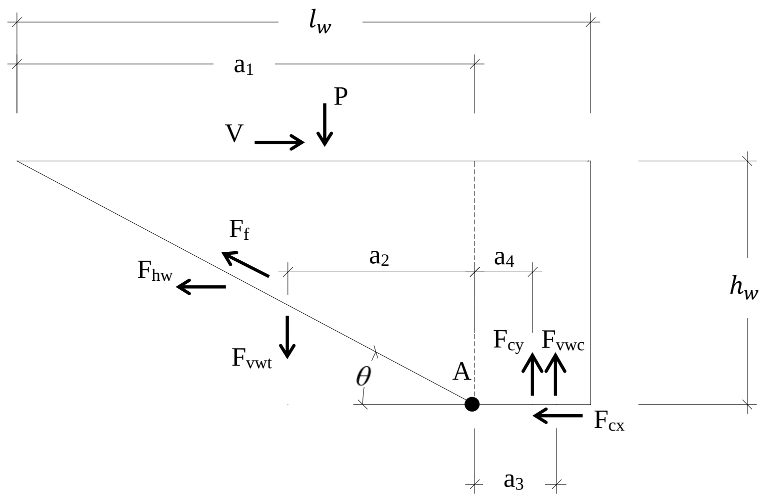

a) Modified free-body diagram

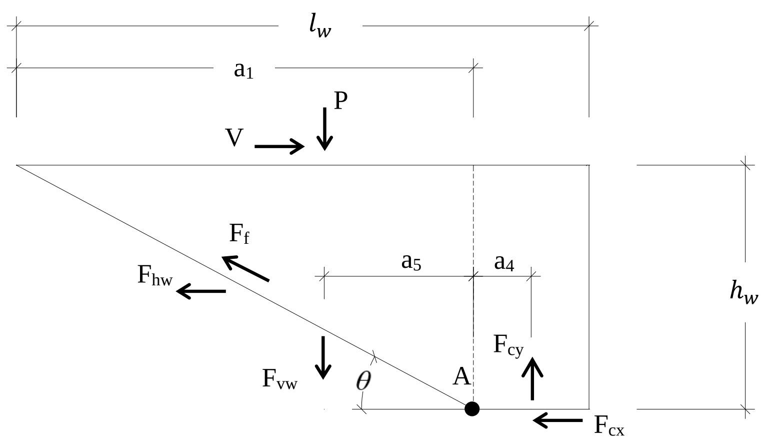

b) Simplified free-body diagram

Figure 6.5. Free-body diagram for the modified Gulec and Whittaker equation for peak strengt h

Regression analysis was performed using MATLAB R2012b to determine the values of the coefficients in (6.4), as described above. The walls with no boundary elements were chosen from the database of 74 rectangular walls. A total of 13 walls were selected: two from Cardenas, two from Greifenhagen and nine from Sheu. Shear-critical walls without boundary elements tested at UB, SW2 through SW10, were added to these 13 walls. For the cyclically loaded specimens (including UB walls SW2 through SW10), the peak shear strength was set equal to the average of the peak strengths in the first and third quadrants of loading. The coefficients determined from the regression analysis using the 22 walls without boundary elements are provided in (6.5):

$$V_n = \frac{1.11\sqrt{f_c^{'}}A_{eff} + 0.25F_{vw} + 0.08F_{hw} + 0.21P}{\left(h_w/l_w\right)^{0.81}} \tag{6.5}$$

The predicted peak shear strength of the 22 walls using (6.5) is shown in Table 6.8. The ratios of the predicted to experimental peak strength, shown in the last column of Table 6.8, had a mean value of 1.0 (the input constraint) and an improved coefficient of variation of 0.08. Similar to the original equation, the small value of the coefficient for the horizontal reinforcement indicates that the contribution of the horizontal reinforcement to peak shear strength is small. Equation (6.5) can be generalized and simplified to the following expression:

$$V_n = \frac{1.1\sqrt{f_c^{'}}A_{eff} + 0.25F_{vw} + 0.2P}{\left(h_w/l_w\right)^{0.8}} \tag{6.6}$$

Predictions using this equation are provided in Figure 6.1 as Luna (2016).

Table 6.8. Predicted peak shear strength of rectangular walls without boundary elements using Equation 6.5

Researcher	Wall	V_{peak} (kips)	V_n (Eqn. 6.5) (kips)	$\frac{V_n}{V_{peak}}$
Cardenas	SW-8	128.1	127.6	1.00
	SW-13	142.1	135.7	0.95
Greifenhagen	M1	45.5	47.3	1.04
	M2	45.7	44.3	0.97
Sheu	SWN-1D	67.2	69.2	1.03
	SWN-5D	55.1	52.7	0.96
	SW-5	54.4	63.4	1.17
	SW9	55.8	56.2	1.01
	SW11	49.8	56.2	1.13
	SW12	55.8	57.2	1.03
	SW13	54.7	54.6	1.00
	SW17	40.5	42.0	1.04
	SW19	35.2	37.4	1.06
Luna	SW2	526.0	438.0	0.83
	SW3	423.0	349.9	0.83
	SW4	221.0	215.8	0.98
	SW5	633.0	592.5	0.94
	SW6	491.0	442.0	0.90
	SW7	297.0	297.3	1.00
	SW8	584.0	568.6	0.97
	SW9	627.0	541.8	0.86
	SW10	512.0	530.2	1.04
			Average	1.00

6.5 Moehle (2015) equation for peak shear strength

Moehle (2015) presents an expression to estimate the peak shear strength of a low aspect ratio RC wall. The formula is based on the idealized crack pattern and free-body diagrams shown in Figure 6.6. In his formulation, diagonal cracking is assumed to occur at a constant angle θ with respect to the horizontal, and normal and shear stresses along a diagonal crack are resisted only by reinforcement, that is, the effect of aggregate interlock is not included. A further simplification is made by assuming that the stress in the horizontal and vertical reinforcement is f_y. Summing moments about the mid-bottom of the compression strut shown in Figure 6.6b:

$$v_n x b_w h_w - n_u x b_w \frac{h_w}{\tan\theta} - A_{sy} f_y \frac{x}{s_x} \frac{h_w}{\tan\theta} = 0 \tag{6.7}$$

where v_n is the uniform shear stress acting at the top and bottom of the strut; x and b_w are the width and thickness of the compression strut, respectively; h_w is the height of the wall; A_{sy} is the area of vertical reinforcement evenly spaced at a distance s_x; and f_y is the yield stress of the reinforcement. Equation (6.7) was assumed to apply along the length of the wall, l_w, giving:

$$V_n = v_n l_w b_w = \left(n_u l_w b_w - \frac{A_{sy} f_y l_w}{s_x} \right) \frac{1}{\tan\theta} = \left(N_u + \rho_l f_y A_{cv} \right) \frac{1}{\tan\theta} \tag{6.8}$$

where V_n is the peak shear strength, N_u is the total axial load, ρ_l is the vertical reinforcement ratio, A_{cv} is the gross-cross sectional area of the wall and θ is the angle of the crack with respect to the horizontal. The equation does not include horizontal reinforcement ratio but the presence of horizontal reinforcement stressed to f_y is assumed. The assumption that (6.7) applies along the length of the wall is studied in the following section. If (6.7) is assumed to apply only over the fraction of the length of the wall that can develop compression struts under unidirectional loading, which is a function of aspect ratio, (6.8) will overestimate nominal shear strength. Moehle notes the equation can be interpreted as the product of the effective normal force (the terms inside the parentheses) and a friction coefficient $1/\tan\theta$, and can be used to define the interface shear strength between the wall and foundation.

Wood (1990) proposed an equation (see Section 2.4) for the shear strength of low-rise walls that takes a similar form to Equation 6.8: $A_v f_y / 4$, where A_v is the area of the vertical reinforcement crossing the (horizontal) shear plane. Although the Wood and Moehle equations have a similar functional form, one is empirical and based on shear friction (Wood) and the other is based on diagonal compression struts (Moehle) that have been observed in experiments. Importantly, the model assumed by Moehle is supported by data presented in this report whereas the shear-friction model is not: walls do not slide until after peak strength is achieved.

Equation (6.7) was formulated using the free body diagram of a concrete compression strut shown in Figure 6.6b. Equation (6.7) is suitable for that fraction of the length of the wall where compression struts can form. For the other part of the wall, segment c-d-e in Figure 6.6c, the assumption is not suitable. For walls with a very low aspect ratio, length c-d in Figure 6.6 will be a small fraction of and (6.8) should yield reasonable estimates of the peak strength.

Moehle recognized the importance of the distributed horizontal reinforcement for the equilibrium of segment c-d-e shown in Figure 6.6c. The horizontal reinforcement is needed to transfer lateral forces from segment c-d-e to the remainder of the wall. Moehle also identified that concrete at the toe of the wall (point e in segment c-d-e) must be resisting compression to maintain equilibrium of the segment.

Moehle's equation was used to predict the peak strength of all the walls tested at UB, except for SW1, SW11 and SW12. The idealized cracking pattern used in the formulation of Moehle's equation is different from the cracking patterns observed on SW1, SW11 and SW12. Wall SW1 was the tallest of the walls tested and its cracks were due to both shear and flexure (see Figure 4.3a). Walls SW11 and SW12 had boundary elements, which changed the orientation of the cracks from diagonal to horizontal at the web-boundary element junctions (see panels k and l of Figure 4.3). Moehle (2015) presents similar horizontal cracking patterns in the boundary flanges of slender structural walls.

The estimated peak shear strengths of walls SW2 through SW10 per Moehle (2015) are listed in the last column of Table 6.2. The angle of inclination of the cracks, θ, was assumed to be 45°. The ratio of the predicted peak strength to the measured peak strength is presented in the last column of Table 6.3. The peak strengths of SW2 through SW7 are predicted reasonably well whereas the peak strength of walls SW8, SW9 and SW10 are over-estimated by a factor of more than 1.5 if no upper limit is imposed to address diagonal compression failure. The vertical reinforcement ratio in SW2 through SW7 was 1% and less. As shown in panels a through g of Figure 4.6, the vertical reinforcement in these walls had yielded at peak strength, which supports a key assumption in the Moehle formulation. The vertical reinforcement ratio in SW8, SW9 and SW10 was 1.5%, with corresponding horizontal reinforcement ratios of 1.5%, 0.67% and 0.33%. The assumption that all horizontal and vertical reinforcement has yielded at peak shear strength does not hold for these three walls. Panels h, i and j of Figure 4.6 show that strain in many vertical rebar in SW8, SW9 and SW10, respectively, was less than the yield value at peak shear strength.

The equation formulated by Moehle provides insight into force transfer in low aspect ratio walls at peak strength. Reasonable assumptions were made to simplify the problem and Moehle did not have the data presented previously in this report. The Moehle equation can be improved using the cracking patterns and data from the strain gages and Krypton LED sensors, obtained from the testing of the 12 shear walls, as presented in the next section.

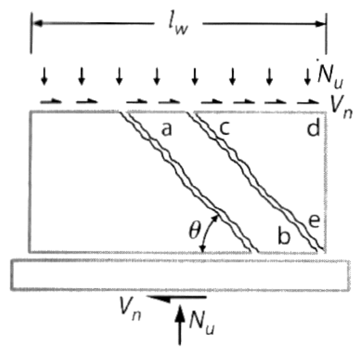

a) Idealized cracks

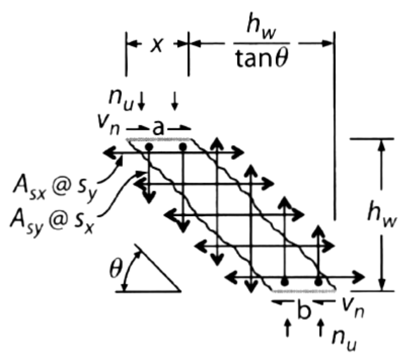

b) Free-body diagram of compression strut a-b

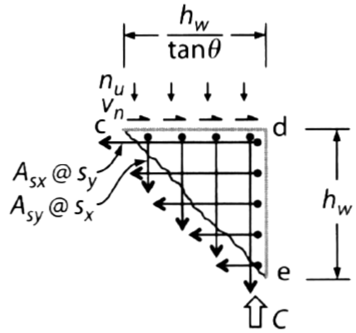

c) Free-body diagram of segment c-d-e

Figure 6.6. Idealized forces on a low aspect ratio RC wall (Moehle, 2015, reproduced with per mission from McGraw-Hill Education)

6.6 Peak shear strength of low aspect ratio RC walls without boundary elements

Data from the tests of the 12 RC shear walls described in Chapter 3 and Chapter 4 provide information to help understand how forces are transferred through a wall. The data from the strain gages, strain distributions on the faces of the walls calculated from the Krypton LED data and the cracking patterns can be used to develop free-body diagrams of different segments of the wall and to estimate the magnitude of the forces in reinforcement and the strains in the concrete. These data are used to derive predictive equations for peak shear strength of rectangular low aspect ratio, RC walls.

An equation for peak in-plane shear strength is presented in this section for walls without boundary elements and it utilizes a formulation similar to Moehle's. Those segments of a low-rise wall with significantly different strains at peak strength were identified in Section 4.6. Figure 6.7 cartoons the three segments, observed cracking pattern and forces acting on a wall. The shear strains at peak shear strength in segment B are substantially greater than those in segments A and C. The toe of the wall shown in the bottom left corner of segment A (open red circle) can resist compression and shearing forces because the inclined cracks do not propagate to the corner as assumed in the idealized cracking pattern of Figure 6.7. The distance from the bottom end of the wall to the bottom of the diagonal crack in segment A is designated as *c*. The patterns of concrete cracking at peak shear strength in SW3 and SW8 at peak strength are shown in Figure 6.8, with length *c* highlighted with an open red circle. (The patterns of concrete cracking for all the walls are presented in Figure 4.4.) Three representative concrete compression struts (or simply struts) are drawn in segment B. (The number of struts in section B can be less or more than three.) Variables *p* and *v* represent the axial load per unit length and shear force per unit length at the centerline of horizontal loading, respectively, noting that the assumption of uniform shear force per unit length of wall was not validated in the experiments of Chapter 3 or in prior tests, and may not occur in the field. No axial load was applied to the 12 walls tested at UB and their self-weight is insignificant for the purpose of calculations of shear strength. Cracks are assumed to propagate at a constant angle, θ, with respect to the horizontal. Variables h_w and l_w are the height (distance between foundation and centerline of loading) and length of the wall, respectively.

Information from Sections 4.5, 4.6 and 6.5 are summarized here because they are used to formulate an equation for the peak shear strength of walls without boundary elements.

1) The idealized cracking pattern presented in Figure 6.7 is applicable for walls SW2 through SW10. The cracking patterns observed on SW1, SW11 and SW12 were different from that shown in Figure 6.7. Cracks in SW1 were due to shear and flexure (see Figure 4.4a) and the cracks in the boundary elements of walls SW11 and SW12 (see panels k and l of Figure 4.4) were horizontal.
2) All vertical reinforcement yielded in tension (over the height of the wall) for walls SW2 through SW7 (walls with vertical reinforcement ratio of 1% and less). Many vertical bars in walls SW8 through SW10 (walls with vertical reinforcement ratio of 1.5%) did not yield in tension.
3) The strain in the horizontal reinforcement of walls SW2 through SW10 was greatest in the mid-section of the walls and relatively small at the ends. The strains in segments A of SW2 through SW10, as calculated using the Krypton LED data, were relatively small.

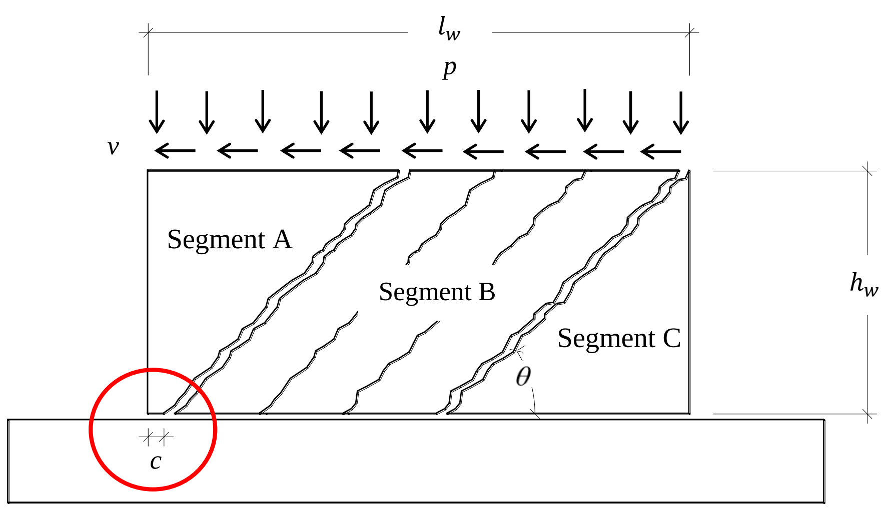

Figure 6.7. Different sections and idealized cracking pattern of a low aspect ratio rectangular R C wall without boundary elements

The free-body diagram of segment B of the wall is shown in Figure 6.9. Actions F_v and F_h are the total forces carried by the vertical and horizontal reinforcement, respectively, that cross a diagonal crack. Action F_s is the force associated with aggregate interlock. Variable x is the horizontal projection of the width of the strut. Summing moments about the mid-bottom of a strut:

$$vxh_w = F_y \frac{h_w}{\tan\theta} + px\frac{h_w}{\tan\theta} + F_s(x\sin\theta) \tag{6.9}$$

where F_y is the axial force in the vertical reinforcement over distance *x*. The strains in the vertical reinforcement in segment B of SW2 through SW7 at peak shear strength were between 6 millistrain ($\simeq 3\varepsilon_y$) and 20 millistrain ($\simeq 10\varepsilon_y$), where ε_y is the yield strain. For walls SW8, SW9 and SW10, the corresponding strains were between one and six millistrain. (The strains on the vertical reinforcement are shown in Figure 4.8.) The force on the vertical reinforcement F_y, shown in Figure 6.9b is:

$$F_y = \rho_l t_w x f_{\bar{y}} \tag{6.10}$$

where ρ_l is the vertical reinforcement ratio, t_w is the thickness of the wall, and $f_{\bar{y}}$ is the stress in the vertical reinforcement, and equal to: a) the average of the measured yield strength (f_y) and measured ultimate strength (f_u) of the reinforcement to account for cyclic hardening of the vertical reinforcement in walls SW2 through SW7, and b) the measured yield strength (f_y) for walls SW8, SW9 and SW10.

The strains in the horizontal reinforcement of walls SW2 through SW10 are shown in Figure 4.8. In these walls, the strains are greatest in the mid-section (mid-length) of the wall and small at the ends. Based on the gage data at peak strength, $0.25e_y$ is a conservative (low) estimate of the strain in the horizontal reinforcement at the boundaries of segments A and B, and of segments B and C. The net effect of the forces in the horizontal reinforcement at the two sides of segment B on the moment at the mid-bottom of a strut is assumed to be negligible. Assuming a uniform distribution of applied shear along the horizontal projection of segment B, and using (6.10) for F_y, the shear resistance of segment B can be estimated as:

$$\begin{aligned} v\left(l_w - \frac{h_w}{\tan\theta} - c\right)h_w &= \rho_l t_w f_{\bar{y}}\left(l_w - \frac{h_w}{\tan\theta} - c\right)\frac{h_w}{\tan\theta} + \ldots \\ &\ldots + p\left(l_w - \frac{h_w}{\tan\theta} - c\right)\frac{h_w}{\tan\theta} + F_s\left(l_w - \frac{h_w}{\tan\theta} - c\right)\sin\theta \end{aligned} \tag{6.11}$$

The total lateral resistance provided by segment B of the wall, V_{nb}, is given by:

$$V_{nb} = v\left(l_w - \frac{h_w}{\tan\theta} - c\right) = \rho_l t_w f_{\bar{y}}\left(l_w - \frac{h_w}{\tan\theta} - c\right)\frac{1}{\tan\theta} + \ldots$$
$$\ldots + p\left(l_w - \frac{h_w}{\tan\theta} - c\right)\frac{1}{\tan\theta} + F_s\left(l_w - \frac{h_w}{\tan\theta} - c\right)\frac{\sin\theta}{h_w} \tag{6.12}$$

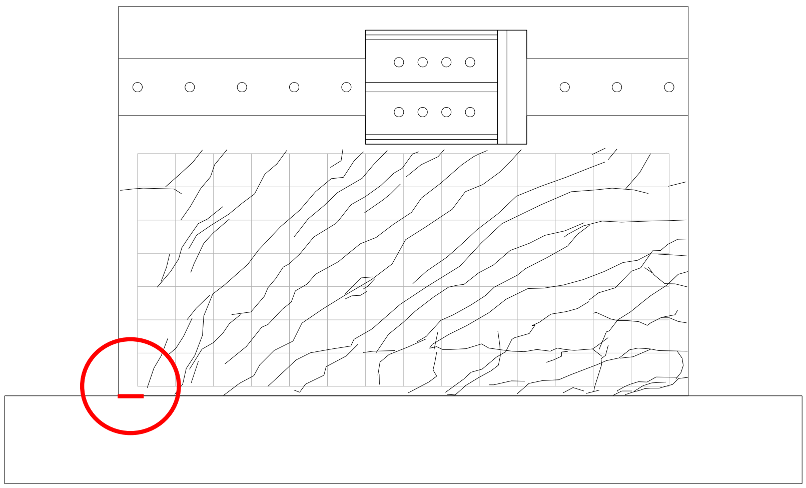

a) SW3

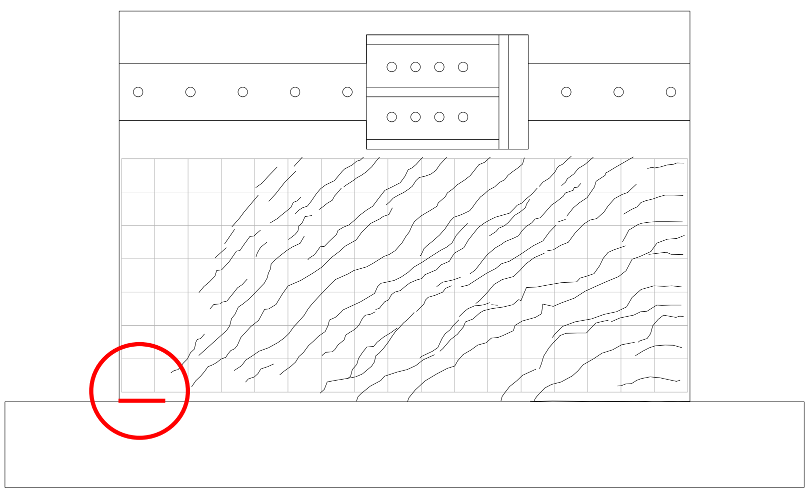

b) SW8

Figure 6.8. Cracking patterns at peak strength of walls SW3 and SW8

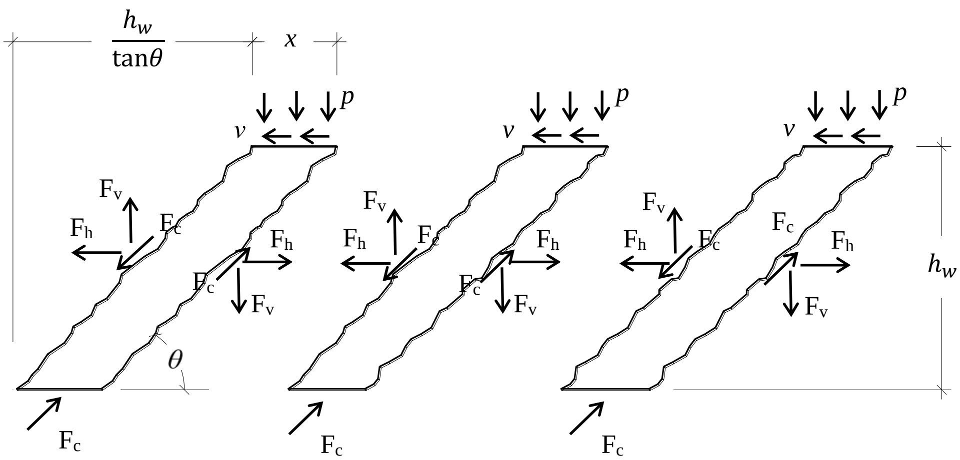

a) Forces in the concrete compression struts

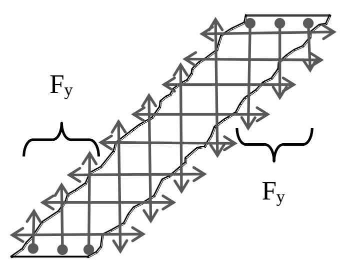

b) Forces in reinforcement

Figure 6.9. Free-body diagram of segment B of a wall without boundary elements

Force F_s is associated with aggregate interlock (or friction forces). There is considerable uncertainty in the magnitude of this force (Gulec and Whittaker 2009). Moehle (2015) conservatively assumed that the normal and shear stresses along a diagonal crack were resisted only by the reinforcement and that assumption is adopted here because it is impossible to assess the width of the cracks away from the surface of the 12 walls tested as part of this research project.

Accordingly, the term that includes F_s in (6.12) is set equal to zero. Equation (6.12) can be rewritten as:

$$V_{nb} = \rho_l t_w f_{\bar{y}} \left(l_w - \frac{h_w}{\tan\theta} - c \right) \frac{1}{\tan\theta} + p \left(l_w - \frac{h_w}{\tan\theta} - c \right) \frac{1}{\tan\theta} \tag{6.13}$$

or

$$V_{nb} = \left(\rho_l t_w f_{\bar{y}} + p \right) \left(l_w - \frac{h_w}{\tan\theta} - c \right) \frac{1}{\tan\theta} \tag{6.14}$$

Segments A and C contribute to the peak shear resistance of low aspect ratio walls. Consider first Figure 6.10a that presents a free-body diagram of segment A. Actions F_{cy} and F_{cx} are the normal and shear forces acting at the bottom of segment A. The other variables were defined previously. Summing forces in the vertical direction and ignoring the vertical component of aggregate interlock for the reason previously given:

$$F_{cy} = F_v + p \left(\frac{h_w}{\tan\theta} + c \right) \tag{6.15}$$

where F_v is equal to

$$F_v = \rho_l t_w \left(\frac{h_w}{\tan\theta} \right) f_{\bar{y}} \tag{6.16}$$

where $f_{\bar{y}}$ is set equal to the average of measured yield and ultimate strength of the reinforcement for walls SW2 through SW7. The strains in the vertical reinforcement at the boundary of segments A and C of walls SW8, SW9 and SW10 ranged between 0.1 and 1.0 millistrain and so $f_{\bar{y}}$ is set equal to $0.25 f_y$ in (6.16) for these walls. Denoting f_c as the axial stress in the concrete at the bottom of segment A, F_{cy} is:

$$F_{cy} = f_c c t_w \tag{6.17}$$

and using (6.15), (6.16) and (6.17), c can be written as:

$$c = \frac{\left(\rho_l t_w f_{\bar{y}} + p \right) \left(\dfrac{h_w}{\tan\theta} \right)}{f_c t_w + p} \tag{6.18}$$

Shear force F_{cx} can be estimated by multiplying F_{cy} by a coefficient of friction, μ. If V_{na} is the contribution to the shear resistance of segment A:

$$V_{na} = F_{cx} = \mu F_{cy} \tag{6.19}$$

and

$$V_{na} = \mu\left[\left(\rho_l t_w f_{\bar{y}} + p\right)\left(\frac{h_w}{\tan\theta}\right) + pc\right] \tag{6.20}$$

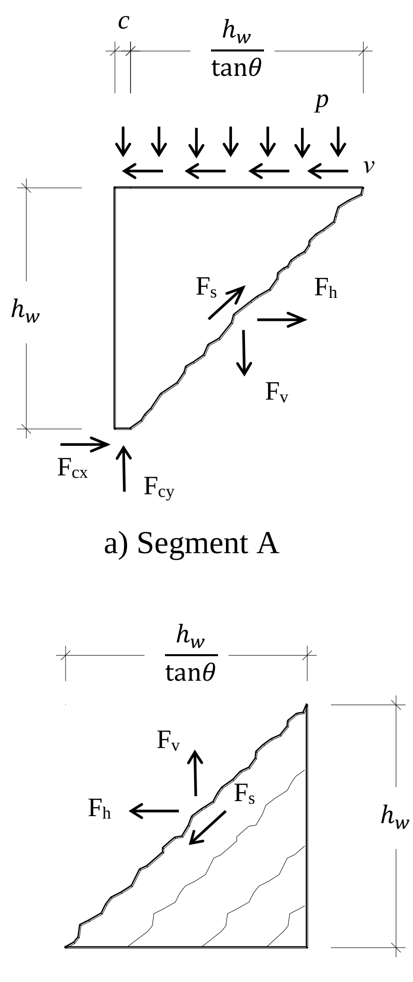

a) Segment A

b) Segment C

Figure 6.10. Free-body diagram of segments A and C of a wall without boundary elements

Consider second Figure 6.10b that presents a free-body diagram of segment C. The sum of forces in the horizontal reinforcement in segment C at peak strength, which is equal to the shear resistance of the segment, V_{nc}, can be estimated using strain gage data from the horizontal reinforcement (see Figure 4.9). A conservative (low) estimate of the strain in the horizontal reinforcement at the boundary of segments B and C (and A and B) is $0.25F_y$. Accordingly, V_{nc} can be estimated as:

$$V_{nc} = \rho_t h_w t_w \left(0.25 f_y\right) \tag{6.21}$$

The total lateral resistance (peak shear strength) of a wall without boundary elements, V_n, is the sum of V_{na}, V_{nb} and V_{nc} and is given by:

$$\begin{aligned} V_n &= \mu\left[\left(\rho_l t_w f_{\bar{y}} + p\right)\left(\frac{h_w}{\tan\theta}\right) + pc\right] + \ldots \\ &\ldots + \left(\rho_l t_w f_{\bar{y}} + p\right)\left(l_w - \frac{h_w}{\tan\theta} - c\right)\frac{1}{\tan\theta} + \ldots \\ &\ldots + 0.25\rho_t h_w t_w f_y \end{aligned} \tag{6.22}$$

Equation (6.22) can be simplified by setting θ equal to 40° (see Table 4.2), which is likely appropriate for walls with aspect ratios between 0.25 and 0.75 and low axial compressive stresses. (Angle θ will decrease with a significant increase in axial compressive stress.)

$$\begin{aligned} V_n &= \mu\left[\left(\rho_l t_w f_{\bar{y}} + p\right)\left(1.2h_w\right) + pc\right] + \ldots \\ &\ldots + 1.2\left(\rho_l t_w f_{\bar{y}} + p\right)\left(l_w - 1.2h_w - c\right) + \ldots \\ &\ldots + 0.25\rho_t h_w t_w f_y \end{aligned} \tag{6.23}$$

To judge the accuracy of this equation for the shear-critical walls SW2 through SW10, p is set to zero and (6.23) can be further simplified to:

$$V_n = 1.2\mu\rho_l t_w h_w f_{\bar{y}} + 1.2\rho_l t_w f_{\bar{y}}\left(l_w - 1.2h_w - c\right) + 0.25\rho_t t_w h_w f_y \tag{6.24}$$

or

$$V_n = 1.2\mu\rho_l A_{cv}\frac{h_w}{l_w} f_{\bar{y}} + 1.2\rho_l A_{cv} f_{\bar{y}}\left(1 - 1.2\frac{h_w}{l_w} - \frac{c}{l_w}\right) + 0.25\rho_t A_{cv}\frac{h_w}{l_w} f_y \tag{6.25}$$

where A_{cv} is the gross cross sectional area of the wall. The variables in (6.25) are vertical and horizontal reinforcement ratios, aspect ratio, gross cross-sectional area of the wall, yield and ultimate strength of the reinforcement, applied normal force and a length of the wall in compression. To estimate the length c, a value of $0.8f_c^{'}$ is assumed: less than the measured uniaxial compressive strength because there was no evidence of spalling of concrete at the compression toes of walls at peak shear strength. The values of c calculated using (6.18) are listed in Table 6.9.

Table 6.9. Distance, c

Wall	c (in)
SW2	10.4
SW3	6.2
SW4	6.4
SW5	12
SW6	9.1
SW7	4.5
SW8	7
SW9	5.7
SW10	5.3

The shear force transfer across the wall-to-foundation interface in segment A will be limited by a) principal tensile strength of concrete, and b) shear friction. To calculate capacity based on a), the concrete is assumed not to be reinforced, to have a tensile strength of $0.15f_c'$, and loaded in uniaxial plane stress: a normal stress corresponding to F_{cy} and a shear stress. If the normal stress is $0.8f_c'$ and the corresponding shear stress is $0.4f_c'$, the corresponding principal stresses are $0.96f_c'$ (compression) and $-0.16f_c'$ (tension): the ratio of shear stress to normal stress is 0.5.

Shear-friction calculations can be informed by the studies of Mattock (1976, 1977), which form the basis of the provisions in ACI 318. Consider first, the test series B of Mattock (1976) (see Tables 2.1 and 2.3 of that report), wherein samples with roughened surfaces and pre-cracked interfaces were tested under monotonically increasing shear force to failure; the reported compressive strength of the concrete was approximately 6000 psi. The interfaces in Mattock's 1976 tests used reinforcement placed perpendicular to the shear plane to generate normal force, which is not the case here: normal force is provided by concrete in compression and not yielded reinforcement. Table 3.1A of Mattock (1976) provides relevant monotonic test data. For normal stress between 226 psi and 1576 psi, the ultimate shear stress ranged between 487 and 1700 psi, with the ratio of shear stress to normal stress of between 2.05 and 1.07, namely, greater than 1.0. Consider second, the test series M of Mattock (1977) (see Tables 2.1 and 2.3 of that report), wherein samples with roughened surfaces and pre-cracked interfaces were tested under both monotonically increasing and reversed cyclic incremented shear force to failure; the reported compressive strength of the concrete in these tests was approximately 6000 psi. The interfaces in Mattock's 1977 tests also used reinforcement placed perpendicular to the shear plane to generate normal force. Table 4.1 of Mattock (1977) reports relevant data; the ratio of the measured cyclic to monotonic shears strengths were 0.88 (M2C to M2M) and 0.92 (M3C to M3M), noting that the incremented cyclic loading was applied over 46 (M2C) and 47 (M3C) cycles: many more cycles than that expected in design basis earthquake shaking and imposed in the tests described in Chapter 4. A substantial reduction in the number of reversed cycles to failure would increase the ratio from the average of 0.90 to close to 1.0 (i.e., the monotonic shear strength).

Accordingly, a coefficient of friction, μ, equal to 0.5 is assumed here for the calculation of V_{na}, which caps the shear stress at $0.4f_c'$ and satisfies both the principal tensile stress-based calculation above and is substantially less that the shear-friction strength supported by Mattock's monotonic and cyclic tests. (Note the maximum value of the normal stress (product of the reinforcement ratio and yield strength) of 1576 psi in the 1976 monotonic tests was equal to approximately $0.25f_c'$ and smaller than the normal stress assumed here of $0.8f_c'$.)

The first, second and third terms in (6.25) correspond to V_{na}, V_{nb} and V_{nc}, respectively. The calculated values of the three terms in (6.25) and the predicted peak shear strength for walls SW2 through SW10 are listed in Table 6.10. A coefficient of friction, μ, equal to 0.5 is assumed: less than the value of 1.0 given in ACI 318-14 for a concrete-to-concrete interface but reasonable given that the toes of the walls had experienced tensile and compressive loadings prior to the cycle to peak strength. The ratio of the predicted peak shear strength to measured peak shear strength (listed in the last column of Table 6.1) of walls SW2 through SW10 range between 0.78 (SW9) and 1.1 (SW5), with an average of 0.94. Excluding the walls that failed in diagonal compression, SW8 and SW9, the average is 0.96. The contributions of the horizontal reinforcement, V_{nc}, to the peak strength of the walls is relatively small, which supports the findings of Section 4.2 and observations by Barda et al. (1977), Gulec and Whittaker (2011) and Moehle (2015).

Table 6.10. Shear strength of walls SW2 through SW10

Wall	V_{na} (kips)	V_{nb} (kips)	V_{nc} (kips)	V_n (kips)	$\frac{V_n}{V_{peak}}$
SW2	234	228	82	544	1.03
SW3	157	173	55	384	0.91
SW4	87	95	29	211	0.95
SW5	166	477	55	698	1.10
SW6	111	335	37	484	0.98
SW7	55	178	18	251	0.84
SW8	78	338	131	547	0.94
SW9	78	351	58	487	0.78
SW10	78	354	29	461	0.9
				Average	0.94

Although the contribution of the horizontal reinforcement to the peak shear strength of a low-rise wall is relatively small, a sufficient amount of horizontal reinforcement is needed to transfer the lateral load from the centerline of loading of the wall to the different segments of the wall and to confine the concrete in the compression struts, where confinement here relates to maintaining the integrity of the compression struts (see Section 23.5 of ACI 318-14). A portion of the lateral load in segment A (see Figure 6.10a) is transmitted to segments B and C by the horizontal reinforcement. Lateral force in segment C is transferred to the foundation via compression struts that form in in segment C: see Figure 6.10b.

It is common practice to assume that walls are uniformly loaded in shear. On the basis of q equal to 40º, segments A (and C) and B should resist 39% (64%) and 61% (36%) of the total lateral force, respectively, for an aspect ratio of 0.33 (0.54), where the percentage assigned to segment A (and C) is given by the ratio of the projected horizontal length of the crack, $h_w/\tan q$, to the length of the wall, l_w. On the basis of the values of V_{na}, V_{nb} and V_{nc} in Table 6.10, segments A and C (B) resist approximately 30% (70%) of the total lateral force for the walls with an aspect ratio of 0.33 (SW5, SW6, and SW7) and approximately 60% (40%) of the walls with an aspect ratio of 0.54 (SW2, SW3, and SW4). (Walls SW8 and SW9 failed in diagonal compression and so are excluded from the this discussion.) This result indicated the loading plates redistribute shear over the length of the wall during the tests, which would suggest that floor diaphragms should be reinforced for this purpose in the field.

The shear resistance of the wall provided by segment B will be limited by the compressive strength of its struts. Consider again the free-body diagram of segment B presented in Figure 6.9. Assuming the force in the horizontal reinforcement on the two sides of a strut are not significantly different, the compressive force at the bottom of a strut, F_c, can be estimated by summing horizontal forces along the horizontal projection of segment B. That is:

$$v_n x = F_c \cos\theta \tag{6.26}$$

If f_c is the compressive stress in a strut, F_c can be expressed as

$$F_c = f_c (x \sin\theta) t_w \tag{6.27}$$

Considering all the struts in segment B of the wall, the lateral force in segment B, V_{nb}, can be expressed in terms of f_c as

$$V_{nb} = f_c \sin\theta \cos\theta t_w \left(l_w - \frac{h_w}{\tan\theta} - c \right) \tag{6.28}$$

Using (6.14) and (6.28), an approximate value of the compressive stress of the struts in segment B, f_c, can be calculated as:

$$f_c \sin\theta \cos\theta t_w \left(l_w - \frac{h_w}{\tan\theta} - c \right) = \left(\rho_l t_w f_{\bar{y}} + p \right) \left(l_w - \frac{h_w}{\tan\theta} - c \right) \frac{1}{\tan\theta} \tag{6.29}$$

Using a value of 40° for θ and simplifying, (6.29) becomes:

$$f_c = 2.4 \left(\rho_l f_{\bar{y}} + \frac{p}{t_w} \right) \tag{6.30}$$

For walls SW2 through SW10, (6.30) can be written as:

$$f_c = 2.4 \rho_l f_{\bar{y}} \tag{6.31}$$

Values of f_c for walls SW2 through SW10 per (6.31) are listed in Table 6.11. The ratios of f_c to $f_c^{'}$ are also listed in Table 6.11. For walls SW2 through SW7, walls with vertical reinforcement ratio of 1% and less, the ratio of f_c to $f_c^{'}$ ranged between 0.16 (SW3 and SW4) and 0.48 (SW5). For walls SW8, SW9 and SW10 (walls with vertical reinforcement ratio of 1.5%), the ratios are 0.69, 0.57 and 0.53, respectively. Walls that are heavily reinforced, assumed here to be a few multiples of the minimum reinforcement ratio specified in ACI 318 (= 0.0025 for Grade 60 rebar), may fail in diagonal compression: excessive axial stress in the diagonal struts that transfer horizontal shearing force to the foundation. Based on the values of the ratio of f_c to $f_c^{'}$ for walls

SW8 and SW9 that failed in diagonal compression, it is reasonable to limit f_c to $0.5 f_c^{'}$. Compression struts also form in segment C. Assuming an axial stress in these struts of $0.5 f_c^{'}$, the diagonal compression strength of the wall can be estimated as:

$$V_n = f_c \sin q \cos q t_w l_w \tag{6.32}$$

For a strut angle of 40 degrees to the horizontal (see Table 4.2), (6.32) corresponds to a horizontal shearing stress of $0.25 f_c^{'}$, which in turn maps to $15.8\sqrt{f_c^{'}}$ for concrete with a uniaxial compressive strength of 4000 psi. Given that the maximum average shear stress at peak strength for SW8 and SW9 ranged between $10\sqrt{f_c^{'}}$ and $11\sqrt{f_c^{'}}$ (see Table 6.1), it is reasonable to retain the ACI 318-14 limit on nominal shear stress of $10\sqrt{f_c^{'}}$.

Table 6.11. Compressive stress on the struts in segment B

Wall	f_c (ksi)	$\frac{f_c}{f_c^{'}}$
SW2	1.82	0.26
SW3	1.22	0.16
SW4	0.67	0.16
SW5	2.05	0.48
SW6	1.37	0.36
SW7	0.67	0.18
SW8	2.43	0.69
SW9	2.43	0.57
SW10	2.43	0.53

The nominal shear strength of a rectangular, low aspect ratio RC wall without boundary elements can be estimated as:

$$\begin{aligned} V_n &= 0.6\frac{h_w}{l_w}\left(\rho_l A_{cv} f_{\bar{y}} + pl_w\right) + 0.5pc + 1.2\left(\rho_l A_{cv} f_{\bar{y}} + pl_w\right)\left(1 - 1.2\frac{h_w}{l_w} - \frac{c}{l_w}\right) + \ldots \\ &\ldots + 0.25\rho_t \frac{h_w}{l_w} A_{cv} f_y \le 10\sqrt{f_c^{'}} A_{cv} \end{aligned} \tag{6.33}$$

or

$$V_n = 1.2\left(\rho_l A_{cv} f_{\bar{y}} + p l_w\right)\left(1 - 0.7\frac{h_w}{l_w} - \frac{c}{l_w}\right) + \ldots$$
$$\ldots + 0.25\rho_t \frac{h_w}{l_w} A_{cv} f_y + 0.5pc \le 10\sqrt{f_c^{'}} A_{cv} \qquad (6.34)$$

where all terms have been defined previously, $q = 40^{\circ}$, and $m = 0.5$. In (6.34), $f_{\bar{y}}$ is set equal to $1.25 f_y$, which requires that the vertical rebar be developed for this stress or greater (perhaps $1.5 f_y$ based on the test data) at the upper ends of the compression struts.

6.7 Peak shear strength of low aspect ratio RC walls with boundary elements

The patterns of cracks in concrete for the walls with boundary elements, SW11 and SW12, are shown in panels k and l of Figure 4.4. The reinforcement in the boundary elements changed the orientation of the diagonal cracks to horizontal at the web-boundary element junctions. The segments of SW11 and SW12 with significantly different strains at peak strength are identified in Section 4.6. Figure 6.11 identifies these segments, the observed patterns of cracks and the forces acting on the wall, where l_{be} is the length of each boundary element (equal to 16 inches for SW11 and SW12), l_{web} is the length of the web of the wall between the two boundary elements, and ρ_{be} is the boundary element reinforcement ratio defined as the area of vertical reinforcement ($A_{s,be}$) in one boundary element divided by the area of that boundary element ($l_{be} \times t_w$), and all other variables were defined previously. Herein, the formulation of (6.22) is extended to accommodate the presence of boundary elements, each of which is assumed to be loaded by an axial force *P*.

The free-body diagram of segment A of the wall with boundary elements is shown in Figure 6.12a. The shearing force at the bottom of segment A, $V_{na,be}$, is calculated similarly to (6.20). The distance *c* is set equal to the length of the boundary element, l_{be}, based on the patterns of cracking observed in the tests of SW11 and SW12. The normal force F_{cy} in (6.20) will increase by an amount equal to the concentrated load on the boundary element, *P*. The strains in the vertical reinforcement in the webs of SW11 and SW12 were mostly between 1 and 6 millistrain (see panels k and l of Figure 4.8) and so the stress in this rebar is assumed to be f_y. The shear force $V_{na,be}$ can be written as:

$$V_{na,be} = \mu\left[\left(\rho_l t_w f_y + p\right)\left(\frac{h_w}{\tan\theta}\right) + pl_{be} + P\right] \tag{6.35}$$

Similar to (6.21), the contribution of the horizontal reinforcement to the lateral resistance of the wall with boundary elements, $V_{nc,be}$, is given by:

$$V_{nc,be} = \rho_t h_w t_w \left(0.25 f_y\right) \tag{6.36}$$

where all variables have been defined previously.

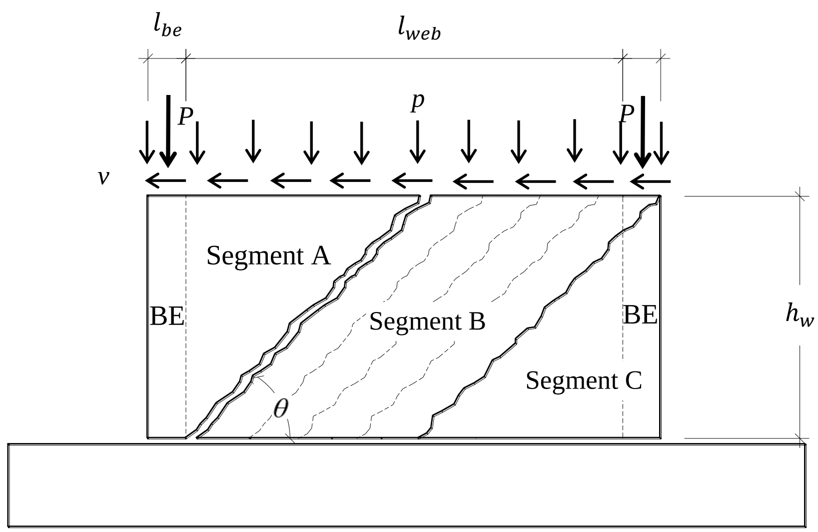

Figure 6.11. Different sections and idealized cracking pattern of a low aspect ratio rectangular RC wall with boundary elements

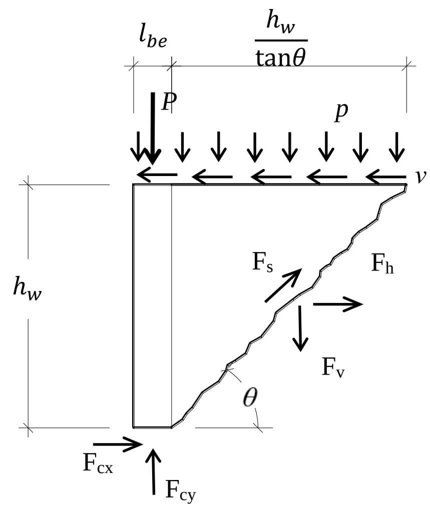

a) Segment A

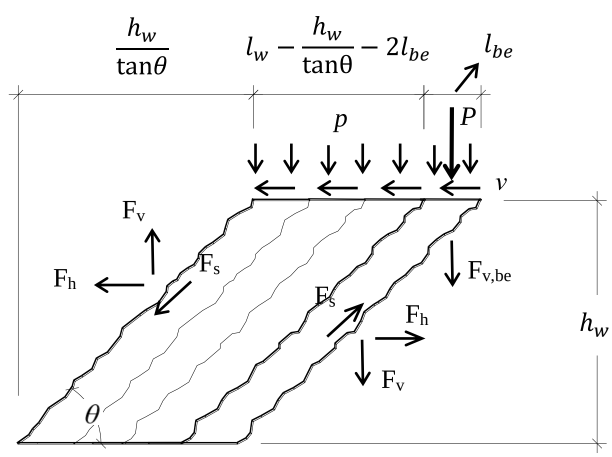

b) Segment B

Figure 6.12. Free-body diagram of segments A and B of a wall with boundary elements

The free body diagram of segment B is presented in Figure 6.12b. Following the formulation for (6.14), the total lateral resistance provided by segment B for the walls with boundary elements, $V_{nb,be}$, is given by:

$$V_{nb,be} = \left(\rho_l t_w f_y + p\right)\left(l_w - \frac{h_w}{\tan\theta} - 2l_{be}\right)\frac{1}{\tan\theta} + \ldots$$
$$\ldots + \left(\rho_{be} t_w f_{\bar{y}} + p\right)\left(l_{be}\right)\frac{1}{\tan\theta} + P\frac{1}{\tan\theta} \tag{6.37}$$

where the axial force on the right boundary element is assigned to segment B, identically to the boundary element vertical reinforcement. The strains in the vertical reinforcement of the boundary elements of SW11 and SW12 ranged between 2 and 20 millistrain (see panels k and l of Figure 4.8) and the stress in this vertical reinforcement is taken as $f_{\bar{y}}$ (i.e., the average of the yield and ultimate strengths) to account for cyclic strain hardening.

The diagonal tension shear strength of a wall with boundary elements, $V_{n,be}$, is the sum of $V_{na,be}$, $V_{nb,be}$ and $V_{nc,be}$:

$$V_{n,be} = \mu\left[\left(\rho_l t_w f_y + p\right)\left(\frac{h_w}{\tan\theta}\right) + pl_{be} + P\right] + \ldots$$
$$\ldots + \left(\rho_l t_w f_y + p\right)\left(l_w - \frac{h_w}{\tan\theta} - 2l_{be}\right)\frac{1}{\tan\theta} + \ldots$$
$$\ldots + \left(\rho_{be} t_w f_{\bar{y}} + p\right)\left(l_{be}\right)\frac{1}{\tan\theta} + P\frac{1}{\tan\theta} + \ldots$$
$$\ldots + \rho_t h_w t_w \left(0.25 f_y\right) \tag{6.38}$$

Setting $q = 40^{\circ}$, $\mu = 0.5$, and simplifying, (6.38) becomes:

$$V_{n,be} = 0.6h_w\left(\rho_l t_w f_y + p\right) + 1.7\left(pl_{be} + P\right)$$
$$\ldots + 1.2\left(\rho_l t_w f_y + p\right)\left(l_w - 1.2h_w - 2l_{be}\right) + \ldots$$
$$\ldots + 1.2\left(\rho_{be} A_{s,be} f_{\bar{y}}\right) + 0.25\rho_t h_w t_w f_y \tag{6.39}$$

For walls SW11 and SW12 for which p and P are zero, (6.39) can be further simplified to:

$$V_{n,be} = 0.6\rho_l t_w h_w f_y + 1.2\rho_l t_w f_y\left(l_w - 1.2h_w - 2l_{be}\right) + \ldots$$
$$\ldots + 1.2\rho_{be} l_{be} t_w f_{\bar{y}} + 0.25\rho_t h_w t_w f_y \tag{6.40}$$

In (6.40), the first term on the right side corresponds to $V_{na,be}$, the sum of the second and third terms correspond to $V_{nb,be}$, and the fourth term corresponds to $V_{nc,be}$. The calculated values of $V_{na,be}$, $V_{nb,be}$ and $V_{nc,be}$ and the predicted peak shear strength for walls SW11 and SW12 are listed in Table 6.12. Similar to the walls without boundary elements, the contribution of the horizontal reinforcement to peak strength, $V_{nc,be}$, is small. The average of the ratios of the predicted peak shear strength to the measured peak shear strength (listed in the last column of Table 6.1) for SW11 and SW12 is 1.01. The strengths of SW11 and SW12 associated with a diagonal compression failure is 679 kips for both, and greater than those associated with a diagonal tension failure.

Table 6.12. Predicted peak shear strength for SW11 and SW12

Wall	$V_{na,be}$ (kips)	$V_{nb,be}$ (kips)	$V_{nc,be}$ (kips)	$V_{n,be}$ (kips)	$\frac{V_{n,be}}{V_{peak}}$
SW11	140	238	58	436	1.05
SW12	69	281	29	379	0.97
				Average	1.01

The nominal shear strength of a rectangular, low aspect ratio RC wall with boundary elements contained within the web of the wall can be estimated by simplifying (6.39) as:

$$\begin{aligned} V_{n,be} &= 1.2\left(\rho_l t_w f_y + p\right)\left(l_w - 0.7h_w - 2l_{be}\right) + 1.7\left(pl_{be} + P\right)\ldots \\ &\ldots + 1.2\rho_{be} A_{s,be} f_{\bar{y}} + 0.25\rho_t h_w t_w f_y \le 10\sqrt{f_c'} A_{cv} \end{aligned} \tag{6.41}$$

or

$$\begin{aligned} V_{n,be} &= 1.2\left(\rho_l A_{cv} f_y + p\right)\left(1 - 0.7\frac{h_w}{l_w} - 2\frac{l_{be}}{l_w}\right) + 1.7\left(pl_{be} + P\right)\ldots \\ &\ldots + 1.2\rho_{be} A_{s,be} f_{\bar{y}} + 0.25\rho_t A_{cv}\frac{h_w}{l_w} f_y \le 10\sqrt{f_c'} A_{cv} \end{aligned} \tag{6.42}$$

where all terms have been defined previously, $q = 40^{\circ}$, and $\mu = 0.5$. In (6.42), $f_{\bar{y}}$ is set equal to $1.25 f_y$, which requires that the vertical rebar be developed for this stress or greater at the upper ends of the boundary elements.

6.8 Loss of stiffness and strength resistance in low aspect ratio walls

The data of Section 4.2 makes it clear that low aspect ratio shear walls that do not include boundary elements rapidly lose strength and stiffness at cycling to displacements greater than that associated with peak strength. Pinching of the hysteresis loops that is clearly evident in all 12 walls (Section 4.2) was exacerbated by the absence of axial compressive force acting on the wall. Lateral strength will be lost from segment C as the tension end of the wall separates from the foundation at significant lateral displacements and the load path from the wall into the foundation, via a concrete-to-concrete interface is lost.

The lateral stiffness of low aspect ratio walls is derived, post cracking, primarily from the axial stiffness of the diagonal compression struts that form regardless of reinforcement ratio. The axial stiffness of the struts degrades under repeated cyclic loading, whereupon the struts that form under push loading are cracked under pull loading (see the cracking patterns in Figures 4.4). Such cracking degrades the strength and stiffness of the individual struts, leading to a loss of strength and stiffness in the wall. Struts in walls constructed with high web reinforcement ratios (much greater than the ACI-318 minimum) and closely spaced rebar are expected to maintain their stiffness and strength at greater drift ratios than those in walls that are lightly reinforced with widely spaced rebar: curtains of closely spaced rebar confine the concrete in the struts and limit crack widths, both of which contribute to improved cyclic behavior of low aspect ratio walls.

Of all the walls tested at the University at Buffalo, the poorest performance could be assigned to SW10, which failed due to diagonal tension associated with yielding of the horizontal reinforcement. The horizontal reinforcement ratio in this wall (=0.33%) was slightly greater than the ACI 318 limit of 0.25%. The post-peak strength deformation in this wall was concentrated in the crack that is clearly evident in Figure 4.5j and Figure 4.6b: strain capacity of the horizontal rebar that crossed the crack effectively limited the displacement capacity of the wall.

Of all the walls tested UB, the best performance could be assigned to those with boundary elements, namely, SW11 and SW12. The boundary elements preserved the integrity of the walls and did not permit the inclined cracks to propagate to the toes of the walls: the cracks turned horizontal at the web-boundary element junctions. The boundary elements enabled shearing forces to be passed through the intact compression toe of the wall, helping maintain the peak shear strength at story drifts much greater than that associated with peak strength.

6.9 Closing thoughts

The data, analysis and theory presented in this chapter could be used to alter design practice for the construction of low aspect ratio walls in buildings and safety-related nuclear structures.

The formulation proposed by Moehle (2015) for the peak shear resistance of low aspect ratio walls represents a significant improvement on equations in codes and standards in the United

States. His equation identifies the importance of a) vertical reinforcement ratio, and b) applied axial compression, on peak shear strength. Herein, Moehle's equation has been extended based on data collected during the testing of SW1 through SW12: data not available to him. This data has allowed some assumptions to be supported and others to be set aside. An updated equation for peak shear strength of walls without and with boundary elements is provided. These equations, with $f_{\bar{y}}$ set equal to f_y, could be implemented in ACI 318 and ACI 349. For this equation to be valid and useful for earthquake-resistant design, the peak strength should be retained at displacements substantially greater than that associated with peak strength for which a) boundary elements may be required, and b) adequate horizontal web reinforcement is provided to confine the diagonal compression struts.

It is not possible to make definitive statements regarding minimum reinforcement requirements in low aspect ratio walls based on 12 tests. However, based on these 12 tests and analysis of data:

1) Low aspect ratio walls should be equipped with special zones of reinforcement, of the type utilized on SW11 and SW12, to maintain the integrity of the wall boundaries and delay loss of strength and stiffness.
2) The use of Type 2 mechanical splices at wall-to-foundation junctions does not compromise the shear strength of low aspect ratio walls.
3) Walls with disparate ratios of vertical and horizontal reinforcement should be discouraged. Equal ratios in the vertical and horizontal directions should be encouraged, with the horizontal ratio being based on the vertical ratio, as calculated using (6.23).
4) The seismic performance of walls with light web reinforcement, of the order of the ACI minimum, will likely be poor in design basis shaking (for buildings) and beyond design basis shaking (for nuclear power plants). A value greater than the current ACI minimum should be used but the additional tests will likely be required to support a code change.

Alternate equations for the peak shear strength of low aspect ratio walls have been derived on the basis of test data and simplified analysis models, including (6.6), (6.34) and (6.42). These equations are more robust than that proposed in Chapter 18 of ACI-318-14 for the seismic design of reinforced concrete shear walls, which may be appropriate for flexure-critical (tall) walls but has no physical basis for shear-critical walls such as those tested as part of this research project.

CHAPTER 7

SUMMARY, CONCLUSIONS AND RECOMMENDATIONS

7.1 Summary

Twelve large-size, rectangular, low aspect ratio, reinforced concrete (RC), shear walls were built and tested at the Network for Earthquake Engineering Simulation (NEES) facility at University at Buffalo (UB). Financial support was provided by the US National Science Foundation (NSF) under Grant No. CMMI-0829978. The general objective of this research was to analyze data from tests of the 12 RC walls to improve the understanding of the seismic behavior of such walls.

A literature review of topics related to the experimental and analytical studies of low aspect ratio RC walls was performed. The experimental research programs conducted by other researchers were summarized. The different failure modes of low aspect ratio RC walls were discussed. Equations for peak shear strength available in literature and building codes, and prior work done on the effective stiffness of low aspect ratio walls were presented.

Detailed descriptions of the experimental program, including pre-test numerical analysis, construction of the tests specimens, material properties, test setup, instrumentation, loading protocol and tests procedures, were provided. The pre-test numerical analysis of the walls was performed using the non-linear finite element program VecTor2 ver. 2.8 (Vecchio and Wong, 2002) to help design and detail the test specimens and fixture. The 12 specimens were named SW1 through SW12. The construction and testing of the 12 specimens was executed in two phases: Phase I (SW1-SW7) and Phase II (SW8-SW12). The Phase I walls were constructed and tested first. The Phase II walls were designed after preliminary analysis of data from the testing of the Phase I walls.

The cyclic performance of the 12 walls was documented comprehensively. Data from the tests of the walls were analyzed to better understand the behavior of low aspect ratio walls during earthquake shaking. Global-force displacement relationships were presented and analyzed. The different cracking patterns and modes of failure of the walls were described. Strains in reinforcement acquired from the strain gages and strain distributions calculated from the Krypton LED sensors were studied and discussed. The contributions of flexure, shear and sliding to the total lateral drift were calculated and reported. Data from the tests have been curated and archived at NEES Project Warehouse (Luna et al., 2013a and 2013b).

The initial stiffness of the 12 wall specimens calculated from test data were compared with those predicted using strength-of-material formulations and recommendations from widely used standards in the United States (e.g., ASCE 43-05 (ASCE, 2005) and ASCE 41-13 (ASCE, 2013)). The effects of cracking, restrained shrinkage and out-of-plane displacement on the initial stiffness of the wall specimens were discussed. Recommendations for the values of shear and flexural rigidities for use in practice were provided.

The peak shear strength of the 12 wall specimens were compared and contrasted with equations in the literature and building codes and standards in the United States. The effects of out-of-plane displacement and twisting on peak shear strength of the walls in the first and third quadrants of loading were discussed. New equations for the peak in-plane shear strength of low aspect ratio rectangular walls, with and without boundary elements, were proposed.

7.2 Conclusions

The key conclusions from the analysis of the performance, lateral stiffness and peak shear strength of the 12 RC shear wall specimens are presented below.

7.2.1 Specimen performance

1. The effect of horizontal reinforcement ratio on the peak shear strength of a shear-critical wall is small above a certain threshold value that is sufficient to maintain the integrity of the diagonal compression struts.
2. Boundary elements help maintain peak shear strength at displacements beyond peak strength.
3. Low aspect ratio walls are prone to base sliding after the peak shear strength is attained. The significant pinching of the hysteresis loops is attributed to sliding.
4. The shear resistance of walls without boundary elements degrades rapidly with repeated cycling at lateral displacements equal to or greater than that associated with peak shear strength.
5. Web reinforcement confines concrete compression struts and its volume and distribution are coupled with diagonal compression failure. For those walls that failed in diagonal

compression, the walls with lower web reinforcement ratios achieved lower peak average shear stress than walls with higher reinforcement ratios.

6. Type-2 mechanical couplers (defined in ACI 318-14 (ACI, 2014)) on vertical reinforcement appear to have no significant effect on the cyclic response of low aspect ratio walls.
7. The average angle of the diagonal cracks in the web of the walls with respect to the horizontal are 46º, 41º and 42º for walls with aspect ratios of 0.94, 0.54 and 0.33, respectively.

7.2.2 Lateral stiffness

1. There is a large discrepancy between the initial stiffness measured in the tests and the initial stiffness calculated using ASCE 43-05 for *uncracked* wall sections. The secant stiffness at peak shear strength was significantly smaller than the effective stiffness recommended by ASCE 43-05 and ASCE 41-13 for *cracked* wall sections. The discrepancy is attributed to restrained shrinkage at the base of the tested walls.
2. Restrained shrinkage can be mimicked in LS-DYNA by imposing a thermal loading over a height of the wall near the point of restraint (the foundation block in this instance). The numerical studies showed that restrained shrinkage of the magnitude reported by prior researchers has a significant effect on the lateral stiffness of low aspect ratio shear walls, with reductions of more than a factor of 2 from theoretical values.
3. Restrained shrinkage of the magnitude considered here has no meaningful effect on peak shear strength and post-peak-strength response.
4. Finite element analysis confirmed the effect of axial compressive load on the lateral behavior of low aspect ratio shear walls: initial stiffness, peak strength and post-peak response. Axial compressive load increases initial stiffness and peak strength, and offsets the effect of restrained shrinkage on initial stiffness.
5. Reasonable estimates of the initial stiffness of the 12 walls were obtained using effective flexural and shear stiffness equal to $0.5E_cI_g$ and $0.35G_cA_g$, respectively, for drifts less than 0.1% and lateral forces less than 40% of peak strength. These reductions from the *uncracked* values are reasonable if the axial compressive loads are small. The lateral

stiffness will decrease from these *cracked* values as the imposed lateral loads and deformations are increased.

7.3 Peak shear strength

1. There is a significant scatter in the shear strength of the twelve walls predicted using equations from chapters 11 and 18 of ACI 318-14, Barda et al. (1977) and Wood (1990): confirming the prior observation of Gulec et al. (2008).
2. In the absence of out-of-plane displacement and twisting, the peak shear strength of a wall in the first and third quadrants of loading are expected to be similar. Large out-of-plane displacements and twisting result in significant differences in first and third quadrant peak strengths.
3. New equations for the in-plane peak shear strength of rectangular, low aspect ratio walls, with and without boundary elements, have been proposed for use in design practice. These equations are based on internal force-resisting mechanisms derived from strain and deformation measurements and observations of cracking patterns made during testing.
4. The peak shear strength of a low aspect ratio wall is a function of the vertical reinforcement ratio, aspect ratio and applied axial force. The horizontal reinforcement ratio plays a secondary role in peak shear strength, supporting the findings in Chapter 4 and those of Barda et al. (1977), Gulec and Whittaker (2011) and Moehle (2015).

7.4 Recommendations for detailing of low aspect ratio walls

Recommendations for the seismic detailing of low aspect ratio walls are provided below.

1. Low aspect ratio walls should be equipped with special zones of transverse reinforcement, of the type utilized on SW11 and SW12. Although the 90º hooks on the horizontal web reinforcement were maintained (i.e., did not straighten) at large lateral displacements, the presence of the boundary-element transverse reinforcement changed the orientation of the cracking at the toes of the walls, maintained the integrity of the wall boundaries and delayed the loss of lateral strength and stiffness.
2. Walls with disparate ratios of vertical and horizontal reinforcement should be discouraged. Equal ratios in the vertical and horizontal directions are encouraged, with the horizontal

ratio being based on the vertical ratio, as calculated using the new equations for peak shear strength.

3. The seismic performance of walls with light web reinforcement, of the order of the ACI minimum, will likely be poor in design basis shaking (for buildings) and beyond design basis shaking (for nuclear power plants). A value greater than the current ACI minimum should be used but the additional tests will likely be required to support a code change.

CHAPTER 8

REFERENCES

American Concrete Institute (ACI). (1992). "Prediction of creep, shrinkage, and temperature effects in concrete structures (ACI 209R-92)." Farmington Hills, MI.

American Concrete Institute (ACI). (2005). "Acceptance criteria for moment frames based on structural testing (ACI 374.1-05) and commentary." Farmington Hills, MI.

American Concrete Institute (ACI). (2013). "Guide for testing reinforced concrete structural elements under slowly applied simulated seismic loads (ACI 374.2R-13)." Farmington Hills, MI.

American Concrete Institute (ACI). (2014). "Building code requirements for structural concrete (ACI 318-14) and commentary." Farmington Hills, MI.

American Society for Testing and Materials (ASTM). (2005). "Standard test method for compressive strength of cylindrical concrete specimens (ASTM C39/C39M-05)." West Conshohocken, PA.

American Society for Testing and Materials (ASTM). (2008). "Standard practice for making and curing concrete test specimens in the field (ASTM C31/C31M-08)." West Conshohocken, PA.

American Society for Testing and Materials (ASTM). (2010). "Standard test method for obtaining and testing drilled cores and sawed beams of concrete (ASTM C42/C42M-10)." West Conshohocken, PA.

American Society for Testing and Materials (ASTM). (2013). "Standard specification for high-strength low-alloy columbium-vanadium structural steel (ASTM A572/A572M-13)." West Conshohocken, PA.

American Society for Testing and Materials (ASTM). (2014). "Standard specification for deformed and plain carbon-steel bars for concrete reinforcement (ASTM A615/A615M-14)." West Conshohocken, PA.

American Society for Testing and Materials (ASTM). (2014). "Standard specification for deformed and plain low-alloy steel bars for concrete reinforcement (ASTM A706/A706M-14)." West Conshohocken, PA.

American Society of Civil Engineers (ASCE). (2005). "Seismic design criteria for structures, systems, and components in nuclear facilities (ASCE/SEI 43-05)." Reston, VA.

American Society of Civil Engineers (ASCE). (2013). "Seismic rehabilitation of buildings (ASCE/SEI 41-13)." ASCE, Reston, VA.

Applied Technology Council (ATC). (1992). "Guidelines for cyclic seismic testing of component of steel structures (ATC-24)." Redwood City, CA.

Athanasopoulou, A. (2010). "Shear strength and drift capacity of reinforced concrete and high-performance fiber reinforced concrete low-rise walls subjected to displacement reversals." PhD Dissertation, University of Michigan, Ann Arbor, MI.

Barda, F., Hanson, J. M., and Corley, W. G. (1977). "Shear strength of low-rise walls with boundary elements." *Reinforced Concrete Structures in Seismic Zones, ACI*, (SP-53), 149-202.

Birely, A. C. (2012). "Seismic performance of slender reinforced concrete structural walls." PhD Dissertation, University of Washington, Seattle, WA.

Broadhouse, B. J. (1986). *DRASTIC: A computer code for dynamic analysis of stress transients in reinforced concrete*, UKAEA Atomic Energy Establishment.

Broadhouse, B. J. (1995). "The Winfrith concrete model in LS-DYNA3D." Report: SPD/D (95) - 363.

Carino, N., and Clifton, J. R. (1995). "Prediction of cracking in reinforced concrete structures." *NISTIR 5634*, National Institute of Standards and Technology, Gaithersburg, MD.

Cowper, G. R. (1966). "The shear coefficient in Timoshenko's beam theory." *Journal of Applied Mechanics*, 33(2), 335-340.

Dassault Systemes Simulia Corp. (2010). ABAQUS/CAE version 6.10-EF. Providence, RI.

Del Carpio Ramos, M., Whittaker, A. S., and Gulec, C. K. (2012). "An evaluation of predictive equations for the peak shear strength of low-aspect ratio reinforced concrete walls." *Journal of Earthquake Engineering*, 16(2), 159-187.

El-Sokkary, H., and Galal, K. (2013). "Seismic behavior of RC shear walls strengthened with fiber-reinforced polymer." *Journal of Composites for Construction*, 17(5), 603-613.

Epackachi, S. (2014). "Experimental, numerical and analytical studies on the seismic response of steelplate concrete (SC) composite shear walls." PhD Dissertation, University at Buffalo, Buffalo, NY.

Epackachi, S., Luna, B. N., and Whittaker, A. S. (2015). "Numerical investigation of the in-plane behavior of low aspect ratio reinforced concrete shear walls." *Proc., 23rd International Conference on Structural Mechanics in Reactor Technology (SMiRT 23)*, Manchester, UK.

Farrar, C. R., and Baker, W. E. (1993). "Experimental assessment of low-aspect-ratio, reinforced concrete shear wall stiffness." *Earthquake Engineering and Structural Dynamics*, 22, 373-387.

Farrar, C. R., Baker, W. E., and Dove, R. C. (1991). "Static and simulated seismic testing of the TRG-7 through -16 shear wall structures." *NUREG/CR-5660*, US Nuclear Regulatory Commission, Washington, DC.

Farrar, C. R., Bennett, J. G., Dunwoody, W. E., and Baker, W. E. (1990). "The seismic category I structures program results for FY 1987." *NUREG/CR-5369*, US Nuclear Regulatory Commission, Washington, DC.

Farvashany, F. E., Foster, S. J., and Rangan, B. V. (2008). "Strength and deformation of high-strength concrete shearwalls." *ACI Structural Journal*, 105(1), 21-29.

GigaPan Systems. (2013). http://www.gigapansystems.com/. Accessed August 1, 2013.

Gilbert, R. I. (1992). "Shrinkage cracking in fully restrained concrete members." *ACI Structural Journal*, 89(2), 141-149.

Gulec, C. K., and Whittaker, A. S. (2009). "Performance-based assessment and design of squat reinforced concrete shear walls." *Technical Report MCEER-09-0010*, University at Buffalo, Buffalo, NY.

Gulec, C. K., and Whittaker, A. S. (2011). "Empirical equations for peak shear strength of low aspect ratio reinforced concrete walls." *ACI Structural Journal*, 108(1), 80-89.

Gulec, C. K., Whittaker, A. S., and Hooper, J. D. (2010). "Fragility functions for low aspect ratio reinforced concrete walls." *Engineering Structures*, 32, 2894-2901.

Gulec, C. K., Whittaker, A. S., and Stojadinovic, B. (2008). "Shear strength of squat rectangular reinforced concrete walls." *ACI Structural Journal*, 105(4), 488-497.

Hibbitt, Karlsson & Sorensen, Inc. (2004). ABAQUS/CAE version 6.5.1. Pawtucket, RI.

Inada, Y. (1986). "Relationship between force and displacement in RC structures for nuclear reactors (in Japanese)." PhD Dissertation, University of Tokyo, Tokyo, Japan.

Kuang, J. S., and Ho, Y. B. (2008). "Seismic behavior and ductility of squat reinforced concrete shear walls with nonseismic detailing." *ACI Structural Journal*, 105(2), 225-231.

Lee, K. H., Goel, S. C., and Stojadinovic, B. (2000). "Boundary effects in steel moment connections." *Proc., 12th World Conference on Earthquake Engineering*, Auckland, New Zealand.

Livermore Software Technology Corp. (LSTC). (2012). "Keyword user's manual, Volume I." LS-DYNA Version 971 R6.0.0, Livermore, CA.

Livermore Software Technology Corp. (LSTC). (2012). "Keyword user's manual, Volume II." LS-DYNA Version 971 R6.0.0, Livermore, CA.

Luna, B. N., Rivera, J. P., Rocks, J. F., Goksu, C., Weinreber, S., and Whittaker, A. S. (2013). "University at Buffalo - low aspect ratio rectangular reinforced concrete shear wall (phase

I) - specimens SW1, SW2, SW3, SW4, SW5, SW6, SW7," Network for Earthquake Engineering Simulation (distributor), Dataset, DOIs:10.4231/D3542J820, 10.4231/D38W3825B, 10.4231/D32B8VB8X, 10.4231/D3639K516, 10.4231/D3RX93D28, 10.4231/D3WP9T661, 10.4231/D31G0HV0P.

Luna, B. N., Rivera, J. P., Rocks, J. F., Goksu, C., Weinreber, S., and Whittaker, A. S. (2013). "University at Buffalo - low aspect ratio rectangular reinforced concrete shear wall (phase II) - specimens SW8, SW9, SW10, SW11, SW12," Network for Earthquake Engineering Simulation (distributor), Dataset, DOIs:10.4231/D3XP6V35S, 10.4231/D3SX6492H, 10.4231/D3P55DG82, 10.4231/D3JD4PP4X, 10.4231/D3DN3ZW0S.

Maier, J., and Thürlimann, B. (1985). "Bruchversuche an stahlbetonscheiben."Institut für Baustatik und Konstruktion, Eidgenössische Technische Hochschule (ETH) Zürich, Zürich, Switzerland, 130 pp.

MathWorks, Inc. (2006). MATLAB R2006b. Natick, MA.

MathWorks, Inc. (2012). MATLAB R2012b. Natick, MA.

Mattock, A. H. (1976). "Shear transfer under monotonic loading, across an interface between concretes cast at different times, final report, part 1." *Report No. SM 76-3*, University of Washington, Seattle, Washington.

Mattock, A. H. (1977). "Shear transfer under monotonic loading, across an interface between concretes cast at different times, final report, part 2." *Report No. SM 77-1*, University of Washington, Seattle, Washington.

Moehle, J. (2015). *Seismic design of reinforced concrete buildings*, McGraw-Hill Education, New York.

Murray, R. C., Basak, A. K., Bennett, J. G., Farrar, C. R., Gupta, A. K., Hadjian, A. H., Hashimoto, P. S., Hossain, Q. A., Kenneally, R. M., Kennedy, R. P., Nuta, D. A., Oleck Jr., R. F., Singh, A. K., Tang, H. T., and Tsai, N. C. (1994). *Stiffness of low rise reinforced concrete shear walls*, American Society of Civil Engineers, New York, NY.

Nikon Metrology, Inc. (2013). "Krypton K600 optical measurement system." http://www.nikonmetrology.com/. Accessed August 1, 2013.

Orakcal, K., Massone, L. M., and Wallace, J. W. (2009). "Shear strength of lightly reinforced wall piers and spandrels." *ACI Structural Journal*, 106(4).

Ottosen, N. S. (1977). "A failure criterion for concrete." *Journal of the Engineering Mechanics Division*, 103(4), 527-535.

Palermo, D., and Vecchio, F. J. (2002). "Behavior and analysis of reinforced concrete walls subjected to reversed cyclic loading." *Publication No. 2002-01*, Department of Civil Engineering, University of Toronto, Canada.

Park, H. G., Lee, J. H., Shin, H. M., and Baek, J. W. (2014). "Shear strength of low-rise RC walls with grade 550 MPa bars." *International Proceedings of Chemical, Biological and Environmental Engineering*, 62(1), 34-39. (in Korean).

Parulekar, Y. M., Reddy, G. R., Vaze, K. K., Pegon, P., and Wenzel, H. (2014). "Simulation of reinforced concrete short shear wall subjected to cyclic loading." *Nuclear Engineering and Design*, 270, 344-350.

Paulay, T., and Priestley, M. J. (1992). *Seismic design of reinforced concrete and masonry buildings*, John Wiley & Sons, Inc.

Popovics, S. (1973). "A numerical approach to the complete stress-strain curve of concrete." *Cement and Concrete Research*, 3(5), 583-599.

Raoufi, K. (2011). "Restrained shrinkage cracking of concrete: the influence of damage localization." PhD Dissertation, Purdue University, West Lafayette, IN.

Renton, J. D. (1991). "Generalized beam theory applied to shear stiffness." *International Journal of Solids and Structures*, 27(15), 1955-1967.

Rivera, J. (2018). "Seismic damage assessment of low aspect ratio reinforced concrete shear walls." PhD Dissertation, University at Buffalo, Buffalo, NY.

Rivera, J., Luna, B. N. and Whittaker, A. S. (2018). "Seismic damage assessment of low aspect ratio reinforced concrete shear walls." *Technical Report MCEER*, University at Buffalo, Buffalo, NY.

Rothe, D. (1992). "Untersuchungen zum nichtlinearen verhalten von stahlbeton wandschieben unter erdbebenbeanspruchung." PhD Dissertation, der Technischen Hochschule Darmstadt, Darmstadt, Germany.

Sika Corporation U.S. (2013). "SikaTop 123 Plus." http://usa.sika.com/. Accessed August 1, 2013.

Sozen, M. A., and Moehle, J. P. (1993). "Stiffness of reinforced concrete walls resisting in-plane shear." *Report No. EPRI TR-102731*, Electrical Power Research Institute, Palo Alto, CA.

Thomson, E. D., Perdomo, M. E., Picón, R., Marante, M. E., and Flórez-López, J. (2009). "Simplified model for damage in squat RC shear walls." *Engineering Structures*, 31(10), 2215-2223.

Timoshenko, S. (1940). *Strength of materials, Part I*, D. Van Nostrand Company, Inc., New York, NY.

Tokyo Sokki Kenkyujo Co., Ltd. (2013). "YFLA-5-5L strain gage." http://www.tml.jp/e/. Accessed August 1, 2013.

USG Corporation. (2014). "Hydro-Stone gypsum cement." http://www.usg.com/. Accessed May 1, 2014.

Vecchio, F. J., and Collins, M. P. (1986). "The modified compression field theory for reinforced concrete elements subjected to shear." *ACI Journal*, 83(2), 219-231.

Vecchio, F. J., and Wong, P. S. (2002). "VecTor2 and FormWorks user's manual." University of Toronto, Toronto, Canada.

Whyte, C. A., and Stojadinovic, B. (2013). "Hybrid simulation of the seismic response of squat reinforced concrete shear walls." *PEER Report 2013/02*, Pacific Earthquake Engineering Research Center, University of California, Berkeley, CA.

Wood, S. L. (1990). "Shear strength of low-rise reinforced concrete walls." *ACI Structural Journal*, 87(1), 99-107.

TRC Companies, Inc. (2010). XTRACT version 3.0.8. Lowell, MA.

APPENDIX A

SPECIMEN CONSTRUCTION DRAWINGS AND LOADING APPARATUS

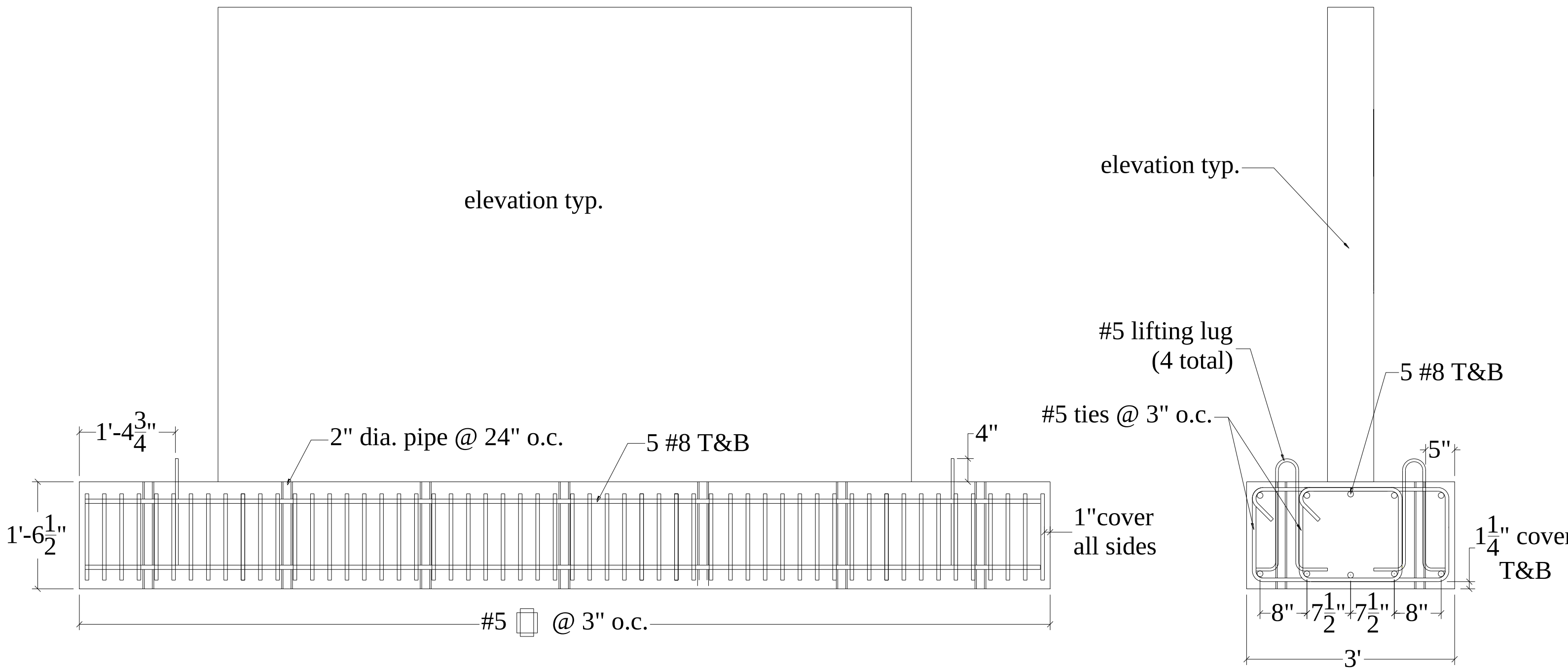

Figure A.1. Typical foundation drawings (Phase I Specimens)

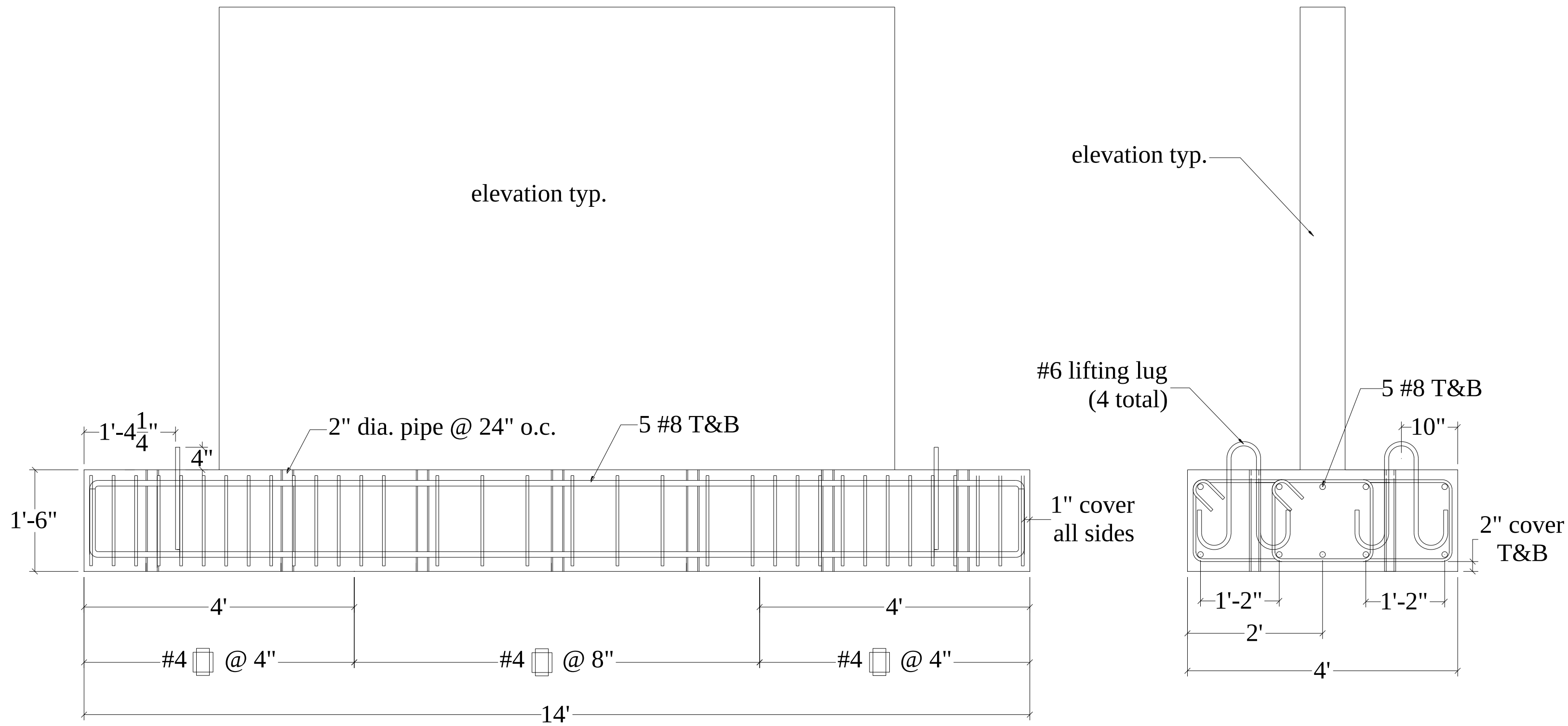

Figure A2. Typical foundation drawings (Phase II specimens)

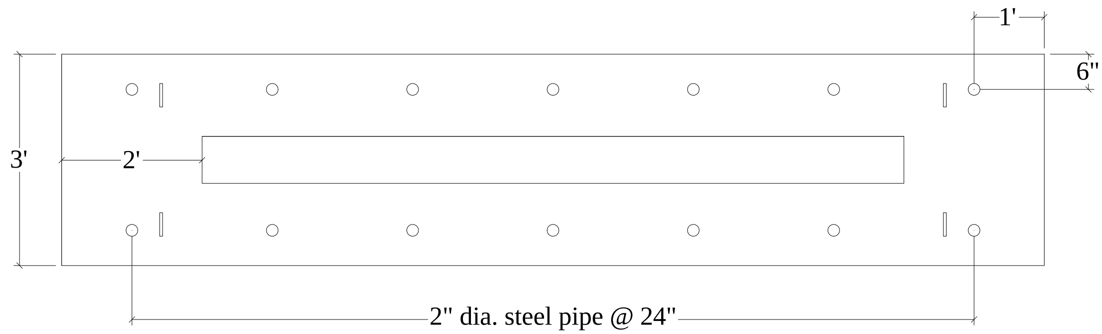

Figure A.3. Typical foundation thru-hole layout for the installation of Dywidag bars (Phase I specimens)

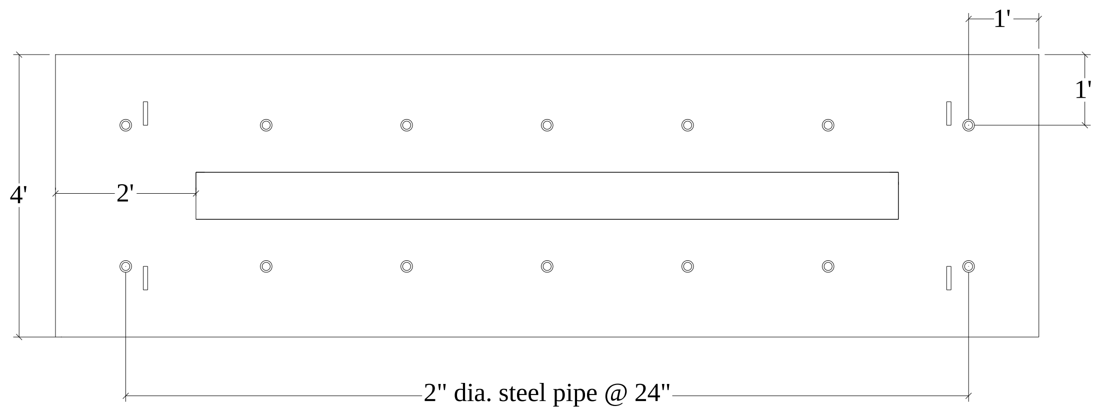

Figure A.4. Typical foundation thru-hole layout for the installation of Dywidag bars (Phase II specimens)

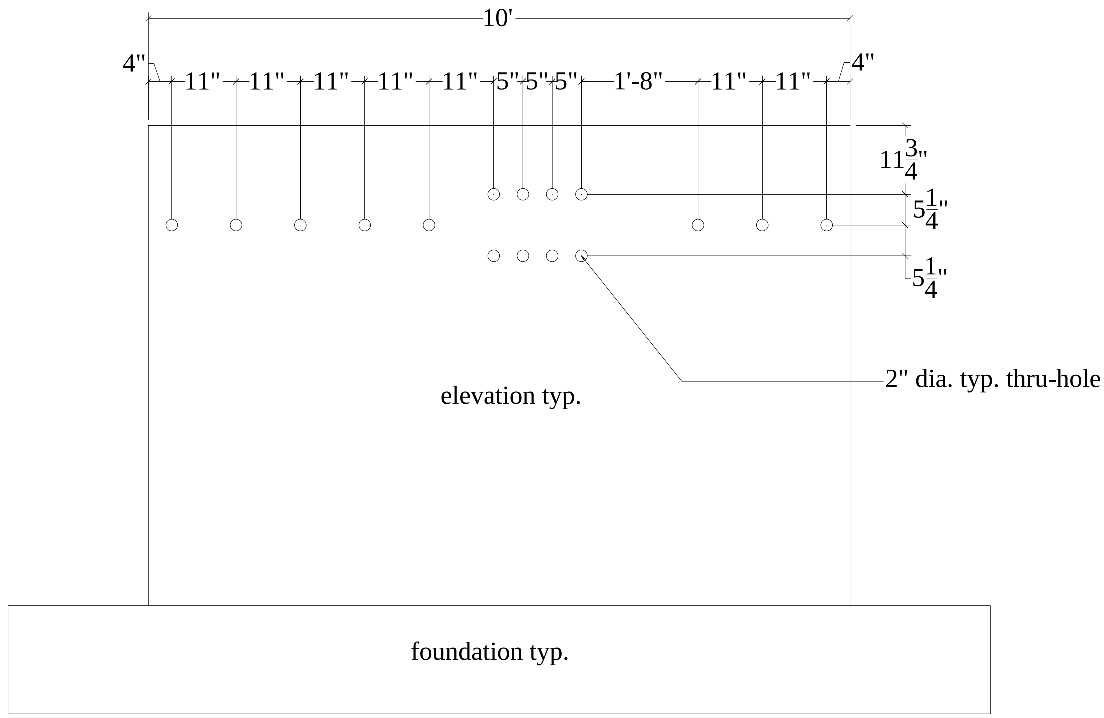

Figure A.5. Typical thru-hole layout for the installation of loading apparatus

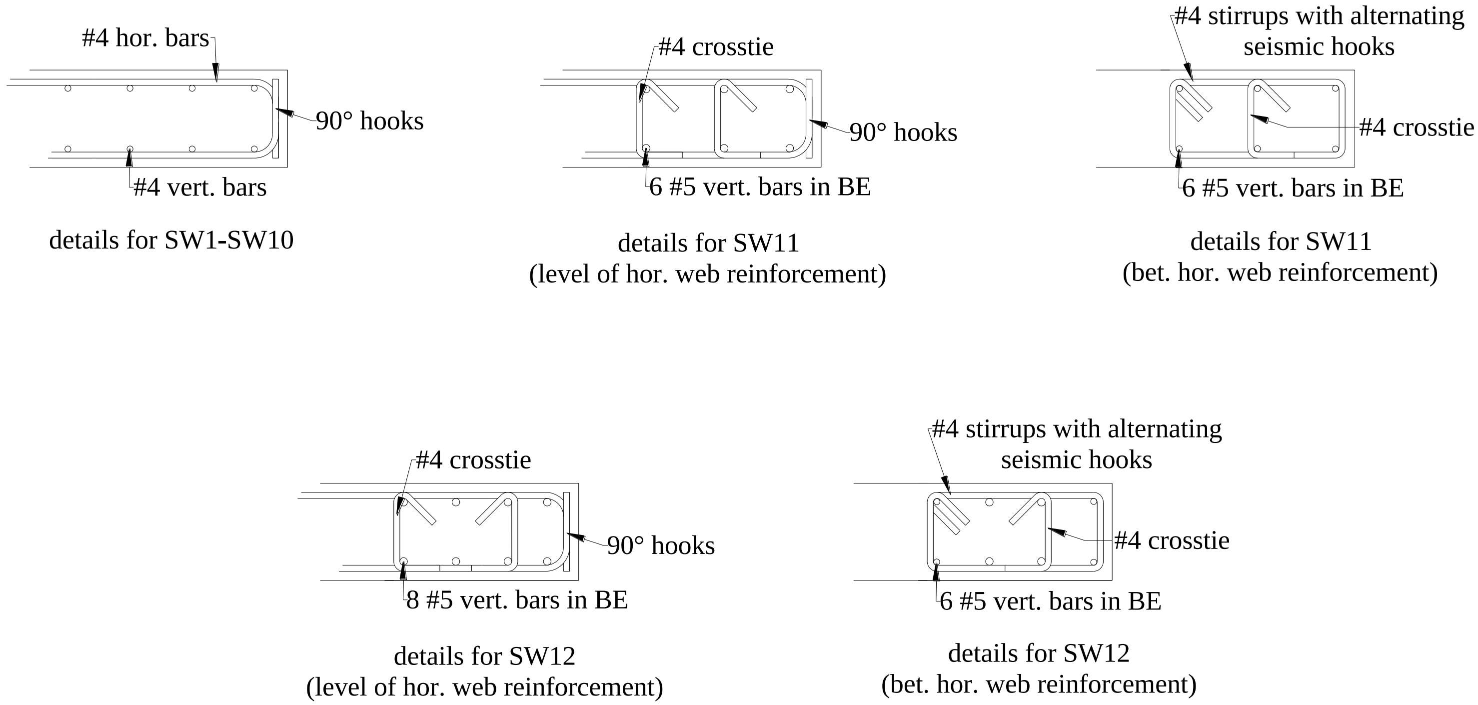

Figure A.6. Wall boundary details

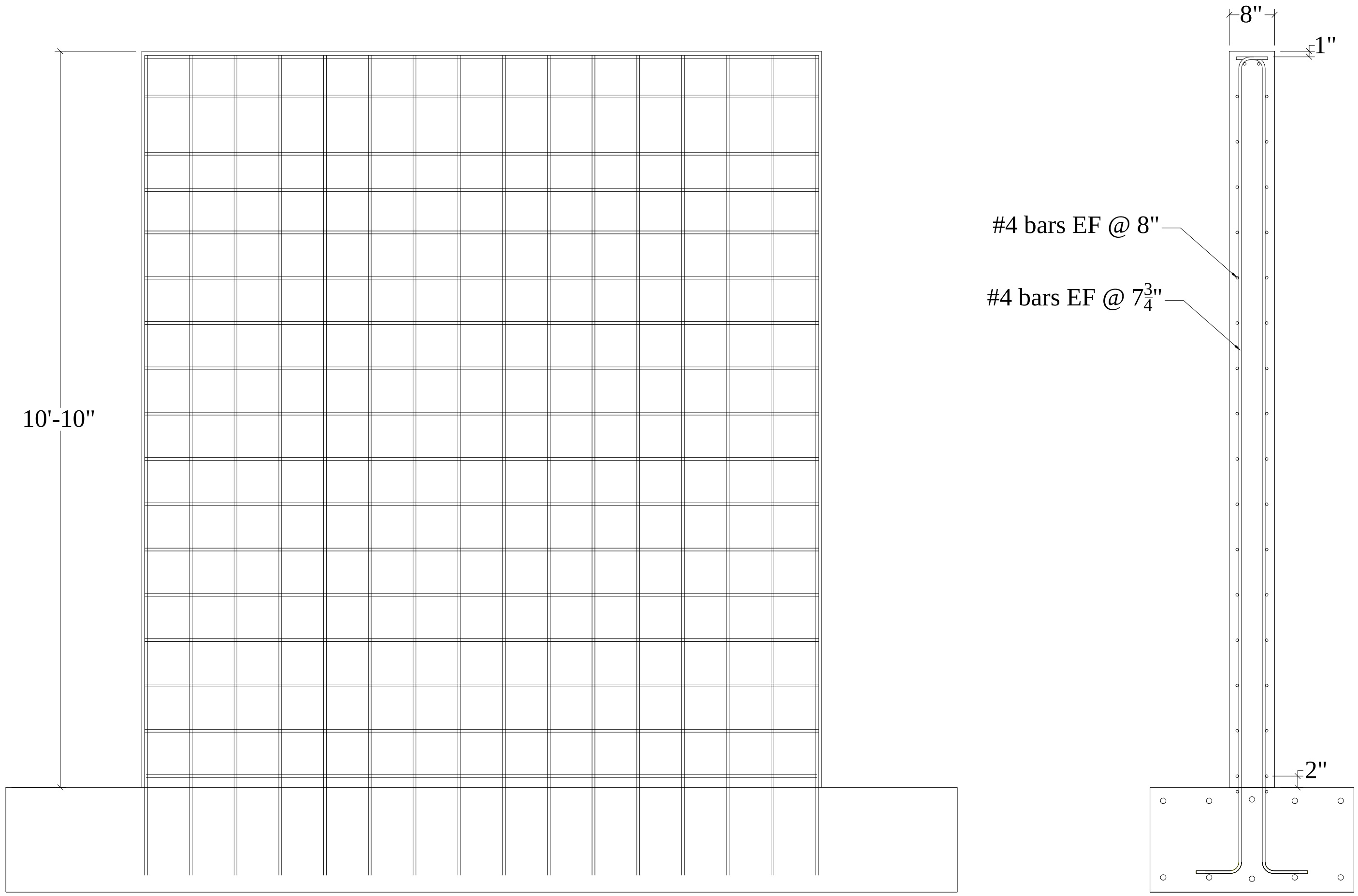

Figure A.7. Reinforcement details for SW1

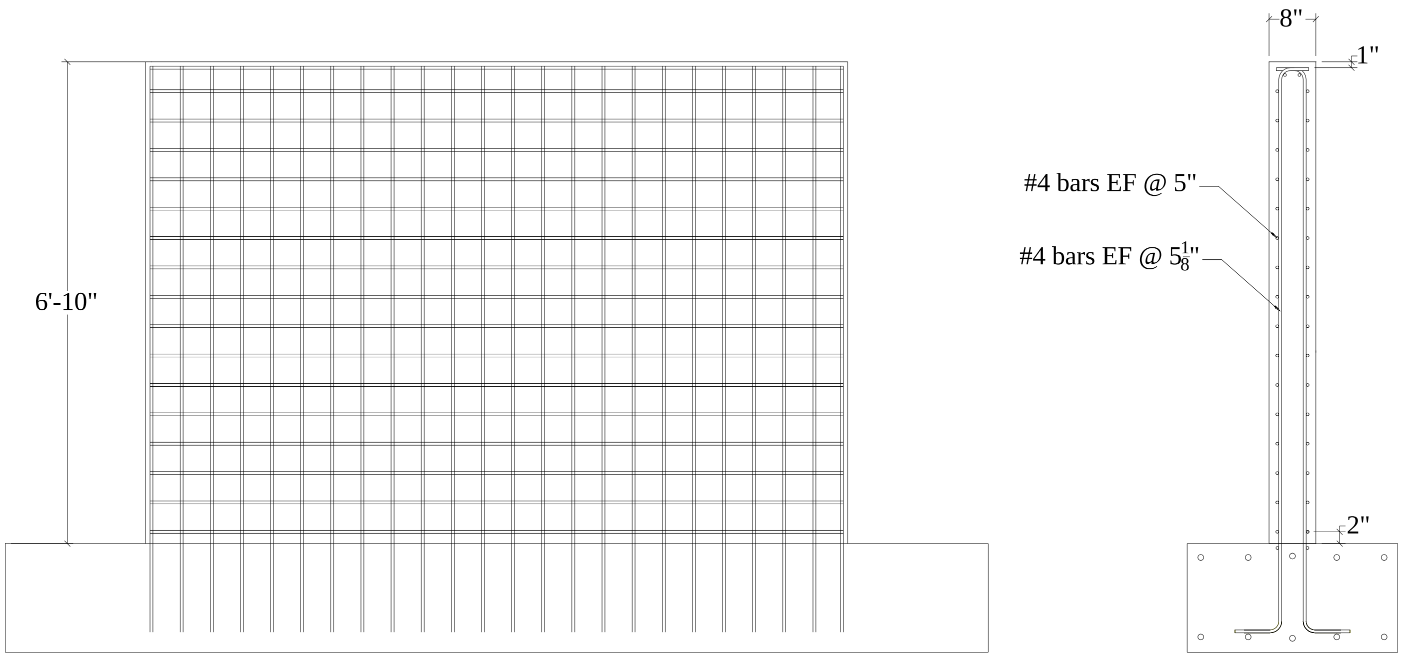

Figure A.8. Reinforcement details for SW2

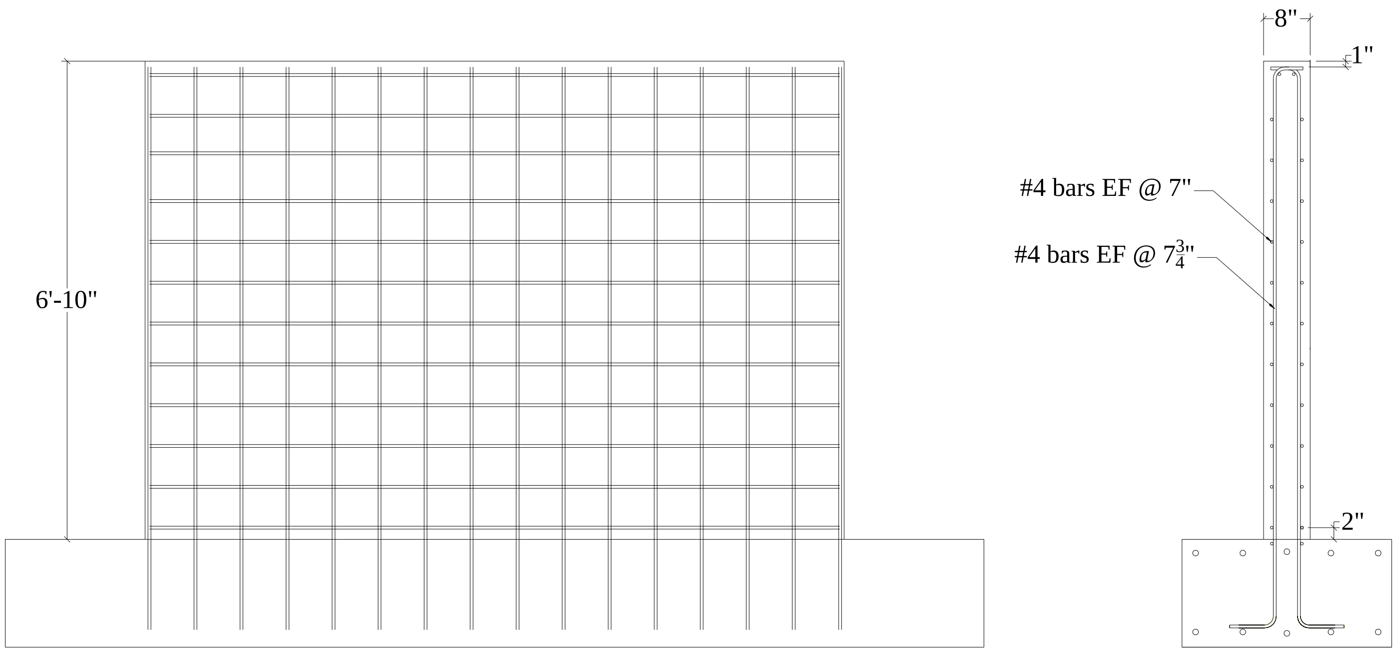

Figure A.9. Reinforcement details for SW3

Figure A.10. Reinforcement details for SW4

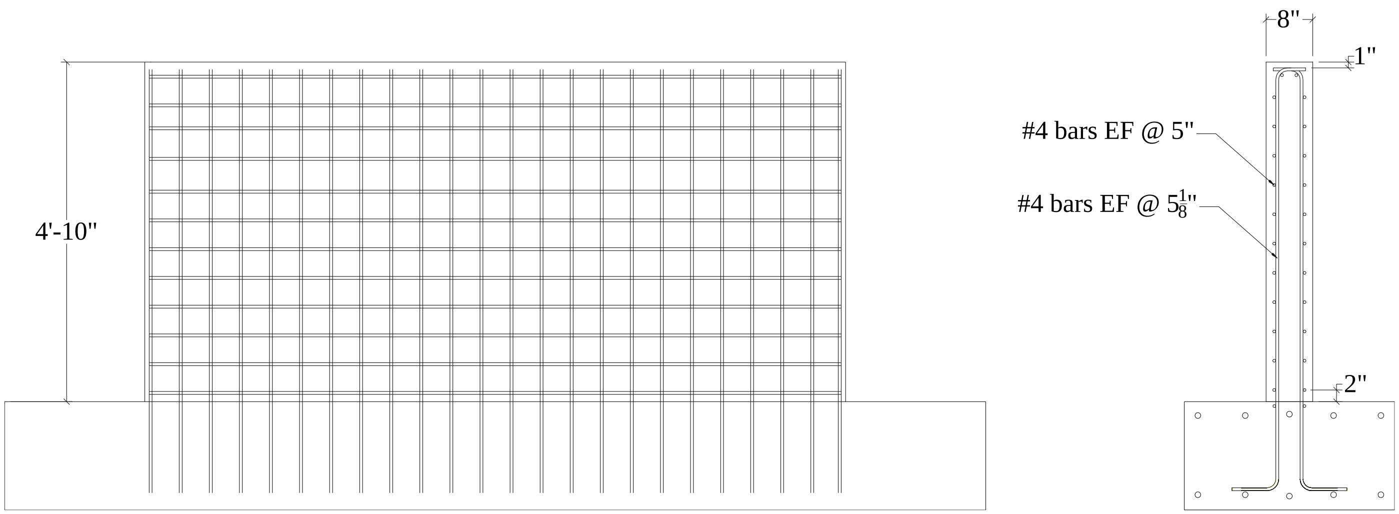

Figure A.11. Reinforcement details for SW5

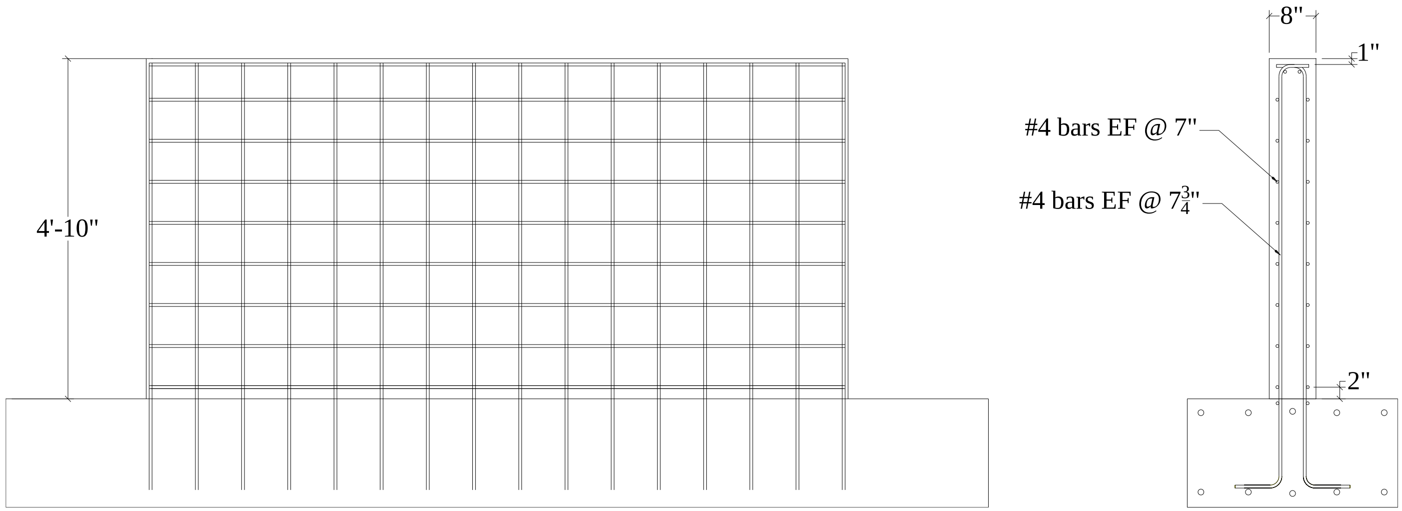

Figure A.12. Reinforcement details for SW6

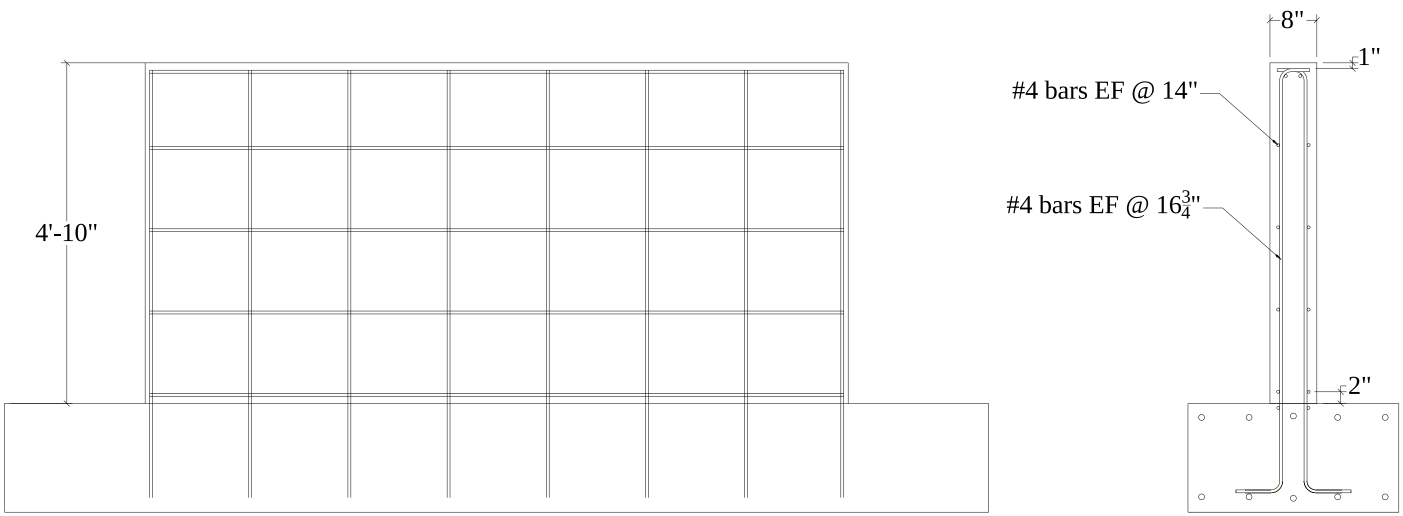

Figure A.13. Reinforcement details for SW7

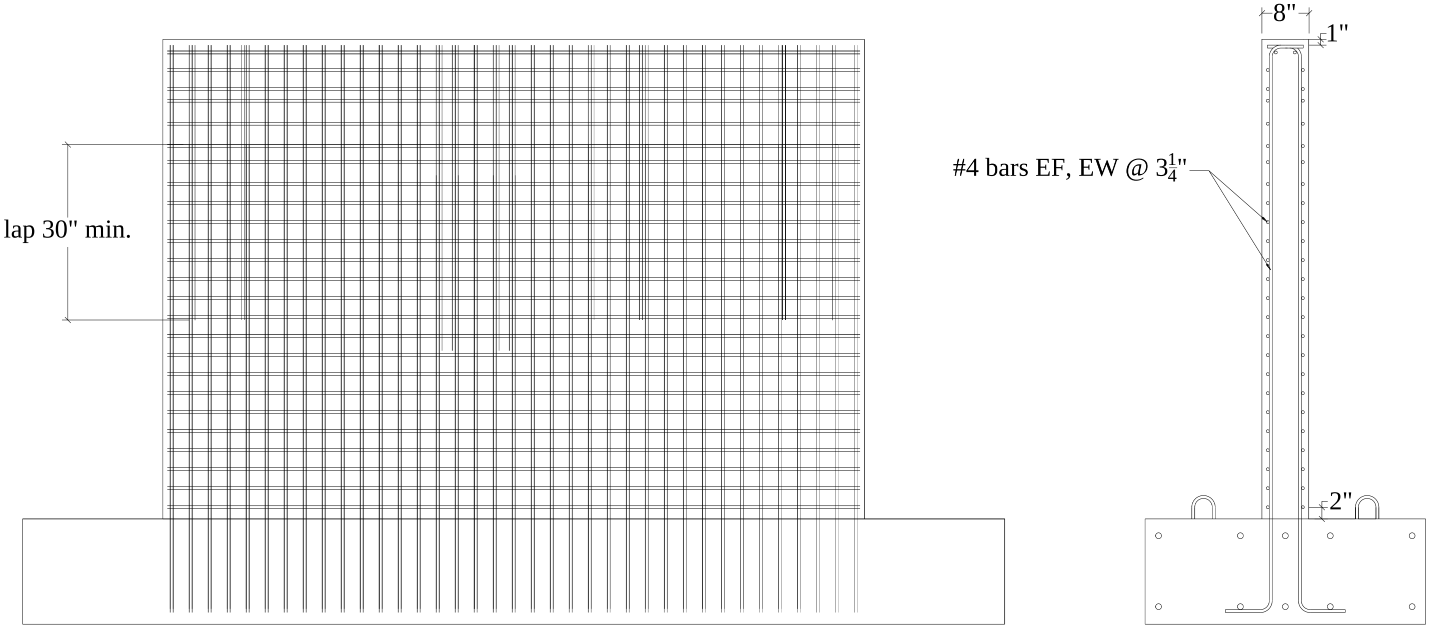

Figure A.14. Reinforcement details for SW8

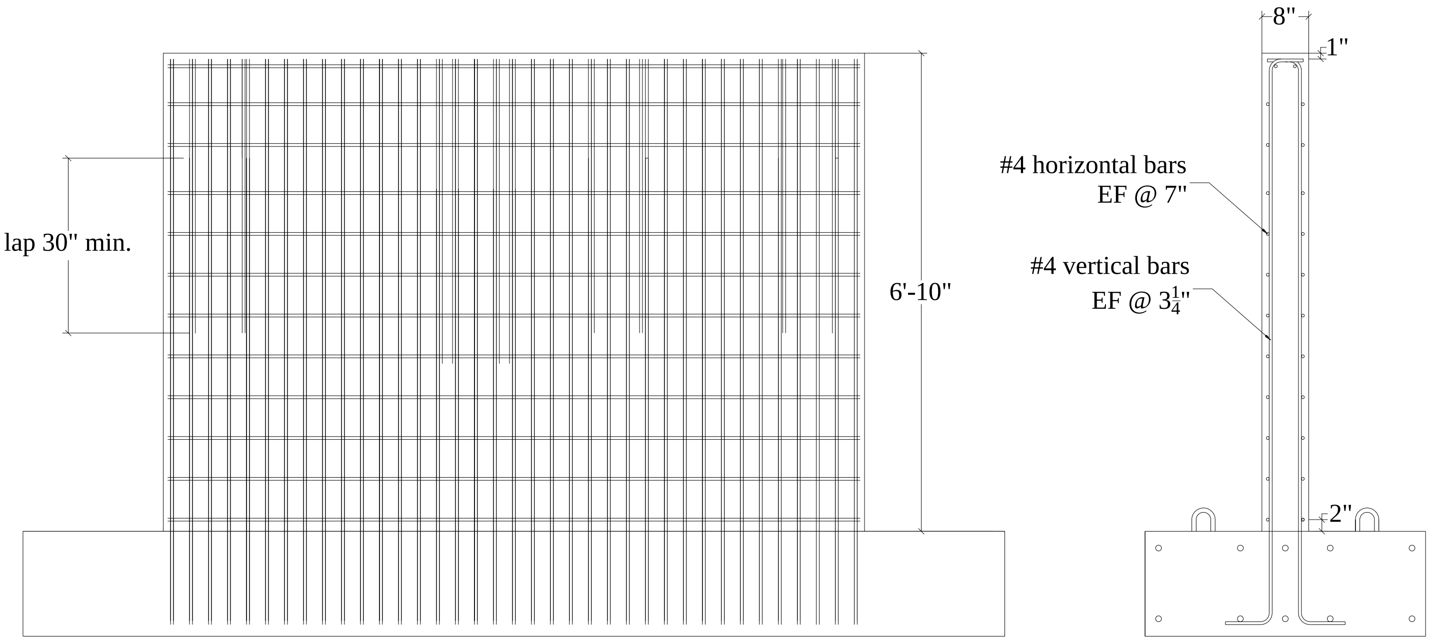

Figure A.15. Reinforcement details for SW9

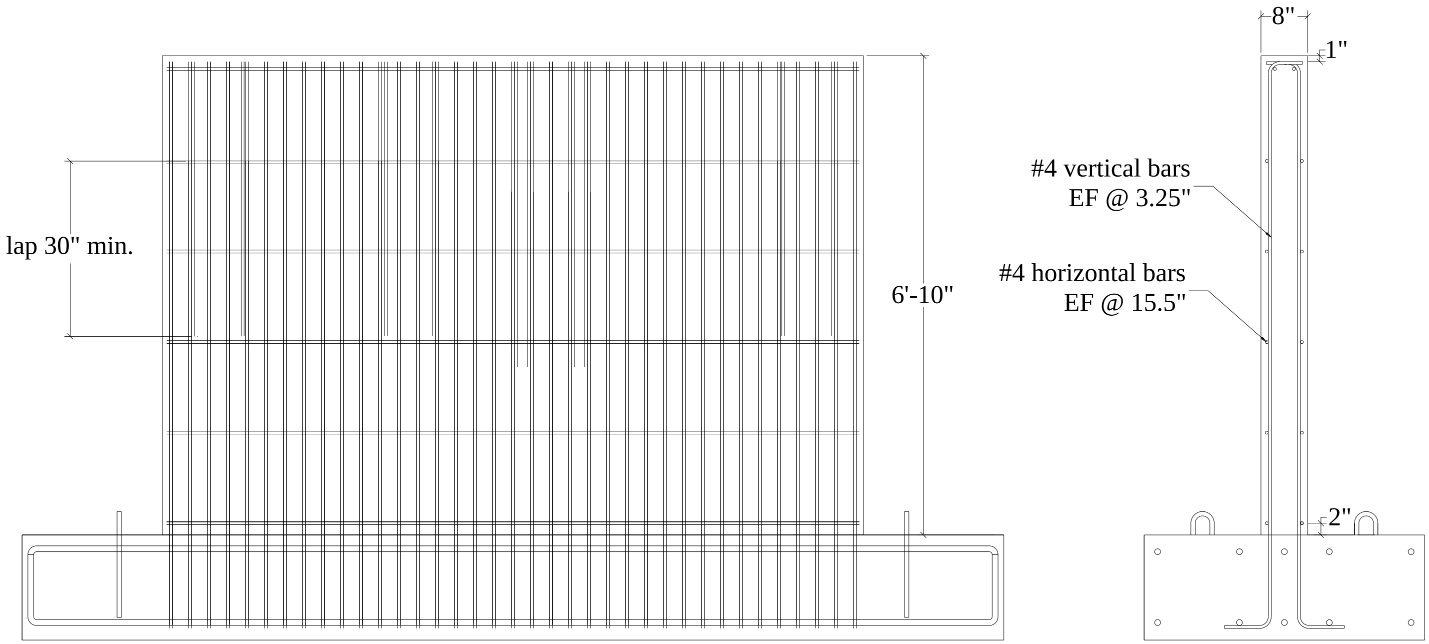

Figure A.16. Reinforcement details for SW10

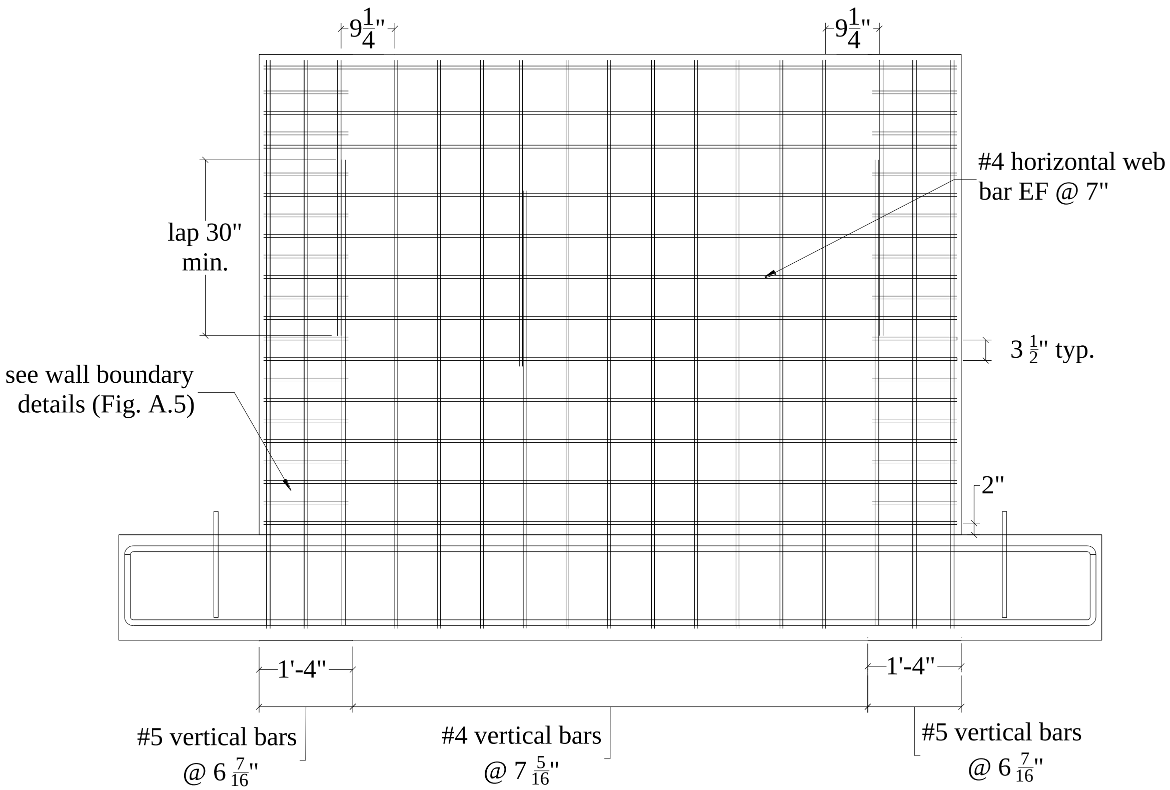

Figure A.17. Reinforcement details for SW11

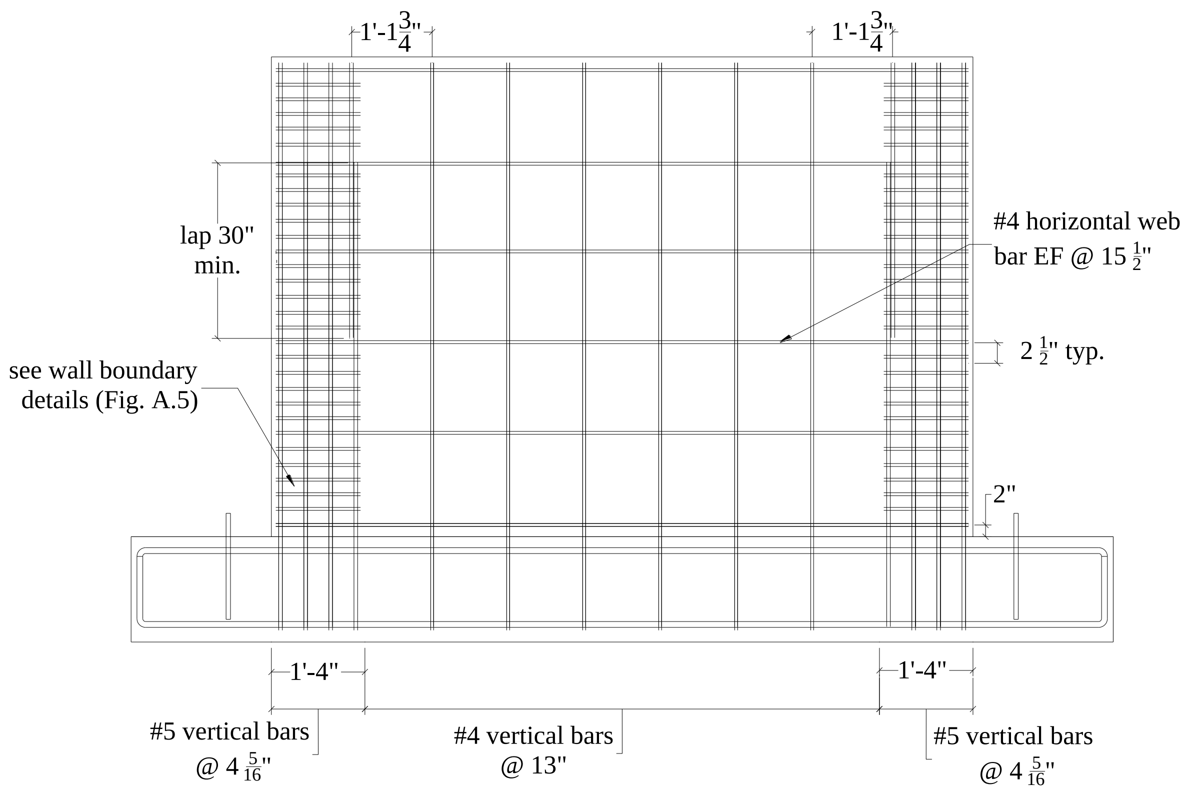

Figure A.18. Reinforcement details for SW12

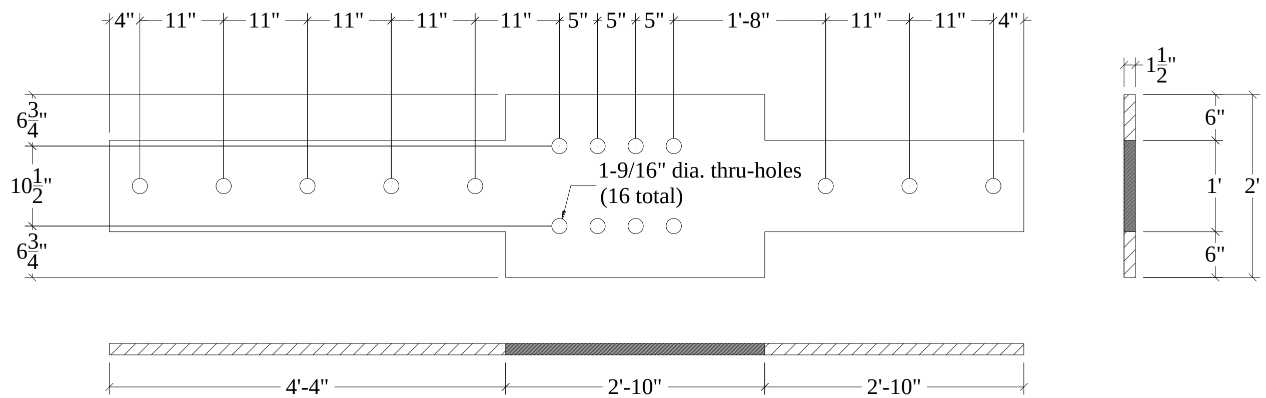

Figure A.19. Loading plate details

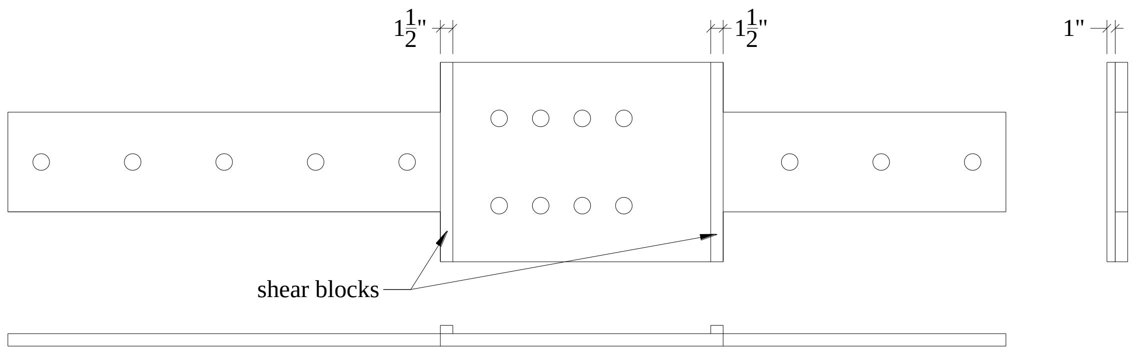

Figure A.20. Loading plate with the additional shear blocks

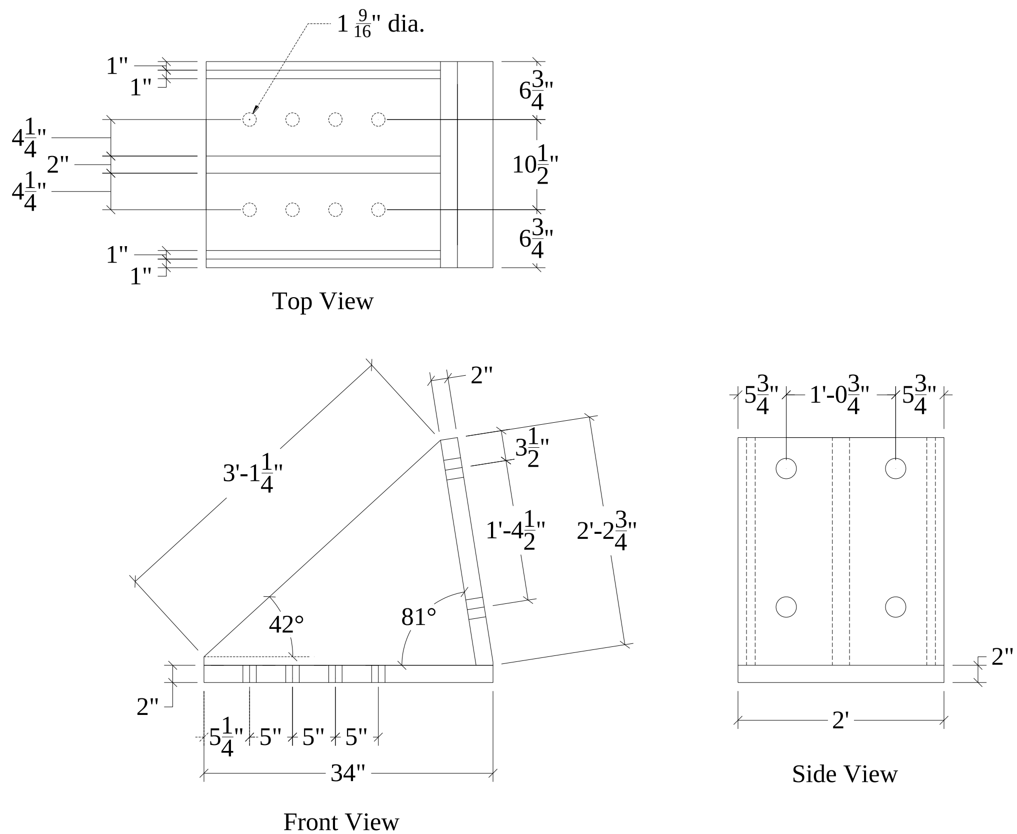

Figure A.21. Loading bracket details

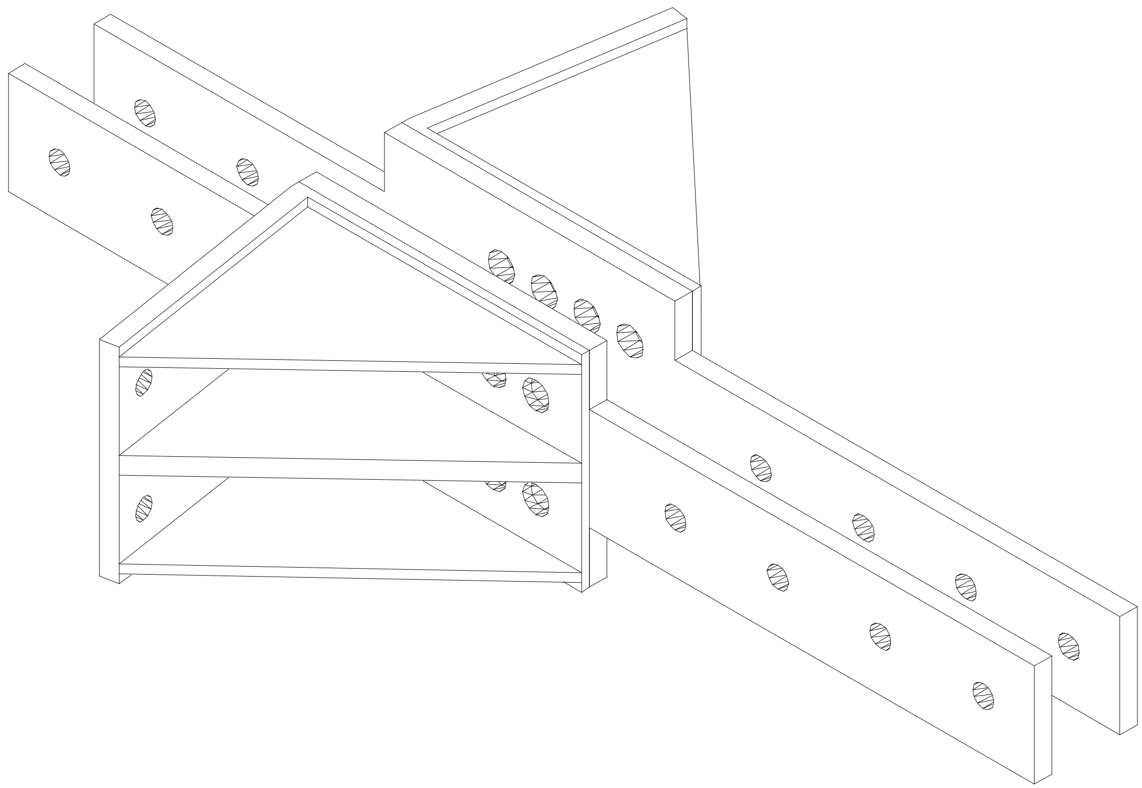

Figure A.22. Isometric drawing of the loading apparatus

APPENDIX B
STRUT-AND-TIE MODEL OF THE FOUNDATION OF SW8

Strut-and-tie modeling technique is useful to analyze reinforced concrete components with discontinuities and complex geometry. The foundations of the wall specimens have discontinuous regions (interface between wall and foundation and the thru-holes for the Dywidag bars), which makes strut-and-tie modeling suitable for its analysis.

The height of the stirrups for the foundations of the Phase II walls were fabricated 2 inches shorter than what was specified and this prompted a reevaluation of the design of the foundation of the Phase II specimens. Strut-and-tie models of the critical zones of the foundation of SW8, the wall with the largest reinforcement ratio, were used to examine the effects of the reduced height of the reinforcement cages.

The initial task was to determine the maximum tensile force that could be transferred to the critical zone of the foundation as a result of the lateral load applied at the centerline of loading of the wall. Figure B.1 is a plan view of specimen SW8 with the critical zones of the foundation highlighted by red boxes. Each section of wall above a critical zone of the foundation contained 14 #4 vertical reinforcement. The maximum tensile force that could be transferred to this part of the foundation is equal to the sum of the yield forces on the 14 vertical reinforcement (assuming that tensile yielding of the vertical reinforcement on the critical zone will occur during a loading cycle). Assuming an upper value of the yield stress of 80 ksi for the reinforcement, the maximum tensile force on the critical zone (T) is equal to

$$T = 14 * 0.2 * 80 = 224 \text{ kips} \tag{C.1}$$

The strut-and-tie model of the critical zone of the foundation in the longitudinal and transverse directions is shown in Figure B.2. The compression struts are marked by the blue dashed lines and the tension ties are marked by the solid blue lines. Forces T_1, T_2 and T_3 represent the forces on the Dywidag bars. Force T was assumed to act at the centroid of the vertical reinforcement within the critical zone and at the bottom of the foundation where the 90 degree hooks of the vertical reinforcement of the wall were installed. The centroids of the vertical reinforcement in the critical zones are marked with solid red circles in Figure B.1 and Figure B.2.

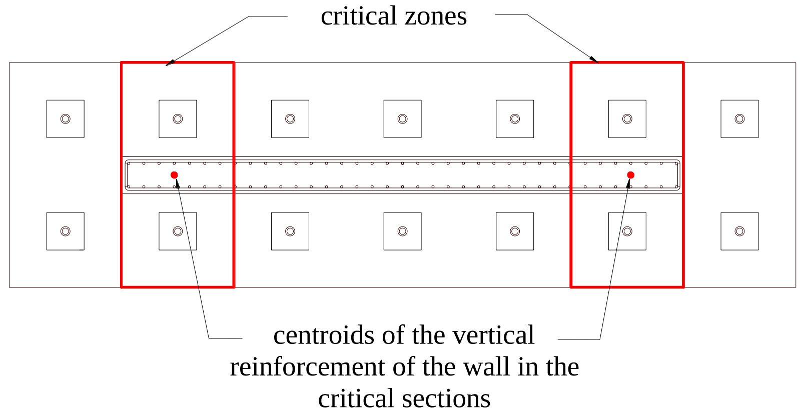

Figure B.1. Critical zones of the foundation of SW8

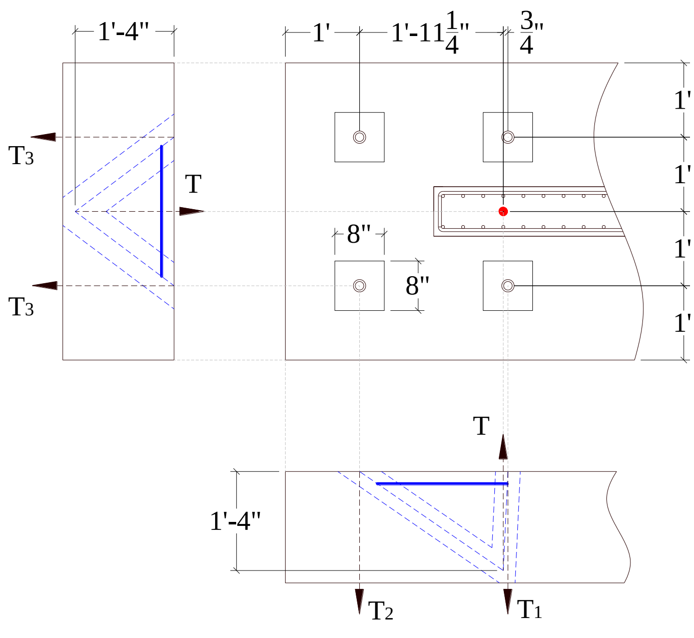

Figure B.2. Strut-and-tie model of the critical zone (longitudinal and transverse directions)

Figure B.3 shows the idealized free-body diagram of the nodes of the strut-and-tie model in the transverse direction. Force F_c and F_t are acting on the compression struts and tension tie, respectively. (A similar free-body diagram was prepared for the strut-and-tie model in the longitudinal direction.) The tensile force T was transferred to the compression struts at node A. The vertical components of the forces in the compression struts were resisted by the Dywidag bars (at nodes B and C). The horizontal components of the forces in the compression struts were resisted by the tension tie.

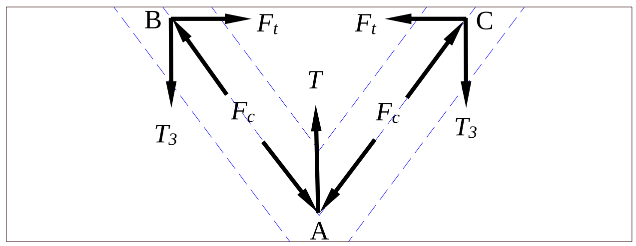

Figure B.3. Idealized free-body diagram of the nodes of the strut-and-tie model (transverse dir ection)

The forces in the compression struts and tension ties were determined by equilibrium equations. The force on the tension tie in the transverse direction was calculated to be equal to 84 kips. This force on the tension tie was resisted by the top transverse reinforcement of the foundation. There were six transverse reinforcement along the 2 feet length of the critical zone to resist the 84 kips. Assuming a yield stress of 60 ksi, the total force that can be supported by the six transverse reinforcement was 72 kips, which was less than the 86 kips required. An additional four #4 transverse bars were added in the critical zone to increase the force capacity in the transverse direction. The details of the additional transverse reinforcement are shown in Figure B.4. For the longitudinal direction, the force on the tension tie was calculated to be 20 kips. There were 5 #8 longitudinal bars on top section of the foundation reinforcement. The total force that can be supported was 237 kips (assuming a yield stress of 60 ksi), which was significantly greater than the 20 kips required. Supplemental reinforcement was provided in the longitudinal direction in the top section of the foundation reinforcement to decrease the space between the longitudinal bars. Two #6 and two #4 bars, 6 feet long, were added along the longitudinal direction in the top section of the foundation of SW8 (Figure B.5). Two #6 bars, 6 feet long, were added along the longitudinal direction in the top section of the foundations of SW9 through SW12 (Figure B.6).

The concrete cover on top and bottom of the foundation was increased to 2 inches to account for the reduction in height of the stirrups. The tails of the vertical reinforcement in the wall were placed below the #8 longitudinal bars. Details of the modifications are shown in the section view in Figure B.4.

The Dywidag bars have $1-1/2$ inches thick steel washers with a cross section of about 8×8 inches. The concrete compression struts transfer the vertical components of the force to the Dywidag bars through these washers. The required width of the compression struts on both the longitudinal and transverse strut-and-tie models were checked and were all less than 8 inches.

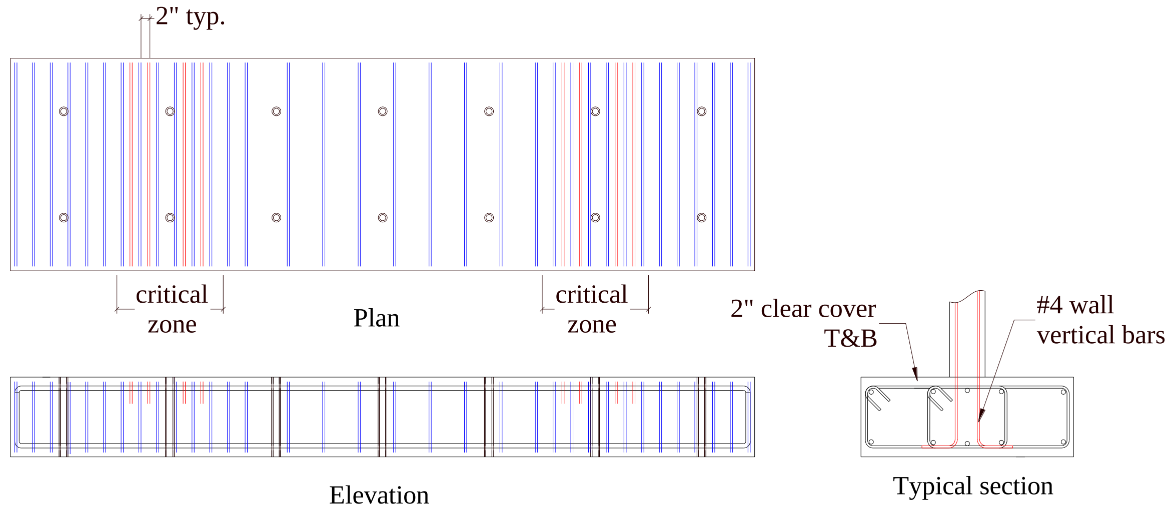

Figure B.4. Supplemental transverse reinforcement

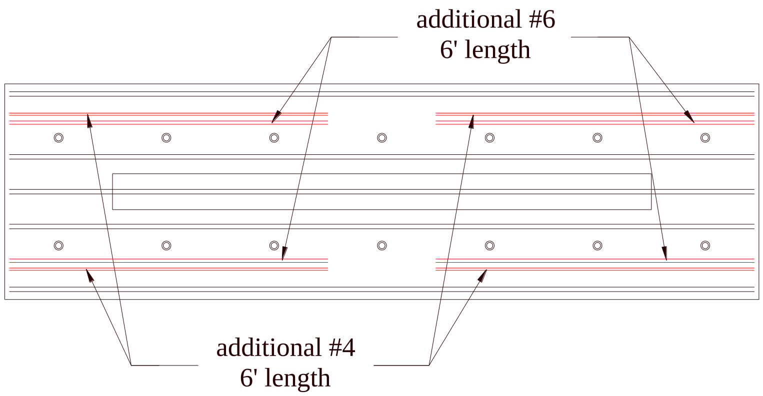

Figure B.5. Supplemental longitudinal reinforcement on the top section of rebar cage (SW8)

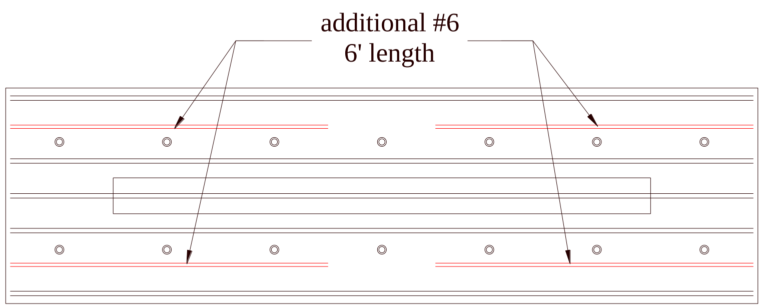

Figure B.6. Supplemental longitudinal reinforcement on the top section of rebar cage (SW9-SW12)

APPENDIX C
SPECIMEN INSTRUMENTATIONS AND LABORATORY EQUIPMENT SPECIFICATIONS

C.1 Introduction

Section C.2 presents the instrumentation plans for each wall specimen. Drawings that show the locations of 1) Krypton LED sensors, 2) strain gages on vertical reinforcement, 3) strain gages on the horizontal reinforcement, and 4) string potentiometers and Temposonics are presented for each wall. The locations of the linear potentiometers for SW4 are also shown. The following are abbreviations used in the drawings and their corresponding descriptions: SP – string potentiometer, TP – Temposonic, LP – linear potentiometer and S – strain gage.

Section C.3 presents the specifications of the laboratory equipment used during testing. The equipment included: 1) MTS actuator model 243.90T, 2) SAC series D62 string potentiometer, 3) MTS Temposonic, 4) LW12 linear potentiometer, 5) Krypton K600 system, 6) YFLA-5-5L strain gages, and 6) Pacific Instruments model 6000 data acquisition system.

C.2 Instrumentation drawings

C.2.1 Krypton LED sensors

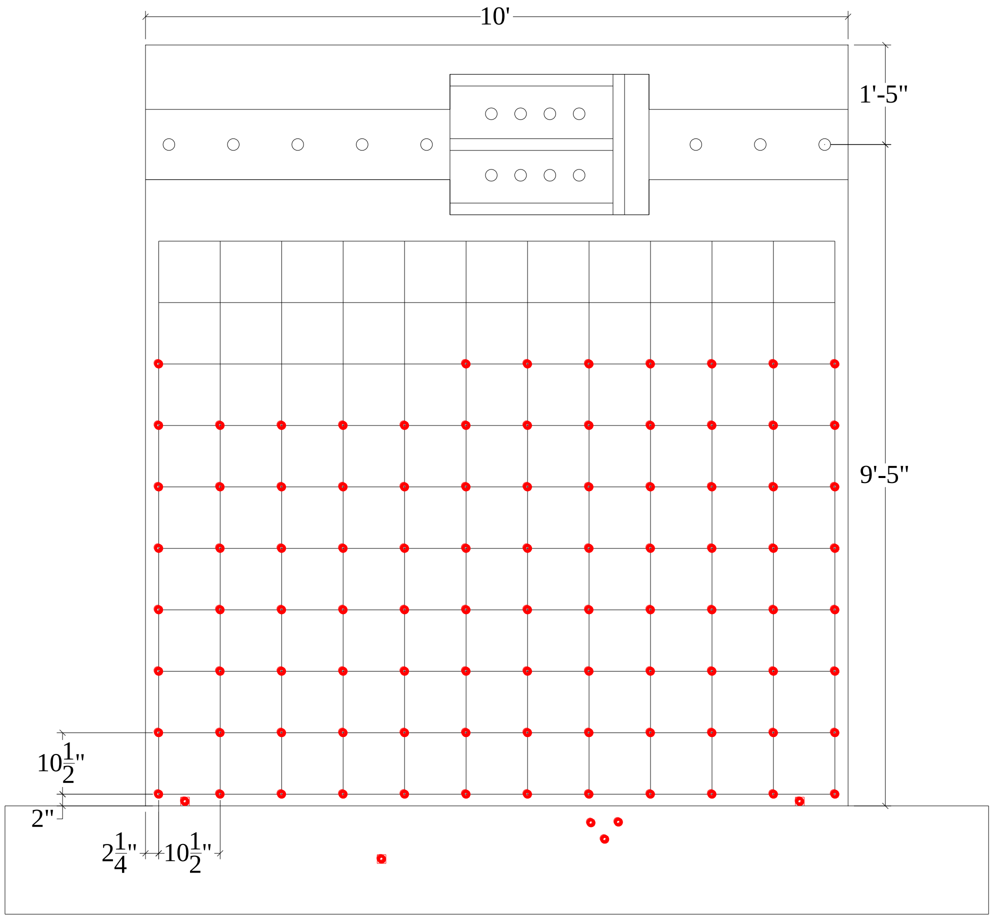

Figure C.1. Krypton LED sensors for SW1

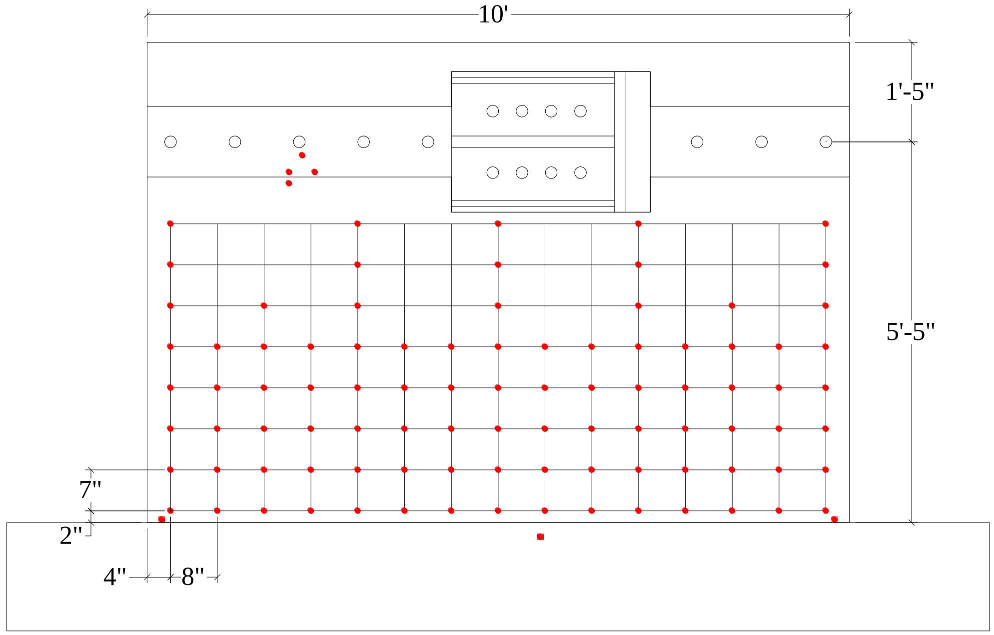

Figure C.2. Krypton LED sensors for SW2

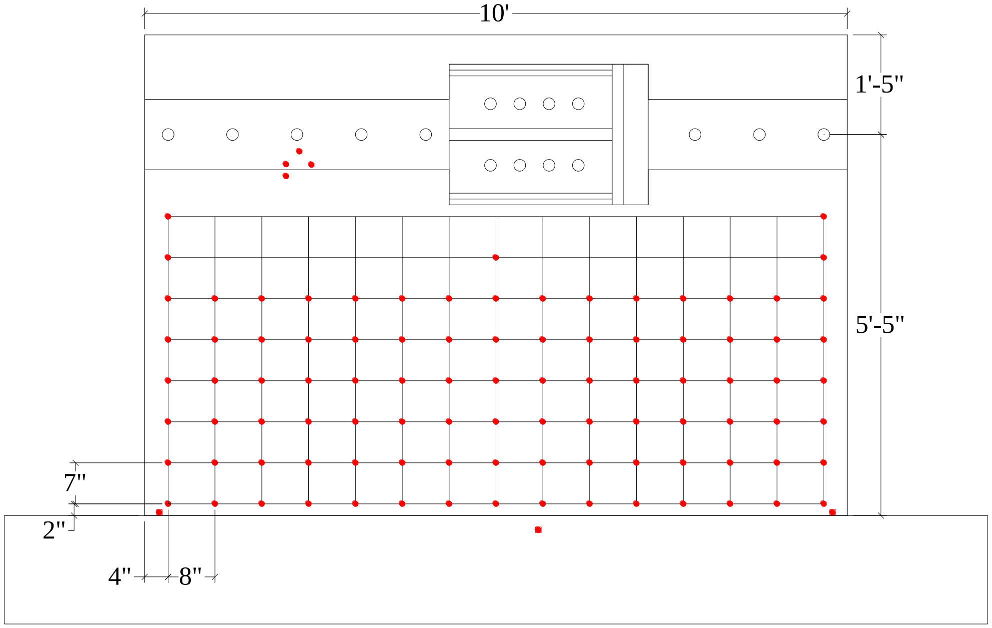

Figure C.3. Krypton LED sensors for SW3

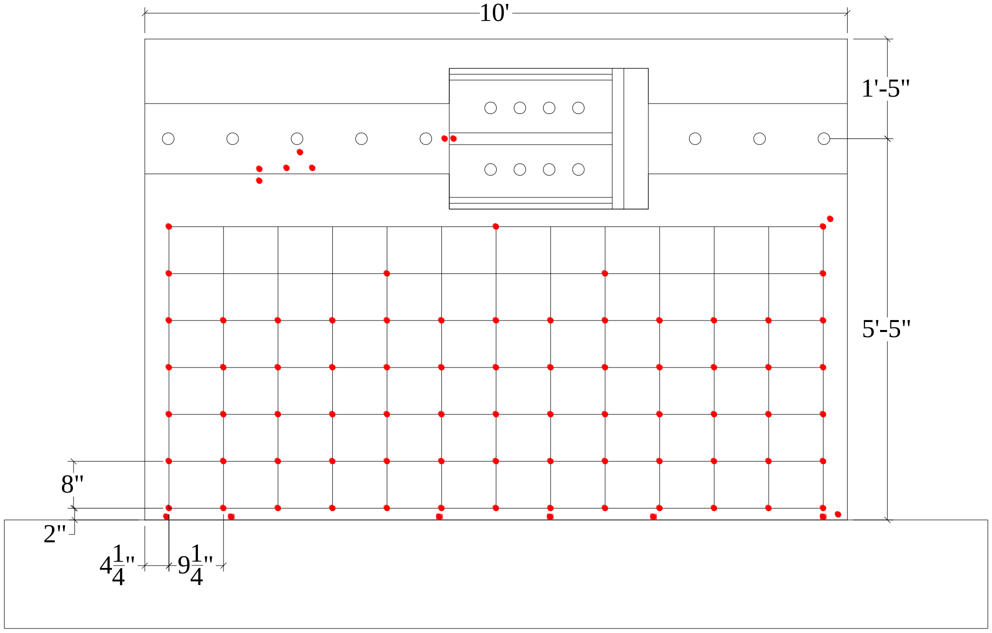

Figure C.4. Krypton LED sensors for SW4

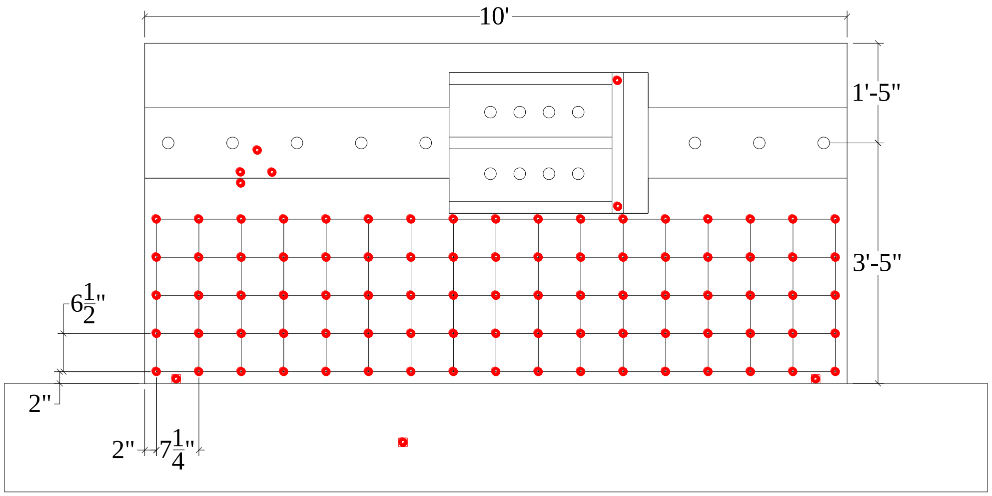

Figure C.5. Krypton LED sensors for SW5

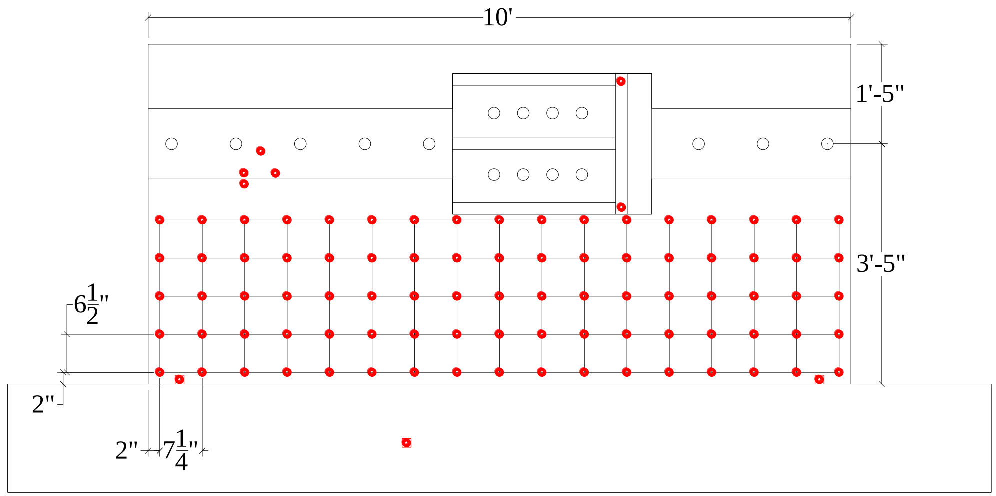

Figure C.6. Krypton LED sensors for SW6

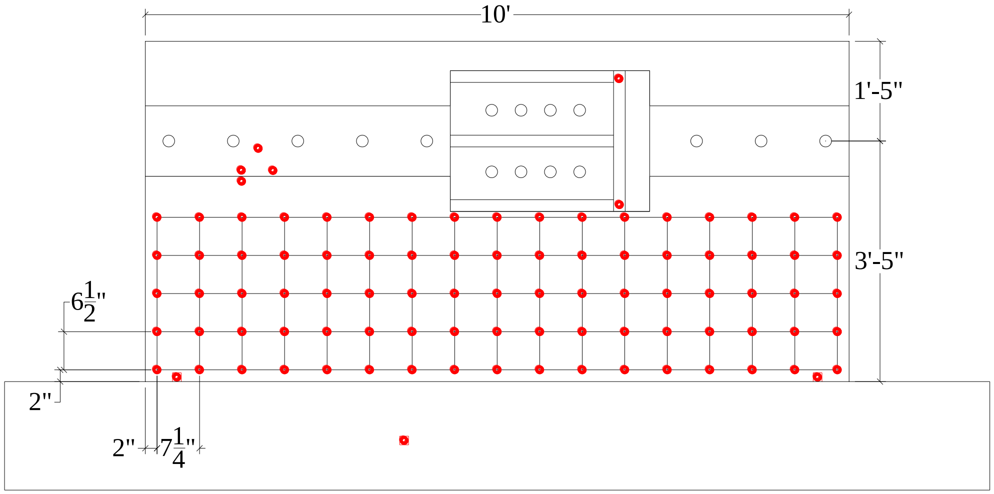

Figure C.7. Krypton LED sensors for SW7

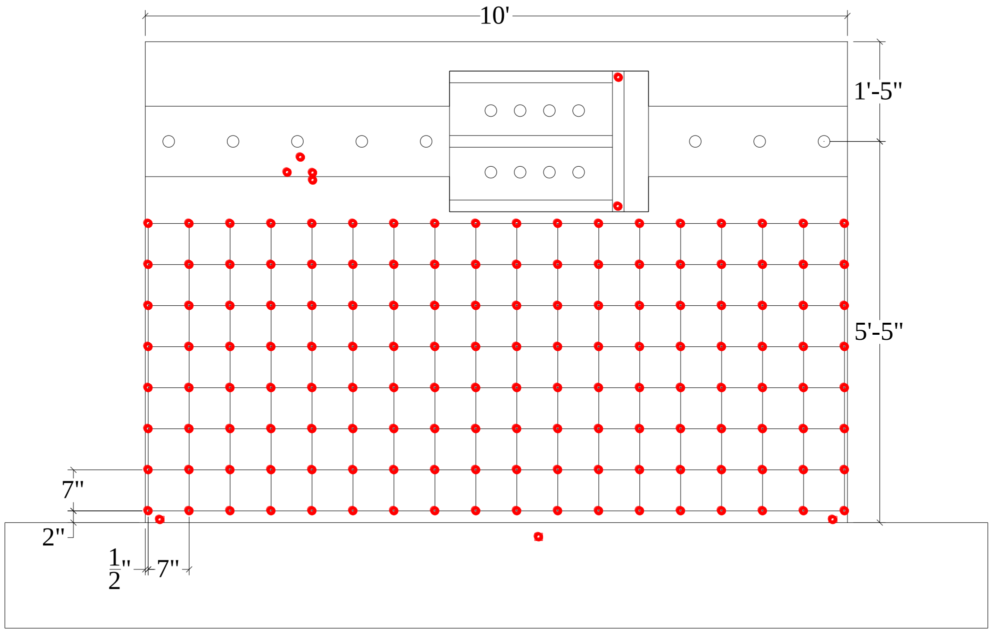

Figure C.8. Krypton LED sensors for SW8

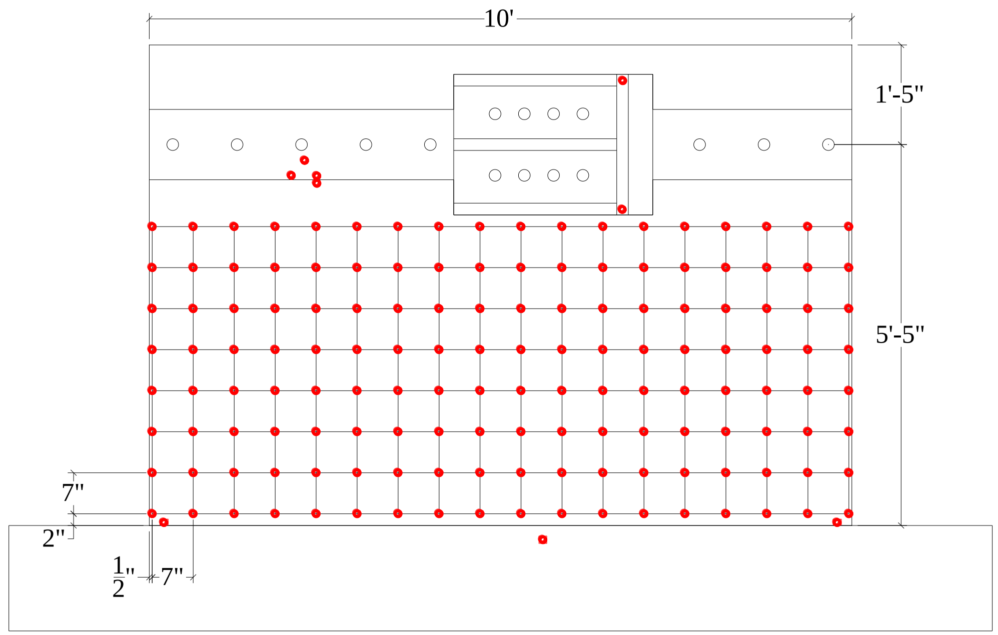

Figure C.9. Krypton LED sensors for SW9

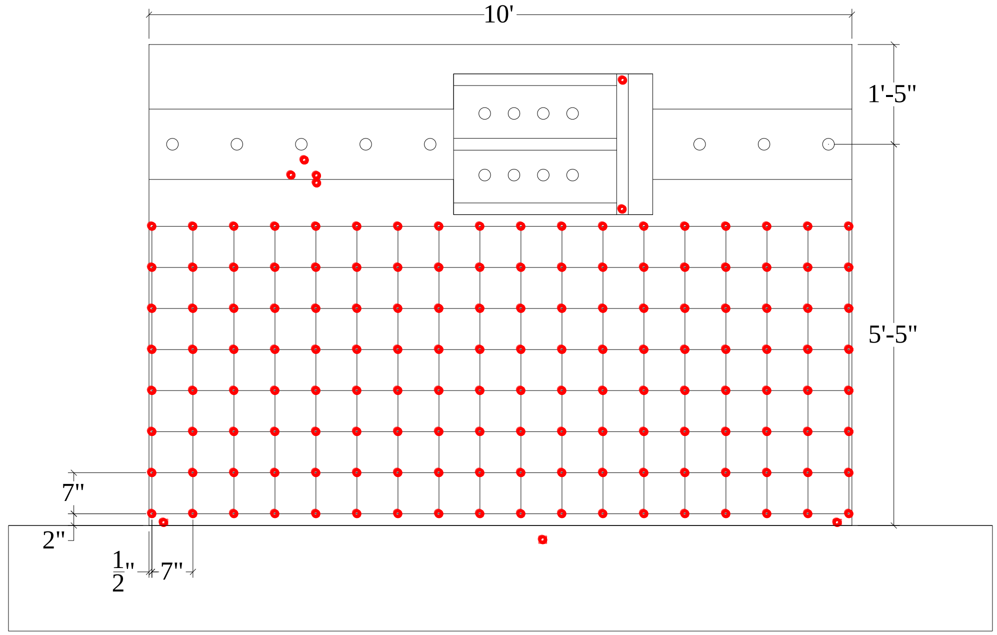

Figure C.10. Krypton LED sensors for SW10

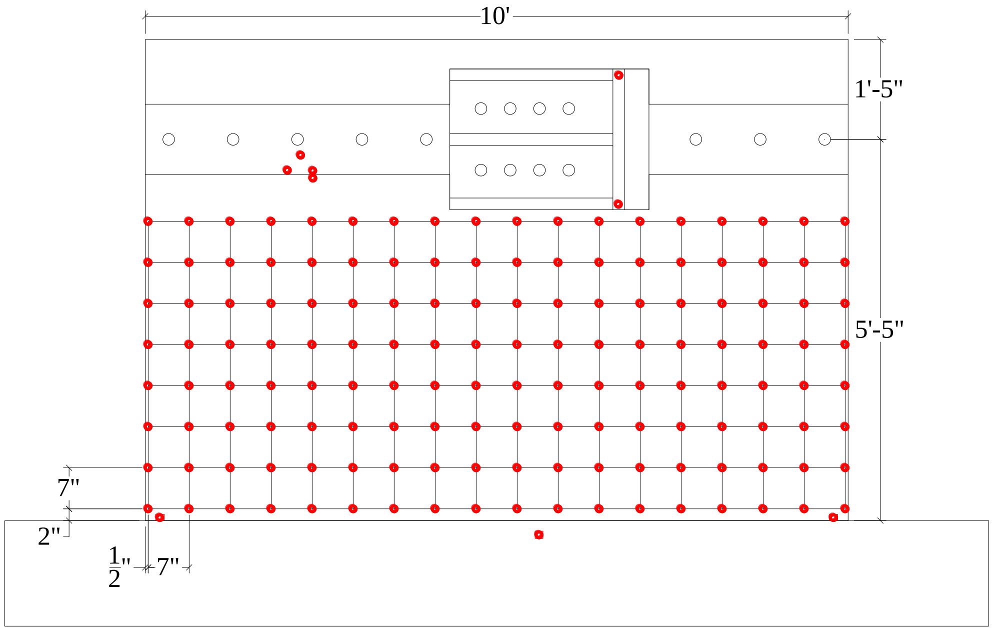

Figure C.11. Krypton LED sensors for SW11

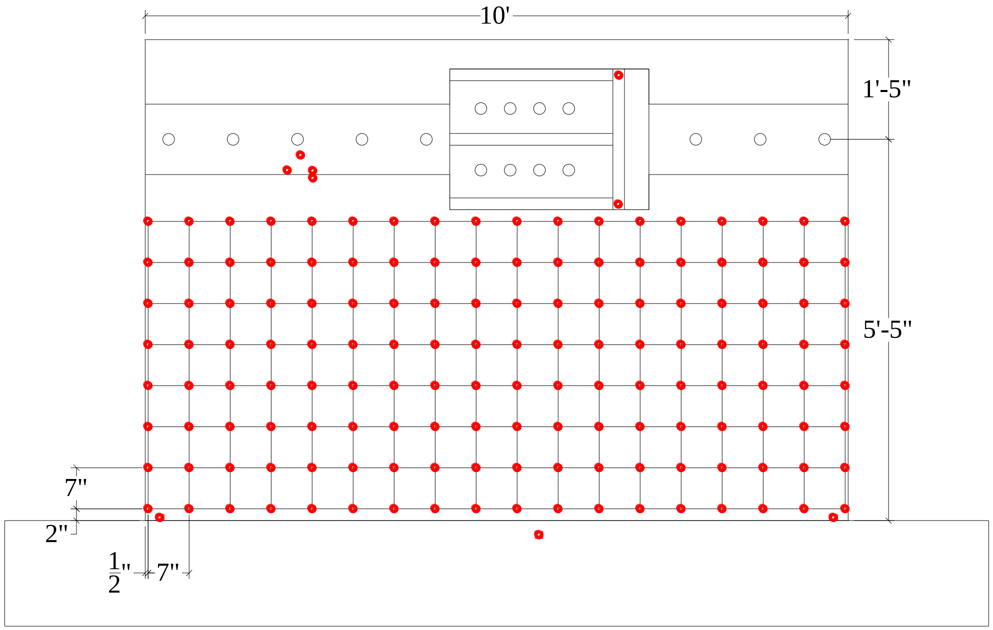

Figure C.12. Krypton LED sensors for SW12

C.2.2 Strain gages on the vertical reinforcements

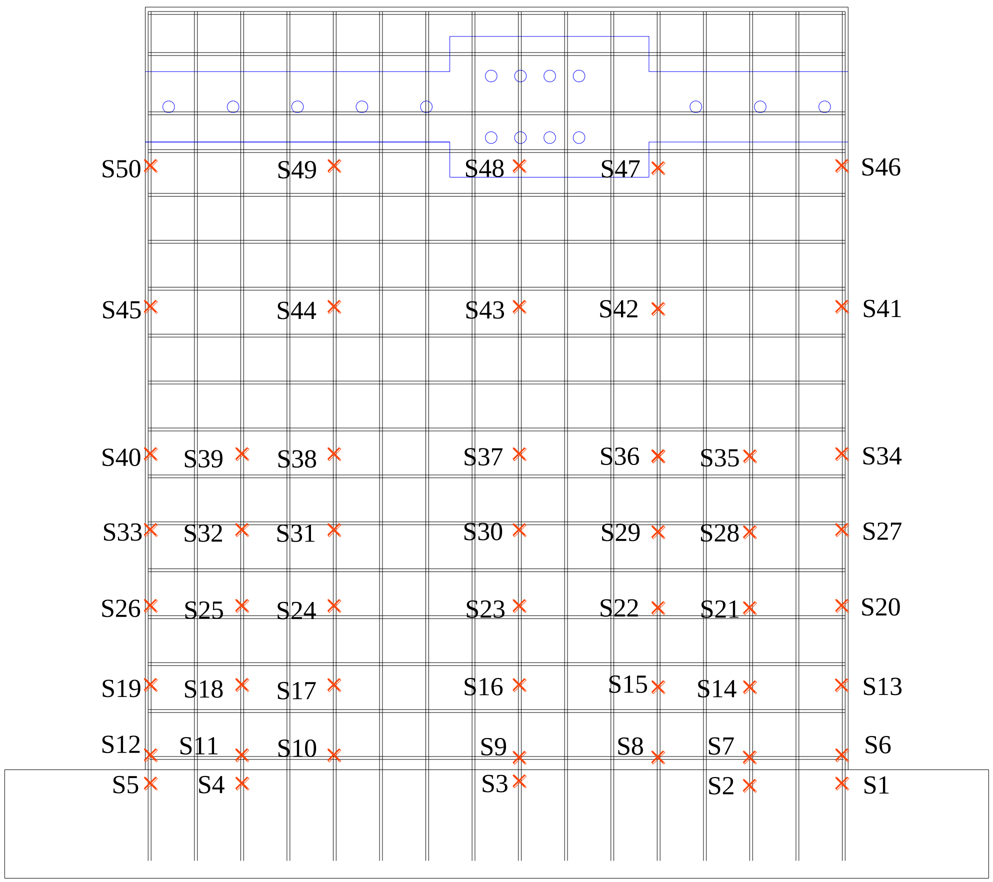

Figure C.13. Strain gages on the vertical reinforcements for SW1

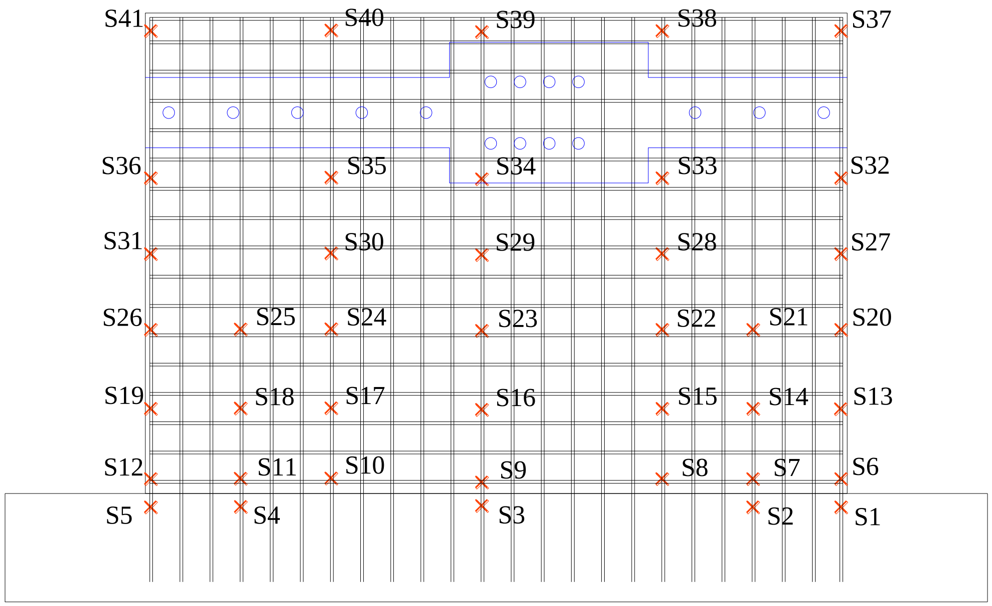

Figure C.14. Strain gages on the vertical reinforcements for SW2

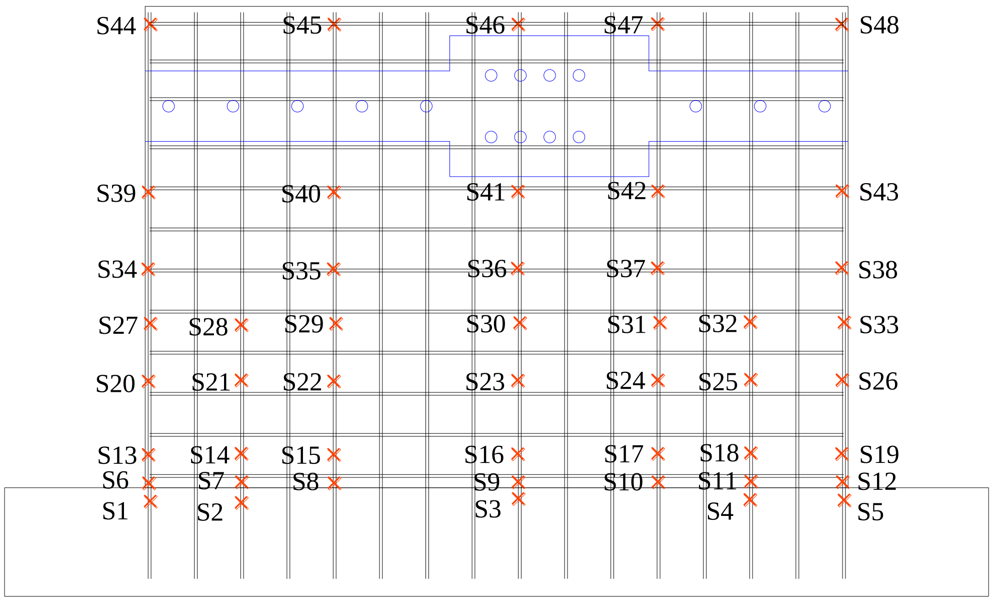

Figure C.15. Strain gages on the vertical reinforcements for SW3

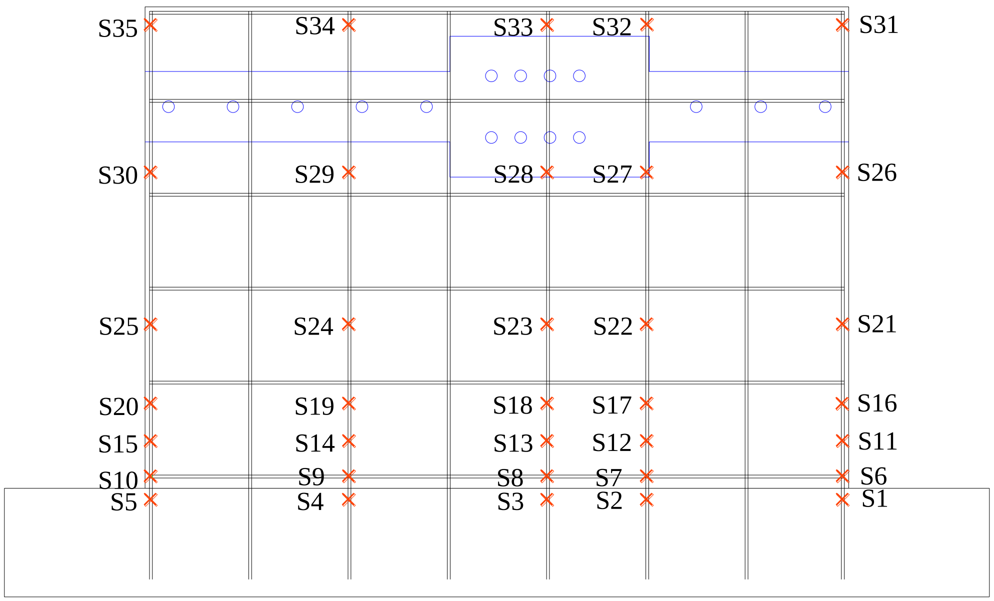

Figure C.16. Strain gages on the vertical reinforcements for SW4

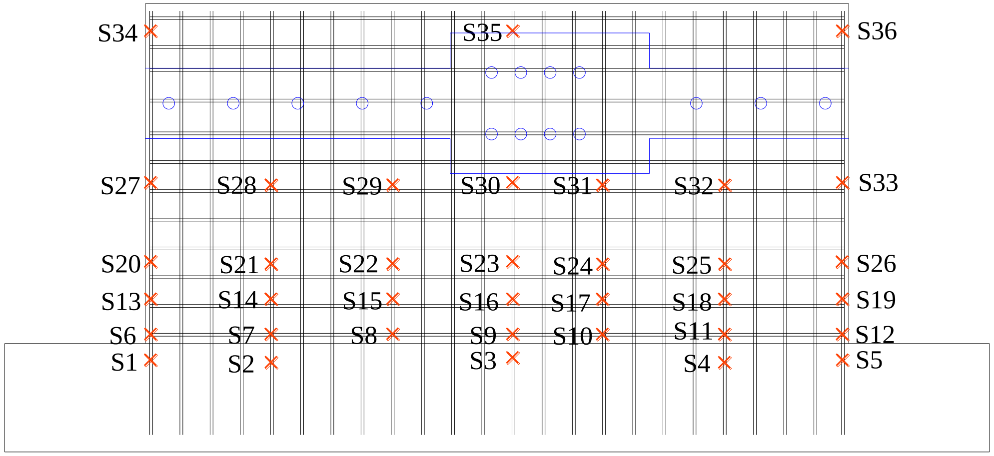

Figure C.17. Strain gages on the vertical reinforcements for SW5

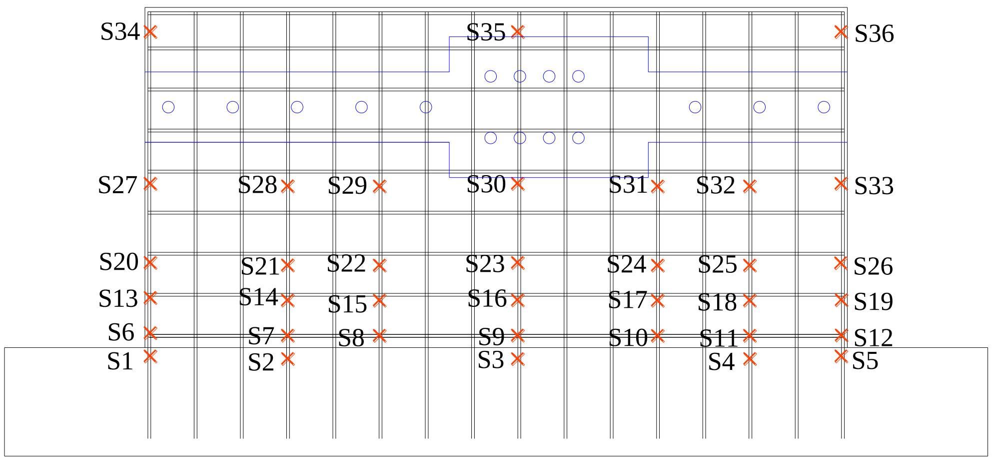

Figure C.18. Strain gages on the vertical reinforcements for SW6

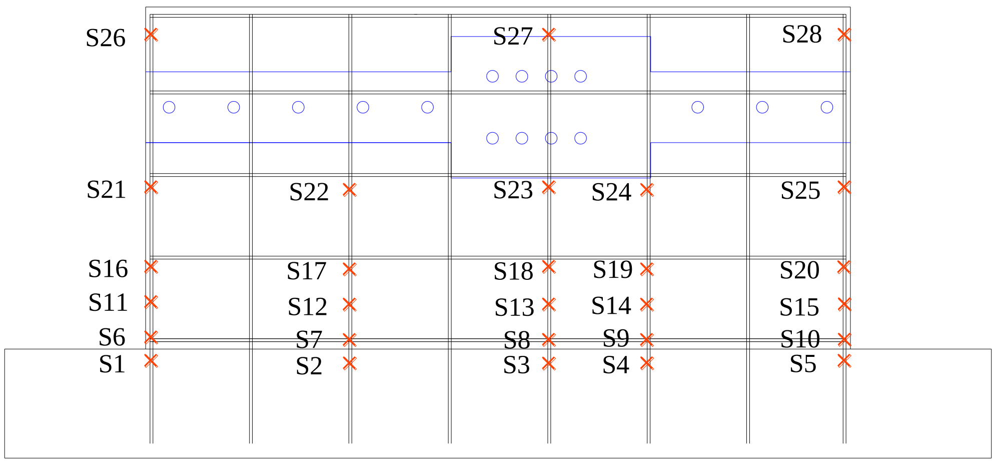

Figure C.19. Strain gages on the vertical reinforcements for SW7

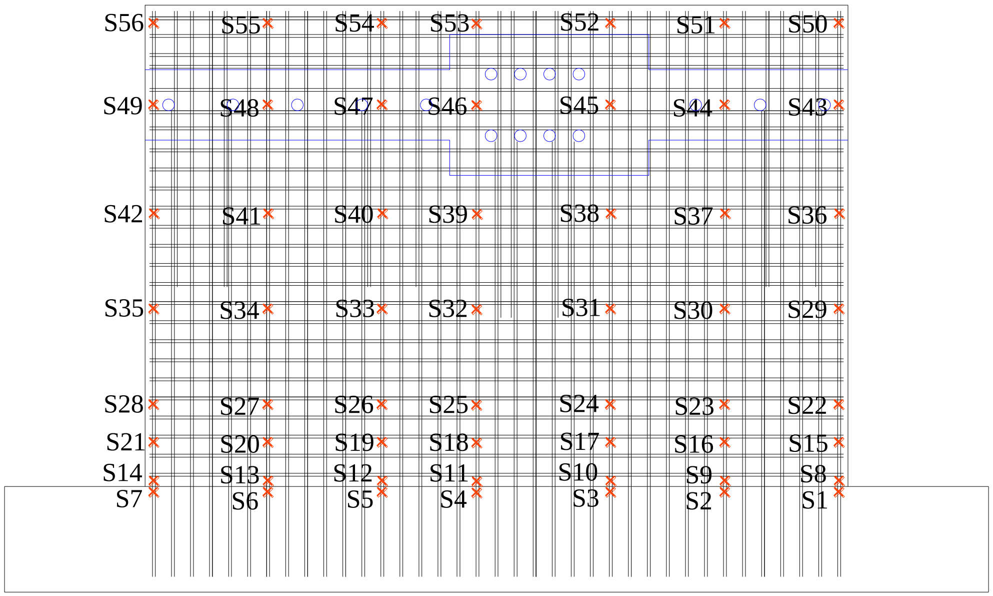

Figure C.20. Strain gages on the vertical reinforcements for SW8

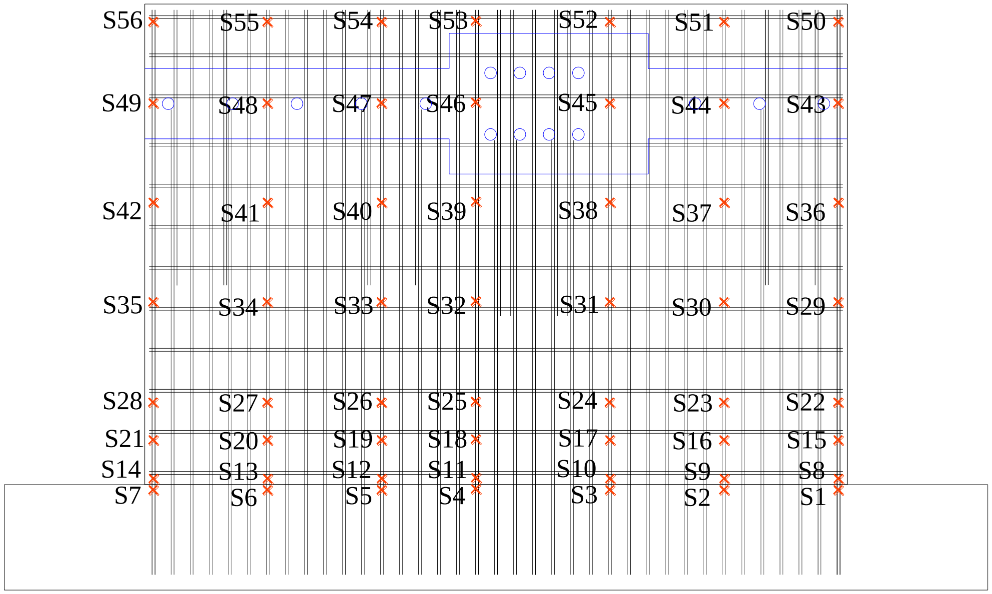

Figure C.21. Strain gages on the vertical reinforcements for SW9

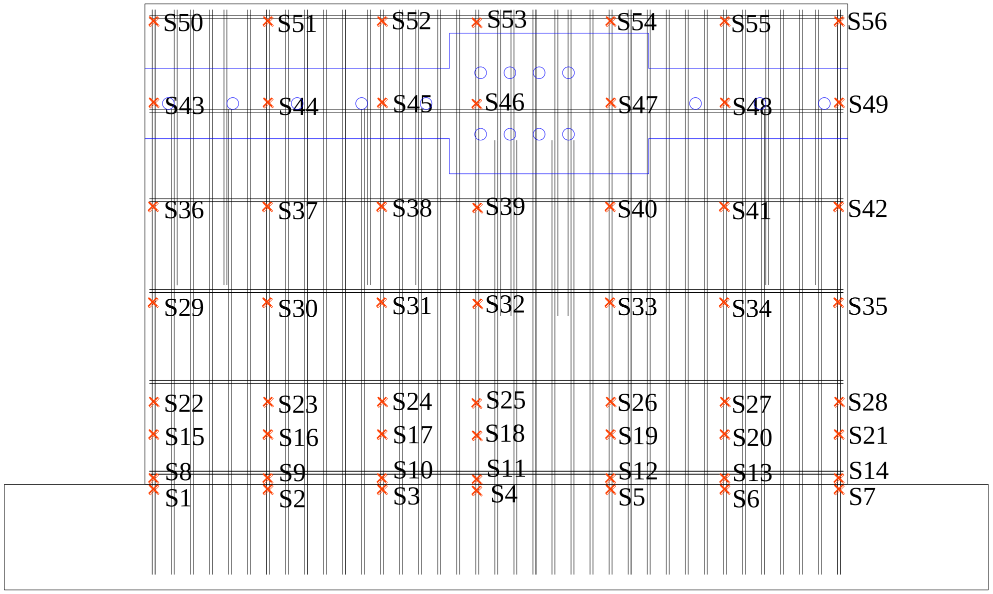

Figure C.22. Strain gages on the vertical reinforcements for SW10

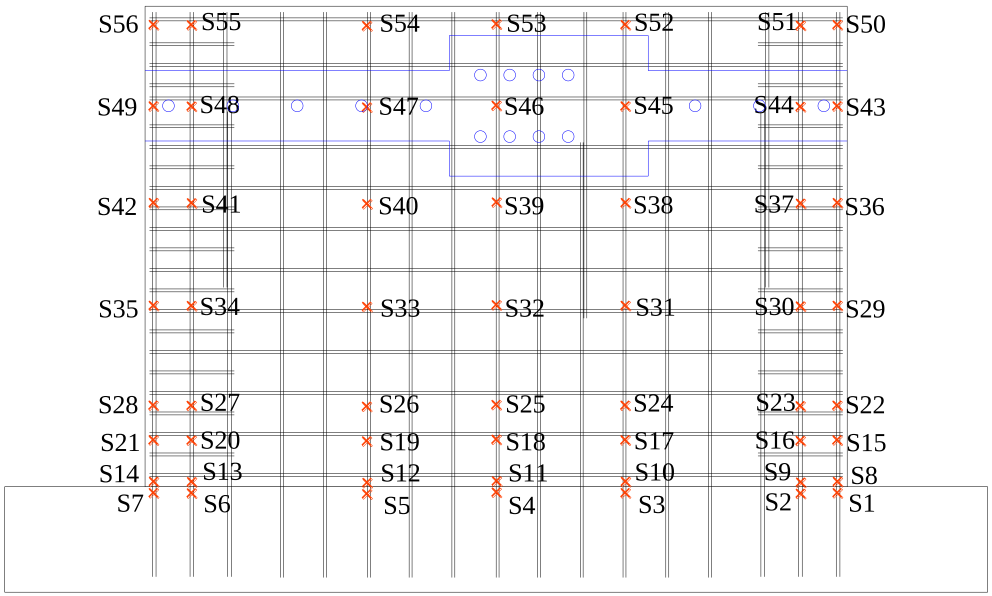

Figure C.23. Strain gages on the vertical reinforcements for SW11

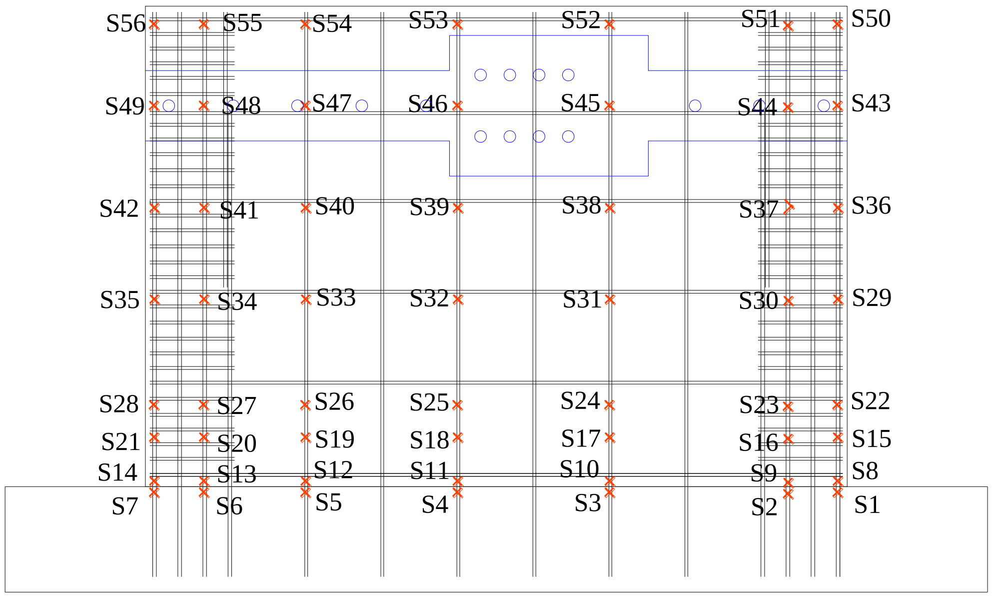

Figure C.24. Strain gages on the vertical reinforcements for SW12

C.2.3 Strain gages on the horizontal reinforcements

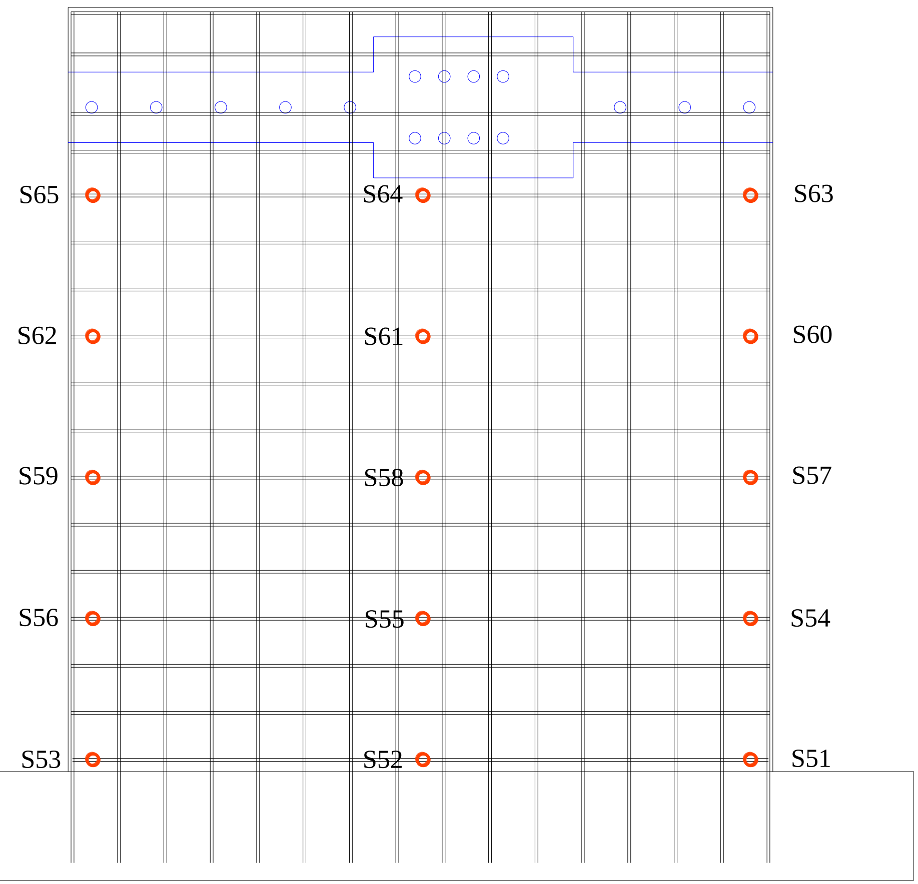

Figure C.25. Strain gages on the horizontal reinforcements for SW1

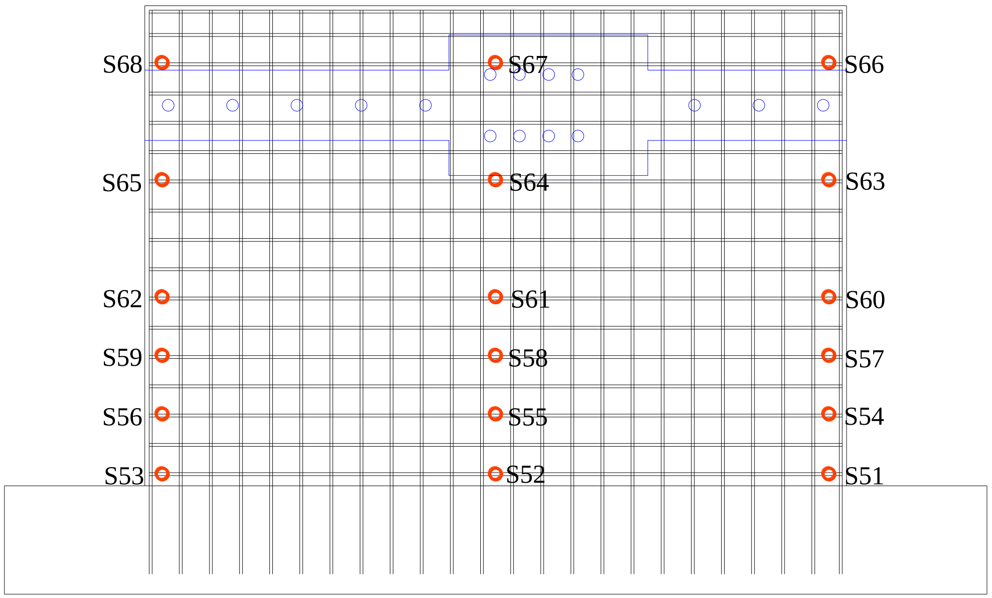

Figure C.26. Strain gages on the horizontal reinforcements for SW2

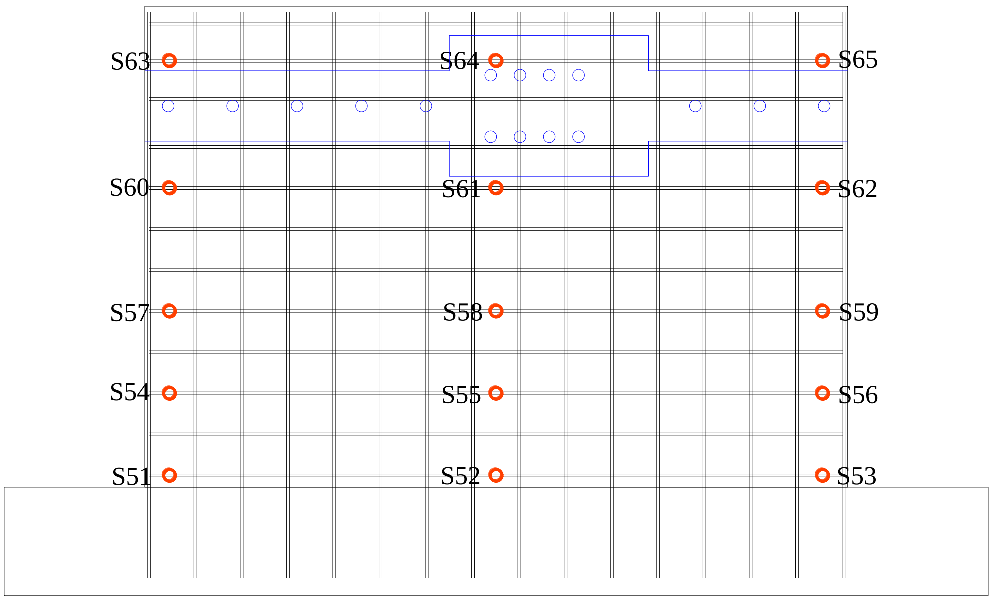

Figure C.27. Strain gages on the horizontal reinforcements for SW3

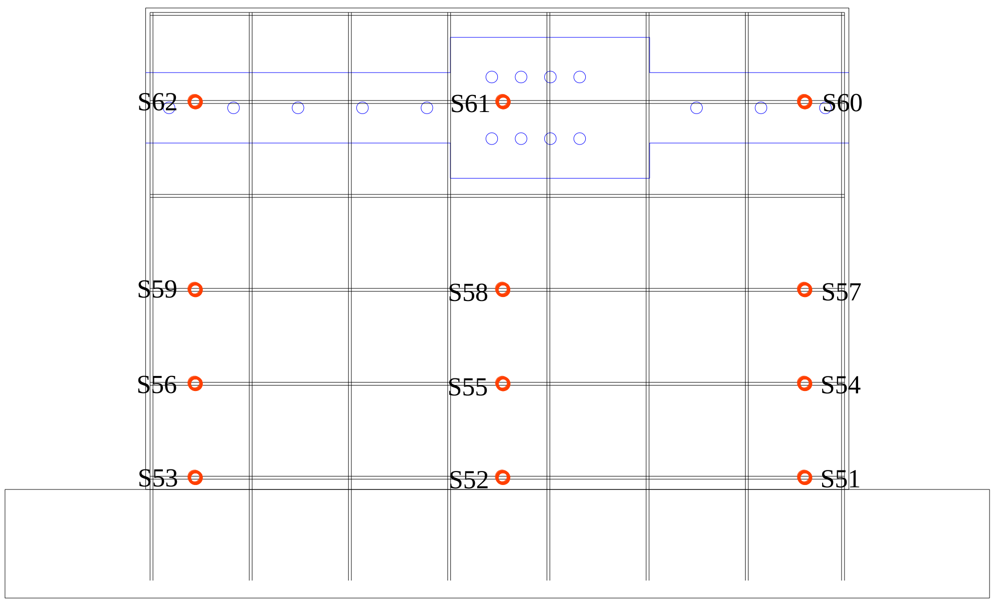

Figure C.28. Strain gages on the horizontal reinforcements for SW4

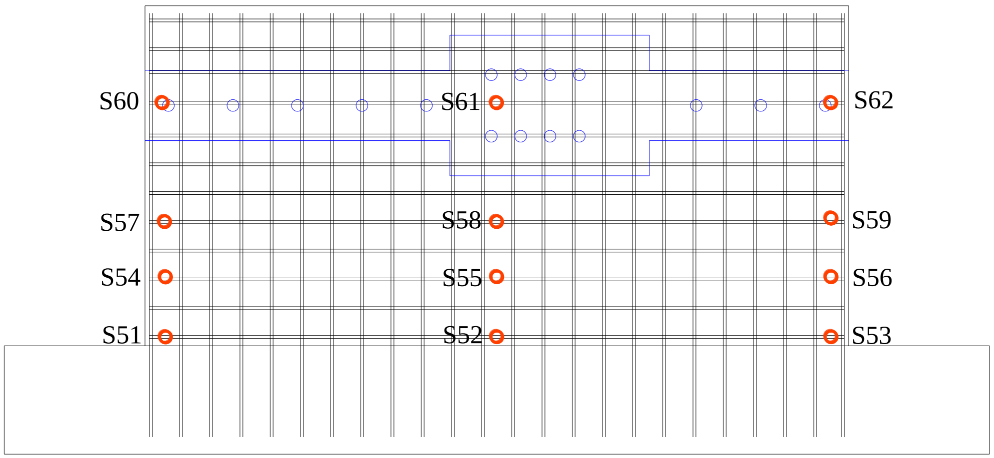

Figure C.29. Strain gages on the horizontal reinforcements for SW5

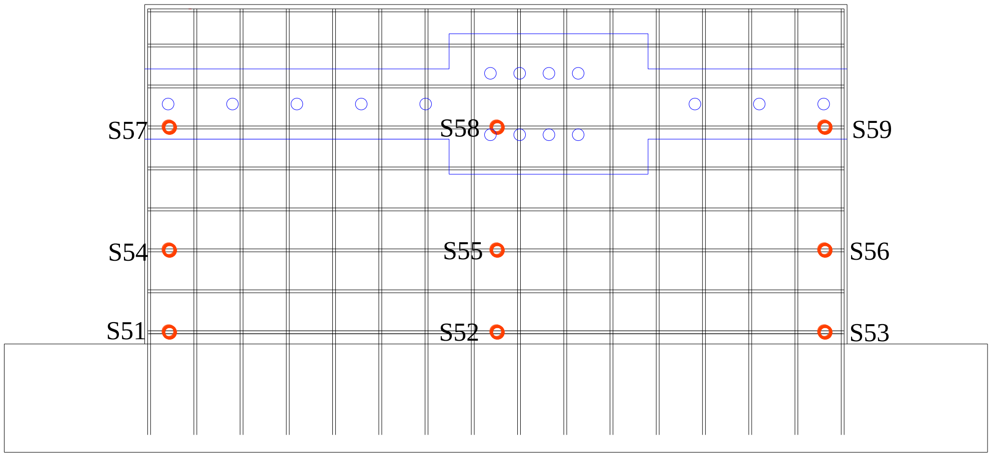

Figure C.30. Strain gages on the horizontal reinforcements for SW6

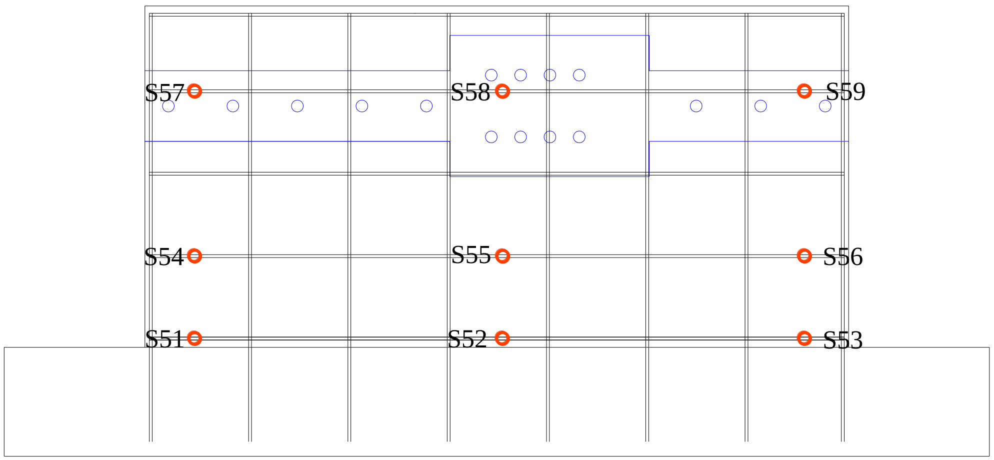

Figure C.31. Strain gages on the horizontal reinforcements for SW7

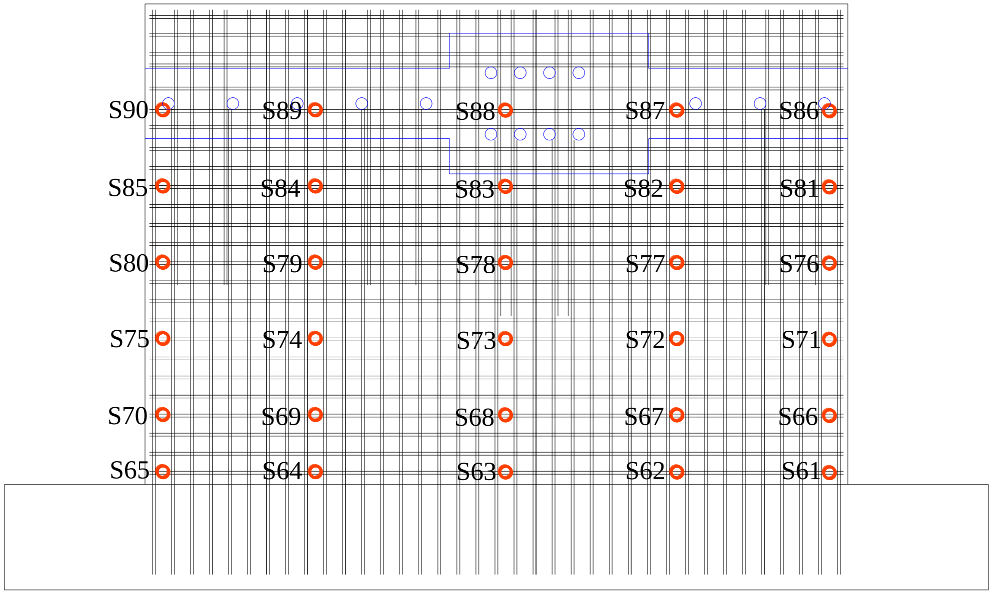

Figure C.32. Strain gages on the horizontal reinforcements for SW8

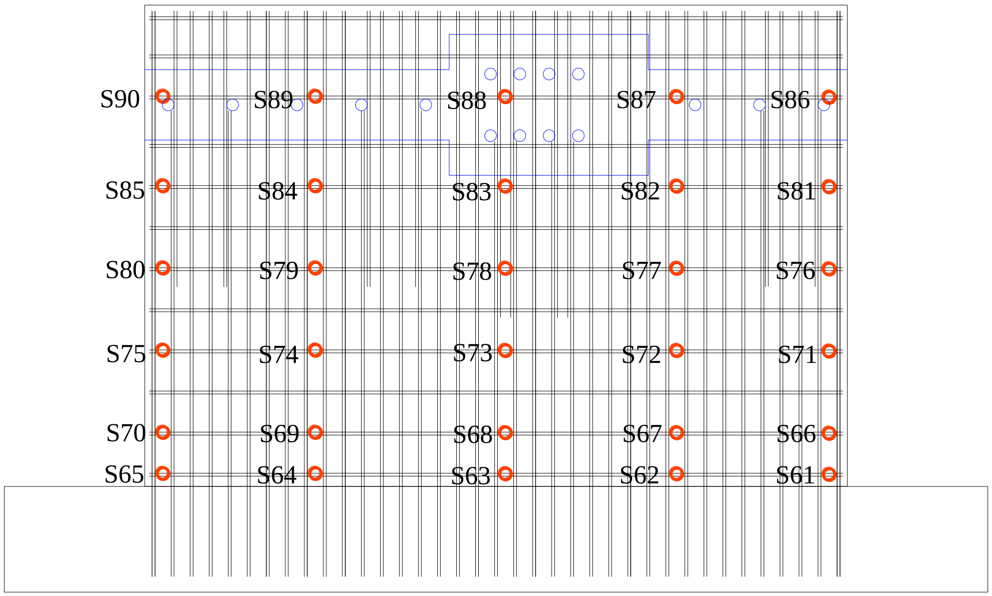

Figure C.33. Strain gages on the horizontal reinforcements for SW9

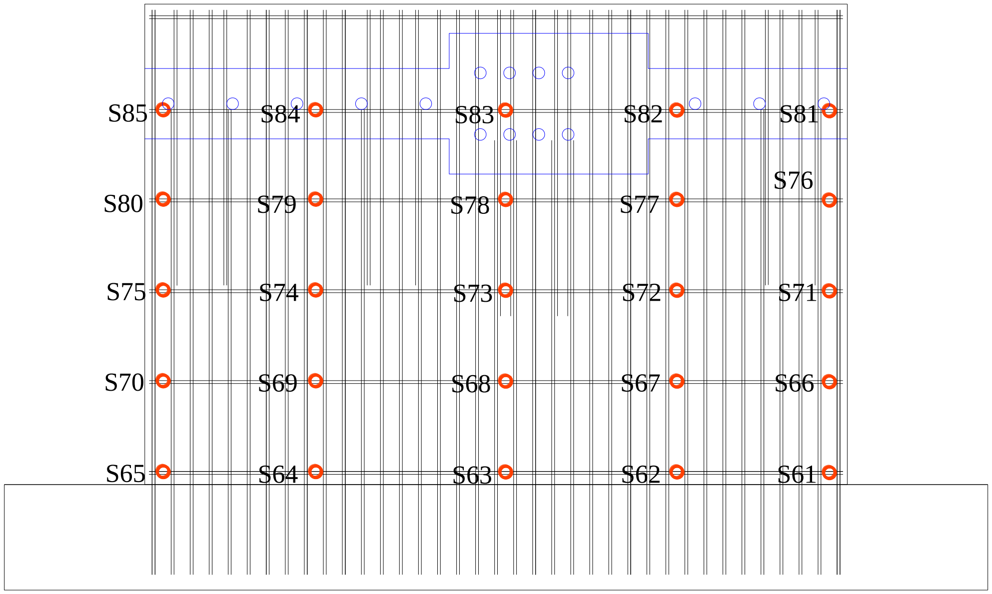

Figure C.34. Strain gages on the horizontal reinforcements for SW10

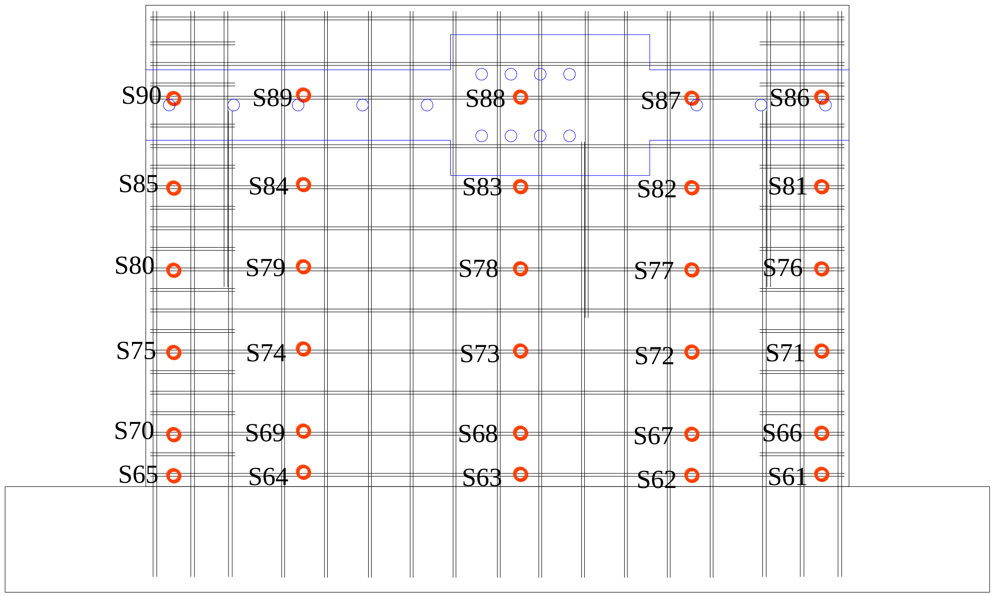

Figure C.35. Strain gages on the horizontal reinforcements for SW11

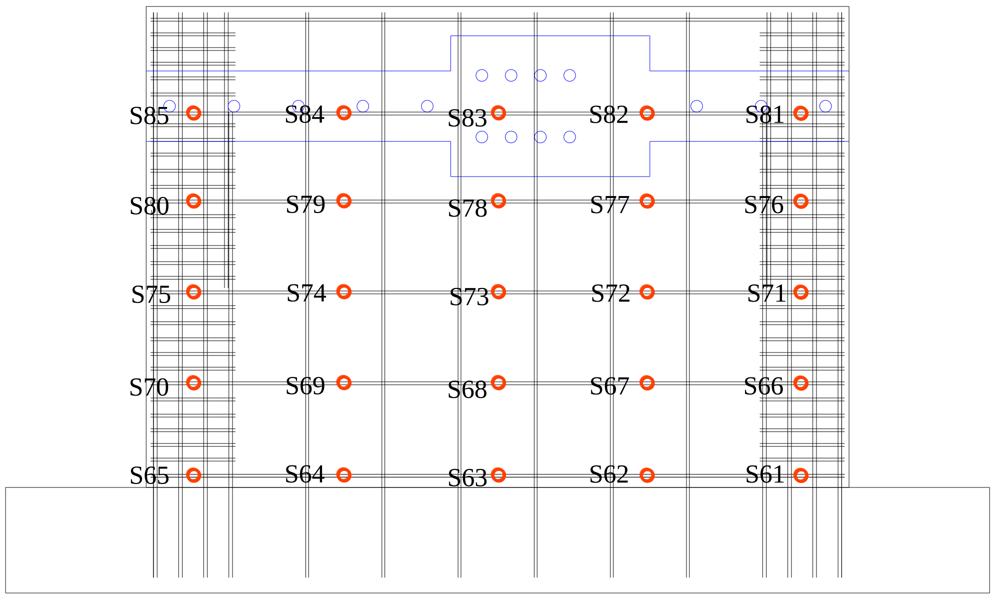

Figure C.36. Strain gages on the horizontal reinforcements for SW12

C.2.4 In-plane and out-of-plane string potentiometers and Temposonics

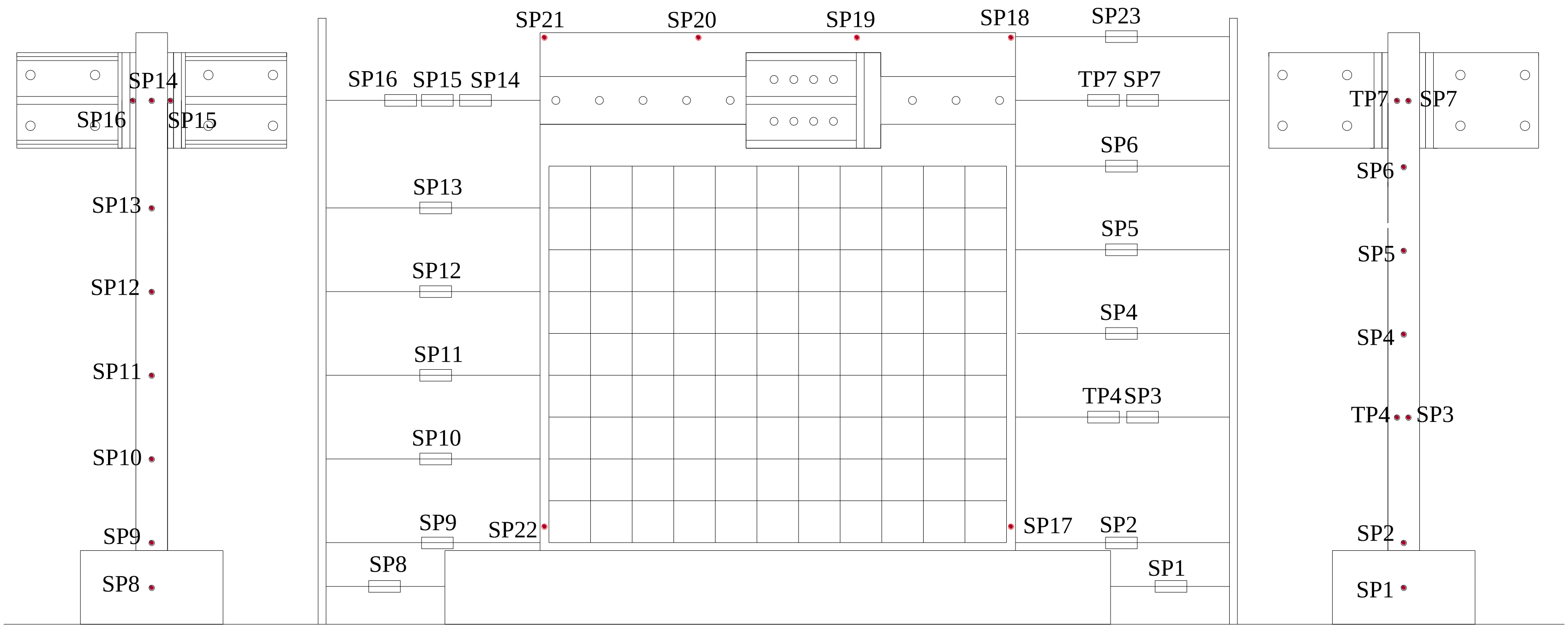

Figure C.37. In-plane and out-of-plane string potentiometers and Temposonics for SW1

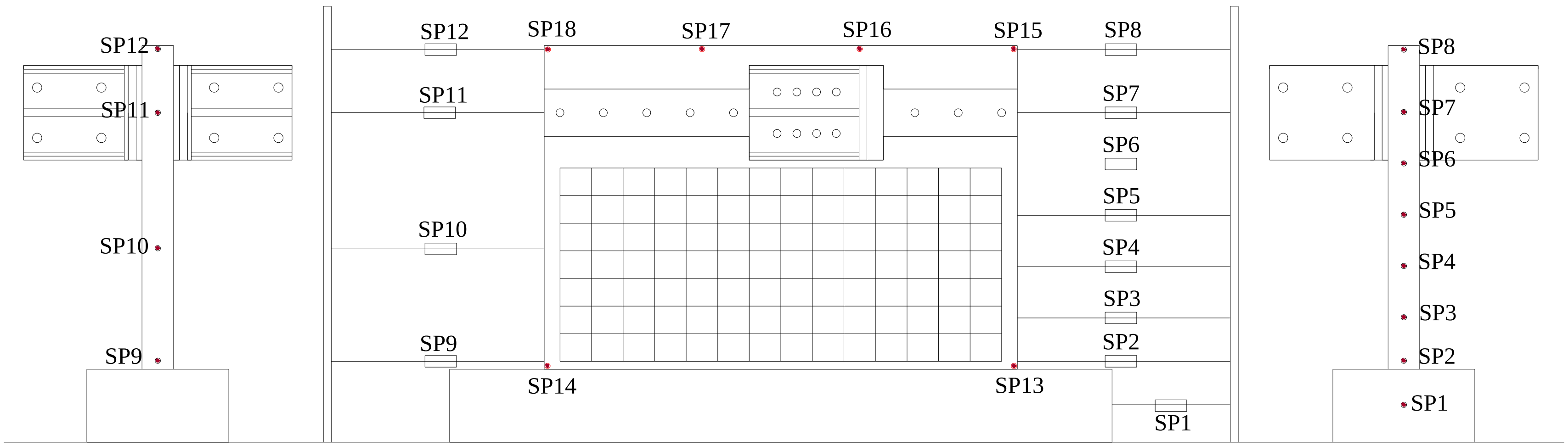

Figure C.38. In-plane and out-of-plane string potentiometers and Temposonics for SW2

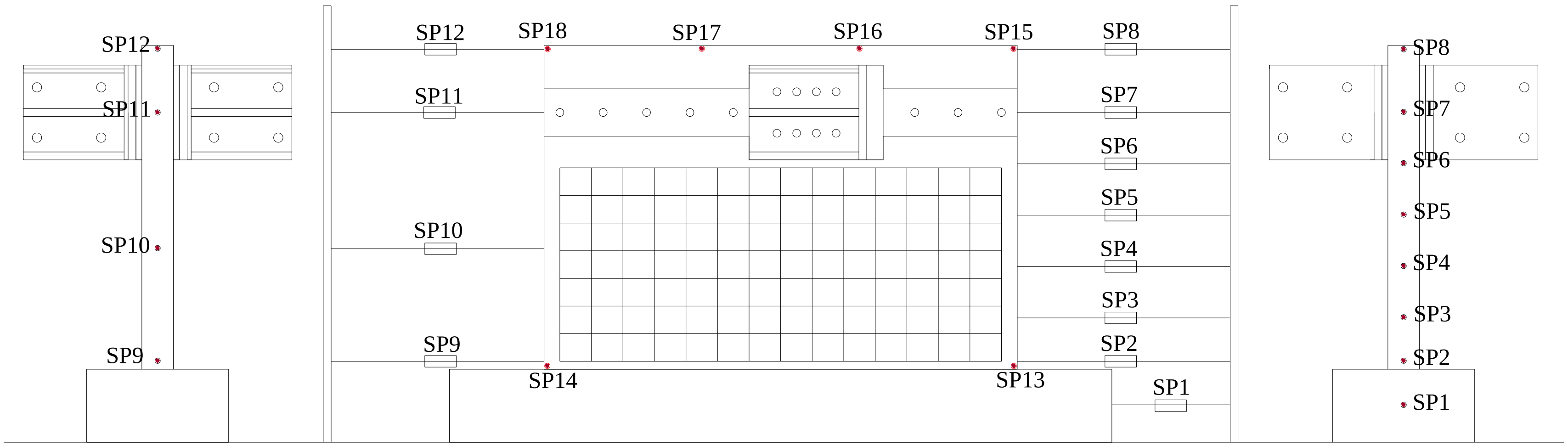

Figure C.39. In-plane and out-of-plane string potentiometers and Temposonics for SW3

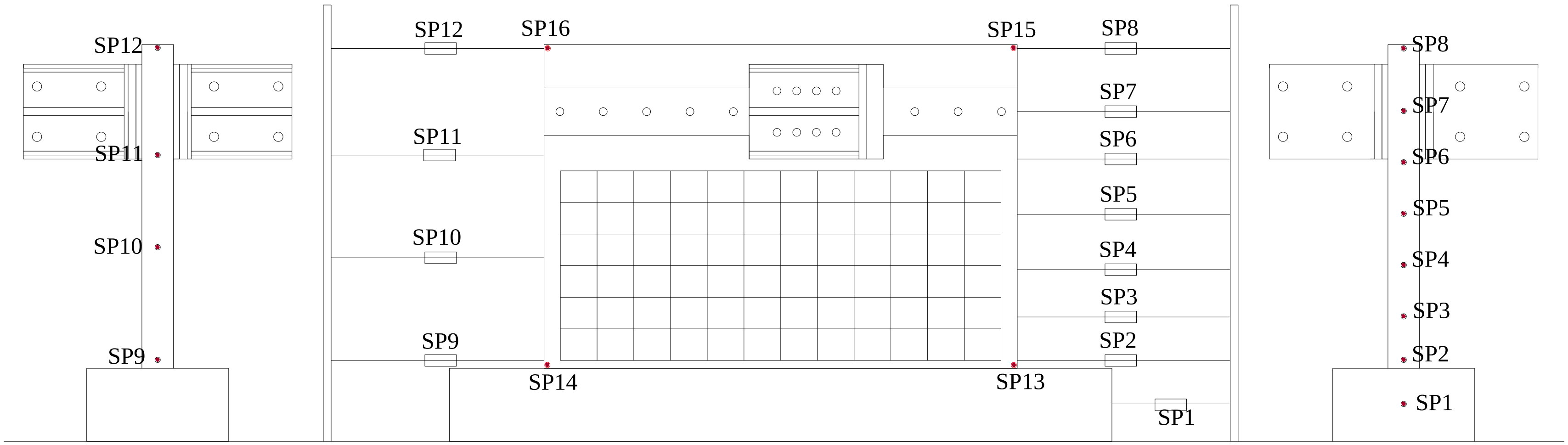

Figure C.40. In-plane and out-of-plane string potentiometers and Temposonics for SW4

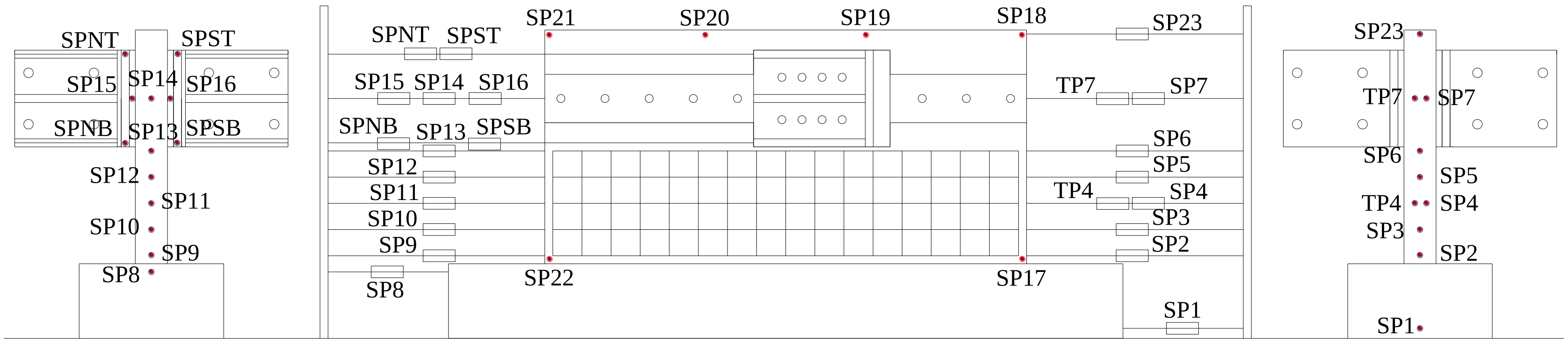

Figure C.41. In-plane and out-of-plane string potentiometers and Temposonics for SW5

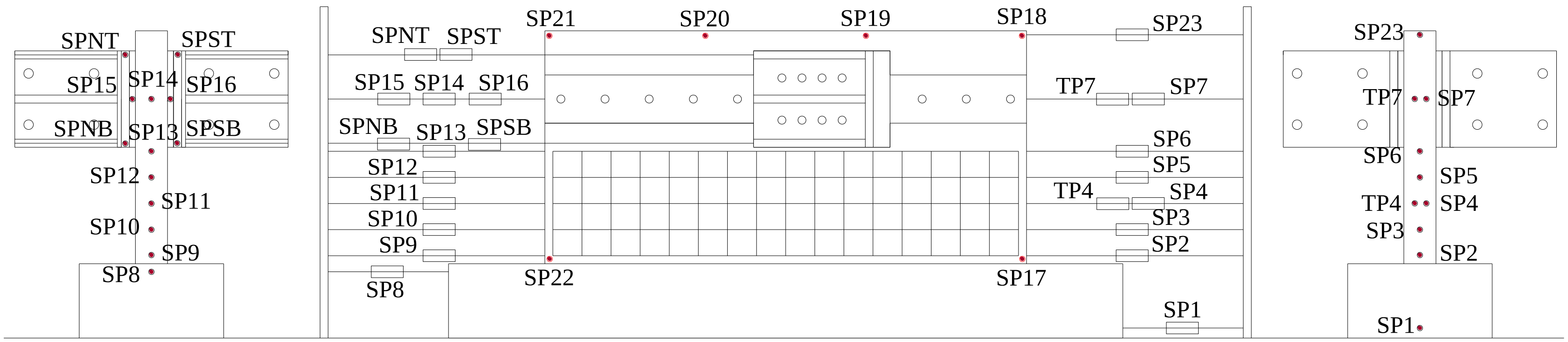

Figure C.42. In-plane and out-of-plane string potentiometers and Temposonics for SW6

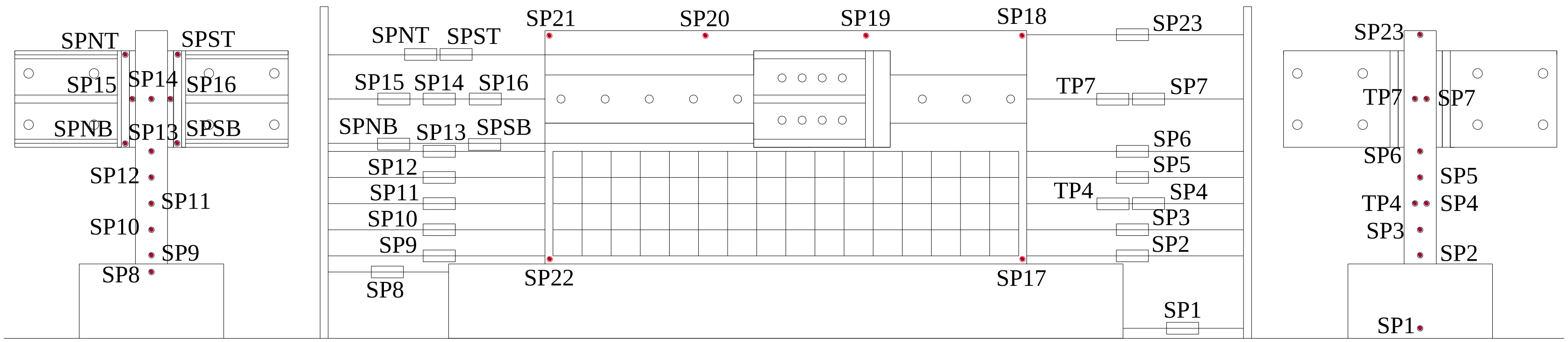

Figure C.43. In-plane and out-of-plane string potentiometers and Temposonics for SW7

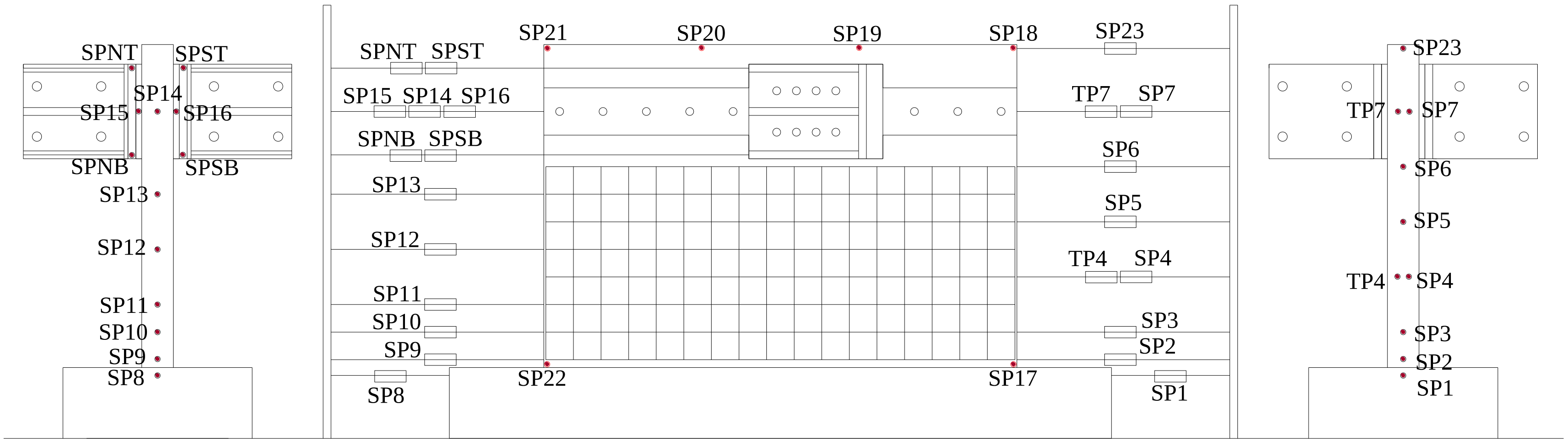

Figure C.44. In-plane and out-of-plane string potentiometers and Temposonics for SW8

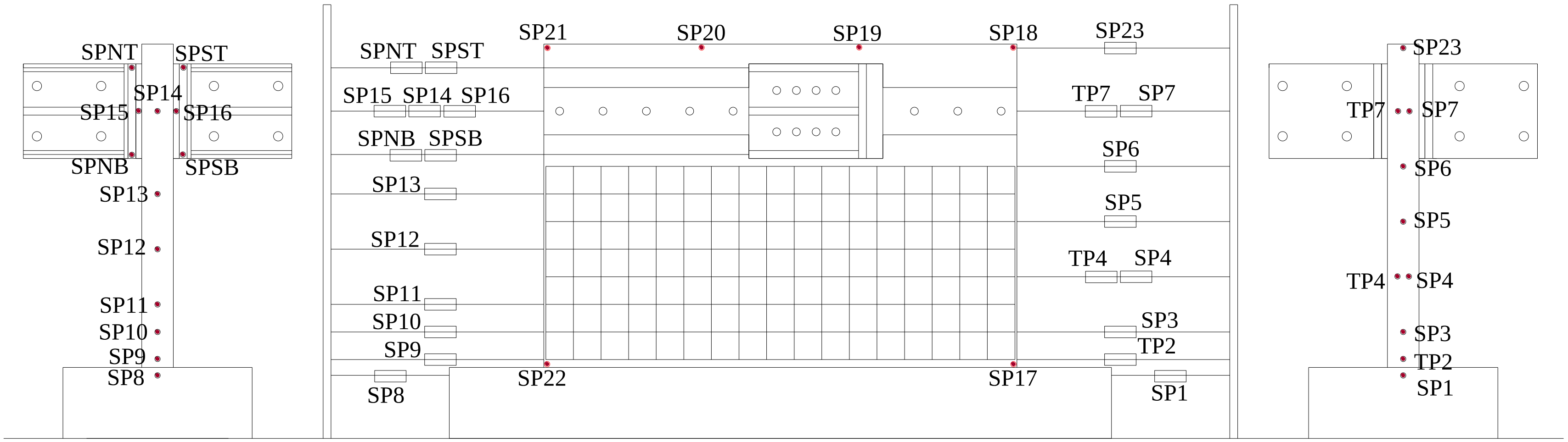

Figure C.45. In-plane and out-of-plane string potentiometers and Temposonics for SW9

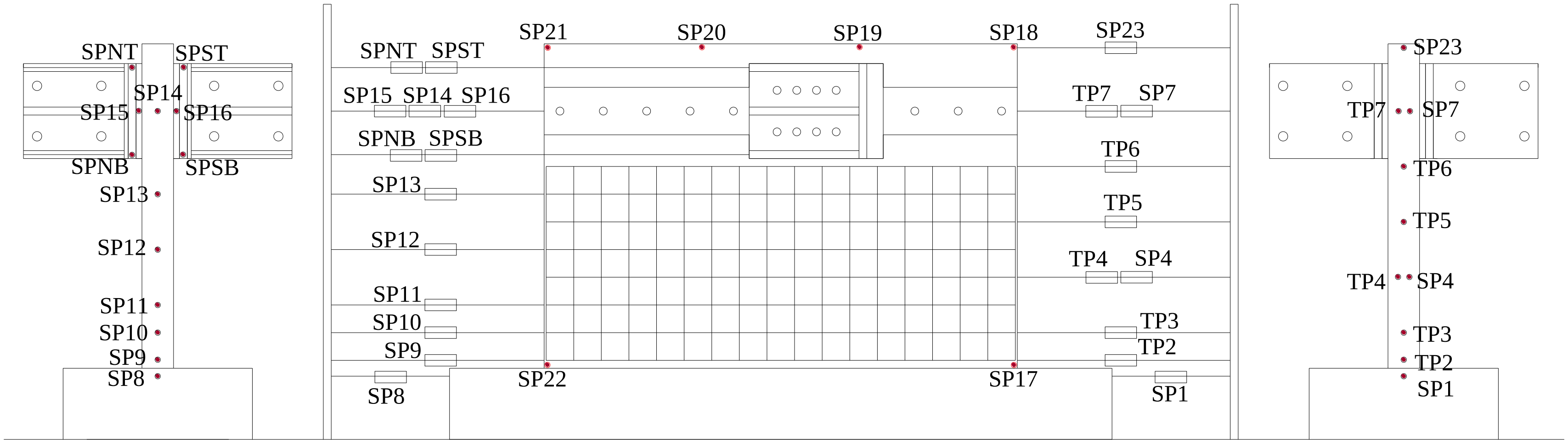

Figure C.46. In-plane and out-of-plane string potentiometers and Temposonics for SW10

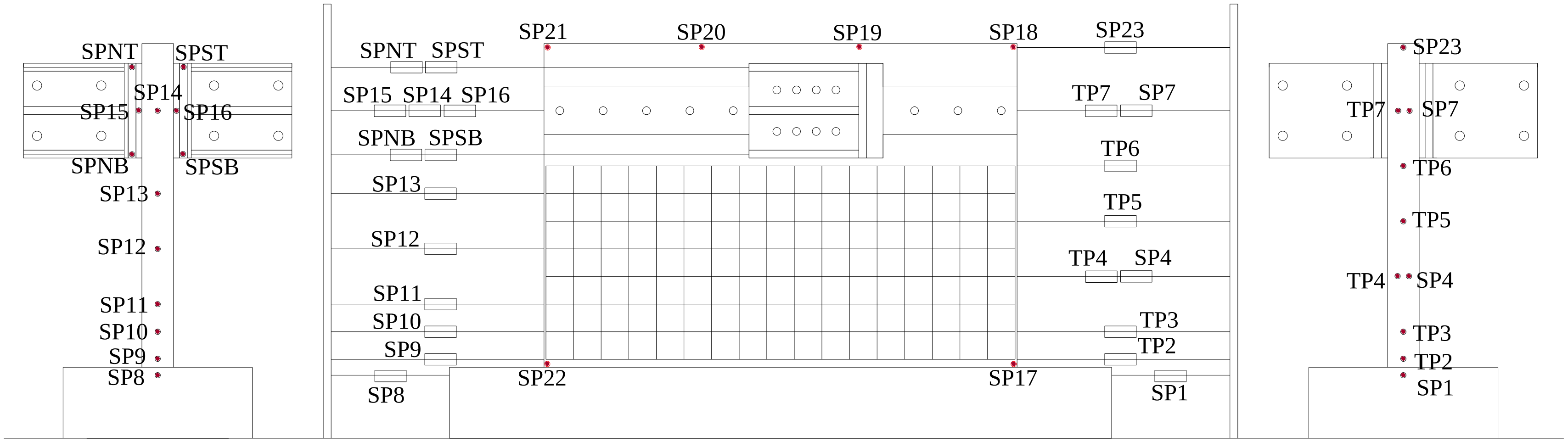

Figure C.47. In-plane and out-of-plane string potentiometers and Temposonics for SW11

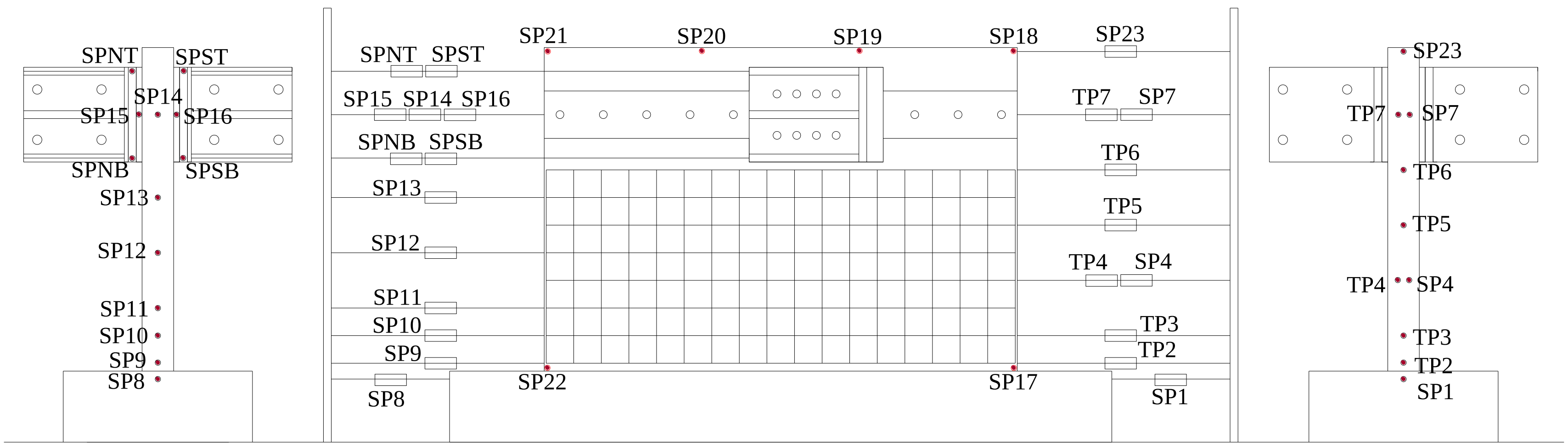

Figure C.48. In-plane and out-of-plane string potentiometers and Temposonics for SW12

C.3 Laboratory equipment specifications

C.3.1 MTS Systems Corporation servo-controlled static rated actuator model 243.90T (source: SEESL website, http://seesl.buffalo.edu)

Table C.1. MTS 243.90T actuator specifications

Parameter	Specification
Load Capacity	
Tension	440 kips
Compression	600 kips
Stroke	40 in.
Servovalve Type	MTS 252.25
Servo Controller	MTS 406, 458, 407, FlexTest
Servovalve	15 gpm
Peak Velocity*	0.393 in./sec

* Velocity assumes no load on actuator

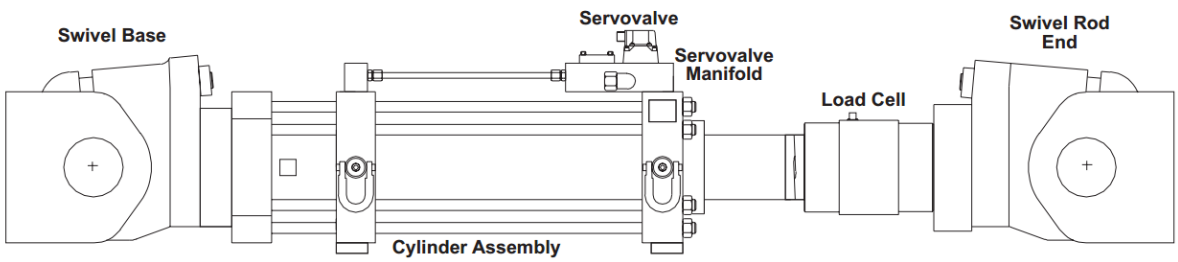

Figure C.49. MTS 243.90T actuator assembly

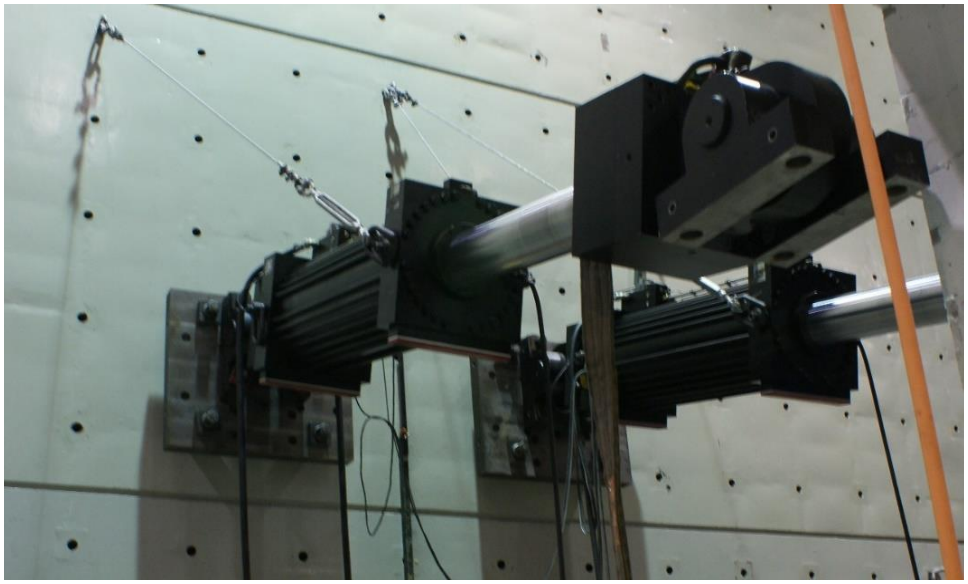

Figure C.50. MTS 243.90T actuators attached to the SEESL strong wall (pistons extended)

C.3.2 Space Age Control series D62 string potentiometers (source: SEESL website, http://seesl.buffalo.edu)

Table C.2. D62 string potentiometer specifications

Parameter	Specification
Power Requirement	5 to 26 VDC
Current	35 mA max at 5 VDC
Logic Output	open collector with Schmitt trigger and 10 Kohm pull-up resistor (push-pull differential line driver)
Power Consumption	150 mW max, 16 mA sink current at 0.40 VDC
Travel: Electrical, Mechanical	360° continuous
Mechanical Life	100 million shaft revolutions min
Resolution	8192 quadrature pulses per revolution
Output	2-bit (quadrature) code, A leads B by 90° w/CW
Operating Temperature	-4° to 212° F (-20° to 100° C)
Shock / Vibration	50 g for 11 ms / 50 to 500 Hz at 20 g
Case/Drum Materials	precision-machined, anodized 2024 aluminum
Displacement Cable	0.027 inch (0.6858 mm) diameter, 7-by-7 stranded stainless steel, 90-lb (400-N) min breaking strength
Displacement Cable Hardware	1 each of 300196 loop sleeve, 300292 copper sleeve, 300688 ball-end plug, 300495 pull ring, 160026 brass swivel, and 301003 nickel swivel; all items provided uncrimped
Nominal Mass	11 oz (312 g)
Environmental Sealing	NEMA 4X / IP 66Part Numbers

Figure C.51. Series D62 string potentiometer

C.3.3 MTS Temposonic^{TM} brand linear displacement transducer system with analog output (source: SEESL website, http://seesl.buffalo.edu)

The Temposonics^{TM} brand linear displacement transducer precisely senses the position of an external magnet to measure displacements with high resolution. The system measures the time interval between an interrogating pulse and a return pulse. The interrogating pulse is transmitted through the transducer waveguide and the return pulse is generated by a permanent magnet representing the displacement to be measured. The system includes a linear displacement transducer, a magnet, and the electronics necessary to generate the interrogating pulse, sense the return pulse and develop an analog output signal.

Table C.3. MTS Temposonic specifications

Parameter	Specification
Input Voltage	+15 Vdc (± 2%) @ 250 mA with <1% ripple -15 Vdc (± 2%) @ 65 mA with <1% ripple
Displacement	4 in. or 8 in.
Nonlinearity	< ± 0.05% full scale or min ± 0.0001 in
Repeatability	± 0.001% of full scale or 0.001
Frequency Response	200 Hz to 50 Hz (typical)
Transducer Temperature Coefficient	10 ppm/ºF
Operating Temperature	35 ºF to 150 ºF
Output	0 to 10 Vdc and a TTL compatible, pulse-width modu lated output
Output Impedance	< 10 ohms
Velocity Output	± 10 Vdc traveling away from the head assembly; -10 Vdc traveling toward the head assembly

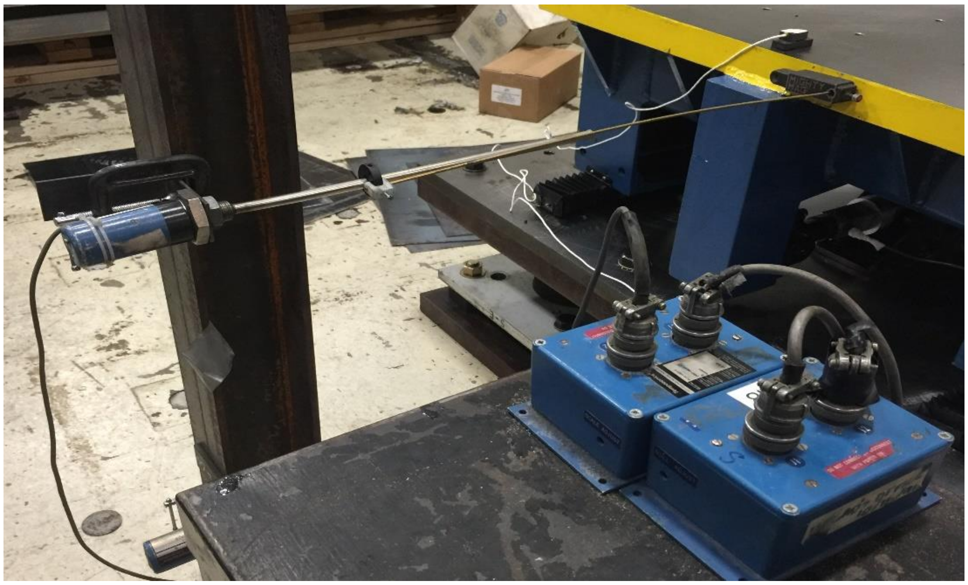

Figure C.52. MTS Temposonic assembly

C.3.4 LW12 wirebound precision linear motion potentiometer (source: manufacturer's website, http://www.etisystems.com)

Table C.4. LW12 linear potentiometer specifications

Parameter	Specification
Life Expectancy	20 million strokes
Resistance Tolerance	5%
Linearity Tolerance	0.5% to 1.5%
Power Rating	0.2 to 1.2 Watt
Electrical Stroke	1" to 4"
Friction	1.8 oz.
Unit Weight	10 to 35 grams

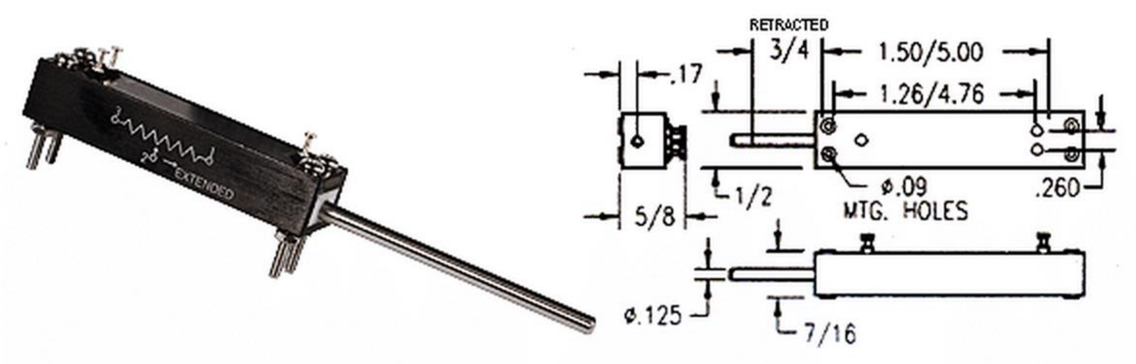

Figure C.53. LW12 linear potentiometer assembly

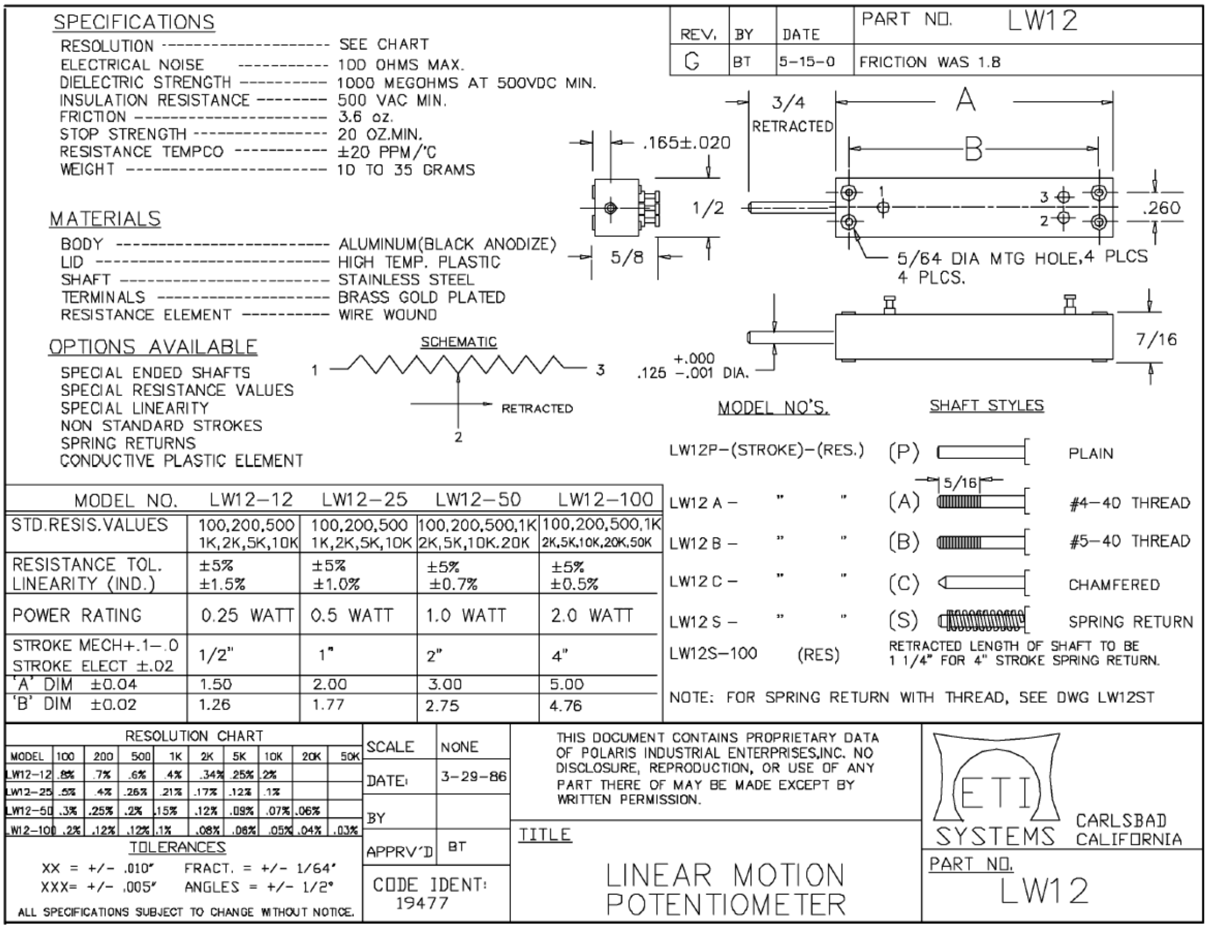

SPECIFICATIONS

- RESOLUTION -------------------- SEE CHART
- ELECTRICAL NOISE ----------- 100 OHMS MAX.
- DIELECTRIC STRENGTH ---------- 1000 MEGOHMS AT 500VDC MIN.
- INSULATION RESISTANCE -------- 500 VAC MIN.
- FRICTION ---------------------- 3.6 oz.
- STOP STRENGTH --------------- 20 OZ.MIN.
- RESISTANCE TEMPCO ----------- ±20 PPM/°C
- WEIGHT ---------------------- 10 TO 35 GRAMS

MATERIALS

- BODY ------------------------ ALUMINUM(BLACK ANODIZE)
- LID -------------------------- HIGH TEMP. PLASTIC
- SHAFT ----------------------- STAINLESS STEEL
- TERMINALS ------------------ BRASS GOLD PLATED
- RESISTANCE ELEMENT ---------- WIRE WOUND

OPTIONS AVAILABLE

- SPECIAL ENDED SHAFTS
- SPECIAL RESISTANCE VALUES
- SPECIAL LINEARITY
- NON STANDARD STROKES
- SPRING RETURNS
- CONDUCTIVE PLASTIC ELEMENT

REV.	BY	DATE	PART NO. LW12
G	BT	5-15-0	FRICTION WAS 1.8

MODEL NO.	LW12-12	LW12-25	LW12-50	LW12-100
STD.RESIS.VALUES	100,200,500 1K,2K,5K,10K	100,200,500 1K,2K,5K,10K	100,200,500,1K 2K,5K,10K.20K	100,200,500,1K 2K,5K,10K,20K,50K
RESISTANCE TOL. LINEARITY (IND.)	±5% ±1.5%	±5% ±1.0%	±5% ±0.7%	±5% ±0.5%
POWER RATING	0.25 WATT	0.5 WATT	1.0 WATT	2.0 WATT
STROKE MECH+.1−.0 STROKE ELECT ±.02	1/2"	1"	2"	4"
'A' DIM ±0.04	1.50	2.00	3.00	5.00
'B' DIM ±0.02	1.26	1.77	2.75	4.76

MODEL NO'S. / SHAFT STYLES

LW12P−(STROKE)−(RES.)	(P)	PLAIN
LW12 A − " "	(A)	#4−40 THREAD
LW12 B − " "	(B)	#5−40 THREAD
LW12 C − " "	(C)	CHAMFERED
LW12 S − " "	(S)	SPRING RETURN
LW12S−100 (RES)		RETRACTED LENGTH OF SHAFT TO BE 1 1/4" FOR 4" STROKE SPRING RETURN.

NOTE: FOR SPRING RETURN WITH THREAD, SEE DWG LW12ST

RESOLUTION CHART

MODEL	100	200	500	1K	2K	5K	10K	20K	50K
LW12−12	.8%	.7%	.6%	.4%	.34%	.25%	.2%		
LW12−25	.5%	.4%	.26%	.21%	.17%	.12%	.1%		
LW12−50	.3%	.25%	.2%	.15%	.12%	.09%	.07%	.06%	
LW12−100	.2%	.12%	.12%	.1%	.08%	.06%	.05%	.04%	.03%

TOLERANCES

XX = +/− .010" FRACT. = +/− 1/64"
XXX= +/− .005" ANGLES = +/− 1/2°

ALL SPECIFICATIONS SUBJECT TO CHANGE WITHOUT NOTICE.

SCALE	NONE
DATE:	3−29−86
BY	
APPRV'D	BT
CODE IDENT: 19477	

THIS DOCUMENT CONTAINS PROPRIETARY DATA OF POLARIS INDUSTRIAL ENTERPRISES,INC. NO DISCLOSURE, REPRODUCTION, OR USE OF ANY PART THERE OF MAY BE MADE EXCEPT BY WRITTEN PERMISSION.

TITLE

LINEAR MOTION POTENTIOMETER

ETI SYSTEMS CARLSBAD CALIFORNIA

PART NO. LW12

Figure C.54. LW12 linear potentiometer data sheet

C.3.5 Krypton K600 Portable CMM System (source: SEESL website, http://seesl.buffalo.edu)

The Krypton K600 camera system measures the three-dimensional positions of infrared LED sensors using linear CCD cameras. The position in space of each LED sensor is calculated through triangulation. In a single setup, it covers a field of view consisting of three different zones. The different zones and their dimensions are shown in Figure C.55 (and are summarized in Table C.6). The LED sensors can be positioned between 1.5 to 6 meters (approximately) from the camera. When tracking in two-dimensions, a maximum area of approximately 3.6 meters x 2.6 meters can be covered when the camera is placed at around 6 meters from the LED sensors. The accuracies on the different zones of measurements are presented in Table C.7.

Table C.5. Krypton K600 specifications

Parameter	Specification
Dimensions	1140 mm x 170 mm x 210 mm
Weight	18 kg
Sampling rate	3000 / (# of LEDs)
Resolution	2 microns at 2.5 m distance from the camera
Measurement Volume	17 m^3

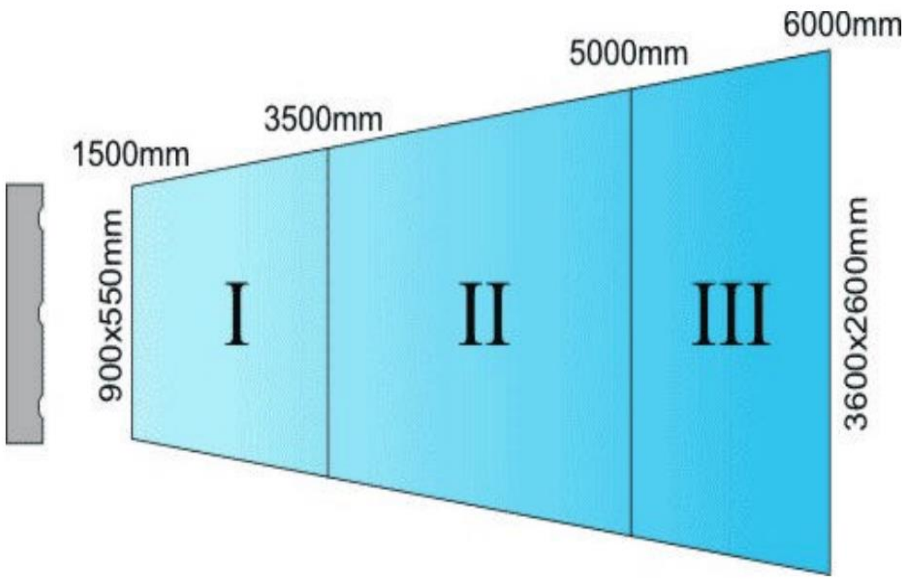

Figure C.55. Krypton K600 camera field of view

Table C.6. Krypton K600 camera field of view

Zone	Height (m)	Width (m)	Distance (m)
0	0.9	0.5	1.5 (min)
I	1.7	1.8	3.5 (max)
II	2.4	3.3	5.0 (max)
III	2.6	3.6	6.0 (max)

Table C.7. Krypton K600 accuracies on the different zones

Zone	Volumetric	Single Point
I	90mm + 10mm/m	60mm + 7mm/m
II	90mm + 25mm/m	60mm + 17mm/m
III	190mm + 25mm/m	130mm + 17mm/m

Figure C.56. Krypton K600 camera assembly

C.3.6 YFLA-5-5L strain gages

The YFLA-5-5L strain gages are made by Tokyo Sokki Kenkyujo Co., Ltd. (http://www.tml.jp/e) and exclusively distributed in the United States by Texas Measurements, Inc. (http://www.straingage.com). The YFLA-5-5L is designed for measurement of large strain (15-20%). It has a gage length and width of 5 mm and 2 mm, respectively. The backing length and width are 12 mm and 4 mm, respectively. The resistance of the gage is 120 ohms.

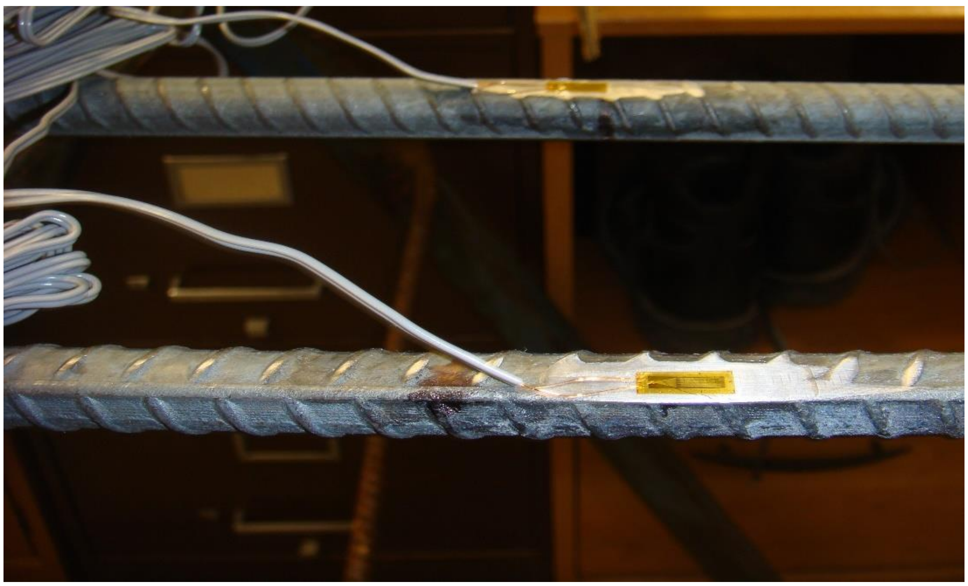

Figure C.57. YFLA-5-5L strain gages

C.3.7 GigaPan camera system

A GigaPan setup consists of a high resolution digital camera attached to a robotic panohead mounted on a tripod. The robotic panohead makes it possible to take a series of high resolution pictures of small portions of the wall. The GigaPan Stitch software then assembles, aligns and blends the individual images into one large panorama.

Figure C.58. The GigaPan system (source: http://gigapan.com)

C.3.8 Pacific Instruments model 6000 data acquisition system (Source: SEESL website, http://seesl.buffalo.edu)

The 6000 Mainframe has an IEEE-488 interface for control and data output with mounting for 16 input and output modules. The Mainframe is running Version 8.1 of PI660 software. The system was configured for 132 channels at the time of testing of the wall specimens. It can support up to 31 additional slave enclosures or up to 32,000 channels.

Figure C.59. Pacific Instruments model 6000 data acquisition system

APPENDIX D

REFERENCE DISPLACEMENTS AND LOADING PROTOCOLS

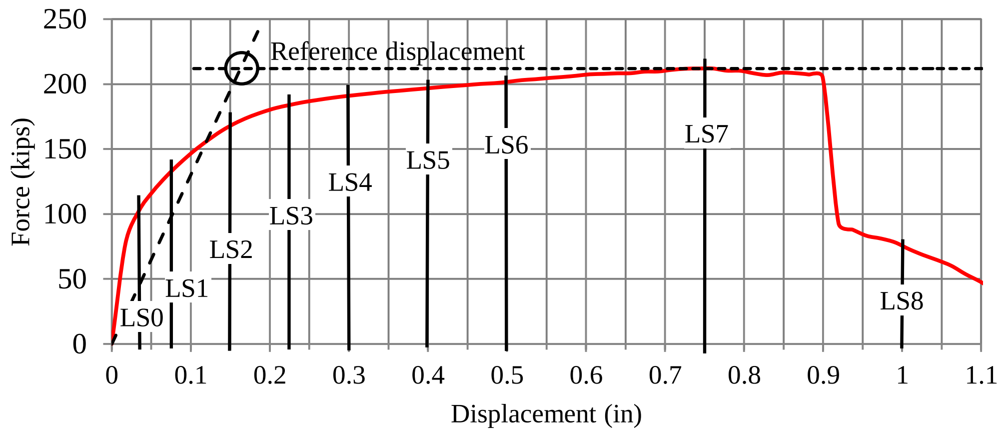

Figure D.1. Reference displacement for SW1

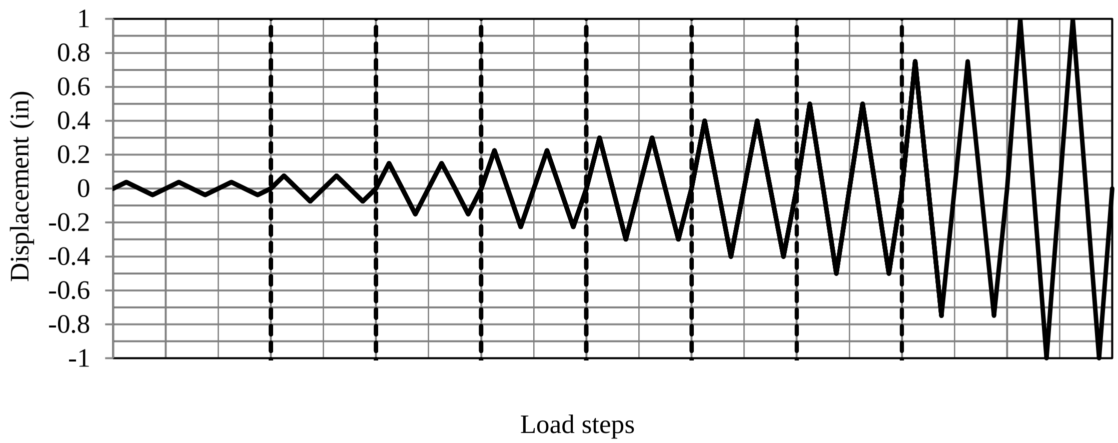

Figure D.2. Loading protocol for SW1

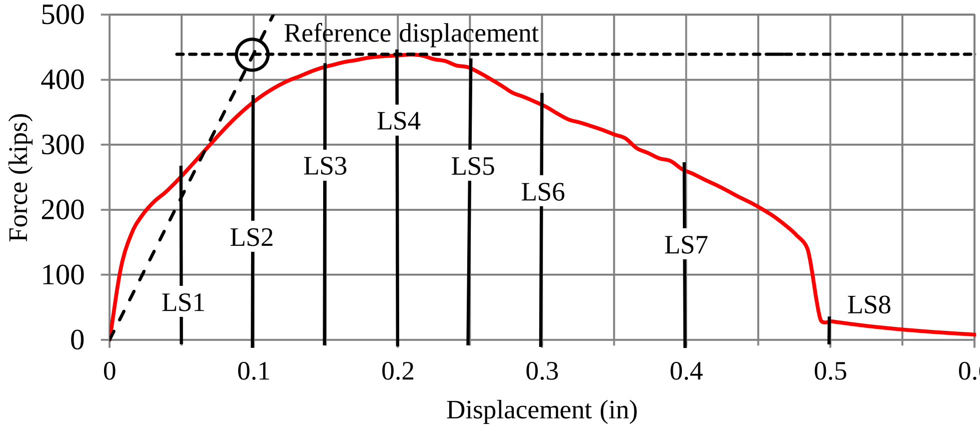

Figure D.3. Reference displacement for SW2

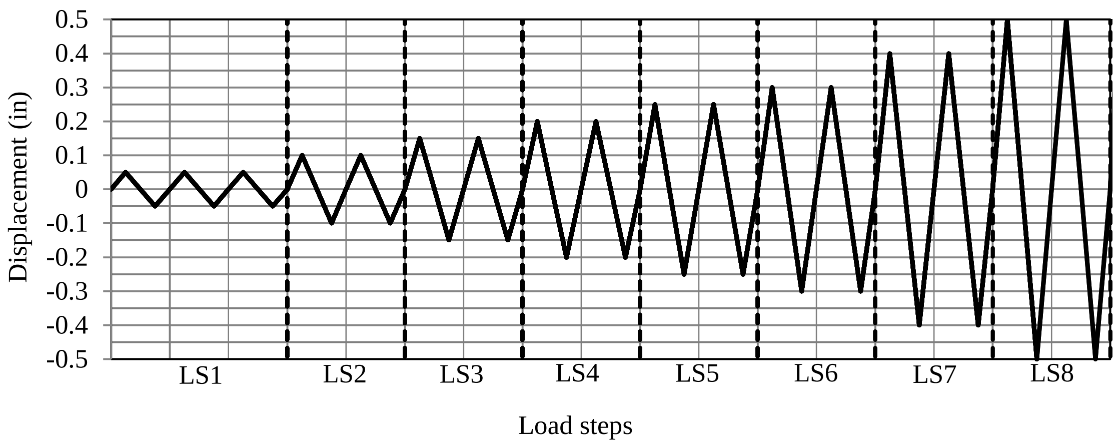

Figure D.4. Loading protocol for SW2

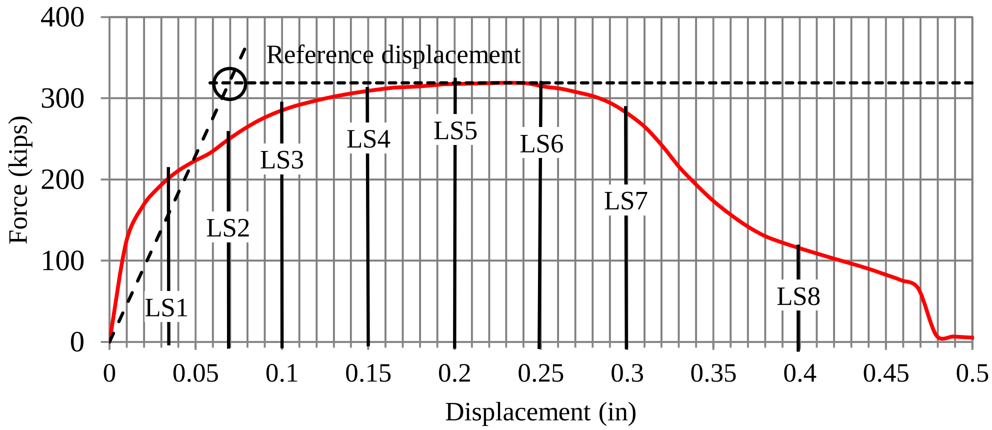

Figure D.5. Reference displacement for SW3

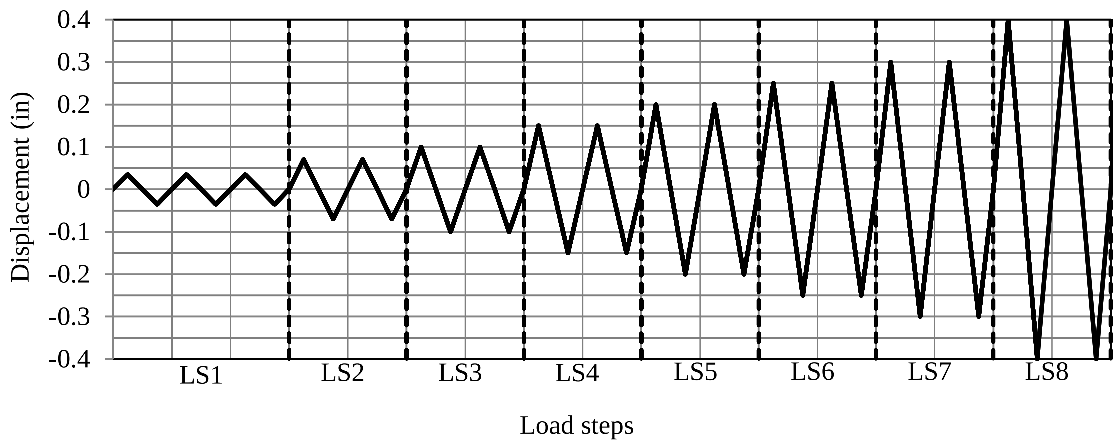

Figure D.6. Loading protocol for SW3

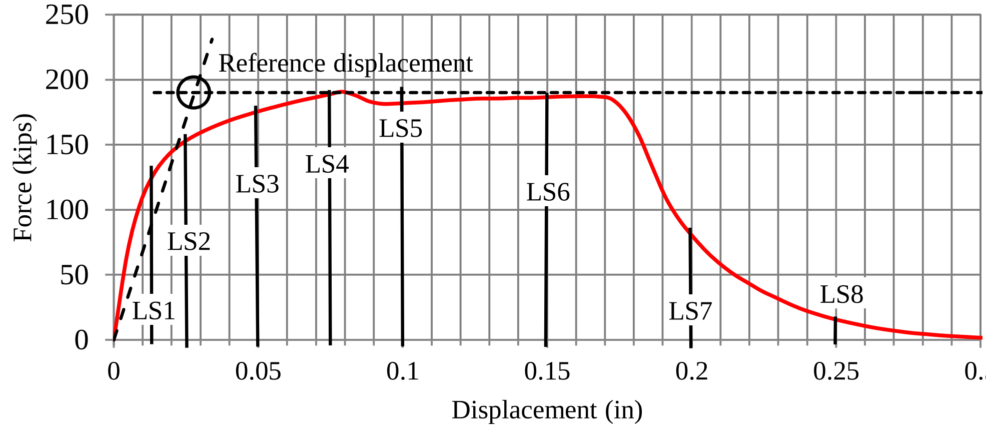

Figure D.7. Reference displacement for SW4

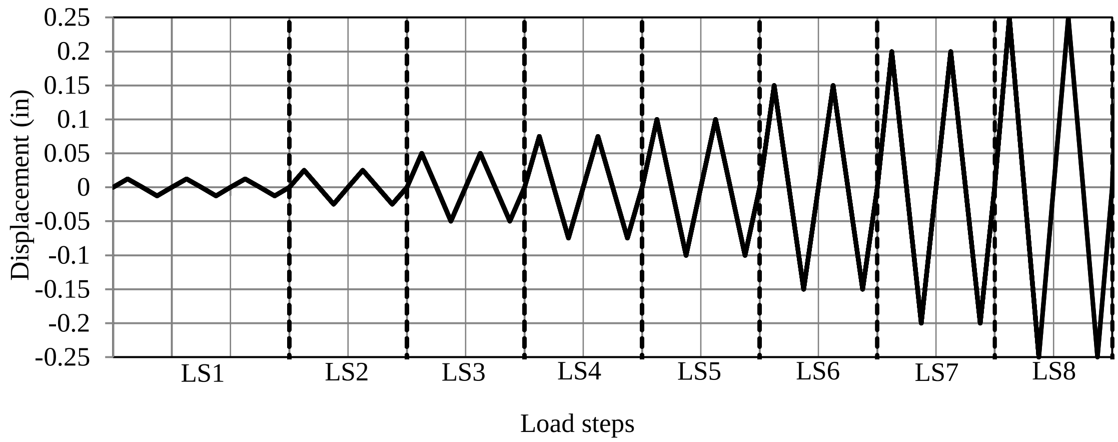

Figure D.8. Loading protocol for SW4

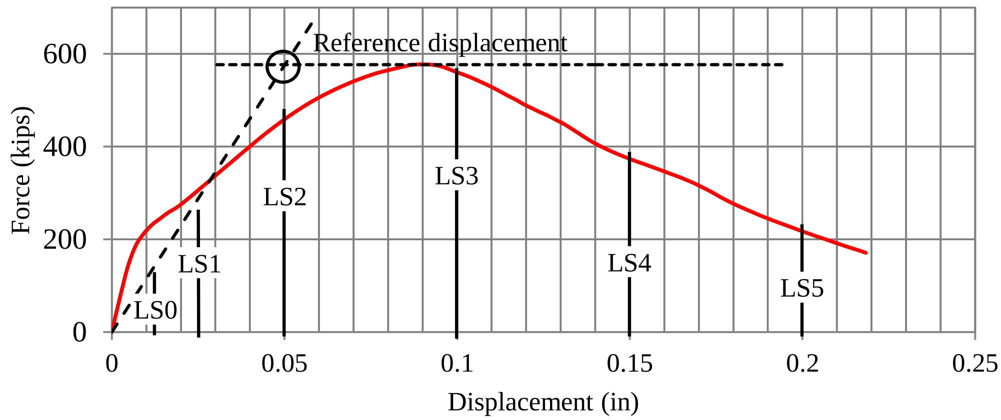

Figure D.9. Reference displacement for SW5

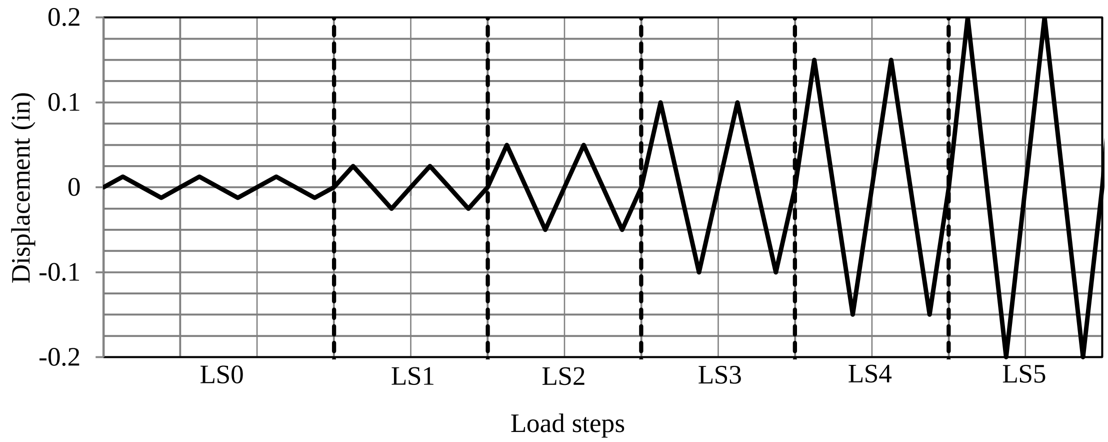

Figure D.10. Loading protocol for SW5

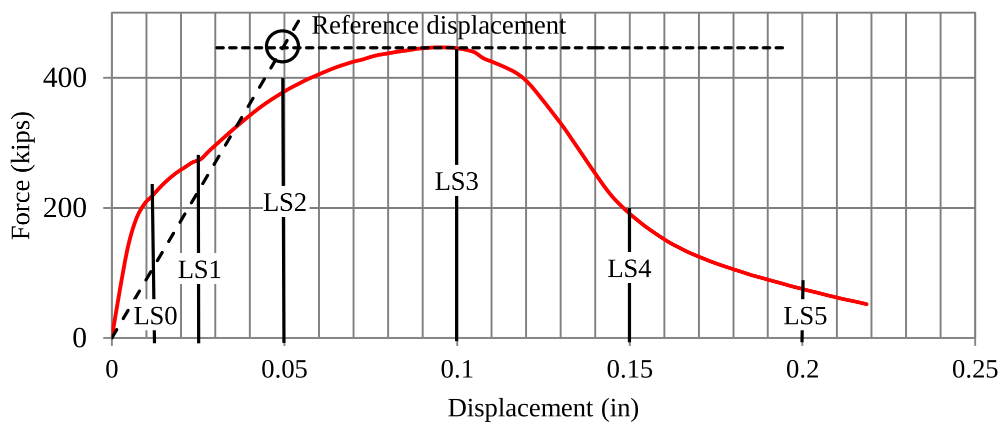

Figure D.11. Reference displacement for SW6

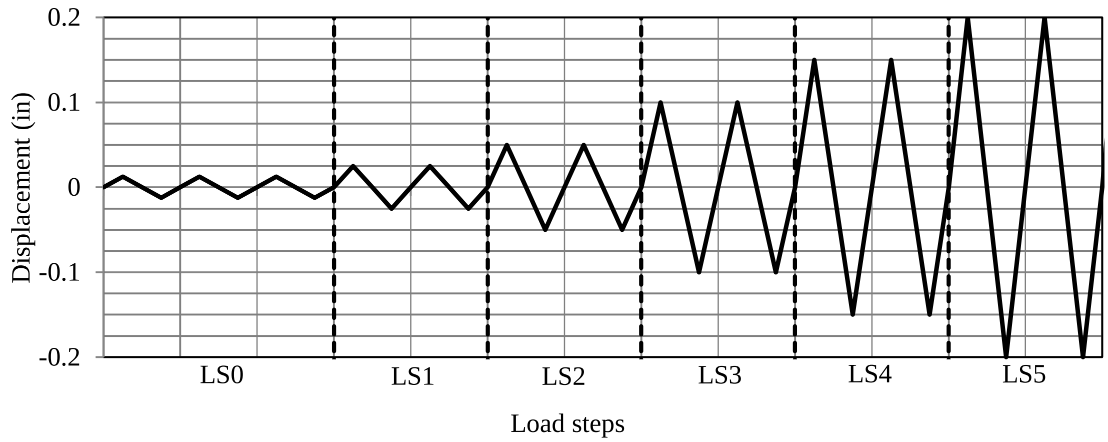

Figure D.12. Loading protocol for SW6

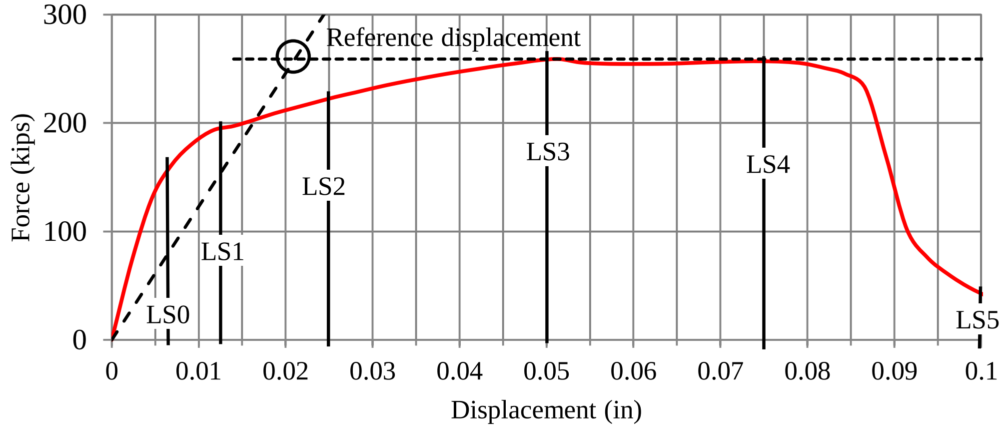

Figure D.13. Reference displacement for SW7

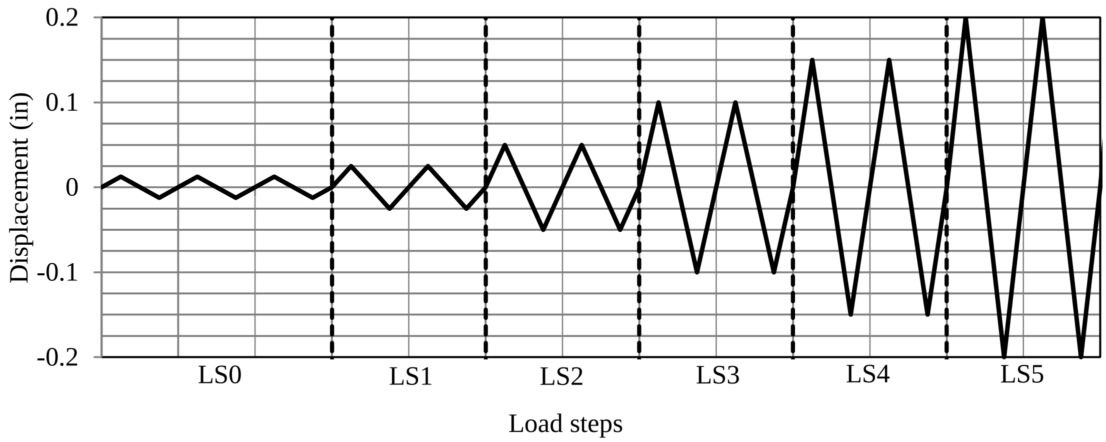

Figure D.14. Loading protocol for SW7

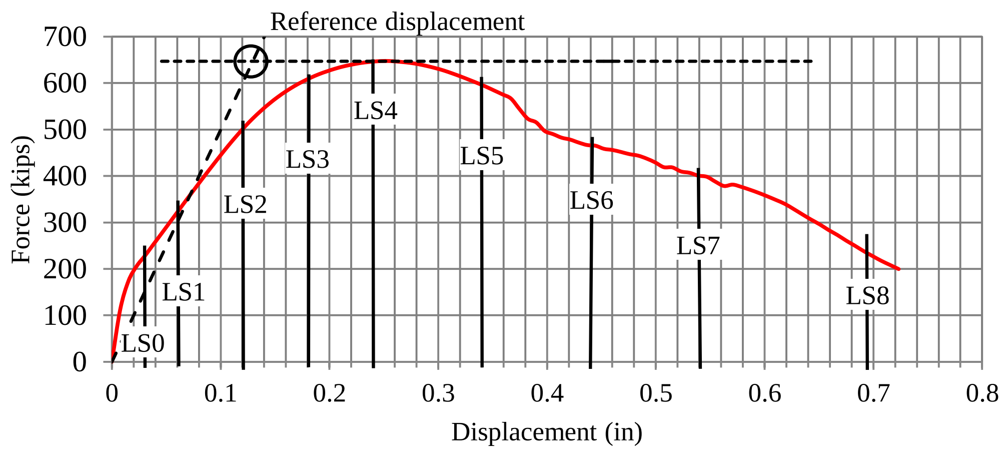

Figure D.15. Reference displacement for SW8

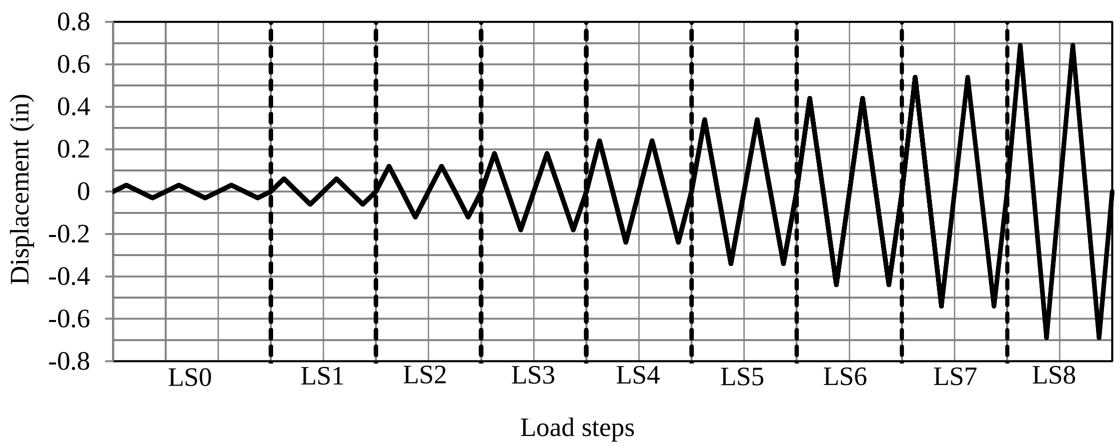

Figure D.16. Loading protocol for SW8

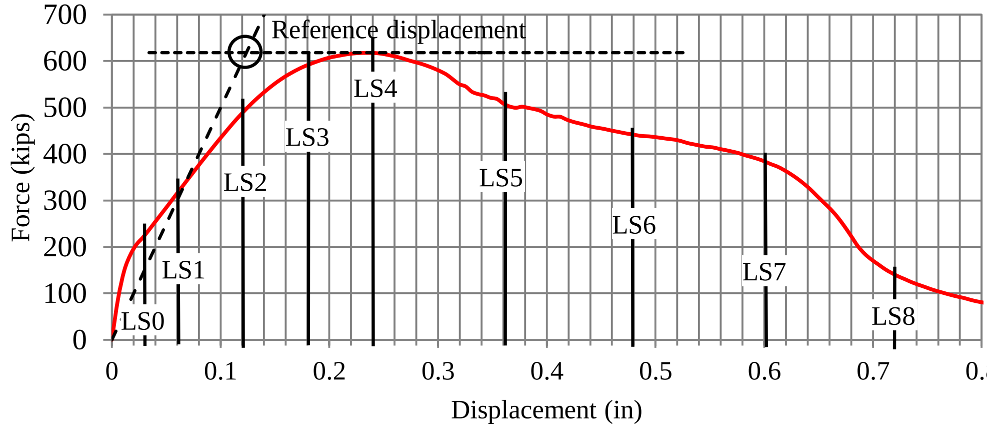

Figure D.17. Reference displacement for SW9

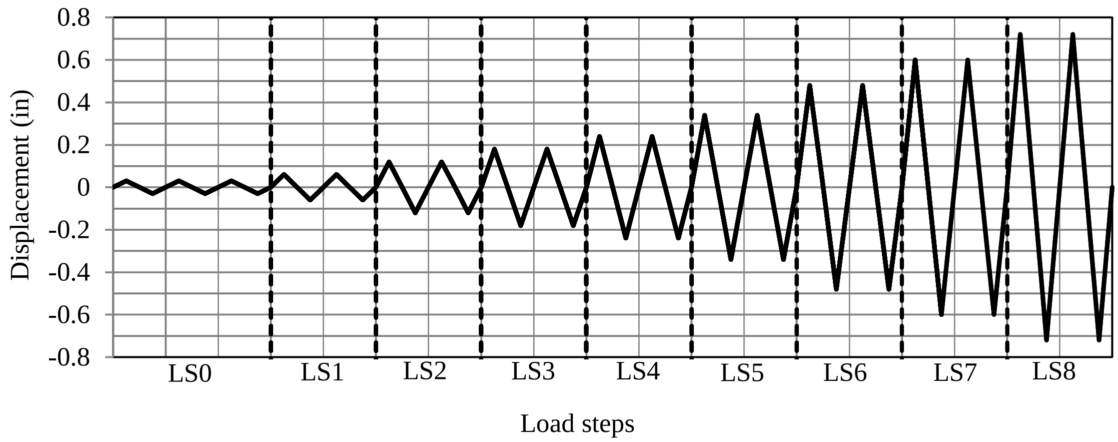

Figure D.18. Loading protocol for SW9

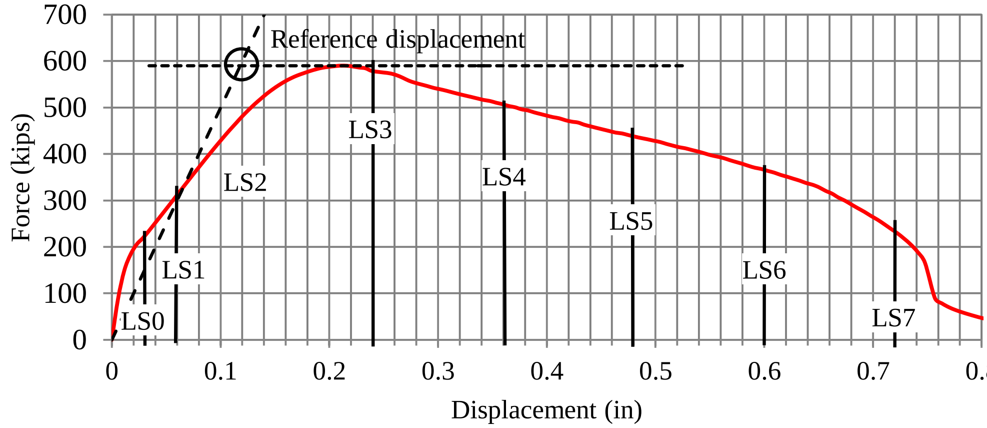

Figure D.19. Reference displacement for SW10

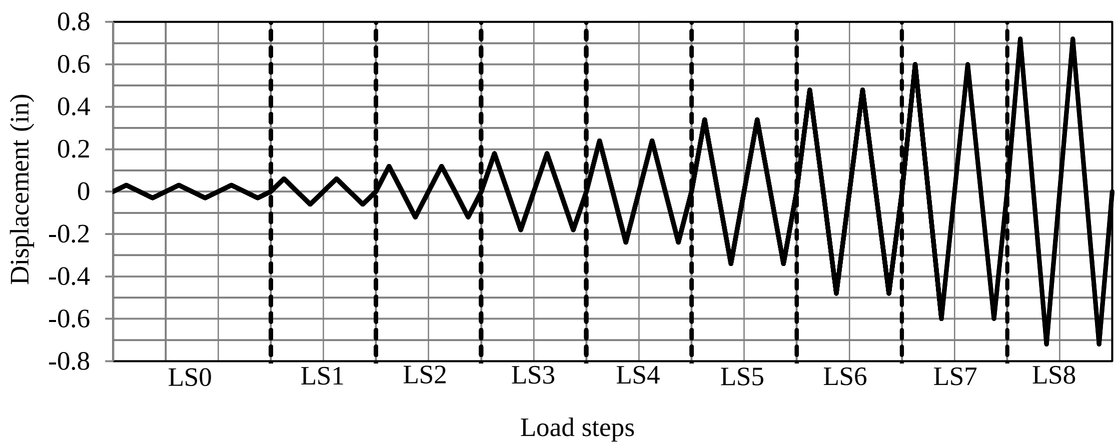

Figure D.20. Loading protocol for SW10

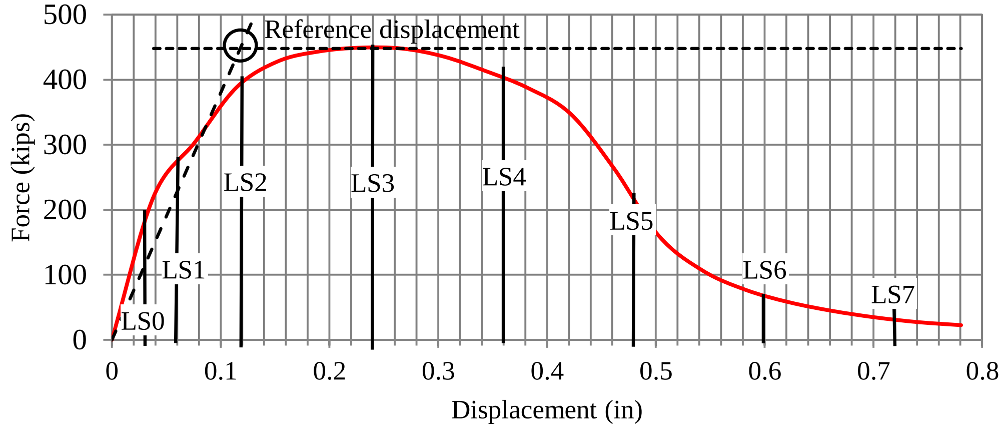

Figure D.21. Reference displacement for SW11

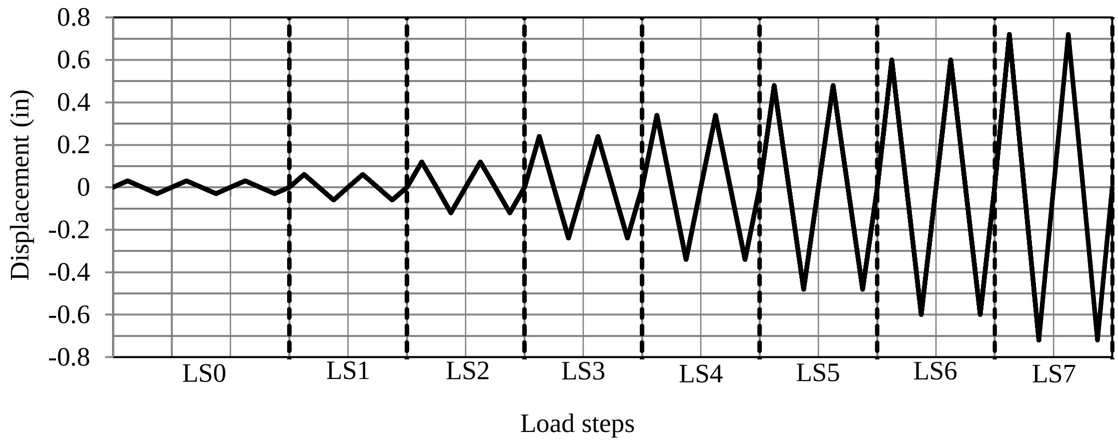

Figure D.22. Loading protocol for SW11

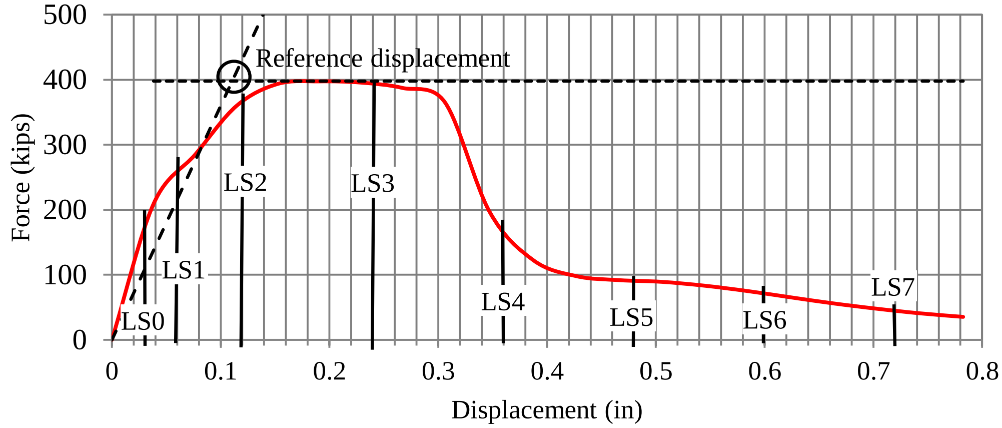

Figure D.23. Reference displacement for SW12

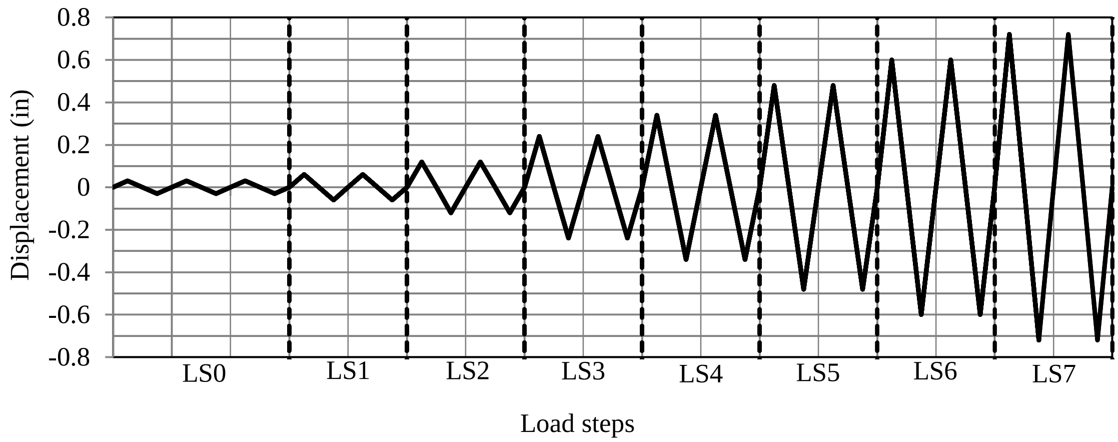

Figure D.24. Loading protocol for SW12

APPENDIX E

PHOTOGRAPHS OF TEST SPECIMENS

E.1 SW1

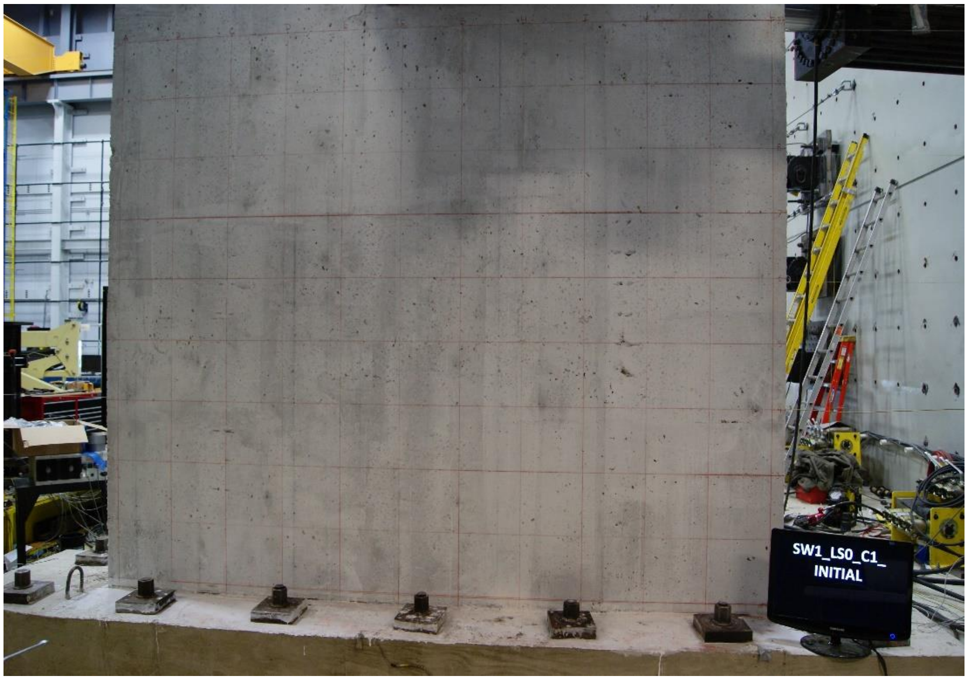

Figure E.1. SW1 before testing

Figure E.2. Damage to SW1 at 0.62% drift ratio

Figure E.3. Damage to SW1 at -0.61% drift ratio

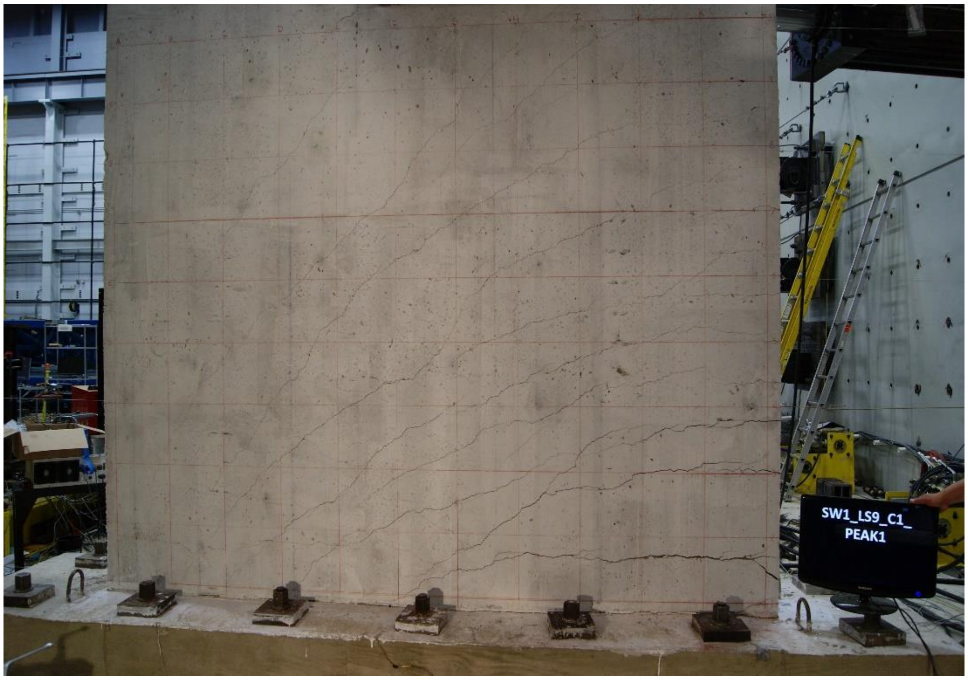

Figure E.4. Damage to SW1 at 1.30% drift ratio (peak strength)

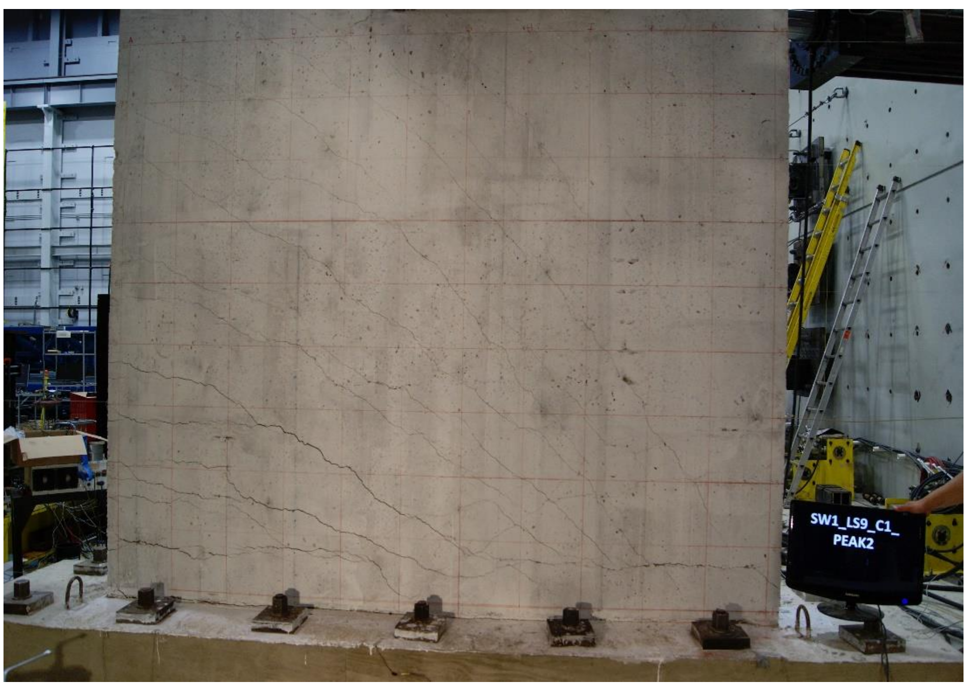

Figure E.5. Damage to SW1 at -1.28% drift ratio

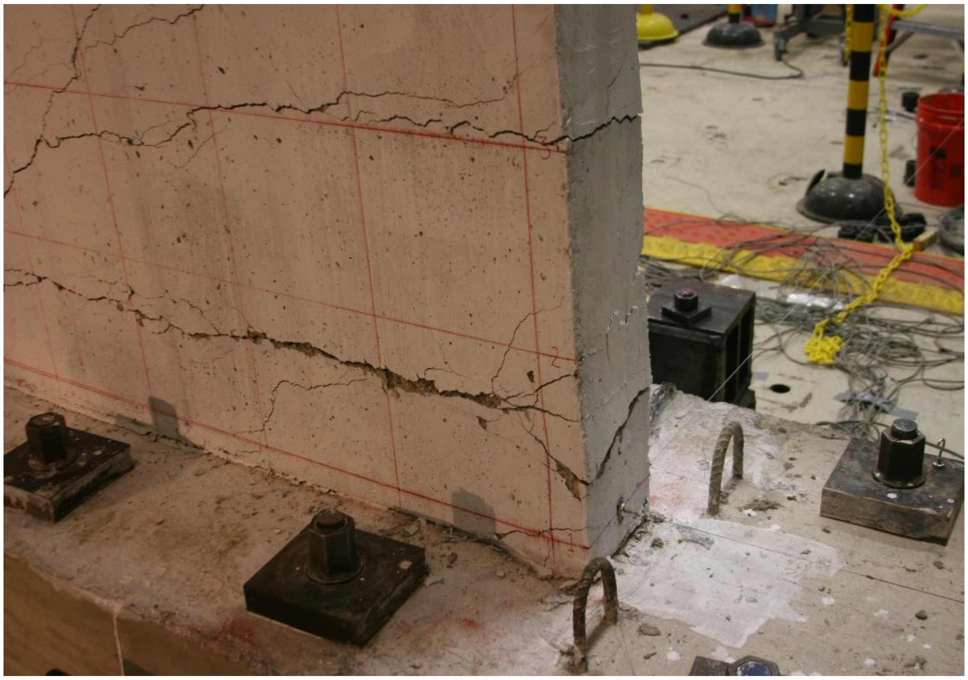
Figure E.6. Damage to SW1 at 1.67% drift ratio

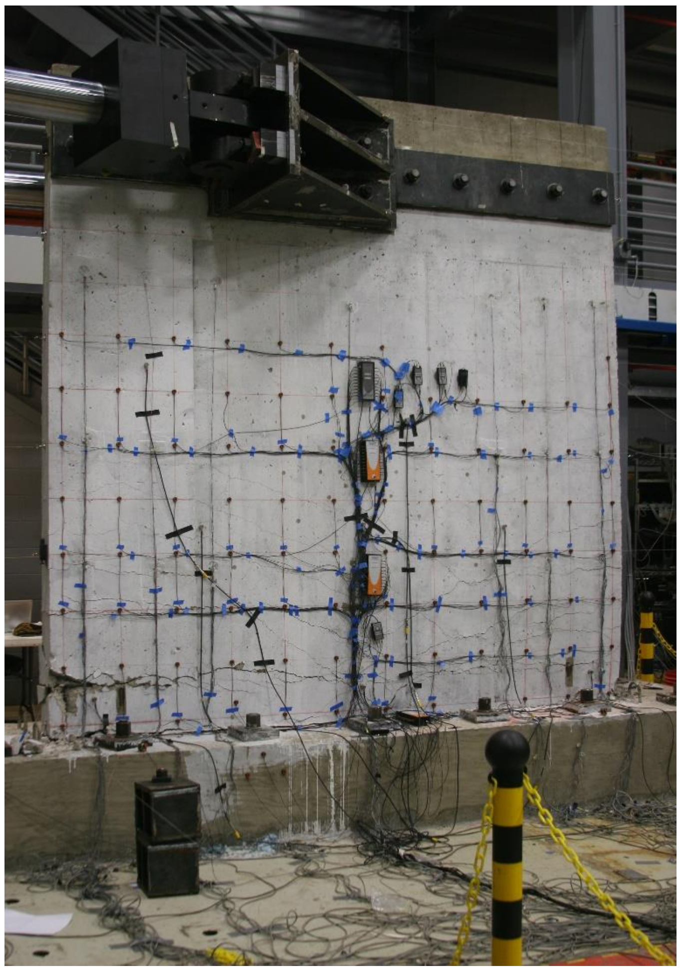

Figure E.7. Damage to SW1 at the end of testing

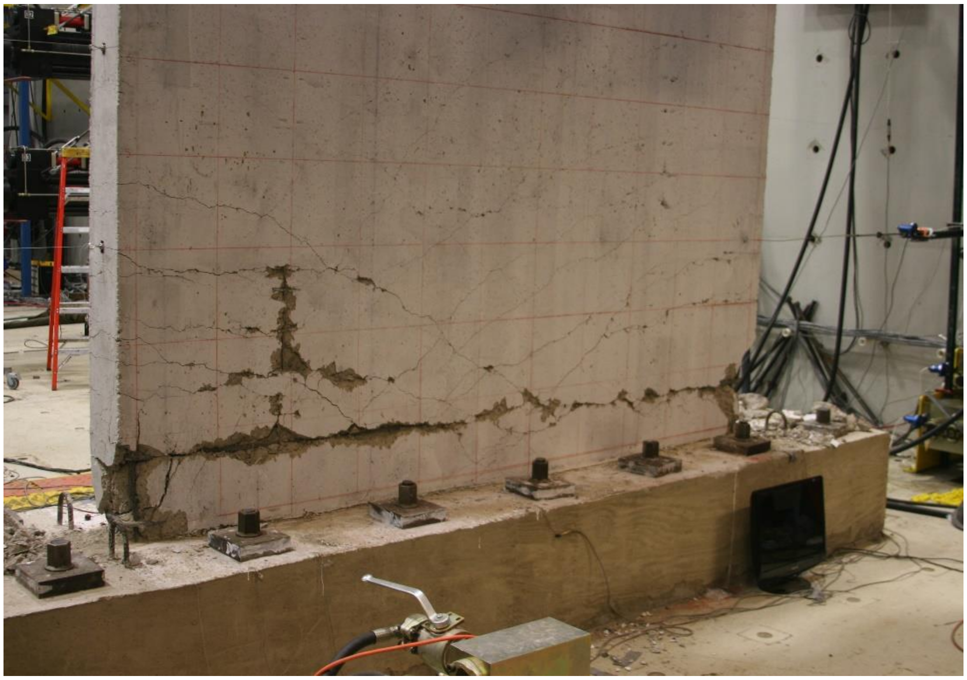

Figure E.8. Damage to SW1 at the end of testing

Figure E.9. Damage to SW1 at the end of testing

Figure E.10. Damage to SW1 at the end of testing

Figure E.11. Damage to SW1 at the end of testing

E.2 SW2

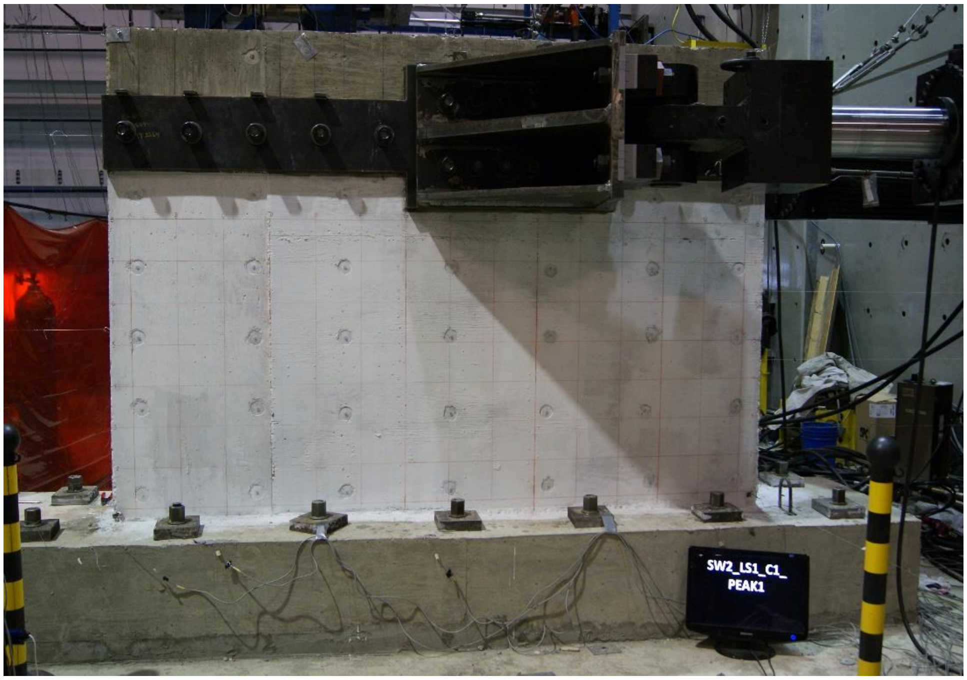

Figure E.12. SW2 before testing

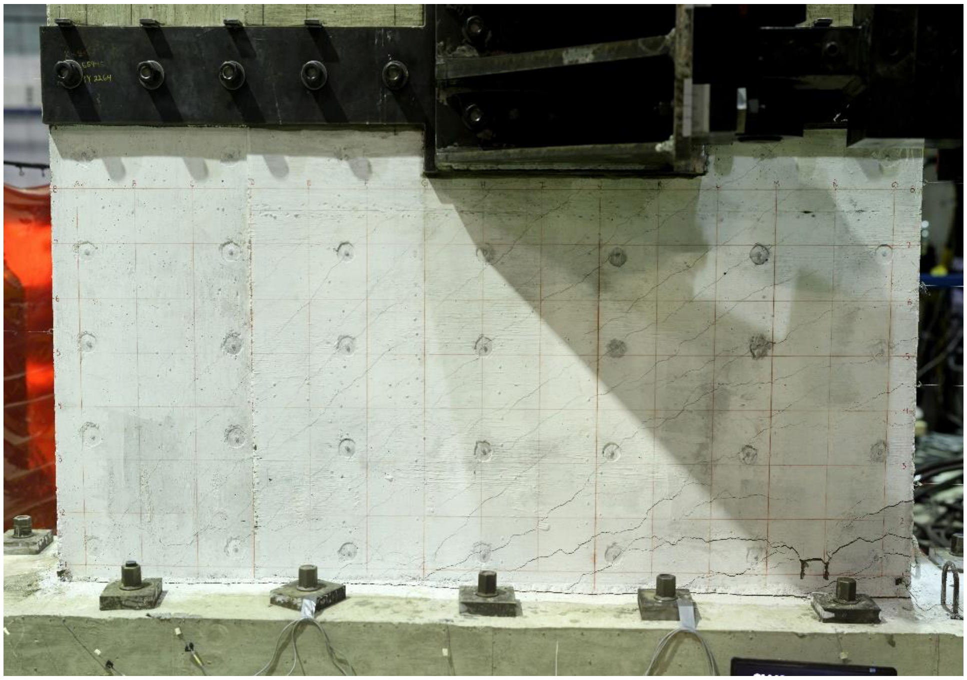
Figure E.13. Damage to SW2 at 1.25% drift ratio (peak strength)

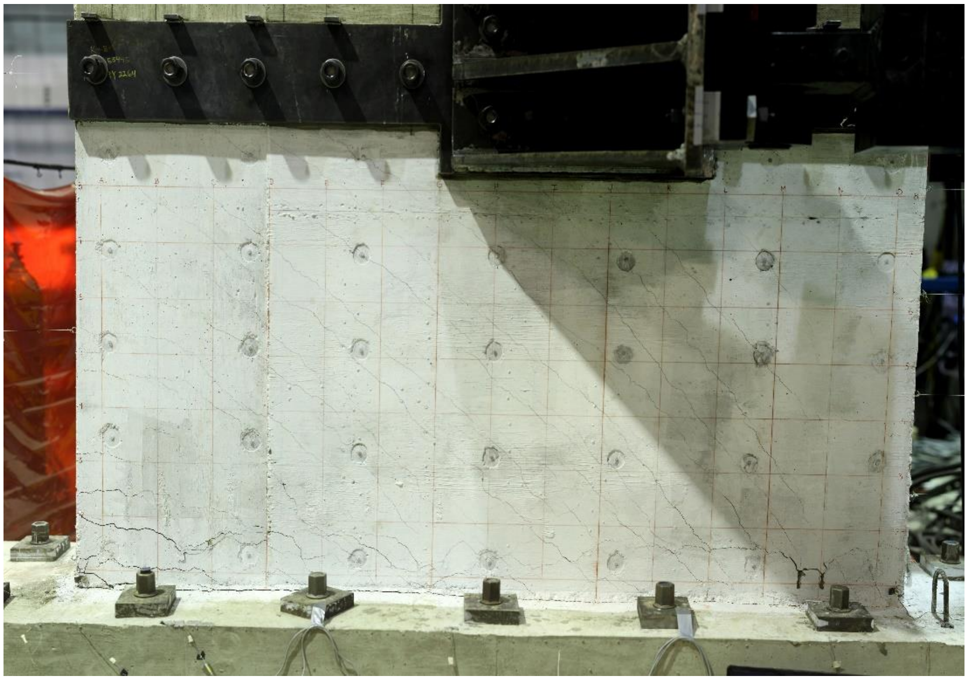

Figure E.14. Damage to SW2 at -1.28% drift ratio

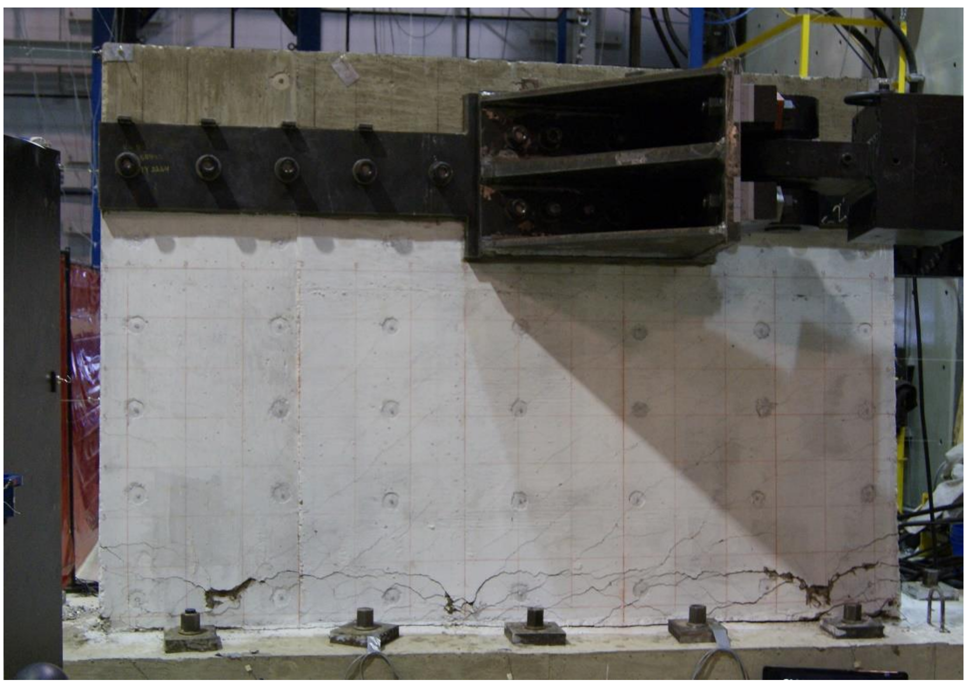

Figure E.15. Damage to SW2 at the end of testing

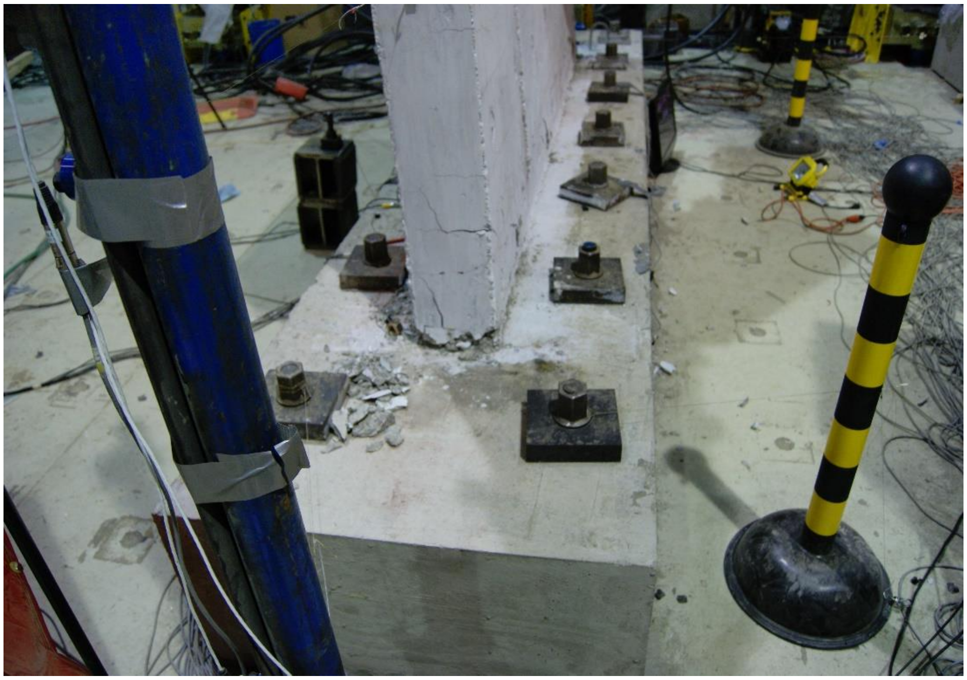
Figure E.16. Damage to SW2 at the end of testing

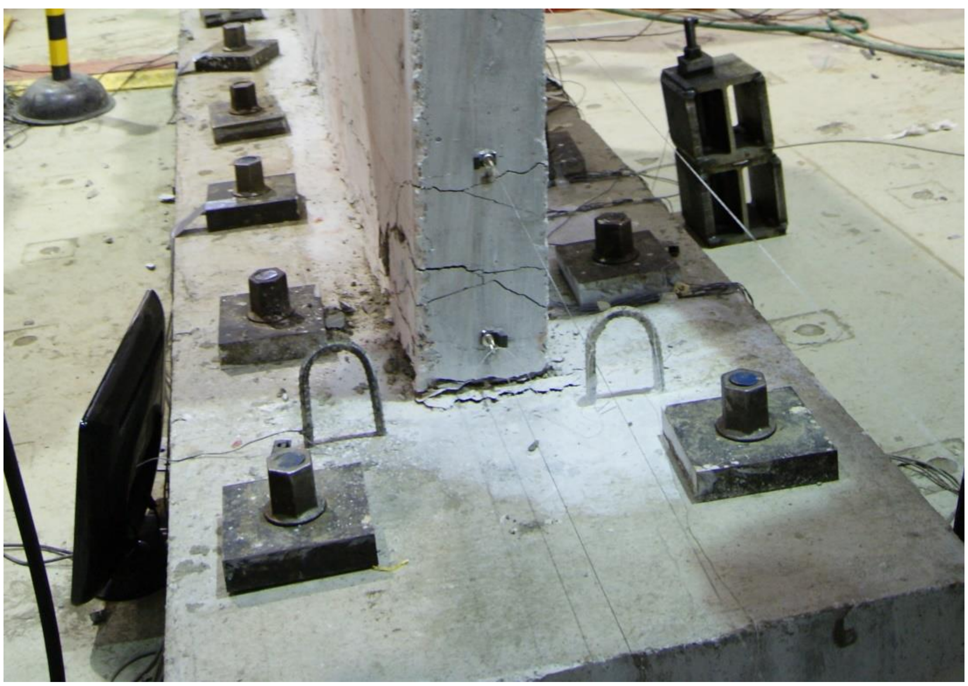
Figure E.17. Damage to SW2 at the end of testing

E.3 SW3

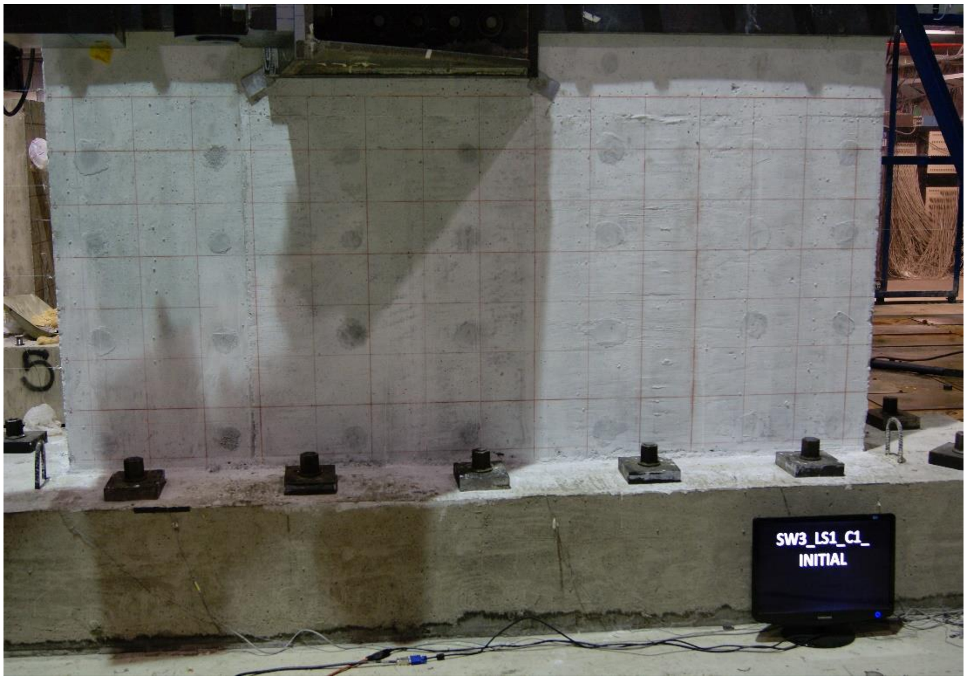

Figure E.18. SW3 before testing

Figure E.19. Damage to SW3 at 0.75% drift ratio

Figure E.20. Damage to SW3 at -0.76% drift ratio

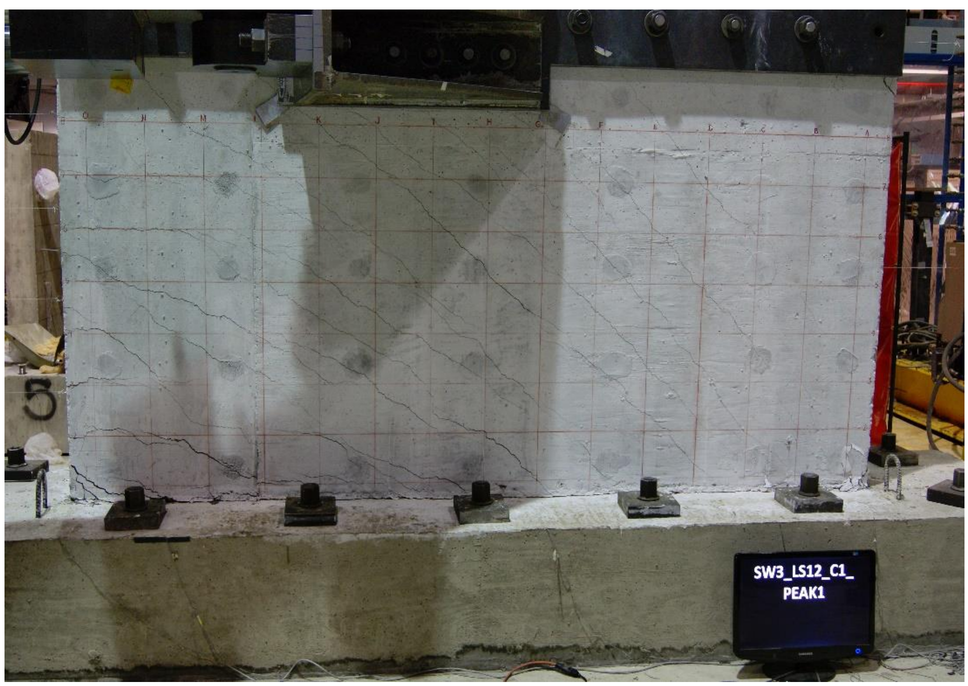

Figure E.21. Damage to SW3 at 2.09% drift ratio (peak strength)

Figure E.22. Damage to SW3 at -1.96% drift ratio

Figure E.23. Damage to SW3 at the end of testing

Figure E.24. Damage to SW3 at the end of testing

Figure E.25. Damage to SW3 at the end of testing

E.4 SW4

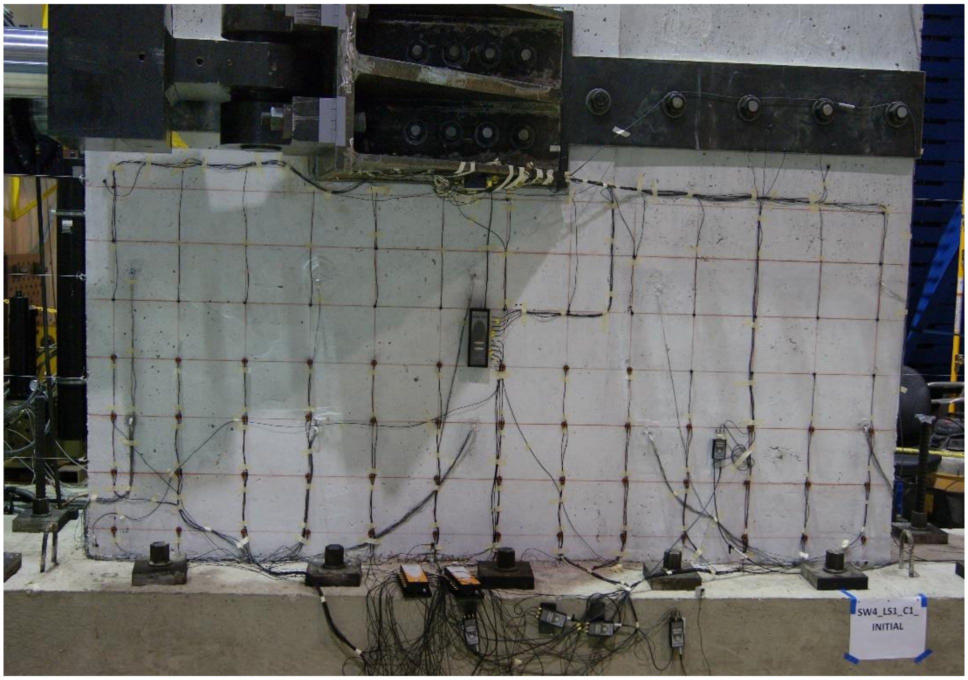

Figure E.26. SW4 before testing

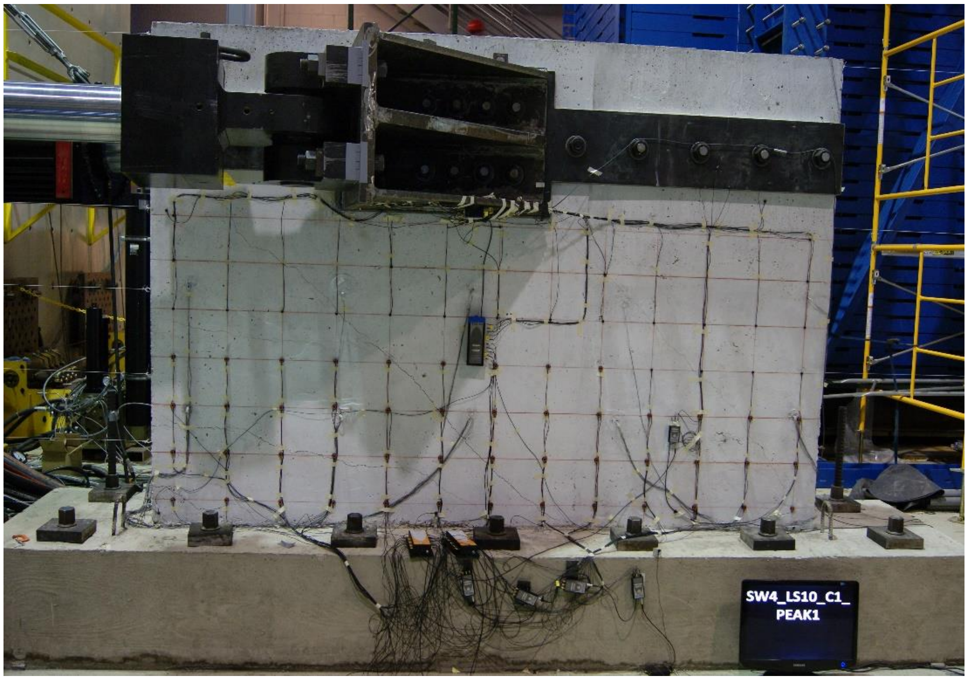

Figure E.27. Damage to SW4 at 0.60% drift ratio

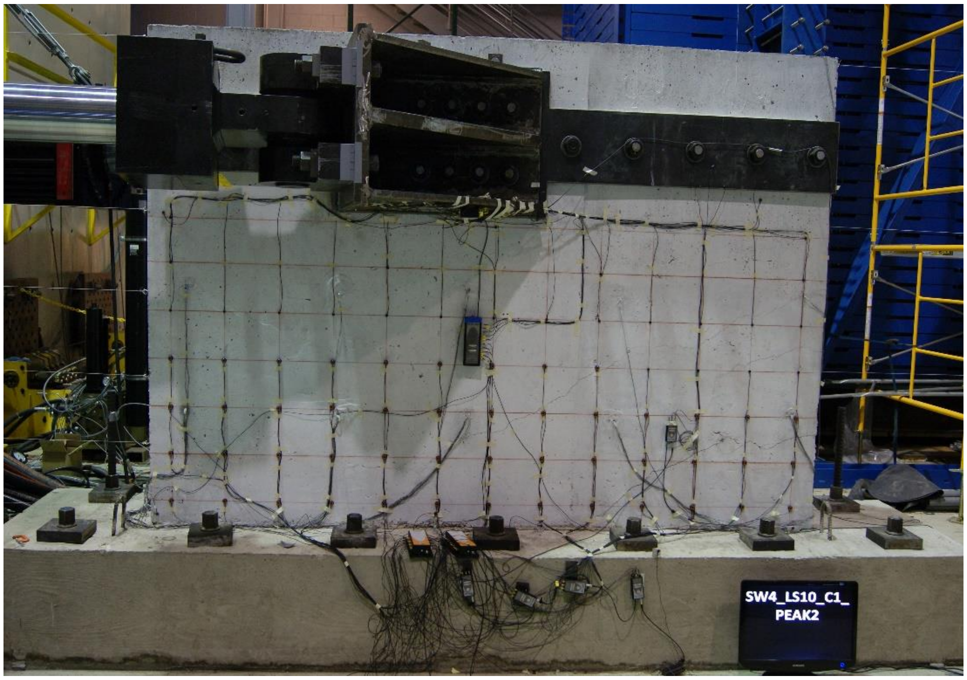

Figure E.28. Damage to SW4 at -0.55% drift ratio

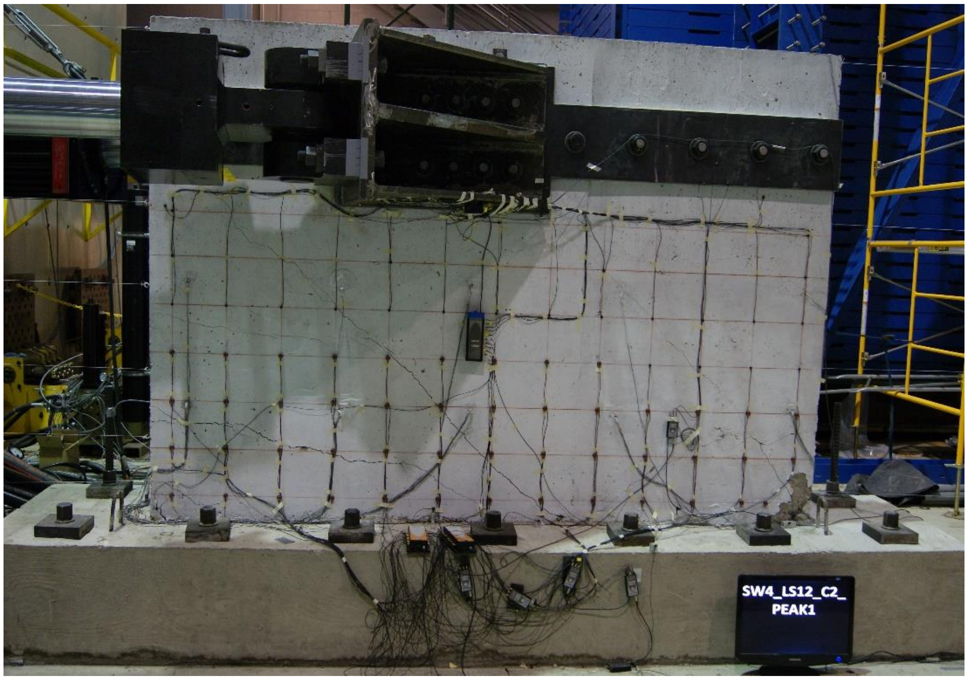

Figure E.29. Damage to SW4 at 1.08% drift ratio (peak strength)

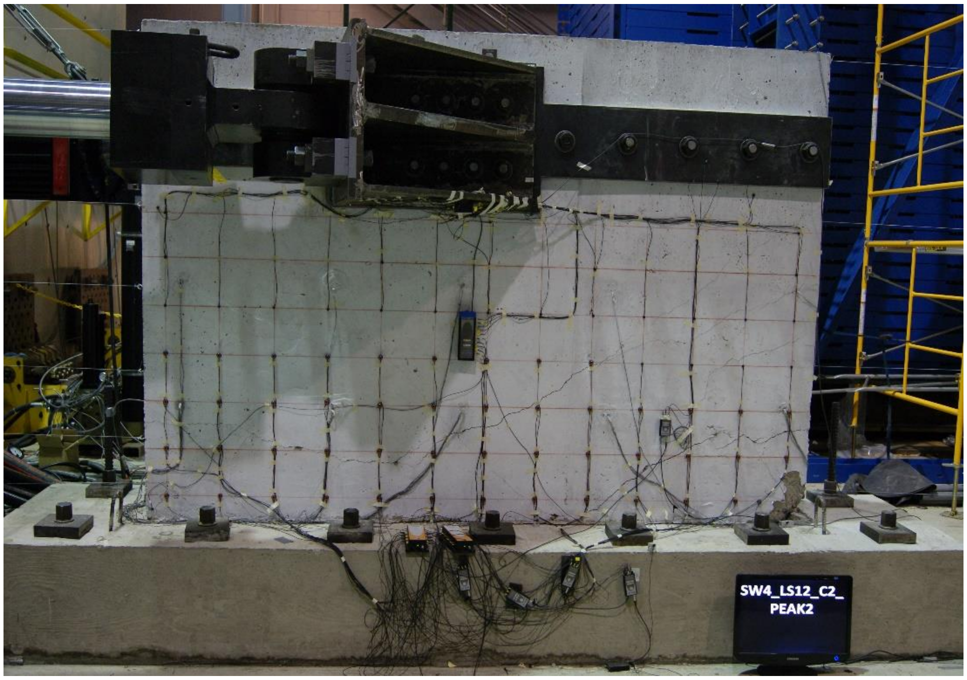

Figure E.30. Damage to SW4 at -1.06% drift ratio

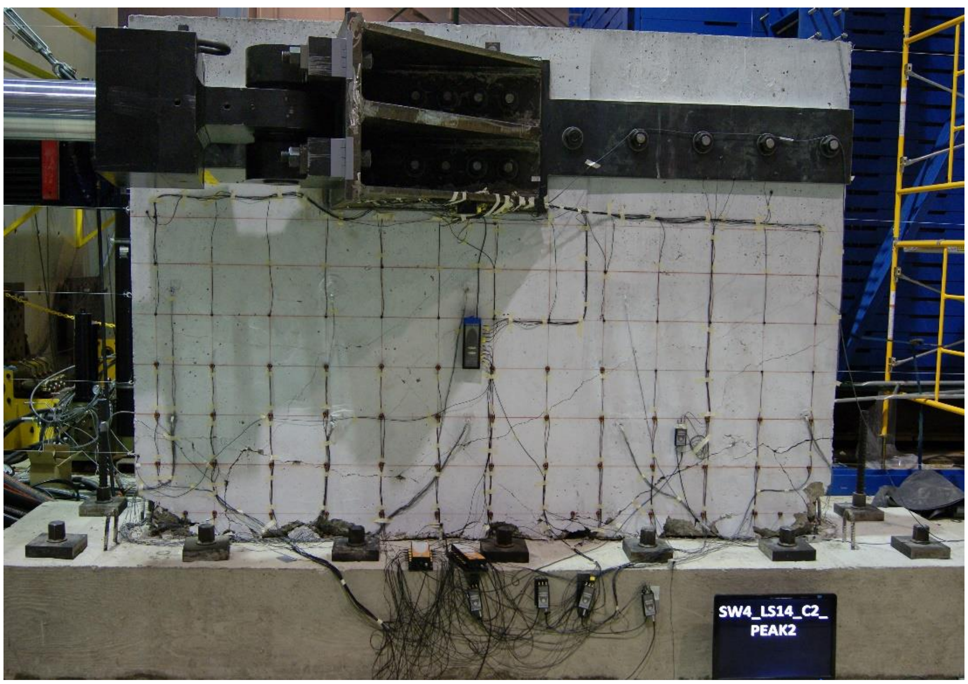

Figure E.31. Damage to SW4 at the end of testing

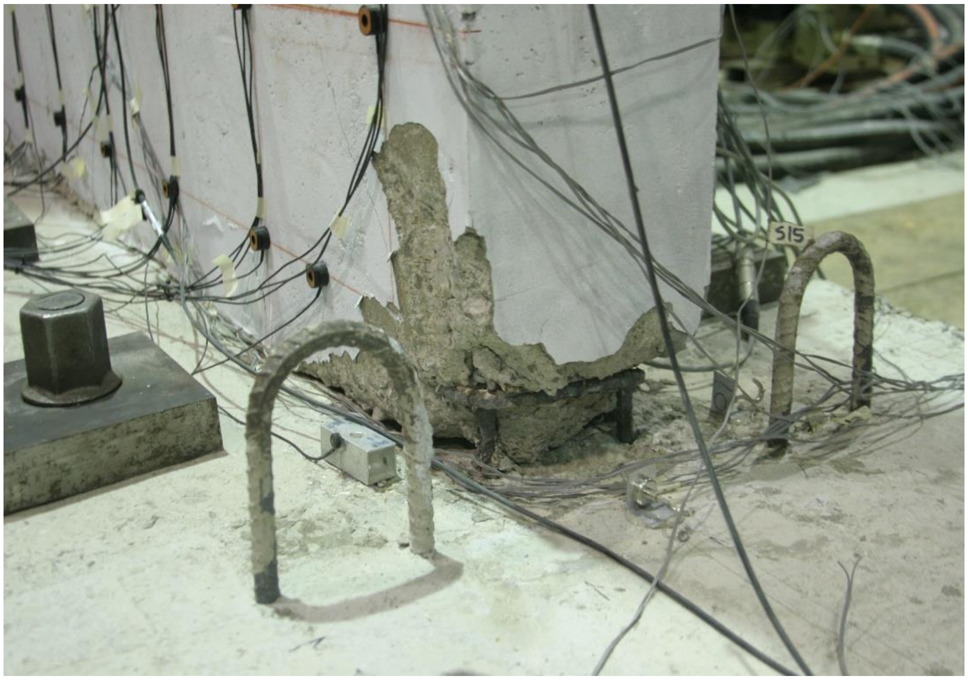

Figure E.32. Damage to SW4 at the end of testing

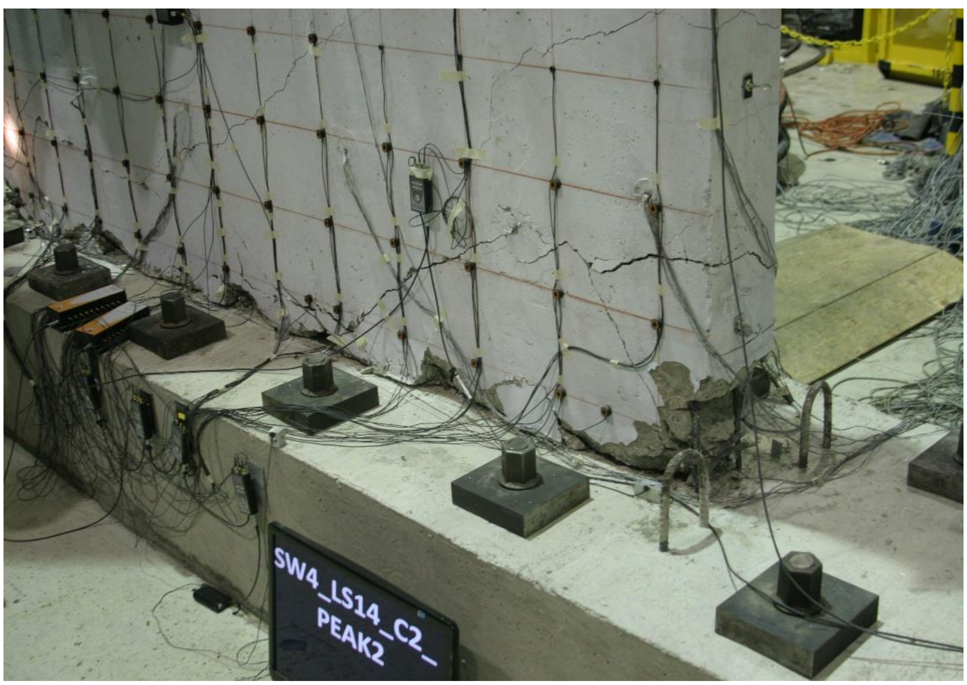

Figure E.33. Damage to SW4 at the end of testing

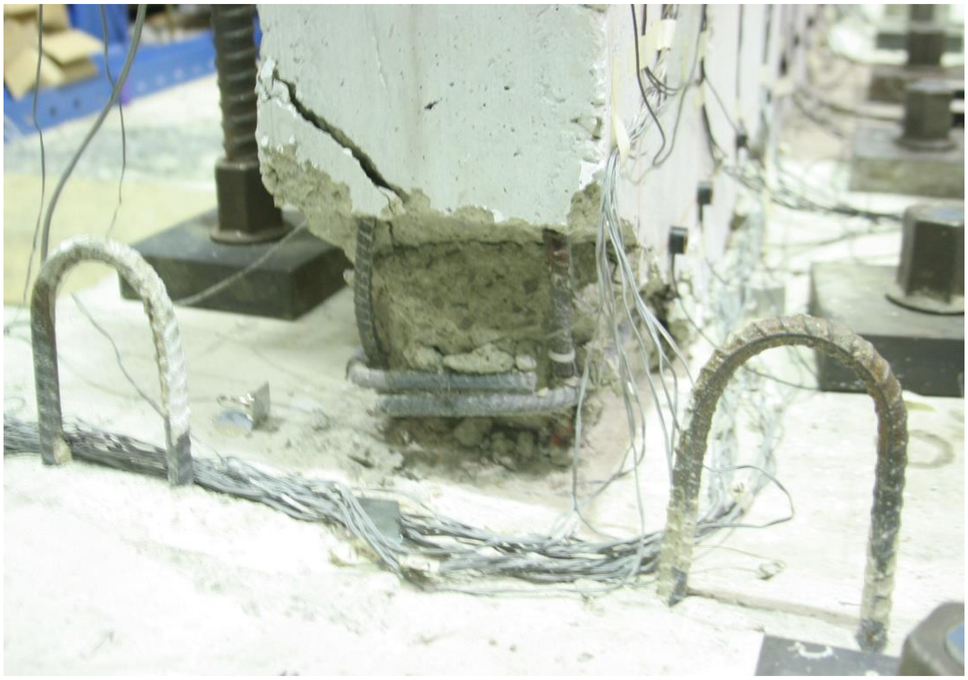
Figure E.34. Damage to SW4 at the end of testing

E.5 SW5

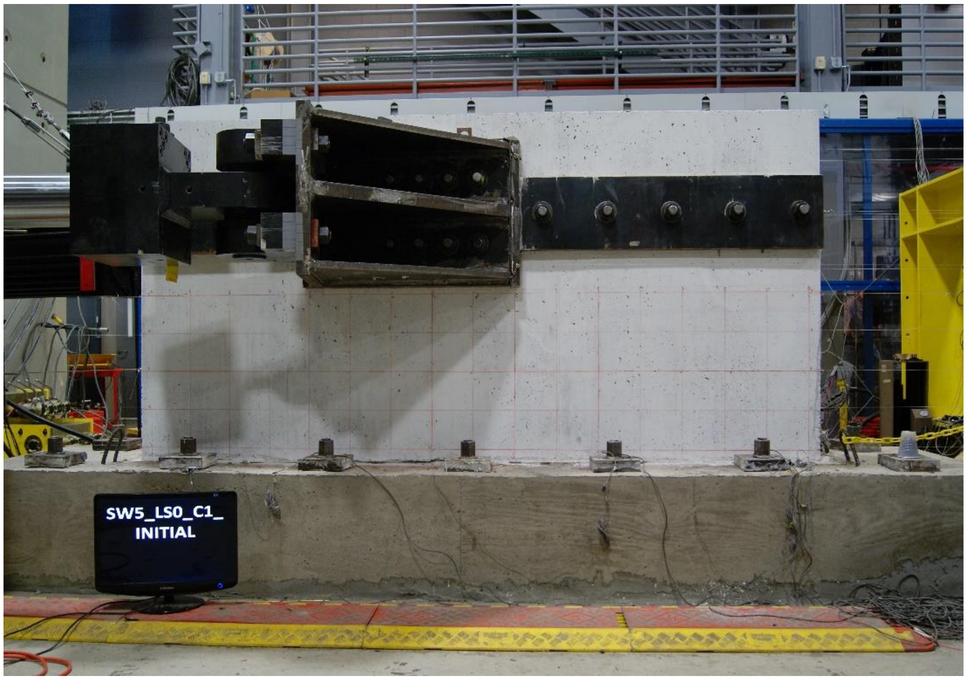

Figure E.35. SW5 before testing

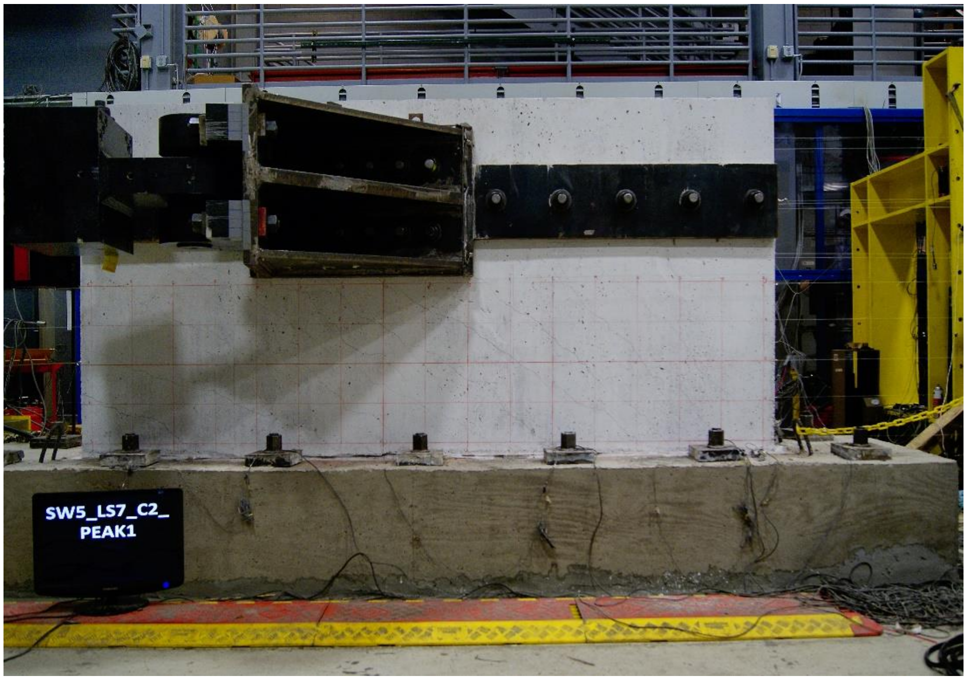

Figure E.36. Damage to SW5 at 0.67% drift ratio

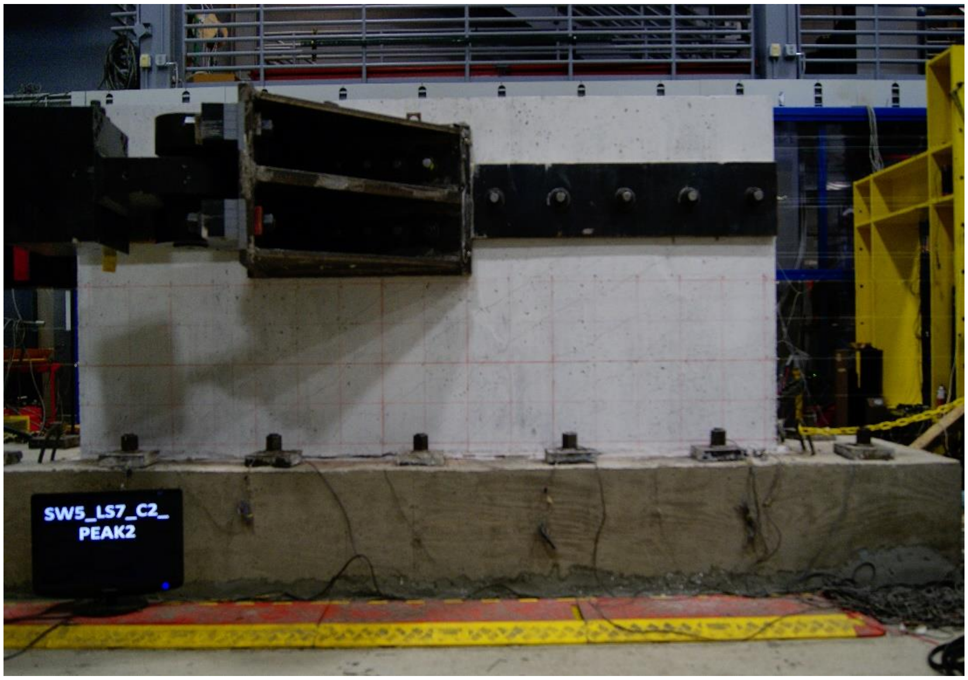

Figure E.37. Damage to SW5 at -0.59% drift ratio

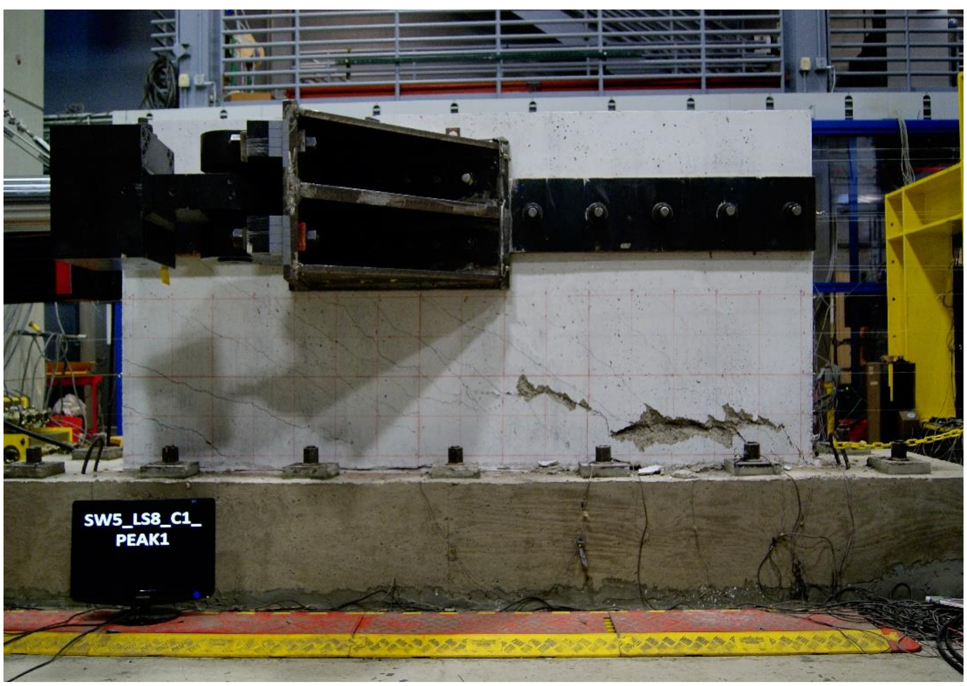

Figure E.38. Damage to SW5 at 0.89% drift ratio (peak strength)

Figure E.39. Damage to SW5 at -1.31% drift ratio

Figure E.40. Damage to SW5 at the end of testing

Figure E.41. Damage to SW5 at the end of testing

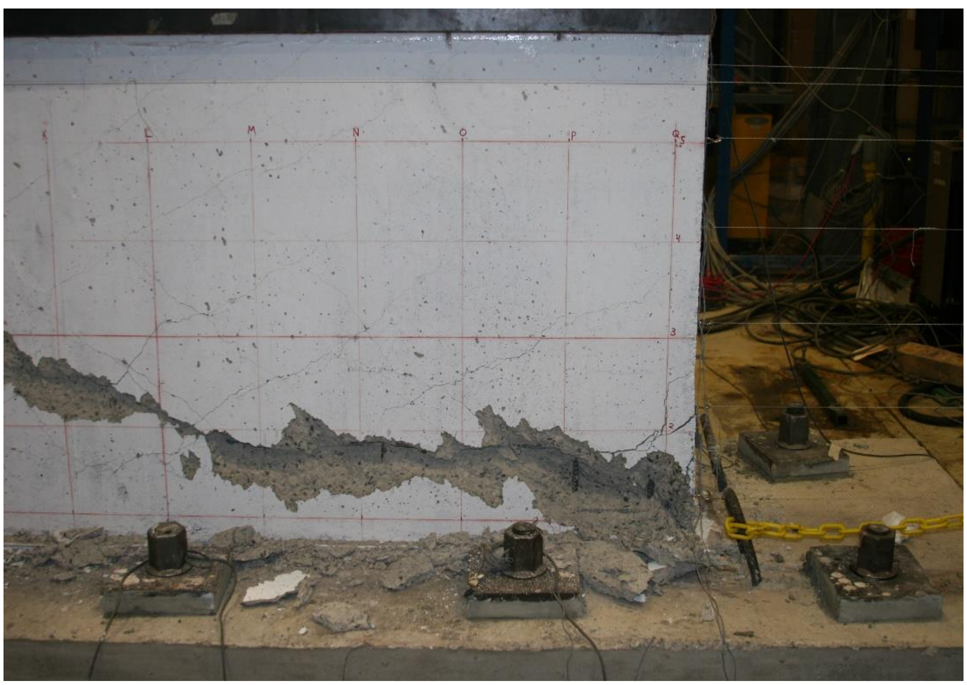
Figure E.42. Damage to SW5 at the end of testing

E.6 SW6

Figure E.43. SW6 before testing

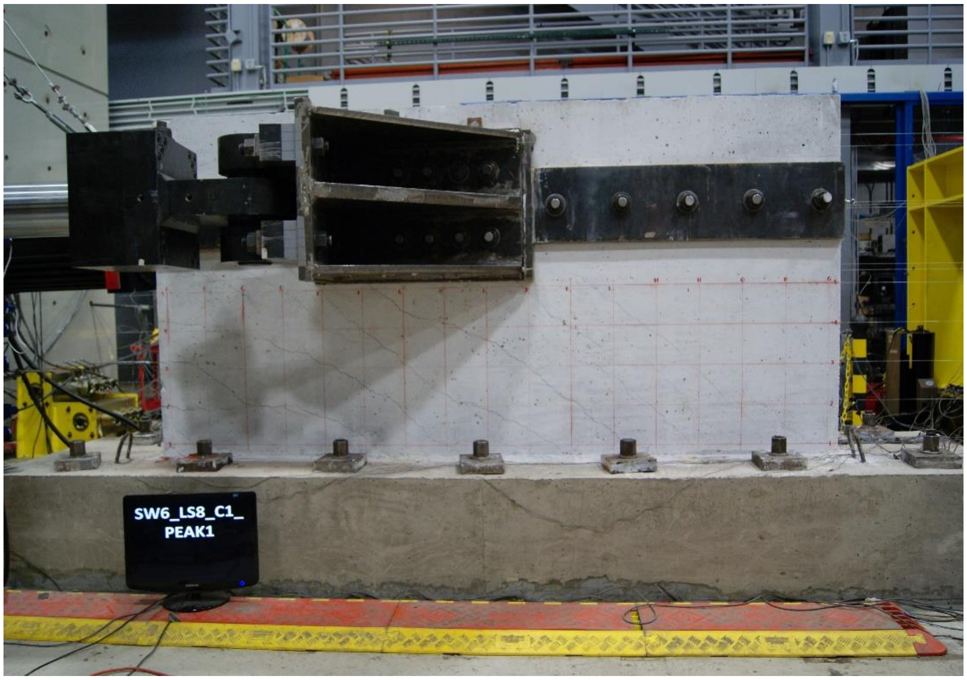

Figure E.44. Damage to SW6 at 0.81% drift ratio (peak strength)

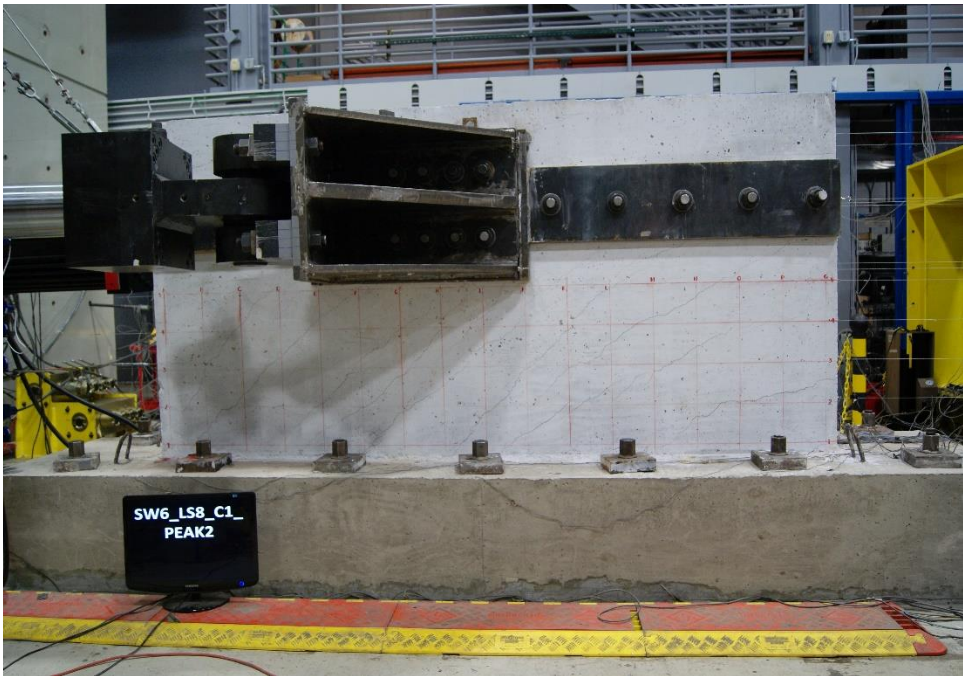

Figure E.45. Damage to SW6 at -0.81% drift ratio

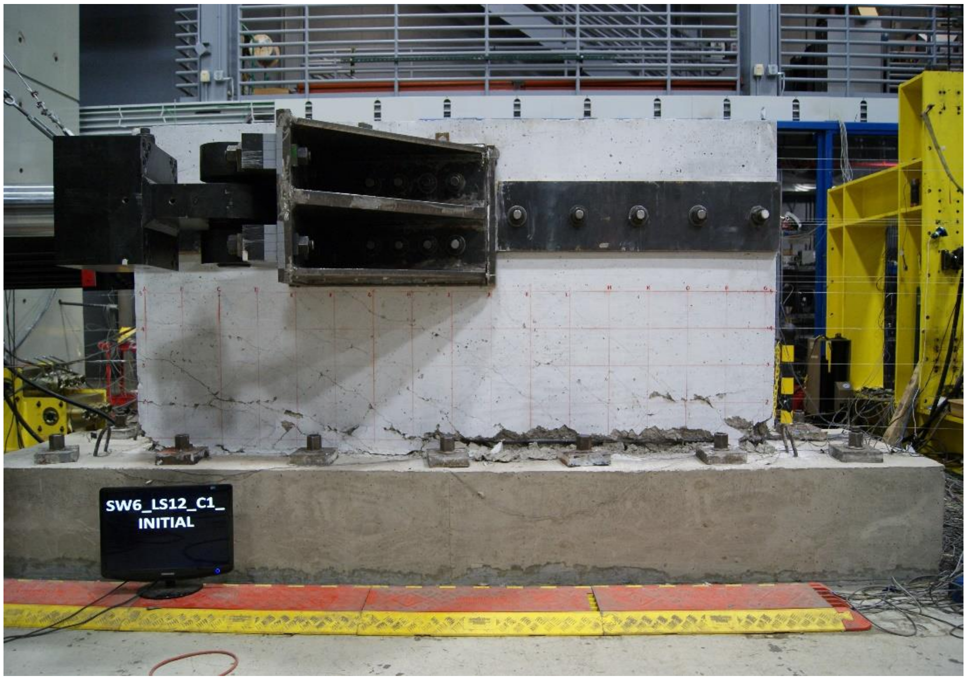

Figure E.46. Damage to SW6 at the end of testing

Figure E.47. Damage to SW6 at the end of testing

Figure E.48. Damage to SW6 at the end of testing

E.7 SW7

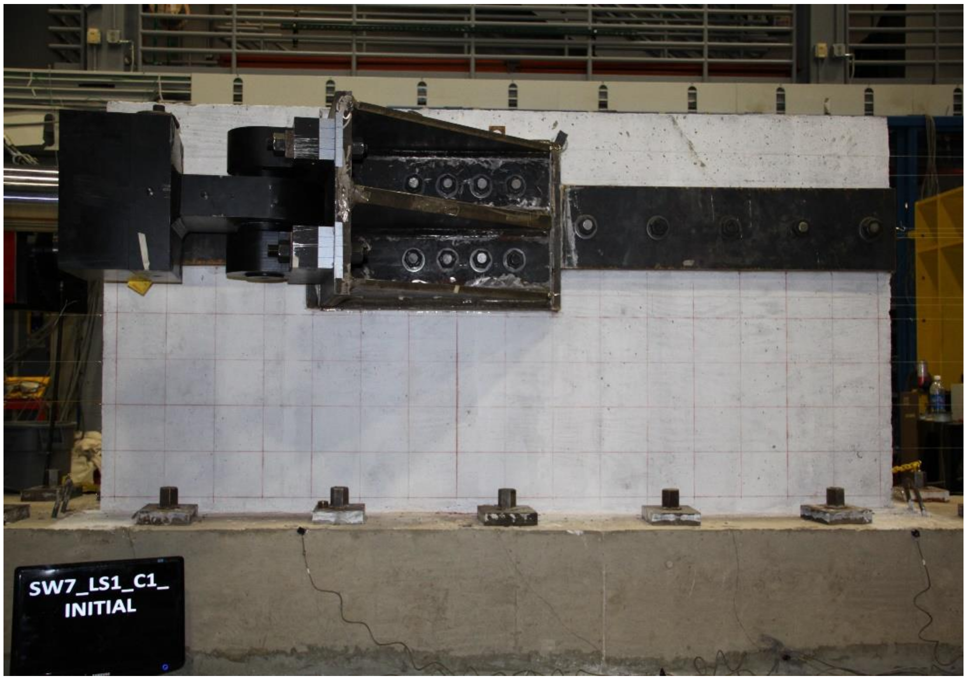

Figure E.49. SW7 before testing

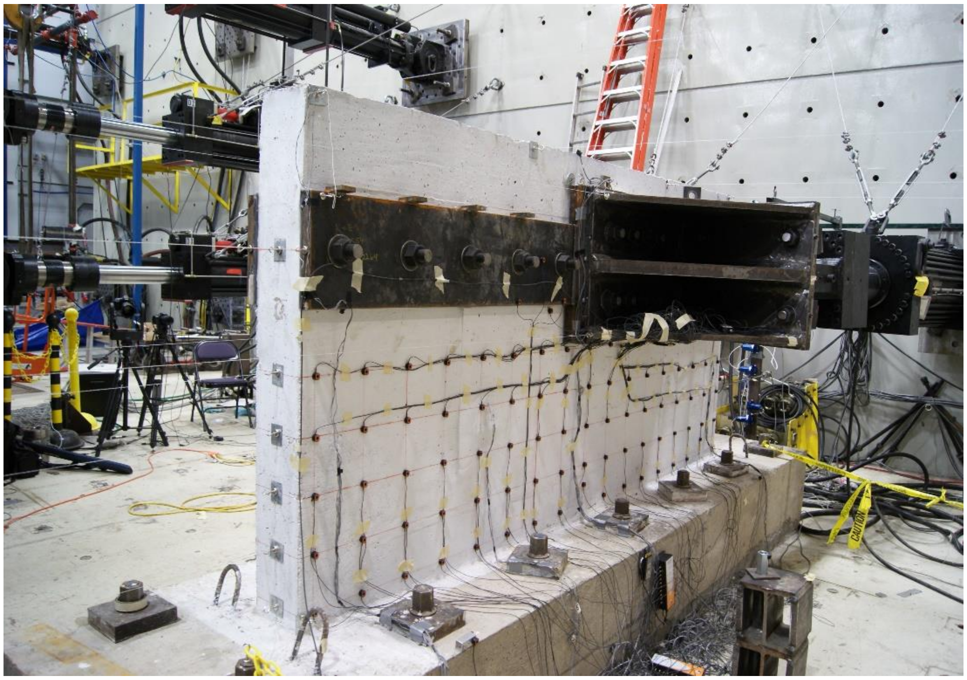
Figure E.50. SW7 before testing

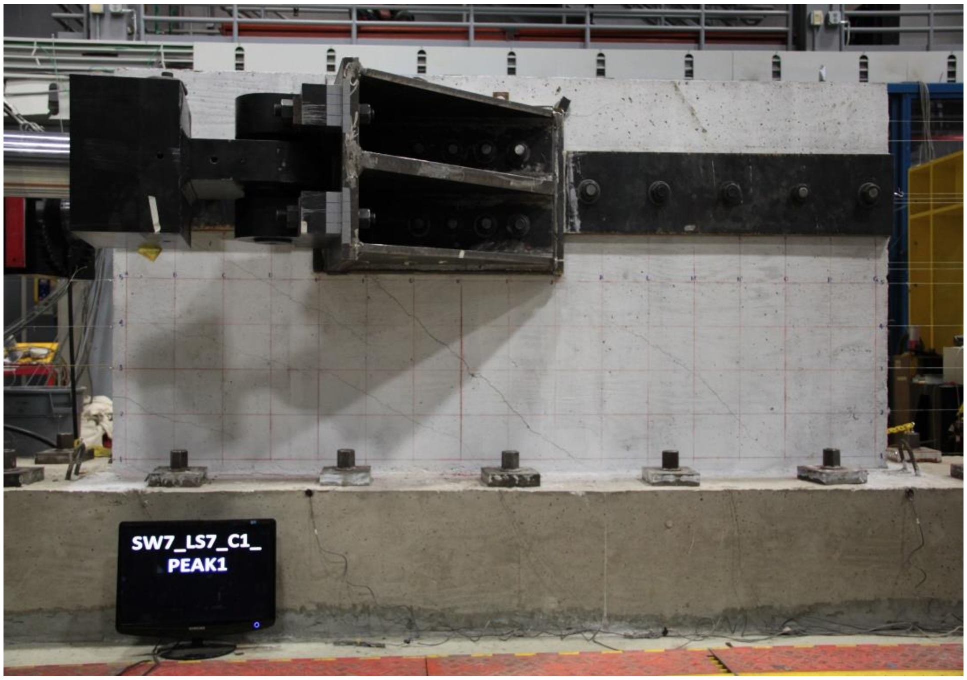

Figure E.51. Damage to SW7 at 0.45% drift ratio (peak strength)

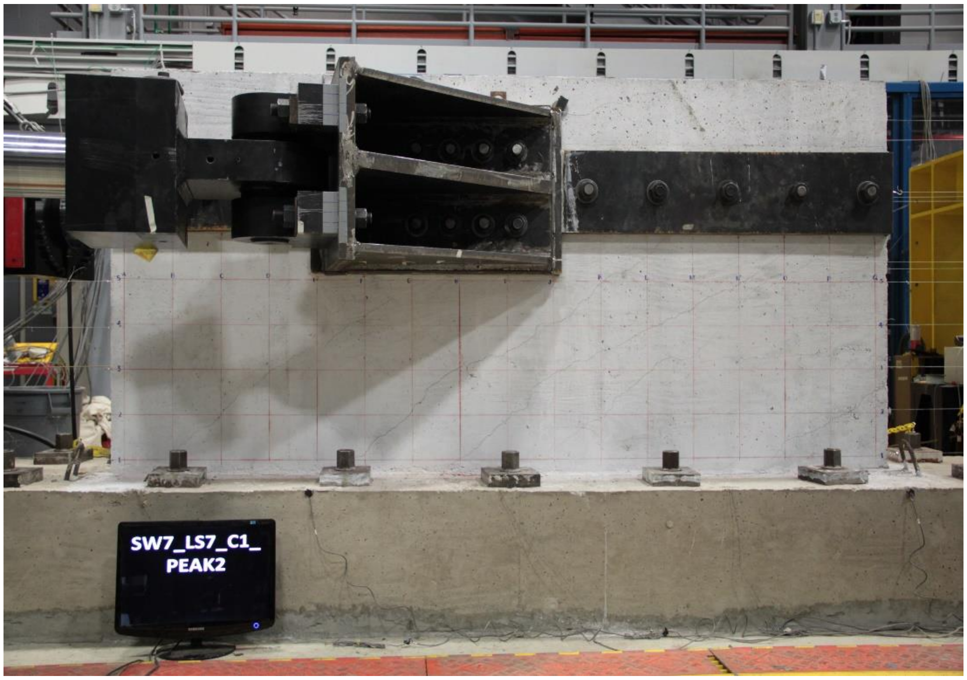

Figure E.52. Damage to SW7 at -0.41% drift ratio

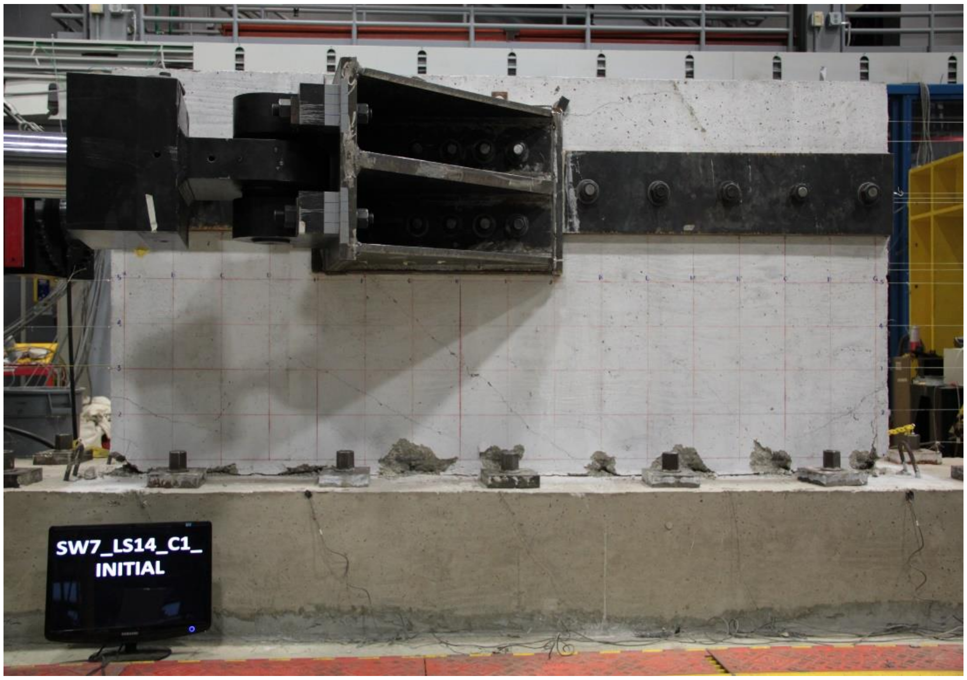

Figure E.53. Damage to SW7 at the end of testing


Figure E.54. Damage to SW7 at the end of testing

Figure E.55. Damage to SW7 at the end of testing

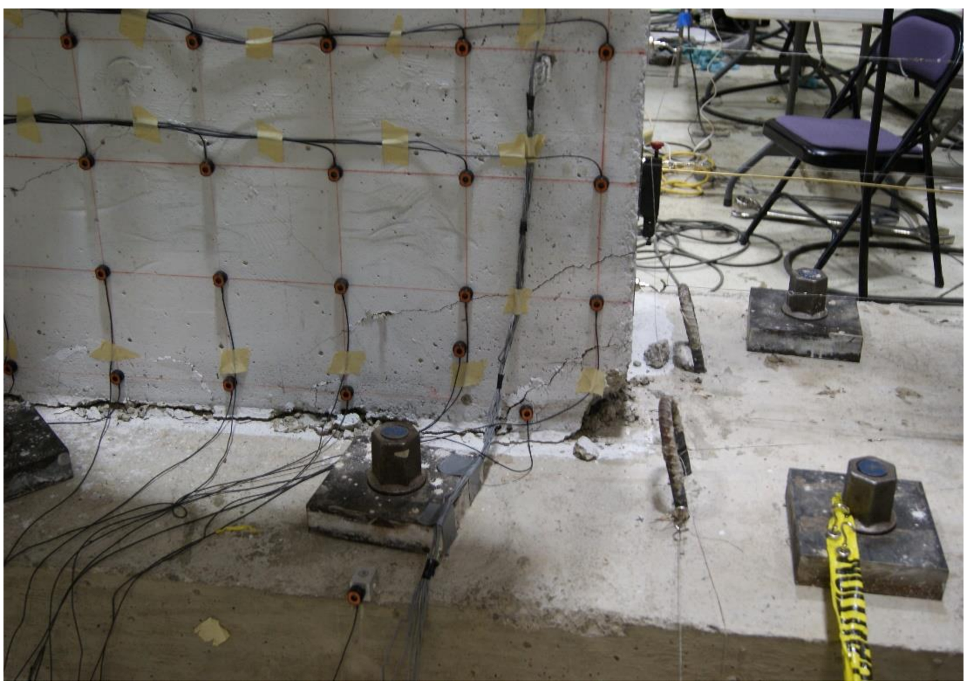

Figure E.56. Damage to SW7 at the end of testing

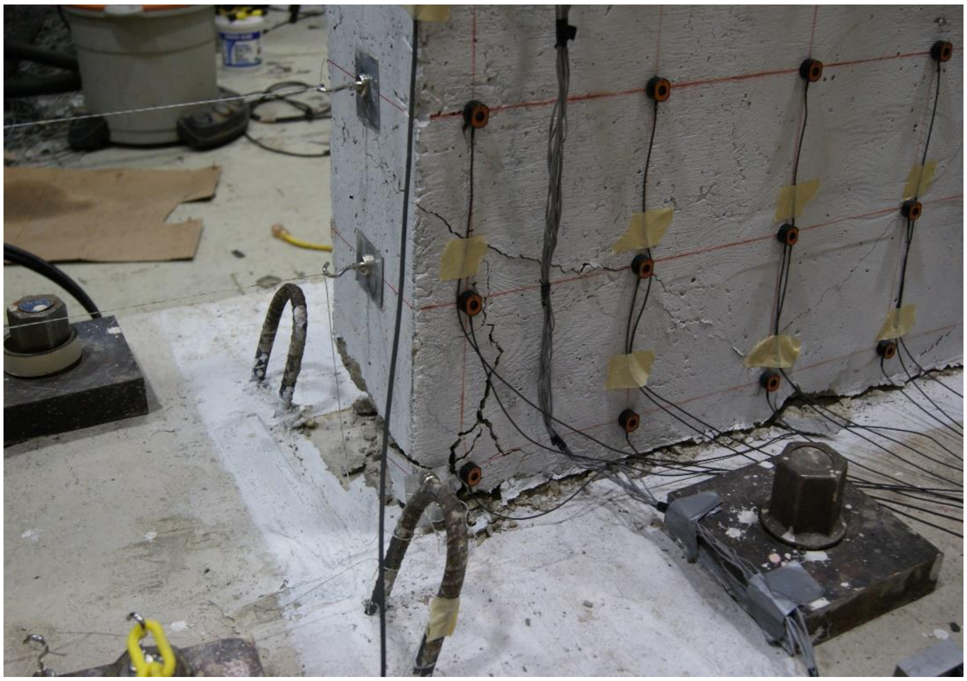
Figure E.57. Damage to SW7 at the end of testing

E.8 SW8

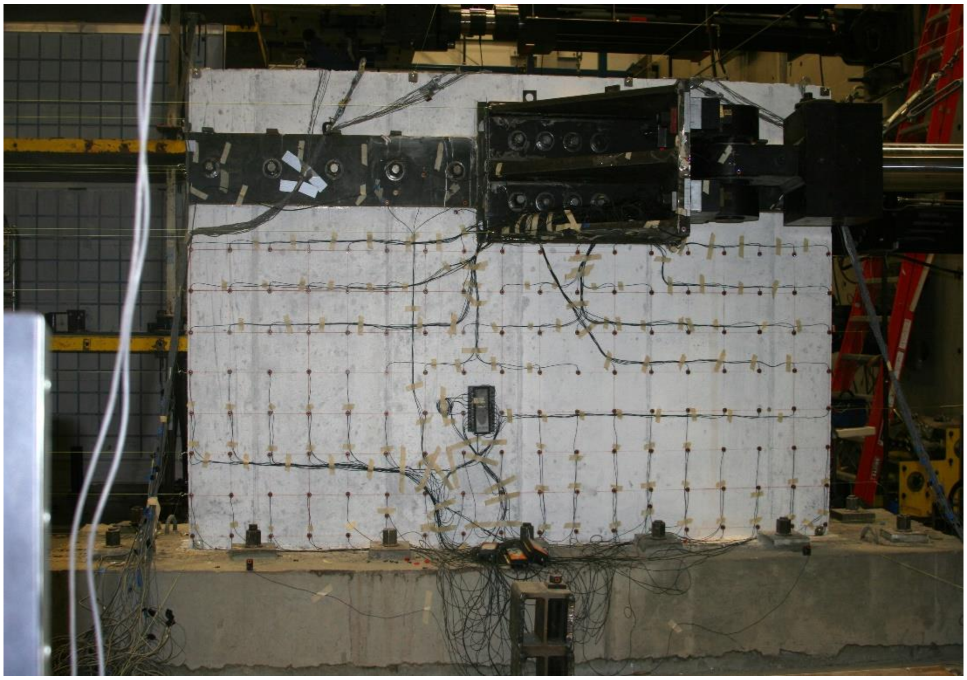

Figure E.58. SW8 before testing

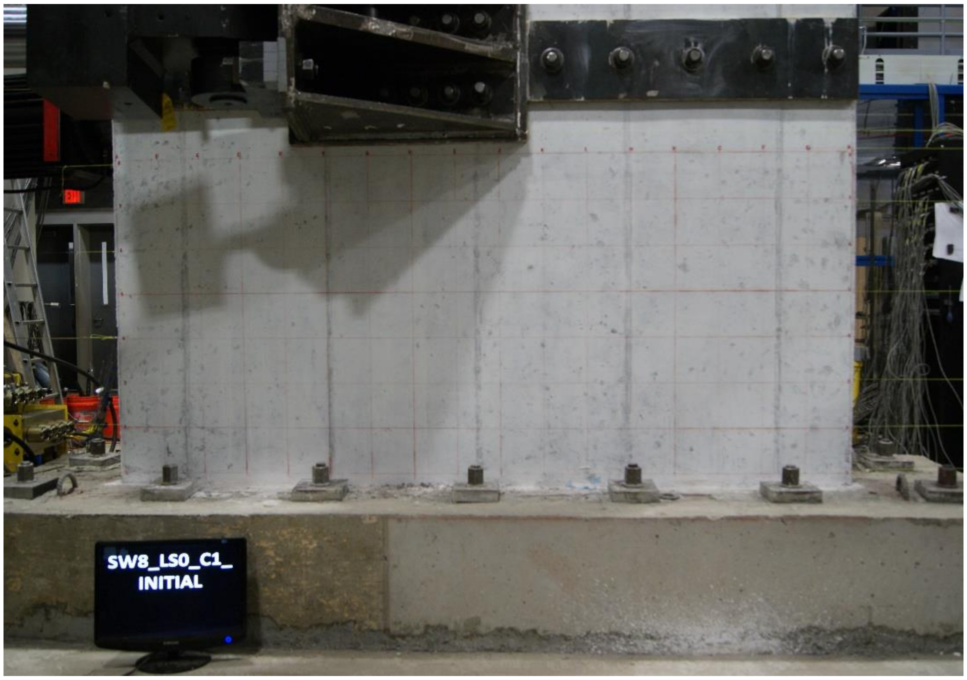

Figure E.59. SW8 before testing

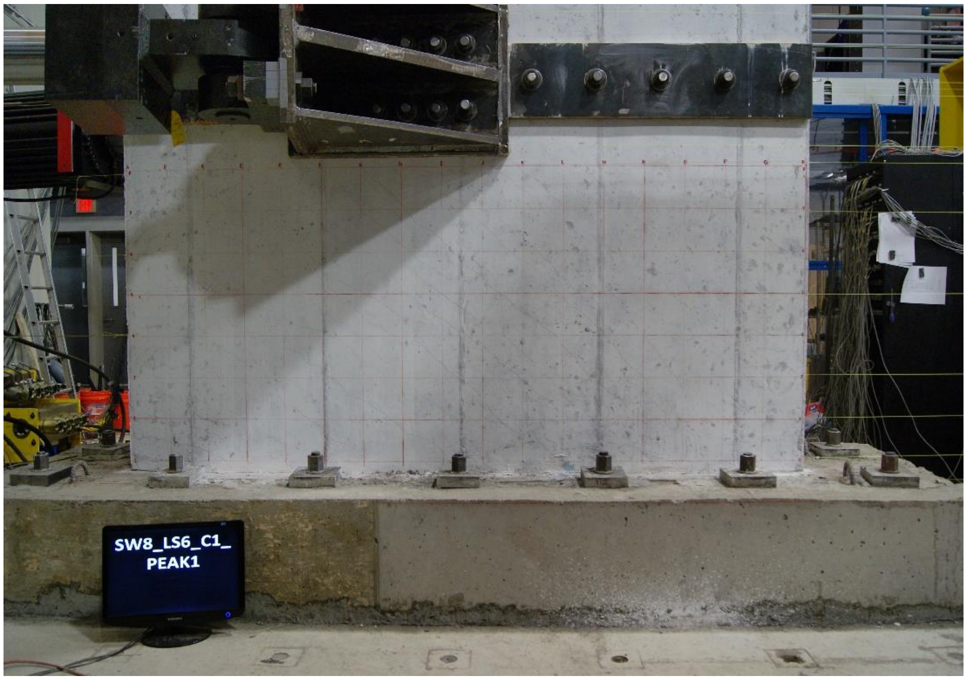

Figure E.60. Damage to SW8 at 0.70% drift ratio (peak strength)

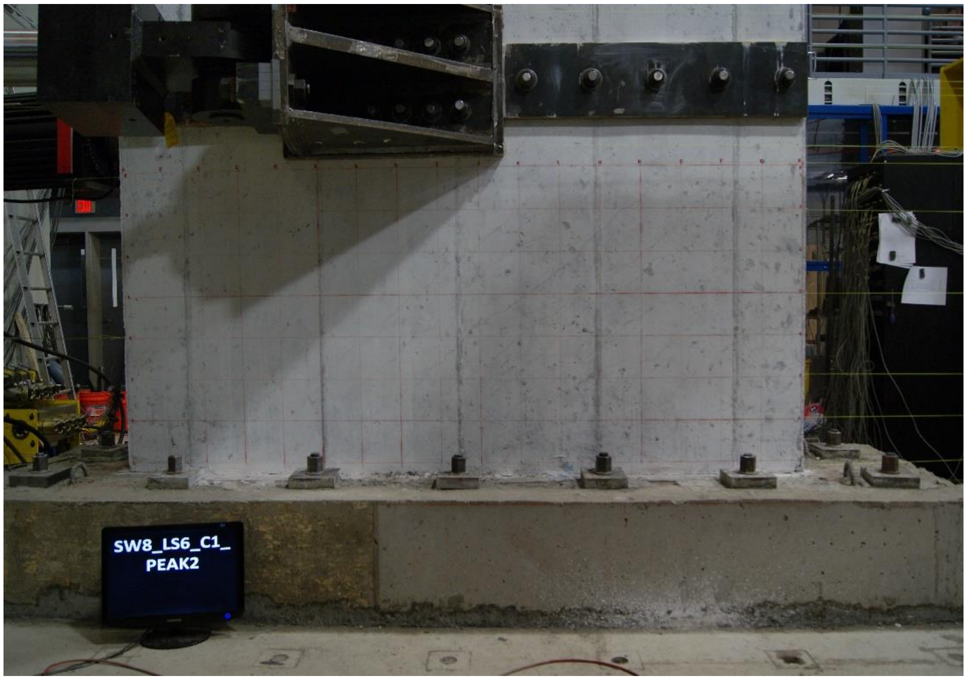

Figure E.61. Damage to SW8 at -0.65% drift ratio

Figure E.62. Damage to SW8 at 0.91% drift ratio

Figure 0.1. Damage to SW8 at -0.86% drift ratio

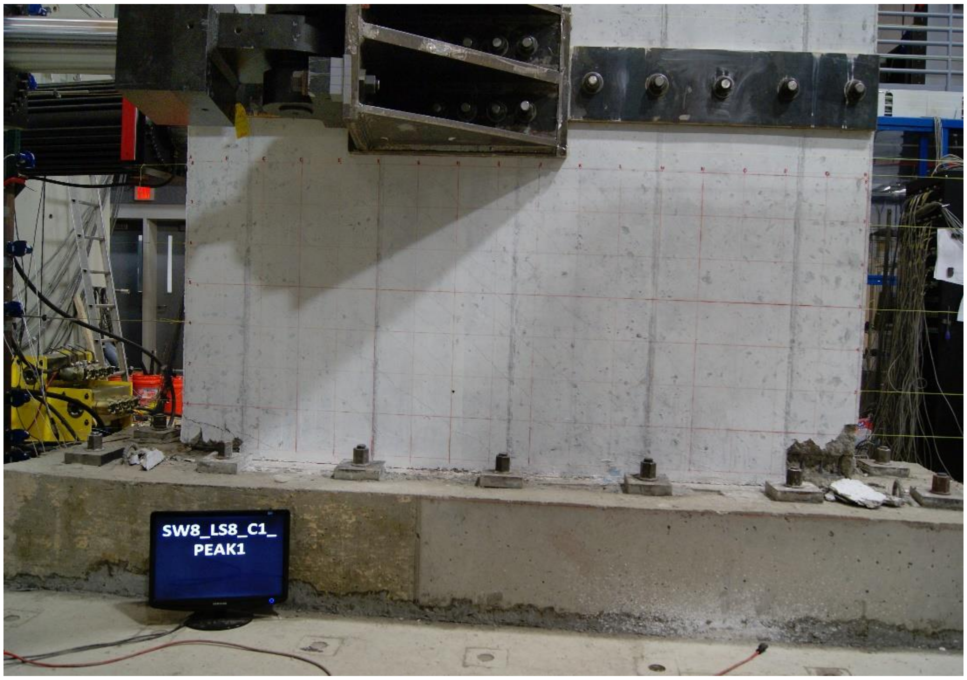

Figure E.64. Damage to SW8 at 1.31% drift ratio

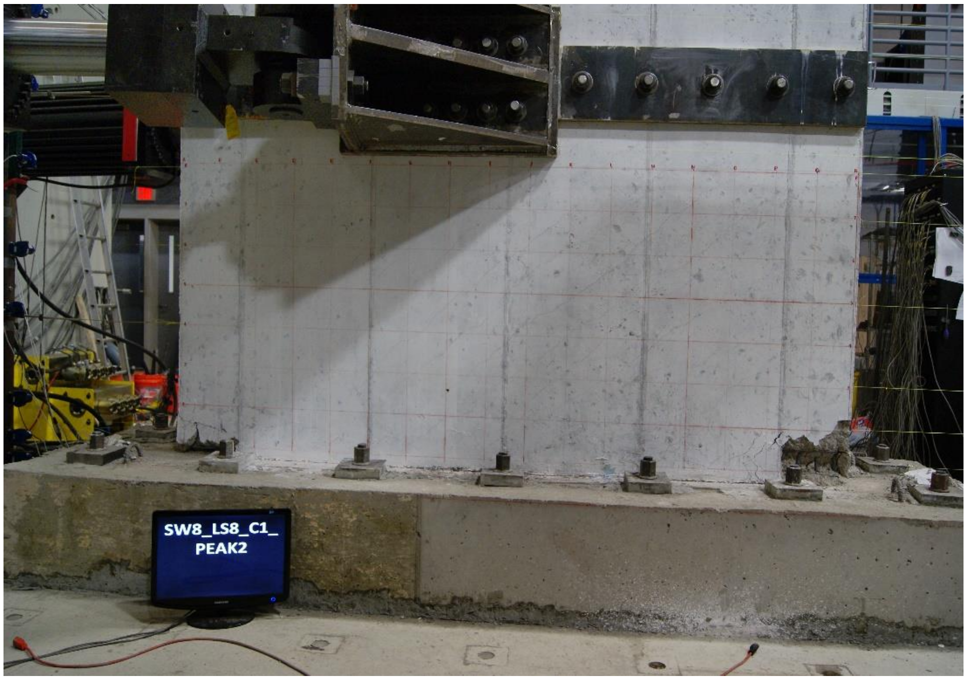

Figure E.65. Damage to SW8 at -1.28% drift ratio

Figure E.66. Damage to SW8 following two cycles to 1.3% drift ratio

Figure E.67. Damage to SW8 following two cycles to 1.3% drift ratio

Figure E.68. Damage to SW8 following two cycles to 1.3% drift ratio

Figure E.69. Damage to SW8 following two cycles to 1.3% drift ratio

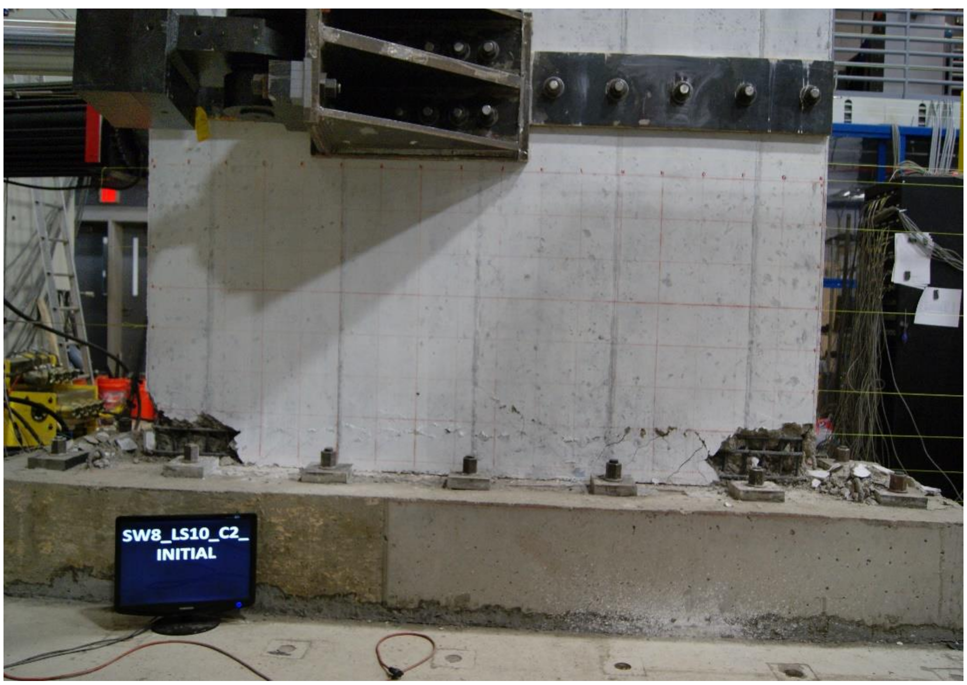

Figure E.70. Damage to SW8 at the end of testing

E.9 SW9

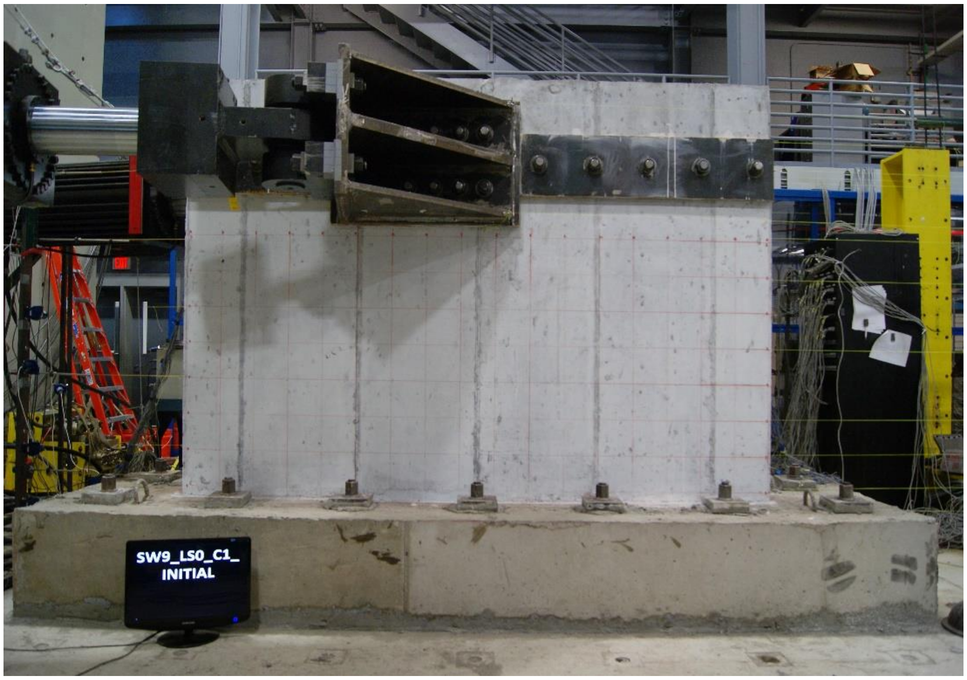

Figure E.71. SW9 before testing

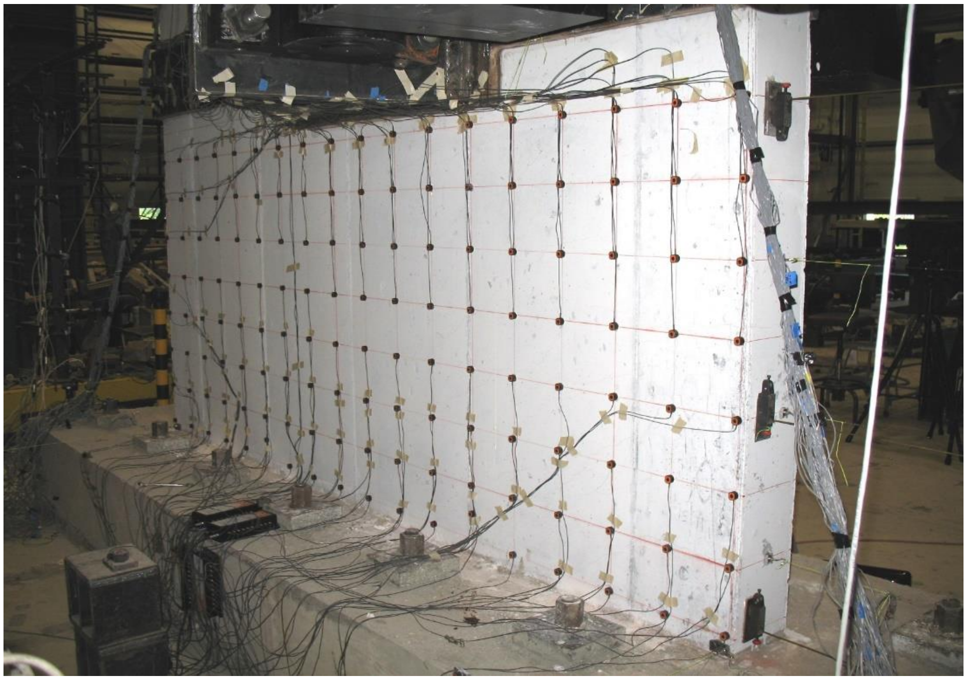

Figure E.72. SW9 before testing

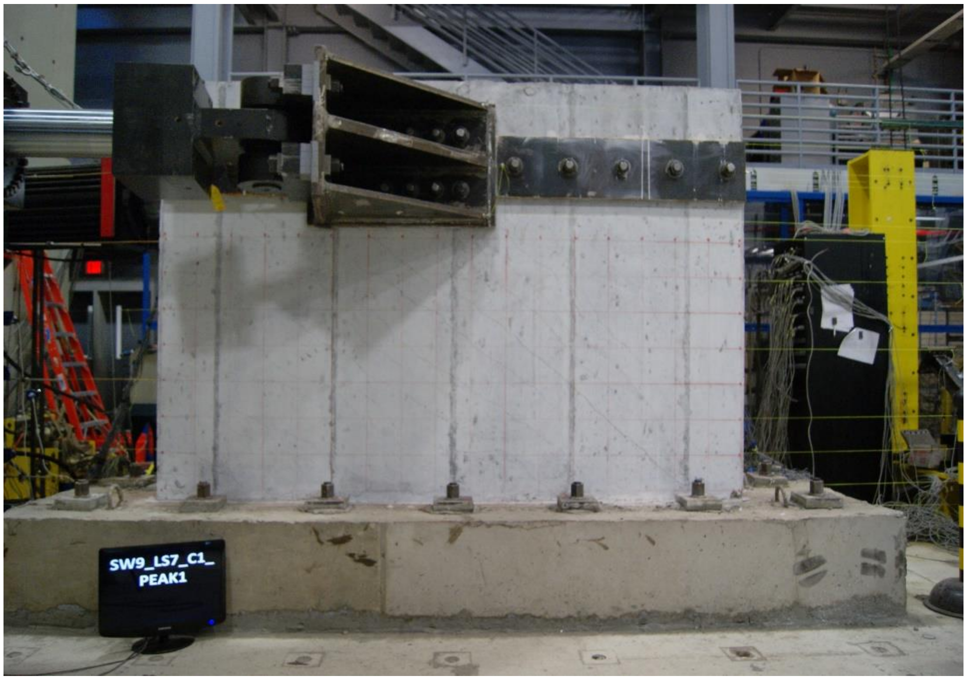

Figure E.73. Damage to SW9 at 0.76% drift ratio

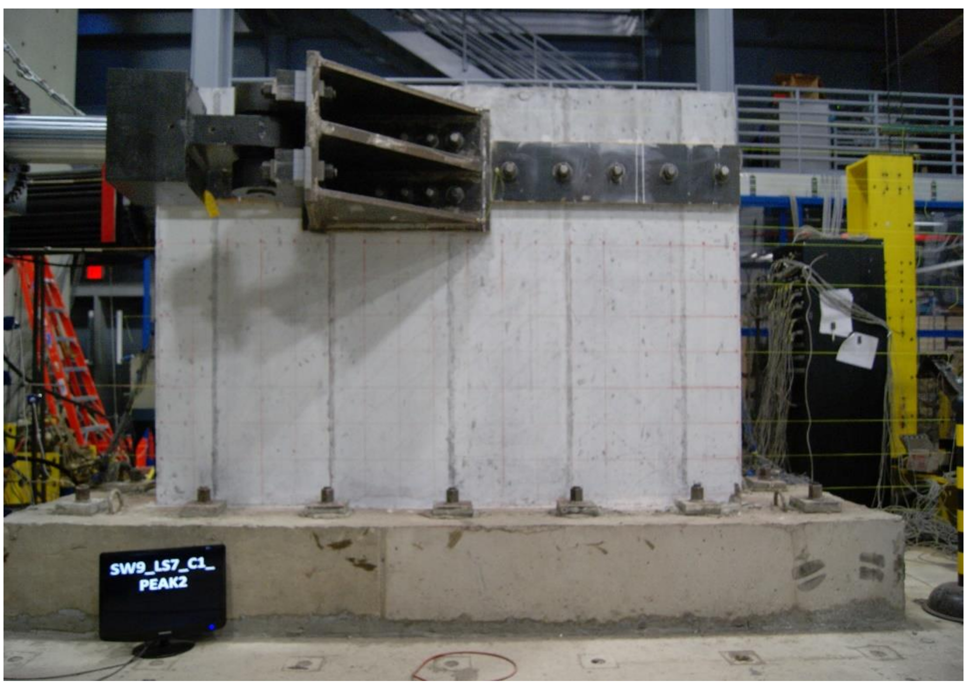

Figure E.74. Damage to SW9 at -0.78% drift ratio (peak strength)

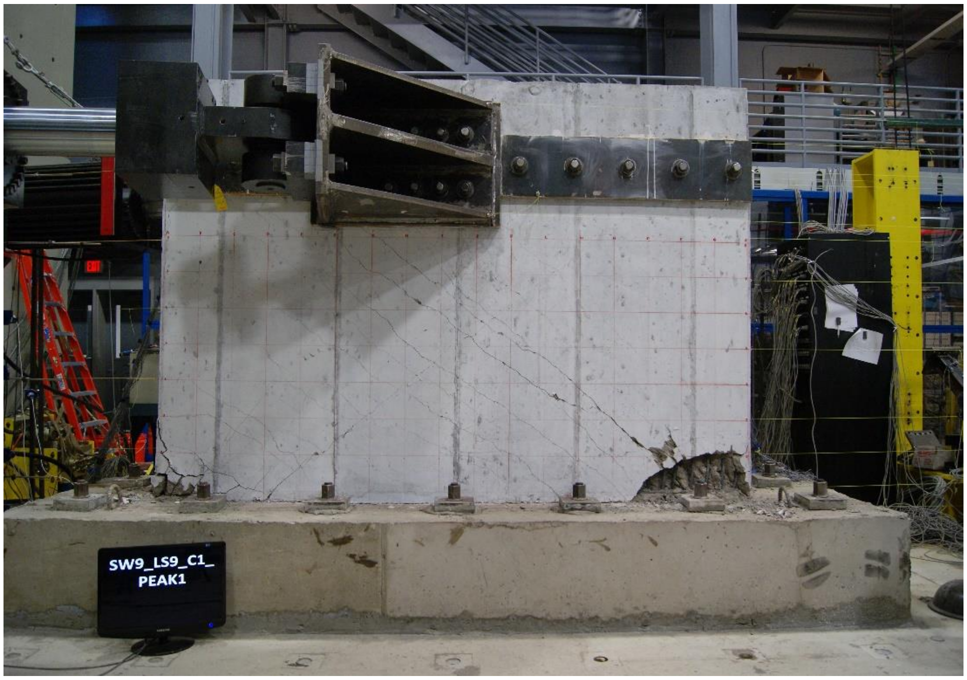

Figure E.75. Damage to SW9 at 1.72% drift ratio

Figure E.76. Damage to SW9 at -1.72% drift ratio


Figure E.77. Damage to SW9 at the end of testing


Figure E.78. Damage to SW9 at the end of testing


Figure E.79. Damage to SW9 at the end of testing


Figure E.80. Damage to SW9 at the end of testing

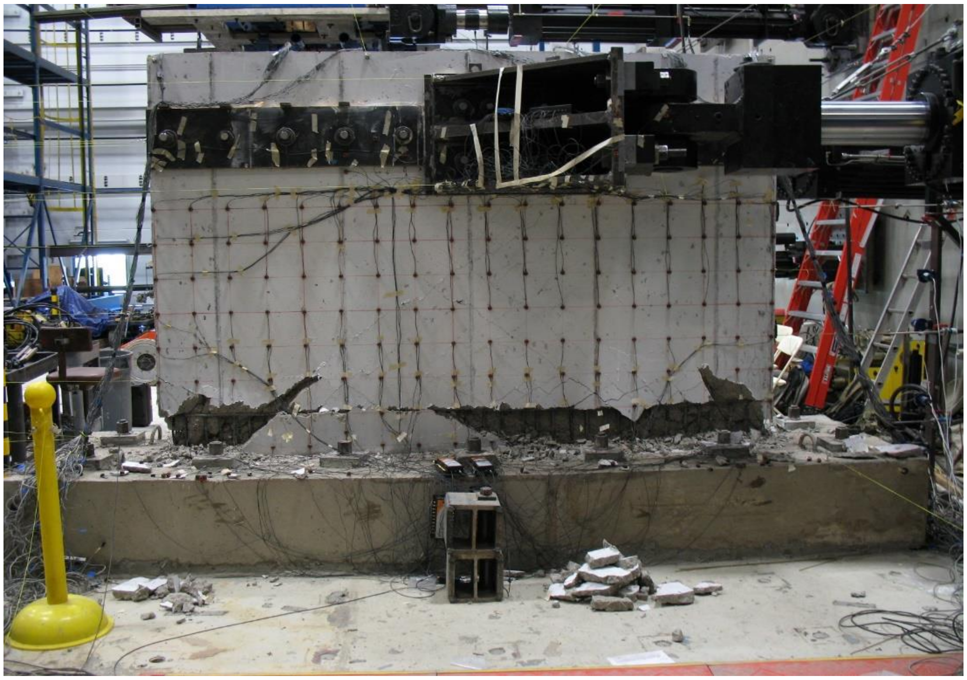
Figure E.81. Damage to SW9 at the end of testing

E.10 SW10

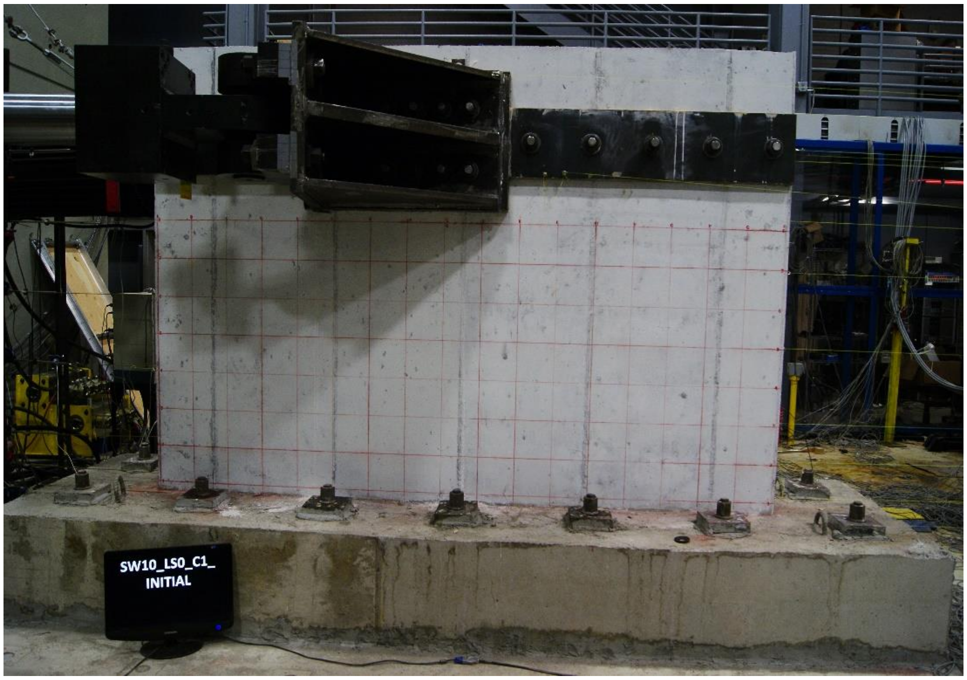

Figure E.82. SW10 before testing

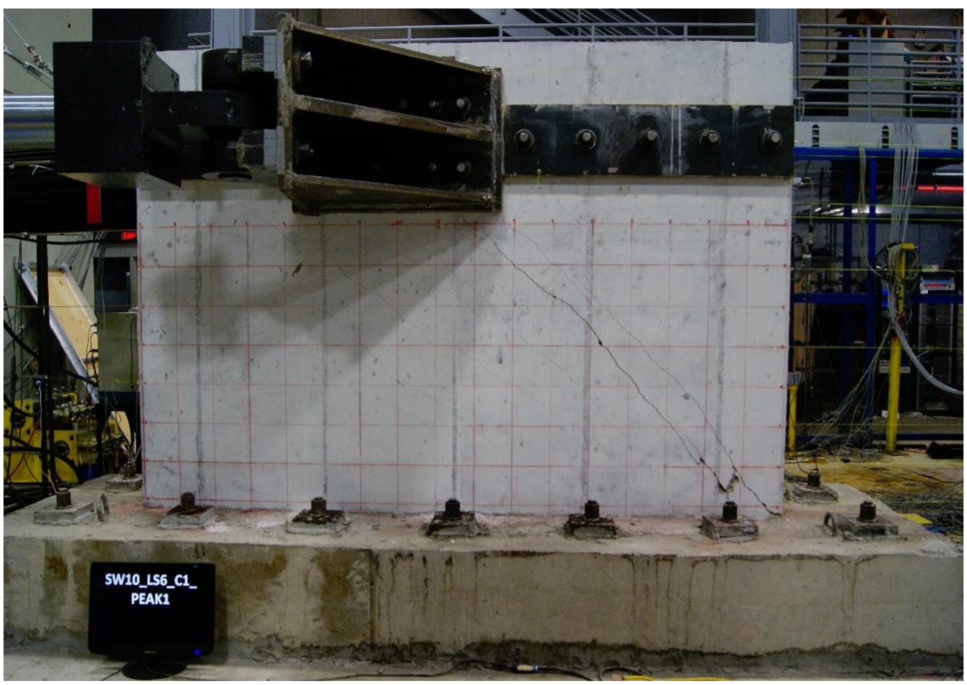

Figure E.83. Damage to SW1 at 0.52% drift ratio

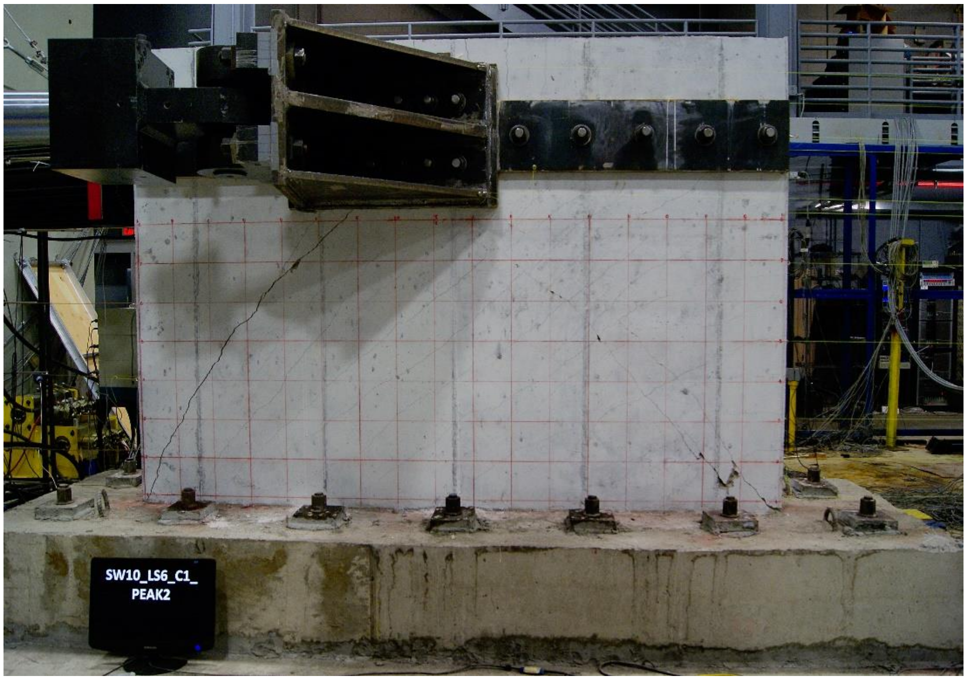

Figure E.84. Damage to SW10 at -0.58% drift ratio (peak strength)

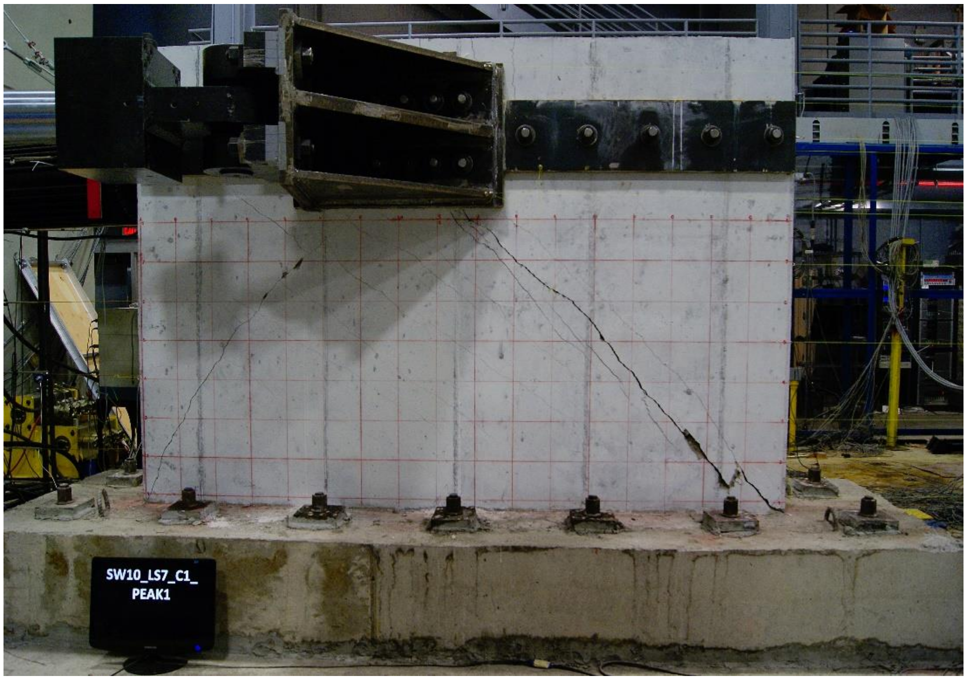

Figure E.85. Damage to SW10 at 0.93% drift ratio

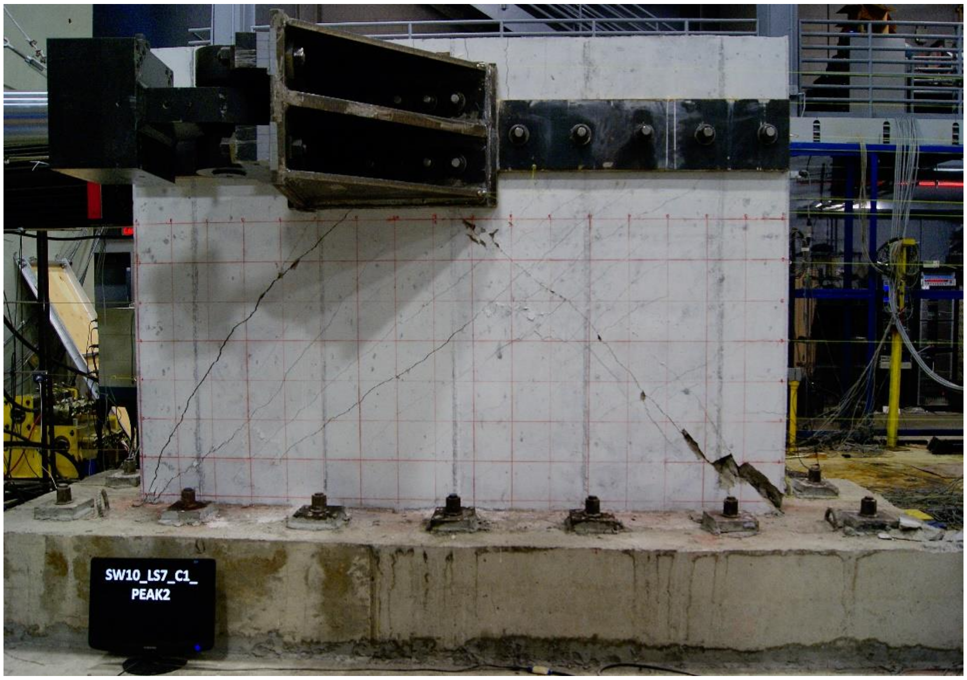

Figure E.86. Damage to SW10 at -0.87% drift ratio

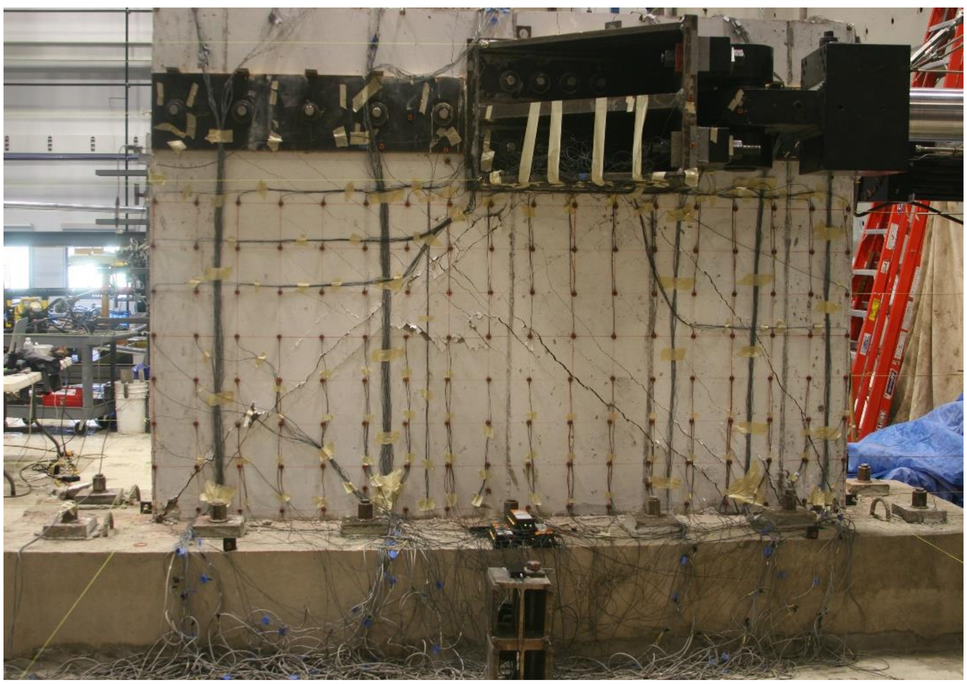
Figure E.87. Damage to SW10 at -0.87% drift ratio

Figure E.88. Damage to SW10 at -0.87% drift ratio

Figure E.89. Damage to SW10 at the end of testing


Figure E.90. Damage to SW10 at the end of testing

E.11 SW11

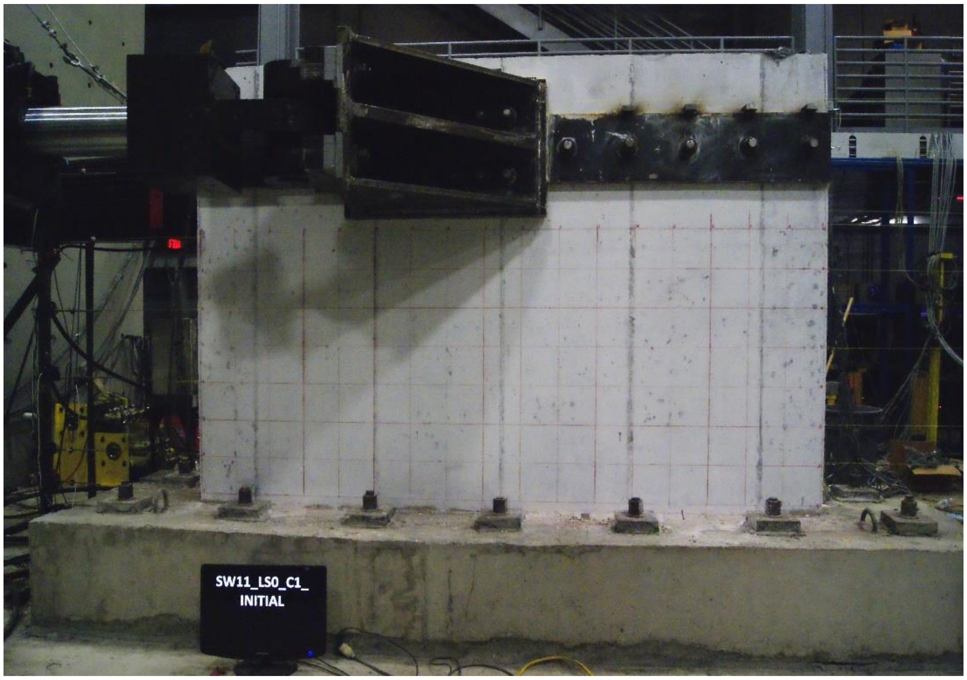

Figure E.91. SW11 before testing

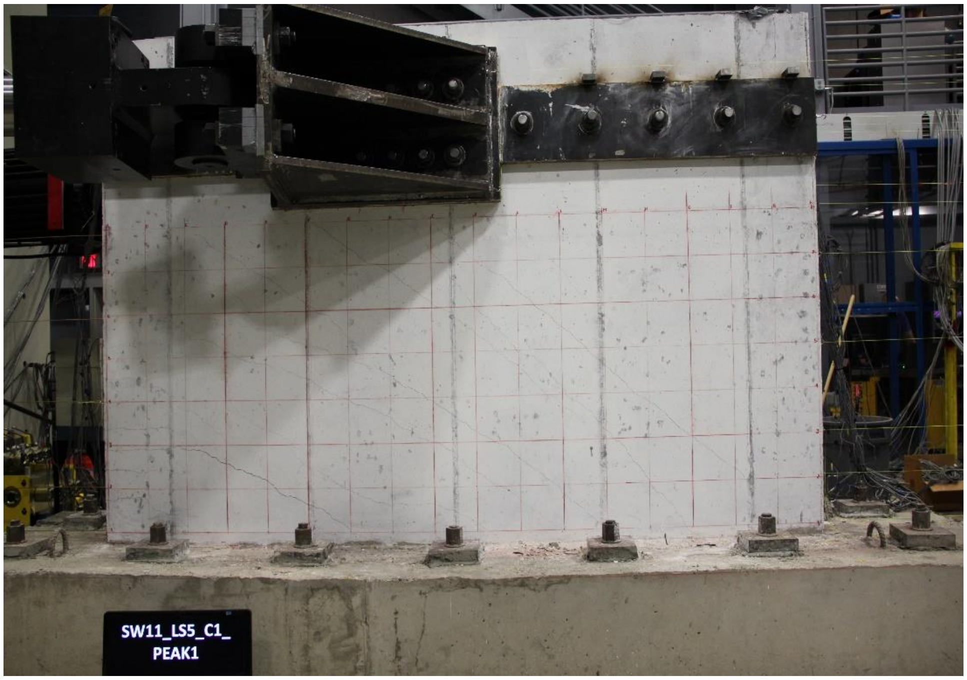

Figure E.92. Damage to SW11 at 0.56% drift ratio (peak strength)

Figure E.93. Damage to SW11 at -0.57% drift ratio

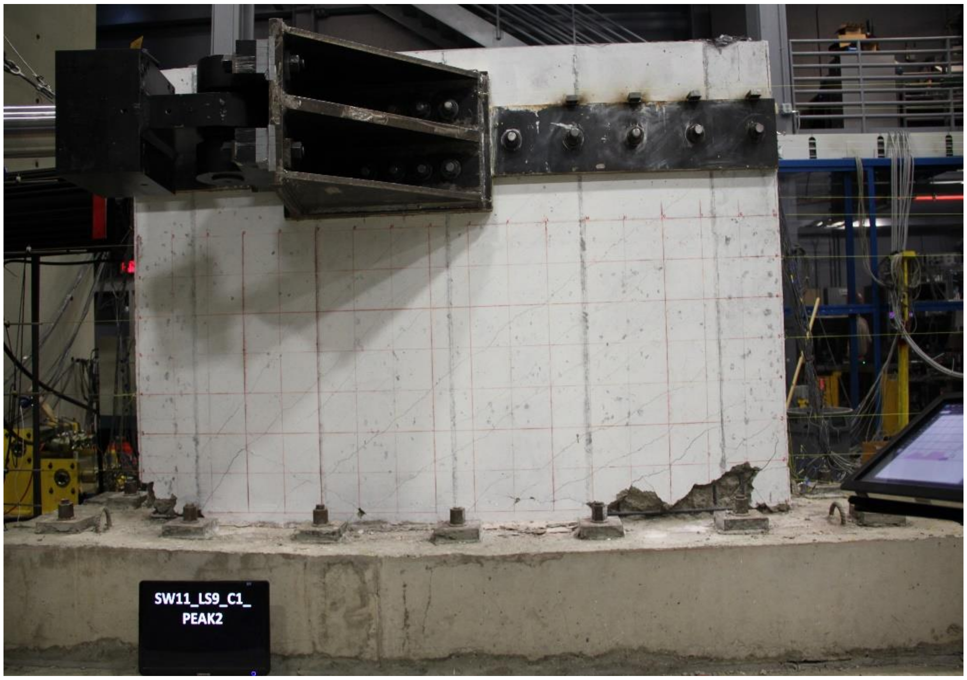

Figure E.94. Damage to SW11 at –1.75% drift ratio

Figure E.95. Damage to SW11 at 2.4% drift ratio

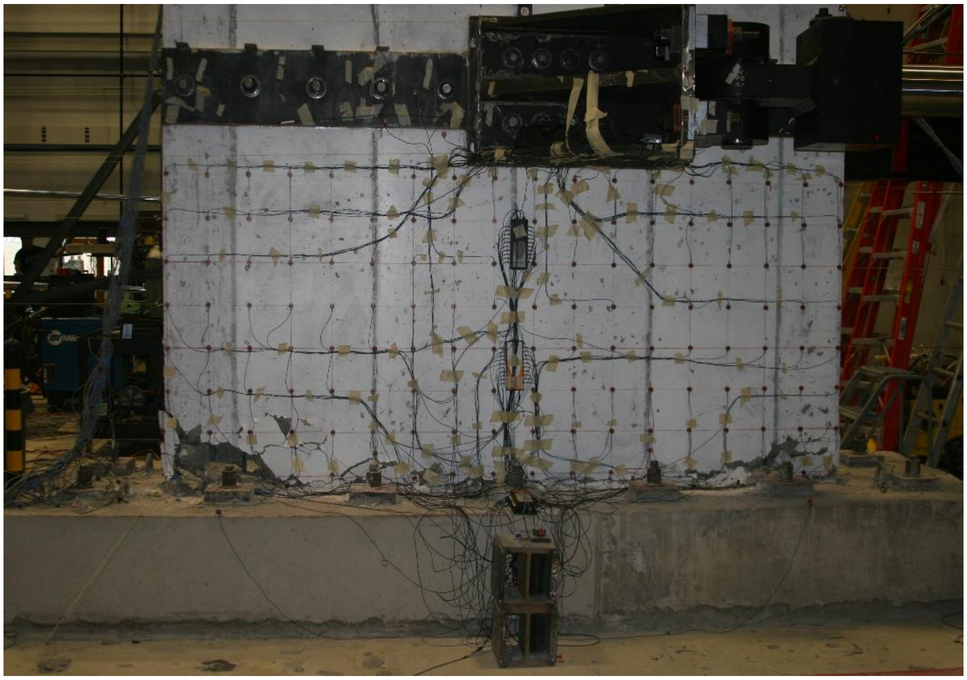
Figure E.96. Damage to SW11 at the end of testing

Figure E.97. Damage to SW11 at the end of testing

Figure E.98. Damage to SW11 at the end of testing

E.12 SW12

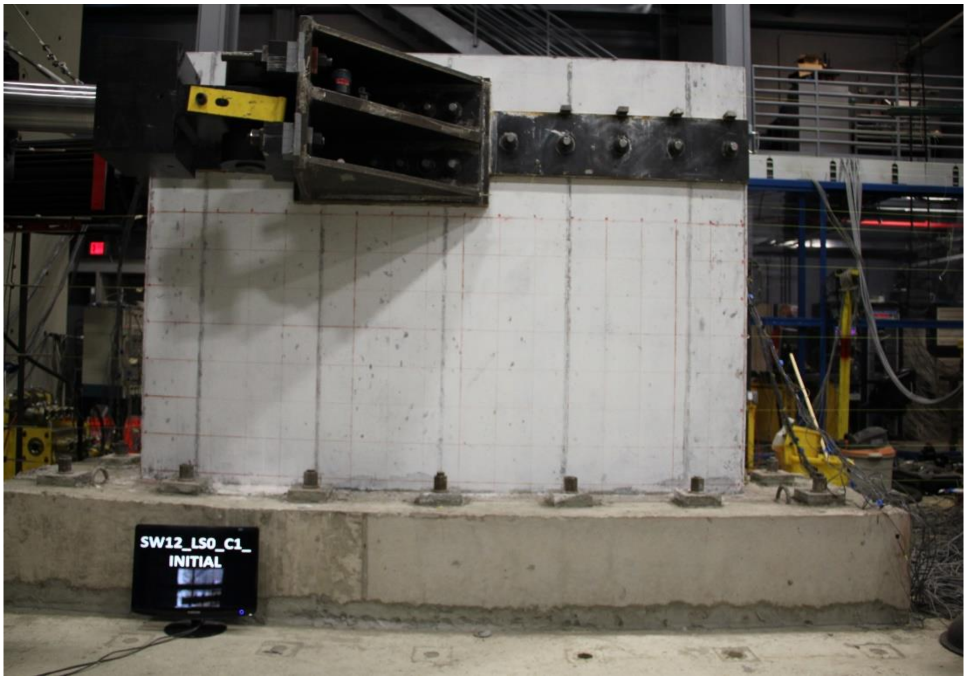

Figure E.99. SW12 before testing

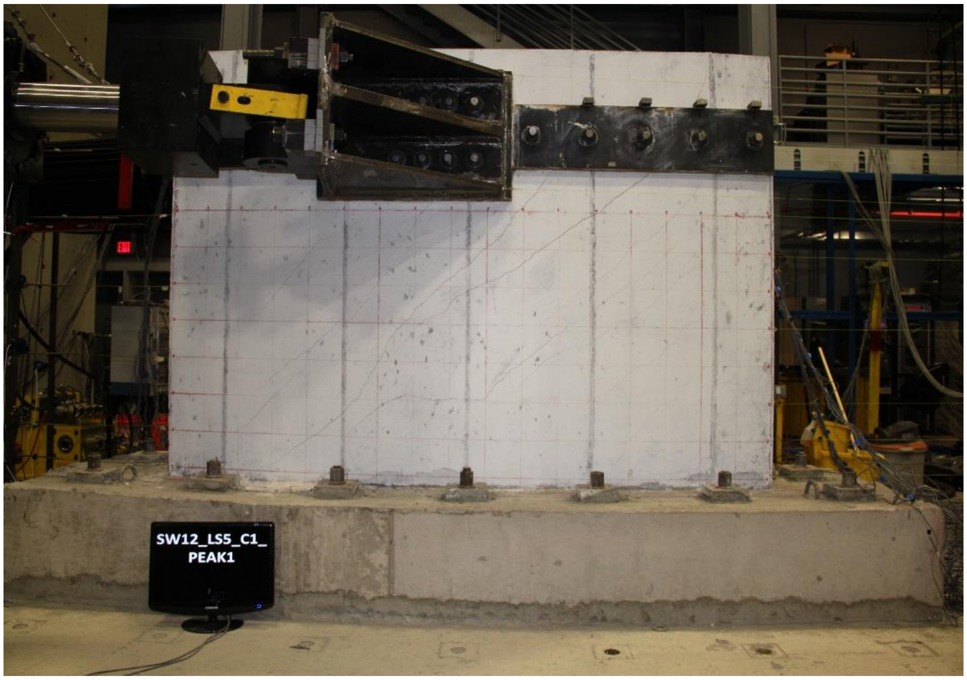

Figure E.100. Damage to SW12 at 0.54% drift ratio

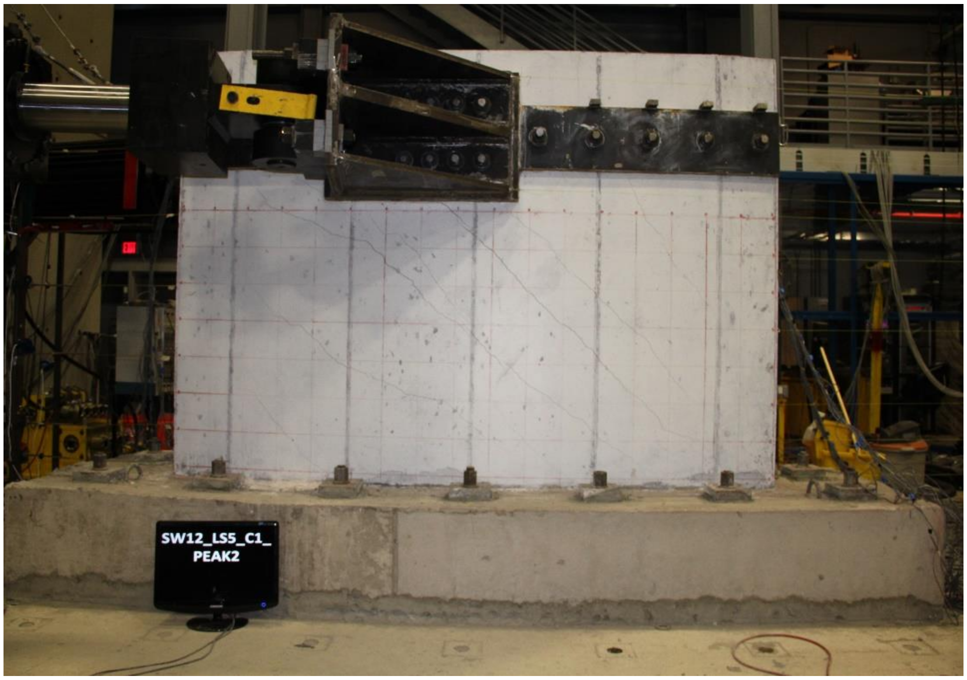

Figure E.101. Damage to SW12 at -0.54% drift ratio

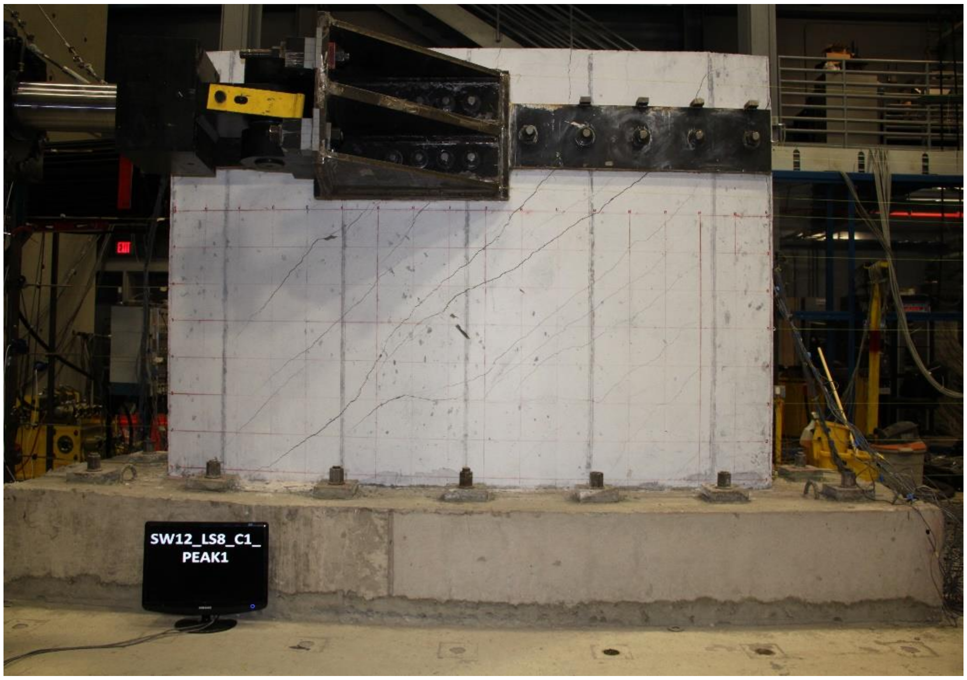

Figure E.102. Damage to SW12 at 1.24% drift ratio

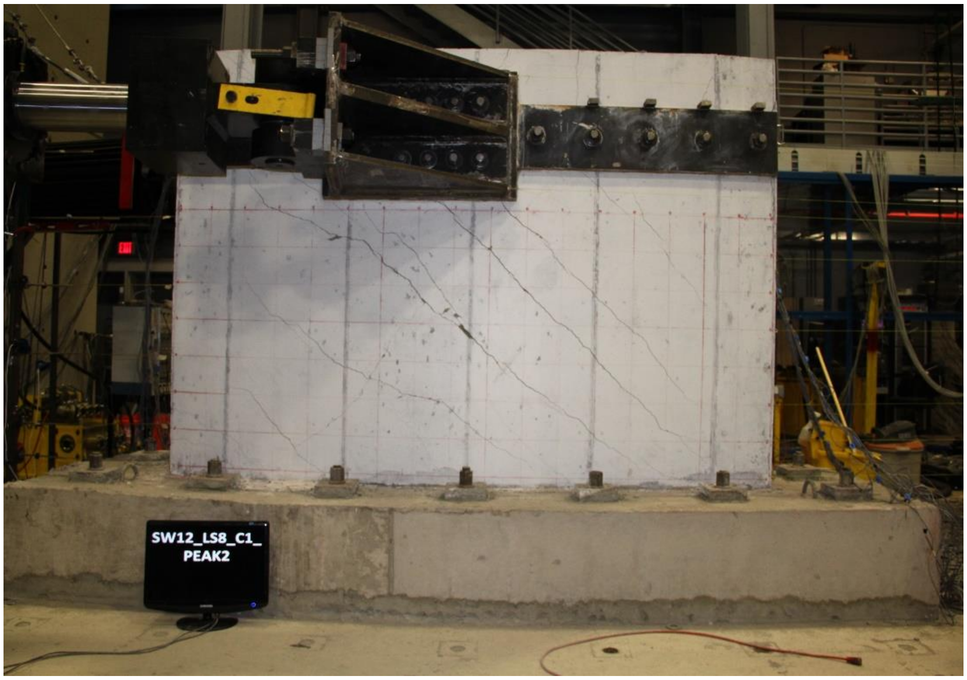

Figure E.103. Damage to SW12 at -1.24% drift ratio (peak strength)

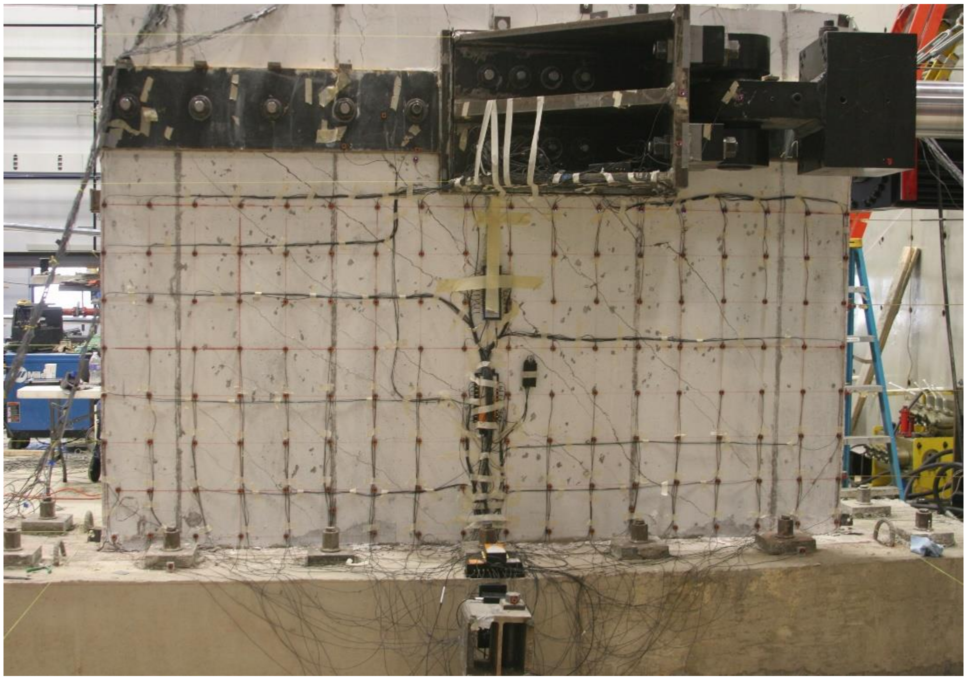
Figure E.104. Damage to SW12 at 1.63% drift ratio

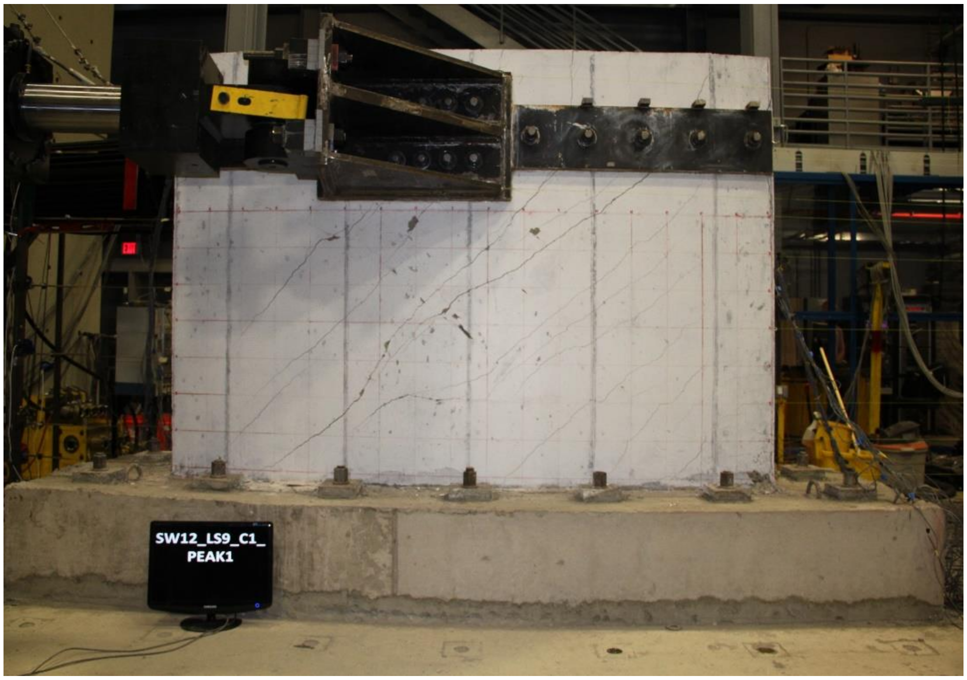

Figure E.105. Damage to SW12 at 1.63% drift ratio

Figure 0.2. Damage to SW12 at -1.64% drift ratio

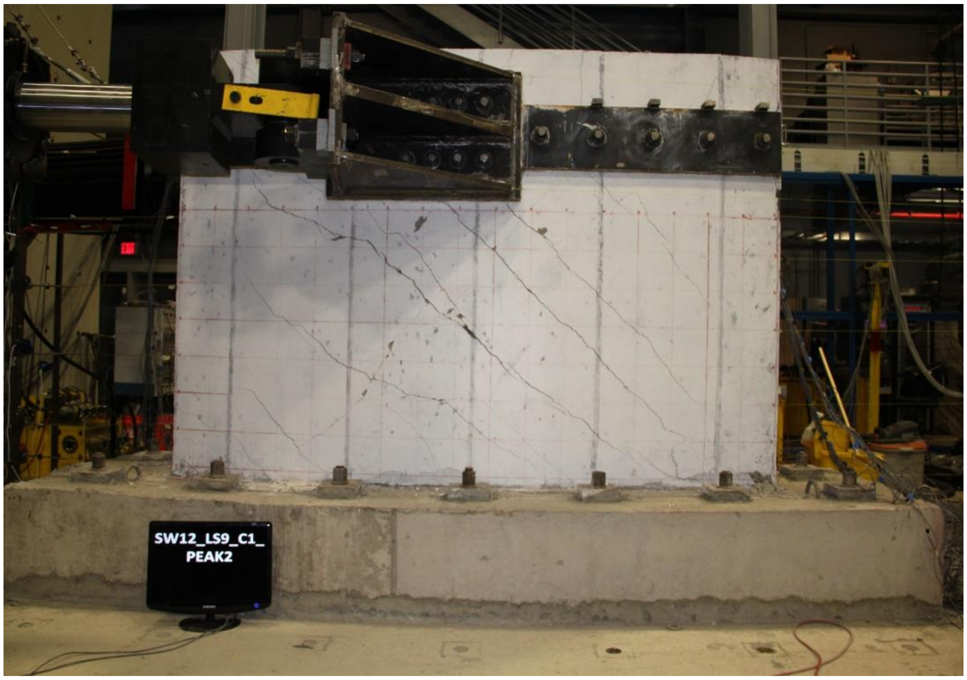

Figure E.107. Damage to SW12 at -1.64% drift ratio


Figure E.108. Damage to SW12 at the end of testing


Figure E.109. Damage to SW12 at the end of testing

MCEER Technical Reports

MCEER publishes technical reports on a variety of subjects written by authors funded through MCEER. These reports can be downloaded from the MCEER website at http://www.buffalo.edu/mceer. They can also be requested through NTIS, P.O. Box 1425, Springfield, Virginia 22151. NTIS accession numbers are shown in parenthesis, if available.

NCEER-87-0001 "First-Year Program in Research, Education and Technology Transfer," 3/5/87, (PB88-134275, A04, MF-A01).

NCEER-87-0002 "Experimental Evaluation of Instantaneous Optimal Algorithms for Structural Control," by R.C. Lin, T.T. Soong and A.M. Reinhorn, 4/20/87, (PB88-134341, A04, MF-A01).

NCEER-87-0003 "Experimentation Using the Earthquake Simulation Facilities at University at Buffalo," by A.M. Reinhorn and R.L. Ketter, not available.

NCEER-87-0004 "The System Characteristics and Performance of a Shaking Table," by J.S. Hwang, K.C. Chang and G.C. Lee, 6/1/87, (PB88-134259, A03, MF-A01). This report is available only through NTIS (see address given above).

NCEER-87-0005 "A Finite Element Formulation for Nonlinear Viscoplastic Material Using a Q Model," by O. Gyebi and G. Dasgupta, 11/2/87, (PB88-213764, A08, MF-A01).

NCEER-87-0006 "Symbolic Manipulation Program (SMP) - Algebraic Codes for Two and Three Dimensional Finite Element Formulations," by X. Lee and G. Dasgupta, 11/9/87, (PB88-218522, A05, MF-A01).

NCEER-87-0007 "Instantaneous Optimal Control Laws for Tall Buildings Under Seismic Excitations," by J.N. Yang, A. Akbarpour and P. Ghaemmaghami, 6/10/87, (PB88-134333, A06, MF-A01). This report is only available through NTIS (see address given above).

NCEER-87-0008 "IDARC: Inelastic Damage Analysis of Reinforced Concrete Frame - Shear-Wall Structures," by Y.J. Park, A.M. Reinhorn and S.K. Kunnath, 7/20/87, (PB88-134325, A09, MF-A01). This report is only available through NTIS (see address given above).

NCEER-87-0009 "Liquefaction Potential for New York State: A Preliminary Report on Sites in Manhattan and Buffalo," by M. Budhu, V. Vijayakumar, R.F. Giese and L. Baumgras, 8/31/87, (PB88-163704, A03, MF-A01). This report is available only through NTIS (see address given above).

NCEER-87-0010 "Vertical and Torsional Vibration of Foundations in Inhomogeneous Media," by A.S. Veletsos and K.W. Dotson, 6/1/87, (PB88-134291, A03, MF-A01). This report is only available through NTIS (see address given above).

NCEER-87-0011 "Seismic Probabilistic Risk Assessment and Seismic Margins Studies for Nuclear Power Plants," by Howard H.M. Hwang, 6/15/87, (PB88-134267, A03, MF-A01). This report is only available through NTIS (see address given above).

NCEER-87-0012 "Parametric Studies of Frequency Response of Secondary Systems Under Ground-Acceleration Excitations," by Y. Yong and Y.K. Lin, 6/10/87, (PB88-134309, A03, MF-A01). This report is only available through NTIS (see address given above).

NCEER-87-0013 "Frequency Response of Secondary Systems Under Seismic Excitation," by J.A. HoLung, J. Cai and Y.K. Lin, 7/31/87, (PB88-134317, A05, MF-A01). This report is only available through NTIS (see address given above).

NCEER-87-0014 "Modelling Earthquake Ground Motions in Seismically Active Regions Using Parametric Time Series Methods," by G.W. Ellis and A.S. Cakmak, 8/25/87, (PB88-134283, A08, MF-A01). This report is only available through NTIS (see address given above).

NCEER-87-0015 "Detection and Assessment of Seismic Structural Damage," by E. DiPasquale and A.S. Cakmak, 8/25/87, (PB88-163712, A05, MF-A01). This report is only available through NTIS (see address given above).

NCEER-87-0016 "Pipeline Experiment at Parkfield, California," by J. Isenberg and E. Richardson, 9/15/87, (PB88-163720, A03, MF-A01). This report is available only through NTIS (see address given above).

NCEER-87-0017 "Digital Simulation of Seismic Ground Motion," by M. Shinozuka, G. Deodatis and T. Harada, 8/31/87, (PB88-155197, A04, MF-A01). This report is available only through NTIS (see address given above).

NCEER-87-0018 "Practical Considerations for Structural Control: System Uncertainty, System Time Delay and Truncation of Small Control Forces," J.N. Yang and A. Akbarpour, 8/10/87, (PB88-163738, A08, MF-A01). This report is only available through NTIS (see address given above).

NCEER-87-0019 "Modal Analysis of Nonclassically Damped Structural Systems Using Canonical Transformation," by J.N. Yang, S. Sarkani and F.X. Long, 9/27/87, (PB88-187851, A04, MF-A01).

NCEER-87-0020 "A Nonstationary Solution in Random Vibration Theory," by J.R. Red-Horse and P.D. Spanos, 11/3/87, (PB88-163746, A03, MF-A01).

NCEER-87-0021 "Horizontal Impedances for Radially Inhomogeneous Viscoelastic Soil Layers," by A.S. Veletsos and K.W. Dotson, 10/15/87, (PB88-150859, A04, MF-A01).

NCEER-87-0022 "Seismic Damage Assessment of Reinforced Concrete Members," by Y.S. Chung, C. Meyer and M. Shinozuka, 10/9/87, (PB88-150867, A05, MF-A01). This report is available only through NTIS (see address given above).

NCEER-87-0023 "Active Structural Control in Civil Engineering," by T.T. Soong, 11/11/87, (PB88-187778, A03, MF-A01).

NCEER-87-0024 "Vertical and Torsional Impedances for Radially Inhomogeneous Viscoelastic Soil Layers," by K.W. Dotson and A.S. Veletsos, 12/87, (PB88-187786, A03, MF-A01).

NCEER-87-0025 "Proceedings from the Symposium on Seismic Hazards, Ground Motions, Soil-Liquefaction and Engineering Practice in Eastern North America," October 20-22, 1987, edited by K.H. Jacob, 12/87, (PB88-188115, A23, MF-A01). This report is available only through NTIS (see address given above).

NCEER-87-0026 "Report on the Whittier-Narrows, California, Earthquake of October 1, 1987," by J. Pantelic and A. Reinhorn, 11/87, (PB88-187752, A03, MF-A01). This report is available only through NTIS (see address given above).

NCEER-87-0027 "Design of a Modular Program for Transient Nonlinear Analysis of Large 3-D Building Structures," by S. Srivastav and J.F. Abel, 12/30/87, (PB88-187950, A05, MF-A01). This report is only available through NTIS (see address given above).

NCEER-87-0028 "Second-Year Program in Research, Education and Technology Transfer," 3/8/88, (PB88-219480, A04, MF-A01).

NCEER-88-0001 "Workshop on Seismic Computer Analysis and Design of Buildings With Interactive Graphics," by W. McGuire, J.F. Abel and C.H. Conley, 1/18/88, (PB88-187760, A03, MF-A01). This report is only available through NTIS (see address given above).

NCEER-88-0002 "Optimal Control of Nonlinear Flexible Structures," by J.N. Yang, F.X. Long and D. Wong, 1/22/88, (PB88-213772, A06, MF-A01).

NCEER-88-0003 "Substructuring Techniques in the Time Domain for Primary-Secondary Structural Systems," by G.D. Manolis and G. Juhn, 2/10/88, (PB88-213780, A04, MF-A01).

NCEER-88-0004 "Iterative Seismic Analysis of Primary-Secondary Systems," by A. Singhal, L.D. Lutes and P.D. Spanos, 2/23/88, (PB88-213798, A04, MF-A01).

NCEER-88-0005 "Stochastic Finite Element Expansion for Random Media," by P.D. Spanos and R. Ghanem, 3/14/88, (PB88-213806, A03, MF-A01).

NCEER-88-0006 "Combining Structural Optimization and Structural Control," by F.Y. Cheng and C.P. Pantelides, 1/10/88, (PB88-213814, A05, MF-A01).

NCEER-88-0007 "Seismic Performance Assessment of Code-Designed Structures," by H.H-M. Hwang, J-W. Jaw and H-J. Shau, 3/20/88, (PB88-219423, A04, MF-A01). This report is only available through NTIS (see address given above).

NCEER-88-0008 "Reliability Analysis of Code-Designed Structures Under Natural Hazards," by H.H-M. Hwang, H. Ushiba and M. Shinozuka, 2/29/88, (PB88-229471, A07, MF-A01). This report is only available through NTIS (see address given above).

NCEER-88-0009 "Seismic Fragility Analysis of Shear Wall Structures," by J-W Jaw and H.H-M. Hwang, 4/30/88, (PB89-102867, A04, MF-A01).

NCEER-88-0010 "Base Isolation of a Multi-Story Building Under a Harmonic Ground Motion - A Comparison of Performances of Various Systems," by F-G Fan, G. Ahmadi and I.G. Tadjbakhsh, 5/18/88, (PB89-122238, A06, MF-A01). This report is only available through NTIS (see address given above).

NCEER-88-0011 "Seismic Floor Response Spectra for a Combined System by Green's Functions," by F.M. Lavelle, L.A. Bergman and P.D. Spanos, 5/1/88, (PB89-102875, A03, MF-A01).

NCEER-88-0012 "A New Solution Technique for Randomly Excited Hysteretic Structures," by G.Q. Cai and Y.K. Lin, 5/16/88, (PB89-102883, A03, MF-A01).

NCEER-88-0013 "A Study of Radiation Damping and Soil-Structure Interaction Effects in the Centrifuge," by K. Weissman, supervised by J.H. Prevost, 5/24/88, (PB89-144703, A06, MF-A01).

NCEER-88-0014 "Parameter Identification and Implementation of a Kinematic Plasticity Model for Frictional Soils," by J.H. Prevost and D.V. Griffiths, not available.

NCEER-88-0015 "Two- and Three- Dimensional Dynamic Finite Element Analyses of the Long Valley Dam," by D.V. Griffiths and J.H. Prevost, 6/17/88, (PB89-144711, A04, MF-A01).

NCEER-88-0016 "Damage Assessment of Reinforced Concrete Structures in Eastern United States," by A.M. Reinhorn, M.J. Seidel, S.K. Kunnath and Y.J. Park, 6/15/88, (PB89-122220, A04, MF-A01). This report is only available through NTIS (see address given above).

NCEER-88-0017 "Dynamic Compliance of Vertically Loaded Strip Foundations in Multilayered Viscoelastic Soils," by S. Ahmad and A.S.M. Israil, 6/17/88, (PB89-102891, A04, MF-A01).

NCEER-88-0018 "An Experimental Study of Seismic Structural Response With Added Viscoelastic Dampers," by R.C. Lin, Z. Liang, T.T. Soong and R.H. Zhang, 6/30/88, (PB89-122212, A05, MF-A01). This report is available only through NTIS (see address given above).

NCEER-88-0019 "Experimental Investigation of Primary - Secondary System Interaction," by G.D. Manolis, G. Juhn and A.M. Reinhorn, 5/27/88, (PB89-122204, A04, MF-A01).

NCEER-88-0020 "A Response Spectrum Approach For Analysis of Nonclassically Damped Structures," by J.N. Yang, S. Sarkani and F.X. Long, 4/22/88, (PB89-102909, A04, MF-A01).

NCEER-88-0021 "Seismic Interaction of Structures and Soils: Stochastic Approach," by A.S. Veletsos and A.M. Prasad, 7/21/88, (PB89-122196, A04, MF-A01). This report is only available through NTIS (see address given above).

NCEER-88-0022 "Identification of the Serviceability Limit State and Detection of Seismic Structural Damage," by E. DiPasquale and A.S. Cakmak, 6/15/88, (PB89-122188, A05, MF-A01). This report is available only through NTIS (see address given above).

NCEER-88-0023 "Multi-Hazard Risk Analysis: Case of a Simple Offshore Structure," by B.K. Bhartia and E.H. Vanmarcke, 7/21/88, (PB89-145213, A05, MF-A01).

NCEER-88-0024 "Automated Seismic Design of Reinforced Concrete Buildings," by Y.S. Chung, C. Meyer and M. Shinozuka, 7/5/88, (PB89-122170, A06, MF-A01). This report is available only through NTIS (see address given above).

NCEER-88-0025 "Experimental Study of Active Control of MDOF Structures Under Seismic Excitations," by L.L. Chung, R.C. Lin, T.T. Soong and A.M. Reinhorn, 7/10/88, (PB89-122600, A04, MF-A01).

NCEER-88-0026 "Earthquake Simulation Tests of a Low-Rise Metal Structure," by J.S. Hwang, K.C. Chang, G.C. Lee and R.L. Ketter, 8/1/88, (PB89-102917, A04, MF-A01).

NCEER-88-0027 "Systems Study of Urban Response and Reconstruction Due to Catastrophic Earthquakes," by F. Kozin and H.K. Zhou, 9/22/88, (PB90-162348, A04, MF-A01).

NCEER-88-0028 "Seismic Fragility Analysis of Plane Frame Structures," by H.H-M. Hwang and Y.K. Low, 7/31/88, (PB89-131445, A06, MF-A01).

NCEER-88-0029 "Response Analysis of Stochastic Structures," by A. Kardara, C. Bucher and M. Shinozuka, 9/22/88, (PB89-174429, A04, MF-A01).

NCEER-88-0030 "Nonnormal Accelerations Due to Yielding in a Primary Structure," by D.C.K. Chen and L.D. Lutes, 9/19/88, (PB89-131437, A04, MF-A01).

NCEER-88-0031 "Design Approaches for Soil-Structure Interaction," by A.S. Veletsos, A.M. Prasad and Y. Tang, 12/30/88, (PB89-174437, A03, MF-A01). This report is available only through NTIS (see address given above).

NCEER-88-0032 "A Re-evaluation of Design Spectra for Seismic Damage Control," by C.J. Turkstra and A.G. Tallin, 11/7/88, (PB89-145221, A05, MF-A01).

NCEER-88-0033 "The Behavior and Design of Noncontact Lap Splices Subjected to Repeated Inelastic Tensile Loading," by V.E. Sagan, P. Gergely and R.N. White, 12/8/88, (PB89-163737, A08, MF-A01).

NCEER-88-0034 "Seismic Response of Pile Foundations," by S.M. Mamoon, P.K. Banerjee and S. Ahmad, 11/1/88, (PB89-145239, A04, MF-A01).

NCEER-88-0035 "Modeling of R/C Building Structures With Flexible Floor Diaphragms (IDARC2)," by A.M. Reinhorn, S.K. Kunnath and N. Panahshahi, 9/7/88, (PB89-207153, A07, MF-A01).

NCEER-88-0036 "Solution of the Dam-Reservoir Interaction Problem Using a Combination of FEM, BEM with Particular Integrals, Modal Analysis, and Substructuring," by C-S. Tsai, G.C. Lee and R.L. Ketter, 12/31/88, (PB89-207146, A04, MF-A01).

NCEER-88-0037 "Optimal Placement of Actuators for Structural Control," by F.Y. Cheng and C.P. Pantelides, 8/15/88, (PB89-162846, A05, MF-A01).

NCEER-88-0038 "Teflon Bearings in Aseismic Base Isolation: Experimental Studies and Mathematical Modeling," by A. Mokha, M.C. Constantinou and A.M. Reinhorn, 12/5/88, (PB89-218457, A10, MF-A01). This report is available only through NTIS (see address given above).

NCEER-88-0039 "Seismic Behavior of Flat Slab High-Rise Buildings in the New York City Area," by P. Weidlinger and M. Ettouney, 10/15/88, (PB90-145681, A04, MF-A01).

NCEER-88-0040 "Evaluation of the Earthquake Resistance of Existing Buildings in New York City," by P. Weidlinger and M. Ettouney, 10/15/88, not available.

NCEER-88-0041 "Small-Scale Modeling Techniques for Reinforced Concrete Structures Subjected to Seismic Loads," by W. Kim, A. El-Attar and R.N. White, 11/22/88, (PB89-189625, A05, MF-A01).

NCEER-88-0042 "Modeling Strong Ground Motion from Multiple Event Earthquakes," by G.W. Ellis and A.S. Cakmak, 10/15/88, (PB89-174445, A03, MF-A01).

NCEER-88-0043 "Nonstationary Models of Seismic Ground Acceleration," by M. Grigoriu, S.E. Ruiz and E. Rosenblueth, 7/15/88, (PB89-189617, A04, MF-A01).

NCEER-88-0044 "SARCF User's Guide: Seismic Analysis of Reinforced Concrete Frames," by Y.S. Chung, C. Meyer and M. Shinozuka, 11/9/88, (PB89-174452, A08, MF-A01).

NCEER-88-0045 "First Expert Panel Meeting on Disaster Research and Planning," edited by J. Pantelic and J. Stoyle, 9/15/88, (PB89-174460, A05, MF-A01).

NCEER-88-0046 "Preliminary Studies of the Effect of Degrading Infill Walls on the Nonlinear Seismic Response of Steel Frames," by C.Z. Chrysostomou, P. Gergely and J.F. Abel, 12/19/88, (PB89-208383, A05, MF-A01).

NCEER-88-0047 "Reinforced Concrete Frame Component Testing Facility - Design, Construction, Instrumentation and Operation," by S.P. Pessiki, C. Conley, T. Bond, P. Gergely and R.N. White, 12/16/88, (PB89-174478, A04, MF-A01).

NCEER-89-0001 "Effects of Protective Cushion and Soil Compliancy on the Response of Equipment Within a Seismically Excited Building," by J.A. HoLung, 2/16/89, (PB89-207179, A04, MF-A01).

NCEER-89-0002 "Statistical Evaluation of Response Modification Factors for Reinforced Concrete Structures," by H.H-M. Hwang and J-W. Jaw, 2/17/89, (PB89-207187, A05, MF-A01).

NCEER-89-0003 "Hysteretic Columns Under Random Excitation," by G-Q. Cai and Y.K. Lin, 1/9/89, (PB89-196513, A03, MF-A01).

NCEER-89-0004 "Experimental Study of `Elephant Foot Bulge' Instability of Thin-Walled Metal Tanks," by Z-H. Jia and R.L. Ketter, 2/22/89, (PB89-207195, A03, MF-A01).

NCEER-89-0005 "Experiment on Performance of Buried Pipelines Across San Andreas Fault," by J. Isenberg, E. Richardson and T.D. O'Rourke, 3/10/89, (PB89-218440, A04, MF-A01). This report is available only through NTIS (see address given above).

NCEER-89-0006 "A Knowledge-Based Approach to Structural Design of Earthquake-Resistant Buildings," by M. Subramani, P. Gergely, C.H. Conley, J.F. Abel and A.H. Zaghw, 1/15/89, (PB89-218465, A06, MF-A01).

NCEER-89-0007 "Liquefaction Hazards and Their Effects on Buried Pipelines," by T.D. O'Rourke and P.A. Lane, 2/1/89, (PB89-218481, A09, MF-A01).

NCEER-89-0008 "Fundamentals of System Identification in Structural Dynamics," by H. Imai, C-B. Yun, O. Maruyama and M. Shinozuka, 1/26/89, (PB89-207211, A04, MF-A01).

NCEER-89-0009 "Effects of the 1985 Michoacan Earthquake on Water Systems and Other Buried Lifelines in Mexico," by A.G. Ayala and M.J. O'Rourke, 3/8/89, (PB89-207229, A06, MF-A01).

NCEER-89-R010 "NCEER Bibliography of Earthquake Education Materials," by K.E.K. Ross, Second Revision, 9/1/89, (PB90-125352, A05, MF-A01). This report is replaced by NCEER-92-0018.

NCEER-89-0011 "Inelastic Three-Dimensional Response Analysis of Reinforced Concrete Building Structures (IDARC-3D), Part I - Modeling," by S.K. Kunnath and A.M. Reinhorn, 4/17/89, (PB90-114612, A07, MF-A01). This report is available only through NTIS (see address given above).

NCEER-89-0012 "Recommended Modifications to ATC-14," by C.D. Poland and J.O. Malley, 4/12/89, (PB90-108648, A15, MF-A01).

NCEER-89-0013 "Repair and Strengthening of Beam-to-Column Connections Subjected to Earthquake Loading," by M. Corazao and A.J. Durrani, 2/28/89, (PB90-109885, A06, MF-A01).

NCEER-89-0014 "Program EXKAL2 for Identification of Structural Dynamic Systems," by O. Maruyama, C-B. Yun, M. Hoshiya and M. Shinozuka, 5/19/89, (PB90-109877, A09, MF-A01).

NCEER-89-0015 "Response of Frames With Bolted Semi-Rigid Connections, Part I - Experimental Study and Analytical Predictions," by P.J. DiCorso, A.M. Reinhorn, J.R. Dickerson, J.B. Radziminski and W.L. Harper, 6/1/89, not available.

NCEER-89-0016 "ARMA Monte Carlo Simulation in Probabilistic Structural Analysis," by P.D. Spanos and M.P. Mignolet, 7/10/89, (PB90-109893, A03, MF-A01).

NCEER-89-P017 "Preliminary Proceedings from the Conference on Disaster Preparedness - The Place of Earthquake Education in Our Schools," Edited by K.E.K. Ross, 6/23/89, (PB90-108606, A03, MF-A01).

NCEER-89-0017 "Proceedings from the Conference on Disaster Preparedness - The Place of Earthquake Education in Our Schools," Edited by K.E.K. Ross, 12/31/89, (PB90-207895, A012, MF-A02). This report is available only through NTIS (see address given above).

NCEER-89-0018 "Multidimensional Models of Hysteretic Material Behavior for Vibration Analysis of Shape Memory Energy Absorbing Devices, by E.J. Graesser and F.A. Cozzarelli, 6/7/89, (PB90-164146, A04, MF-A01).

NCEER-89-0019 "Nonlinear Dynamic Analysis of Three-Dimensional Base Isolated Structures (3D-BASIS)," by S. Nagarajaiah, A.M. Reinhorn and M.C. Constantinou, 8/3/89, (PB90-161936, A06, MF-A01). This report has been replaced by NCEER-93-0011.

NCEER-89-0020 "Structural Control Considering Time-Rate of Control Forces and Control Rate Constraints," by F.Y. Cheng and C.P. Pantelides, 8/3/89, (PB90-120445, A04, MF-A01).

NCEER-89-0021 "Subsurface Conditions of Memphis and Shelby County," by K.W. Ng, T-S. Chang and H-H.M. Hwang, 7/26/89, (PB90-120437, A03, MF-A01).

NCEER-89-0022 "Seismic Wave Propagation Effects on Straight Jointed Buried Pipelines," by K. Elhmadi and M.J. O'Rourke, 8/24/89, (PB90-162322, A10, MF-A02).

NCEER-89-0023 "Workshop on Serviceability Analysis of Water Delivery Systems," edited by M. Grigoriu, 3/6/89, (PB90-127424, A03, MF-A01).

NCEER-89-0024 "Shaking Table Study of a 1/5 Scale Steel Frame Composed of Tapered Members," by K.C. Chang, J.S. Hwang and G.C. Lee, 9/18/89, (PB90-160169, A04, MF-A01).

NCEER-89-0025 "DYNA1D: A Computer Program for Nonlinear Seismic Site Response Analysis - Technical Documentation," by Jean H. Prevost, 9/14/89, (PB90-161944, A07, MF-A01). This report is available only through NTIS (see address given above).

NCEER-89-0026 "1:4 Scale Model Studies of Active Tendon Systems and Active Mass Dampers for Aseismic Protection," by A.M. Reinhorn, T.T. Soong, R.C. Lin, Y.P. Yang, Y. Fukao, H. Abe and M. Nakai, 9/15/89, (PB90-173246, A10, MF-A02). This report is available only through NTIS (see address given above).

NCEER-89-0027 "Scattering of Waves by Inclusions in a Nonhomogeneous Elastic Half Space Solved by Boundary Element Methods," by P.K. Hadley, A. Askar and A.S. Cakmak, 6/15/89, (PB90-145699, A07, MF-A01).

NCEER-89-0028 "Statistical Evaluation of Deflection Amplification Factors for Reinforced Concrete Structures," by H.H.M. Hwang, J-W. Jaw and A.L. Ch'ng, 8/31/89, (PB90-164633, A05, MF-A01).

NCEER-89-0029 "Bedrock Accelerations in Memphis Area Due to Large New Madrid Earthquakes," by H.H.M. Hwang, C.H.S. Chen and G. Yu, 11/7/89, (PB90-162330, A04, MF-A01).

NCEER-89-0030 "Seismic Behavior and Response Sensitivity of Secondary Structural Systems," by Y.Q. Chen and T.T. Soong, 10/23/89, (PB90-164658, A08, MF-A01).

NCEER-89-0031 "Random Vibration and Reliability Analysis of Primary-Secondary Structural Systems," by Y. Ibrahim, M. Grigoriu and T.T. Soong, 11/10/89, (PB90-161951, A04, MF-A01).

NCEER-89-0032 "Proceedings from the Second U.S. - Japan Workshop on Liquefaction, Large Ground Deformation and Their Effects on Lifelines, September 26-29, 1989," Edited by T.D. O'Rourke and M. Hamada, 12/1/89, (PB90-209388, A22, MF-A03).

NCEER-89-0033 "Deterministic Model for Seismic Damage Evaluation of Reinforced Concrete Structures," by J.M. Bracci, A.M. Reinhorn, J.B. Mander and S.K. Kunnath, 9/27/89, (PB91-108803, A06, MF-A01).

NCEER-89-0034 "On the Relation Between Local and Global Damage Indices," by E. DiPasquale and A.S. Cakmak, 8/15/89, (PB90-173865, A05, MF-A01).

NCEER-89-0035 "Cyclic Undrained Behavior of Nonplastic and Low Plasticity Silts," by A.J. Walker and H.E. Stewart, 7/26/89, (PB90-183518, A10, MF-A01).

NCEER-89-0036 "Liquefaction Potential of Surficial Deposits in the City of Buffalo, New York," by M. Budhu, R. Giese and L. Baumgrass, 1/17/89, (PB90-208455, A04, MF-A01).

NCEER-89-0037 "A Deterministic Assessment of Effects of Ground Motion Incoherence," by A.S. Veletsos and Y. Tang, 7/15/89, (PB90-164294, A03, MF-A01).

NCEER-89-0038 "Workshop on Ground Motion Parameters for Seismic Hazard Mapping," July 17-18, 1989, edited by R.V. Whitman, 12/1/89, (PB90-173923, A04, MF-A01).

NCEER-89-0039 "Seismic Effects on Elevated Transit Lines of the New York City Transit Authority," by C.J. Costantino, C.A. Miller and E. Heymsfield, 12/26/89, (PB90-207887, A06, MF-A01).

NCEER-89-0040 "Centrifugal Modeling of Dynamic Soil-Structure Interaction," by K. Weissman, Supervised by J.H. Prevost, 5/10/89, (PB90-207879, A07, MF-A01).

NCEER-89-0041 "Linearized Identification of Buildings With Cores for Seismic Vulnerability Assessment," by I-K. Ho and A.E. Aktan, 11/1/89, (PB90-251943, A07, MF-A01).

NCEER-90-0001 "Geotechnical and Lifeline Aspects of the October 17, 1989 Loma Prieta Earthquake in San Francisco," by T.D. O'Rourke, H.E. Stewart, F.T. Blackburn and T.S. Dickerman, 1/90, (PB90-208596, A05, MF-A01).

NCEER-90-0002 "Nonnormal Secondary Response Due to Yielding in a Primary Structure," by D.C.K. Chen and L.D. Lutes, 2/28/90, (PB90-251976, A07, MF-A01).

NCEER-90-0003 "Earthquake Education Materials for Grades K-12," by K.E.K. Ross, 4/16/90, (PB91-251984, A05, MF-A05). This report has been replaced by NCEER-92-0018.

NCEER-90-0004 "Catalog of Strong Motion Stations in Eastern North America," by R.W. Busby, 4/3/90, (PB90-251984, A05, MF-A01).

NCEER-90-0005 "NCEER Strong-Motion Data Base: A User Manual for the GeoBase Release (Version 1.0 for the Sun3)," by P. Friberg and K. Jacob, 3/31/90 (PB90-258062, A04, MF-A01).

NCEER-90-0006 "Seismic Hazard Along a Crude Oil Pipeline in the Event of an 1811-1812 Type New Madrid Earthquake," by H.H.M. Hwang and C-H.S. Chen, 4/16/90, (PB90-258054, A04, MF-A01).

NCEER-90-0007 "Site-Specific Response Spectra for Memphis Sheahan Pumping Station," by H.H.M. Hwang and C.S. Lee, 5/15/90, (PB91-108811, A05, MF-A01).

NCEER-90-0008 "Pilot Study on Seismic Vulnerability of Crude Oil Transmission Systems," by T. Ariman, R. Dobry, M. Grigoriu, F. Kozin, M. O'Rourke, T. O'Rourke and M. Shinozuka, 5/25/90, (PB91-108837, A06, MF-A01).

NCEER-90-0009 "A Program to Generate Site Dependent Time Histories: EQGEN," by G.W. Ellis, M. Srinivasan and A.S. Cakmak, 1/30/90, (PB91-108829, A04, MF-A01).

NCEER-90-0010 "Active Isolation for Seismic Protection of Operating Rooms," by M.E. Talbott, Supervised by M. Shinozuka, 6/8/9, (PB91-110205, A05, MF-A01).

NCEER-90-0011 "Program LINEARID for Identification of Linear Structural Dynamic Systems," by C-B. Yun and M. Shinozuka, 6/25/90, (PB91-110312, A08, MF-A01).

NCEER-90-0012 "Two-Dimensional Two-Phase Elasto-Plastic Seismic Response of Earth Dams," by A.N. Yiagos, Supervised by J.H. Prevost, 6/20/90, (PB91-110197, A13, MF-A02).

NCEER-90-0013 "Secondary Systems in Base-Isolated Structures: Experimental Investigation, Stochastic Response and Stochastic Sensitivity," by G.D. Manolis, G. Juhn, M.C. Constantinou and A.M. Reinhorn, 7/1/90, (PB91-110320, A08, MF-A01).

NCEER-90-0014 "Seismic Behavior of Lightly-Reinforced Concrete Column and Beam-Column Joint Details," by S.P. Pessiki, C.H. Conley, P. Gergely and R.N. White, 8/22/90, (PB91-108795, A11, MF-A02).

NCEER-90-0015 "Two Hybrid Control Systems for Building Structures Under Strong Earthquakes," by J.N. Yang and A. Danielians, 6/29/90, (PB91-125393, A04, MF-A01).

NCEER-90-0016 "Instantaneous Optimal Control with Acceleration and Velocity Feedback," by J.N. Yang and Z. Li, 6/29/90, (PB91-125401, A03, MF-A01).

NCEER-90-0017 "Reconnaissance Report on the Northern Iran Earthquake of June 21, 1990," by M. Mehrain, 10/4/90, (PB91-125377, A03, MF-A01).

NCEER-90-0018 "Evaluation of Liquefaction Potential in Memphis and Shelby County," by T.S. Chang, P.S. Tang, C.S. Lee and H. Hwang, 8/10/90, (PB91-125427, A09, MF-A01).

NCEER-90-0019 "Experimental and Analytical Study of a Combined Sliding Disc Bearing and Helical Steel Spring Isolation System," by M.C. Constantinou, A.S. Mokha and A.M. Reinhorn, 10/4/90, (PB91-125385, A06, MF-A01). This report is available only through NTIS (see address given above).

NCEER-90-0020 "Experimental Study and Analytical Prediction of Earthquake Response of a Sliding Isolation System with a Spherical Surface," by A.S. Mokha, M.C. Constantinou and A.M. Reinhorn, 10/11/90, (PB91-125419, A05, MF-A01).

NCEER-90-0021 "Dynamic Interaction Factors for Floating Pile Groups," by G. Gazetas, K. Fan, A. Kaynia and E. Kausel, 9/10/90, (PB91-170381, A05, MF-A01).

NCEER-90-0022 "Evaluation of Seismic Damage Indices for Reinforced Concrete Structures," by S. Rodriguez-Gomez and A.S. Cakmak, 9/30/90, PB91-171322, A06, MF-A01).

NCEER-90-0023 "Study of Site Response at a Selected Memphis Site," by H. Desai, S. Ahmad, E.S. Gazetas and M.R. Oh, 10/11/90, (PB91-196857, A03, MF-A01).

NCEER-90-0024 "A User's Guide to Strongmo: Version 1.0 of NCEER's Strong-Motion Data Access Tool for PCs and Terminals," by P.A. Friberg and C.A.T. Susch, 11/15/90, (PB91-171272, A03, MF-A01).

NCEER-90-0025 "A Three-Dimensional Analytical Study of Spatial Variability of Seismic Ground Motions," by L-L. Hong and A.H.-S. Ang, 10/30/90, (PB91-170399, A09, MF-A01).

NCEER-90-0026 "MUMOID User's Guide - A Program for the Identification of Modal Parameters," by S. Rodriguez-Gomez and E. DiPasquale, 9/30/90, (PB91-171298, A04, MF-A01).

NCEER-90-0027 "SARCF-II User's Guide - Seismic Analysis of Reinforced Concrete Frames," by S. Rodriguez-Gomez, Y.S. Chung and C. Meyer, 9/30/90, (PB91-171280, A05, MF-A01).

NCEER-90-0028 "Viscous Dampers: Testing, Modeling and Application in Vibration and Seismic Isolation," by N. Makris and M.C. Constantinou, 12/20/90 (PB91-190561, A06, MF-A01).

NCEER-90-0029 "Soil Effects on Earthquake Ground Motions in the Memphis Area," by H. Hwang, C.S. Lee, K.W. Ng and T.S. Chang, 8/2/90, (PB91-190751, A05, MF-A01).

NCEER-91-0001 "Proceedings from the Third Japan-U.S. Workshop on Earthquake Resistant Design of Lifeline Facilities and Countermeasures for Soil Liquefaction, December 17-19, 1990," edited by T.D. O'Rourke and M. Hamada, 2/1/91, (PB91-179259, A99, MF-A04).

NCEER-91-0002 "Physical Space Solutions of Non-Proportionally Damped Systems," by M. Tong, Z. Liang and G.C. Lee, 1/15/91, (PB91-179242, A04, MF-A01).

NCEER-91-0003 "Seismic Response of Single Piles and Pile Groups," by K. Fan and G. Gazetas, 1/10/91, (PB92-174994, A04, MF-A01).

NCEER-91-0004 "Damping of Structures: Part 1 - Theory of Complex Damping," by Z. Liang and G. Lee, 10/10/91, (PB92-197235, A12, MF-A03).

NCEER-91-0005 "3D-BASIS - Nonlinear Dynamic Analysis of Three Dimensional Base Isolated Structures: Part II," by S. Nagarajaiah, A.M. Reinhorn and M.C. Constantinou, 2/28/91, (PB91-190553, A07, MF-A01). This report has been replaced by NCEER-93-0011.

NCEER-91-0006 "A Multidimensional Hysteretic Model for Plasticity Deforming Metals in Energy Absorbing Devices," by E.J. Graesser and F.A. Cozzarelli, 4/9/91, (PB92-108364, A04, MF-A01).

NCEER-91-0007 "A Framework for Customizable Knowledge-Based Expert Systems with an Application to a KBES for Evaluating the Seismic Resistance of Existing Buildings," by E.G. Ibarra-Anaya and S.J. Fenves, 4/9/91, (PB91-210930, A08, MF-A01).

NCEER-91-0008 "Nonlinear Analysis of Steel Frames with Semi-Rigid Connections Using the Capacity Spectrum Method," by G.G. Deierlein, S-H. Hsieh, Y-J. Shen and J.F. Abel, 7/2/91, (PB92-113828, A05, MF-A01).

NCEER-91-0009 "Earthquake Education Materials for Grades K-12," by K.E.K. Ross, 4/30/91, (PB91-212142, A06, MF-A01). This report has been replaced by NCEER-92-0018.

NCEER-91-0010 "Phase Wave Velocities and Displacement Phase Differences in a Harmonically Oscillating Pile," by N. Makris and G. Gazetas, 7/8/91, (PB92-108356, A04, MF-A01).

NCEER-91-0011 "Dynamic Characteristics of a Full-Size Five-Story Steel Structure and a 2/5 Scale Model," by K.C. Chang, G.C. Yao, G.C. Lee, D.S. Hao and Y.C. Yeh," 7/2/91, (PB93-116648, A06, MF-A02).

NCEER-91-0012 "Seismic Response of a 2/5 Scale Steel Structure with Added Viscoelastic Dampers," by K.C. Chang, T.T. Soong, S-T. Oh and M.L. Lai, 5/17/91, (PB92-110816, A05, MF-A01).

NCEER-91-0013 "Earthquake Response of Retaining Walls; Full-Scale Testing and Computational Modeling," by S. Alampalli and A-W.M. Elgamal, 6/20/91, not available.

NCEER-91-0014 "3D-BASIS-M: Nonlinear Dynamic Analysis of Multiple Building Base Isolated Structures," by P.C. Tsopelas, S. Nagarajaiah, M.C. Constantinou and A.M. Reinhorn, 5/28/91, (PB92-113885, A09, MF-A02).

NCEER-91-0015 "Evaluation of SEAOC Design Requirements for Sliding Isolated Structures," by D. Theodossiou and M.C. Constantinou, 6/10/91, (PB92-114602, A11, MF-A03).

NCEER-91-0016 "Closed-Loop Modal Testing of a 27-Story Reinforced Concrete Flat Plate-Core Building," by H.R. Somaprasad, T. Toksoy, H. Yoshiyuki and A.E. Aktan, 7/15/91, (PB92-129980, A07, MF-A02).

NCEER-91-0017 "Shake Table Test of a 1/6 Scale Two-Story Lightly Reinforced Concrete Building," by A.G. El-Attar, R.N. White and P. Gergely, 2/28/91, (PB92-222447, A06, MF-A02).

NCEER-91-0018 "Shake Table Test of a 1/8 Scale Three-Story Lightly Reinforced Concrete Building," by A.G. El-Attar, R.N. White and P. Gergely, 2/28/91, (PB93-116630, A08, MF-A02).

NCEER-91-0019 "Transfer Functions for Rigid Rectangular Foundations," by A.S. Veletsos, A.M. Prasad and W.H. Wu, 7/31/91, not available.

NCEER-91-0020 "Hybrid Control of Seismic-Excited Nonlinear and Inelastic Structural Systems," by J.N. Yang, Z. Li and A. Danielians, 8/1/91, (PB92-143171, A06, MF-A02).

NCEER-91-0021 "The NCEER-91 Earthquake Catalog: Improved Intensity-Based Magnitudes and Recurrence Relations for U.S. Earthquakes East of New Madrid," by L. Seeber and J.G. Armbruster, 8/28/91, (PB92-176742, A06, MF-A02).

NCEER-91-0022 "Proceedings from the Implementation of Earthquake Planning and Education in Schools: The Need for Change - The Roles of the Changemakers," by K.E.K. Ross and F. Winslow, 7/23/91, (PB92-129998, A12, MF-A03).

NCEER-91-0023 "A Study of Reliability-Based Criteria for Seismic Design of Reinforced Concrete Frame Buildings," by H.H.M. Hwang and H-M. Hsu, 8/10/91, (PB92-140235, A09, MF-A02).

NCEER-91-0024 "Experimental Verification of a Number of Structural System Identification Algorithms," by R.G. Ghanem, H. Gavin and M. Shinozuka, 9/18/91, (PB92-176577, A18, MF-A04).

NCEER-91-0025 "Probabilistic Evaluation of Liquefaction Potential," by H.H.M. Hwang and C.S. Lee," 11/25/91, (PB92-143429, A05, MF-A01).

NCEER-91-0026 "Instantaneous Optimal Control for Linear, Nonlinear and Hysteretic Structures - Stable Controllers," by J.N. Yang and Z. Li, 11/15/91, (PB92-163807, A04, MF-A01).

NCEER-91-0027 "Experimental and Theoretical Study of a Sliding Isolation System for Bridges," by M.C. Constantinou, A. Kartoum, A.M. Reinhorn and P. Bradford, 11/15/91, (PB92-176973, A10, MF-A03).

NCEER-92-0001 "Case Studies of Liquefaction and Lifeline Performance During Past Earthquakes, Volume 1: Japanese Case Studies," Edited by M. Hamada and T. O'Rourke, 2/17/92, (PB92-197243, A18, MF-A04).

NCEER-92-0002 "Case Studies of Liquefaction and Lifeline Performance During Past Earthquakes, Volume 2: United States Case Studies," Edited by T. O'Rourke and M. Hamada, 2/17/92, (PB92-197250, A20, MF-A04).

NCEER-92-0003 "Issues in Earthquake Education," Edited by K. Ross, 2/3/92, (PB92-222389, A07, MF-A02).

NCEER-92-0004 "Proceedings from the First U.S. - Japan Workshop on Earthquake Protective Systems for Bridges," Edited by I.G. Buckle, 2/4/92, (PB94-142239, A99, MF-A06).

NCEER-92-0005 "Seismic Ground Motion from a Haskell-Type Source in a Multiple-Layered Half-Space," A.P. Theoharis, G. Deodatis and M. Shinozuka, 1/2/92, not available.

NCEER-92-0006 "Proceedings from the Site Effects Workshop," Edited by R. Whitman, 2/29/92, (PB92-197201, A04, MF-A01).

NCEER-92-0007 "Engineering Evaluation of Permanent Ground Deformations Due to Seismically-Induced Liquefaction," by M.H. Baziar, R. Dobry and A-W.M. Elgamal, 3/24/92, (PB92-222421, A13, MF-A03).

NCEER-92-0008 "A Procedure for the Seismic Evaluation of Buildings in the Central and Eastern United States," by C.D. Poland and J.O. Malley, 4/2/92, (PB92-222439, A20, MF-A04).

NCEER-92-0009 "Experimental and Analytical Study of a Hybrid Isolation System Using Friction Controllable Sliding Bearings," by M.Q. Feng, S. Fujii and M. Shinozuka, 5/15/92, (PB93-150282, A06, MF-A02).

NCEER-92-0010 "Seismic Resistance of Slab-Column Connections in Existing Non-Ductile Flat-Plate Buildings," by A.J. Durrani and Y. Du, 5/18/92, (PB93-116812, A06, MF-A02).

NCEER-92-0011 "The Hysteretic and Dynamic Behavior of Brick Masonry Walls Upgraded by Ferrocement Coatings Under Cyclic Loading and Strong Simulated Ground Motion," by H. Lee and S.P. Prawel, 5/11/92, not available.

NCEER-92-0012 "Study of Wire Rope Systems for Seismic Protection of Equipment in Buildings," by G.F. Demetriades, M.C. Constantinou and A.M. Reinhorn, 5/20/92, (PB93-116655, A08, MF-A02).

NCEER-92-0013 "Shape Memory Structural Dampers: Material Properties, Design and Seismic Testing," by P.R. Witting and F.A. Cozzarelli, 5/26/92, (PB93-116663, A05, MF-A01).

NCEER-92-0014 "Longitudinal Permanent Ground Deformation Effects on Buried Continuous Pipelines," by M.J. O'Rourke, and C. Nordberg, 6/15/92, (PB93-116671, A08, MF-A02).

NCEER-92-0015 "A Simulation Method for Stationary Gaussian Random Functions Based on the Sampling Theorem," by M. Grigoriu and S. Balopoulou, 6/11/92, (PB93-127496, A05, MF-A01).

NCEER-92-0016 "Gravity-Load-Designed Reinforced Concrete Buildings: Seismic Evaluation of Existing Construction and Detailing Strategies for Improved Seismic Resistance," by G.W. Hoffmann, S.K. Kunnath, A.M. Reinhorn and J.B. Mander, 7/15/92, (PB94-142007, A08, MF-A02).

NCEER-92-0017 "Observations on Water System and Pipeline Performance in the Limón Area of Costa Rica Due to the April 22, 1991 Earthquake," by M. O'Rourke and D. Ballantyne, 6/30/92, (PB93-126811, A06, MF-A02).

NCEER-92-0018 "Fourth Edition of Earthquake Education Materials for Grades K-12," Edited by K.E.K. Ross, 8/10/92, (PB93-114023, A07, MF-A02).

NCEER-92-0019 "Proceedings from the Fourth Japan-U.S. Workshop on Earthquake Resistant Design of Lifeline Facilities and Countermeasures for Soil Liquefaction," Edited by M. Hamada and T.D. O'Rourke, 8/12/92, (PB93-163939, A99, MF-E11).

NCEER-92-0020 "Active Bracing System: A Full Scale Implementation of Active Control," by A.M. Reinhorn, T.T. Soong, R.C. Lin, M.A. Riley, Y.P. Wang, S. Aizawa and M. Higashino, 8/14/92, (PB93-127512, A06, MF-A02).

NCEER-92-0021 "Empirical Analysis of Horizontal Ground Displacement Generated by Liquefaction-Induced Lateral Spreads," by S.F. Bartlett and T.L. Youd, 8/17/92, (PB93-188241, A06, MF-A02).

NCEER-92-0022 "IDARC Version 3.0: Inelastic Damage Analysis of Reinforced Concrete Structures," by S.K. Kunnath, A.M. Reinhorn and R.F. Lobo, 8/31/92, (PB93-227502, A07, MF-A02).

NCEER-92-0023 "A Semi-Empirical Analysis of Strong-Motion Peaks in Terms of Seismic Source, Propagation Path and Local Site Conditions, by M. Kamiyama, M.J. O'Rourke and R. Flores-Berrones, 9/9/92, (PB93-150266, A08, MF-A02).

NCEER-92-0024 "Seismic Behavior of Reinforced Concrete Frame Structures with Nonductile Details, Part I: Summary of Experimental Findings of Full Scale Beam-Column Joint Tests," by A. Beres, R.N. White and P. Gergely, 9/30/92, (PB93-227783, A05, MF-A01).

NCEER-92-0025 "Experimental Results of Repaired and Retrofitted Beam-Column Joint Tests in Lightly Reinforced Concrete Frame Buildings," by A. Beres, S. El-Borgi, R.N. White and P. Gergely, 10/29/92, (PB93-227791, A05, MF-A01).

NCEER-92-0026 "A Generalization of Optimal Control Theory: Linear and Nonlinear Structures," by J.N. Yang, Z. Li and S. Vongchavalitkul, 11/2/92, (PB93-188621, A05, MF-A01).

NCEER-92-0027 "Seismic Resistance of Reinforced Concrete Frame Structures Designed Only for Gravity Loads: Part I - Design and Properties of a One-Third Scale Model Structure," by J.M. Bracci, A.M. Reinhorn and J.B. Mander, 12/1/92, (PB94-104502, A08, MF-A02).

NCEER-92-0028 "Seismic Resistance of Reinforced Concrete Frame Structures Designed Only for Gravity Loads: Part II - Experimental Performance of Subassemblages," by L.E. Aycardi, J.B. Mander and A.M. Reinhorn, 12/1/92, (PB94-104510, A08, MF-A02).

NCEER-92-0029 "Seismic Resistance of Reinforced Concrete Frame Structures Designed Only for Gravity Loads: Part III - Experimental Performance and Analytical Study of a Structural Model," by J.M. Bracci, A.M. Reinhorn and J.B. Mander, 12/1/92, (PB93-227528, A09, MF-A01).

NCEER-92-0030 "Evaluation of Seismic Retrofit of Reinforced Concrete Frame Structures: Part I - Experimental Performance of Retrofitted Subassemblages," by D. Choudhuri, J.B. Mander and A.M. Reinhorn, 12/8/92, (PB93-198307, A07, MF-A02).

NCEER-92-0031 "Evaluation of Seismic Retrofit of Reinforced Concrete Frame Structures: Part II - Experimental Performance and Analytical Study of a Retrofitted Structural Model," by J.M. Bracci, A.M. Reinhorn and J.B. Mander, 12/8/92, (PB93-198315, A09, MF-A03).

NCEER-92-0032 "Experimental and Analytical Investigation of Seismic Response of Structures with Supplemental Fluid Viscous Dampers," by M.C. Constantinou and M.D. Symans, 12/21/92, (PB93-191435, A10, MF-A03). This report is available only through NTIS (see address given above).

NCEER-92-0033 "Reconnaissance Report on the Cairo, Egypt Earthquake of October 12, 1992," by M. Khater, 12/23/92, (PB93-188621, A03, MF-A01).

NCEER-92-0034 "Low-Level Dynamic Characteristics of Four Tall Flat-Plate Buildings in New York City," by H. Gavin, S. Yuan, J. Grossman, E. Pekelis and K. Jacob, 12/28/92, (PB93-188217, A07, MF-A02).

NCEER-93-0001 "An Experimental Study on the Seismic Performance of Brick-Infilled Steel Frames With and Without Retrofit," by J.B. Mander, B. Nair, K. Wojtkowski and J. Ma, 1/29/93, (PB93-227510, A07, MF-A02).

NCEER-93-0002 "Social Accounting for Disaster Preparedness and Recovery Planning," by S. Cole, E. Pantoja and V. Razak, 2/22/93, (PB94-142114, A12, MF-A03).

NCEER-93-0003 "Assessment of 1991 NEHRP Provisions for Nonstructural Components and Recommended Revisions," by T.T. Soong, G. Chen, Z. Wu, R-H. Zhang and M. Grigoriu, 3/1/93, (PB93-188639, A06, MF-A02).

NCEER-93-0004 "Evaluation of Static and Response Spectrum Analysis Procedures of SEAOC/UBC for Seismic Isolated Structures," by C.W. Winters and M.C. Constantinou, 3/23/93, (PB93-198299, A10, MF-A03).

NCEER-93-0005 "Earthquakes in the Northeast - Are We Ignoring the Hazard? A Workshop on Earthquake Science and Safety for Educators," edited by K.E.K. Ross, 4/2/93, (PB94-103066, A09, MF-A02).

NCEER-93-0006 "Inelastic Response of Reinforced Concrete Structures with Viscoelastic Braces," by R.F. Lobo, J.M. Bracci, K.L. Shen, A.M. Reinhorn and T.T. Soong, 4/5/93, (PB93-227486, A05, MF-A02).

NCEER-93-0007 "Seismic Testing of Installation Methods for Computers and Data Processing Equipment," by K. Kosar, T.T. Soong, K.L. Shen, J.A. HoLung and Y.K. Lin, 4/12/93, (PB93-198299, A07, MF-A02).

NCEER-93-0008 "Retrofit of Reinforced Concrete Frames Using Added Dampers," by A. Reinhorn, M. Constantinou and C. Li, not available.

NCEER-93-0009 "Seismic Behavior and Design Guidelines for Steel Frame Structures with Added Viscoelastic Dampers," by K.C. Chang, M.L. Lai, T.T. Soong, D.S. Hao and Y.C. Yeh, 5/1/93, (PB94-141959, A07, MF-A02).

NCEER-93-0010 "Seismic Performance of Shear-Critical Reinforced Concrete Bridge Piers," by J.B. Mander, S.M. Waheed, M.T.A. Chaudhary and S.S. Chen, 5/12/93, (PB93-227494, A08, MF-A02).

NCEER-93-0011 "3D-BASIS-TABS: Computer Program for Nonlinear Dynamic Analysis of Three Dimensional Base Isolated Structures," by S. Nagarajaiah, C. Li, A.M. Reinhorn and M.C. Constantinou, 8/2/93, (PB94-141819, A09, MF-A02).

NCEER-93-0012 "Effects of Hydrocarbon Spills from an Oil Pipeline Break on Ground Water," by O.J. Helweg and H.H.M. Hwang, 8/3/93, (PB94-141942, A06, MF-A02).

NCEER-93-0013 "Simplified Procedures for Seismic Design of Nonstructural Components and Assessment of Current Code Provisions," by M.P. Singh, L.E. Suarez, E.E. Matheu and G.O. Maldonado, 8/4/93, (PB94-141827, A09, MF-A02).

NCEER-93-0014 "An Energy Approach to Seismic Analysis and Design of Secondary Systems," by G. Chen and T.T. Soong, 8/6/93, (PB94-142767, A11, MF-A03).

NCEER-93-0015 "Proceedings from School Sites: Becoming Prepared for Earthquakes - Commemorating the Third Anniversary of the Loma Prieta Earthquake," Edited by F.E. Winslow and K.E.K. Ross, 8/16/93, (PB94-154275, A16, MF-A02).

NCEER-93-0016 "Reconnaissance Report of Damage to Historic Monuments in Cairo, Egypt Following the October 12, 1992 Dahshur Earthquake," by D. Sykora, D. Look, G. Croci, E. Karaesmen and E. Karaesmen, 8/19/93, (PB94-142221, A08, MF-A02).

NCEER-93-0017 "The Island of Guam Earthquake of August 8, 1993," by S.W. Swan and S.K. Harris, 9/30/93, (PB94-141843, A04, MF-A01).

NCEER-93-0018 "Engineering Aspects of the October 12, 1992 Egyptian Earthquake," by A.W. Elgamal, M. Amer, K. Adalier and A. Abul-Fadl, 10/7/93, (PB94-141983, A05, MF-A01).

NCEER-93-0019 "Development of an Earthquake Motion Simulator and its Application in Dynamic Centrifuge Testing," by I. Krstelj, Supervised by J.H. Prevost, 10/23/93, (PB94-181773, A-10, MF-A03).

NCEER-93-0020 "NCEER-Taisei Corporation Research Program on Sliding Seismic Isolation Systems for Bridges: Experimental and Analytical Study of a Friction Pendulum System (FPS)," by M.C. Constantinou, P. Tsopelas, Y-S. Kim and S. Okamoto, 11/1/93, (PB94-142775, A08, MF-A02).

NCEER-93-0021 "Finite Element Modeling of Elastomeric Seismic Isolation Bearings," by L.J. Billings, Supervised by R. Shepherd, 11/8/93, not available.

NCEER-93-0022 "Seismic Vulnerability of Equipment in Critical Facilities: Life-Safety and Operational Consequences," by K. Porter, G.S. Johnson, M.M. Zadeh, C. Scawthorn and S. Eder, 11/24/93, (PB94-181765, A16, MF-A03).

NCEER-93-0023 "Hokkaido Nansei-oki, Japan Earthquake of July 12, 1993, by P.I. Yanev and C.R. Scawthorn, 12/23/93, (PB94-181500, A07, MF-A01).

NCEER-94-0001 "An Evaluation of Seismic Serviceability of Water Supply Networks with Application to the San Francisco Auxiliary Water Supply System," by I. Markov, Supervised by M. Grigoriu and T. O'Rourke, 1/21/94, (PB94-204013, A07, MF-A02).

NCEER-94-0002 "NCEER-Taisei Corporation Research Program on Sliding Seismic Isolation Systems for Bridges: Experimental and Analytical Study of Systems Consisting of Sliding Bearings, Rubber Restoring Force Devices and Fluid Dampers," Volumes I and II, by P. Tsopelas, S. Okamoto, M.C. Constantinou, D. Ozaki and S. Fujii, 2/4/94, (PB94-181740, A09, MF-A02 and PB94-181757, A12, MF-A03).

NCEER-94-0003 "A Markov Model for Local and Global Damage Indices in Seismic Analysis," by S. Rahman and M. Grigoriu, 2/18/94, (PB94-206000, A12, MF-A03).

NCEER-94-0004 "Proceedings from the NCEER Workshop on Seismic Response of Masonry Infills," edited by D.P. Abrams, 3/1/94, (PB94-180783, A07, MF-A02).

NCEER-94-0005 "The Northridge, California Earthquake of January 17, 1994: General Reconnaissance Report," edited by J.D. Goltz, 3/11/94, (PB94-193943, A10, MF-A03).

NCEER-94-0006 "Seismic Energy Based Fatigue Damage Analysis of Bridge Columns: Part I - Evaluation of Seismic Capacity," by G.A. Chang and J.B. Mander, 3/14/94, (PB94-219185, A11, MF-A03).

NCEER-94-0007 "Seismic Isolation of Multi-Story Frame Structures Using Spherical Sliding Isolation Systems," by T.M. Al-Hussaini, V.A. Zayas and M.C. Constantinou, 3/17/94, (PB94-193745, A09, MF-A02).

NCEER-94-0008 "The Northridge, California Earthquake of January 17, 1994: Performance of Highway Bridges," edited by I.G. Buckle, 3/24/94, (PB94-193851, A06, MF-A02).

NCEER-94-0009 "Proceedings of the Third U.S.-Japan Workshop on Earthquake Protective Systems for Bridges," edited by I.G. Buckle and I. Friedland, 3/31/94, (PB94-195815, A99, MF-A06).

NCEER-94-0010 "3D-BASIS-ME: Computer Program for Nonlinear Dynamic Analysis of Seismically Isolated Single and Multiple Structures and Liquid Storage Tanks," by P.C. Tsopelas, M.C. Constantinou and A.M. Reinhorn, 4/12/94, (PB94-204922, A09, MF-A02).

NCEER-94-0011 "The Northridge, California Earthquake of January 17, 1994: Performance of Gas Transmission Pipelines," by T.D. O'Rourke and M.C. Palmer, 5/16/94, (PB94-204989, A05, MF-A01).

NCEER-94-0012 "Feasibility Study of Replacement Procedures and Earthquake Performance Related to Gas Transmission Pipelines," by T.D. O'Rourke and M.C. Palmer, 5/25/94, (PB94-206638, A09, MF-A02).

NCEER-94-0013 "Seismic Energy Based Fatigue Damage Analysis of Bridge Columns: Part II - Evaluation of Seismic Demand," by G.A. Chang and J.B. Mander, 6/1/94, (PB95-18106, A08, MF-A02).

NCEER-94-0014 "NCEER-Taisei Corporation Research Program on Sliding Seismic Isolation Systems for Bridges: Experimental and Analytical Study of a System Consisting of Sliding Bearings and Fluid Restoring Force/Damping Devices," by P. Tsopelas and M.C. Constantinou, 6/13/94, (PB94-219144, A10, MF-A03).

NCEER-94-0015 "Generation of Hazard-Consistent Fragility Curves for Seismic Loss Estimation Studies," by H. Hwang and J-R. Huo, 6/14/94, (PB95-181996, A09, MF-A02).

NCEER-94-0016 "Seismic Study of Building Frames with Added Energy-Absorbing Devices," by W.S. Pong, C.S. Tsai and G.C. Lee, 6/20/94, (PB94-219136, A10, A03).

NCEER-94-0017 "Sliding Mode Control for Seismic-Excited Linear and Nonlinear Civil Engineering Structures," by J. Yang, J. Wu, A. Agrawal and Z. Li, 6/21/94, (PB95-138483, A06, MF-A02).

NCEER-94-0018 "3D-BASIS-TABS Version 2.0: Computer Program for Nonlinear Dynamic Analysis of Three Dimensional Base Isolated Structures," by A.M. Reinhorn, S. Nagarajaiah, M.C. Constantinou, P. Tsopelas and R. Li, 6/22/94, (PB95-182176, A08, MF-A02).

NCEER-94-0019 "Proceedings of the International Workshop on Civil Infrastructure Systems: Application of Intelligent Systems and Advanced Materials on Bridge Systems," Edited by G.C. Lee and K.C. Chang, 7/18/94, (PB95-252474, A20, MF-A04).

NCEER-94-0020 "Study of Seismic Isolation Systems for Computer Floors," by V. Lambrou and M.C. Constantinou, 7/19/94, (PB95-138533, A10, MF-A03).

NCEER-94-0021 "Proceedings of the U.S.-Italian Workshop on Guidelines for Seismic Evaluation and Rehabilitation of Unreinforced Masonry Buildings," Edited by D.P. Abrams and G.M. Calvi, 7/20/94, (PB95-138749, A13, MF-A03).

NCEER-94-0022 "NCEER-Taisei Corporation Research Program on Sliding Seismic Isolation Systems for Bridges: Experimental and Analytical Study of a System Consisting of Lubricated PTFE Sliding Bearings and Mild Steel Dampers," by P. Tsopelas and M.C. Constantinou, 7/22/94, (PB95-182184, A08, MF-A02).

NCEER-94-0023 “Development of Reliability-Based Design Criteria for Buildings Under Seismic Load,” by Y.K. Wen, H. Hwang and M. Shinozuka, 8/1/94, (PB95-211934, A08, MF-A02).

NCEER-94-0024 “Experimental Verification of Acceleration Feedback Control Strategies for an Active Tendon System,” by S.J. Dyke, B.F. Spencer, Jr., P. Quast, M.K. Sain, D.C. Kaspari, Jr. and T.T. Soong, 8/29/94, (PB95-212320, A05, MF-A01).

NCEER-94-0025 “Seismic Retrofitting Manual for Highway Bridges,” Edited by I.G. Buckle and I.F. Friedland, published by the Federal Highway Administration (PB95-212676, A15, MF-A03).

NCEER-94-0026 “Proceedings from the Fifth U.S.-Japan Workshop on Earthquake Resistant Design of Lifeline Facilities and Countermeasures Against Soil Liquefaction,” Edited by T.D. O’Rourke and M. Hamada, 11/7/94, (PB95-220802, A99, MF-E08).

NCEER-95-0001 "Experimental and Analytical Investigation of Seismic Retrofit of Structures with Supplemental Damping: Part 1 - Fluid Viscous Damping Devices," by A.M. Reinhorn, C. Li and M.C. Constantinou, 1/3/95, (PB95-266599, A09, MF-A02).

NCEER-95-0002 "Experimental and Analytical Study of Low-Cycle Fatigue Behavior of Semi-Rigid Top-And-Seat Angle Connections," by G. Pekcan, J.B. Mander and S.S. Chen, 1/5/95, (PB95-220042, A07, MF-A02).

NCEER-95-0003 "NCEER-ATC Joint Study on Fragility of Buildings," by T. Anagnos, C. Rojahn and A.S. Kiremidjian, 1/20/95, (PB95-220026, A06, MF-A02).

NCEER-95-0004 "Nonlinear Control Algorithms for Peak Response Reduction," by Z. Wu, T.T. Soong, V. Gattulli and R.C. Lin, 2/16/95, (PB95-220349, A05, MF-A01).

NCEER-95-0005 "Pipeline Replacement Feasibility Study: A Methodology for Minimizing Seismic and Corrosion Risks to Underground Natural Gas Pipelines," by R.T. Eguchi, H.A. Seligson and D.G. Honegger, 3/2/95, (PB95-252326, A06, MF-A02).

NCEER-95-0006 "Evaluation of Seismic Performance of an 11-Story Frame Building During the 1994 Northridge Earthquake," by F. Naeim, R. DiSulio, K. Benuska, A. Reinhorn and C. Li, not available.

NCEER-95-0007 "Prioritization of Bridges for Seismic Retrofitting," by N. Basöz and A.S. Kiremidjian, 4/24/95, (PB95-252300, A08, MF-A02).

NCEER-95-0008 "Method for Developing Motion Damage Relationships for Reinforced Concrete Frames," by A. Singhal and A.S. Kiremidjian, 5/11/95, (PB95-266607, A06, MF-A02).

NCEER-95-0009 "Experimental and Analytical Investigation of Seismic Retrofit of Structures with Supplemental Damping: Part II - Friction Devices," by C. Li and A.M. Reinhorn, 7/6/95, (PB96-128087, A11, MF-A03).

NCEER-95-0010 "Experimental Performance and Analytical Study of a Non-Ductile Reinforced Concrete Frame Structure Retrofitted with Elastomeric Spring Dampers," by G. Pekcan, J.B. Mander and S.S. Chen, 7/14/95, (PB96-137161, A08, MF-A02).

NCEER-95-0011 "Development and Experimental Study of Semi-Active Fluid Damping Devices for Seismic Protection of Structures," by M.D. Symans and M.C. Constantinou, 8/3/95, (PB96-136940, A23, MF-A04).

NCEER-95-0012 "Real-Time Structural Parameter Modification (RSPM): Development of Innervated Structures," by Z. Liang, M. Tong and G.C. Lee, 4/11/95, (PB96-137153, A06, MF-A01).

NCEER-95-0013 "Experimental and Analytical Investigation of Seismic Retrofit of Structures with Supplemental Damping: Part III - Viscous Damping Walls," by A.M. Reinhorn and C. Li, 10/1/95, (PB96-176409, A11, MF-A03).

NCEER-95-0014 "Seismic Fragility Analysis of Equipment and Structures in a Memphis Electric Substation," by J-R. Huo and H.H.M. Hwang, 8/10/95, (PB96-128087, A09, MF-A02).

NCEER-95-0015 "The Hanshin-Awaji Earthquake of January 17, 1995: Performance of Lifelines," Edited by M. Shinozuka, 11/3/95, (PB96-176383, A15, MF-A03).

NCEER-95-0016 "Highway Culvert Performance During Earthquakes," by T.L. Youd and C.J. Beckman, available as NCEER-96-0015.

NCEER-95-0017 "The Hanshin-Awaji Earthquake of January 17, 1995: Performance of Highway Bridges," Edited by I.G. Buckle, 12/1/95, not available.

NCEER-95-0018 "Modeling of Masonry Infill Panels for Structural Analysis," by A.M. Reinhorn, A. Madan, R.E. Valles, Y. Reichmann and J.B. Mander, 12/8/95, (PB97-110886, MF-A01, A06).

NCEER-95-0019 "Optimal Polynomial Control for Linear and Nonlinear Structures," by A.K. Agrawal and J.N. Yang, 12/11/95, (PB96-168737, A07, MF-A02).

NCEER-95-0020 "Retrofit of Non-Ductile Reinforced Concrete Frames Using Friction Dampers," by R.S. Rao, P. Gergely and R.N. White, 12/22/95, (PB97-133508, A10, MF-A02).

NCEER-95-0021 "Parametric Results for Seismic Response of Pile-Supported Bridge Bents," by G. Mylonakis, A. Nikolaou and G. Gazetas, 12/22/95, (PB97-100242, A12, MF-A03).

NCEER-95-0022 "Kinematic Bending Moments in Seismically Stressed Piles," by A. Nikolaou, G. Mylonakis and G. Gazetas, 12/23/95, (PB97-113914, MF-A03, A13).

NCEER-96-0001 "Dynamic Response of Unreinforced Masonry Buildings with Flexible Diaphragms," by A.C. Costley and D.P. Abrams," 10/10/96, (PB97-133573, MF-A03, A15).

NCEER-96-0002 "State of the Art Review: Foundations and Retaining Structures," by I. Po Lam, not available.

NCEER-96-0003 "Ductility of Rectangular Reinforced Concrete Bridge Columns with Moderate Confinement," by N. Wehbe, M. Saiidi, D. Sanders and B. Douglas, 11/7/96, (PB97-133557, A06, MF-A02).

NCEER-96-0004 "Proceedings of the Long-Span Bridge Seismic Research Workshop," edited by I.G. Buckle and I.M. Friedland, not available.

NCEER-96-0005 "Establish Representative Pier Types for Comprehensive Study: Eastern United States," by J. Kulicki and Z. Prucz, 5/28/96, (PB98-119217, A07, MF-A02).

NCEER-96-0006 "Establish Representative Pier Types for Comprehensive Study: Western United States," by R. Imbsen, R.A. Schamber and T.A. Osterkamp, 5/28/96, (PB98-118607, A07, MF-A02).

NCEER-96-0007 "Nonlinear Control Techniques for Dynamical Systems with Uncertain Parameters," by R.G. Ghanem and M.I. Bujakov, 5/27/96, (PB97-100259, A17, MF-A03).

NCEER-96-0008 "Seismic Evaluation of a 30-Year Old Non-Ductile Highway Bridge Pier and Its Retrofit," by J.B. Mander, B. Mahmoodzadegan, S. Bhadra and S.S. Chen, 5/31/96, (PB97-110902, MF-A03, A10).

NCEER-96-0009 "Seismic Performance of a Model Reinforced Concrete Bridge Pier Before and After Retrofit," by J.B. Mander, J.H. Kim and C.A. Ligozio, 5/31/96, (PB97-110910, MF-A02, A10).

NCEER-96-0010 "IDARC2D Version 4.0: A Computer Program for the Inelastic Damage Analysis of Buildings," by R.E. Valles, A.M. Reinhorn, S.K. Kunnath, C. Li and A. Madan, 6/3/96, (PB97-100234, A17, MF-A03).

NCEER-96-0011 "Estimation of the Economic Impact of Multiple Lifeline Disruption: Memphis Light, Gas and Water Division Case Study," by S.E. Chang, H.A. Seligson and R.T. Eguchi, 8/16/96, (PB97-133490, A11, MF-A03).

NCEER-96-0012 "Proceedings from the Sixth Japan-U.S. Workshop on Earthquake Resistant Design of Lifeline Facilities and Countermeasures Against Soil Liquefaction, Edited by M. Hamada and T. O'Rourke, 9/11/96, (PB97-133581, A99, MF-A06).

NCEER-96-0013 "Chemical Hazards, Mitigation and Preparedness in Areas of High Seismic Risk: A Methodology for Estimating the Risk of Post-Earthquake Hazardous Materials Release," by H.A. Seligson, R.T. Eguchi, K.J. Tierney and K. Richmond, 11/7/96, (PB97-133565, MF-A02, A08).

NCEER-96-0014 "Response of Steel Bridge Bearings to Reversed Cyclic Loading," by J.B. Mander, D-K. Kim, S.S. Chen and G.J. Premus, 11/13/96, (PB97-140735, A12, MF-A03).

NCEER-96-0015 "Highway Culvert Performance During Past Earthquakes," by T.L. Youd and C.J. Beckman, 11/25/96, (PB97-133532, A06, MF-A01).

NCEER-97-0001 "Evaluation, Prevention and Mitigation of Pounding Effects in Building Structures," by R.E. Valles and A.M. Reinhorn, 2/20/97, (PB97-159552, A14, MF-A03).

NCEER-97-0002 "Seismic Design Criteria for Bridges and Other Highway Structures," by C. Rojahn, R. Mayes, D.G. Anderson, J. Clark, J.H. Hom, R.V. Nutt and M.J. O'Rourke, 4/30/97, (PB97-194658, A06, MF-A03).

NCEER-97-0003 “Proceedings of the U.S.-Italian Workshop on Seismic Evaluation and Retrofit,” Edited by D.P. Abrams and G.M. Calvi, 3/19/97, (PB97-194666, A13, MF-A03).

NCEER-97-0004 "Investigation of Seismic Response of Buildings with Linear and Nonlinear Fluid Viscous Dampers," by A.A. Seleemah and M.C. Constantinou, 5/21/97, (PB98-109002, A15, MF-A03).

NCEER-97-0005 "Proceedings of the Workshop on Earthquake Engineering Frontiers in Transportation Facilities," edited by G.C. Lee and I.M. Friedland, 8/29/97, (PB98-128911, A25, MR-A04).

NCEER-97-0006 "Cumulative Seismic Damage of Reinforced Concrete Bridge Piers," by S.K. Kunnath, A. El-Bahy, A. Taylor and W. Stone, 9/2/97, (PB98-108814, A11, MF-A03).

NCEER-97-0007 "Structural Details to Accommodate Seismic Movements of Highway Bridges and Retaining Walls," by R.A. Imbsen, R.A. Schamber, E. Thorkildsen, A. Kartoum, B.T. Martin, T.N. Rosser and J.M. Kulicki, 9/3/97, (PB98-108996, A09, MF-A02).

NCEER-97-0008 "A Method for Earthquake Motion-Damage Relationships with Application to Reinforced Concrete Frames," by A. Singhal and A.S. Kiremidjian, 9/10/97, (PB98-108988, A13, MF-A03).

NCEER-97-0009 "Seismic Analysis and Design of Bridge Abutments Considering Sliding and Rotation," by K. Fishman and R. Richards, Jr., 9/15/97, (PB98-108897, A06, MF-A02).

NCEER-97-0010 "Proceedings of the FHWA/NCEER Workshop on the National Representation of Seismic Ground Motion for New and Existing Highway Facilities," edited by I.M. Friedland, M.S. Power and R.L. Mayes, 9/22/97, (PB98-128903, A21, MF-A04).

NCEER-97-0011 "Seismic Analysis for Design or Retrofit of Gravity Bridge Abutments," by K.L. Fishman, R. Richards, Jr. and R.C. Divito, 10/2/97, (PB98-128937, A08, MF-A02).

NCEER-97-0012 "Evaluation of Simplified Methods of Analysis for Yielding Structures," by P. Tsopelas, M.C. Constantinou, C.A. Kircher and A.S. Whittaker, 10/31/97, (PB98-128929, A10, MF-A03).

NCEER-97-0013 "Seismic Design of Bridge Columns Based on Control and Repairability of Damage," by C-T. Cheng and J.B. Mander, 12/8/97, (PB98-144249, A11, MF-A03).

NCEER-97-0014 "Seismic Resistance of Bridge Piers Based on Damage Avoidance Design," by J.B. Mander and C-T. Cheng, 12/10/97, (PB98-144223, A09, MF-A02).

NCEER-97-0015 “Seismic Response of Nominally Symmetric Systems with Strength Uncertainty,” by S. Balopoulou and M. Grigoriu, 12/23/97, (PB98-153422, A11, MF-A03).

NCEER-97-0016 “Evaluation of Seismic Retrofit Methods for Reinforced Concrete Bridge Columns,” by T.J. Wipf, F.W. Klaiber and F.M. Russo, 12/28/97, (PB98-144215, A12, MF-A03).

NCEER-97-0017 “Seismic Fragility of Existing Conventional Reinforced Concrete Highway Bridges,” by C.L. Mullen and A.S. Cakmak, 12/30/97, (PB98-153406, A08, MF-A02).

NCEER-97-0018 “Loss Asssessment of Memphis Buildings,” edited by D.P. Abrams and M. Shinozuka, 12/31/97, (PB98-144231, A13, MF-A03).

NCEER-97-0019 “Seismic Evaluation of Frames with Infill Walls Using Quasi-static Experiments,” by K.M. Mosalam, R.N. White and P. Gergely, 12/31/97, (PB98-153455, A07, MF-A02).

NCEER-97-0020 “Seismic Evaluation of Frames with Infill Walls Using Pseudo-dynamic Experiments,” by K.M. Mosalam, R.N. White and P. Gergely, 12/31/97, (PB98-153430, A07, MF-A02).

NCEER-97-0021 “Computational Strategies for Frames with Infill Walls: Discrete and Smeared Crack Analyses and Seismic Fragility,” by K.M. Mosalam, R.N. White and P. Gergely, 12/31/97, (PB98-153414, A10, MF-A02).

NCEER-97-0022 "Proceedings of the NCEER Workshop on Evaluation of Liquefaction Resistance of Soils," edited by T.L. Youd and I.M. Idriss, 12/31/97, (PB98-155617, A15, MF-A03).

MCEER-98-0001 "Extraction of Nonlinear Hysteretic Properties of Seismically Isolated Bridges from Quick-Release Field Tests," by Q. Chen, B.M. Douglas, E.M. Maragakis and I.G. Buckle, 5/26/98, (PB99-118838, A06, MF-A01).

MCEER-98-0002 "Methodologies for Evaluating the Importance of Highway Bridges," by A. Thomas, S. Eshenaur and J. Kulicki, 5/29/98, (PB99-118846, A10, MF-A02).

MCEER-98-0003 "Capacity Design of Bridge Piers and the Analysis of Overstrength," by J.B. Mander, A. Dutta and P. Goel, 6/1/98, (PB99-118853, A09, MF-A02).

MCEER-98-0004 "Evaluation of Bridge Damage Data from the Loma Prieta and Northridge, California Earthquakes," by N. Basoz and A. Kiremidjian, 6/2/98, (PB99-118861, A15, MF-A03).

MCEER-98-0005 "Screening Guide for Rapid Assessment of Liquefaction Hazard at Highway Bridge Sites," by T. L. Youd, 6/16/98, (PB99-118879, A06, not available on microfiche).

MCEER-98-0006 "Structural Steel and Steel/Concrete Interface Details for Bridges," by P. Ritchie, N. Kauhl and J. Kulicki, 7/13/98, (PB99-118945, A06, MF-A01).

MCEER-98-0007 "Capacity Design and Fatigue Analysis of Confined Concrete Columns," by A. Dutta and J.B. Mander, 7/14/98, (PB99-118960, A14, MF-A03).

MCEER-98-0008 "Proceedings of the Workshop on Performance Criteria for Telecommunication Services Under Earthquake Conditions," edited by A.J. Schiff, 7/15/98, (PB99-118952, A08, MF-A02).

MCEER-98-0009 "Fatigue Analysis of Unconfined Concrete Columns," by J.B. Mander, A. Dutta and J.H. Kim, 9/12/98, (PB99-123655, A10, MF-A02).

MCEER-98-0010 "Centrifuge Modeling of Cyclic Lateral Response of Pile-Cap Systems and Seat-Type Abutments in Dry Sands," by A.D. Gadre and R. Dobry, 10/2/98, (PB99-123606, A13, MF-A03).

MCEER-98-0011 "IDARC-BRIDGE: A Computational Platform for Seismic Damage Assessment of Bridge Structures," by A.M. Reinhorn, V. Simeonov, G. Mylonakis and Y. Reichman, 10/2/98, (PB99-162919, A15, MF-A03).

MCEER-98-0012 "Experimental Investigation of the Dynamic Response of Two Bridges Before and After Retrofitting with Elastomeric Bearings," by D.A. Wendichansky, S.S. Chen and J.B. Mander, 10/2/98, (PB99-162927, A15, MF-A03).

MCEER-98-0013 "Design Procedures for Hinge Restrainers and Hinge Sear Width for Multiple-Frame Bridges," by R. Des Roches and G.L. Fenves, 11/3/98, (PB99-140477, A13, MF-A03).

MCEER-98-0014 "Response Modification Factors for Seismically Isolated Bridges," by M.C. Constantinou and J.K. Quarshie, 11/3/98, (PB99-140485, A14, MF-A03).

MCEER-98-0015 "Proceedings of the U.S.-Italy Workshop on Seismic Protective Systems for Bridges," edited by I.M. Friedland and M.C. Constantinou, 11/3/98, (PB2000-101711, A22, MF-A04).

MCEER-98-0016 "Appropriate Seismic Reliability for Critical Equipment Systems: Recommendations Based on Regional Analysis of Financial and Life Loss," by K. Porter, C. Scawthorn, C. Taylor and N. Blais, 11/10/98, (PB99-157265, A08, MF-A02).

MCEER-98-0017 "Proceedings of the U.S. Japan Joint Seminar on Civil Infrastructure Systems Research," edited by M. Shinozuka and A. Rose, 11/12/98, (PB99-156713, A16, MF-A03).

MCEER-98-0018 "Modeling of Pile Footings and Drilled Shafts for Seismic Design," by I. PoLam, M. Kapuskar and D. Chaudhuri, 12/21/98, (PB99-157257, A09, MF-A02).

MCEER-99-0001 "Seismic Evaluation of a Masonry Infilled Reinforced Concrete Frame by Pseudodynamic Testing," by S.G. Buonopane and R.N. White, 2/16/99, (PB99-162851, A09, MF-A02).

MCEER-99-0002 "Response History Analysis of Structures with Seismic Isolation and Energy Dissipation Systems: Verification Examples for Program SAP2000," by J. Scheller and M.C. Constantinou, 2/22/99, (PB99-162869, A08, MF-A02).

MCEER-99-0003 "Experimental Study on the Seismic Design and Retrofit of Bridge Columns Including Axial Load Effects," by A. Dutta, T. Kokorina and J.B. Mander, 2/22/99, (PB99-162877, A09, MF-A02).

MCEER-99-0004 "Experimental Study of Bridge Elastomeric and Other Isolation and Energy Dissipation Systems with Emphasis on Uplift Prevention and High Velocity Near-source Seismic Excitation," by A. Kasalanati and M. C. Constantinou, 2/26/99, (PB99-162885, A12, MF-A03).

MCEER-99-0005 "Truss Modeling of Reinforced Concrete Shear-flexure Behavior," by J.H. Kim and J.B. Mander, 3/8/99, (PB99-163693, A12, MF-A03).

MCEER-99-0006 "Experimental Investigation and Computational Modeling of Seismic Response of a 1:4 Scale Model Steel Structure with a Load Balancing Supplemental Damping System," by G. Pekcan, J.B. Mander and S.S. Chen, 4/2/99, (PB99-162893, A11, MF-A03).

MCEER-99-0007 "Effect of Vertical Ground Motions on the Structural Response of Highway Bridges," by M.R. Button, C.J. Cronin and R.L. Mayes, 4/10/99, (PB2000-101411, A10, MF-A03).

MCEER-99-0008 "Seismic Reliability Assessment of Critical Facilities: A Handbook, Supporting Documentation, and Model Code Provisions," by G.S. Johnson, R.E. Sheppard, M.D. Quilici, S.J. Eder and C.R. Scawthorn, 4/12/99, (PB2000-101701, A18, MF-A04).

MCEER-99-0009 "Impact Assessment of Selected MCEER Highway Project Research on the Seismic Design of Highway Structures," by C. Rojahn, R. Mayes, D.G. Anderson, J.H. Clark, D'Appolonia Engineering, S. Gloyd and R.V. Nutt, 4/14/99, (PB99-162901, A10, MF-A02).

MCEER-99-0010 "Site Factors and Site Categories in Seismic Codes," by R. Dobry, R. Ramos and M.S. Power, 7/19/99, (PB2000-101705, A08, MF-A02).

MCEER-99-0011 "Restrainer Design Procedures for Multi-Span Simply-Supported Bridges," by M.J. Randall, M. Saiidi, E. Maragakis and T. Isakovic, 7/20/99, (PB2000-101702, A10, MF-A02).

MCEER-99-0012 "Property Modification Factors for Seismic Isolation Bearings," by M.C. Constantinou, P. Tsopelas, A. Kasalanati and E. Wolff, 7/20/99, (PB2000-103387, A11, MF-A03).

MCEER-99-0013 "Critical Seismic Issues for Existing Steel Bridges," by P. Ritchie, N. Kauhl and J. Kulicki, 7/20/99, (PB2000-101697, A09, MF-A02).

MCEER-99-0014 "Nonstructural Damage Database," by A. Kao, T.T. Soong and A. Vender, 7/24/99, (PB2000-101407, A06, MF-A01).

MCEER-99-0015 "Guide to Remedial Measures for Liquefaction Mitigation at Existing Highway Bridge Sites," by H.G. Cooke and J. K. Mitchell, 7/26/99, (PB2000-101703, A11, MF-A03).

MCEER-99-0016 "Proceedings of the MCEER Workshop on Ground Motion Methodologies for the Eastern United States," edited by N. Abrahamson and A. Becker, 8/11/99, (PB2000-103385, A07, MF-A02).

MCEER-99-0017 "Quindío, Colombia Earthquake of January 25, 1999: Reconnaissance Report," by A.P. Asfura and P.J. Flores, 10/4/99, (PB2000-106893, A06, MF-A01).

MCEER-99-0018 "Hysteretic Models for Cyclic Behavior of Deteriorating Inelastic Structures," by M.V. Sivaselvan and A.M. Reinhorn, 11/5/99, (PB2000-103386, A08, MF-A02).

MCEER-99-0019 "Proceedings of the 7th U.S.- Japan Workshop on Earthquake Resistant Design of Lifeline Facilities and Countermeasures Against Soil Liquefaction," edited by T.D. O'Rourke, J.P. Bardet and M. Hamada, 11/19/99, (PB2000-103354, A99, MF-A06).

MCEER-99-0020 "Development of Measurement Capability for Micro-Vibration Evaluations with Application to Chip Fabrication Facilities," by G.C. Lee, Z. Liang, J.W. Song, J.D. Shen and W.C. Liu, 12/1/99, (PB2000-105993, A08, MF-A02).

MCEER-99-0021 "Design and Retrofit Methodology for Building Structures with Supplemental Energy Dissipating Systems," by G. Pekcan, J.B. Mander and S.S. Chen, 12/31/99, (PB2000-105994, A11, MF-A03).

MCEER-00-0001 "The Marmara, Turkey Earthquake of August 17, 1999: Reconnaissance Report," edited by C. Scawthorn; with major contributions by M. Bruneau, R. Eguchi, T. Holzer, G. Johnson, J. Mander, J. Mitchell, W. Mitchell, A. Papageorgiou, C. Scaethorn, and G. Webb, 3/23/00, (PB2000-106200, A11, MF-A03).

MCEER-00-0002 "Proceedings of the MCEER Workshop for Seismic Hazard Mitigation of Health Care Facilities," edited by G.C. Lee, M. Ettouney, M. Grigoriu, J. Hauer and J. Nigg, 3/29/00, (PB2000-106892, A08, MF-A02).

MCEER-00-0003 "The Chi-Chi, Taiwan Earthquake of September 21, 1999: Reconnaissance Report," edited by G.C. Lee and C.H. Loh, with major contributions by G.C. Lee, M. Bruneau, I.G. Buckle, S.E. Chang, P.J. Flores, T.D. O'Rourke, M. Shinozuka, T.T. Soong, C-H. Loh, K-C. Chang, Z-J. Chen, J-S. Hwang, M-L. Lin, G-Y. Liu, K-C. Tsai, G.C. Yao and C-L. Yen, 4/30/00, (PB2001-100980, A10, MF-A02).

MCEER-00-0004 "Seismic Retrofit of End-Sway Frames of Steel Deck-Truss Bridges with a Supplemental Tendon System: Experimental and Analytical Investigation," by G. Pekcan, J.B. Mander and S.S. Chen, 7/1/00, (PB2001-100982, A10, MF-A02).

MCEER-00-0005 "Sliding Fragility of Unrestrained Equipment in Critical Facilities," by W.H. Chong and T.T. Soong, 7/5/00, (PB2001-100983, A08, MF-A02).

MCEER-00-0006 "Seismic Response of Reinforced Concrete Bridge Pier Walls in the Weak Direction," by N. Abo-Shadi, M. Saiidi and D. Sanders, 7/17/00, (PB2001-100981, A17, MF-A03).

MCEER-00-0007 "Low-Cycle Fatigue Behavior of Longitudinal Reinforcement in Reinforced Concrete Bridge Columns," by J. Brown and S.K. Kunnath, 7/23/00, (PB2001-104392, A08, MF-A02).

MCEER-00-0008 "Soil Structure Interaction of Bridges for Seismic Analysis," I. PoLam and H. Law, 9/25/00, (PB2001-105397, A08, MF-A02).

MCEER-00-0009 "Proceedings of the First MCEER Workshop on Mitigation of Earthquake Disaster by Advanced Technologies (MEDAT-1), edited by M. Shinozuka, D.J. Inman and T.D. O'Rourke, 11/10/00, (PB2001-105399, A14, MF-A03).

MCEER-00-0010 "Development and Evaluation of Simplified Procedures for Analysis and Design of Buildings with Passive Energy Dissipation Systems, Revision 01," by O.M. Ramirez, M.C. Constantinou, C.A. Kircher, A.S. Whittaker, M.W. Johnson, J.D. Gomez and C. Chrysostomou, 11/16/01, (PB2001-105523, A23, MF-A04).

MCEER-00-0011 "Dynamic Soil-Foundation-Structure Interaction Analyses of Large Caissons," by C-Y. Chang, C-M. Mok, Z-L. Wang, R. Settgast, F. Waggoner, M.A. Ketchum, H.M. Gonnermann and C-C. Chin, 12/30/00, (PB2001-104373, A07, MF-A02).

MCEER-00-0012 "Experimental Evaluation of Seismic Performance of Bridge Restrainers," by A.G. Vlassis, E.M. Maragakis and M. Saiid Saiidi, 12/30/00, (PB2001-104354, A09, MF-A02).

MCEER-00-0013 "Effect of Spatial Variation of Ground Motion on Highway Structures," by M. Shinozuka, V. Saxena and G. Deodatis, 12/31/00, (PB2001-108755, A13, MF-A03).

MCEER-00-0014 "A Risk-Based Methodology for Assessing the Seismic Performance of Highway Systems," by S.D. Werner, C.E. Taylor, J.E. Moore, II, J.S. Walton and S. Cho, 12/31/00, (PB2001-108756, A14, MF-A03).

MCEER-01-0001 "Experimental Investigation of P-Delta Effects to Collapse During Earthquakes," by D. Vian and M. Bruneau, 6/25/01, (PB2002-100534, A17, MF-A03).

MCEER-01-0002 "Proceedings of the Second MCEER Workshop on Mitigation of Earthquake Disaster by Advanced Technologies (MEDAT-2)," edited by M. Bruneau and D.J. Inman, 7/23/01, (PB2002-100434, A16, MF-A03).

MCEER-01-0003 "Sensitivity Analysis of Dynamic Systems Subjected to Seismic Loads," by C. Roth and M. Grigoriu, 9/18/01, (PB2003-100884, A12, MF-A03).

MCEER-01-0004 "Overcoming Obstacles to Implementing Earthquake Hazard Mitigation Policies: Stage 1 Report," by D.J. Alesch and W.J. Petak, 12/17/01, (PB2002-107949, A07, MF-A02).

MCEER-01-0005 "Updating Real-Time Earthquake Loss Estimates: Methods, Problems and Insights," by C.E. Taylor, S.E. Chang and R.T. Eguchi, 12/17/01, (PB2002-107948, A05, MF-A01).

MCEER-01-0006 "Experimental Investigation and Retrofit of Steel Pile Foundations and Pile Bents Under Cyclic Lateral Loadings," by A. Shama, J. Mander, B. Blabac and S. Chen, 12/31/01, (PB2002-107950, A13, MF-A03).

MCEER-02-0001 "Assessment of Performance of Bolu Viaduct in the 1999 Duzce Earthquake in Turkey" by P.C. Roussis, M.C. Constantinou, M. Erdik, E. Durukal and M. Dicleli, 5/8/02, (PB2003-100883, A08, MF-A02).

MCEER-02-0002 "Seismic Behavior of Rail Counterweight Systems of Elevators in Buildings," by M.P. Singh, Rildova and L.E. Suarez, 5/27/02. (PB2003-100882, A11, MF-A03).

MCEER-02-0003 "Development of Analysis and Design Procedures for Spread Footings," by G. Mylonakis, G. Gazetas, S. Nikolaou and A. Chauncey, 10/02/02, (PB2004-101636, A13, MF-A03, CD-A13).

MCEER-02-0004 "Bare-Earth Algorithms for Use with SAR and LIDAR Digital Elevation Models," by C.K. Huyck, R.T. Eguchi and B. Houshmand, 10/16/02, (PB2004-101637, A07, CD-A07).

MCEER-02-0005 "Review of Energy Dissipation of Compression Members in Concentrically Braced Frames," by K.Lee and M. Bruneau, 10/18/02, (PB2004-101638, A10, CD-A10).

MCEER-03-0001 "Experimental Investigation of Light-Gauge Steel Plate Shear Walls for the Seismic Retrofit of Buildings" by J. Berman and M. Bruneau, 5/2/03, (PB2004-101622, A10, MF-A03, CD-A10).

MCEER-03-0002 "Statistical Analysis of Fragility Curves," by M. Shinozuka, M.Q. Feng, H. Kim, T. Uzawa and T. Ueda, 6/16/03, (PB2004-101849, A09, CD-A09).

MCEER-03-0003 "Proceedings of the Eighth U.S.-Japan Workshop on Earthquake Resistant Design f Lifeline Facilities and Countermeasures Against Liquefaction," edited by M. Hamada, J.P. Bardet and T.D. O'Rourke, 6/30/03, (PB2004-104386, A99, CD-A99).

MCEER-03-0004 "Proceedings of the PRC-US Workshop on Seismic Analysis and Design of Special Bridges," edited by L.C. Fan and G.C. Lee, 7/15/03, (PB2004-104387, A14, CD-A14).

MCEER-03-0005 "Urban Disaster Recovery: A Framework and Simulation Model," by S.B. Miles and S.E. Chang, 7/25/03, (PB2004-104388, A07, CD-A07).

MCEER-03-0006 "Behavior of Underground Piping Joints Due to Static and Dynamic Loading," by R.D. Meis, M. Maragakis and R. Siddharthan, 11/17/03, (PB2005-102194, A13, MF-A03, CD-A00).

MCEER-04-0001 "Experimental Study of Seismic Isolation Systems with Emphasis on Secondary System Response and Verification of Accuracy of Dynamic Response History Analysis Methods," by E. Wolff and M. Constantinou, 1/16/04 (PB2005-102195, A99, MF-E08, CD-A00).

MCEER-04-0002 "Tension, Compression and Cyclic Testing of Engineered Cementitious Composite Materials," by K. Kesner and S.L. Billington, 3/1/04, (PB2005-102196, A08, CD-A08).

MCEER-04-0003 "Cyclic Testing of Braces Laterally Restrained by Steel Studs to Enhance Performance During Earthquakes," by O.C. Celik, J.W. Berman and M. Bruneau, 3/16/04, (PB2005-102197, A13, MF-A03, CD-A00).

MCEER-04-0004 "Methodologies for Post Earthquake Building Damage Detection Using SAR and Optical Remote Sensing: Application to the August 17, 1999 Marmara, Turkey Earthquake," by C.K. Huyck, B.J. Adams, S. Cho, R.T. Eguchi, B. Mansouri and B. Houshmand, 6/15/04, (PB2005-104888, A10, CD-A00).

MCEER-04-0005 "Nonlinear Structural Analysis Towards Collapse Simulation: A Dynamical Systems Approach," by M.V. Sivaselvan and A.M. Reinhorn, 6/16/04, (PB2005-104889, A11, MF-A03, CD-A00).

MCEER-04-0006 "Proceedings of the Second PRC-US Workshop on Seismic Analysis and Design of Special Bridges," edited by G.C. Lee and L.C. Fan, 6/25/04, (PB2005-104890, A16, CD-A00).

MCEER-04-0007 "Seismic Vulnerability Evaluation of Axially Loaded Steel Built-up Laced Members," by K. Lee and M. Bruneau, 6/30/04, (PB2005-104891, A16, CD-A00).

MCEER-04-0008 "Evaluation of Accuracy of Simplified Methods of Analysis and Design of Buildings with Damping Systems for Near-Fault and for Soft-Soil Seismic Motions," by E.A. Pavlou and M.C. Constantinou, 8/16/04, (PB2005-104892, A08, MF-A02, CD-A00).

MCEER-04-0009 "Assessment of Geotechnical Issues in Acute Care Facilities in California," by M. Lew, T.D. O'Rourke, R. Dobry and M. Koch, 9/15/04, (PB2005-104893, A08, CD-A00).

MCEER-04-0010 "Scissor-Jack-Damper Energy Dissipation System," by A.N. Sigaher-Boyle and M.C. Constantinou, 12/1/04 (PB2005-108221).

MCEER-04-0011 "Seismic Retrofit of Bridge Steel Truss Piers Using a Controlled Rocking Approach," by M. Pollino and M. Bruneau, 12/20/04 (PB2006-105795).

MCEER-05-0001 "Experimental and Analytical Studies of Structures Seismically Isolated with an Uplift-Restraint Isolation System," by P.C. Roussis and M.C. Constantinou, 1/10/05 (PB2005-108222).

MCEER-05-0002 "A Versatile Experimentation Model for Study of Structures Near Collapse Applied to Seismic Evaluation of Irregular Structures," by D. Kusumastuti, A.M. Reinhorn and A. Rutenberg, 3/31/05 (PB2006-101523).

MCEER-05-0003 "Proceedings of the Third PRC-US Workshop on Seismic Analysis and Design of Special Bridges," edited by L.C. Fan and G.C. Lee, 4/20/05, (PB2006-105796).

MCEER-05-0004 "Approaches for the Seismic Retrofit of Braced Steel Bridge Piers and Proof-of-Concept Testing of an Eccentrically Braced Frame with Tubular Link," by J.W. Berman and M. Bruneau, 4/21/05 (PB2006-101524).

MCEER-05-0005 "Simulation of Strong Ground Motions for Seismic Fragility Evaluation of Nonstructural Components in Hospitals," by A. Wanitkorkul and A. Filiatrault, 5/26/05 (PB2006-500027).

MCEER-05-0006 "Seismic Safety in California Hospitals: Assessing an Attempt to Accelerate the Replacement or Seismic Retrofit of Older Hospital Facilities," by D.J. Alesch, L.A. Arendt and W.J. Petak, 6/6/05 (PB2006-105794).

MCEER-05-0007 "Development of Seismic Strengthening and Retrofit Strategies for Critical Facilities Using Engineered Cementitious Composite Materials," by K. Kesner and S.L. Billington, 8/29/05 (PB2006-111701).

MCEER-05-0008 "Experimental and Analytical Studies of Base Isolation Systems for Seismic Protection of Power Transformers," by N. Murota, M.Q. Feng and G-Y. Liu, 9/30/05 (PB2006-111702).

MCEER-05-0009 "3D-BASIS-ME-MB: Computer Program for Nonlinear Dynamic Analysis of Seismically Isolated Structures," by P.C. Tsopelas, P.C. Roussis, M.C. Constantinou, R. Buchanan and A.M. Reinhorn, 10/3/05 (PB2006-111703).

MCEER-05-0010 "Steel Plate Shear Walls for Seismic Design and Retrofit of Building Structures," by D. Vian and M. Bruneau, 12/15/05 (PB2006-111704).

MCEER-05-0011 "The Performance-Based Design Paradigm," by M.J. Astrella and A. Whittaker, 12/15/05 (PB2006-111705).

MCEER-06-0001 "Seismic Fragility of Suspended Ceiling Systems," H. Badillo-Almaraz, A.S. Whittaker, A.M. Reinhorn and G.P. Cimellaro, 2/4/06 (PB2006-111706).

MCEER-06-0002 "Multi-Dimensional Fragility of Structures," by G.P. Cimellaro, A.M. Reinhorn and M. Bruneau, 3/1/06 (PB2007-106974, A09, MF-A02, CD A00).

MCEER-06-0003 "Built-Up Shear Links as Energy Dissipators for Seismic Protection of Bridges," by P. Dusicka, A.M. Itani and I.G. Buckle, 3/15/06 (PB2006-111708).

MCEER-06-0004 "Analytical Investigation of the Structural Fuse Concept," by R.E. Vargas and M. Bruneau, 3/16/06 (PB2006-111709).

MCEER-06-0005 "Experimental Investigation of the Structural Fuse Concept," by R.E. Vargas and M. Bruneau, 3/17/06 (PB2006-111710).

MCEER-06-0006 "Further Development of Tubular Eccentrically Braced Frame Links for the Seismic Retrofit of Braced Steel Truss Bridge Piers," by J.W. Berman and M. Bruneau, 3/27/06 (PB2007-105147).

MCEER-06-0007 "REDARS Validation Report," by S. Cho, C.K. Huyck, S. Ghosh and R.T. Eguchi, 8/8/06 (PB2007-106983).

MCEER-06-0008 "Review of Current NDE Technologies for Post-Earthquake Assessment of Retrofitted Bridge Columns," by J.W. Song, Z. Liang and G.C. Lee, 8/21/06 (PB2007-106984).

MCEER-06-0009 "Liquefaction Remediation in Silty Soils Using Dynamic Compaction and Stone Columns," by S. Thevanayagam, G.R. Martin, R. Nashed, T. Shenthan, T. Kanagalingam and N. Ecemis, 8/28/06 (PB2007-106985).

MCEER-06-0010 "Conceptual Design and Experimental Investigation of Polymer Matrix Composite Infill Panels for Seismic Retrofitting," by W. Jung, M. Chiewanichakorn and A.J. Aref, 9/21/06 (PB2007-106986).

MCEER-06-0011 "A Study of the Coupled Horizontal-Vertical Behavior of Elastomeric and Lead-Rubber Seismic Isolation Bearings," by G.P. Warn and A.S. Whittaker, 9/22/06 (PB2007-108679).

MCEER-06-0012 "Proceedings of the Fourth PRC-US Workshop on Seismic Analysis and Design of Special Bridges: Advancing Bridge Technologies in Research, Design, Construction and Preservation," Edited by L.C. Fan, G.C. Lee and L. Ziang, 10/12/06 (PB2007-109042).

MCEER-06-0013 "Cyclic Response and Low Cycle Fatigue Characteristics of Plate Steels," by P. Dusicka, A.M. Itani and I.G. Buckle, 11/1/06 06 (PB2007-106987).

MCEER-06-0014 "Proceedings of the Second US-Taiwan Bridge Engineering Workshop," edited by W.P. Yen, J. Shen, J-Y. Chen and M. Wang, 11/15/06 (PB2008-500041).

MCEER-06-0015 "User Manual and Technical Documentation for the REDARS^{TM} Import Wizard," by S. Cho, S. Ghosh, C.K. Huyck and S.D. Werner, 11/30/06 (PB2007-114766).

MCEER-06-0016 "Hazard Mitigation Strategy and Monitoring Technologies for Urban and Infrastructure Public Buildings: Proceedings of the China-US Workshops," edited by X.Y. Zhou, A.L. Zhang, G.C. Lee and M. Tong, 12/12/06 (PB2008-500018).

MCEER-07-0001 "Static and Kinetic Coefficients of Friction for Rigid Blocks," by C. Kafali, S. Fathali, M. Grigoriu and A.S. Whittaker, 3/20/07 (PB2007-114767).

MCEER-07-0002 "Hazard Mitigation Investment Decision Making: Organizational Response to Legislative Mandate," by L.A. Arendt, D.J. Alesch and W.J. Petak, 4/9/07 (PB2007-114768).

MCEER-07-0003 "Seismic Behavior of Bidirectional-Resistant Ductile End Diaphragms with Unbonded Braces in Straight or Skewed Steel Bridges," by O. Celik and M. Bruneau, 4/11/07 (PB2008-105141).

MCEER-07-0004 "Modeling Pile Behavior in Large Pile Groups Under Lateral Loading," by A.M. Dodds and G.R. Martin, 4/16/07(PB2008-105142).

MCEER-07-0005 "Experimental Investigation of Blast Performance of Seismically Resistant Concrete-Filled Steel Tube Bridge Piers," by S. Fujikura, M. Bruneau and D. Lopez-Garcia, 4/20/07 (PB2008-105143).

MCEER-07-0006 "Seismic Analysis of Conventional and Isolated Liquefied Natural Gas Tanks Using Mechanical Analogs," by I.P. Christovasilis and A.S. Whittaker, 5/1/07, not available.

MCEER-07-0007 "Experimental Seismic Performance Evaluation of Isolation/Restraint Systems for Mechanical Equipment – Part 1: Heavy Equipment Study," by S. Fathali and A. Filiatrault, 6/6/07 (PB2008-105144).

MCEER-07-0008 "Seismic Vulnerability of Timber Bridges and Timber Substructures," by A.A. Sharma, J.B. Mander, I.M. Friedland and D.R. Allicock, 6/7/07 (PB2008-105145).

MCEER-07-0009 "Experimental and Analytical Study of the XY-Friction Pendulum (XY-FP) Bearing for Bridge Applications," by C.C. Marin-Artieda, A.S. Whittaker and M.C. Constantinou, 6/7/07 (PB2008-105191).

MCEER-07-0010 "Proceedings of the PRC-US Earthquake Engineering Forum for Young Researchers," Edited by G.C. Lee and X.Z. Qi, 6/8/07 (PB2008-500058).

MCEER-07-0011 "Design Recommendations for Perforated Steel Plate Shear Walls," by R. Purba and M. Bruneau, 6/18/07, (PB2008-105192).

MCEER-07-0012 "Performance of Seismic Isolation Hardware Under Service and Seismic Loading," by M.C. Constantinou, A.S. Whittaker, Y. Kalpakidis, D.M. Fenz and G.P. Warn, 8/27/07, (PB2008-105193).

MCEER-07-0013 "Experimental Evaluation of the Seismic Performance of Hospital Piping Subassemblies," by E.R. Goodwin, E. Maragakis and A.M. Itani, 9/4/07, (PB2008-105194).

MCEER-07-0014 "A Simulation Model of Urban Disaster Recovery and Resilience: Implementation for the 1994 Northridge Earthquake," by S. Miles and S.E. Chang, 9/7/07, (PB2008-106426).

MCEER-07-0015 "Statistical and Mechanistic Fragility Analysis of Concrete Bridges," by M. Shinozuka, S. Banerjee and S-H. Kim, 9/10/07, (PB2008-106427).

MCEER-07-0016 "Three-Dimensional Modeling of Inelastic Buckling in Frame Structures," by M. Schachter and AM. Reinhorn, 9/13/07, (PB2008-108125).

MCEER-07-0017 "Modeling of Seismic Wave Scattering on Pile Groups and Caissons," by I. Po Lam, H. Law and C.T. Yang, 9/17/07 (PB2008-108150).

MCEER-07-0018 "Bridge Foundations: Modeling Large Pile Groups and Caissons for Seismic Design," by I. Po Lam, H. Law and G.R. Martin (Coordinating Author), 12/1/07 (PB2008-111190).

MCEER-07-0019 "Principles and Performance of Roller Seismic Isolation Bearings for Highway Bridges," by G.C. Lee, Y.C. Ou, Z. Liang, T.C. Niu and J. Song, 12/10/07 (PB2009-110466).

MCEER-07-0020 "Centrifuge Modeling of Permeability and Pinning Reinforcement Effects on Pile Response to Lateral Spreading," by L.L Gonzalez-Lagos, T. Abdoun and R. Dobry, 12/10/07 (PB2008-111191).

MCEER-07-0021 "Damage to the Highway System from the Pisco, Perú Earthquake of August 15, 2007," by J.S. O'Connor, L. Mesa and M. Nykamp, 12/10/07, (PB2008-108126).

MCEER-07-0022 "Experimental Seismic Performance Evaluation of Isolation/Restraint Systems for Mechanical Equipment – Part 2: Light Equipment Study," by S. Fathali and A. Filiatrault, 12/13/07 (PB2008-111192).

MCEER-07-0023 "Fragility Considerations in Highway Bridge Design," by M. Shinozuka, S. Banerjee and S.H. Kim, 12/14/07 (PB2008-111193).

MCEER-07-0024 "Performance Estimates for Seismically Isolated Bridges," by G.P. Warn and A.S. Whittaker, 12/30/07 (PB2008-112230).

MCEER-08-0001 "Seismic Performance of Steel Girder Bridge Superstructures with Conventional Cross Frames," by L.P. Carden, A.M. Itani and I.G. Buckle, 1/7/08, (PB2008-112231).

MCEER-08-0002 "Seismic Performance of Steel Girder Bridge Superstructures with Ductile End Cross Frames with Seismic Isolators," by L.P. Carden, A.M. Itani and I.G. Buckle, 1/7/08 (PB2008-112232).

MCEER-08-0003 "Analytical and Experimental Investigation of a Controlled Rocking Approach for Seismic Protection of Bridge Steel Truss Piers," by M. Pollino and M. Bruneau, 1/21/08 (PB2008-112233).

MCEER-08-0004 "Linking Lifeline Infrastructure Performance and Community Disaster Resilience: Models and Multi-Stakeholder Processes," by S.E. Chang, C. Pasion, K. Tatebe and R. Ahmad, 3/3/08 (PB2008-112234).

MCEER-08-0005 "Modal Analysis of Generally Damped Linear Structures Subjected to Seismic Excitations," by J. Song, Y-L. Chu, Z. Liang and G.C. Lee, 3/4/08 (PB2009-102311).

MCEER-08-0006 "System Performance Under Multi-Hazard Environments," by C. Kafali and M. Grigoriu, 3/4/08 (PB2008-112235).

MCEER-08-0007 "Mechanical Behavior of Multi-Spherical Sliding Bearings," by D.M. Fenz and M.C. Constantinou, 3/6/08 (PB2008-112236).

MCEER-08-0008 "Post-Earthquake Restoration of the Los Angeles Water Supply System," by T.H.P. Tabucchi and R.A. Davidson, 3/7/08 (PB2008-112237).

MCEER-08-0009 "Fragility Analysis of Water Supply Systems," by A. Jacobson and M. Grigoriu, 3/10/08 (PB2009-105545).

MCEER-08-0010 "Experimental Investigation of Full-Scale Two-Story Steel Plate Shear Walls with Reduced Beam Section Connections," by B. Qu, M. Bruneau, C-H. Lin and K-C. Tsai, 3/17/08 (PB2009-106368).

MCEER-08-0011 "Seismic Evaluation and Rehabilitation of Critical Components of Electrical Power Systems," S. Ersoy, B. Feizi, A. Ashrafi and M. Ala Saadeghvaziri, 3/17/08 (PB2009-105546).

MCEER-08-0012 "Seismic Behavior and Design of Boundary Frame Members of Steel Plate Shear Walls," by B. Qu and M. Bruneau, 4/26/08 . (PB2009-106744).

MCEER-08-0013 "Development and Appraisal of a Numerical Cyclic Loading Protocol for Quantifying Building System Performance," by A. Filiatrault, A. Wanitkorkul and M. Constantinou, 4/27/08 (PB2009-107906).

MCEER-08-0014 "Structural and Nonstructural Earthquake Design: The Challenge of Integrating Specialty Areas in Designing Complex, Critical Facilities," by W.J. Petak and D.J. Alesch, 4/30/08 (PB2009-107907).

MCEER-08-0015 "Seismic Performance Evaluation of Water Systems," by Y. Wang and T.D. O'Rourke, 5/5/08 (PB2009-107908).

MCEER-08-0016 "Seismic Response Modeling of Water Supply Systems," by P. Shi and T.D. O'Rourke, 5/5/08 (PB2009-107910).

MCEER-08-0017 "Numerical and Experimental Studies of Self-Centering Post-Tensioned Steel Frames," by D. Wang and A. Filiatrault, 5/12/08 (PB2009-110479).

MCEER-08-0018 "Development, Implementation and Verification of Dynamic Analysis Models for Multi-Spherical Sliding Bearings," by D.M. Fenz and M.C. Constantinou, 8/15/08 (PB2009-107911).

MCEER-08-0019 "Performance Assessment of Conventional and Base Isolated Nuclear Power Plants for Earthquake Blast Loadings," by Y.N. Huang, A.S. Whittaker and N. Luco, 10/28/08 (PB2009-107912).

MCEER-08-0020 "Remote Sensing for Resilient Multi-Hazard Disaster Response – Volume I: Introduction to Damage Assessment Methodologies," by B.J. Adams and R.T. Eguchi, 11/17/08 (PB2010-102695).

MCEER-08-0021 "Remote Sensing for Resilient Multi-Hazard Disaster Response – Volume II: Counting the Number of Collapsed Buildings Using an Object-Oriented Analysis: Case Study of the 2003 Bam Earthquake," by L. Gusella, C.K. Huyck and B.J. Adams, 11/17/08 (PB2010-100925).

MCEER-08-0022 "Remote Sensing for Resilient Multi-Hazard Disaster Response – Volume III: Multi-Sensor Image Fusion Techniques for Robust Neighborhood-Scale Urban Damage Assessment," by B.J. Adams and A. McMillan, 11/17/08 (PB2010-100926).

MCEER-08-0023 "Remote Sensing for Resilient Multi-Hazard Disaster Response – Volume IV: A Study of Multi-Temporal and Multi-Resolution SAR Imagery for Post-Katrina Flood Monitoring in New Orleans," by A. McMillan, J.G. Morley, B.J. Adams and S. Chesworth, 11/17/08 (PB2010-100927).

MCEER-08-0024 "Remote Sensing for Resilient Multi-Hazard Disaster Response – Volume V: Integration of Remote Sensing Imagery and VIEWS^{TM} Field Data for Post-Hurricane Charley Building Damage Assessment," by J.A. Womble, K. Mehta and B.J. Adams, 11/17/08 (PB2009-115532).

MCEER-08-0025 "Building Inventory Compilation for Disaster Management: Application of Remote Sensing and Statistical Modeling," by P. Sarabandi, A.S. Kiremidjian, R.T. Eguchi and B. J. Adams, 11/20/08 (PB2009-110484).

MCEER-08-0026 "New Experimental Capabilities and Loading Protocols for Seismic Qualification and Fragility Assessment of Nonstructural Systems," by R. Retamales, G. Mosqueda, A. Filiatrault and A. Reinhorn, 11/24/08 (PB2009-110485).

MCEER-08-0027 "Effects of Heating and Load History on the Behavior of Lead-Rubber Bearings," by I.V. Kalpakidis and M.C. Constantinou, 12/1/08 (PB2009-115533).

MCEER-08-0028 "Experimental and Analytical Investigation of Blast Performance of Seismically Resistant Bridge Piers," by S.Fujikura and M. Bruneau, 12/8/08 (PB2009-115534).

MCEER-08-0029 "Evolutionary Methodology for Aseismic Decision Support," by Y. Hu and G. Dargush, 12/15/08.

MCEER-08-0030 "Development of a Steel Plate Shear Wall Bridge Pier System Conceived from a Multi-Hazard Perspective," by D. Keller and M. Bruneau, 12/19/08 (PB2010-102696).

MCEER-09-0001 "Modal Analysis of Arbitrarily Damped Three-Dimensional Linear Structures Subjected to Seismic Excitations," by Y.L. Chu, J. Song and G.C. Lee, 1/31/09 (PB2010-100922).

MCEER-09-0002 "Air-Blast Effects on Structural Shapes," by G. Ballantyne, A.S. Whittaker, A.J. Aref and G.F. Dargush, 2/2/09 (PB2010-102697).

MCEER-09-0003 "Water Supply Performance During Earthquakes and Extreme Events," by A.L. Bonneau and T.D. O'Rourke, 2/16/09 (PB2010-100923).

MCEER-09-0004 "Generalized Linear (Mixed) Models of Post-Earthquake Ignitions," by R.A. Davidson, 7/20/09 (PB2010-102698).

MCEER-09-0005 "Seismic Testing of a Full-Scale Two-Story Light-Frame Wood Building: NEESWood Benchmark Test," by I.P. Christovasilis, A. Filiatrault and A. Wanitkorkul, 7/22/09 (PB2012-102401).

MCEER-09-0006 "IDARC2D Version 7.0: A Program for the Inelastic Damage Analysis of Structures," by A.M. Reinhorn, H. Roh, M. Sivaselvan, S.K. Kunnath, R.E. Valles, A. Madan, C. Li, R. Lobo and Y.J. Park, 7/28/09 (PB2010-103199).

MCEER-09-0007 "Enhancements to Hospital Resiliency: Improving Emergency Planning for and Response to Hurricanes," by D.B. Hess and L.A. Arendt, 7/30/09 (PB2010-100924).

MCEER-09-0008 "Assessment of Base-Isolated Nuclear Structures for Design and Beyond-Design Basis Earthquake Shaking," by Y.N. Huang, A.S. Whittaker, R.P. Kennedy and R.L. Mayes, 8/20/09 (PB2010-102699).

MCEER-09-0009 "Quantification of Disaster Resilience of Health Care Facilities," by G.P. Cimellaro, C. Fumo, A.M Reinhorn and M. Bruneau, 9/14/09 (PB2010-105384).

MCEER-09-0010 "Performance-Based Assessment and Design of Squat Reinforced Concrete Shear Walls," by C.K. Gulec and A.S. Whittaker, 9/15/09 (PB2010-102700).

MCEER-09-0011 "Proceedings of the Fourth US-Taiwan Bridge Engineering Workshop," edited by W.P. Yen, J.J. Shen, T.M. Lee and R.B. Zheng, 10/27/09 (PB2010-500009).

MCEER-09-0012 "Proceedings of the Special International Workshop on Seismic Connection Details for Segmental Bridge Construction," edited by W. Phillip Yen and George C. Lee, 12/21/09 (PB2012-102402).

MCEER-10-0001 "Direct Displacement Procedure for Performance-Based Seismic Design of Multistory Woodframe Structures," by W. Pang and D. Rosowsky, 4/26/10 (PB2012-102403).

MCEER-10-0002 "Simplified Direct Displacement Design of Six-Story NEESWood Capstone Building and Pre-Test Seismic Performance Assessment," by W. Pang, D. Rosowsky, J. van de Lindt and S. Pei, 5/28/10 (PB2012-102404).

MCEER-10-0003 "Integration of Seismic Protection Systems in Performance-Based Seismic Design of Woodframed Structures," by J.K. Shinde and M.D. Symans, 6/18/10 (PB2012-102405).

MCEER-10-0004 "Modeling and Seismic Evaluation of Nonstructural Components: Testing Frame for Experimental Evaluation of Suspended Ceiling Systems," by A.M. Reinhorn, K.P. Ryu and G. Maddaloni, 6/30/10 (PB2012-102406).

MCEER-10-0005 "Analytical Development and Experimental Validation of a Structural-Fuse Bridge Pier Concept," by S. El-Bahey and M. Bruneau, 10/1/10 (PB2012-102407).

MCEER-10-0006 "A Framework for Defining and Measuring Resilience at the Community Scale: The PEOPLES Resilience Framework," by C.S. Renschler, A.E. Frazier, L.A. Arendt, G.P. Cimellaro, A.M. Reinhorn and M. Bruneau, 10/8/10 (PB2012-102408).

MCEER-10-0007 "Impact of Horizontal Boundary Elements Design on Seismic Behavior of Steel Plate Shear Walls," by R. Purba and M. Bruneau, 11/14/10 (PB2012-102409).

MCEER-10-0008 "Seismic Testing of a Full-Scale Mid-Rise Building: The NEESWood Capstone Test," by S. Pei, J.W. van de Lindt, S.E. Pryor, H. Shimizu, H. Isoda and D.R. Rammer, 12/1/10 (PB2012-102410).

MCEER-10-0009 "Modeling the Effects of Detonations of High Explosives to Inform Blast-Resistant Design," by P. Sherkar, A.S. Whittaker and A.J. Aref, 12/1/10 (PB2012-102411).

MCEER-10-0010 "L'Aquila Earthquake of April 6, 2009 in Italy: Rebuilding a Resilient City to Withstand Multiple Hazards," by G.P. Cimellaro, I.P. Christovasilis, A.M. Reinhorn, A. De Stefano and T. Kirova, 12/29/10.

MCEER-11-0001 "Numerical and Experimental Investigation of the Seismic Response of Light-Frame Wood Structures," by I.P. Christovasilis and A. Filiatrault, 8/8/11 (PB2012-102412).

MCEER-11-0002 "Seismic Design and Analysis of a Precast Segmental Concrete Bridge Model," by M. Anagnostopoulou, A. Filiatrault and A. Aref, 9/15/11.

MCEER-11-0003 'Proceedings of the Workshop on Improving Earthquake Response of Substation Equipment," Edited by A.M. Reinhorn, 9/19/11 (PB2012-102413).

MCEER-11-0004 "LRFD-Based Analysis and Design Procedures for Bridge Bearings and Seismic Isolators," by M.C. Constantinou, I. Kalpakidis, A. Filiatrault and R.A. Ecker Lay, 9/26/11.

MCEER-11-0005 "Experimental Seismic Evaluation, Model Parameterization, and Effects of Cold-Formed Steel-Framed Gypsum Partition Walls on the Seismic Performance of an Essential Facility," by R. Davies, R. Retamales, G. Mosqueda and A. Filiatrault, 10/12/11.

MCEER-11-0006 "Modeling and Seismic Performance Evaluation of High Voltage Transformers and Bushings," by A.M. Reinhorn, K. Oikonomou, H. Roh, A. Schiff and L. Kempner, Jr., 10/3/11.

MCEER-11-0007 "Extreme Load Combinations: A Survey of State Bridge Engineers," by G.C. Lee, Z. Liang, J.J. Shen and J.S. O'Connor, 10/14/11.

MCEER-12-0001 "Simplified Analysis Procedures in Support of Performance Based Seismic Design," by Y.N. Huang and A.S. Whittaker.

MCEER-12-0002 "Seismic Protection of Electrical Transformer Bushing Systems by Stiffening Techniques," by M. Koliou, A. Filiatrault, A.M. Reinhorn and N. Oliveto, 6/1/12.

MCEER-12-0003 "Post-Earthquake Bridge Inspection Guidelines," by J.S. O'Connor and S. Alampalli, 6/8/12.

MCEER-12-0004 "Integrated Design Methodology for Isolated Floor Systems in Single-Degree-of-Freedom Structural Fuse Systems," by S. Cui, M. Bruneau and M.C. Constantinou, 6/13/12.

MCEER-12-0005 "Characterizing the Rotational Components of Earthquake Ground Motion," by D. Basu, A.S. Whittaker and M.C. Constantinou, 6/15/12.

MCEER-12-0006 "Bayesian Fragility for Nonstructural Systems," by C.H. Lee and M.D. Grigoriu, 9/12/12.

MCEER-12-0007 "A Numerical Model for Capturing the In-Plane Seismic Response of Interior Metal Stud Partition Walls," by R.L. Wood and T.C. Hutchinson, 9/12/12.

MCEER-12-0008 "Assessment of Floor Accelerations in Yielding Buildings," by J.D. Wieser, G. Pekcan, A.E. Zaghi, A.M. Itani and E. Maragakis, 10/5/12.

MCEER-13-0001 "Experimental Seismic Study of Pressurized Fire Sprinkler Piping Systems," by Y. Tian, A. Filiatrault and G. Mosqueda, 4/8/13.

MCEER-13-0002 "Enhancing Resource Coordination for Multi-Modal Evacuation Planning," by D.B. Hess, B.W. Conley and C.M. Farrell, 2/8/13.

MCEER-13-0003 "Seismic Response of Base Isolated Buildings Considering Pounding to Moat Walls," by A. Masroor and G. Mosqueda, 2/26/13.

MCEER-13-0004 "Seismic Response Control of Structures Using a Novel Adaptive Passive Negative Stiffness Device," by D.T.R. Pasala, A.A. Sarlis, S. Nagarajaiah, A.M. Reinhorn, M.C. Constantinou and D.P. Taylor, 6/10/13.

MCEER-13-0005 "Negative Stiffness Device for Seismic Protection of Structures," by A.A. Sarlis, D.T.R. Pasala, M.C. Constantinou, A.M. Reinhorn, S. Nagarajaiah and D.P. Taylor, 6/12/13.

MCEER-13-0006 "Emilia Earthquake of May 20, 2012 in Northern Italy: Rebuilding a Resilient Community to Withstand Multiple Hazards," by G.P. Cimellaro, M. Chiriatti, A.M. Reinhorn and L. Tirca, June 30, 2013.

MCEER-13-0007 "Precast Concrete Segmental Components and Systems for Accelerated Bridge Construction in Seismic Regions," by A.J. Aref, G.C. Lee, Y.C. Ou and P. Sideris, with contributions from K.C. Chang, S. Chen, A. Filiatrault and Y. Zhou, June 13, 2013.

MCEER-13-0008 "A Study of U.S. Bridge Failures (1980-2012)," by G.C. Lee, S.B. Mohan, C. Huang and B.N. Fard, June 15, 2013.

MCEER-13-0009 "Development of a Database Framework for Modeling Damaged Bridges," by G.C. Lee, J.C. Qi and C. Huang, June 16, 2013.

MCEER-13-0010 "Model of Triple Friction Pendulum Bearing for General Geometric and Frictional Parameters and for Uplift Conditions," by A.A. Sarlis and M.C. Constantinou, July 1, 2013.

MCEER-13-0011 "Shake Table Testing of Triple Friction Pendulum Isolators under Extreme Conditions," by A.A. Sarlis, M.C. Constantinou and A.M. Reinhorn, July 2, 2013.

MCEER-13-0012 "Theoretical Framework for the Development of MH-LRFD," by G.C. Lee (coordinating author), H.A Capers, Jr., C. Huang, J.M. Kulicki, Z. Liang, T. Murphy, J.J.D. Shen, M. Shinozuka and P.W.H. Yen, July 31, 2013.

MCEER-13-0013 "Seismic Protection of Highway Bridges with Negative Stiffness Devices," by N.K.A. Attary, M.D. Symans, S. Nagarajaiah, A.M. Reinhorn, M.C. Constantinou, A.A. Sarlis, D.T.R. Pasala, and D.P. Taylor, September 3, 2014.

MCEER-14-0001 "Simplified Seismic Collapse Capacity-Based Evaluation and Design of Frame Buildings with and without Supplemental Damping Systems," by M. Hamidia, A. Filiatrault, and A. Aref, May 19, 2014.

MCEER-14-0002 "Comprehensive Analytical Seismic Fragility of Fire Sprinkler Piping Systems," by Siavash Soroushian, Emmanuel "Manos" Maragakis, Arash E. Zaghi, Alicia Echevarria, Yuan Tian and Andre Filiatrault, August 26, 2014.

MCEER-14-0003 "Hybrid Simulation of the Seismic Response of a Steel Moment Frame Building Structure through Collapse," by M. Del Carpio Ramos, G. Mosqueda and D.G. Lignos, October 30, 2014.

MCEER-14-0004 "Blast and Seismic Resistant Concrete-Filled Double Skin Tubes and Modified Steel Jacketed Bridge Columns," by P.P. Fouche and M. Bruneau, June 30, 2015.

MCEER-14-0005 "Seismic Performance of Steel Plate Shear Walls Considering Various Design Approaches," by R. Purba and M. Bruneau, October 31, 2014.

MCEER-14-0006 "Air-Blast Effects on Civil Structures," by Jinwon Shin, Andrew S. Whittaker, Amjad J. Aref and David Cormie, October 30, 2014.

MCEER-14-0007 "Seismic Performance Evaluation of Precast Girders with Field-Cast Ultra High Performance Concrete (UHPC) Connections," by G.C. Lee, C. Huang, J. Song, and J. S. O'Connor, July 31, 2014.

MCEER-14-0008 "Post-Earthquake Fire Resistance of Ductile Concrete-Filled Double-Skin Tube Columns," by Reza Imani, Gilberto Mosqueda and Michel Bruneau, December 1, 2014.

MCEER-14-0009 "Cyclic Inelastic Behavior of Concrete Filled Sandwich Panel Walls Subjected to In-Plane Flexure," by Y. Alzeni and M. Bruneau, December 19, 2014.

MCEER-14-0010 "Analytical and Experimental Investigation of Self-Centering Steel Plate Shear Walls," by D.M. Dowden and M. Bruneau, December 19, 2014.

MCEER-15-0001 "Seismic Analysis of Multi-story Unreinforced Masonry Buildings with Flexible Diaphragms," by J. Aleman, G. Mosqueda and A.S. Whittaker, June 12, 2015.

MCEER-15-0002 "Site Response, Soil-Structure Interaction and Structure-Soil-Structure Interaction for Performance Assessment of Buildings and Nuclear Structures," by C. Bolisetti and A.S. Whittaker, June 15, 2015.

MCEER-15-0003 "Stress Wave Attenuation in Solids for Mitigating Impulsive Loadings," by R. Rafiee-Dehkharghani, A.J. Aref and G. Dargush, August 15, 2015.

MCEER-15-0004 "Computational, Analytical, and Experimental Modeling of Masonry Structures," by K.M. Dolatshahi and A.J. Aref, November 16, 2015.

MCEER-15-0005 "Property Modification Factors for Seismic Isolators: Design Guidance for Buildings," by W.J. McVitty and M.C. Constantinou, June 30, 2015.

MCEER-15-0006 "Seismic Isolation of Nuclear Power Plants using Sliding Bearings," by Manish Kumar, Andrew S. Whittaker and Michael C. Constantinou, December 27, 2015.

MCEER-15-0007 "Quintuple Friction Pendulum Isolator Behavior, Modeling and Validation," by Donghun Lee and Michael C. Constantinou, December 28, 2015.

MCEER-15-0008 "Seismic Isolation of Nuclear Power Plants using Elastomeric Bearings," by Manish Kumar, Andrew S. Whittaker and Michael C. Constantinou, December 29, 2015.

MCEER-16-0001 "Experimental, Numerical and Analytical Studies on the Seismic Response of Steel-Plate Concrete (SC) Composite Shear Walls," by Siamak Epackachi and Andrew S. Whittaker, June 15, 2016.

MCEER-16-0002 "Seismic Demand in Columns of Steel Frames," by Lisa Shrestha and Michel Bruneau, June 17, 2016.

MCEER-16-0003 "Development and Evaluation of Procedures for Analysis and Design of Buildings with Fluidic Self-Centering Systems" by Shoma Kitayama and Michael C. Constantinou, July 21, 2016.

MCEER-16-0004 "Real Time Control of Shake Tables for Nonlinear Hysteretic Systems," by Ki Pung Ryu and Andrei M. Reinhorn, October 22, 2016.

MCEER-16-0006 "Seismic Isolation of High Voltage Electrical Power Transformers," by Kostis Oikonomou, Michael C. Constantinou, Andrei M. Reinhorn and Leon Kemper, Jr., November 2, 2016.

MCEER-16-0007 "Open Space Damping System Theory and Experimental Validation," by Erkan Polat and Michael C. Constantinou, December 13, 2016.

MCEER-16-0008 "Seismic Response of Low Aspect Ratio Reinforced Concrete Walls for Buildings and Safety-Related Nuclear Applications," by Bismarck N. Luna and Andrew S. Whittaker.

MCEER-16-0009 "Buckling Restrained Braces Applications for Superstructure and Substructure Protection in Bridges," by Xiaone Wei and Michel Bruneau, December 28, 2016.

MCEER-16-0010 "Procedures and Results of Assessment of Seismic Performance of Seismically Isolated Electrical Transformers with Due Consideration for Vertical Isolation and Vertical Ground Motion Effects," by Shoma Kitayama, Michael C. Constantinou and Donghun Lee, December 31, 2016.

MCEER-17-0001 "Diagonal Tension Field Inclination Angle in Steel Plate Shear Walls," by Yushan Fu, Fangbo Wang and Michel Bruneau, February 10, 2017.

MCEER-17-0002 "Behavior of Steel Plate Shear Walls Subjected to Long Duration Earthquakes," by Ramla Qureshi and Michel Bruneau, September 1, 2017.

MCEER-17-0003 "Response of Steel-plate Concrete (SC) Wall Piers to Combined In-plane and Out-of-plane Seismic Loadings," by Brian Terranova, Andrew S. Whittaker, Siamak Epackachi and Nebojsa Orbovic, July 17, 2017.

MCEER-17-0004 "Design of Reinforced Concrete Panels for Wind-borne Missile Impact," by Brian Terranova, Andrew S. Whittaker and Len Schwer, July 18, 2017.

MCEER-17-0005 "A Simple Strategy for Dynamic Substructuring and its Application to Soil-Foundation-Structure Interaction," by Aikaterini Stefanaki and Metttupalayam V. Sivaselvan, December 15, 2017.

MCEER-17-0006 "Dynamics of Cable Structures: Modeling and Applications," by Nicholas D. Oliveto and Mettupalayam V. Sivaselvan, December 1, 2017.

MCEER-17-0007 "Development and Validation of a Combined Horizontal-Vertical Seismic Isolation System for High-Voltage-Power Transformers," by Donghun Lee and Michael C. Constantinou, November 3, 2017.

MCEER-18-0001 “Reduction of Seismic Acceleration Parameters for Temporary Bridge Design,” by Conor Stucki and Michel Bruneau, March 22, 2018.

MCEER-18-0002 “Seismic Response of Low Aspect Ratio Reinforced Concrete Walls,” by Bismarck N. Luna, Jonathan P. Rivera, Siamak Epackachi and Andrew S. Whittaker, April 21, 2018.

EARTHQUAKE ENGINEERING TO EXTREME EVENTS
University at Buffalo, The State University of New York
133A Ketter Hall ▪ Buffalo, New York 14260-4300
Phone: (716) 645-3391 ▪ Fax: (716) 645-3399
Email: *mceer@buffalo.edu* ▪ Web: ***http://mceer.buffalo.edu***
University at Buffalo *The State University of New York*

ISSN 1520-295X